

1485

GPO PRICE \$ _____

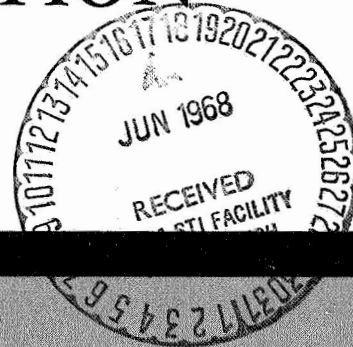
CFSTI PRICE(S) \$ _____

Hard copy (HC) 300

Microfiche (MF) .65

ff 653 July 65

PROTECTION AGAINST SPACE RADIATION



N 68-26128

N 68-261

FACILITY FORM 602

(ACCESSION NUMBER) 627

(PAGES) _____

(NASA CR OR TMX OR AD NUMBER) _____

(THRU) _____

(CODE) 29

(CATEGORY) _____



NASA SP-169

(ANS-SD-5)

PROTECTION AGAINST SPACE RADIATION

The proceedings of the Special Sessions on Protection Against Space Radiation, presented at the thirteenth annual meeting of the American Nuclear Society, San Diego, California, June 11-15, 1967

Edited by

ARTHUR REETZ, JR., AND KERAN O'BRIEN



Scientific and Technical Information Division
OFFICE OF TECHNOLOGY UTILIZATION
NATIONAL AERONAUTICS AND SPACE ADMINISTRATION
1968
Washington, D.C.

NATIONAL AERONAUTICS AND SPACE ADMINISTRATION

**For sale by the Clearinghouse for Federal Scientific and Technical Information
Springfield, Virginia 22151 - CFSTI price \$3.00**

FOREWORD

The Special Sessions on Protection Against Space Radiation were sponsored by the Shielding and Aerospace Divisions of the American Nuclear Society and were included in the 13th Annual Meeting of the American Nuclear Society in San Diego, California, June 11-15, 1967. The Sessions were held in response to requests of researchers in the field of space radiation shielding who felt the need for a symposium similar to previous meetings held at Gatlinburg, Tennessee in 1962 and 1964. So as to avoid adding to the already large number of national technical meetings, the Sessions were held in conjunction with a scheduled Society meeting rather than as a separate topical symposium as before. However, in contrast to the previous symposia, only the shielding aspects of the space radiation problem were emphasized. Introductory discussions dealing with the space radiation environment, radiobiology, and radiation effects on materials and components were limited to a single, comprehensive review paper in each area, whereas previously, complete half-day sessions were devoted to these topics.

Both invited and contributed papers related to the shielding of natural space radiation were given at San Diego. The four principal areas of interest discussed were: (1) Basic interaction and transport of space radiation in materials; (2) methods for space radiation shield penetration calculations; (3) spacecraft shield design, analysis and verification; and (4) advanced shielding concepts for spacecraft.

The proceedings of the San Diego Special Sessions are being published by NASA, in cooperation with the American Nuclear Society Shielding Division, so as to provide a wide dissemination of the excellent papers presented at the meeting. The alternate report number, ANS-SD-5, of the proceedings represents the fifth in a series of special radiation shielding reports prepared by the Shielding Division. The proceedings of the 1962 Symposium at Gatlinburg were published by the USAEC (TID-7652), while the proceedings of the 1964 Symposium were published by NASA (SP-71).

In reviewing these proceedings, it will be obvious that the problems in space radiation shielding are not completely solved. However, a great deal of progress has been made since the 1962 Symposium in Gatlinburg, especially in the acquisition of data with respect to basic interactions and in the development of transport calculation techniques. Relatively speaking, shielding technology is in good shape. At this time it appears that unknowns in the space radiation environment and in the effects of radiation on man remain the largest uncertainty in the problem of protection against space radiation.

Arthur Reetz, Jr.
NASA Headquarters
Washington, D.C.



CONTENTS

SESSION I

Chairman: J. Warren Keller

| | Page |
|--|-------|
| 1 SPACE RADIATION ENVIRONMENT (Invited) Jerry L. Modisette, Joseph W. Snyder, Richard D. Juday | 1 ✓ |
| 2 CURRENT STATUS OF SPACE RADIATION EFFECTS ON MATERIALS AND COMPONENTS (Invited) David L. Dye | 19 ✓ |
| 3 STATUS OF RESEARCH TO DETERMINE RADIOBIOLOGICAL RESPONSE CRITERIA FOR SPACE MISSIONS (Invited) Edwin R. Ballinger | 33 ✓ |
| 4 THE LET SPECTRUM OF GALACTIC RADIATION EXPOSURE IN SPACE AND ITS TRANSITION IN SHIELD OR TISSUE Hermann J. Schaefer | 43 ✓ |
| 5 SPECTRAL CHARACTERISTICS AND DOSE CALCULATIONS FOR THE PRIMARY AND SECONDARY PARTICLES THAT RESULT FROM THE INTERACTION OF THE SOLAR AND GALACTIC COSMIC-RAYS WITH ALUMINUM SHIELDS Stanley B. Curtis, M. C. Wilkinson | 59 ✓ |
| 6 A CORRELATION OF DOSIMETRIC MEASUREMENTS WITH CHARGED PARTICLE ENVIRONMENT OF THE INNER VAN ALLEN BELT Allen L. Thede, George E. Radke | 75 ✓ |
| 7 THE PLASMA RADIATION SHIELD: CONCEPT, AND APPLICATIONS TO SPACE VEHICLES Richard H. Levy, Francis W. French | 93 ✓ |
| 8 THE QUASI-HOLLOW CONDUCTOR MAGNET AS A SPACE SHIELD AGAINST ELECTRONS S. H. Levine, R. Lepper | 189 ✓ |

SESSION II

Chairman: Jim H. Johnson

| | Page |
|---|-------|
| 9 ELECTRON BREMSSTRAHLUNG CROSS-SECTION MEASUREMENTS (Invited) D. H. Rester, W. E. Dance | 215 ✓ |
| 10 AN EXPERIMENTAL STUDY OF THE TRANSPORT OF ELECTRONS THROUGH THICK TARGETS (Invited) C. P. Jupiter, J. A. Lonergan, G. Merkel | 249 ✓ |
| 11 PENETRATION OF ELECTRONS AND ASSOCIATED BREMSSTRAHLUNG THROUGH ALUMINUM TARGETS (Invited) M. J. Berger, S. M. Seltzer | 285 ✓ |
| 12 THE THEORY OF THE TRANSPORT OF RELATIVISTIC ELECTRONS (Invited) Richard Scalettar | 323 ✓ |
| 13 ANGULAR DISTRIBUTIONS OF THICK TARGET BREMSSTRAHLUNG COMPARED WITH EXPERIMENT W. Wayne Scott | 339 ✓ |
| 14 ELECTRON DISTRIBUTION IN A SLOWING-DOWN MEDIUM Dong H. Nguyen, Lawrence M. Grossman | 359 ✓ |
| 15 A PARAMETRIC TECHNIQUE OF COMPUTING PRIMARY ELECTRON DOSE Alva C. Hardy, Manuel D. Lopez, Timothy T. White | 391 ✓ |

SESSION III

Chairman: William A. Anders

| | |
|--|-------|
| 16 HIGH-ENERGY NUCLEON TRANSPORT (Invited) R. G. Alsmiller, Jr. | 403 ✓ |
| 17 NUCLEAR REACTION CROSS SECTIONS FOR SPACECRAFT SHIELD DESIGN (Invited) R. W. Peelle | 429 ✓ |

| | Page |
|--|-------|
| 18 SECONDARY-DOSE EQUIVALENT MODEL AND COMPARISON OF 160-MEV PROTON-INDUCED NEUTRON AND PROTON DOSE WITH A COMPREHENSIVE EXPERIMENT Bobby Liley, Arthur G. Duneer, Jr. | 463 ✓ |
| 19 ANALYTIC REPRESENTATION OF NONELASTIC CROSS SECTIONS AND PARTICLE-EMISSION SPECTRA FROM NUCLEON-NUCLEUS COLLISIONS IN THE ENERGY RANGE 25 TO 400 MEV R. G. Alsmiller, Jr., M. Leimdorfer, J. Barish | 495 ✓ |
| 20 PLANE ISOTROPIC BUILDUP FACTORS FOR BREMSSTRAHLUNG CALCULATIONS M. O. Burrell, J. W. Watts, Jr. | 517 ✓ |
| 21 THE CALCULATION OF ELECTRON AND BREMSSTRAHLUNG DOSE RATES Martin O. Burrell, J. J. Wright, John W. Watts, Jr. | 529 ✓ |
| 22 EVALUATION OF GAMMA PROBE SHIELDING VERIFICATION FOR THE GEMINI AND APOLLO VEHICLES Alva C. Hardy, Joseph W. Snyder | 539 ✓ |
| 23 RADIATION DOSIMETRY FOR MANNED SPACE FLIGHT Robert G. Richmond, William G. Davis, Joseph C. Lill, Carlos S. Warren | 555 ✓ |
| 24 A COMPARISON OF MEASURED TO CALCULATED DOSE FOR THE GEMINI-IV AND VI SPACE FLIGHTS AND WL-304 SPACE PROBE Robert L. Stovall, Roger S. Case, Jr., Joseph F. Janni, Marion F. Schneider | 581 ✓ |

SHIELDING DIVISION INFORMAL SESSION

Chairman: J. R. Beyster

| | |
|--|-------|
| 25 THE APPLICATION OF SPACE SHIELDING TECHNOLOGY TO SPACECRAFT PROBLEMS (Invited) Russell D. Shelton | 611 ✓ |
|--|-------|

SPACE RADIATION ENVIRONMENT

By Jerry L. Modisette, Joseph W. Snyder, and Richard D. Juday

NASA Manned Spacecraft Center

Houston, Texas

Consideration of ionizing radiation in space as a potential hazard to space exploration began with the discovery of the Van Allen belts in 1958 and with the recognition of polar cap absorption events, neutron monitor enhancements, solar radio bursts, magnetic storms, and other disturbances as part of a complex phenomenon associated with solar flare particle events. Several years of data-gathering and analysis have seen the evolution of the spacecraft designer's concept of the radiation problem from an almost insurmountable obstacle to a rather routine task; now the major difficulty is the assignment of the proper amount of resources to the problem so that the risk due to radiation is commensurate with other risks requiring similar resources, in the form of money, spacecraft weight, or operational constraints.

The change in outlook has been partly because of the better understanding of the nature and magnitude of space radiation. Early estimates of the number of particles in a solar flare particle event, for example, were as much as two orders of magnitude greater than currently accepted values. Some of the change is also because the individuals responsible for radiation environment engineering now have more experience in the field and have largely abandoned an ultra-conservative approach based on their uncertainties in favor of more exact definitions of the problems.

The radiation environment in space consists of cosmic rays, Van Allen radiation, solar flare particle events, and whatever radiation man generates or takes with him. The description of the radiation environment requires a knowledge of the particle flux as a function of energy, species, location in space, and time. For cosmic rays all of these relations are well known. For Van Allen radiation the spatial variations are complex, and for the outer belts temporal variations become important. The essence of the solar flare particle events is their temporal variation, taking the form of irregular occurrence and wide variation in the particle flux from event to event.

This paper will attempt to describe current practices in specifying space radiation environments for engineering purposes, and to discuss areas of current activity or controversy.

Cosmic Rays

The term "cosmic rays" refers to particles originating outside the solar system, having energies up to perhaps 10^{19} electron volts. Solar flare particles are sometimes referred to as solar cosmic rays, but such terminology is not generally accepted.

The flux of cosmic rays ranges from about $2/\text{cm}^2\text{-sec}$ at solar maximum to about $4/\text{cm}^2\text{-sec}$ at solar minimum above 40 MeV. At solar maximum most of the particles are above 1 BeV as the solar wind and interplanetary magnetic field excludes lower energy particles from the solar system. From the shape of the cosmic ray spectrum (Figure 1), there appears to be some attenuation of particles below about 5 BeV at all times during the sunspot cycle, leading to an interesting question of what the flux of low energy particles will be as one goes away from the sun.

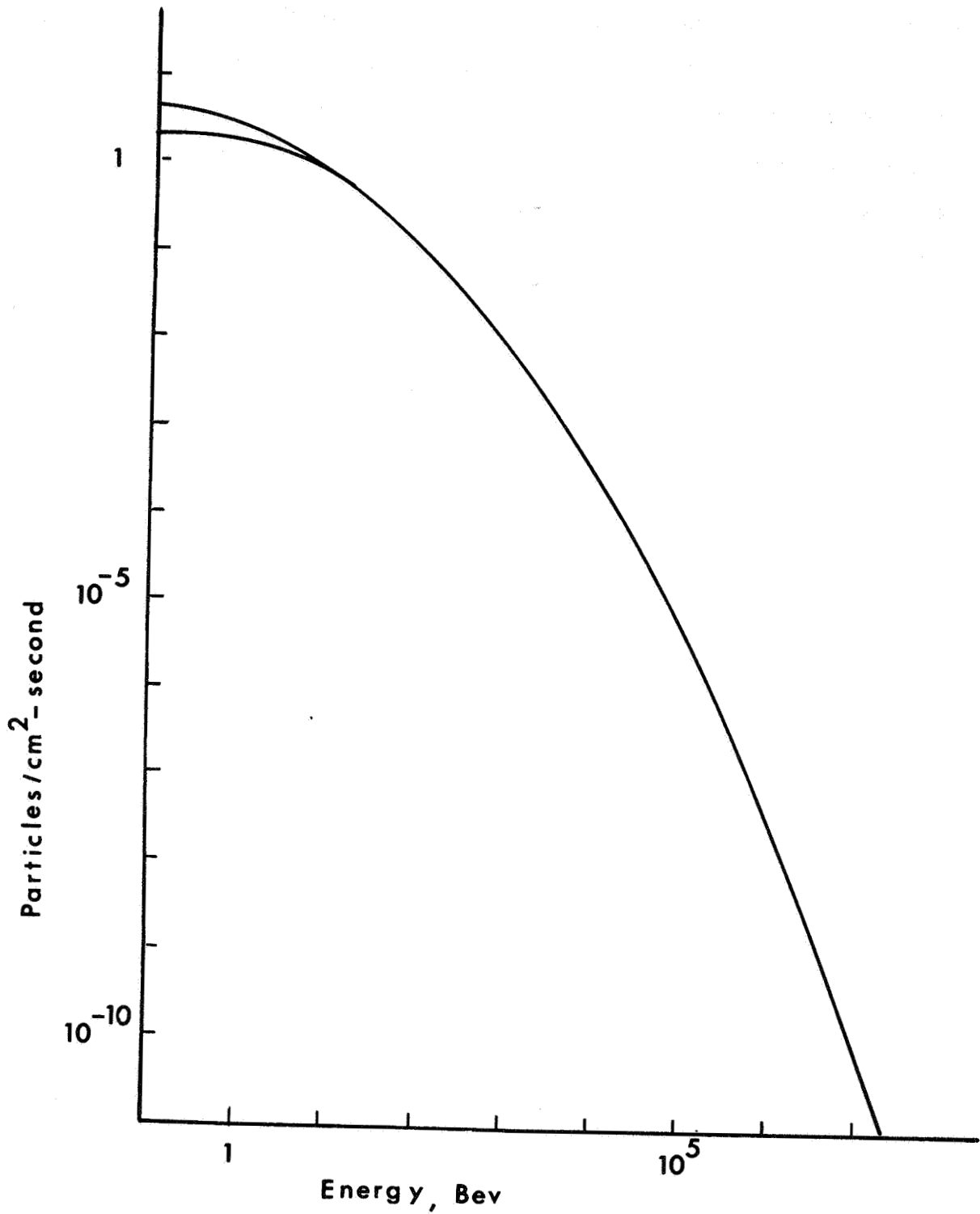


Fig. 1 Cosmic ray spectra

The dose produced by cosmic rays is rather low; 4 minimum ionizing protons per cm² per second produce about 0.01 rads per day. However, the composition leads to some interesting results from the dose due to heavier ions. The following table shows the fraction of various nuclei in the cosmic ray flux. Also shown is the relative dose due to the various species if the energy spectrum per nucleon is the same and the nuclei are completely stripped ($\frac{dE}{dx} \propto z^2$).

| <u>Element</u> | <u>Relative Abundance</u> | <u>Relative Dose</u> |
|---|---------------------------|----------------------|
| ${}^1_1\text{H}$ | 0.86 | 0.86 |
| ${}^2_2\text{He}$ | 0.12 | 0.48 |
| ${}^3_3\text{Li}$ | 0.0008 | 0.0072 |
| ${}^4_4\text{Be}$ ${}^5_5\text{B}$ | 0.002 | 0.032 |
| ${}^6_6\text{C}$ | 0.004 | 0.144 |
| ${}^7_7\text{N}$ | 0.002 | 0.098 |
| ${}^8_8\text{O}$ | 0.003 | 0.192 |
| ${}^9_9\text{F}$ | 0.0002 | 0.0162 |
| ${}^{10}_{10}\text{Ne}$ | 0.0008 | 0.0800 |
| ${}^{11}_{11}\text{Na}$ | 0.0005 | 0.0605 |
| ${}^{12}_{12}\text{Mg}$ | 0.0008 | 0.1152 |
| ${}^{13}_{13}\text{Al}$ | 0.0002 | 0.0338 |
| ${}^{14}_{14}\text{Si}$ | 0.0003 | 0.0588 |
| ${}^{15}_{15}\text{P}$ - ${}^{21}_{21}\text{Sc}$ | 0.0003 | 0.0972 |
| ${}^{22}_{22}\text{Ti}$ - ${}^{28}_{28}\text{Ni}$ | 0.0008 | 0.5000 |

The relative abundances are after Biswas & Fichtel [1964]. It is apparent that a substantial part of the dose comes from heavy nuclei having $\frac{dE}{dx}$ orders of magnitude greater than that of a minimum ionizing proton. Therefore the relative biological effectiveness should be greater than unity. For long duration missions, cosmic rays may require more consideration.

Solar Flare Particle Events

In order to predict the effects of solar proton events upon a particular mission, one must predict the number of events that will be encountered, their fluxes, and their spectra. No way has been found to know any of these parameters far enough in advance to help spacecraft design or mission planners, but several statistical approaches have been used to extrapolate the data on past events into the future. Four of these approaches will be discussed here.

Modisette et al. [1965] plotted proton flux > 30 MeV for various mission lengths during the maximum of the 19th solar cycle (1956-1961) and found a close fit to a log-normal probability distribution (Figure 2). These distributions combined the number of events encountered during a mission and the flux per event into one parameter. By assuming an average spectrum, they were then able to predict dose at various probability levels.

Snyder [1967] plotted dose per event and also found log-normal probability fits (Figure 3). These distributions combined the flux and spectra into one parameter. By assuming a Binomial probability distribution for event frequency, he was also able to predict dose at various probability levels (Figure 4).

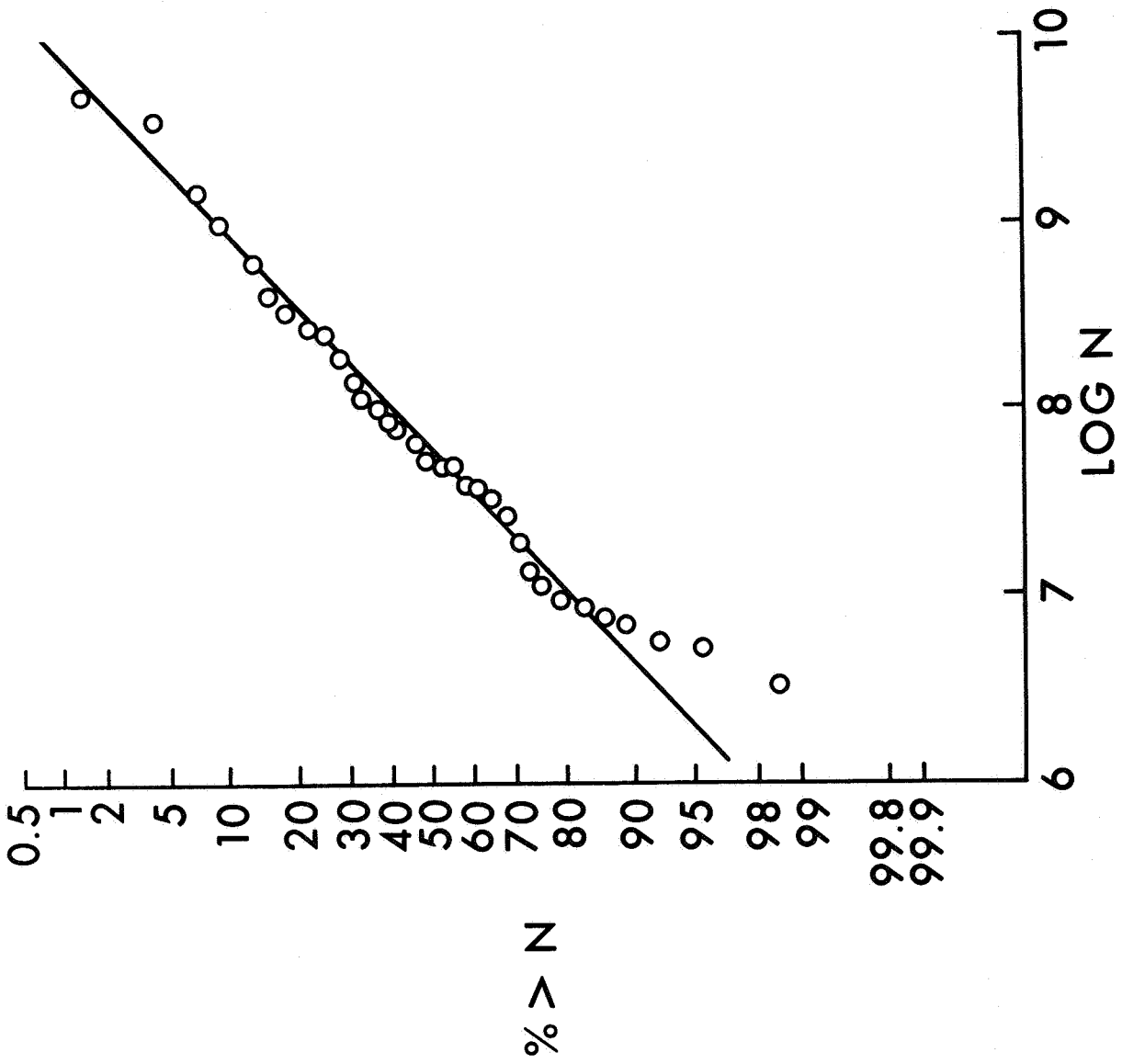


Fig. 2 Distribution of proton fluxes two week mission

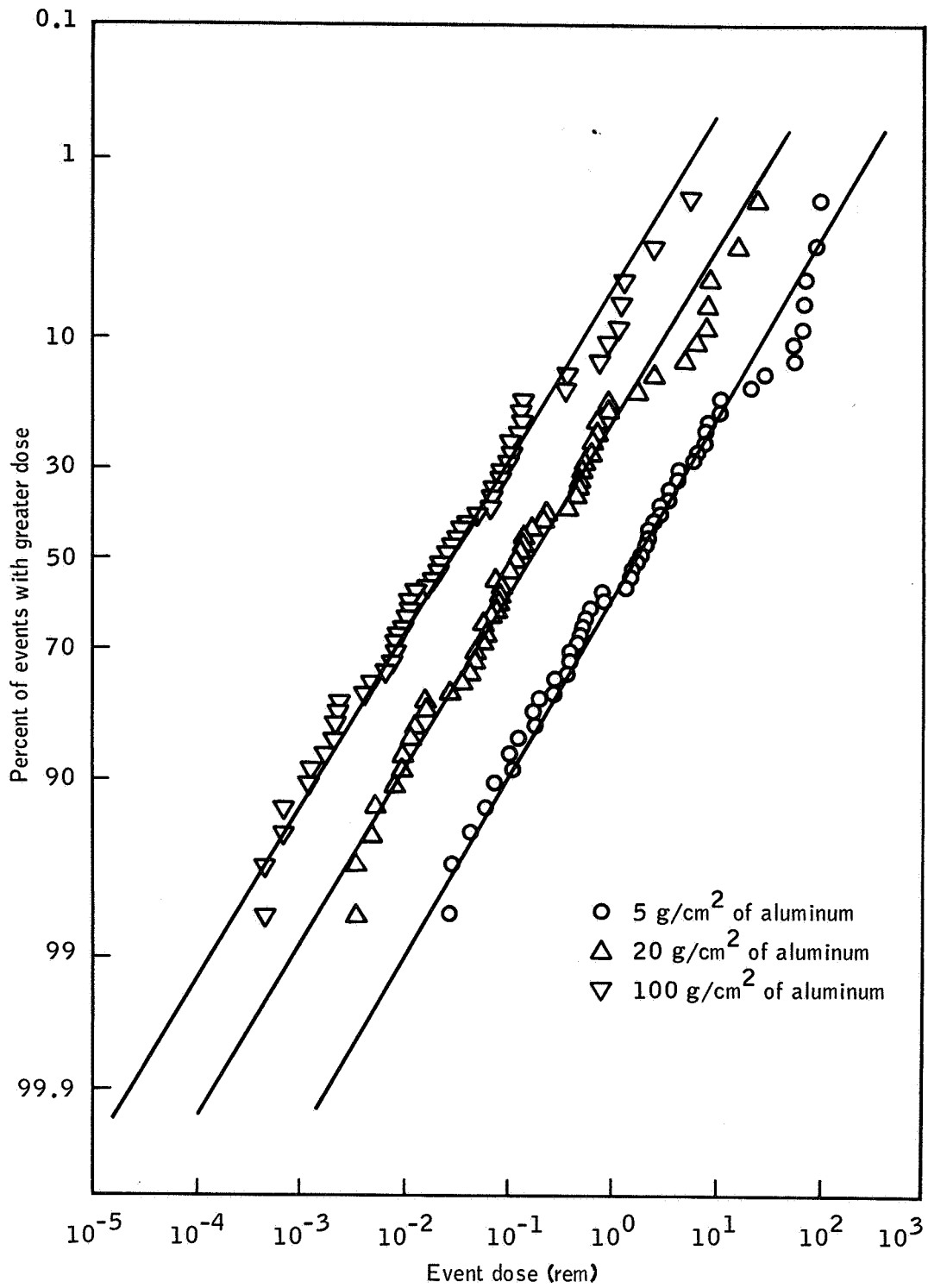


Fig. 3 Dose-per-event probability distributions. Each point represents a proton event from the 19th solar cycle.

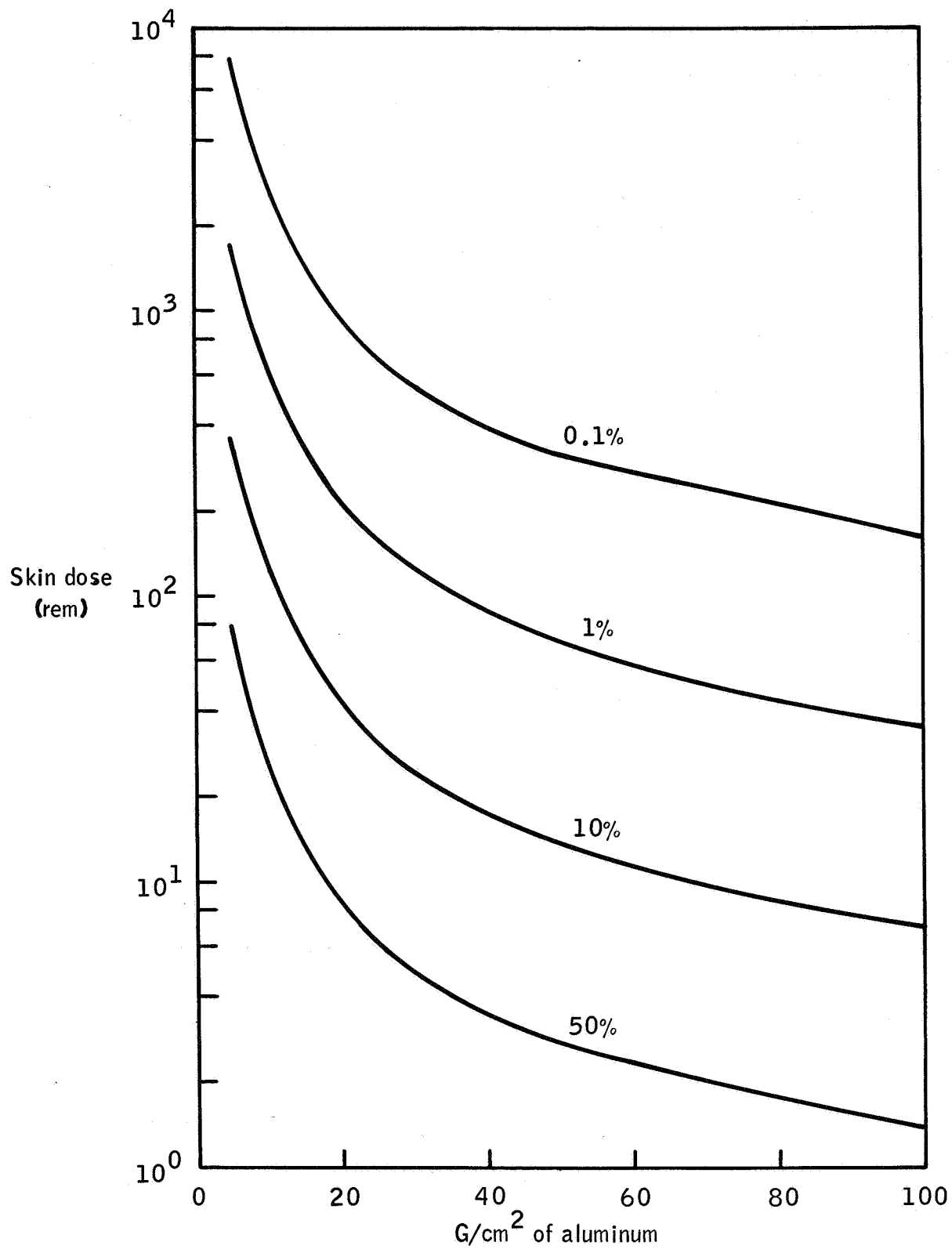


Fig. 4 Dose vs shield thickness for one-year missions at solar maximum. Each curve is labeled with the percentage of missions expected to exceed the doses on that curve.

Both of these methods produced very close to the same results in terms of dose, even though they use different statistical approaches.

Hilberg [1966] used a model event somewhat larger than any seen in the 19th solar cycle for the flux and spectra per event. He used a Poisson probability for the occurrence of large events only, arguing that the smaller events produce only insignificant doses. His results are much lower than the other two approaches.

French [1966] shortcuts all probability distributions and looks for a worst case in the 19th solar cycle for a time period equal to the mission length. When the frequency difference is accounted for, his results are comparable to Hilberg's.

The reason for the difference in results between the first two methods and the last two is simple. The first two approaches assign a low, but finite, probability for encountering an event with a flux much higher than any previously observed; the last two approaches have an upper limit on event flux. For longer missions the one very large event dominates the low probability end of the dose per mission curves, i.e., the probability of getting one event of 200 rad becomes larger than the probability of getting 5 events of 40 rad.

The question of which approach is correct depends on whether there is any limit to the size of a solar flare particle event. If one considers probability levels of, say, 1%, and mission lengths of one year, then one is necessarily

considering the largest event in 100 years. The data on solar flare particle events only covers one sunspot cycle. All of the above analyses involve some assumption about how to extrapolate the distribution of events from one sunspot cycle to cover a longer period. Modisette et al. and Snyder assume the log-normal distributions observed to hold for the range of data available can be extrapolated to lower probabilities and longer missions; Hilberg and French assume the current data to be representative of the largest events which can occur. There is no clear technical basis for a choice at this time, and the situation will not improve very rapidly. Another ten years of observation will double the current data, and will take us to the 5% level for one year missions. The decision, then, becomes one of the degree of conservatism to be adopted, in the light of the cost of assuming a severe environment.

Van Allen Radiation

One of the sources of radiation in manned space flight is high-energy charged particles that have, by mechanisms as yet not entirely explained, become "trapped" in the earth's magnetic field. A trapped particle is one that is constrained to a limited region of space by the magnetic field. It exhibits three cyclic motions--a cyclotron-type circular motion about what is called its guiding center, a bouncing of the guiding center back and forth approximately along a field line between northern and southern points of equal magnetic field strength, and a drift in longitude approximately on a surface of revolution of the magnetic field line about the magnetic axis. A multitude of particles describing these motions form the belt of trapped radiation.

A detector sensitive to "penetrating" radiation will see the trapped radiation separate into two belts. The penetrating components of the inner belt are protons and electrons; of the outer belt, electrons. The inner zone electrons have an appreciable, but quantitatively unknown, fraction of their origin in the beta-decay of fission fragments from high-altitude nuclear explosions. Like the electrons, the inner zone protons show a high degree of time stability. This stability lends itself well to orbital dose integration; one can quite well assume that a dose environment calculated from particle measurements will show the same time stability as the particles.

The outer zone is quite another matter. The electron population is quite sensitive to geomagnetic disturbances, and a number of different behavior patterns have been noted. The problem of a dose environment must be handled statistically, with points separated temporally by more than a few hours treated as independent samples.

There has recently been much interest in the synchronous region (i.e., the locus of positions at which a satellite will, in its orbit, remain fixed in geographic coordinates). Sufficient data have been recorded in that general region (about 22,000 miles altitude in the equatorial plane) to make statistical descriptions of the particle environment [Vette and Lucero, 1967]. The vast majority of the penetrating particles in the synchronous region are electrons. These electrons show a degree of time-instability entirely unlike the stable inner zone of penetrating radiation, which is comprised mostly of protons, with the penetrating electron component for the most part having been artificially injected. The outer zone is then

suitable for statistical description, with points separated by more than a few hours treated as statistically independent. Juday [1967] has converted the statistical electron descriptions into statistical dose descriptions. The manner in which the conversion was made is described here.

The dose rate received behind a shield is, neglecting bremsstrahlung, dependent only on those electrons that can negotiate the shield with some energy remaining; i.e., those with initial energies above the cutoff for the particular range presented by the shield. The specification of the external flux of electrons above the cutoff energy is not all the problem, however, as the dose given by the penetrating electrons is a function of their remaining energy. Even for monoenergetic external electrons, this is not a simple matter, since electrons tend to straggle in energy and spread in angular distribution. This is due to the high ratio of charge to mass for electrons; individual collisions have a wider range of effect on an electron than, say, on a proton.

Thus, given a shield and a flux of electrons above cutoff, the dose rate behind the shield is a function of the flux and how the flux is distributed in energy.

It happens that the energy distributions of electrons in the synchronous region are fit well by exponentials in energy, characterized by their e-folding energies E_0 . Second, the statistical distributions are near log-normal in E_0 . Third, the fluxes of electrons having energies above, say, 1 MeV are likewise log-normal. Fourth, scatter plots of E_0 versus flux show no correlation, so that spectrum and flux are independent parameters for the particle distribution.

The procedure for achieving the distribution of dose rates is schematically illustrated in Figures 5 and 6. In Figure 5, the distribution of E_0 is crossed with the functions giving dose per electron as a function of E_0 . (The latter curve is achieved by the integration of such curves as in Figure 7, which is a direct, point-for-point multiplication of an electron spectrum with dose-per-electron-as-a-function-of-energy curves for various shieldings.) The result in Figure 5 is the distribution of dose per single electron. This being a function solely of spectrum, the situation is as yet independent of flux, as mentioned earlier. Now the two distributions that are to be sampled independently are that of flux of electrons above cutoff energy and that of dose per single electron. That the final dose rate distribution is not so simply achieved as by a point-for-point multiplication of two curves may be seen from the consideration that a medium dose rate can come from large dose per electron and small flux, medium dose per electron and medium flux, etc. Thus, the crossing of the two curves in Figure 6 is handled by independently sampling the two distributions, taking the product of the two samples, and sorting the products into a distribution as indicated by the final part of Figure 6. This distribution of dose rate will be representative of the input particle environment.

Concluding Remarks

The radiation in space due to cosmic rays, solar flare particle events, and Van Allen radiation has been discussed, with emphasis on some of the active areas of research. The general problem of radiation in space appears to be

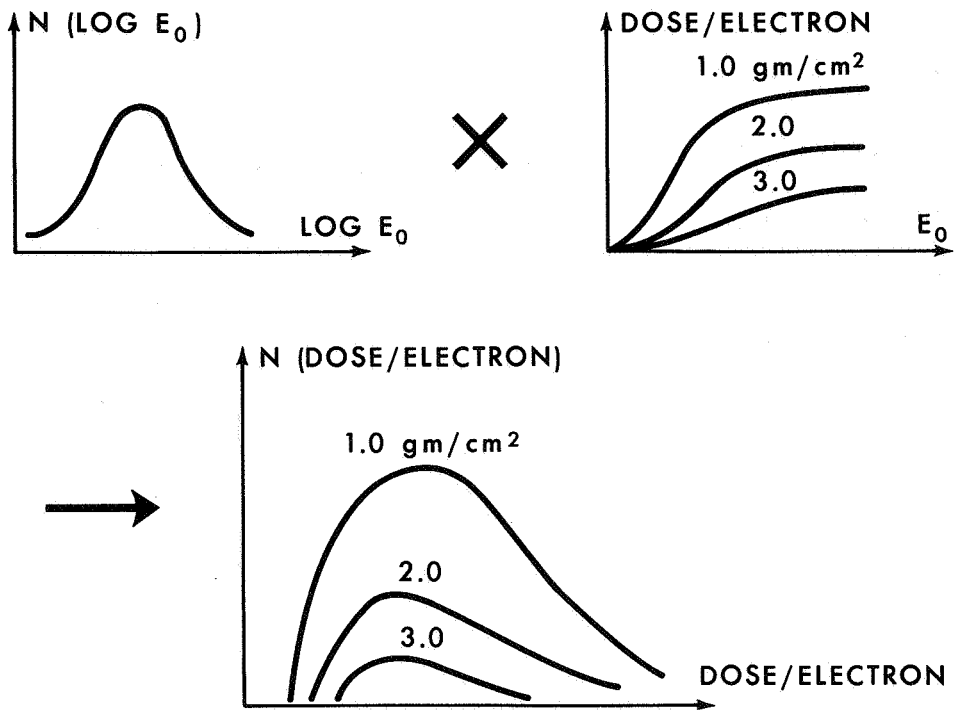


Fig. 5 Distribution of dose with incident electron energy for $E_0 = 0.2$ MeV, various shield thickness

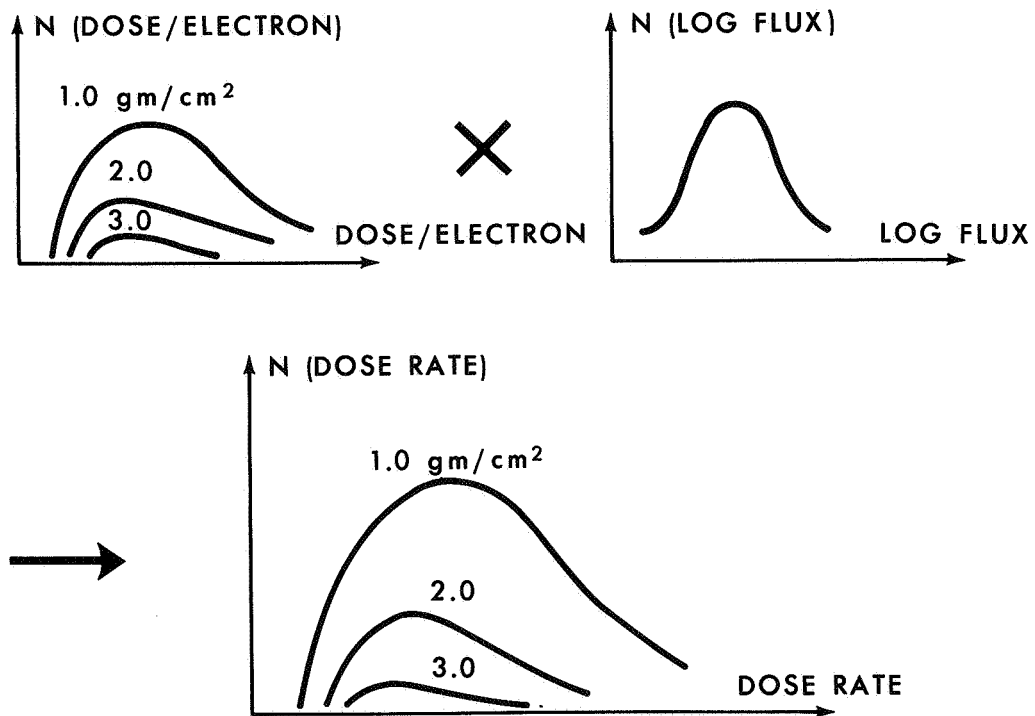


Fig. 6 Distribution of dose with incident electron energy for $E_0 = 0.2$ MeV, various shield thickness

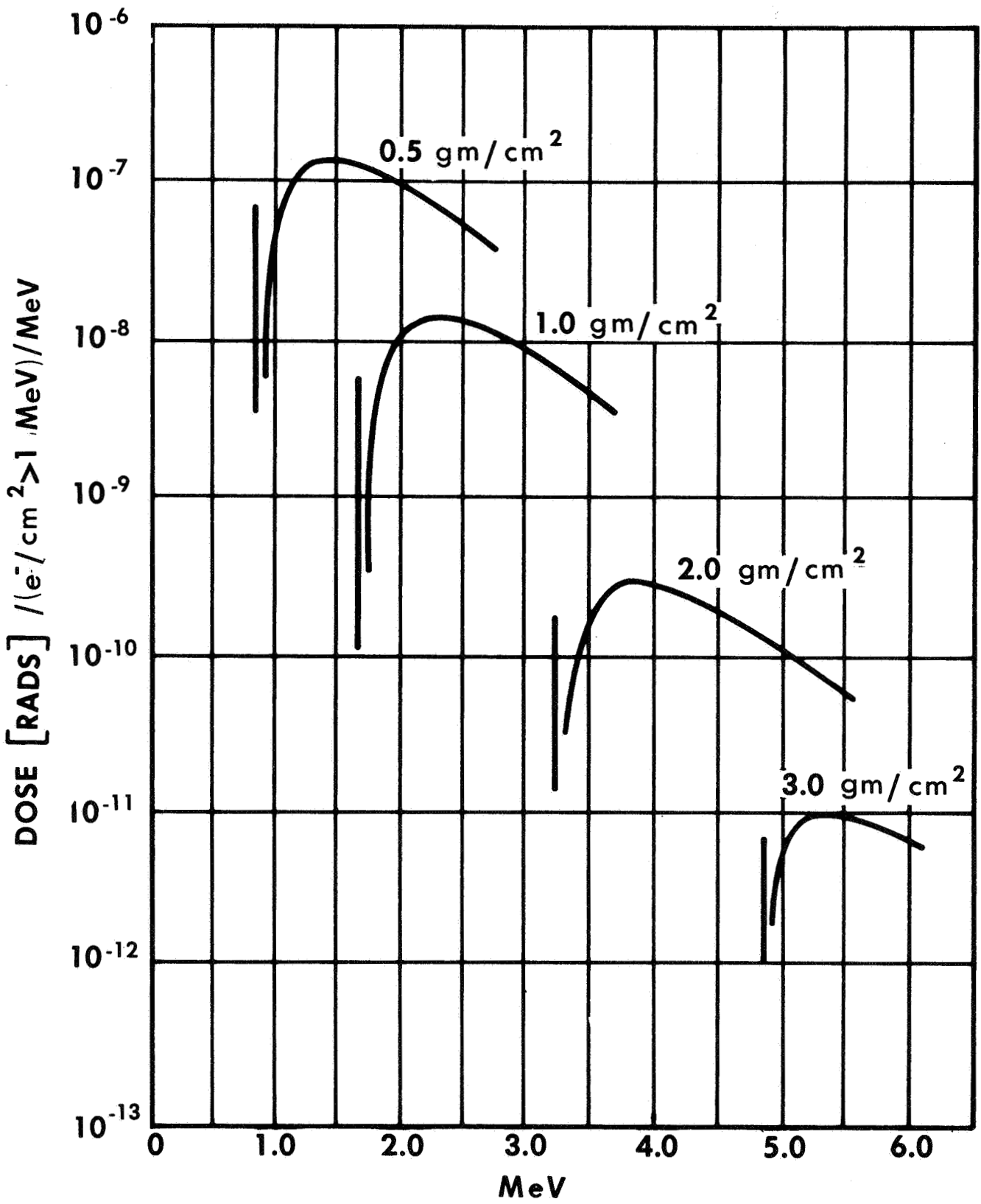


Fig. 7 Energy - distribution of dose-per-electron for exponential spectral parameter of 0.5 MeV

tractable, with most current questions involving the formulation of engineering design approaches which provide the right amount of protection in the light of competing requirements for resources.

One area not covered, but important in an overall solution to the radiation problem in space, is that of operational means of dose reduction, such as moving the crew into a protected region of the spacecraft. Such an approach is currently used for some missions, and requires real time environment analysis on the same level as the design environment analysis discussed here.

References

Biswas, S. and C. E. Fichtel, 1964, "Nuclear Composition and Rigidity Spectra of Solar Cosmic Rays", Astrophys. J., 139, 941-50.

French, F. W., 1966, "Radiation Shielding of Manned Mars Vehicles", J. Spacecraft & Rockets 3, 1544-1546.

Hilberg, R. H., 1966, Private Communication.

Juday, R. D., 1967, "A Statistical Dose Environment at Synchronous Altitudes", In Preparation.

Modisette, J. L., T. M. Vinson, and A. C. Hardy, 1965, "Model Solar Proton Environments for Manned Spacecraft Design", NASA TN D-2746.

Snyder, Joseph W., 1967, "Radiation Hazard to Man from Solar Proton Events", J. Spacecraft & Rockets 4 , 826-828.

Vette, James I., A. B. Lucero, and J. A. Wright, "Models of the Trapped Radiation Environment", NASA SP 3024.



CURRENT STATUS OF SPACE RADIATION EFFECTS ON
MATERIALS AND COMPONENTS

David L. Dye

Missile and Information Systems Division
The Boeing Company
Seattle, Washington

The purpose of this paper is to present some of the space radiation effects data within the context of the physical phenomena which give rise to these effects. Thus it is necessary to discuss the space radiation environments and their basic physical interactions in materials. Only on the basis of good radiation physics can good, i. e., interpretable, experiments be designed to study radiation effects on spacecraft materials and components.

ENVIRONMENT SUMMARY

Only a brief summary of space radiation environment is given here. Much more exists in the literature (Ref. 1 has an extensive bibliography).

The geomagnetically trapped proton flux around the earth has an inner region of high energy and an outer region of low-energy protons. Experimental and theoretical studies of the trapped proton integral energy spectra for these two regions indicate that the flux is $>10^8$ p/cm²-sec at low energy (≤ 100 kev), and much lower at higher energies (>10 Mev). Similarly the natural trapped electron flux appears approximately in two belts, the inner low flux ($\leq 10^4$ cm⁻² sec⁻¹) high energy (>1.6 Mev) region, and the outer higher flux ($\sim 10^8$ cm⁻² sec⁻¹) lower energy (<1 Mev) region, extending out as far as nine or ten earth radii.

An important fact to bear in mind concerning space electron fluxes is their extreme variability with magnetic storms, solar plasma events, and their enhancement from high-altitude nuclear weapon detonations. Some of these variations amount to a factor of 10.

Solar flare event protons have been extensively studied, and the subject is out of our scope here (Ref. 2). However, the incidence of these particles has to be seen in terms of probability of exposure to a given fluence of specified energy spectrum during a period (Ref. 3). For a 230-day Earth-Mars mission the exposure to protons of energies > specified values are given in Table 1. Note the fluence values, for these levels will be referred to in the later discussion of effects.

In interplanetary space there exists the "solar wind" or low-energy particle plasma streaming out from the sun. The proton flux, at the earth's orbit, is about 10^8 p/cm²-sec, and their energies are of the order of a few kev. These particles are responsible for much of the damage to exposed (exterior) materials on spacecraft, since they are continually bombarding during the mission in space.

The solar electromagnetic radiation is still another environmental factor that can damage material surfaces. The ultraviolet (UV) is especially important, since these photons can ionize.

The obvious environmental parameters of pressure (or vacuum), specifically partial pressures of specific reactant gases such as oxygen, water vapor, hydrogen, nitrogen, have been too often neglected in past laboratory studies due to difficulties in simulation and instrumentation. Also the temperature of an exposed or irradiated material influences the effect. The need for control and understanding of these environments will be discussed later.

RADIATION INTERACTIONS

It is the energy deposited by the traversing radiation — particles or photons, or secondaries — that produces effects. The principal interaction mechanisms for effects discussed here are (1) ionization and (2) atomic displacements. The secondary particles mediating the energy transfer in these interactions may be electrons or free radicals.

Table 1. Probability of Accumulating Proton Fluences in a 230-Day Mars Mission*

| Fluence $E > E_0 \rightarrow$ ↓ Energy, E_0 | Protons/cm ² | | | |
|--|-------------------------|-----------------|-----------------|------------------|
| | 10 ⁷ | 10 ⁸ | 10 ⁹ | 10 ¹⁰ |
| 1 Mev | 0.92 | 0.84 | 0.70 | 0.32 |
| 3 Mev | 0.91 | 0.83 | 0.66 | 0.24 |
| 10 Mev | 0.90 | 0.80 | 0.55 | 0.09 |
| 30 Mev | 0.87 | 0.74 | 0.25 | <0.01 |
| 100 Mev | 0.80 | 0.44 | <0.01 | <<0.01 |

*Based on Solar Cycle 19 Data (see Refs. 1 and 2).

References 4 and 5 present range-energy data for various materials for protons and electrons, respectively. There is uncertainty in the range-energy data for protons below 100 keV, and the form of the curves differs markedly at low energy from the power law form due to straggling and other low-energy processes. These data are useful in determining penetration depths into materials and components¹ different damage mechanisms often have different energy dependences due to different dose deposition patterns and depths. Energy is useful as a probing tool to elicit specific damage mechanisms (Refs. 6 and 7).

The low-energy (few keV) particle ranges have submicron values, of the same order as the UV penetration in materials. The low-energy electrons and UV photons deposit energy by ionization processes, sometimes forming free radicals that can produce further chemical reactions. The heavy particles, protons and alphas, and some of the high-energy electrons cause displacements of the lattice atoms in solids, creating both ionizing recoils, and also new electron trapping centers in the material. These new energy levels produce changes in optical absorption properties and in minority carrier lifetime in semiconductors.

An important feature of radiation dose is the linear energy transfer (LET), or dE/dx , or rate of energy loss along the particle tracks. Some chemical degradation mechanisms depend significantly upon LET, which in turn depends inversely on particle energy. The dependence of radiation effects on LET, on total dose, on dose rate, or on particle energy is often a useful tool for studying basic effects mechanisms.

EFFECTS ON MATERIALS

Reflective Surfaces

Vapor-deposited aluminum seriously degrades, forming small ($<1 \mu$ size) blisters after irradiation by 10^{16} low-energy protons/cm² (keV range). The blisters seem to be due to gas evolution under the layer or in the substrate. The worst degradation of reflectance is in the UV rather than in the visible region. A

proprietary (Boeing-developed) barrier layer anodic coating of aluminum gives about a factor of 10 increased resistance, so that 10^{17} 8-kev protons/cm² cause an increase in solar absorptance from 0.12 to 0.23 in this barrier layer anodic coating.

Other reflecting materials tested include SiO-coated and chromium-deposited nickel, and Si₂O₃, SiO, and aluminum layers on sprayed epoxy bases. Using low-energy protons, it was determined that the most significant damage occurs in the SiO layer on the substrate. Lower temperatures inhibit damage, although there is a delayed blistering effect when aluminum-coated aluminum substrate surfaces are warmed up after $>5 \times 10^{16}$ p/cm² (Ref. 8).

Thermal Control Coatings

This is a specialized field all its own, which can only be touched here (Ref. 9). However, one relatively new result has far-reaching significance. Several working groups have recently developed instrumentation by which optical measurements can be made within the irradiation chamber under vacuum, and the uniformly reported result is that measurements made in air afterwards are quite different (Refs. 10 and 11).

Table 2 shows the decrease in reflectance after 50-kev electron irradiations, as measured in vacuum, at 22°C, for a ZnO methyl silicone sample, and the "annealing" of the effect with exposure to air. Note the changes and the annealing in both visible and infrared spectral reflectance. A previous study showed that for these electrons there was no rate effect between 10^{10} and 10^{13} electrons/cm²-sec. The annealing is not yet well understood, although it may be due to oxygen or water vapor. It is observed for many common coatings, and for UV irradiation as well as particles. Also the IR and visible region appear to exhibit different annealing mechanisms.

The equipment with which these measurements were (and are being) made has a temperature-controlled sample exposure wheel that can position a sample array for irradiation by both UV and particles, then can position the samples under an integrating sphere, the sensing head of a DK-2 spectrophotometer. The technical

Table 2. Electron Irradiation-Induced Percentage Loss of Reflectance ZNO-Methyl Silicone
as a Function of Time in Air Before Measurement

| Wavelength (μ) | Visible | | | | | Infrared | | | | | | |
|----------------------|---------|------|-----|-----|-----|----------|-----|-----|-----|--|--|--|
| | 0.42 | 0.55 | 1.0 | 1.2 | 1.5 | 1.7 | 1.9 | 2.1 | 2.3 | | | |
| 0 (in vacuo) | 31% | 20% | 26% | 36% | 53% | 44% | 57% | 55% | 30% | | | |
| 10 (in air) | -- | -- | 11 | 14 | 25 | 22 | 32 | 34 | 20 | | | |
| 57 (in air) | -- | -- | 9 | 11 | 17 | 16 | 23 | 26 | 16 | | | |
| 71 (in air) | 27 | 12 | -- | 7 | 12 | 12 | 17 | 20 | 12 | | | |
| 99 (in air) | -- | -- | 6 | 5 | 9 | 9 | 15 | 17 | 11 | | | |
| 168 (in air) | -- | -- | 4 | 5 | 9 | 9 | 15 | 17 | 11 | | | |
| 184** (in air) | 16 | 8 | 4 | 5 | 9 | 9 | 15 | 17 | 11 | | | |

*After 8×10^{15} 50 keV Electrons/cm² Irradiation.

**The Spectral Reflectance at this Time Approximates That Measured in Vacuo After 5×10^{13} Electrons/cm².

problems of this combined radiation effects test chamber have been solved, and the trouble involved is justified by the need for understanding of damage annealing, and for useful design data for spacecraft. In addition, it appears from recent data on combined UV-electron exposures that the separate effects of these two radiation environments may not be simply additive. In short, there are synergistic effects (Ref. 12). Obviously all old data, not taken in vacuo, or in combined environments becomes immediately suspect, at least until one understands the effects mechanisms well enough to interpret the data.

Photographic Films

A study of film fogging made during the selection of film for the Lunar Orbiter showed that radiation sensitivity generally correlates with grain size. It is possible to alter both film manufacturing and development processes to increase its tolerance to particulate radiation relative to light photons. Kodak SO 243 was chosen for the Lunar Orbiter mission because it could develop contrast after a 30-rad (film) dose, a much higher level than others tested.

A recent film study on 17 various films, shows also that film nuclear sensitivity correlates closely with light sensitivity, as one expects. The most sensitive film studied was Polaroid (10,000), which exhibited an ΔOD of 0.3 for 80 mrad; the least sensitive was Kodak High Definition Aerial film type 4404 (~90 rad) with Type SO 190 next (20 rad). SO 243 is intermediate in sensitivity between these two (Ref. 13).

EFFECTS ON ELECTRONIC COMPONENTS

Silicon Devices Generally

Two effects are to be distinguished, based on two distinct degradation mechanisms: permanent displacement damage to the bulk silicon lattice, and surface ionization-induced damage. In both cases, the damage affects the minority carrier lifetime by creating trapping levels. Heavy particles, and energetic electrons (primary or secondary) can cause the bulk displacements. The change in

lifetime, which affects transistor gain, diode switching time, and solar cell current, approximately follows the relation $\Delta(1/\tau) = k\phi$, where ϕ is the fluence, and each type of particle has a k value. That is, there is an equivalence between different radiation types for causing bulk displacement damage.

Transistors

Table 3 shows equivalences for silicon bulk damage as exhibited by the change of gain of transistors. It should be emphasized these equivalences apply only to bulk displacements, but for this type of damage they allow one to predict transistor gain changes due to exposure to different types of space radiation such as one actually encounters (Ref. 6).

As a function of proton energy bulk displacement production follows a $1/E$ law, theoretically. The particle energy, E , in this law is the energy of the particles actually impinging on the semiconductor material, not on the can. A typical transistor can absorb protons of energy less than about 15 Mev, and appears to distort the $1/E$ law for protons below 20 Mev. Can-off experiments (Ref. 6) show that the $1/E$ law is valid down to about 8 Mev, but for lower energies the damage is less than predicted, being about constant down to 1 Mev before falling off. This is probably due to proton absorption in the outer layers and the transistor itself, so that base region damage is lessened. In view of the large flux of low energy protons in space, the low energy behaviour of this silicon damage is worth noting. Low energy electrons are less effective in transferring energy to the silicon lattice so that below about 200 kev almost all the damage is due to ionization. At higher energies the damage would be expected to follow predictions of a theory of momentum and energy transfer to silicon atoms to produce displacements, with relativistic corrections where needed at very high energies. However, the energy dependent transistor damage data do not fit this theory well except for a small energy range. The damage observed is twice that of theory, suggesting that the defects generated may be divacancies rather than simple vacancy-interstitial defects.

Table 3. Particle-Type Displacement Equivalences, $\Delta(h_{FE}^{-1})$

| Particle Type and Energy | Alpha Particle (5 Mev) | Proton (1 Mev) | Neutron (Reactor Spectrum) | Electron (1 Mev) | Gamma Ray (Co60) |
|--------------------------------|------------------------|----------------------|----------------------------|-----------------------|--------------------|
| Alpha Particle (5 Mev) Can off | 1 | 3.5 | 1.4×10^2 | $*7 \times 10^3$ | 1.5×10^5 |
| Proton (1 Mev) Can off | 2.9×10^{-1} | 1 | 4×10^1 | $*2 \times 10^3$ | 4.3×10^4 |
| Neutron (Reactor) | 7.1×10^{-3} | 2.5×10^{-2} | 1 | $*5 \times 10^1$ | 1.1×10^3 |
| Electron (1 Mev) Can off | $*1.4 \times 10^{-4}$ | $*5 \times 10^{-4}$ | $*2.0 \times 10^{-2}$ | 1 | $*2.2 \times 10^1$ |
| Gamma Ray (Co60) | 6.7×10^{-6} | 2.3×10^{-5} | 9.1×10^{-4} | $*4.5 \times 10^{-2}$ | 1 |

*Transistor cans of 0.17 gm cm^{-2} .

Ionization effects due to both electrons and protons are also seen in the reduced gain of transistors, the increased leakage currents, and reduction of solar cell power. The mechanism seems to be production of long lived surface (and bulk) trapping centers, which can be annealed out at high temperatures. Transistor gain reduction is largest at the low emitter currents, indicating surface effects. For absorbed doses above 10^4 rad(Si), in some devices gain loss greater than X2 occurs, and allowance must be made for this gain loss in circuit design. At doses above about 10^6 rad(Si) the surface effect saturates, and for energetic particles the bulk effects then predominate. In contrast to the bulk damage, the surface, or "non-linear" component does not depend simply on transistor type or F_T .

The question of using Cobalt-60 as a source for qualifying transistors for spaceflight has been studied (Ref. 6). One would hope that the equivalences would allow one to plan a space mission in terms of an equivalent Co-60 irradiation, and then test the electronics. It runs out that Co-60 can simulate the nonlinear changes to I_{CBO} and gain, but one must expose to 10^8 rad(Si) to simulate proton displacement (bulk) damage with Co-60.

Diodes

Radiation-damaged diodes exhibit decreases in forward current output and in recovery time, and increases in reverse leakage current and in reverse breakdown voltage. It may not be easy for an engineer to relate change in inverse lifetime to what happens to his diode in space. For a typical power diode of normal lifetime ~ 1 μ sec, a 10^6 value of $\Delta(1/\tau)$ represents a factor of 2 change, and 10^7 represents a factor of 10 change. A faster switching diode is more radiation resistant. Thus a fluence 10^{12} to 10^{13} protons/cm² or 10^{14} to 10^{15} electrons/cm² of space radiation energies can produce noticeable increases in leakage current and decreases in recovery time or forward current. A (X10) lifetime change would increase the body resistance by a factor of 5 to 10, the leakage current by X10, and decrease the storage time X5.

Solar Cells

The radiation-induced change in lifetime in silicon produces a reduction in the short-circuit current of conventional p-on-n solar cells. In the past few years, lithium doping has been used in solar cells, resulting in increased radiation resistance to over 10^{15} electrons/cm² (1 Mev).

The lithium doping processes provide a new radiation damage center, to which unpaired lithium atoms in the bulk can diffuse. They interact there either to improve the carrier lifetime or to annihilate the damage center. These cells thus appear to be "self annealing" after radiation damage at normal temperatures. At high temperatures, they anneal as do conventional undoped cells.

Recent studies using various energies to probe cell parts have distinguished two damage mechanisms in both conventional and lithium diffusion cells (Ref. 7). Conventional damage, or bulk damage, occurs when particles cause defects in the cell interior of either p-on-n or n-on-p cells. This is the damage produced by penetrating particles (say ≥ 1 Mev protons or electrons). This damage produces a reduction in short-circuit current, and some loss in power; that is, the knee of the V-I curve comes in somewhat. This damage is only partly annealable, and needs high temperatures in conventional cells. It is more easily annealed in Li-doped cells.

Another type of damage is observed in cells when the bombarding particle is of low enough energy to penetrate only into the top layer or the junction. This may be called "surface damage", by analogy with the effects in transistors to be described. The characteristics of surface damage are a lowering of open circuit voltage (rather than short-circuit current) and of the knee of the curve. The V_{OC} change is mostly annealable, at room temperature, but not the power reduction. A study is underway to see how much of this effect is due to charge buildup in the oxide layer over the cell top, and to relate this surface damage to that observed in other semiconductors. Also, a study is underway to investigate means of annealing Li-doped cells in space from the hard space radiation.

SUMMARY AND CONCLUSION

There are still crucial questions being resolved in studies of radiation damage mechanisms in spacecraft materials and components. However, much data exists, and some of it is useful to designers as well as to technologists. The new questions being raised and resolved relate to combined effects of UV and particulate radiation on surface materials as they will be used in vacuo, surface ionization effects in semiconductor electronics — transistors, diodes, and solar cells.

REFERENCES

1. "Space Environment and Simulation of its Effects on Spacecraft", R. R. Brown, Document D2-113005-1, 1966, The Boeing Company, Seattle, Washington.
2. "An Evaluation of The Radiation Hazard Due to Solar Particle Events", W. R. Webber, Document D2-90469, October 1963, The Boeing Company, Seattle, Washington.
3. "Radiation Hazards in Space", D. L. Dye and M. Wilkenson, *Science*, Vol. 147, p. 19, 1 January 1965.
4. "Tables of Energy Losses and Ranges of Heavy Charged Particles", W. H. Barkas and M. J. Berger, NASA — SP 3013, 1964.
5. "Tables of Energy Losses and Ranges of Electrons and Positrons", M. J. Berger, and S. M. Seltzer, NASA — SP 3012, 1964.
6. "Space Radiation Equivalence for Effects on Transistors", (R. R. Brown), Document D2-84088-2, 1966, The Boeing Company, (Final Progress Report on Contract NAS5-9578).
7. "Surface Effects in Silicon Solar Cells", R. R. Brown, IEEE Nuclear Science Symposium, Columbus, Ohio, July, 1967.
8. "Photon Radiation Effects on Solar Concentrator Reflective Panels", R. B. Gillette, Paper at AIAA Thermophysics Specialist Conference, 1967.
9. See Proceedings of the 1967 (and earlier) AIAA Thermophysics Specialist Conference, obtainable from AIAA, 1290 Avenue of the Americas, New York, New York 10019.
10. "In Situ Measurements of Spectral Reflectance of Thermal Control Coatings Irradiated in Vacuo", P. R. Cheever, J. K. Miles, John Romanko, AIAA Paper 67-342 (see Ref. 9).

REFERENCES (Continued)

11. "Space Environment Effects on Thermal Control Coatings", Boeing Document D2-84118-4, Quarterly Progress Report on Contract NAS5-9650.
12. "Space Environment Effects on Thermal Control Coatings", Boeing Document D2-84118-6, Quarterly Progress Report on Contract NAS5-9650.
13. "Sensitivity of Photographic Film to Nuclear Radiation in Near-Earth Missions", E. L. Noon, and R. R. Brown, IEEE Nuclear Science Symposium, Columbus, Ohio, July 1967.

STATUS OF RESEARCH TO DETERMINE RADIOBIOLOGICAL RESPONSE

CRITERIA FOR SPACE MISSIONS*

Edwin R. Ballinger, Colonel, U.S.A.F., M.C.
U.S. Air Force School of Aerospace Medicine
Brooks Air Force Base, Texas

In considering any new concept of dose criteria, one is easily tempted to see what is available in the nature of old, used concepts. Certainly in the past 25 years many of us have been busily concocting dose criteria for anything in sight that looked like a possible or potential hazard. We have prepared dose criteria for weapons testing, nuclear aircraft, nuclear submarines, nuclear rockets, luminous instrument panels, klystron tubes, and foot X-ray machines.

In one program we finally achieved the pinnacle of success as we established criteria for fall-out on aircraft in flight and earned from General Ernest Pinson the observation that we had at long last come up with a magnificent overprotection against a nonexistent hazard.

On the other hand there are cases not quite so frivolous, cases of considerable underprotection as a result of poor or no exposure criteria. These can be found in the studies of radium dial painters, uranium miners, leukemia in physicians, and also can be found under the gray felt gloves worn by some of our older radiologists. Thus, there are criteria and more criteria and in some cases a lack of criteria.

A reasonable approach to the manned space flight problem would be first to determine when and where we may have an existent hazard, and second to look at the composition of this hazard to see how it differs from other situations where we already have ample dose criteria. By identifying these differences, we will also have identified the pivotal factors around which a new criterion must be built. If this be the case, these factors so identified must be taken into account in assessing the status of research to determine radiobiological response criteria for space missions.

In space, between the earth, its moon, Mars, and Venus, are several kinds and locations of ionizing radiations that may or may not be hazardous to man depending upon how well he is protected, how long he remains, and the amount, the kind, and the energy of the radiation present.

*The animals involved in this research were maintained in accordance with the "Guide for Laboratory Animal Facilities and Care" published by the National Academy of Sciences, National Research Council.

We need not dwell on the location of these hazards that are more familiar to the physicist than to the biologist, the solar flare proton radiation beyond the Van Allen belts, the protons and electrons in the Van Allen belts, the trapped electrons beneath as residual from nuclear testing in the upper atmosphere, and, of course, any trapped charged radiation which may exist around other planets or stars possessing a sufficient magnetic field.

We can first compare these radiations of space with those we use clinically and in research. When we do this, we will find several important differences in each of four basic manners in which space radiation varies from that used clinically. These four include radiation type and energy, dose rate, exposure frequency, and dose (Table 1.)

Table 1
Comparison of Clinical, Research, and Space Radiations

| Item | Clinical/Research | Space |
|---------------------------|--|---|
| Radiation type and energy | Co ⁶⁰ γ > 1 Mev β 2-40 Mev P 150-600 Mev | Bremsstrahlung γ < 1 Mev β 0.5-5 Mev P < 100 Mev |
| Dose rate | 50-500 rad/min. | < 0.1 rad/min. |
| Exposure frequency | 1-10 exposures (1-10 days between) | 1-10 exposures (over duration of mission) |
| Dose | 1-1000 rad (partial body) | 1-1000 rad (whole body) |

These differences constitute the factors one must take into account in assessing the present status of research to determine radiobiological response criteria for space missions. They prevent us from seeing what is available in the way of old criteria and make us realize how inadequate most present clinical observations and radiation research experiments are in arriving at any but generalized criteria.

We all strive toward higher energies and higher fluxes for faster exposures, more patients, better statistics, or more time for golf. Thus the true space radiation picture of low dose rates of low energy and poorly penetrating particles involves the very dose rate considerations that the clinician avoids with higher flux and energy equipment. Although there are a few clinical users of protons and electrons who particularly rely upon the Bragg peak to produce maximum effect at a specific depth, more frequently the energy, or a rotational exposure, is chosen with greater regard to protecting or sparing deeper structures.

More specifically, from the first factor of radiation type and energy (Table 1), it is evident that space radiation will involve greater considerations of skin and superficial structure protection than generally practiced clinically, or observed in research. With the exception of whole body gamma exposures, our sources of most pertinent human information are those clinicians using electron irradiation techniques on the skin and underlying tissues. There appears to be fair agreement that mild erythema is unlikely to occur below exposures of 250 rad using 2-12 Mev electrons and that there is no evidence of nausea or other gastrointestinal complaints, nor any evidence of serious alterations in the blood unless due to significant X-ray contamination of the electron beam.

For several years the School of Aerospace Medicine has conducted a series of monoenergetic proton exposures using 6- to 8- pound rhesus primates ranging in eight energy groups from 13 Mev to 2.3 Bev. Clinical manifestations included considerably more gastrointestinal symptomatology at 2.3 Bev than at lower proton energies; some of this increased response may be due to the build up of secondary irradiation or spallation within the body. The extent of this build up was calculated at approximately 43 percent of the incident dose for the 2.3-Bev exposures. Secondary buildup was not significant at energies of 400 Mev and below, and in the range of 100 to 400 Mev the acute manifestations were quite similar to 2-Mev X-rays on a rad-for-rad basis. Protons of energies in the order of 55 Mev penetrated the body tissue to the depth of about 2.5 cm, thus irradiating much of the bone marrow and central nervous system and some of the gastrointestinal tract of the rhesus monkey. The $LD_{50/30}$ at this energy is about 1,150 rad as compared with approximately 700 for gamma. There was depression of white cells and platelets but to a much lesser extent than that seen after X-ray irradiation. Gastrointestinal symptoms occurred with doses above 1,500 rad comparable to those seen at half this dose with X-irradiation. The depth of penetration of a 35-Mev proton is approximately 1.0 cm. Findings are predominantly limited to the cutaneous tissue. Doses in excess of 1,500 rad produced severe skin ulceration within a month. Doses in excess of 900 rad developed incapacitating fibrosis of the skin with chronic ulcerations by the 28th month. Animals receiving 550 rad exhibited marked graying of the hair; otherwise, they are alive and well 3 years after exposure. Cataracts of some degree have developed in 87 per cent of the animals receiving doses in excess of 1,000 rad and 37 per cent of the animals receiving 550 rad. Except for transient white-cell drop, neither hematological nor gastrointestinal organs appear to have been affected by this energy.

In comparing the monkey with man, one must make allowances for the differences in dose depth and hence the increased energy necessary to penetrate to the comparable organ in man. Tables 2 and 3 list proton and electron energies necessary to penetrate the mid-distance in a number of vital organs.

In regard to the second factor in Table 1, dose rate, Wright Langham has described our situation as being concerned with rates far too low to depend upon AEC

Table 2

Proton Penetration in Primate and Man

| Organ | Primate Depth in Tissue (cms) (a) | Proton (Mev to Center) | Approx. Man Depth in Tissue (cms) | Proton (Mev to Center) |
|------------------|---|---------------------------|---|---------------------------|
| Liver | 3.5 | 64 | 12.0 | 130 |
| Kidney | 2.7 | 55 | 8.0 | 100 |
| Marrow (sternal) | 1.1 | 34 | 2.0 | 48 |
| Marrow (pelvic) | 2.1 | 49 | 6.0 | 86 |
| Mid-brain | 3.0 | 60 | 8.0 | 100 |
| Optic lens | 0.6 | 24 | 0.9 | 30 |
| Heart | 3.3 | 62 | 8.0 | 100 |
| GI tract | 2.5 | 52 | 12.0 | 130 |
| Testis | 1.0 | 32 | 1.5 | 40 |
| Ovary | 4.0 | 69 | 10.0 | 120 |

(a) Measured from cross-sectional atlas of anatomy of 3.2-kg MACACA MULATTA: center of organ to nearest skin surface.

Table 3

Electron Penetration in Primate and Man

| Organ | Primate Depth in Tissue (cms) (a) | Electron (Mev)(b) | Approx. Man Depth in Tissue (cms) | Electron (Mev) |
|------------------|---|----------------------|---|-------------------|
| Liver | 3.5 | 9 | 12.0 | 35 |
| Kidney | 2.7 | 7.5 | 8.0 | 20 |
| Marrow (sternal) | 1.1 | 4 | 2.0 | 6 |
| Marrow (pelvic) | 2.1 | 6 | 6.0 | 15 |
| Mid-brain | 3.0 | 8 | 8.0 | 20 |
| Optic lens | 0.6 | 2 | 0.9 | 2.8 |
| Heart | 3.3 | 9 | 8.0 | 20 |
| GI tract | 2.5 | 7 | 12.0 | 35 |
| Testis | 1.0 | 3 | 1.5 | 5 |
| Ovary | 4.0 | 10 | 10.0 | 27 |

(a) Measured from cross-sectional atlas of anatomy of 3.2-kg MACACA MULATTA.

(b) Based on depth which relative ionization decreases to 50% of the maximum in water.

data and far too high to lean upon PHS studies. As these two agencies have provided the preponderant financial support to radiation bioeffects research to date, it is not surprising to see a relative gap in the middle of our dose-rate picture.

Still considering dose rate, we find in general that the lower the rate, the less effective the total dose (Figure 1). For instance, using mice at rates of Co^{60} gamma in the order of 300,000 rad/day, we find an $\text{LD}_{50/30}$ of approximately 775 rad. As we reduce this dose rate by factors of the natural log to 100,000 to 30,000 to 10,000 to 3,000, etc., we find a related increase in $\text{LD}_{50/30}$ dose which, as we go through a factor of 10^3 in dose rate, increases the $\text{LD}_{50/30}$ by a factor of approximately 3.

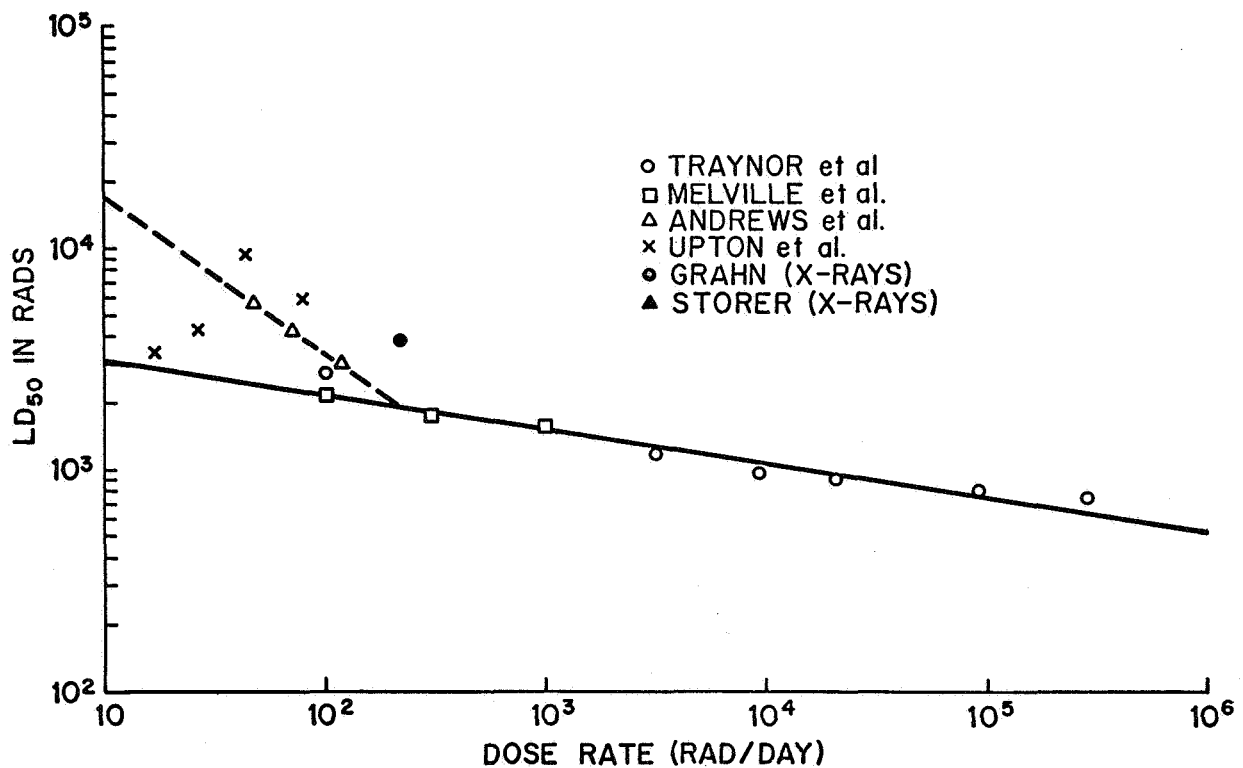


Figure 1—Comparative Data, LD_{50} vs Dose Rate.

From limited primate studies at fewer dose-rate points, a parallel picture is suggested. Examining primate changes more closely at even lower dose rates characteristic of space where $\text{LD}_{50/30}$ is not of primary concern, we see at 15, 10, and 5 rad per day an increasingly higher total dose required to produce hematological changes. Recent gamma data to be repeated using protons in November at the NASA Space Radiation Effects Laboratory suggest involvement of a repair factor which becomes increasingly expressive as we go from 15 rad per day to 5 rad per day and

below. Thus the value of these hematological changes in estimating space radiation dose becomes questionable unless we also have a general idea of the rate of delivery.

When we look at the frequency of exposures (Table 1), we find the clinician seeking the most effective periodicity for tumor regression, while the space researchers seek to find the periodicity for least effect upon anything. Here is where some of Dr. Alpen's work at the U. S. Naval Radiological Defense Laboratory is most pertinent, showing as it does a species difference in degree and in direction as some animals appear to oscillate several times postexposure between a radiosensitive and a radioresistant state. The period for man is not known, but recent work at the School of Aerospace Medicine suggests that rhesus is most sensitive to a second exposure on the 25th to the 30th day.

In seeking to add to our store of space knowledge from examining clinical data, we find few places where whole body exposures are being used, and even fewer that have examined the relationship of surface area to effective dose (Table 1). This relationship is believed to exist for large area exposure as well as for small. As the clinician is primarily interested in the patient and the lesion being treated, he can to some extent be forgiven for failing to observe and record other side effects of radiation that as a psychiatrist, which he must also be, he does not wish to bring to the attention of a very concerned, apprehensive, and not-a-little frightened patient. It is unfortunately this fact that has prevented much clinical dose effect information to go unrecorded and even in fact unobserved. Although our mores do not permit us to expose humans to radiation for research purposes, it is unfortunate that our lack of closer ties with the clinician has to some considerable extent denied us that information which could be observed during the treatment of patients for more legitimate purposes. The estimates for threshold dose for erythema in humans may vary from casual observer to casual observer over a factor of 2 to 3. Associated effects, swelling, itching, and burning, frequently go unrecorded. Although there is a relationship known to exist between area exposed and threshold dose, the clinician is not made aware of our need for this first-hand human data for future space flight considerations. The School of Aerospace Medicine is presently assembling an ad hoc group of clinicians to assist us in this regard.

Whole body exposures are presently being conducted at Stanford University, MIT/Lahey Clinic, and M. D. Anderson Hospital, to name a few. Dr. Ferdinand A. Salzman, MIT, is presently comparing 100 percent O₂ versus hypoxic exposures on the leg, using 2-Mev proton in the treatment of mycosis fungoides. He is, of course, interested in increasing the effectiveness of his exposures by increasing O₂ availability and perhaps metabolism. We should follow this work with considerable interest.

Thus to compare the differences between our clinical and our space situation, we find that:

1. Space radiations are by and large less penetrating, thus less damaging to deeper structures of the body; the gastrointestinal tract will be less involved than the bone marrow, and the skin more involved than either the gastrointestinal tract or bone marrow.
2. The lower dose rates in space can almost axiomatically be said to be less damaging, and thus thresholds for effects as observed at high clinical rates will not necessarily apply in the low dose rates of space. Much work is needed in this region to compare the effects from acutely delivered doses, to the partial or complete absence of effects at lower dose rates. Because of the low energy and low dose rate one can make emphatic the predication that lethality per se is not going to be a radiation problem in any planned situation.
3. Much more is needed in learning man's period of sensitivity to repeated exposures before criteria in this specific can be any more precise than to say "the less frequent the exposure, the better."

Where does this lead us? Can we say that whatever the criteria drawn from clinical and research observations, they can be taken to represent the worst likely effect, rather than that to be normally expected? I believe in general that we can. For in dose rate, in energy, in wide spectral distribution where a smearing of LET and Bragg peak occurs, in frequency and in total dose where on prolonged missions much of the life-support system can be additionally employed as shielding, present clinical and research data do appear to represent the worst rather than the average expected results.

In summarizing our present status of research to determine radiobiological response criteria for space missions, we can say the following:

1. We have a radiation problem in space that appears to be limited to the Van Allen belt, the regions or electromagnetic pathways of solar flares, the near-earth regions of trapped artificially injected electrons from man-made nuclear exercises, and possibly the radiations electromagnetically trapped in the fields of other stars or planets.
2. We cannot lean too heavily on any earlier criteria based upon high energy penetrating radiation given at high dose rates or over a portion of the body.
3. As physical measurements in BL space become more precise, and as more numerous measurements of maximum energies and fluxes from solar flares are gathered as we enter the period of the active sun, our response criteria can become more meaningful as we can further restrict our considerations to certain areas and certain energies and fluxes.

In examining many sources of information for effects of highly penetrating and poorly penetrating ionizing radiations and by separating effects into these categories, we find that 150 rad is about the lowest dose of penetrating radiation to reproducibly produce minimal nausea with concomitant transient alteration in villi of the gastrointestinal tract. In the case of less penetrating radiation, a transient change in the mitotic index of the skin has repeatedly been reported at 100 rad. Early erythema or reddening of the skin reported by several investigators to occur between 200 and 300 rad may constitute a prodromal warning at 300 to 500 rad of the characteristic erythema proper, occurring between the third and fourth week as reported by many electron therapists. As there is little question what nausea or skin inflammation could do to a space mission, it is not unreasonable to assume these effects to be limits beyond which it would be very unwise to stray. As such and to the extent that any space exposure can be called routine, we would support this as a maximum routine dose. Although a routine dose has been defined as any dose that will not produce an alteration in a routine clinically accepted biological test, at dose rates comparable to space, 100 rad may prove to be quite close to this threshold.

There may be occasions when a dose in excess of the routine is contemplated, one which may produce clinically demonstrable but for the most part reversible and transient changes. At lower rates of 5 to 15 rad/day radiation may be of the order of 150 to 300 rad to satisfy one statistically that a 20 percent to 40 percent drop in lymphocytes has occurred. In the region of 300 rad mild erythema has been observed at clinical dose rates using poorly penetrating radiation. To use a limit of 300 rad to the skin with the assumption that dose rate introduces a factor of 2 to 3 in our favor may be the best we can do at this time.

Having suggested a routine and a nonroutine maximum dose, one is faced with the inevitable question, "How much can I take if I have to?" The answer comes out only if we ask, "Have to what?"

For all practical purposes one can repair from whole-body penetrating doses of 150 to 200 rad and skin doses of 400 to 600 rad. Although cataract formation is deemed probable at these higher levels, it is relatively slow in developing and can be removed surgically.

Although an LD_{50} for penetrating radiation has been given as 150 to 200 rad for acutely delivered doses, our earlier described dose-rate study would suggest that a factor of 3 to 4 be applied here, and by so doing to indicate small likelihood of primary radiation death as compared with problems secondary to certain degrees of performance decrement produced by skin doses above 500 rad. We have alive today primates exposed 8 to 10 years ago to low dose rates of penetrating radiation from 2,000 to 4,000 rad.

How good are these numbers? If the dose rates and proton energies which show wide variations between reporting physicists can be averaged, our radiobiological response data may involve a safety factor approaching 2. ^oAt least as much solar flare data as has been collected through the history of mankind's ability to observe and record will be obtained in the next several years as we move through the next period of maximum solar activity. Many of the discrepancies in measurement will be resolved statistically and our response criteria improved in reliability to the extent of the physicists' contributions. With increasing attention on the part of clinicians to the bioeffects of electron and proton irradiations, and with a joint NASA/Air Force committee to this end, the radiobiologist will be able to enhance the validity of these threshold values. A much clearer picture must appear in the early 1970's.

In the early 1970's we are going to need better criteria for prolonged missions, perhaps of several years. Whether beginning a long ballistic trajectory, or a Hohmann minimum energy transfer, the way back is a long one, and the exposure criteria—rigid, restrictive, and conservative at early times—may become increasingly flexible and permissive as the last leg of the flight is entered.

Why use man for such prolonged flights? It would be difficult to find a sane individual to agree to participate in such confinement in a ground-control experiment. We need not belabor the reasons, but at present it appears that the man-machine loop with man onboard gives far greater guarantee of success for such a long-range mission whether he functions only as a repair man, a trouble-shooter, or an observer of a single key function at some time in the long flight. Until nuclear or other exotic power plants can provide the continuous acceleration necessary to accomplish long distance flights in a minimum of time, one of the most trying problems of prolonged flights may be personnel interrelationships. The choice of the magic number of flight crew; the decision on the value of cross-training versus the psychological advantage of deliberately setting each man as a single unique contributing component; the means of protecting man physically against the long periods of inactivity and psychologically against long periods of reduced flow of sensory input—what do these have to do with radiobiology and criteria concepts? These heretofore unrelated factors may find a common ground in the consideration of techniques of preserving the performance integrity of both, for it would seem that many of the present techniques in modifying the effects of radiation may also play a role in modifying man's response to prolonged confinement and isolation. For many years it has been observed that a tie-in apparently exists between the level of metabolic activity and the sensitivity to ionizing radiation—the higher the metabolic activity level, the more sensitive the individual to radiation. Whether this is induced or spontaneous activity is still under examination. Known also is the relationship of oxygen and hypoxia to radiation response. Hypoxia appears to be one of several moderately effective radioprotectants. Similarly thermal effects are thought to play a role in response to radiation. The high LD₅₀ of poikilotherms and the bizarre protection afforded by hibernation in Jacobson's University of Chicago experiment have stimulated increased effort to examine the effects of thermal extremes. It is

possible that the modification of any one of these factors—reduced metabolism, hypoxia, or hypothermia—would be of considerable value in preserving the mental and psychological integrity of space crews subjected to the rigors of space for long periods of time.

If in the middle and late 1970's man is destined to make such flights, it would not be at all surprising that the status of research to determine radiobiological response criteria would flow across and into a second level of involvement, expressing as permissive doses those we are looking at today as modified by the degrees of radioprotection one can achieve by the metabolic modifications just described.

THE LET SPECTRUM OF GALACTIC RADIATION EXPOSURE IN
SPACE AND ITS TRANSITION IN SHIELD OR TISSUE*

Hermann J. Schaefer, Ph.D.

Naval Aerospace Medical Institute
Pensacola, Florida

*This work was conducted under the sponsorship of the Office of Advanced Research and Technology, National Aeronautics and Space Administration. Project R-75.

Opinions or conclusions contained in this paper are those of the author. They are not to be construed as necessarily reflecting the view or the endorsement of the Navy Department.

A complete dosimetric assessment of the galactic radiation hazard to man in space requires analysis of the LET distribution for establishing dose equivalents. Since the primary particle spectrum ranges from $Z = 1$ (protons) to at least $Z = 26$ (Fe nuclei) with energy spectra reaching up into the ultrarelativistic region, the compound LET spectrum is an extremely wide continuum extending from 0.18 kev/micron tissue (minimum LET of protons) to 3600 kev/micron tissue (Bragg peak of Fe nuclei). The build-up of galactic radiation in dense matter and the associated LET transition are not well investigated. Experimental data do exist for the Earth's atmosphere, furnishing a maximum dose rate of 22 millirads/24 hrs as compared to 13.2 millirads/24 hrs for the primaries only. Transfer of these data to dense absorbers is only of limited validity because the charged pi mesons, due to their short lifetime, decay in the rarefied air of the upper stratosphere, yet undergo nuclear collision leading to star formation in dense matter. In a qualitative way, it can be shown that the formation of secondaries from high energy primaries should result in a general shift of the energy dissipation from high to low LET because a large part of the secondaries from high Z primaries is of relativistic energies. Dosimetrically, the most important component of the secondary radiation is the neutrons since they carry RBE and QF factors substantially larger than 1.0. Unfortunately, information on this very component, even for the build-up in the Earth's atmosphere, is incomplete and contradictory with data of different authors differing by a factor of 2. A peculiar transition phenomenon that could be called a pseudo build-up occurs in the initial section of the build-up region for the low energy heavy nuclei of the primary flux which are responsible for the so-called microbeam effects of the galactic radiation exposure. Because the spectrum of the incident radiation has a pronounced maximum at a comparatively large range, the enders frequency increases initially with increasing depth. The position of the maximum of this pseudo build-up occurs at a different depth than that of the main build-up, a circumstance that would have to be taken into consideration in the design of heavy nuclei experimentation.

INTRODUCTION

In discussions of the radiation hazard to man in space, interest has centered in the past primarily on trapped radiation and solar particle beams. For manned space ventures of a more distant future, such as lunar colonization or interplanetary missions, which will entail exposure times in deep space of months or even years, the galactic radiation hazard cannot be disregarded. To be sure, this exposure, since it remains well below the 100 millirad/day level, would not cause concern about possible acute effects that could impair astronaut performance even on an extended mission. What we are dealing with clearly is a chronic exposure at low dose rates which is significant only if long-term effects are considered.

It is a well-established fact in radiobiology that chronic damage from accumulated exposure to low dose rates of high LET radiation is, rem per rem, more severe than that

for standard x- or gamma rays. The reason for it presumably is to be sought in differences in the recovery mechanism in the sense that for high LET radiation, repair of tissue damage is incomplete. Since galactic radiation, acting continuously, represents the most typical chronic low dose rate exposure one can think of, a quantitative analysis of the LET distribution is an essential prerequisite for a full assessment of the long-term damage. In view of the complex composition of the primary galactic radiation and, all the more, of the combined primary and secondary radiation at various depths in a compact absorber, the establishment of the resulting local LET spectra is a task of unusual complexity. The following discourse does not aspire to present a complete solution. It merely discusses the various types of interacting mechanisms involved in the build-up phenomenon in regard to the changes they initiate in the configuration of the LET distribution. For a dosimetric evaluation, a complete analysis of the particle transition of the primary beam as it travels in absorbing material is actually not needed. Obviously, all secondaries of single charge and relativistic speed resulting from nuclear interactions dissipate energy at the same minimum LET. That means their individual particle identity does not have to be determined. As a consequence, the severe limitations that exist at present with regard to a theoretical treatment of the build-up in the multibillion e-volt energy range are alleviated, at least to the extent that reasonable, semiquantitative estimates of the transition of the LET spectrum and the corresponding RBE and QF factors seem possible.

COMPARISON OF FLARE PRODUCED AND GALACTIC RADIATION

Numerous studies have been carried out in the past investigating the problems of shielding and depth dose distribution for the various spectral types of trapped radiation and solar particle beams. Since these efforts have created a general familiarity with the basic characteristics of the pertinent proton spectra and their transition in shielding material or body tissues, it seems indicated to point out the basic difference that exists in this respect between flare produced and galactic particles. Figure 1 gives a direct comparison of the proton energy spectra of a typical large flare (1) and galactic radiation (2, 3). Attention is directed to the difference of a factor of 36 million in the ordinate units for the two spectra that had to be chosen in order to plot both spectra in one graph. Examining the range scale on the upper abscissa, one recognizes the basically different situation with regard to shielding. Taking, for instance, the minimum shielding equivalent of 1.65 g/cm^2 for the Apollo vehicle, one sees immediately that this thickness would provide very substantial protection from the flare beam, yet would cut off only a negligible flux fraction from the galactic beam. In fact, the latter statement does not even tell the whole story. The large fluxes of the galactic beam at 1 Gev and beyond would produce, in the shielding of the Apollo vehicle and all the more in a heavier barrier, a substantial build-up of secondaries, producing, for an astronaut inside the vehicle, a substantially higher exposure than for an astronaut freely floating in space in his space suit far away from any large compact agglomeration of matter.

Unfortunately, as mentioned before, a quantitative theoretical treatment of the build-up for galactic radiation runs into considerable difficulties. Looking at the energy scale on the abscissa of Figure 1, one can distinguish, with regard to the mechanism of energy dissipation of protons in shielding material or tissue, three energy regions. In the first one, extending from zero to about 150 Mev, ordinary ionization is the predominant process of energy dissipation, with the additional energy removed from the primary beam by nuclear collision amounting to only a few per cent. Since the flare spectrum shown in Figure 1 is essentially limited to the energy interval in question, tissue dosages would therefore change only insignificantly by adding the collision term in a dosimetric evaluation.

The second energy interval extends from about 150 Mev to about 400 Mev. In this interval, especially toward its upper end, energy dissipation from secondaries produced locally in nuclear collisions competes with ordinary ionization, and accurate assessment of tissue dosages would require a quantitative analysis of the collision loss. This is not exactly an easy task, but it still can be handled with Monte Carlo methods if a larger computer facility is available (4). Of special importance in such studies is always the neutron component in the collision term because of the high RBE and QF factors that would have to be assigned to the corresponding dose contribution.

The situation changes again in the third interval ranging from 400 Mev into the ultrarelativistic region. At these energy levels, mesons appear as a new type of secondary in the intranuclear cascade and become more and more the determining factor in the build-up as the energy enters the multibillion e-volt level. While the role of the charged pi mesons would still be accessible to a theoretical assessment, the neutral pions initiate photon-electron cascades which determine very prominently that part of the build-up that derives from ultrarelativistic primaries. The development of the photon-electron cascade in the Earth's atmosphere, where it bears the name large air shower, has been studied extensively in theory and experiment. However, the transfer of the pertinent data to compact matter and the complex combination with the nucleon cascade, which continuously feeds new neutral pions into the already existing cascades, so far has deterred theoreticians from any attempt at a computer approach. Similar or possibly even greater difficulties exist in regard to the theoretical treatment of the role of the neutron component in the build-up. At greater depths, i.e., behind very heavy shield thicknesses, neutrons dominate the development and final decay of the nucleon cascade. For an excellent treatment of the subject with particular emphasis on the problems of radiation shielding in space, the reader is referred to a study by Shen (5). In the present discussion, we accept without further proof the fact that a quantitative theoretical treatment of the combined nuclear and photon-electron cascade for the high energy part of the primary galactic beam is out of reach. It should be emphasized that what one faces here is not so much a limitation due to the large number of input parameters for the computational analysis but more so a limitation of inadequate information on the numerical values of those parameters.

Experimental data on the build-up of galactic radiation do exist for the Earth's atmosphere. In fact, most elaborate measurements have been carried out by a number of investigators. However, these data for the tenuous air of the upper atmosphere cannot be transferred directly to a compact material such as the heat shield of a space vehicle. Aside from the different atomic compositions of the two media, the difference in density in connection with the short, mean lifetime of the charged pions causes these particles to decay in the atmosphere, but to undergo nuclear interaction in compact matter. This leads to two basically different types of cascades, the nucleon cascade in the atmosphere and the nucleon-meson cascade in dense material. Even rough estimates of how much this would modify the transition curve in the atmosphere if the latter is visualized as compressed to density one in vertical direction are not available. In the absence of data for compact matter, then, the galactic build-up in the atmosphere as the only available source of information must be resorted to for a first approximation assessment. Figure 2, based on the data of Neher and Anderson (6), shows the altitude profile of the total ionization of the galactic radiation for solar maximum and solar minimum. Since altitude on the abscissa scale is expressed in g/cm^2 of air overhead, the graph can be interpreted directly, with the just-formulated restrictions, as the galactic build-up in a semi-infinite slab of air-equivalent dense material.

For a direct quantitative comparison of the two build-up functions in Figure 2, it is advantageous to normalize the curves to equal dose levels at zero depth in the shield as done in Figure 3. Since conditions at solar minimum, when the screening effect of the interplanetary magnetic field is lowest, are representative for the highest galactic radiation level, it seems appropriate to base the further discussion on the curves for solar minimum in Figures 2 and 3. In doing so one sees from the pertinent curve in Figure 3 that up to the rather heavy shield thickness of about $10 \text{ g}/\text{cm}^2$, no apparent shielding effect exists as far as the absorbed dose is concerned. However, this does not at all mean that the radiation as such does not undergo any transition. Actually, very complex interaction processes occur in the shielding material right from the beginning. It just so happens that, for the galactic spectrum at solar minimum, the processes involved balance out in such a manner that the absorbed dose remains constant over the first $10 \text{ g}/\text{cm}^2$. Hidden behind this constant total energy dissipation are profound continuous changes in number and type of particles and in their energy spectra occurring as the radiation travels through the shield material. Dosimetrically, these changes have to be taken into consideration as one progresses from absorbed doses to dose equivalents since they are accompanied by changes in the local LET spectra of the various beam components.

LET SPECTRUM OF PRIMARY GALACTIC RADIATION

If we visualize, in a conceptual experiment, an infinitesimally small tissue sample freely floating in deep space far away from any compact matter of a stellar body, the galactic radiation will produce, in that sample, an absorbed dose that is in very close approximation, exclusively due to the ionization of the primary particles themselves.

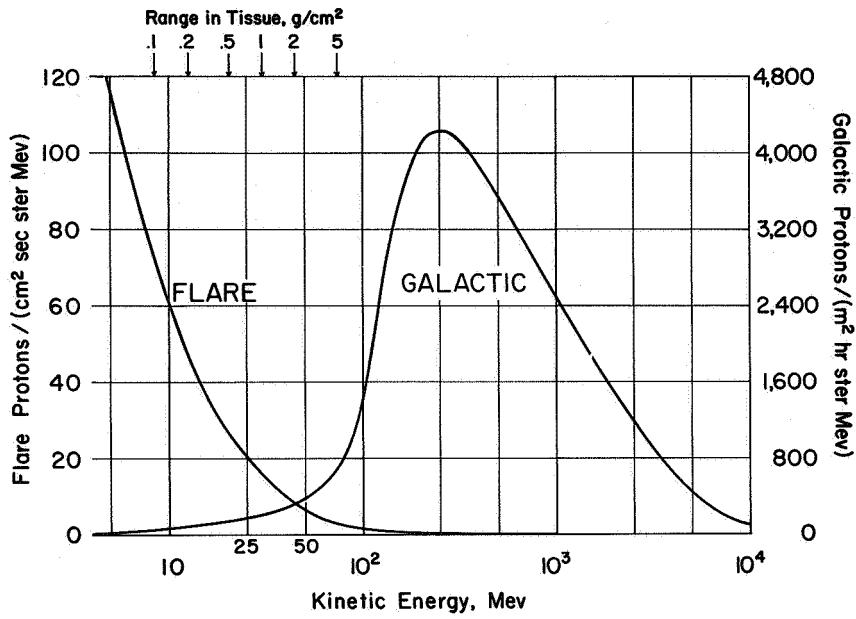


Figure 1

Differential Energy Spectra for Proton Flux of a Large Flare (July 1959) and Galactic Radiation
 (Note greatly different ordinate units!)

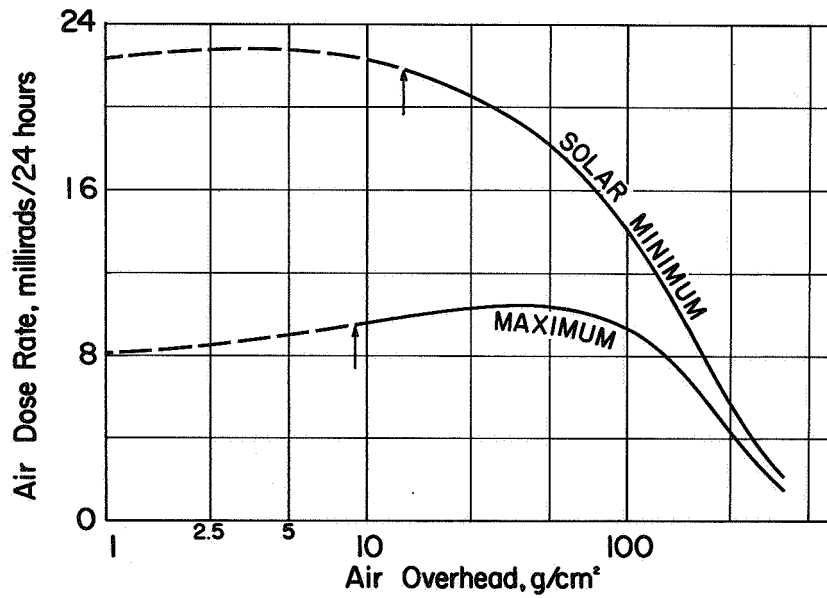


Figure 2

Galactic Radiation Levels in the Earth's Atmosphere as a Function of Pressure Altitude
 (Based on data of reference 6.)

100 Per Cent Skin Dose Rates: July '59 Flare 10 rad/hr Galactic Solar Min. 22 } millirad/24 hrs
 Solar Max. 8 }

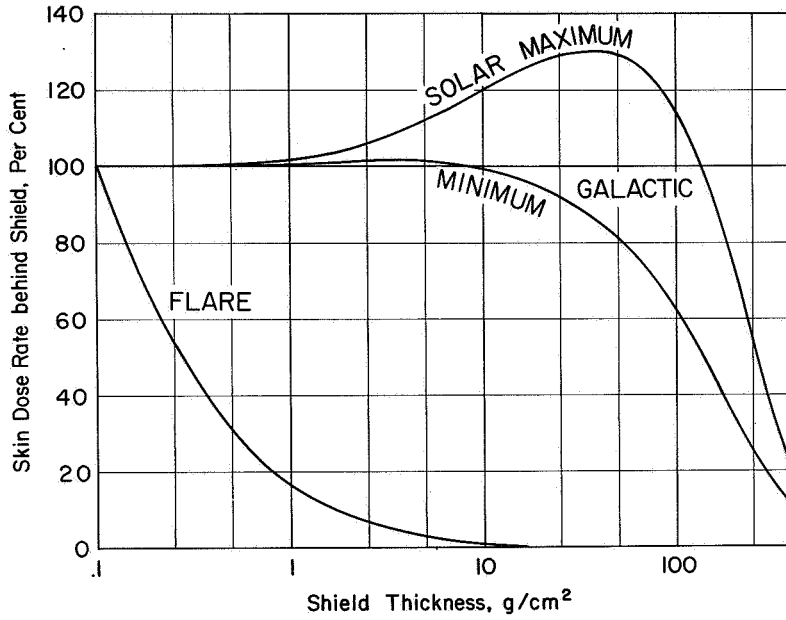


Figure 3

Normalized Galactic Radiation Levels in the Earth's Atmosphere and Corresponding Level for Flare Spectrum of Figure 1

If the particle and energy spectra of this primary flux are known, the accurate determination of absorbed dose and dose equivalent encounters no difficulties. Although at first sight this idealized system would seem of little practical value for dose assessments in actual space systems such as a human target in a vehicle with a heavy heat shield, it does serve well as a baseline from which the transition of the LET spectrum during the build-up of secondaries can be analyzed.

Since the primary radiation is made up of distinctly different Z components, its compound LET distribution is a superposition of overlapping individual distributions covering the enormous LET interval from 0.18 keV/micron T for relativistic protons to 3600 keV/micron T for the Bragg peak of nuclei with a $Z \geq 20$. Based on the best available data on the energy spectra of all Z components of the primary galactic radiation (7), the bottom graph in Figure 4 shows the superposition of the LET distributions of the various Z components. Since the bulk of the differential flux for all components centers on the region of high and very high energies, the LET distributions, in turn, center heavily on the respective minimum LET values of the different Z species, with only a small fraction of the energy dissipation extending toward the upper end of the individual LET scale, i.e., toward the Bragg peak. In order to allow a direct comparison of the heterogeneity in LET, the individual distributions in Figure 4 have been normalized by adjusting the area under each individual distribution to unity. That means the areas for all Z components are equal and do not correspond to the fractional dose rates of the respective components. For this particular information, Table I which lists the values in question in the bottom line should be consulted.

Table I
Dosimetric Data on Primary Galactic Radiation

| Element | | H | He | C | Ne | Ca |
|--------------------|---------|------|------|------------------|------------------|------------------|
| Atomic Number Z | | 1 | 2 | 6 | 10 | 20 |
| LET, | Minimum | 0.18 | 0.73 | 6.6 | 18 | 73 |
| keV/micron T | Maximum | 85 | 240 | 964 | 1420 | 2790 |
| Ionization dose, | | 5.3 | 3.2 | 2.0 ^a | 1.1 ^b | 1.6 ^c |
| millirads/24 hours | | | | | | |
| Mean RBE | | 0.75 | 1.00 | 1.59 | 2.86 | 6.64 |
| Dose equivalent, | | 3.98 | 3.20 | 3.18 | 3.15 | 10.62 |
| millirems/24 hours | | | | | | |

a: For Class Z = 3 to 9; b: For Class Z = 10 to 19; c: For Class Z = 20 to 28.

If we proceed now to the radiobiological interpretation of the compound LET distribution of Figure 4 in terms of dose equivalents, it seems appropriate to compare it to the LET distribution for standard x-rays shown in the center graph of Figure 4. It is seen immediately that galactic radiation encompasses an enormously wider LET range than standard x-rays. In regard to RBE factors, four intervals of the compound galactic LET distribution can be distinguished. The first interval extends from 0.18 to 0.5 keV/micron T. As seen in Figure 4, it is located, with its entire width, below the region of standard x-rays and contains the bulk of the energy dissipation of the primary protons. Of special interest is the close similarity of this LET distribution to that for Co-60 gamma rays as reported by Cormack and Johns (8). Figure 5 shows the two distributions over the same abscissa scale. It should be obvious, from this comparison, that the dose fraction of primary galactic protons should be applied the same RBE, which in clinical radiation therapy and experimental radiobiology has been established for Co-60 gamma rays, i.e., the RBE of 0.6 to 0.8.

The second LET interval of the compound LET distribution for galactic primaries extends from 0.5 keV/micron T to about 3.5 or 5 keV/micron T. This is the region in which most of the energy dissipation of standard x-rays takes place. For the dose fraction in this interval, then, the RBE of 1.0 has to be used by definition. The third interval extends from 3.5 or 5 keV/micron T to 80 or 100 keV/micron T and represents an LET range that could be called the conventional high LET region. Its upper end denotes the maximum LET in the Bragg peak of protons. It is the interval in which the bulk of the energy dissipation of recoil protons from fast and high energy neutrons takes place. The RBE Committee of the ICRP (9) recommends, for this LET interval, an RBE formula which furnishes the curve marked RBE in the center graph of Figure 4 with the right hand ordinate notation. The Committee restricts the use of the formula to a highest LET of 175 keV/micron T. In the graph in Figure 4, the pertinent curve has been arbitrarily extended to higher LET values by gradually saturating the RBE at 10.

The fourth and highest LET interval which begins at about 100 keV/micron T represents an essentially unknown territory as far as experimental data with biological specimens are concerned. On the one hand, studies with alpha particles, which have a maximum LET of 240 keV/micron T in the Bragg peak, clearly indicate for most somatic reactions a reversal of the RBE, i.e., a decreasing efficiency for increasing LET. This effect is presumably due to the so-called "over-kill" or "crowding" effect, meaning that more ionization events than needed for destruction are produced in the microscopic tissue volume where the particle passes. While this "waste" of ionization energy, on the one hand, results in a decreased RBE if the general radiation effect on the whole specimen is compared to standard x-rays, on the other hand, experiments with cosmic ray heavy primaries by Chase (10) and by Eugster (11) have demonstrated that particles with a very high LET, presumably in the 1000 keV/micron T range and beyond, show so-called "microbeam" effectiveness in the sense that a single traversal can lead to complete cellular destruction. As the RBE Committee expressly states (l.c., 9), the ordinary concept of dose and RBE is not applicable to this type of radiation exposure. At present, the problem rests essentially at this negative statement. No alternate concepts for the definition of a special dosimetric unit for microbeam irradiation have been proposed so far, nor are experimental data available on total

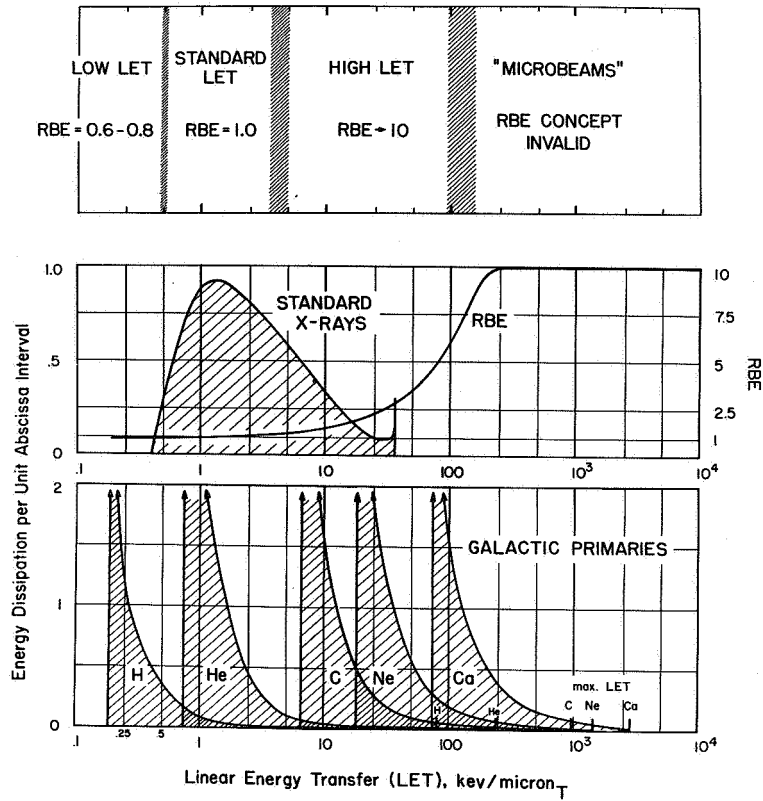


Figure 4

LET Distributions for the Components of Primary Galactic Radiation Compared to those for Standard X-rays and RBE Function Recommended by ICRP

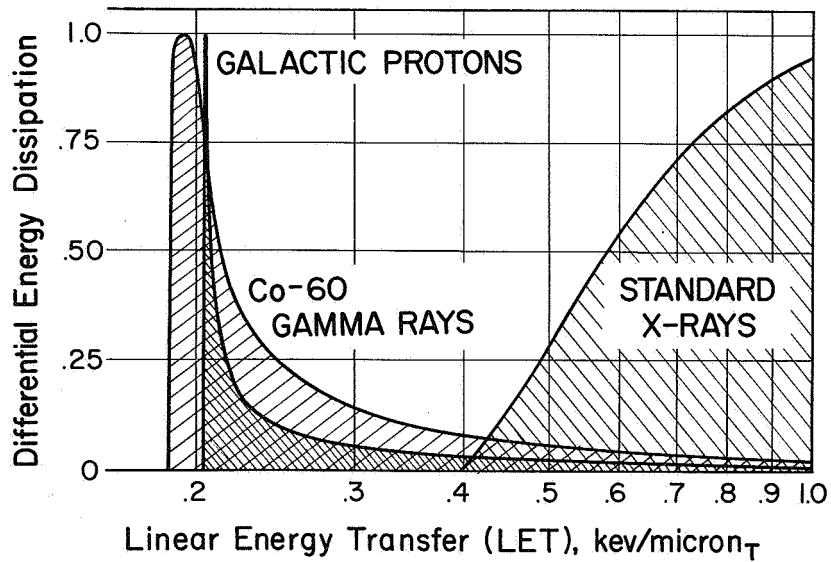


Figure 5

LET Distributions of Primary Galactic Protons and of Co-60 Gamma Rays as Compared to Standard X-rays

body effects of such exposures with mammalian specimens. In view of this gap in present radiobiological knowledge, the dose fraction of galactic exposure in the fourth LET interval in Figure 4 can only be carried in terms of absorbed dose, with the dose equivalent remaining undetermined. Expressed as absorbed dose, the energy dissipation in the LET interval in question is very small, amounting to only a few per cent of the total primary dose. However, the demonstrated microbeam effectiveness on individual cells should caution against an overconfident attitude leaning toward disregarding this part of the galactic radiation exposure.

TRANSITION OF LET DISTRIBUTION IN BUILD-UP REGION

In analyzing the basic mechanism responsible for the build-up, we begin with the primary protons, i.e., with the LET distribution at the extreme left in Figure 4. Quite generally, the first generation secondaries resulting from nuclear interactions of high energy protons are cascade and evaporation particles, with the former being of high energies in the near or full relativistic region and the latter of lower energies down to a few Mev. Most of these particles are of single charge, such as protons and plus- or minus- mesons. Some are neutral mesons and neutrons. A still substantially smaller fraction are secondary alpha particles, and, finally, a very small fraction are heavier nuclei as fragments from disintegration stars or neutron recoil nuclei. Since the bulk of the energy fluence of the primary proton spectrum centers on the energy region around and above 1 Gev, it can be concluded that the bulk of the cascade particles of single charge continue, for several generations, the energy dissipation at minimum LET of the parent primary from which they originated. In other words, where there was before the collision one primary proton of high energy dissipating energy at minimum LET, there will be after the collision several singly charged secondaries of high energy, each dissipating its energy at the same minimum LET. Even if we leave the exact multiplicity as well as other interaction parameters involved undetermined in this rough sketch, we still can see that, for several generations, the secondaries originating from primary protons will dissipate a larger amount of energy per unit length of absorber at minimum LET than the primaries themselves. In other words, the dose contribution of the primary protons of 5.3 millirads/24 hrs will be more than matched by the energy dissipation of their own secondaries. How far downbeam this proposition will hold cannot be determined without more involved assessments. However, the foregoing argumentation does demonstrate that the LET interval below 0.5 kev/micron T at the extreme left in Figure 4 acts as a reservoir into which a substantial part of the energy dissipation from secondaries is fed, at least in the initial steps of the build-up. If we further realize that the interacting mean free paths of the secondaries involved are of the same order as that of the primary protons themselves (about 90 to 120 g/cm² in air), we see that what we just called "initial steps" should cover a sizeable distance even in compact absorbing material. Comparing, for the Earth's atmosphere, the total absorbed dose from all primaries and secondaries as it actually has been measured (22 millirads/24 hrs) and the total absorbed dose from the primaries only as it follows by adding all entries under "Ionization Dose" in Table I (13.2 millirads/24 hrs), we see that only a comparatively small difference (8.8 millirads/24 hrs) remains which must contain, among other contributions, the dose fraction from relativistic secondaries

found above to more than match the 5.3 millirads/24 hrs of the primary protons. This simple estimate strongly suggests that only a rather small part of the dose from secondaries can be due to low energy particles.

A similar argument as was just applied to primary protons holds for primary alpha particles, with the additional provision that most of them will break up, in their first nuclear encounter, into constituent neutrons and protons, thereby not merely maintaining the LET spectrum, but actually degrading it by shifting energy dissipation from the He distribution (Figure 4) to the H distribution. Finally, a similar transition occurs with all still heavier primaries since they also will break up, in their first collision, into fragments of smaller Z-numbers, mainly protons and neutrons but also some alpha particles and a few heavier fragments. In view of the fact that LET changes with the square of the Atomic Number Z, all these transitions constitute a general shifting of energy dissipation on the LET scale from the right to the left (Figure 4), i.e., from regions of higher to lower LET. Again realizing the comparatively small fraction of 8.8 millirads/24 hrs of the total galactic dose of 22 millirads/24 hrs which are not accounted for as to their LET distribution, one wonders whether it is more than a few per cent of the dose from all secondaries that falls into the third area of the top graph of Figure 4, i.e., would have to be assigned RBE values in excess of 1.0.

The most severe limitation of the validity of the foregoing estimates results from the lack of reliable data on the role of neutrons in the build-up phenomenon. That holds for the nucleon cascade in the Earth's atmosphere as well as for the nucleon-meson cascade in dense matter. The data on which the dose/altitude profiles of Figures 2 and 3 are based were obtained with ion chambers made of stainless steel and filled with Argon; therefore, they do not allow any inferences as to the participation of incident or locally produced neutrons in the total ionization. Other data on the galactic neutron dose in the atmosphere are not very well defined either. A report of the ICRP Task Group (12) lists a galactic neutron dose of 0.76 millirads/24 hrs in the atmosphere at 30 g/cm² pressure altitude. These data have been questioned by Watt (13) who arrived at a dose rate twice that large. If one considers that the neutron dose fraction carries an RBE factor substantially larger than 1.0 and that the different reaction mode of charged pions in compact material as compared to the rarefied air of the stratosphere is bound to furnish additional neutrons, one sees that the neutron contribution is of prime importance in the entire build-up problem, particularly from a dosimetric viewpoint where absorbed doses have to be converted to dose equivalents for the final answer.

In weighing the estimates of the dose contributions from the various primary and secondary components presented in this study and combining them with what has just been said about the neutron dose estimates of other authors, one cannot help voicing severe doubts as to the consistency between the measured values of the total ionization and the data on the primary galactic flux. Subtracting the computed dose for the primaries from the measured total dose seems to leave a difference much too small to cover the various contributions from secondaries even if these are entered with their

lowest reasonably acceptable estimates. These discrepancies indicate that, despite a truly enormous effort by cosmic ray physicists over several decades, the build-up phenomenon of galactic radiation in the Earth's atmosphere is not well enough understood at present to allow a more accurate assessment of the galactic dose equivalent in a human body at a specified altitude.

PSEUDO BUILD-UP OF HEAVY FLUX COMPONENTS

A peculiar transition phenomenon occurs in the uppermost section of the LET distribution in the vicinity of the Bragg peak of each individual component of the primary flux. It was mentioned briefly before that the extremely high LET values near the Bragg peaks in the medium high and high Z classes represent, from a radiobiological viewpoint, a special quantity that cannot be adequately described in common dosimetric terms because the ionization trail of a single low energy heavy nucleus constitutes a substantial radiation exposure on the cellular level in tissue that could be likened to a microbeam. Obviously, a separate follow-up of this particular portion of the total energy dissipation during the build-up is of special interest for instance, if the conditions for maximum exposure to these microbeams in a given experimental system are to be determined. Since LET increases with decreasing energy, it is the low energy flux and especially the "enders," i.e., the nuclei reaching the end of their ionization range in tissue, that account for the microbeam part of the total dose. The peculiar transition of this part occurring in the initial section of the build-up region can be explained with the aid of Figure 6. It shows the differential range spectrum of the Neon component which is used in the present discussion as a representative component of the heavy spectrum in general. The group of curves in Figure 6 shows the spectrum for the incident beam and for selected depths up to 10 g/cm^2 . The incident spectrum is based on the best presently available data on the heavy galactic flux at solar minimum (l.c., 7). By subtracting a given absorber depth from the range values of the abscissa, the local range spectrum at that particular depth can be established directly from the incident spectrum. Figure 6 shows the resulting curves. It is seen that, due to the shape of the incident spectrum with a pronounced maximum at a comparatively large range, the left flank of the spectrum rises continuously as the beam proceeds to greater depths. Not until a depth corresponding to the range of maximum flux in the incident spectrum is reached does the initial part of the local spectrum begin to drop. In other words, the local spectrum of the residual primary beam shows a true build-up in its low range section, yet this build-up is in no way connected to any production of secondaries or to any other mechanism of particle multiplication. Explanation of this rests simply on the fact that more particles of the incident flux change from high to low energy and come to rest toward greater depths. Since so far no name has been adopted generally for the phenomenon, it might be called the pseudo build-up.

In the present context it is of special interest to investigate how the pseudo build-up manifests itself in the LET distribution. Figure 7 shows the pertinent distributions for the incident beam and two selected depths. In order to accommodate

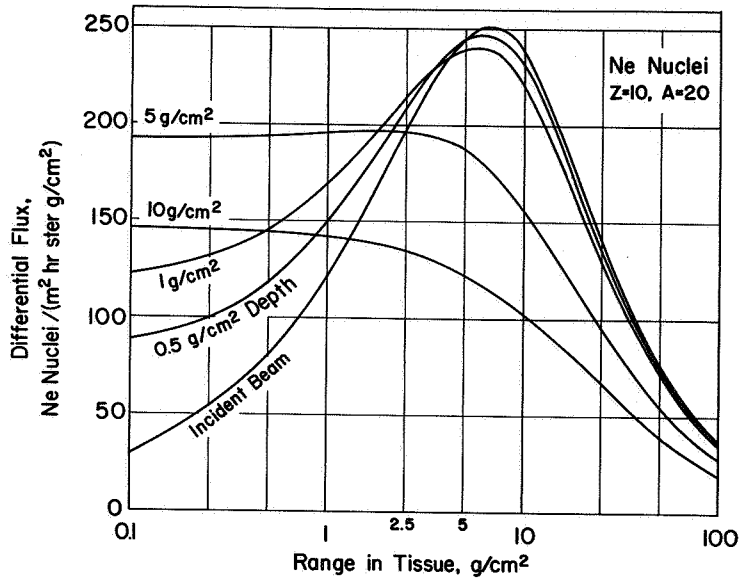


Figure 6

Transition of Differential Range Spectrum for Galactic Neon Nuclei

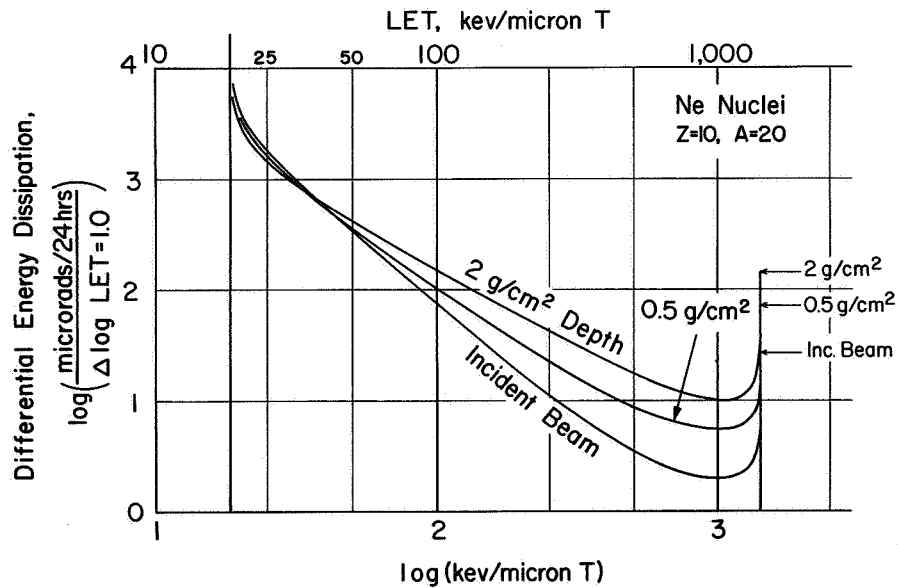


Figure 7

Transition of LET Distribution for Galactic Neon Nuclei
 (Note "pseudo build-up" in high LET region, i.e., increasing energy dissipation for increasing depth.)

the very large range of energy dissipation in one plot, a logarithmic ordinate scale had to be chosen. This should be remembered in comparing Figure 7 with Figure 4 in which a linear ordinate scale is used. It is seen from Figure 7 that the energy distribution in the pseudo build-up increases not merely in close vicinity of the LET value for the Bragg peak, but over a major portion of the full LET scale.

Instead of establishing the LET distributions for different depths, which involves a lengthy computational procedure, one can choose the simpler approach of plotting directly the enders frequency itself as a function of depth as done in an earlier study (14). This shorter method is entirely satisfactory as long as one is merely interested in the general trend and the position of the maximum of the pseudo build-up curve. However, if more detailed information on the pattern of energy dissipation in the tissue structure is required, one has to tackle the full analysis of the LET distribution.

Actual radiobiological experimentation with galactic heavy nuclei has to await the advent of a manned orbital or a lunar laboratory, since delicate techniques and extended exposure times are required. Therefore, a presentation of the data on the pseudo build-up of the other components of the heavy spectrum, as well as a further discussion of the dosimetric problems in such experimentation in general, seems dispensable at this time.

REFERENCES

1. P. S. FREIER and W. R. WEBBER, J. Geophys. Res., 68, 1605 (1963).
2. P. S. FREIER and C. J. WADDINGTON, J. Geophys. Res., 70, 5753 (1965).
3. H. J. SCHAEFER, "A Note on the Galactic Radiation Exposure in Geomagnetically Unprotected Regions of Space," NAMI-982, Naval Aerospace Medical Institute (1966).
4. J. E. TURNER, C. D. ZERBY, R. L. WOODYARD, H. A. WRIGHT, W. E. KINNEY, W. S. SNYDER, and J. NEUFIELD, Health Physics, 10, 783 (1964).
5. S. P. SHEN, Astronautica Acta, 9, 211 (1963).
6. H. V. NEHER and H. R. ANDERSON, J. Geophys. Res., 67, 1309 (1962).
7. H. J. SCHAEFER, "Linear Energy Transfer Spectra and Dose Equivalents of Galactic Radiation Exposure in Space," NAMI-987, Naval Aerospace Medical Institute (1966).
8. D. V. CORMACK and H. E. JOHNS, Brit. J. Radiol., 25, 369 (1952).
9. Report of the RBE Committee to the International Commissions on Radiological Protection and on Radiological Units and Measurements, Health Physics, 9, 357 (1963).
10. H. B. CHASE and J. S. POST, J. Aviat. Med., 27, 533 (1956).
11. J. EUGSTER, Weltraumstrahlung. Medizinischer Verlag Hans Huber, Bern, Switzerland (1955).
12. Report of the ICRP Task Group on the Biological Effects of High-Energy Radiations, Health Physics, 12, 209 (1966).
13. D. E. WATT, Health Physics, 13, 501 (1967).
14. H. J. SCHAEFER, to be published in Proceedings of the Lunar International Laboratory of the XVIIth Congress of the International Astronautical Federation.

SPECTRAL CHARACTERISTICS AND DOSE CALCULATIONS FOR THE
PRIMARY AND SECONDARY PARTICLES THAT RESULT FROM THE INTERACTION OF THE
SOLAR AND GALACTIC COSMIC-RAYS WITH ALUMINUM SHIELDS*

Stanley B. Curtis
UCLRL, Berkeley, California

M. C. Wilkinson
The Boeing Company, Seattle, Washington

Abstract

The importance of the incident galactic and solar cosmic-rays encountered outside the earth's magnetosphere in producing dose is evaluated. It is found that the solar cosmic-ray doses are produced principally by protons with energies at the dose point of between 10 and 100 MeV. Galactic cosmic-ray doses result from a broad range of energies, with the principal contribution coming from the 1 to 10 Gev/nucleon region. The medium and high Z components of the galactic cosmic-rays are important dose contributors for thin ($< 10 \text{ gm/cm}^2$) shielding. Secondary doses depend in a complex way upon the spectral characteristics of the incident particles and the shielding thickness considered.

*This work was performed under NASA contract NASw-1362.

In this paper, we present results of a study to identify the particles and energies which are most important in the evaluation of the radiation hazard to extended manned spaceflight outside the earth's magnetosphere (1). In particular, we have singled out those energies which are most important in depositing dose -- as a function both of interior energy (that is, energy at the dose point) and exterior energy, the initial energy of the particle before entering the shield.

Solar Particle Events

The shape of the solar particle spectra assumed in this study is exponential in rigidity (momentum per unit charge) of the form suggested by Freier and Webber (2):

$$dJ/dP = (J_0/P_0) \exp(-P/P_0)$$

where dJ/dP is the differential rigidity spectrum, J_0 is a measure of the intensity of particles, and P_0 , the characteristic rigidity, is a measure of the steepness of the spectrum.

Most events can be temporally separated into two classes depending on the value of P_0 . They have been called solar cosmic-rays and energetic storm particles (3).

The arrival of the energetic storm particles at the earth is strongly correlated with geomagnetic storm activity. The energetic storm particles are characterized by steep energy spectra with values of P_0 around 10 to 20 MV. They appear for relatively short periods of time compared with the solar cosmic-rays and will generally appear, if at all, some 24 hours or so after the solar flare occurs on the sun. The solar cosmic-ray events are characterized by larger P_0 's, which decrease slowly throughout the event and vary widely from event to event; 40 to 160 MV, (MV - million volts), with 100 MV being a typical value.

In the graphs that follow, we refer to the differential dose distribution and we now define this function. The dose element, dD , is defined

$$dD = (dJ/dE)(dE/dx)dE$$

where dJ/dE is the differential energy spectrum at the dose point and dE/dx is the linear rate of energy loss of a particle of energy E . This can be rewritten

$$dD = (dJ/dE)(dE/dx)Ed(\ln E)$$

Now, we define the differential dose distribution, $F(E)$, as the coefficient in either of the above expressions; that is,

$$dD = F_1(E)d(\ln E)$$

$$dD = F_2(E)dE$$

depending on whether the graphs are plotted as a function of the logarithm of the energy or as a function of the energy itself. In the case of the primary dose, we use the differential in $\ln E$ for convenience. Because of the wide range of primary energies involved, it is convenient to plot the resulting

distribution as a function of $\ln E$. Thus, equal distances along the abscissa have equal weights if the distribution is defined as above. On the other hand, if the energy is plotted linearly, as we do for the secondary particles, the distributions are presented per linear energy interval.

Figure 1 shows the primary differential dose distributions for three shielding thicknesses of aluminum for a proton spectrum with a P_0 equal to 100 MV. The maxima of all curves for thicknesses between 1 and 20 g/cm^2 fall between 10 and 100 MeV. This range, then, is the most important energy range for particles at the dose point for a typical solar particle spectrum.

Figures 2 and 3 give the fraction of the primary dose deposited by protons with exterior or initial energy greater than E plotted as a function of E for variously shaped spectra and for two shielding thicknesses. The energy where the curves reach unity is the energy of a particle having a range equal to the shielding thickness; that is, all particles must have at least that energy in order to penetrate to the dose point. As an example in Figure 2, we see that behind 1 g/cm^2 of aluminum, 20% of the primary dose is deposited by protons of initial energy greater than 60 MeV for a spectrum with P_0 equal to 160 MV.

In Figure 4, the importance of the initial or incident proton energy in producing dose from secondary protons is presented for a shielding thickness of 10 g/cm^2 of aluminum. It is seen that most of the secondary proton dose is produced by incident protons with energies close to the energy needed for the primary particle to reach the dose point. The flattest spectrum ($P_0 = 160$ MV) causes a peak in the distribution at about 130 MeV, slightly over the cutoff energy of 100 MeV for 10 g/cm^2 of aluminum.

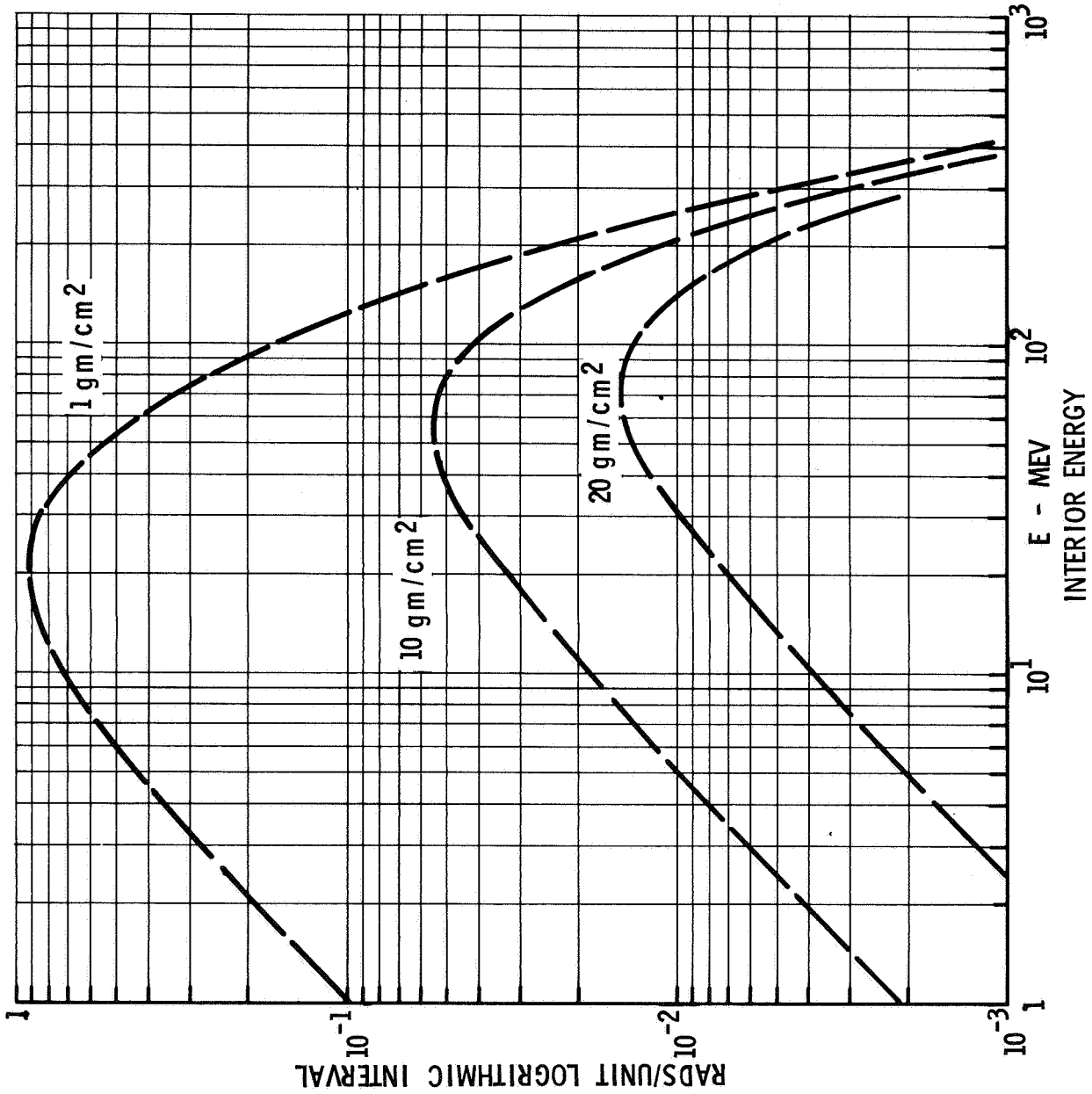


Figure 1—Differential Dose Distributions for 100 MV Rigidity Spectra Protons Incident on Aluminum.

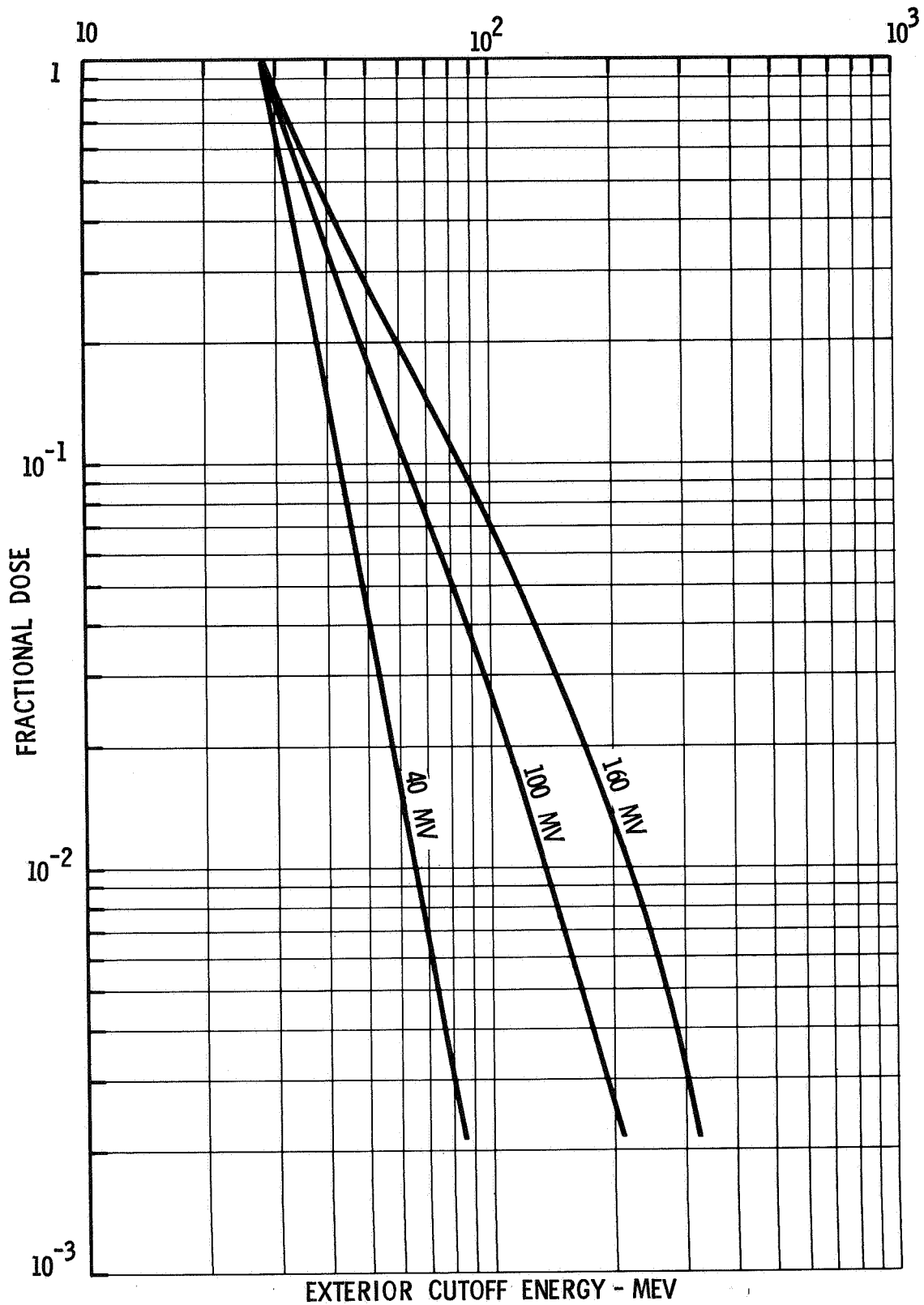


Figure 2—Primary Dose— 1 gm/cm^2 Al.

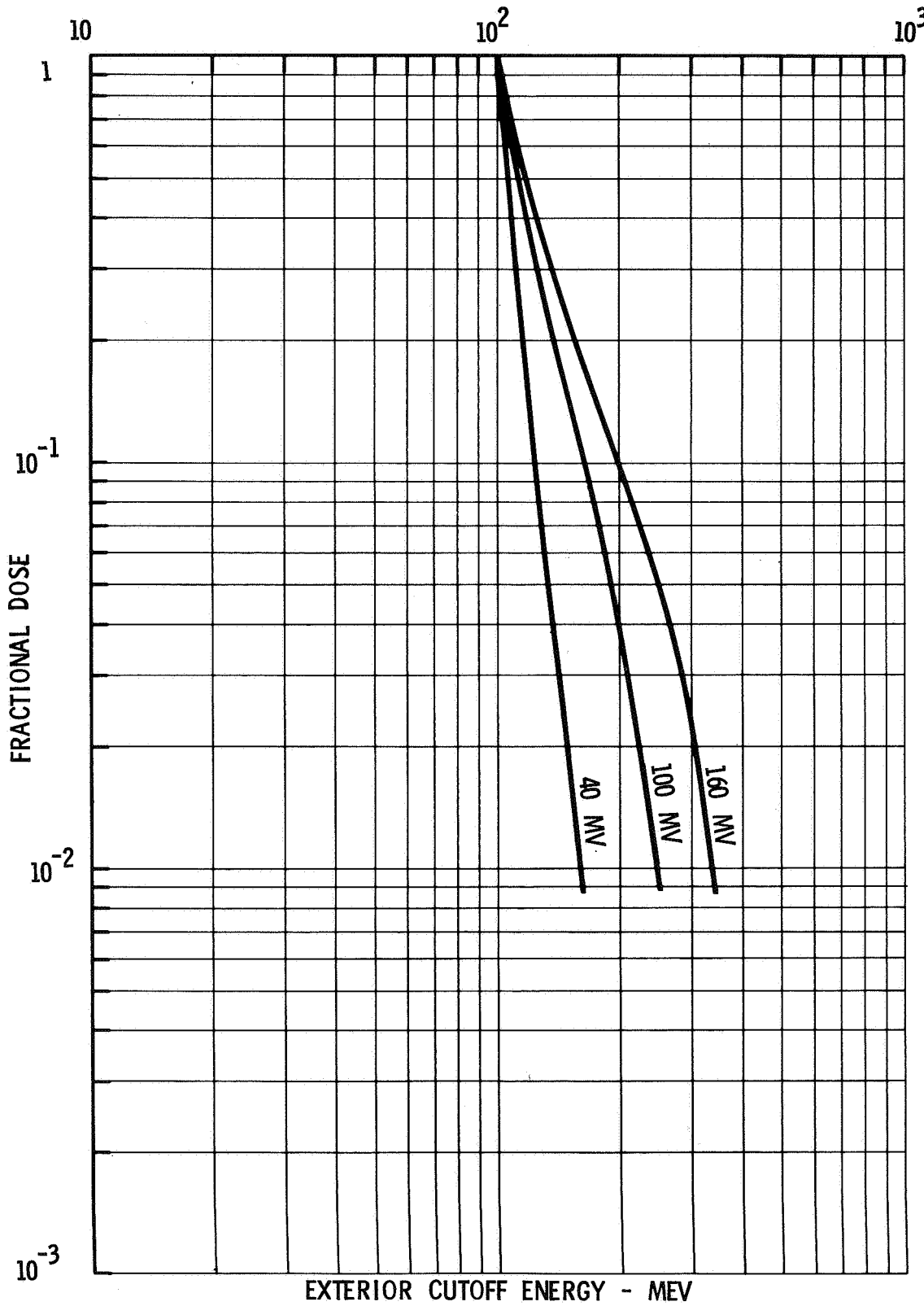


Figure 3—Primary Proton Dose— 10 gm/cm^2 .

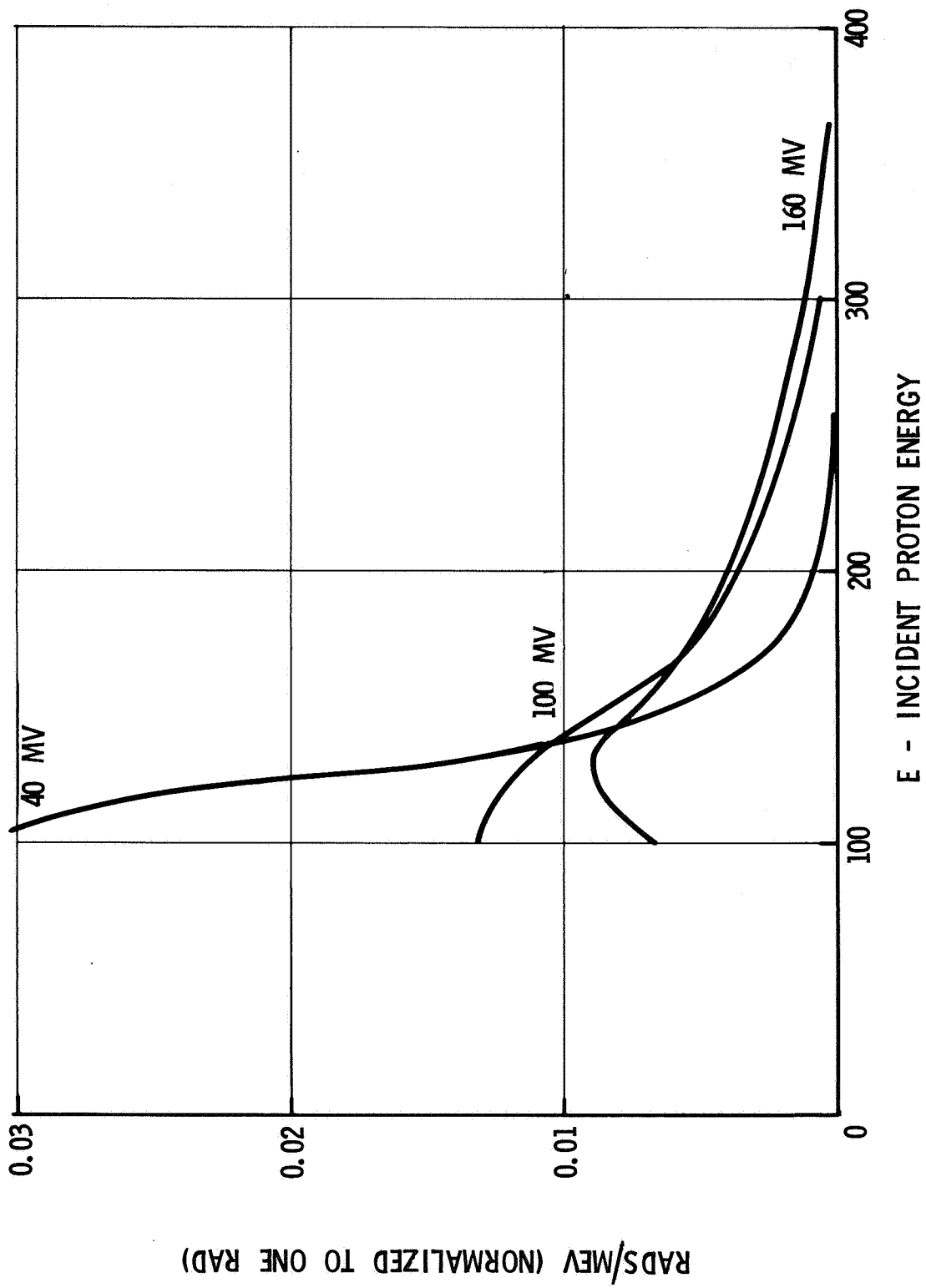


Figure 4--Differential Secondary Proton Dose per Unit Incident Proton Energy--10 gm/cm² A1.

The situation is somewhat different for secondary neutron doses, since neutrons from protons not energetic enough to reach the dose point can contribute to the dose there. This is shown in Figure 5. We see that protons with an incident energy of 30 MeV are important in contributing to the secondary neutron dose at 10 g/cm^2 of aluminum for an event with P_0 equal to 40 MV, even though 30 MeV protons are not energetic enough to reach the dose point. Also of interest is the fact that a wide range of energy is important for the event with P_0 equal to 160 MV. The drop to zero at 400 MeV is an artifact introduced by the fact that no secondaries from incident particles greater than 400 MeV are included in these results. This situation will be corrected when the new secondary production data of Bertini above 400 MeV is incorporated.

Galactic Cosmic-Rays

Recent balloon and satellite data (4) have been compiled and reasonable energy spectra of the various Z-components of the galactic cosmic-rays have been constructed for the solar minimum period (5). These spectra have been used to calculate the free space dose (no shielding) from the various components. Particles with $6 \leq Z \leq 9$ have been designated M particles; and in the calculations we have used $\bar{Z}^2 = 50$, $\bar{A} = 14$ as average values. Similarly, particles with $10 \leq Z \leq 14$ have been designated LH particles ($\bar{Z}^2 = 144$, $\bar{A} = 24$) and particles with $26 \leq Z \leq 28$ have been designated VH particles ($\bar{Z}^2 = 730$, $\bar{A} = 58$). The results are given in Table III. It is interesting to note the large contributions to the total dose from the higher Z components. The dE/dx distributions (LET spectra) are shown in Figure 6. The curves have also been multiplied by the QF defined by the ICRP (6). The shaded area shows the difference between the

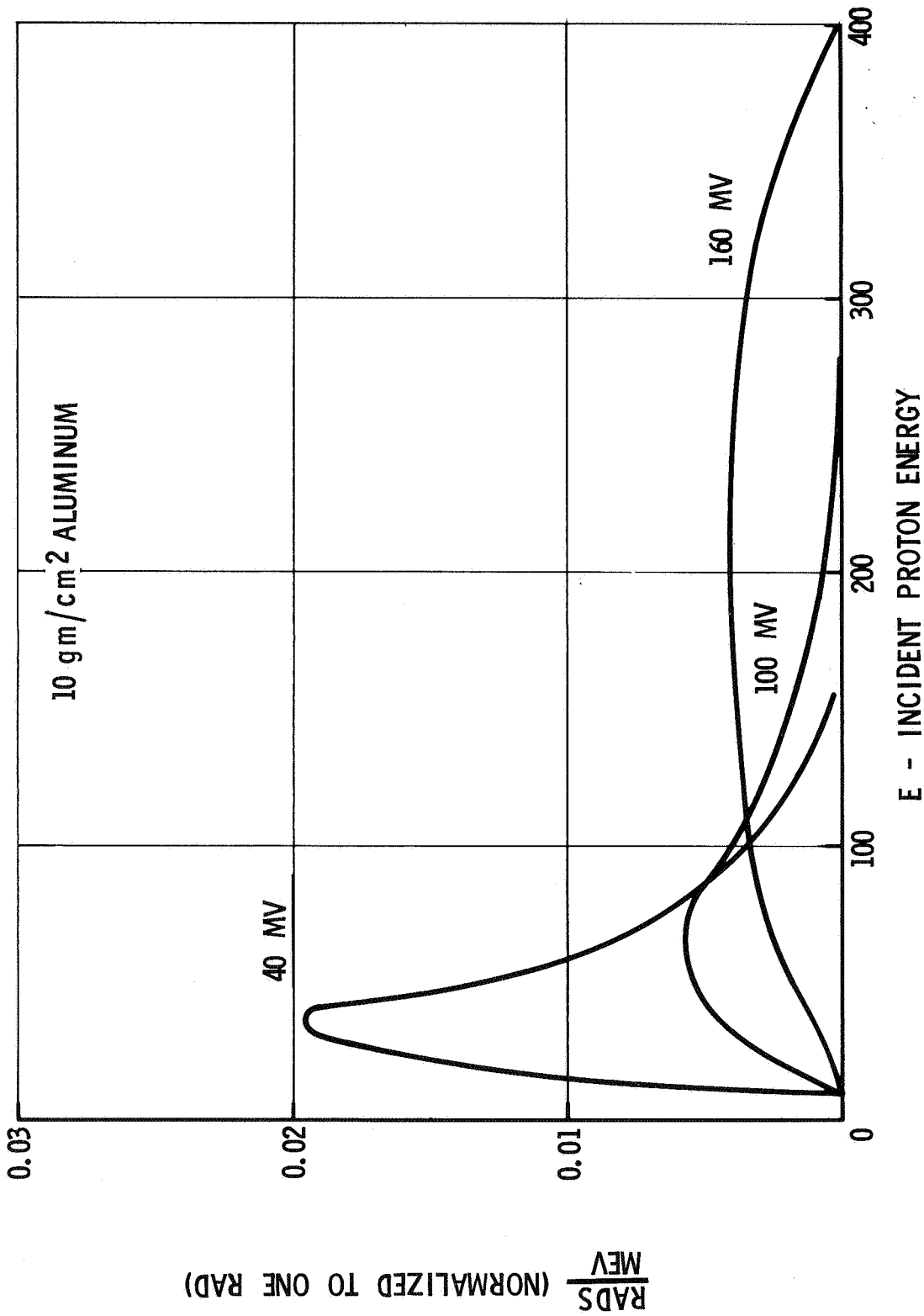


Figure 5—Differential Neutron Dose per Unit Incident Proton Energy.
 (40, 100, 160 MV Proton Spectrum Incident)

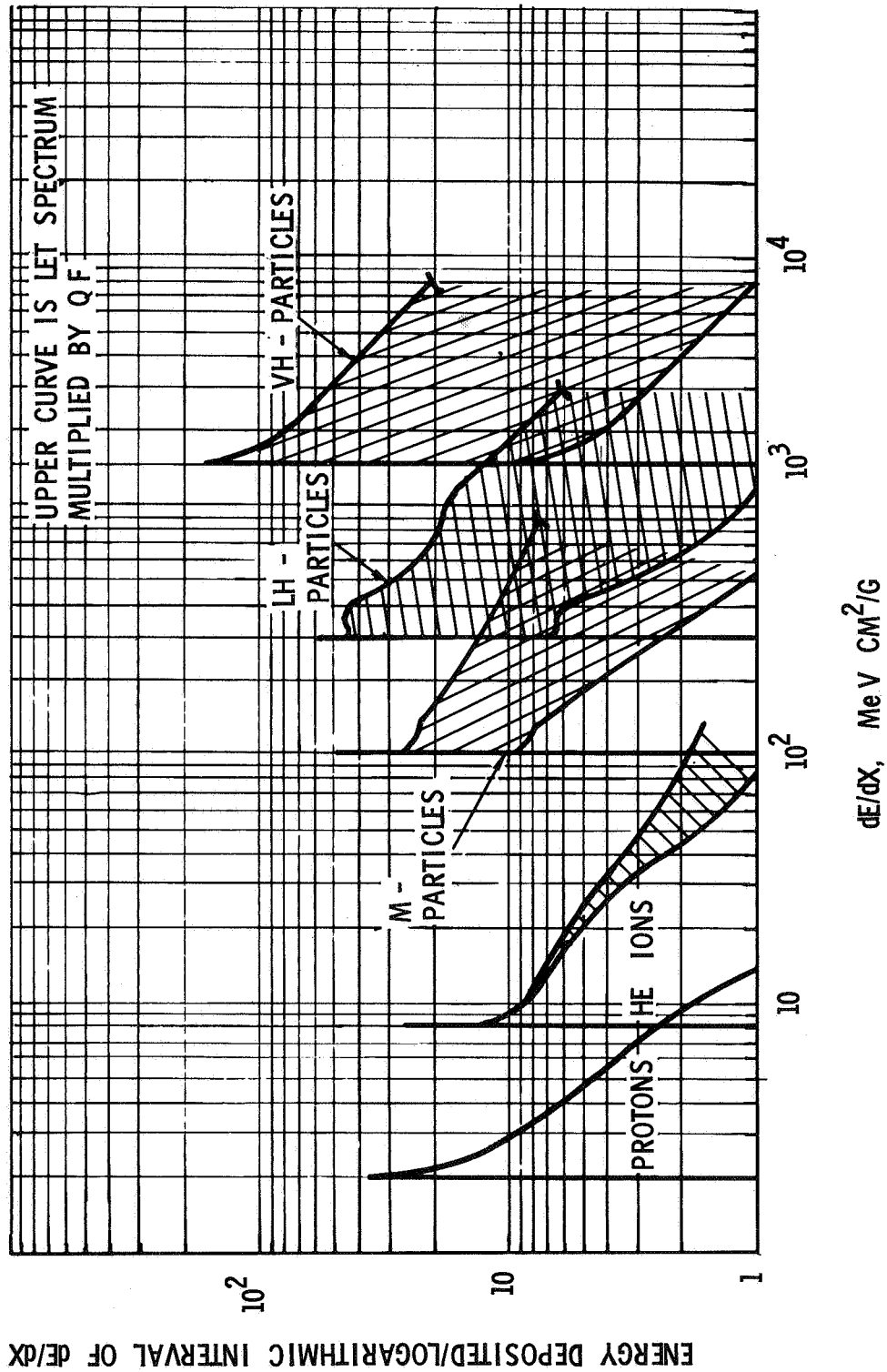


Figure 6—Let Spectrum for Galactic Cosmic Rays under 0.2 g/cm² Water Shielding.

two curves. The area under the upper curve is a measure of the "biologically significant" dose (dose equivalent) and the area under the lower curve is a measure of the energy deposited (rad dose). The true biologically significant dose lies somewhere in between, since the QF is admittedly an upper limit and its use results in numbers that tend to be conservatively high. A rough calculation of the area under the QF-modified curves yields an average "QF" of 4 for the galactic cosmic rays under no shielding.

The heavy particle spectra have been used to calculate the density of stopping particles (sometimes called "thindown hits") as a function of depth in water. These curves are shown in Figure 7. Attenuation of the primary particle intensity by nuclear collision is included, but the contribution from the secondaries produced in such collisions has been neglected. Thus, these curves are lower limits to the true curves, since collisions of both VH and LH particles, for instance, will produce M particles which will stop further on. Such contributions have been neglected here. Even so, it is interesting to note that the density of stopping M particles decreases by only a factor of three between 1 and 15 cm and the density of stopping LH particles decreases by only a factor of four. The reason for this slow fall-off is because of the relatively large fluxes of these particles at high energy. The energy spectra of these particles have broad maxima occurring at around 300 MeV/nucleon.

The proton energy spectra have also been used to calculate the differential primary dose distributions for various shielding thicknesses. The results are shown in Figure 8. It is interesting to note the lack of strong dependence on shielding thickness and the importance of the high energies (100-10,000 MeV)

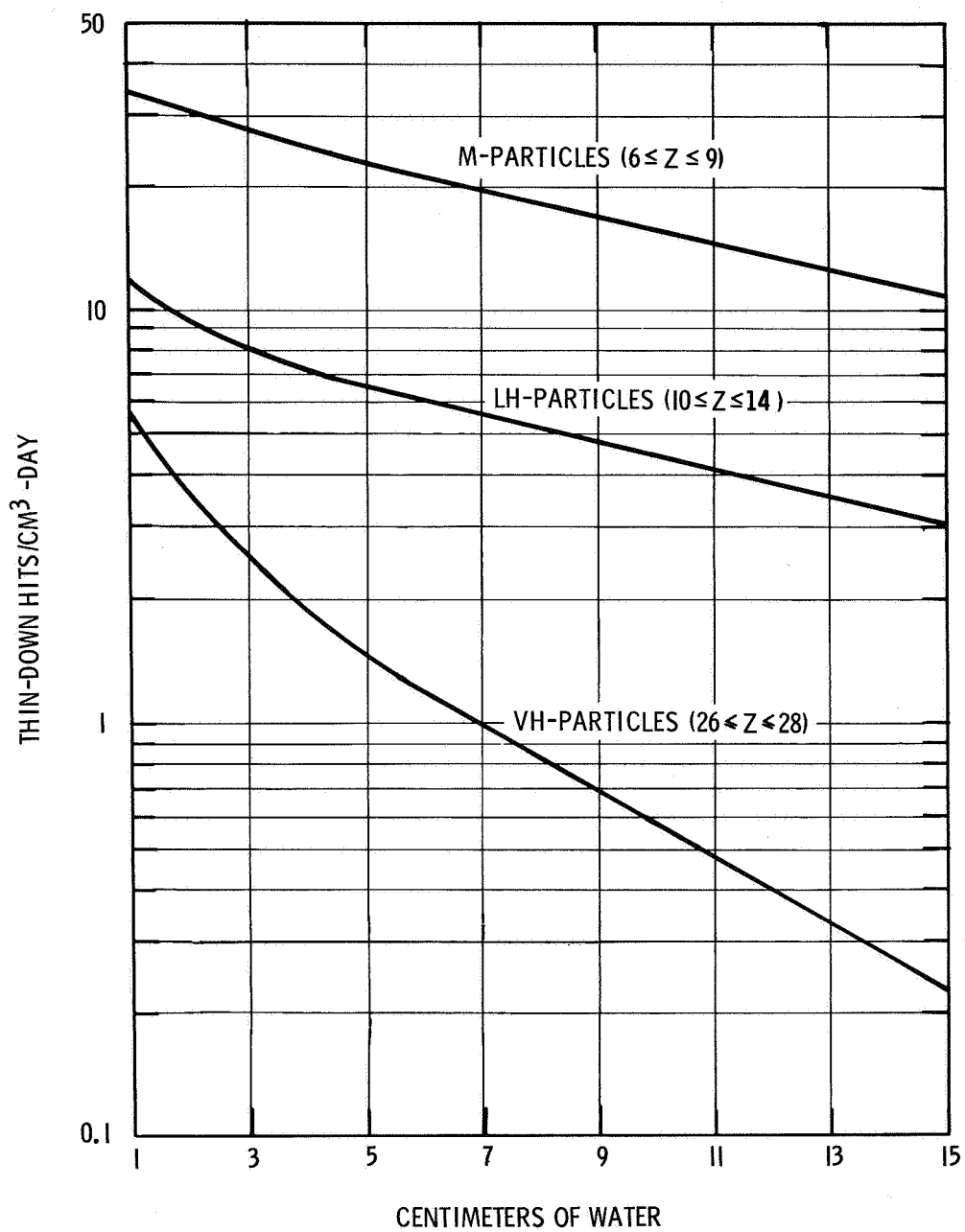


Figure 7—Lower Limits for the Number of Thin-Down Hits per cm³ per Day Neglecting Secondaries.

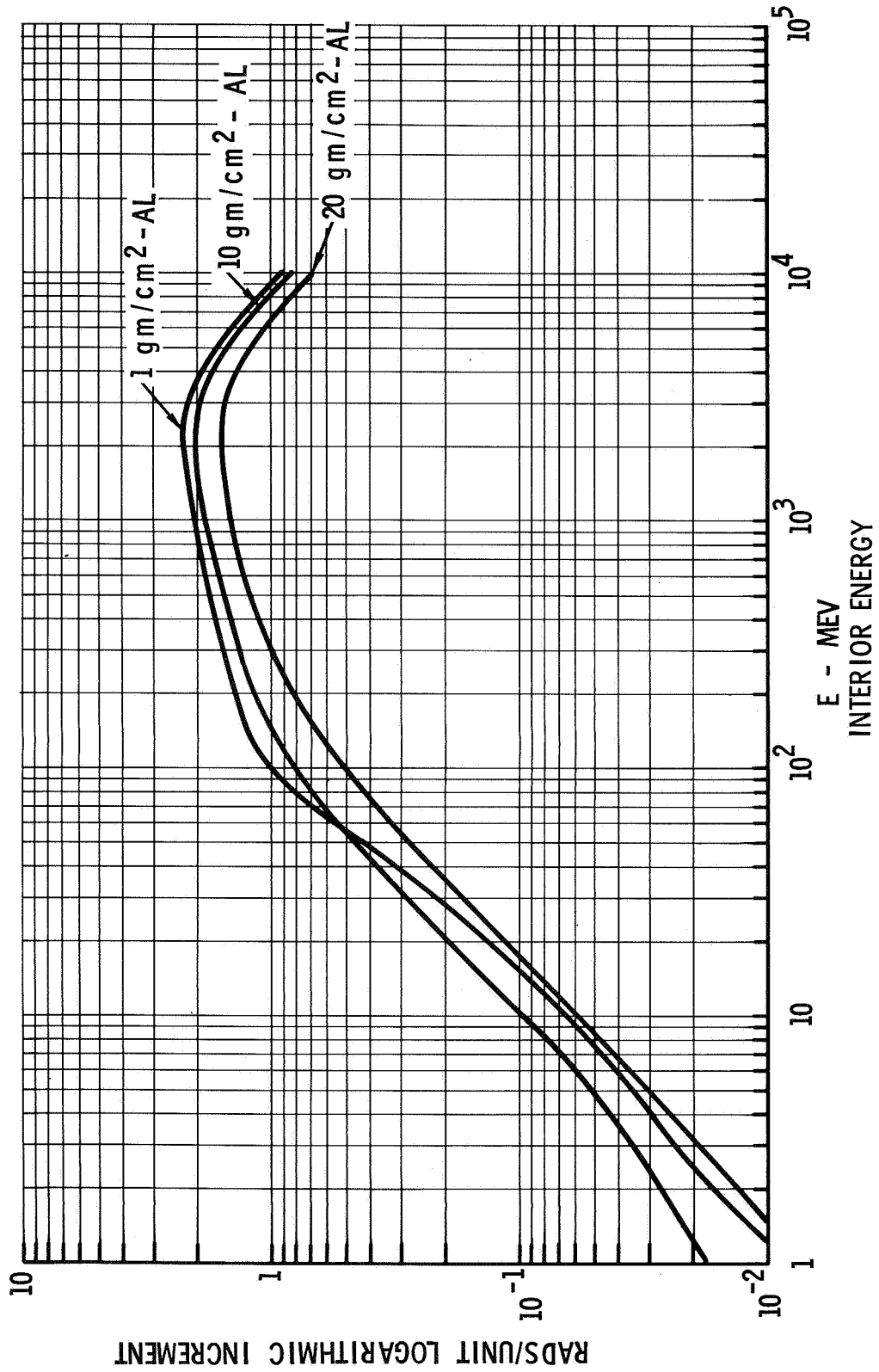


Figure 8-- Differential Dose Distribution for Galactic Cosmic-Ray Protons.

in contributing to the primary dose. It should be mentioned, however, that the secondary dose, which will be important at large shielding thicknesses, has been neglected here because of the lack of secondary production data above 400 MeV. This will be added when the data becomes available.

Conclusions

Although nothing startling has emerged from this study, we now have a quantitative feeling, first, for the importance of various energies of particles in typical solar spectra under various shielding thicknesses and, second, for the importance of the various components of the galactic cosmic-rays, at least under very thin shielding.

We can say that the protons in solar particle events which produce the greatest dose per proton are those which have initial energies slightly greater than necessary to reach the dose point. Protons with energies in the general range from 10 to 100 MeV at the dose point produce a large fraction of the total dose.

Nuclear cascade data are required in the region above 400 MeV to give a complete and accurate picture of the importance of secondaries in very flat solar spectra and in the galactic cosmic rays.

The dose rate from galactic cosmic-rays is low but the higher Z component turns out to be important in producing dose for thin shields and, therefore, even more important in biological terms because of its high dE/dx and increased biological effectiveness. Less is known at thick shielding and certainly more research is indicated both on the physical penetration (i.e., secondary production) and on the biological effects of the heavy particle component.

References

1. A more detailed description of this work can be found in Boeing Document entitled "Study of Radiation Hazards to Man on Extended Missions," Space Physics Group, Space Division, The Boeing Company, Seattle, Washington (1967).
2. P. Freier and W. R. Webber, J. Geophys. Res. 68, 1605 (1963).
3. W. R. Webber, "An Evaluation of Solar-Cosmic-Ray Events During Solar Minimum", D2-84274-1, The Boeing Company, 1966.
4. S. M. Comstock, C. Y. Fan and J. A. Simpson, Astrophys. Jour. 146, 51 (1966), C. Y. Fan, J. E. Lamport, J. A. Simpson and D. R. Smith, J. Geophys. Res. 71, 3289 (1966), and references therein.
5. The compiled spectra may be found in the reference cited in (1) above.
6. Report of the RBE Committee to the ICRP and ICRU, Health Phys. 9, 357 (1963).

A CORRELATION OF DOSIMETRIC MEASUREMENTS
WITH CHARGED PARTICLE ENVIRONMENT
OF THE INNER VAN ALLEN BELT

Allen L. Thede and George E. Radke

Biophysics Branch, Air Force Weapons Laboratory
Kirtland AFB, New Mexico

The principal purpose of the radiation research satellite, OV3-4, was to make simultaneous radiobiological and physical measurements in the radiation environment of the Inner Van Allen Belt. This region of space presents the greatest area of interest to mission planners of manned space activity due mainly to the high energy proton component. Experiments which include simultaneous measurements of the dose rates as well as the particle spectra provide the opportunity to make a more accurate evaluation of the hazards of space radiation.

Measurements of depth dose rate were made by six specially designed tissue equivalent ionization chambers. These chambers were shielded with basic thicknesses of 0.192 gm/cm² aluminum, 0.797, 2.623, and 4.772 gm/cm² Lucite and 4.885 gm/cm² brass. The charged particle environment was determined by an omnidirectional proton and electron spectrometer using solid state detectors. Results of the proton spectral measurements for energies greater than 15 Mev are presented.

Calculated dose rates based on the proton spectral results have been successfully compared with the measured dose rates at points where the electron contribution is negligible. Predicted dose rates were also calculated using the Vette model environment. These values were compared with the measured values and found to be accurate only for thinly shielded chambers. Since the observed proton spectra was much harder than the Vette model, a serious undercalculation or prediction of dose rate resulted for shield thicknesses of greater than 1.0 gm/cm².

I. INTRODUCTION

The radiation research satellite, OV3-4, was launched on 10 June 1966 into an orbit with an inclination of 40.8°. The perigee and apogee were 350 and 2550 nautical miles respectively. The basic satellite was a right octagonal cylinder which was spin stabilized at 40 RPM.

The mission of this satellite was to make simultaneous measurements of the biophysical and physical parameters in the Inner Van Allen Belt. The biophysical measurements consisted of the dose rates behind various types and thicknesses of shielding. The physical charged particle environment was also sampled simultaneously to determine the proton and electron spectra. The region of the Inner Van Allen Belt represents the region of greatest interest to mission planners of manned space activities because of the high energy proton component.

Simultaneous experiments of the type described here will supply data with which to test the accuracy of present methods used to predict dose

rates to be encountered in the Earth's radiation belts. Accurate dose rate predictions are critically dependent on knowledge of the radiation environment, the shielding distribution surrounding the dose point and the radiation transport calculations. Simultaneous measurements will provide knowledge of the physical spectra and the resultant dose rate behind known shielding configurations. The data may then be used to evaluate the accuracy of the transport calculations.

This paper primarily includes results of initial reduction and correlation of the proton data obtained. The measured OV3-4 proton spectra for various points in space are used to calculate the proton component of the dose rate. These proton dose rates have been compared with measured dose rates where electron contributions are minimal. Measured dose rates behind the various shields are also compared with the predicted total dose rates based on the Vette model environment.¹ The Vette dose rates include both the electron and proton contributions.

II. DESCRIPTION OF EXPERIMENT

All experiments aboard this satellite were conceived and developed by the Biophysics Branch of the Air Force Weapons Laboratory (AFWL). Only two of the on-board experiments are discussed here. These experiments are the tissue equivalent ionization chambers and the omnidirectional proton and electron spectrometer.

The dose rates were measured by six tissue equivalent ionization chambers (TEICs). These were highly sensitive sensors made of a tissue equivalent plastic material mated to a unique magnetic amplifier system.² The sensor wall and cavity media simulates the response of muscle tissue to all ionizing radiation. The thickness of each chamber wall was approximately 0.236 gm/cm^2 of conductive tissue equivalent plastic. The sensors were filled with a tissue equivalent gas composed of methane, carbon dioxide and nitrogen. The tissue equivalent gas was necessary to retain the principle of tissue equivalency for heavy charged particles.³ The configuration of a typical chamber is shown in Figure 1.

The dynamic ranges of these instruments allow measurements of dose rates from 1.0 mrad/hr to 10,000 rad/hr for the various chambers. The specific range for each chamber is shown in Table I. The logarithmic response of the electrometer preamplifier, shown in Figure 1, is amplified to provide approximately five decades of dose rate measurement. The range of each sensor was based on the shielding material and thickness shown in Table I. All sensors were located outside of the actual spacecraft structure so that the majority of the shielding was provided by the basic spherical shields.

The spectral data discussed in this presentation were obtained from an omnidirectional spectrometer (OMNI) using solid state detectors.^{4,5} Two ORTEC silicon surface barrier solid state detectors were sandwiched back-to-back to achieve a nominal 2mm depletion depth for each sensor. Ten individual sensors were used in this experiment to sample the proton and electron spectra at all points in the orbit. Five sensors were used for proton detection and five for electrons. Each proton sensor was shielded with specific thicknesses of material as shown in Figure 2 and Table II. These thicknesses and the electronic discriminator bias established the principal energy range of sensitivity for each sensor.

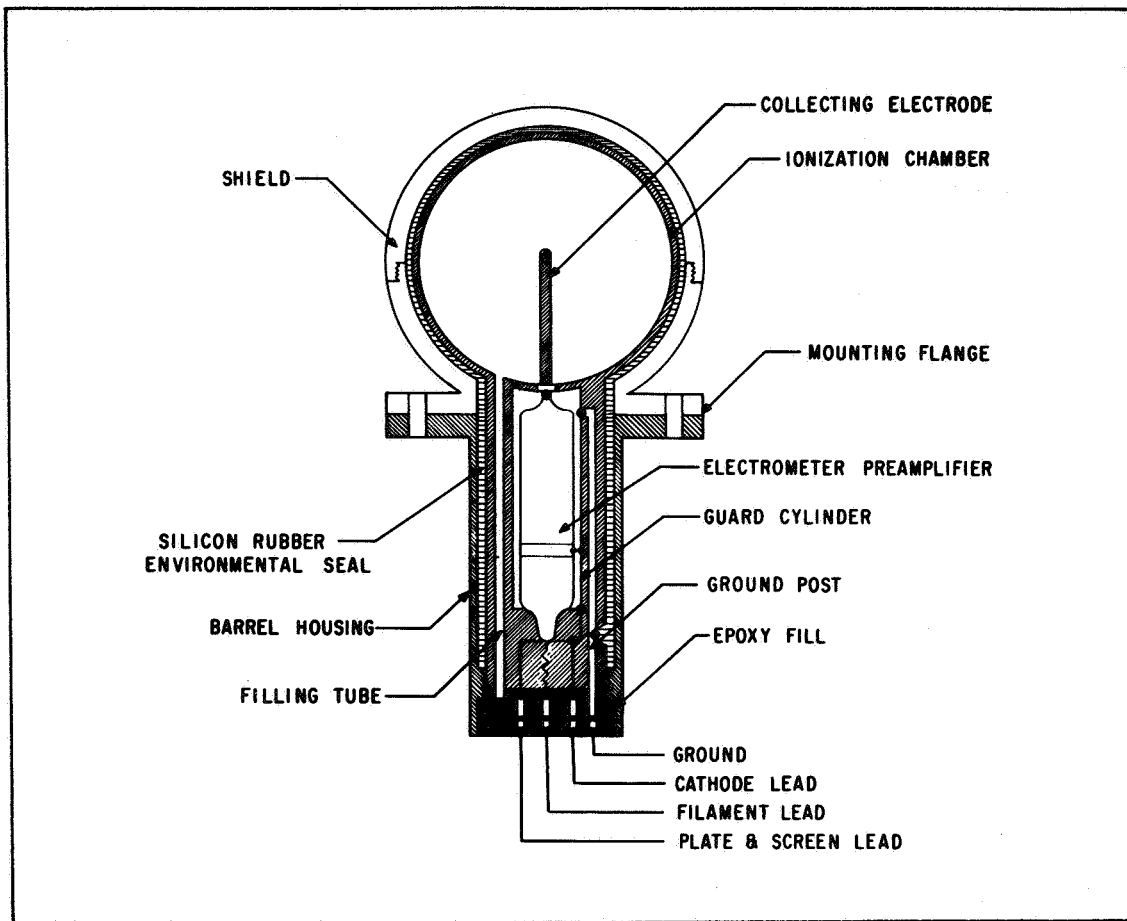


Figure 1. Typical Tissue Equivalent Ionization Chamber Construction

Table I. TEIC Characteristics

| TEIC No. | Volume (cc) | Dose Rate Range (Rad/hr) | Shield Description (gm/cm ²) | Proton Energy Threshold (Mev) |
|----------|----------------|-----------------------------|---|-------------------------------------|
| 1 | 5 | 0.100 - 10000 | 0.192 Aluminum | 17.5 |
| 2 | 25 | 0.010 - 1000 | 0.797 Lucite | 32.0 |
| 3 | 25 | 0.010 - 1000 | 2.623 Lucite | 57.5 |
| 4 | 25 | 0.001 - 100 | 4.485 Brass | 60.0 |
| 5 | 220 | 0.0001 - 10 | 0.192 Aluminum | 17.5 |
| 6 | 25 | 0.001 - 100 | 4.772 Lucite | 78.5 |

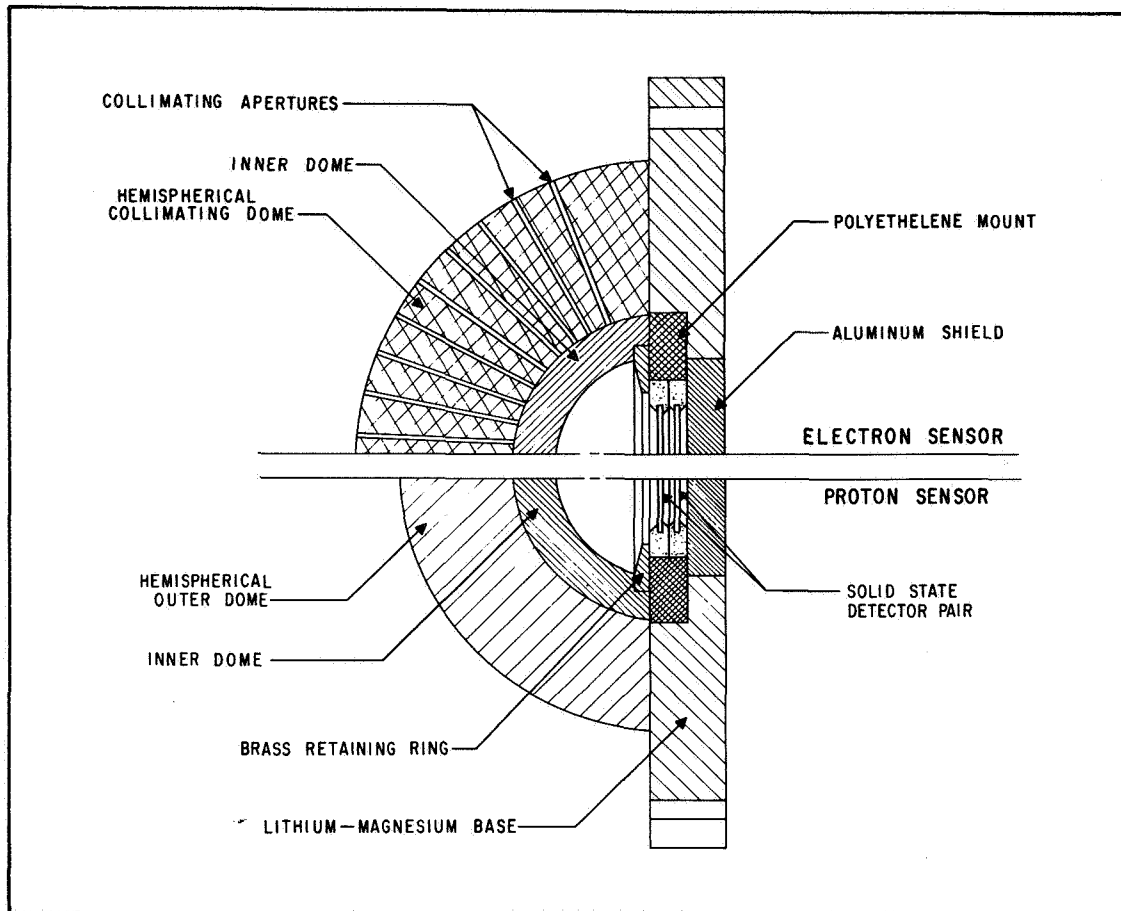


Figure 2. Typical Omnidirectional Spectrometer Sensor Construction

TABLE II. OMNI Characteristics

| Channel | Energy Range (Mev) | Dome Thickness (gm/cm ²) | | Discriminator Bias (Mev) |
|---------|-----------------------|--------------------------------------|------------|-----------------------------|
| | | Inner | Outer | |
| Prot A | 15 - 30 | 0.0017 Alum | 0.153 Poly | 9 |
| B | 30 - 55 | 0.0017 Alum | 0.798 Poly | 9 |
| C | 55 - 105 | 2.38 Copper | 1.000 Poly | 9 |
| D | 105 - 170 | 11.20 Copper | 1.000 Poly | 9 |
| E | >170 | 9.70 Copper | 2.000 Poly | 2 |
| Elec A | >0.1 | 0.0017 Alum | 1.61 Poly* | 0.1 |
| B | >0.4 | 0.0736 Poly | " " | 0.2 |
| C | >1.2 | 0.251 Poly | " " | 0.7 |
| D | >2.2 | 0.549 Poly | " " | 1.7 |
| E | >4.4 | 1.56 Poly | " " | 2.35 |

* With Collimating Apertures

The electron sensors were similar, except for the outer shielding domes which were provided with collimating holes to sufficiently reduce the count rates in the electron channels.

A triaxial magnetometer was provided on an 18-inch boom. These data were used primarily to determine the pitch angle orientation with respect to the magnetic field and were used in reduction of the OMNI data discussed in the next section.

III. METHOD OF ANALYSIS

The basic methods used in the analysis of the data from OV3-4 were as follows. The shielding distributions for the dose points (detector positions) of the satellite were determined using the NASA Manned Spacecraft Shield Thickness Calculation Program (BIOSEC).⁶ Basic cartesian coordinates were used to describe the most significant components of the structure in terms of basic geometric forms of hexahedrons, spheres, hemispheres, and cylinders. A total of 311 shields were used to describe the spacecraft in this manner.

The thickness distribution for a typical OMNI sensor (proton D), as determined by the sectoring process used in BIOSEC, is shown in Figure 3. This distribution illustrates the fractional portion of the total solid angle shielded by a thickness less than T , in gm/cm^2 aluminum equivalent material. Note that approximately 40% of the shielding is less than the basic 11.0 gm/cm^2 thickness due to the combined domes as indicated in Table II. This lower thickness region is viewed by the rear of the sensor. All of the OMNI sensors had approximately 30% of the total solid angle shielded by the thicknesses determined by the domes on the front. The overall response, however, depends very critically on the stopping power of the shielding in all directions.

The TEICs were shielded to a greater extent by the basic thicknesses shown in Table I. Four of the TEICs were located on the top corners of the cylindrical spacecraft and two were located on extended booms. The top mounted sensors (#1, #2, #4, and #5) had approximately 60% of the total solid angle shielded by its own spherical shield. In the case of the boom mounted TEICs, this value increased to 80%.

The thin OMNI detectors and shielding non-symmetry combined with the spacecraft spin rate and pitch angle distribution of particles created an oscillation in the data train. This oscillation was removed by application of suitable data reduction techniques for sinusoidal oscillatory data. The analysis of the OMNI data considered the shielding distributions, detector responses, environmental pitch angle distributions and other basic calibration data. These functions were used to generate overall response functions for all sensors.

A typical response function for the OMNI Channel D proton sensor is shown in Figure 4. It illustrates the response for a particular pitch angle distribution of particles and a single spacecraft orientation with the magnetic field line. A family of these responses have been generated for each sensor and were chosen for use accordingly. Note that this particular sensor responds significantly to protons having energies outside of the design range of 105 to 170 Mev. A higher response is apparent, however, in that range. All proton sensors respond to energies outside of their design

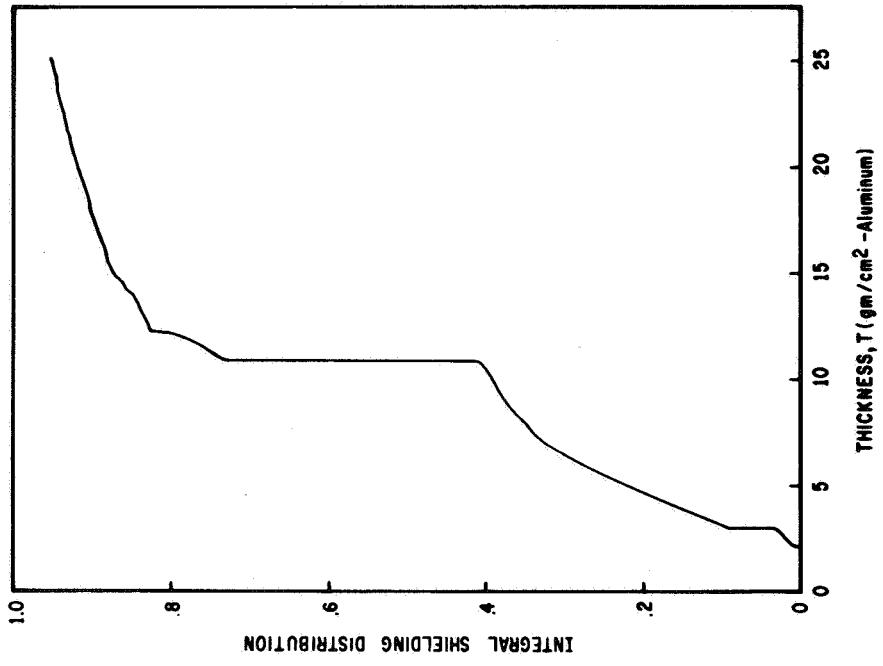


Figure 3. Fraction of Total Solid Angle Shielded by a Thickness less than T for the Proton D OMNI Sensor.

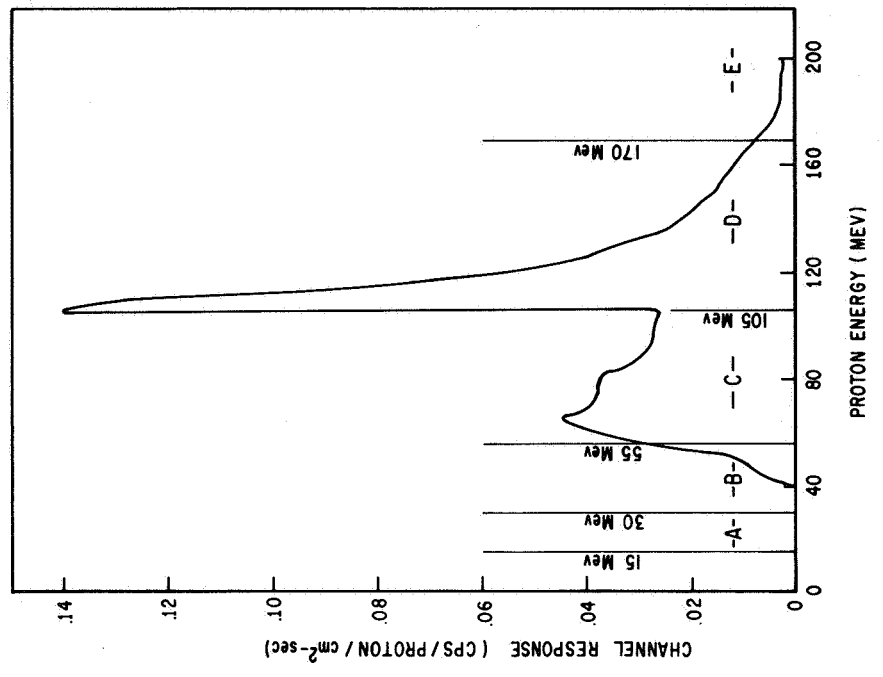


Figure 4. Typical Channel D Proton Response per Unit Incident Proton Flux.

ranges, so that it was necessary to divide the functions into separate sub-intervals indicated in Figure 4. Each of the subintervals correspond to the "high-response" range of a particular sensor.

The OMNI proton data were reduced by simultaneous correlation of all channels of data. The total response of any one channel or sensor is made up of partial responses of several subintervals throughout the energy range. This total response (CR_i) of any one channel may be defined analytically as

$$CR_i = \sum_{j=1}^5 r_{ij} (A_j - A_{j+1}) \quad (1)$$

where r_{ij} = effective response of the i th channel to protons in the j th energy subinterval (CPS/proton/cm² - sec)

$A_j - A_{j+1}$ = total omnidirectional flux in the j th subinterval (Protons/cm²-sec)

The integral omnidirectional proton spectra were defined during the analysis, for each energy subinterval, by the relation

$$\phi_j(E) = A_j e^{-\frac{(E - E_j)}{E_{oj}}} \quad (2)$$

where A_j = omnidirectional flux for energies greater than the lower energy E_j of the subinterval (protons/cm² - sec)

E_{oj} = exponential parameter determining the spectral shape of the integral flux in the j th subinterval (Mev)

An initial spectral shape was assumed to be represented by the first set of five OMNI proton responses. This spectral shape was based on a set of arbitrary E_{oj} values. Effective subinterval responses r_{ij} were generated, based on the spacecraft pitch angle and spectral shape. A set of five equations of the form shown in Equation 1 was therefore defined. The variables in these equations were the total omnidirectional fluxes in the subintervals and were determined by simultaneous solution of the five equations. The initial solution defined a new spectral shape, and the process was repeated until an insignificant change was noted in the spectrum. This spectral shape was then used to initialize the iteration for the next point in space to be processed.

Dose rates were calculated using the measured omnidirectional proton spectra. The calculational process was developed from the relation

$$DR = K \int_{E_{in}=0}^{\infty} \phi'(E_{in}) L(E_{in}) dE_{in} \quad (3)$$

where $\phi'(E_{in})$ = transmitted differential proton spectrum (protons/cm²-sec-Mev)

$L(E_{in})$ = linear energy transfer in tissue (Mev-cm²/gm-proton)

E_{in} = transmitted energy at the dose point (Mev)

K = factor converting the dose rate into rad/hr.

This formula cannot be used directly, however, because $\phi'(E_{in})$ is not immediately known. If we let E_{ex} be the external energy needed by a proton to penetrate to the dose point with an energy of E_{in} , then, for a given shielding distribution, E_{ex} can be computed from E_{in} , or vice versa. In the computations, E_{in} and $L(E_{in})$ were determined from E_{ex} using the range energy and stopping power tables of Janni.⁷ If nuclear interactions are neglected, conservation of protons gives the relation

$$\phi'(E_{in}) dE_{in} = \phi(E_{ex}) dE_{ex} \quad (4)$$

where $\phi(E_{ex})$ is the external differential proton spectrum. By direct substitution of (4) into (3), we get

$$DR = \int_{E_{in}=0}^{\infty} \phi(E_{ex}) L(E_{in}) dE_{ex} \quad (5)$$

which is the relation actually used in the calculations.

Total dose rates were also calculated using the AFWL Space Radiation Shielding Codes.⁸ These calculated dose rates were based on the Vette model environment and included both proton and electron components. The shielding description of each dose point was also used in these calculations.

IV. PRESENTATION OF DATA

Unless otherwise indicated, the data will be presented with respect to the earth's magnetic field, B, and the McIlwain parameter, L.⁹ The spectra which have been determined from the OMNI measurements are presented in the form of integral profiles shown in Figures 5 through 7 for the magnetic shell parameters of L = 1.5, 1.7, and 2.0 earth radii respectively. Each curve represents the free space integral omnidirectional flux above the reference energy indicated. The Vette model spectra is shown for comparison purposes and will be referred to in the following discussion of the data results.

The comparison between the OV3-4 and Vette fluxes above 15 Mev is good for the values of L shown. Note the trend to higher measured values at the higher values of B. The profiles representing energies greater than 30 Mev are somewhat lower in magnitude than the Vette model but compare favorably for low values of B. The greater hardness of the measured spectra for all values of L is obvious when comparisons are made for energies greater than 50 Mev. Spectral softening may be noticed as the value of L increases.

The accuracy of the OMNI proton fluxes is variable and depends on the energy point of the spectra. The absolute error of the integral proton

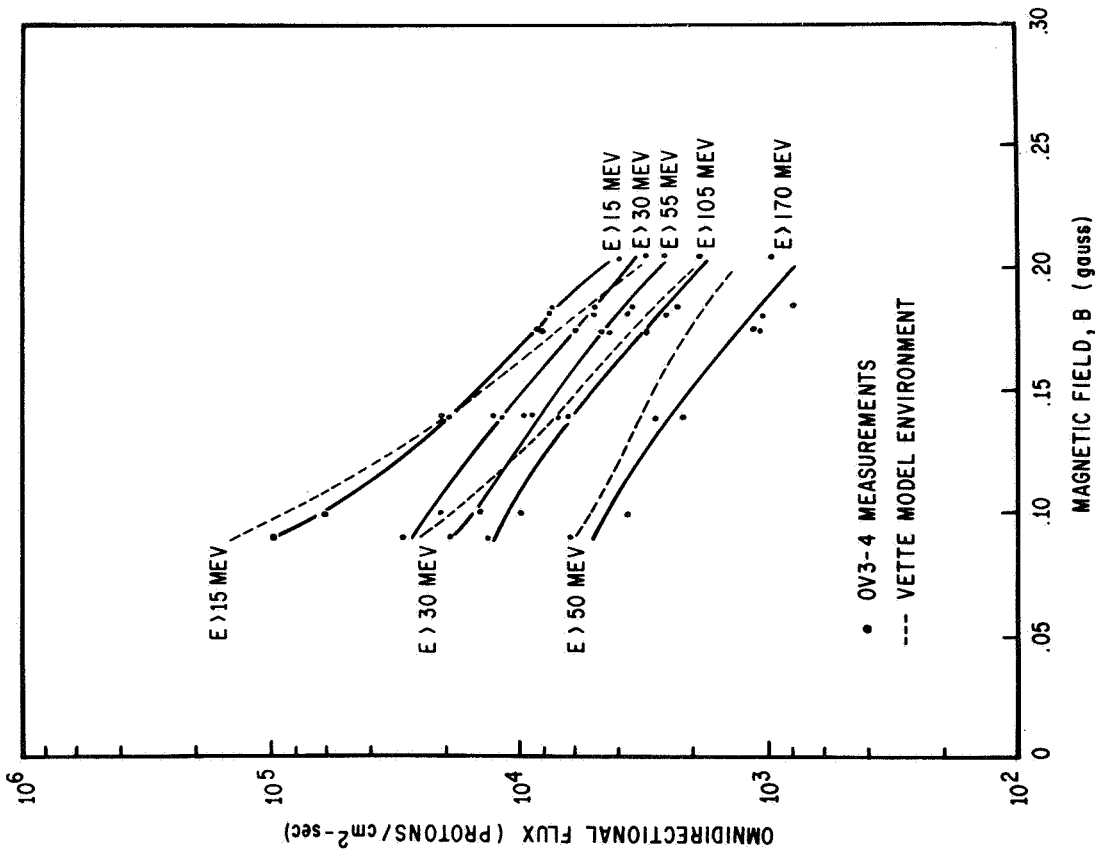


Figure 5. Integral Omnidirectional Proton Flux Profiles as a Function of the Magnetic Field B for Shell Parameter L = 1.5.

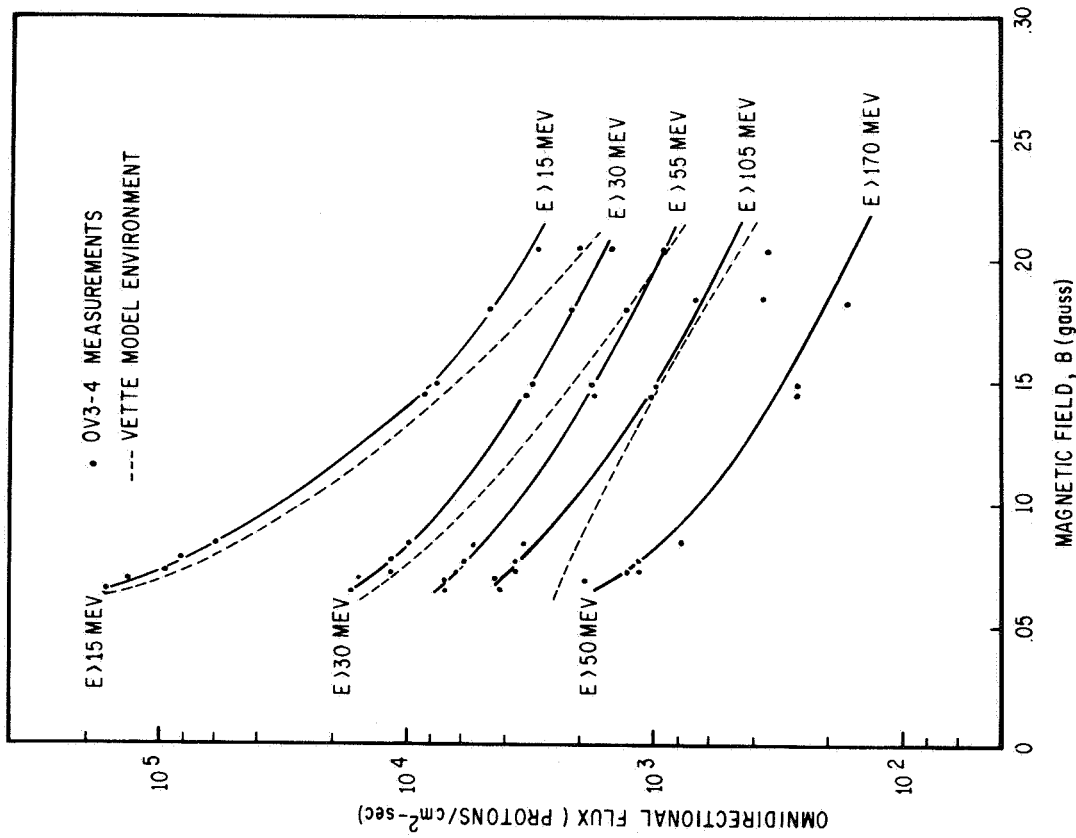


Figure 6. Integral Omnidirectional Proton Flux Profiles as a Function of the Magnetic Field B for Shell Parameter L = 1.7.

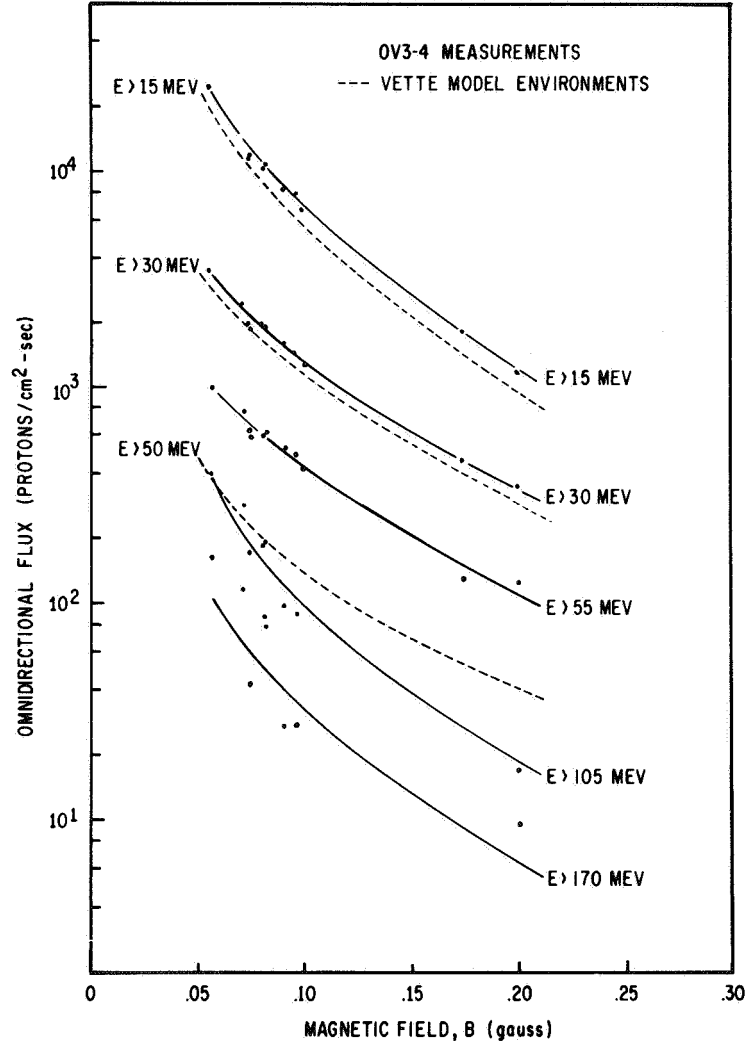


Figure 7. Integral Omnidirectional Proton Flux Profiles as a Function of the Magnetic Field B for Shell Parameter $L = 2.0$.

measurements for energies greater than 15 Mev is between $\pm 10\%$ and $\pm 30\%$. These errors are dependent on the point in space and the condition of the raw data used.

Table III indicates the comparison of the measured and calculated components of the total dose rates for various selected points in (B,L) space. The calculated proton and electron dose rates were obtained using both the Vette model environment and the OMNI spectral measurements. The electron spectral values used for the OMNI electron dose calculations are preliminary only. The total calculated dose rates are also included for the comparison with the TEIC experimental measurements.

Table III. Comparison of Calculated Proton and Electron Dose Rates Using the Vette and OMNI Spectra

| L (Earth Radii) | B (Gauss) | TEIC No. | CALCULATED PROTON DOSE RATE (Rad/hr) | | CALCULATED ELECTRON DOSE RATE (Rad/hr) | | TOTAL DOSE RATE (Rad/hr) | | |
|-----------------|-----------|----------|--------------------------------------|------|--|-------|--------------------------|-------|--------------|
| | | | VETTE | OMNI | VETTE | OMNI* | CALCULATED | | EXPERIMENTAL |
| | | | | | | | VETTE | OMNI* | TEIC |
| 1.3 | .168 | 1 | 9.30 | 7.00 | 130. | 152. | 139. | 159. | 180. |
| | | 2 | 3.80 | 5.00 | 37.0 | 28.9 | 40.8 | 33.9 | 22.7 |
| | | 3 | .852 | 2.72 | 1.30 | .670 | 2.15 | 3.39 | 4.80 |
| | | 4 | .780 | 2.85 | .130 | .150 | .910 | 3.00 | 3.42 |
| 1.5 | .092 | 1 | 130. | 88.0 | 350. | 340. | 480. | 428. | 500. |
| | | 2 | 32.0 | 19.3 | 78.0 | 44.2 | 110. | 63.5 | 80.0 |
| | | 3 | 2.19 | 8.96 | 1.45 | .490 | 3.64 | 9.45 | 16.5 |
| | | 4 | 2.02 | 8.50 | .350 | .340 | 2.37 | 8.84 | 15.0 |
| 1.5 | .175 | 1 | 5.30 | 5.80 | 44.0 | 24.0 | 49.3 | 29.8 | 35.0 |
| | | 2 | 3.00 | 3.60 | 10.0 | 3.08 | 13.0 | 6.68 | 6.38 |
| | | 3 | 1.27 | 2.25 | .188 | .035 | 1.46 | 2.29 | 3.00 |
| | | 4 | 1.15 | 2.10 | .044 | .024 | 1.19 | 2.12 | 2.61 |
| 1.7 | .064 | 1 | 120. | 165. | 31.0 | 15.0 | 151. | 180. | 125. |
| | | 2 | 20.0 | 23.0 | 6.30 | 1.49 | 26.3 | 24.5 | 17.0 |
| | | 3 | 1.26 | 8.40 | .087 | .016 | 1.35 | 8.42 | 8.40 |
| | | 4 | 1.17 | 3.70 | .031 | .015 | 1.20 | 3.72 | 5.36 |
| 1.7 | .178 | 1 | 2.95 | 4.00 | 1.45 | .750 | 4.40 | 4.75 | 4.70 |
| | | 2 | 1.27 | 2.40 | .275 | .074 | 1.53 | 2.47 | 1.70 |
| | | 3 | .456 | 1.00 | .004 | .001 | .460 | 1.00 | 1.25 |
| | | 4 | .410 | .740 | .001 | ---- | .411 | .740 | .670 |
| 2.0 | .056 | 1 | 18.0 | 25.0 | .790 | .221 | 18.8 | 25.2 | 21.0 |
| | | 2 | 4.40 | 3.40 | .270 | .020 | 4.66 | 3.42 | 2.76 |
| | | 3 | .250 | 1.30 | .015 | ---- | .265 | 1.30 | 1.20 |
| | | 4 | .212 | .620 | ---- | ---- | .212 | .620 | .670 |
| 2.0 | .174 | 1 | 1.65 | 1.85 | .040 | .091 | 1.69 | 1.94 | 2.40 |
| | | 2 | .600 | .480 | .014 | .008 | .614 | .488 | .638 |
| | | 3 | .035 | .280 | .001 | ---- | .036 | .280 | .235 |
| | | 4 | .029 | .115 | ---- | ---- | .029 | .115 | .147 |

* The OMNI electron dose rates are based on preliminary electron spectra and are included for preliminary consideration only.

Figures 8 through 11 present the correlation of measured dose rates as indicated by four of the shielded TEICs and the calculated dose rates based on the simultaneous spectral measurements. Also shown are the predicted dose rates for the same L shell values using the Vette model environment. The dose rates measured by TEICs #3 and #4 are primarily due to the penetrating component of the high energy proton environment with a small percentage of Bremsstrahlung production due to the incident electron flux. The greater contribution to dose rate is produced by the proton environment in all chambers for L values between 1.7 and 2.5 earth radii.

The TEIC measurements are subject to a maximum error of $\pm 25\%$. The accuracy of calculated dose rates using the OMNI spectra are limited to that of the spectra used as well as the spectral energy range dominating the dose conversion process. These calculations are also dependent on the accuracy of the sectoring analysis performed. Radiation transport theory was the most accurately known and introduced no appreciable error. The calculations of proton doses for the TEIC #1 shielding configuration are between $\pm 10\%$ and $\pm 30\%$.

Referring to Figures 5 through 7, it was noted that the OMNI proton spectra was harder than that indicated by Vette, especially for energies greater than 50 Mev. Accordingly, higher dose rate measurements by TEIC #3 and TEIC #4 are to be expected and were actually observed. Vette calculated dose rates are low by a factor of 7 for some areas of space covered by this satellite. The OMNI calculated dose rates for these more heavily shielded chambers are consistent with the actual measured values.

The dose rates behind the thin shields are dependent primarily on the magnitude of the integral flux above their lower energy thresholds rather than the spectral shape. In general, the dose rates calculated for TEIC #1 using the Vette spectra accurately represents the measured values. This is reasonable since the Vette low energy proton fluxes compare favorably with the OMNI measurements.

The calculations using the Vette model environment for TEIC #2 are somewhat higher than would be expected when the OMNI and Vette spectra are compared. Although the comparison is not significantly outside the error limits established, it is an interesting observation and requires some explanation. In both cases the method of defining the integral spectra with exponential fits of subintervals introduces some discontinuities in the differential spectra. The severity of this discontinuity depends on the slopes of the spectral subintervals.

Since the lower energy thresholds of TEIC #2 and TEIC #4, for example, are near the points of discontinuity (30 Mev and 55 Mev respectively) the effective error is more critical. The shape of typical spectra, in general, would cause an over-calculation for TEIC #2 and an under-calculation for TEIC #4. The discontinuities exist in the OMNI calculations of the dose rate but are not as severe as for the Vette values, due to the greater spectral hardness of the OMNI spectra.

In general, the correlation of the OMNI calculated dose rates and TEIC measurements manifests itself in the profiles of Figures 8 through 11. The comparison is equally good for all values of B. This basic correlation indicates internal consistency of the spectrometric and dosimetric measurements. Greater validity may be associated with the spectral shapes since the calculated dose rates for the various chambers depend on different components of the spectral range.

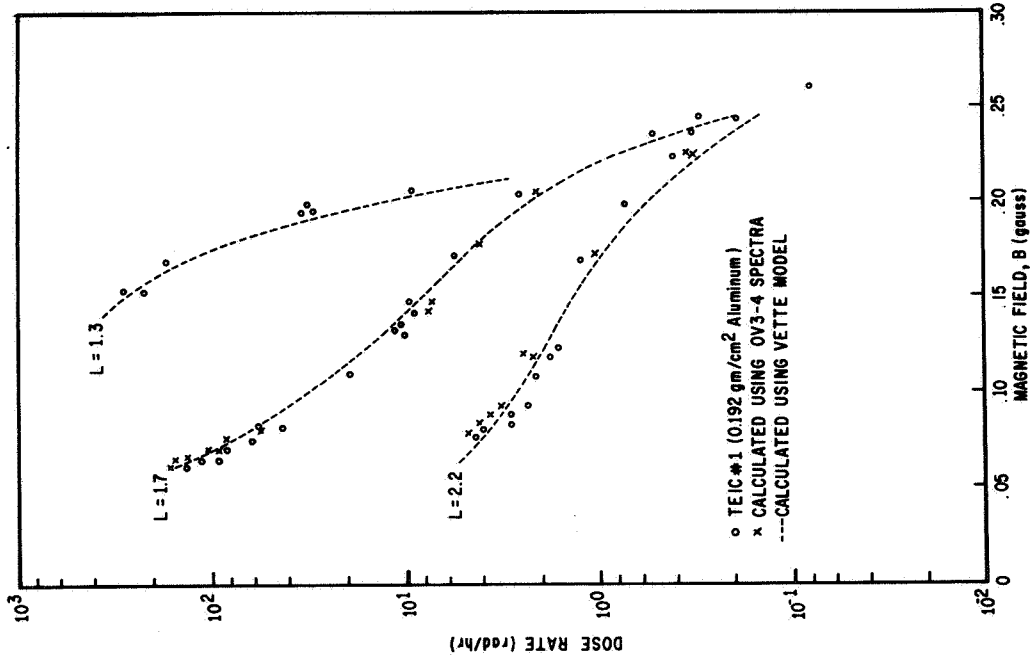
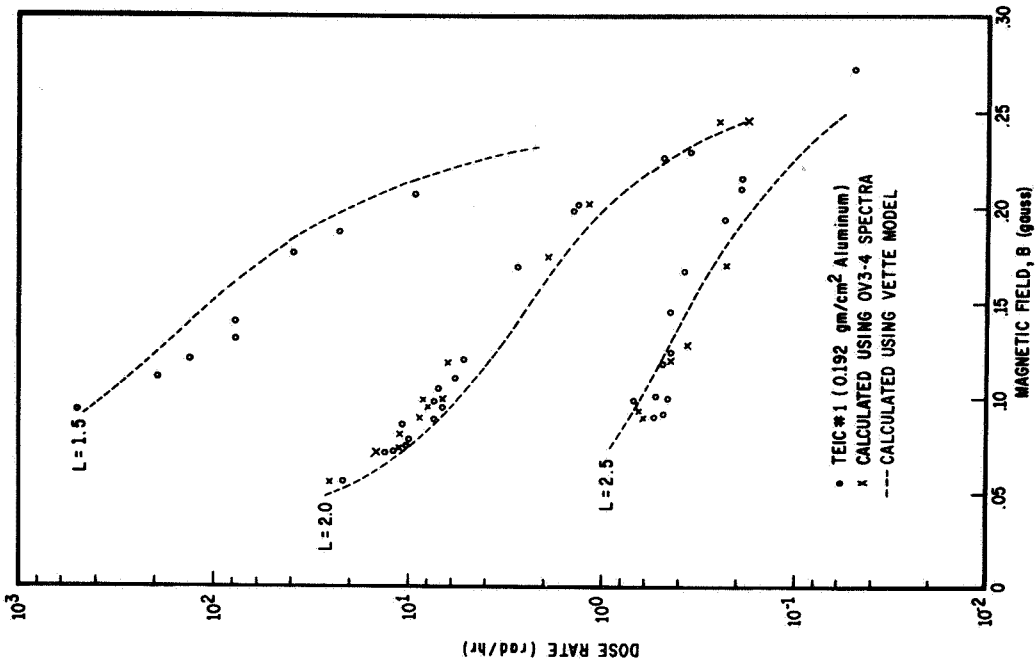


Figure 8. Correlation of Dose Rate Profiles for TEIC #1 as a Function of the Magnetic Field B and Shell Parameter L.

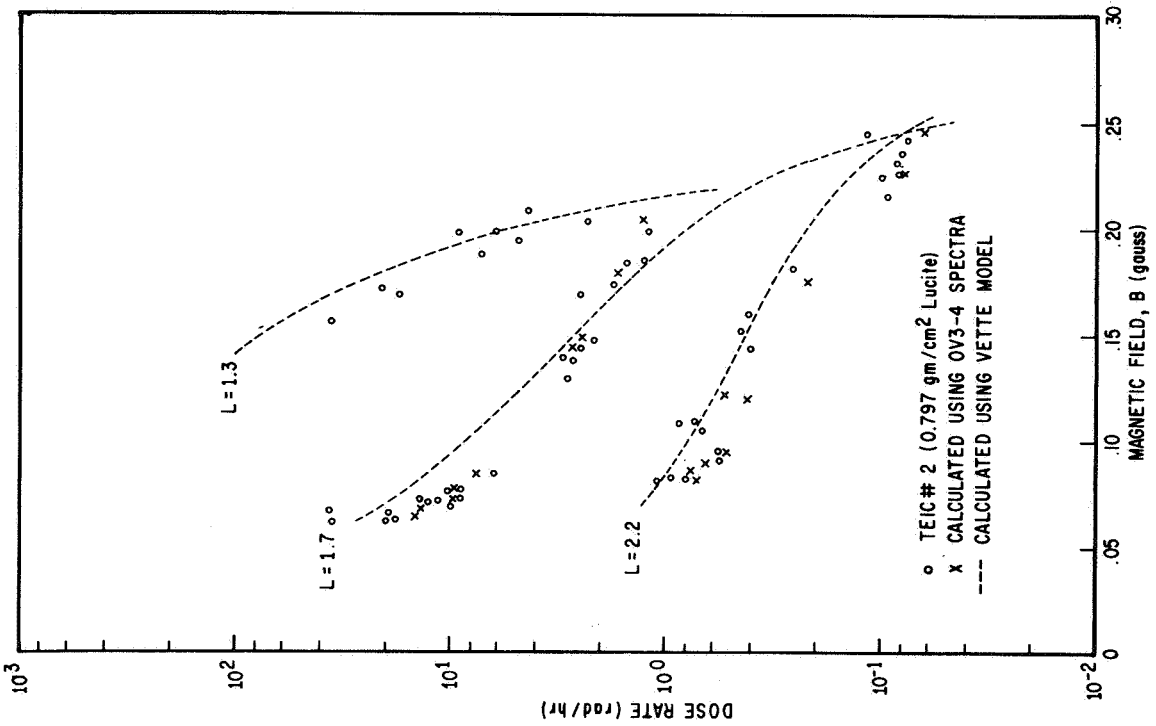
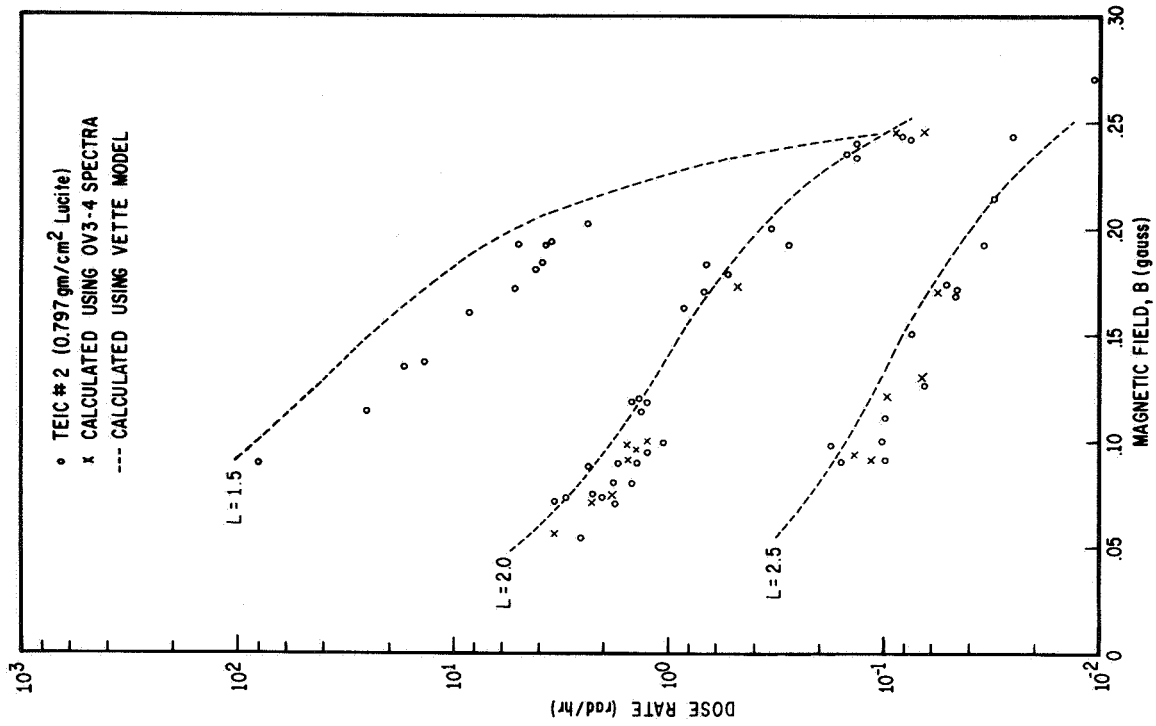


Figure 9. Correlation of Dose Rate Profiles for TEIC #2 as a Function of the Magnetic Field B and Shell Parameter L.

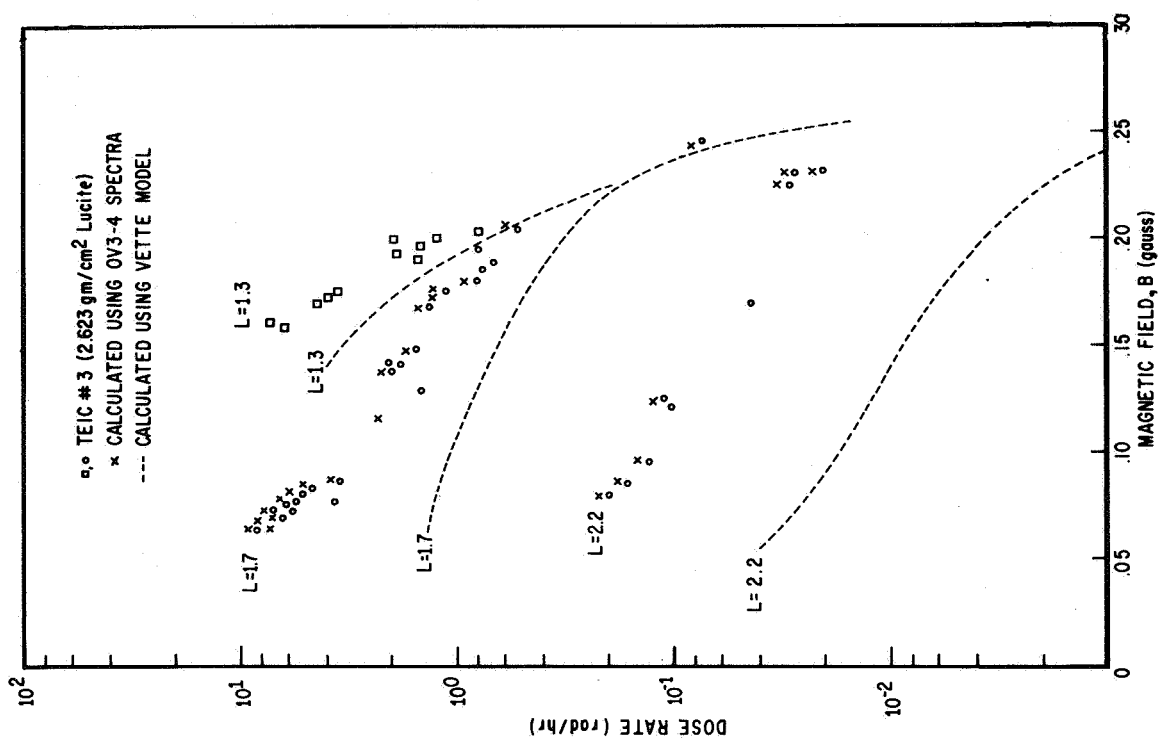
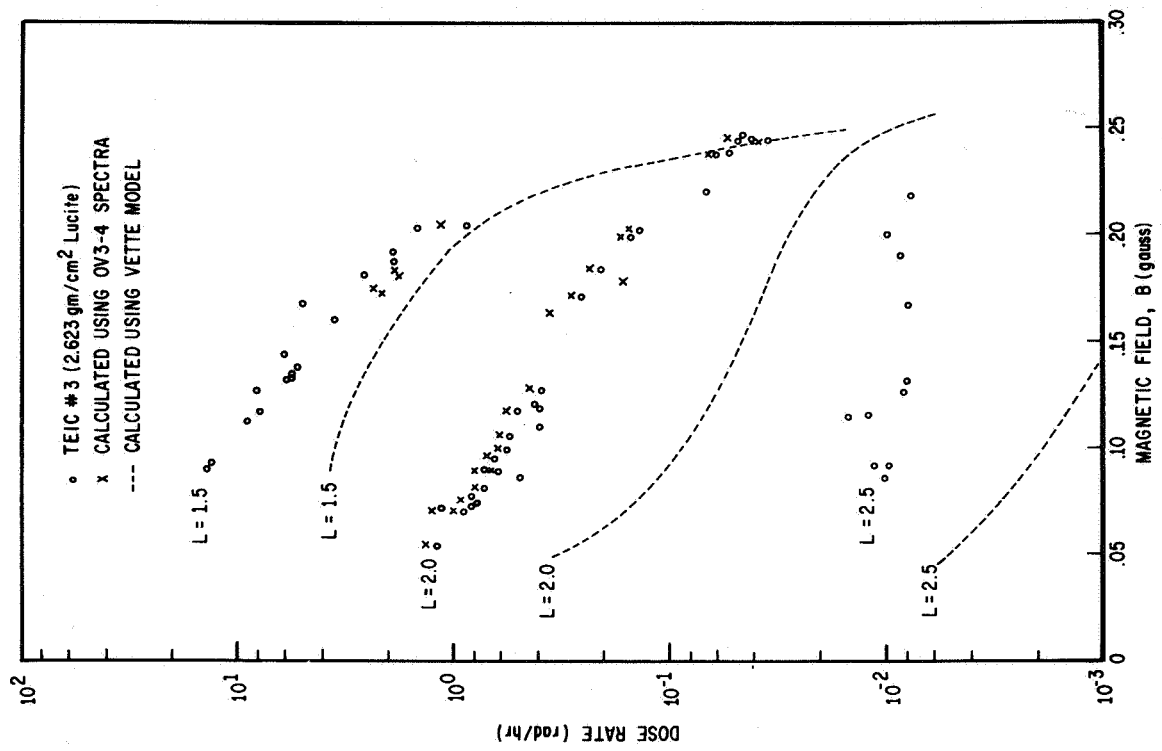


Figure 10. Correlation of Dose Rate Profiles for TEIC #3 as a Function of the Magnetic Field B and Shell Parameter L.

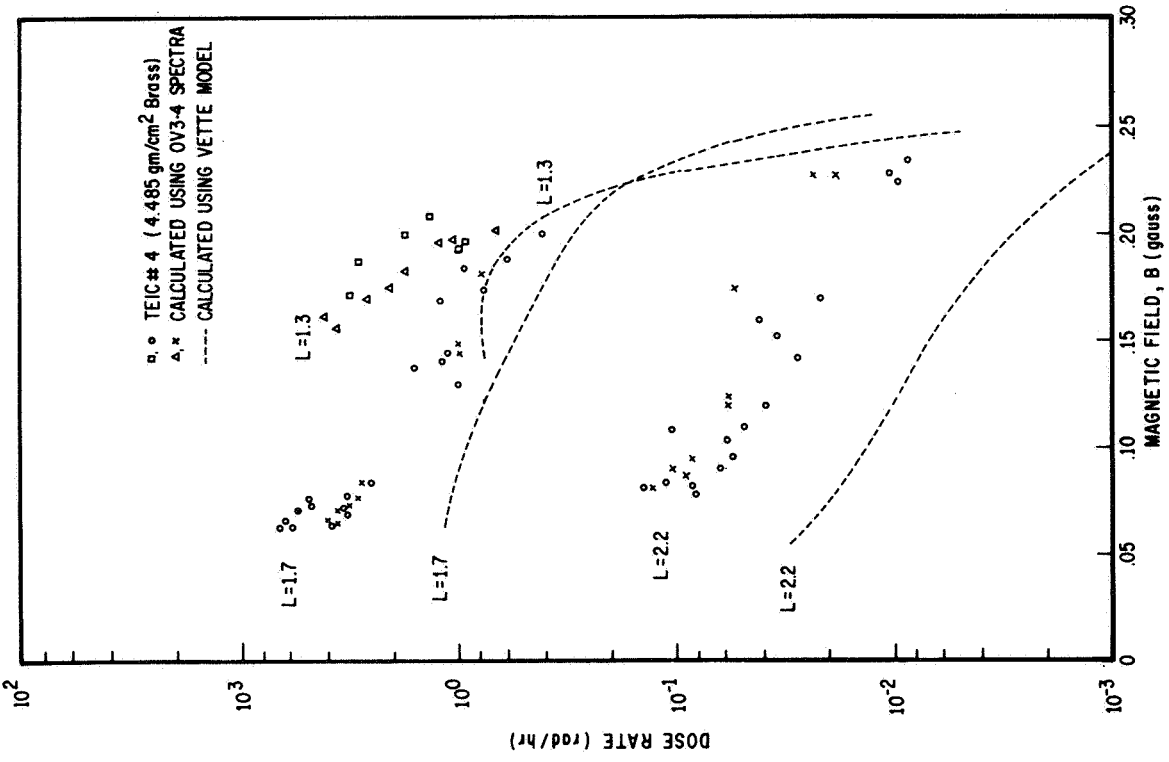
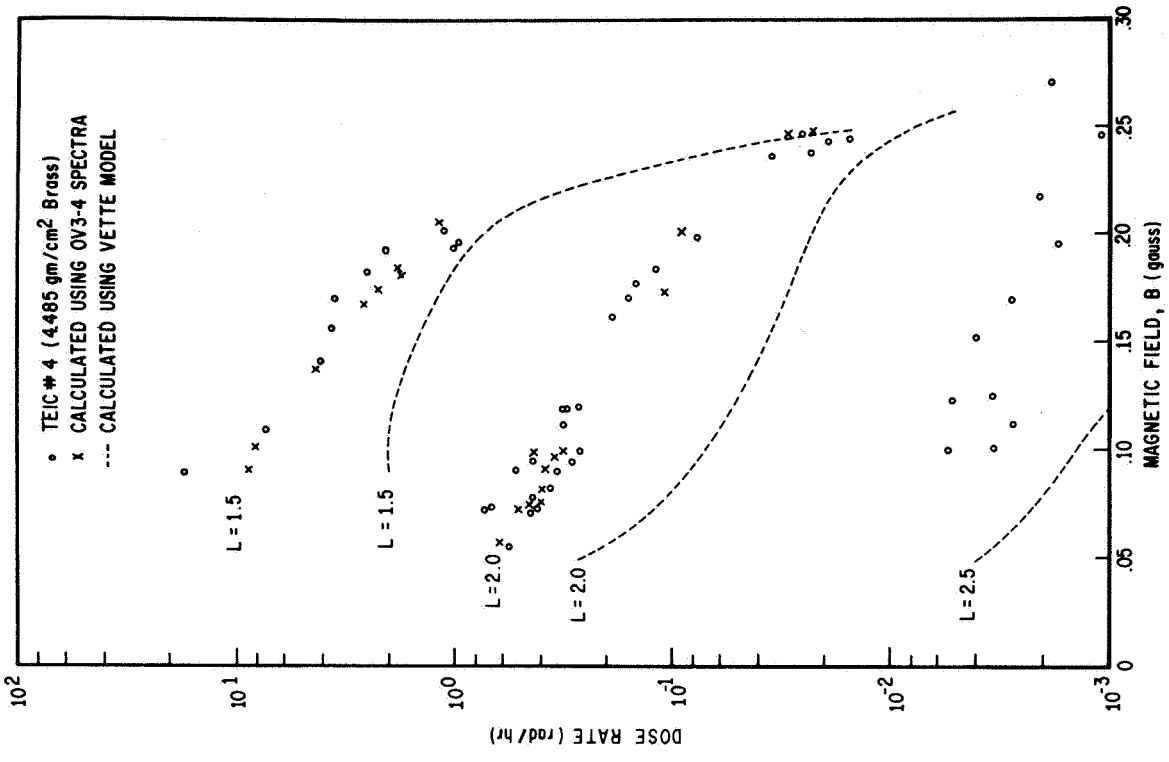


Figure 11. Correlation of Dose Rate Profiles for TEIC #4 as a Function of the Magnetic Field B and Shell Parameter L.

V. CONCLUSIONS

The conclusions and recommendations to be made from the data and the results presented are several in number. Favorable consideration must be given to the experimental philosophy and the dosimetric instrumentation. A more accurate environmental description in the form of spectral data must be provided for use within dose prediction programs.

It has been shown that simultaneous measurements of biophysical and physical parameters is a valid philosophy in the assessment of radiation hazards in space. This is illustrated by the data presented and the correlation success. The correlation consistency further validates the spectral measurements. The results of final data analysis will increase the confidence in the radiation transport techniques used in the prediction programs being developed.

The dosimetry instrumentation which has been used in this experiment has demonstrated the validity of the technique of measuring dose rate in a charged particle environment. This type of dosimetry has proven its value and is worthy of forming the basis of a radiation monitoring system aboard future manned spacecraft.

The dose calculations based on the Vette model environment compared favorably with the measured dose for the thin shielding of less than 1.0 gm/cm^2 . Dose calculations for the heavier shielded ionization chambers, however, were sometimes a factor of 10 too low. Since the proton cutoff energies for TEICs #3 and #4 are above 50 Mev as shown in Table II, this discrepancy is probably due to the uncertainty in the description of the model environment for the higher spectral energies.

A typical manned spacecraft provides a large amount of shielding in excess of 1.0 gm/cm^2 , with a smaller amount less than this thickness. The predictions of skin and eye dose (surface dose) depend to a great extent upon the lower energy protons which can penetrate the thin shielding. The vital organs and bone marrow, however, are generally shielded by at least 2.5 gm/cm^2 of tissue in addition to the spacecraft structure. This added body self shielding will stop protons with energies less than 50 Mev making higher energy protons the dominant hazard to the internal organs. The dose calculations for the internal organs will be in more serious error than those made for surface doses. These facts emphasize the need for a more accurate description of the trapped high energy proton environment.

Acknowledgements

The authors wish to express thanks to F.E. Holly, Audrey Kirkpatrick, J.F. Janni and R.S. Case for their valuable contributions and assistance given in the experimental phases and data analysis processes.

REFERENCES

1. Vette, J.K., "Models of the Trapped Radiation Environment", NASA-SP-3024, National Aeronautics and Space Administration, 1966
2. Schneider, M.F., "Advanced Spaceborne Dosimetry Instrumentation", WL-TDR-64-96, AF Weapons Laboratory, December 1965
3. Schneider, M.F., "Calibration of Dose Measuring Ionization Chambers Using High Energy Proton Beams", WL-TR-66-30, AF Weapons Laboratory, 1967
4. Burton, B.S., "Design and Construction of an Electron-Proton Spectrometer", AFWL-TR-65-186, AF Weapons Laboratory, August 1966
5. Hall, B.C., "Electronics Development for Space Research Applications", AFWL-TR-65-123, AF Weapons Laboratory, March 1966
6. Malone, C.F., "Program L015, Shield Thickness Calculation Program (BIOSEC), Volume I - Computer Program Users Manual", National Aeronautics and Space Administration, 14 May 1965
7. Janni, J.F., "Calculations of Energy Loss, Range, Pathlength, Straggling, Multiple Scattering, and Probability of Inelastic Nuclear Collisions for 0.1 to 1000 Mev Protons", AFWL-TR-65-150, AF Weapons Laboratory, September 1966
8. Barton, J.A., Mar, B.W., et al., "Computer Codes for Space Radiation Environment and Shielding", WL-TR-64-71, Vol. I, August 1964
9. McIlwain, C.E., "Coordinates for Mapping the Distribution of Magnetically Trapped Particles", Journal of Geophysical Research, 66, p. 3681, 1961

THE PLASMA RADIATION SHIELD: CONCEPT, AND
APPLICATIONS TO SPACE VEHICLES*

by

Richard H. Levy, Francis W. French**
Avco Everett Research Laboratory

The Plasma Radiation Shield is an active device using free electrons electric and magnetic fields for the purpose of shielding astronauts from energetic solar flare-produced protons. The concept of Plasma Radiation Shielding is reviewed in the light of current studies. The available evidence indicates that the concept is physically sound, but important practical questions remain in at least two areas: these have to do with establishment and control of the extremely high voltages required, and with integration of the concept into a realistic space vehicle design.

*This work was supported by National Aeronautics and Space Administration, George C. Marshall Space Flight Center, under Contract NAS8-20310.

**Senior Consultant Engineer, Avco Space Systems Division, Lowell, Mass.

1. PREFACE

The Plasma Radiation Shield is an active device intended to protect astronauts on long missions in deep space from the penetrating proton radiation that follows large solar flares. The nature of the Plasma Radiation Shield is such that it is not by any means certain that it will be successful. However, if it is successful, it offers the prospect of radiation shielding at a comparatively low cost in weight, provided that certain features of the device prove to be compatible with broader aspects of the space mission profile. Research on the Plasma Radiation Shielding principle, although far from finished, has yielded encouraging results to the point that it seems worthwhile to consider in a preliminary way the broader problems that must be dealt with if the concept is to be useful in a practical sense. In this context, the present paper is intended to accomplish the following objectives:

1. To explain the fundamentals of the Plasma Radiation Shielding concept;
2. To outline the present status of research on basic aspects of the concept, with particular emphasis on the uncertainties still to be resolved;
3. To extract from the above a list of possible problem areas likely to arise in integrating the Plasma Radiation Shield with a realistic spacecraft design;
4. To discuss these problem areas in general terms, quantitatively where possible. These discussions are viewed as being essentially preliminary to a more thorough systems type study.

The organization of this paper is as follows: In Section 2 we give a very brief summary of the nature of the space radiation shielding problem. This summary points to the desirability of finding unconventional light-weight shielding methods. We discuss electrostatic and magnetic shielding, and conclude that neither of these schemes looks promising. This leaves the Plasma Radiation Shield as the only advanced shielding concept still in the

running; the basic principles of the Plasma Radiation Shield are thoroughly discussed in Section 3. The two basic design parameters in the Plasma Radiation Shield are the size and the voltage. The size is determined by such straightforward factors as the crew size, and compatibility with launch vehicles. The determination of the voltage is more complicated, and is the subject of Section 4. We conclude that the range from 30-60 million volts is likely to be of interest. The following sections (5 through 8) take up particular problems of importance in adapting the Plasma Radiation Shield concept to a space vehicle. These are, respectively, restrictions on the configuration, the superconducting coils, the vacuum requirements, and other miscellaneous problems. Section 9 offers our conclusions from the study; these are principally that we have succeeded in isolating the most difficult practical problems associated with the Plasma Radiation Shield, that these problems appear difficult but not insuperable, and that studies in greater depth are definitely required before firmer conclusions about the merits of the Plasma Radiation Shield can be reached. An appendix discusses the present status of research on the physics of the underlying concept. Here again, in spite of favorable initial results, much work remains to be done.

2. SPACE RADIATION SHIELDING

Manned space vehicles outside the geomagnetic field on lunar and interplanetary missions are subjected to the hazards of the unattenuated space radiation environment. Of the two principal components of this environment,* the galactic and the solar flare radiations, the latter is generally considered the more important because of the large fluxes associated with it.** The solar flare radiation hazard is compounded on long duration missions because of the integrated effects of the doses received over the extended mission. Vehicles orbiting the earth at high (e. g., synchronous) altitudes are subjected to much the same environmental components as well as to the protons and electrons associated with the outer edges of the trapped radiation belts. Since inadequate radiation protection can result in absorbed doses that cause discomfort, illness, and even (in extreme cases) death to the crew, it is apparent that provisions must be made to limit the anticipated radiation doses to acceptable levels.

There is a wide variation in opinion (e. g., Refs. 1 to 30) concerning the degree of hazard posed to astronauts by solar flares. This lack of agreement can be attributed to two factors. First, adequate quantitative data on the space radiation environment has only been obtained through one

* We restrict ourselves to considering the radiation hazard due to naturally occurring charged particles. On the one hand, the dangerous portion of the solar electromagnetic radiation spectrum (principally the far UV) is easily screened; on the other hand, there is no appreciable component of neutron radiation present in space.

** This is a fortunate accident, because the energies of the galactic radiation are so large that shielding against them is an order of magnitude more demanding than in the case of solar flares, and, for practical purposes, can be considered essentially impossible. Astronauts in the foreseeable future will have to live with the galactic radiation; this situation is not ideal, but, in quantitative terms, is probably acceptable.

solar cycle. This data suggests that it will be very difficult to make a useful art out of forecasting the occurrence of major flares. Further, the wide range in intensity of different flares makes it difficult to predict the confidence levels appropriate to the more intense flares. Thus, postulation of radiation conditions to be encountered on future flights based on this modest experience is questionable. Second, information on the response of the human body to the type of radiations encountered in space is limited. This deficiency is due to the lack of experience with a natural source of protons on earth, difficulties in simulating the fluxes of high energy particles in the laboratory, and humanistic considerations which preclude the use of human subjects for hazardous experiments.

The simplest method of providing radiation protection is to use bulk shielding material to stop the incident radiations. For solar flare protons and alpha particles, the most appropriate materials have low atomic numbers (e.g., water, polyethylene). For long-duration missions, the amount of shielding required can be reduced if the recovery capacity of the human body is taken into consideration. However, there are many uncertainties involved in formulating a radiation tolerance criterion on this basis,^{27, 31} and the shielding requirements, while reduced, are still substantial. As an example, the amounts of polyethylene shielding required on a two-year Martian mission are given in Ref. 27 to be 17 gm/cm^2 using a cumulative dose criterion and 7 gm/cm^2 using a criterion that takes into account biological recovery. On the other hand, much larger figures have recently been suggested,^{26, 31} depending on the desired probability of not exceeding some stated dose and the phase of the solar cycle. Some of these figures are given in Table 2.1.

If it is desired to completely shield a cylindrical vehicle 15 ft ($\sim 4.6 \text{ m}$) in diameter by 25 ft ($\sim 7.6 \text{ m}$) long with 7 gm/cm^2 of material, the shielding material would weigh about 22,000 lbs ($\sim 10,000 \text{ kg}$). An alternate procedure to shielding the entire vehicle is to shield only a minimum-size storm cellar to which the crew can retire in the event of severe solar flares. This approach, however, severely restricts the activities of the crew and probably rules out normal flight and scientific duties for the duration of the flare. This restriction could be particularly compromising to the success

TABLE 2.1
Current Estimates of Shielding Thicknesses Required on Interplanetary Flights*

| Dose to the blood-forming organs (rem) | Reliability | Phase of the Solar Cycle | Material | Shielding Thickness | |
|--|----------------|--------------------------|--------------|--------------------------------|------------------------|
| | | | | 380 days Venus orbiter mission | 650 days Mars fly-by |
| 100 | 99% } 99.9% | Minimum | Polyethylene | 1 gm/cm ² | 2 gm/cm ² |
| | | Maximum | | 15 gm/cm ² | 21 gm/cm ² |
| | | Minimum | Aluminum | 3 gm/cm ² | 4.5 gm/cm ² |
| | | Maximum | | 22 gm/cm ² | 30 gm/cm ² |
| | | Maximum | Aluminum | 105 gm/cm ² | |
| 200 | 99% } 99.9% | Maximum | Polyethylene | 8.5 gm/cm ² | 10 gm/cm ² |
| | | | Aluminum | 12 gm/cm ² | 17 gm/cm ² |
| | | | Polyethylene | 37 gm/cm ² | 54 gm/cm ² |
| | | | Aluminum | 51 gm/cm ² | 73 gm/cm ² |

*The data in this table is based on the work of J. Snyder and A. Hardy of the Manned Space Craft Center, Houston, Texas.

of the mission if a solar flare occurs during a crucial phase of the flight. What is clearly needed, then, is a system that will provide adequate radiation protection, not interfere with the normal functioning of the spacecraft, and be relatively light in weight.

From this brief survey of the space radiation shielding problem as a whole, we wish only to draw the following conclusion: a large uncertainty presently exists concerning the shielding that will ultimately be required. It is therefore manifestly worthwhile to consider whether, by unconventional means, the degree of protection afforded by a given weight can be substantially increased. This conclusion launches us into a brief review of advanced concepts in radiation shielding. To the knowledge of the present authors, all advanced radiation shielding schemes so far put forward have depended on the fact that the solar flare protons (and alphas) which constitute the hazard are charged particles and can therefore be acted upon by electromagnetic forces. The first of these schemes is "Pure Magnetic Shielding."

2.1 Pure Magnetic Shielding

It has long been known that the spectrum of cosmic rays or solar flare protons measured near the top of the atmosphere exhibits a low-energy cut-off which is a strong function of geomagnetic latitude.³² This phenomenon is due to the fact that charged particles are able to cross a quantity of magnetic field lines that increase with their energy; it is clearly possible for a particle to arrive at either magnetic pole without crossing a single field line; on the other hand, the equatorial regions are strongly protected by the geomagnetic field. "Equatorial" in this sense means within, say, 45° of the geomagnetic equator. Since all U. S. manned space flights to date have taken place in this general region, it follows that the astronauts have up to the present been protected against solar flares by the earth's magnetic field. It is clearly possible to achieve a protective effect of this type for space vehicles far from the earth by carrying an appropriate magnetic field coil; this possibility (known as pure magnetic shielding) has been studied a good deal.³³⁻⁴² We note first that the method is equally valid for charged particles of either sign. It appears that the method has a certain promise^{43, 44} when it is desired to shield against electrons in the energy range up to several MeV; these occur in the form of trapped particles at

certain locations in the geomagnetic field, but are essentially unknown in deep space. Magnetic radiation shielding of the type in which the field extends to "infinity" is particularly attractive in this application since the radiation hazard caused by the electrons is not due so much to the penetration of the primary electrons, as to the comparatively long range of the secondary x-rays and γ -rays produced by stopping the electrons. These secondaries are absent in the magnetic radiation shield.

Whereas pure magnetic radiation shielding against trapped electrons looks attractive today, the same cannot be said of using pure magnetic radiation shielding against solar flare protons in deep space. The reasons for this situation are strictly quantitative; the solar flare protons against which it is desired to shield have higher rigidities than the trapped electrons, and therefore require more intense magnetic fields to do the job. The situation has been studied both roughly and carefully; the conclusion is always that except for cases where it is desired to stop very energetic (~ 2 BeV) protons from penetrating into large volumes, the weight advantage of pure magnetic shielding over solid shielding is not great enough to compensate for the substantially reduced reliability and increased complexity of the active system. This conclusion can probably be regarded as definitive.

2.2 Pure Electrostatic Shielding

Two forms of pure electrostatic shielding against solar flare protons have been suggested, but in our opinion neither of these presently looks attractive. In one scheme,³⁵ the space vehicle is pictured as being constructed of two concentric shells, these shells to act as a charged capacitor. In this arrangement the space vehicle as a whole is electrically neutral. In the other arrangement,⁴⁵ the space vehicle is considered as a charged conductor at some potential relative to "infinity."^{*} Without going into great detail the difficulty with the first scheme is technical; the largest steady voltages produced on earth between conductors are found in Van de Graaff machines. The massiveness of these machines, which nevertheless cannot attain voltages as high as 20 MV, speaks for itself. It is virtually certain

*The meaning of this is explained in detail in connection with the Plasma Radiation Shield.

that the insulators that would be required by an electrostatic space shielding system would weigh far more than the solid material required to do the same shielding job.

The difficulty with the second scheme is, perhaps, slightly less obvious. It might be thought in the first instance that the very high vacuum prevailing in deep space would itself be a very good insulator. This is not the case, however, since the solar wind fills the planetary system with free protons and electrons to a density of about $10/\text{cc}$. These charges are free to respond to an electric field of the type here considered and would discharge any substantial potential of either sign in a very short time. This is particularly true if (as is always the case) one tried to maintain the space vehicle positive as a protection against energetic protons. The free electrons in space would discharge the potential in a time so short that the scheme becomes quite unrealistic.

From the foregoing it is clear that (in our opinion) neither pure magnetic nor pure electrostatic radiation shielding looks attractive; furthermore, the limitations on both these methods are of a sufficiently fundamental character that it is very unlikely that our conclusions could be substantially modified by technological developments. This situation leaves the field of "active" radiation shielding open to the only other scheme of this type which has been put forward. This is the so-called "Plasma Radiation Shielding" scheme which is the principal subject of this paper and to which we now turn our attention.

3. THE PLASMA RADIATION SHIELDING CONCEPT

3.1 Plasma Radiation Shielding

The Plasma Radiation Shield^{46, 47} involves the use of both electric and magnetic fields, but the specific purposes of the two fields are as follows: the electric field is the direct means of providing the shielding against energetic protons, while the magnetic field has the sole purpose of supporting the electric field. It follows that the electric field that is required for the Plasma Radiation Shield is just the same as that required for the pure electrostatic shield. We therefore require the establishment of a voltage on the order of 30-100 MV, i. e., higher than has ever been achieved on earth. Now, while the achievement of such voltages must obviously remain in doubt until positively demonstrated, we hope to show in this paper that under the special conditions of deep space there are sound reasons to hope that such voltages are in fact attainable.

In the remainder of this section, we will present the basic features of the Plasma Radiation Shield. The sections that follow are devoted to preliminary discussion of various aspects of the Plasma Radiation Shield viewed as a single system in an integrated space vehicle. An appendix describes the current status of research on the problems associated with the basic physics of the Plasma Radiation Shielding concept.

3.2 Electrostatics

We consider first the electrostatic meaning of "potential of a space vehicle with respect to infinity." Now engineers in general are used (for good reasons) to considering virtually any electrical device in terms of the voltages applied or induced between pairs of terminals. In view of this, it is a surprising fact that the concept of a voltage between a conductor and infinity is normally the very first subject introduced in elementary electrostatics. We generally consider a conducting sphere of radius a carrying a positive charge Q on its surface; the electric field produced by this arrangement (in the absence of other charges) is radially outwards from the

surface of the sphere. The magnitude of this radial electric field at radius $r(> a)$ is $E = \frac{Q}{4\pi\epsilon_0 r^2}$ and this field can be derived from a potential

$$\phi = \frac{Q}{4\pi\epsilon_0 r} \quad (3.2.1)$$

In defining the potential an arbitrary constant may always be added; in this case we have assumed that $\phi = 0$ at a large distance from the sphere. It follows that the sphere is at a potential

$$\phi(a) = \frac{Q}{4\pi\epsilon_0 a} \quad (3.2.2)$$

above the potential of distant space. A way of interpreting this statement in terms relevant to the Plasma Radiation Shield is as follows: the work necessary to bring a proton (of charge $+e$) from infinity to the surface of our sphere is just $e\phi(a) = \frac{eQ}{4\pi\epsilon_0 a}$. In space the only source of this energy is the kinetic energy of the proton when at infinity; only if this exceeds the quantity $e\phi(a)$ will the proton be able to reach the surface of the sphere. Measuring this kinetic energy in electron volts we find (since the charges on an electron and a proton are of equal magnitude) that the sphere is electrostatically shielded against protons having less than $\phi(a)$ electron volts. If we wish to exclude protons up to 50 MeV, $\phi(a)$ must have the value 5×10^7 volts.

For a capacitor of capacitance C , the charge and the voltage are related by the formula

$$Q = C\phi \quad (3.2.3)$$

Comparing this with the formula (2) we see that the capacitance of the isolated sphere is $C = 4\pi\epsilon_0 a$. Thus, a two-meter radius isolated sphere

has the capacitance 222×10^{-12} farads = 222 picofarads. It follows that if we wish $\phi(a)$ to be 5×10^7 volts, the charge Q must be 11.1×10^{-3} coulombs = 11.1 millicoulombs.

Now, as was explained in connection with pure electrostatic radiation shielding, the arrangement described is not, as it stands, satisfactory. This is because a positive charge of the magnitude being considered would attract electrons from the surrounding space plasma at a rate so large as to make the whole concept useless. In the Plasma Radiation Shield, the vehicle is surrounded by a cloud of free electrons, the cloud being held in place by a magnetic field. Now the voltage across the electron cloud is always fixed by shielding considerations, but the details of the way in which the electron cloud is distributed are quite difficult to calculate. However, any given distribution can be characterized by a capacitance C , which, through (3.2.3) will determine the required charge. In this section we shall discuss briefly two geometrical arrangements which are intended to convey a general picture of the electrostatic arrangement of the Plasma Radiation Shield, without simulating the geometrical details.

Consider first the situation that arises if the sphere of the previous example is surrounded by a larger concentric conducting sphere of radius b' . The capacitance between the two spheres is

$$C = \frac{4\pi\epsilon_0 ab'}{b' - a} = 4\pi\epsilon_0 a \frac{1}{1 - \frac{a}{b'}} \quad (3.2.4)$$

If $b' = 4$ meters and a remains 2 meters, this is 444 picofarads. To maintain a potential difference of 5×10^7 volts between the spheres requires a charge of 22.2 millicoulombs. Now, if the large sphere carries a charge of - 22.2 millicoulombs, the combination of two spheres carries no net charge, and it follows that the electric field is entirely confined to the space between the two spheres. Thus it does not attract electrons from the surrounding space plasma and thereby overcomes the objection to the single sphere model. In terms of the Plasma Radiation Shield the inner sphere is

not only at a potential 5×10^7 volts higher than the outer sphere; it is also 5×10^7 volts above the potential of "infinity". Suppose that the outer sphere is transparent to protons; then a proton of 50 MeV kinetic energy approaching the arrangement from a large distance will be unaware of the existence of the spheres until it penetrates the outer one. Then, as it travels into regions of higher potential its kinetic energy will fall until it is brought to rest at the surface of the inner sphere. At this point, it will start to fall back towards the outer sphere. When it recrosses the surface of this sphere, it will have reacquired its initial energy of 50 MeV and will retain this energy in its further travels.

The example just discussed is in many ways a fair idealization of the electrostatic aspects of the Plasma Radiation Shield, even though the spherical geometry is not representative of the Plasma Radiation Shield. If we continue to ignore this difference, we can regard the inner sphere as representing the space vehicle. But we have already (in the discussion of pure electrostatic radiation shielding) dismissed the possibility that the outer sphere could be a solid electrode for the reason that the insulators separating the spheres would surely weigh more than a solid material radiation shield. In the Plasma Radiation Shield the outer sphere is replaced by a distributed cloud of electrons held in place by a magnetic field of moderate intensity. Therefore, in our second example, we imagine a cloud of electrons to be distributed around the inner sphere in such a manner that their number density n_e (i. e., the mean number of electrons per cubic meter) is a function only of r . For the moment we shall just suppose that they are held in place by "magic". Later we shall discuss this obviously vital question in detail. Clearly, the electron cloud is completely transparent to incoming protons in the sense of the discussion of proton reflection given earlier.

Poisson's equation connects the potential with the charge density. In the present spherically symmetric situation we have:

$$\frac{1}{r^2} \frac{d}{dr} \left[r^2 \frac{d\phi}{dr} \right] = \frac{n_e(r)e}{\epsilon_0}$$

Now for simplicity, suppose that the electron distribution is one of constant density n_e extending between the surface of the inner sphere (radius a) and some larger radius b . This distributed electron cloud represents the outer sphere of the previous example; the electron cloud therefore contains a total charge $-Q$ given by:

$$Q = \frac{4}{3} \pi (b^3 - a^3) n_e e \quad (3.2.5)$$

The appropriate solution of Poisson's equation, valid for $a \leq r \leq b$ can now be shown to be:

$$\phi(r) = \frac{Q}{4\pi\epsilon_0 r} \frac{(b-r)^2(b+r/2)}{(b^3 - a^3)} \quad (3.2.6)$$

The potential at $r = b$ is zero, as is also the potential of all points $r > b$. The electric field at $r = b$ is also zero because there is no net charge inside this radius. The electric field also vanishes for $r > b$. It follows now that the potential of the "space vehicle" is higher than the potential at "infinity" by the amount

$$\phi(a) = \frac{Q}{4\pi\epsilon_0 a} \frac{(b-a)(b+a/2)}{b^2 + ab + a^2} \quad (3.2.7)$$

For a given value of $\phi(a)$, $\phi(r)$ can be written in the form:

$$\phi(r) = \phi(a) \cdot \frac{(1 - r/b)^2(1 + 2b/r)}{(1 - a/b)^2(1 + 2b/a)} \quad (3.2.8)$$

For various values of b/a , this variation in $\phi(r)$ across the electron

cloud is shown in Fig. 3.1.

Formula (3.2.3) allows the calculation of an equivalent capacitance for the system of sphere plus electron cloud given by:

$$C = 4\pi\epsilon_0 a \frac{b^2 + ab + a^2}{(b - a)(b + a/2)} .$$

Comparing this with (3.2.4), we see that our arrangement is equivalent electrically to the concentric sphere arrangement discussed earlier where the radius of the outer sphere is given by:

$$b' = \frac{2}{3} \frac{b^2 + ab + a^2}{b + a} .$$

If, for example, the distributed electron cloud extends from $a = 2\text{m}$ to $b = 5.46\text{m}$ ($= 2\sqrt{3} + 2$) m , it follows that $b' = 4$ meters. Thus an electron cloud of uniform density extending over a radius ratio of $5.46 : 2$ corresponds electrostatically to the example quoted before of two concentric spheres with a radius ratio of $4 : 2$. For this example we also calculate the required electron density in the cloud; this follows from the fact that $Q = 22.2$ millicoulombs and from equation (3.2.4) we find: $n_e = 2.1 \times 10^{14}$ electrons/ $\text{m}^3 = 2.1 \times 10^8$ electrons/cc. The total number of electrons in the cloud is just Q/e . This is $N_e = 1.38 \times 10^{17}$ electrons. The support of such an enormous number of electrons is obviously not a trivial matter, and we shall come to this question after taking one more number out of the present analysis. The value of the radial electric field at the surface of the sphere is $E(a) = \frac{Q}{4\pi\epsilon_0 a^2}$. For the numbers quoted, this has the value 5×10^7 volts/meter or .5 million volts/cm. This large value of the electric field raises questions of its own to which we shall return (in 3.5). For the moment we observe that the density of positive charge on the outside surface of the "Plasma Radiation Shield" is $Q/4\pi a^2 = .44 \times 10^{-3}$ coulombs/ m^2 . The electric field just calculated exerts a force on this charge layer equal to

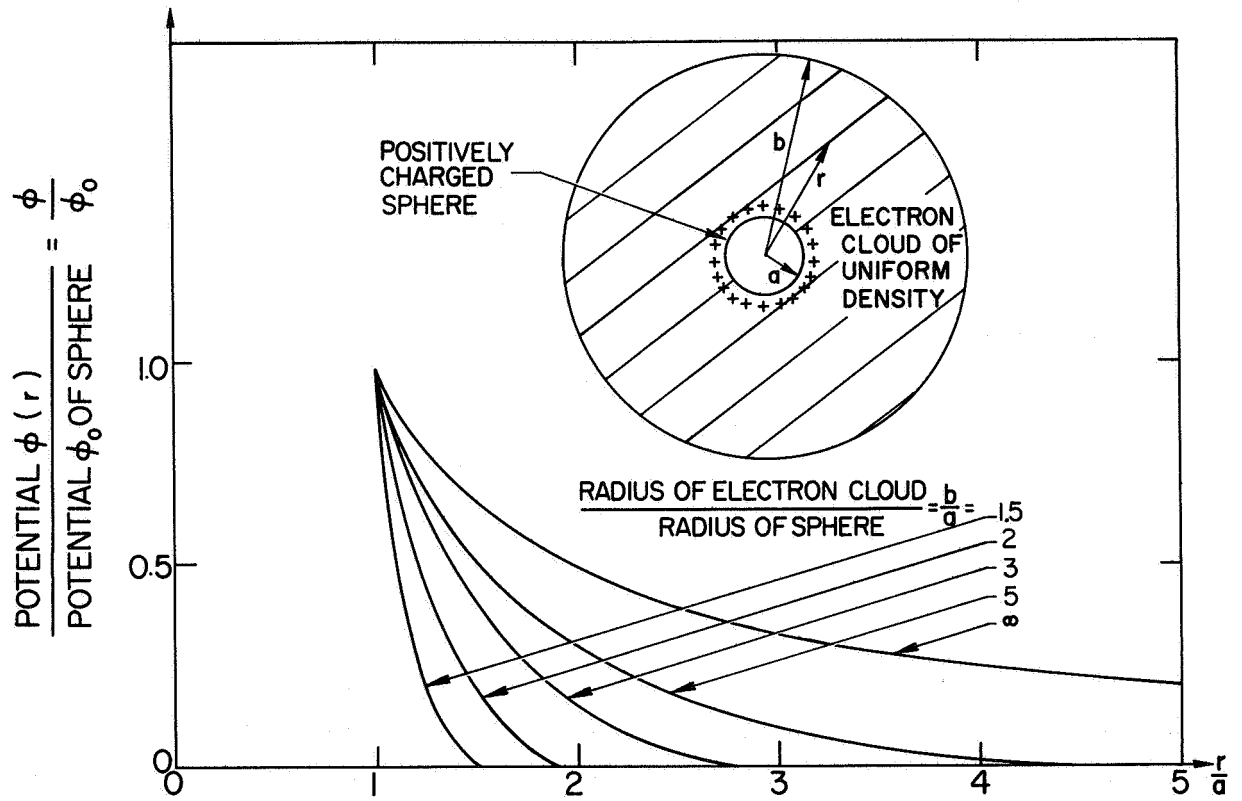


Fig. 3.1 Distribution of potential outside a charged sphere in the presence of an electron cloud of uniform density extending from the sphere (radius a) to radius b . The negative charge in the electron cloud is equal in magnitude to the positive charge on the sphere.

$.11 \times 10^5$ newtons/m² \approx .11 atmospheres. This force can also be thought of as the force of attraction between the positive charge $+Q$ on the inner sphere and the negative charge $-Q$ in the electron cloud. The nature of this force is the same as that of a gas atmosphere at this pressure inside the sphere; the magnitude would not be such as to cause much of a structural problem.

The preceding discussion of the electrostatic situation near a "Plasma Radiation Shield" of spherical geometry gives an idea of the way in which the electric fields are distributed around the space vehicle, and also gives a preliminary indication of the orders of magnitude of the quantities involved; we turn next to the means by which a magnetic field can be used to hold the electron cloud in place.

3.3 The Magnetic Field

The force exerted on an electron of charge $-e$ moving with velocity \underline{v} in a magnetic field \underline{B} is $-e(\underline{v} \times \underline{B})$. This force has no component parallel to \underline{B} , and from this observation follow important consequences. For, should there be any electric field in the direction of the magnetic field, the electrons will respond immediately by flowing along it until it is essentially nullified. It follows that after a very short time magnetic field lines (or at least those portions of the magnetic field lines on which there are electrons) will have no electric field along them, or, what is the same thing, they will become equipotentials. Now, since "infinity" and the space vehicle are supposed to differ in potential by 5×10^7 volts, there can be no lines of force which in one place are near the space vehicle and in another place far away from it. There is really only one kind of magnetic field geometry that satisfies both this requirement and the additional requirement that the field be outside the space vehicle, and that is, in its simplest form, the magnetic field due to loop of current, illustrated in Fig. 3.2. To be more precise, one would like to make the surface of the vehicle correspond in form to a given magnetic field line. This can be accomplished in a large variety of ways, but all these are topologically the same as the single loop coil shown in Fig. 3.2. Thus, the simple observation that $\underline{v} \times \underline{B}$ is perpendicular to \underline{B} leads us to reject the possibility of a spherical Plasma Radiation Shield

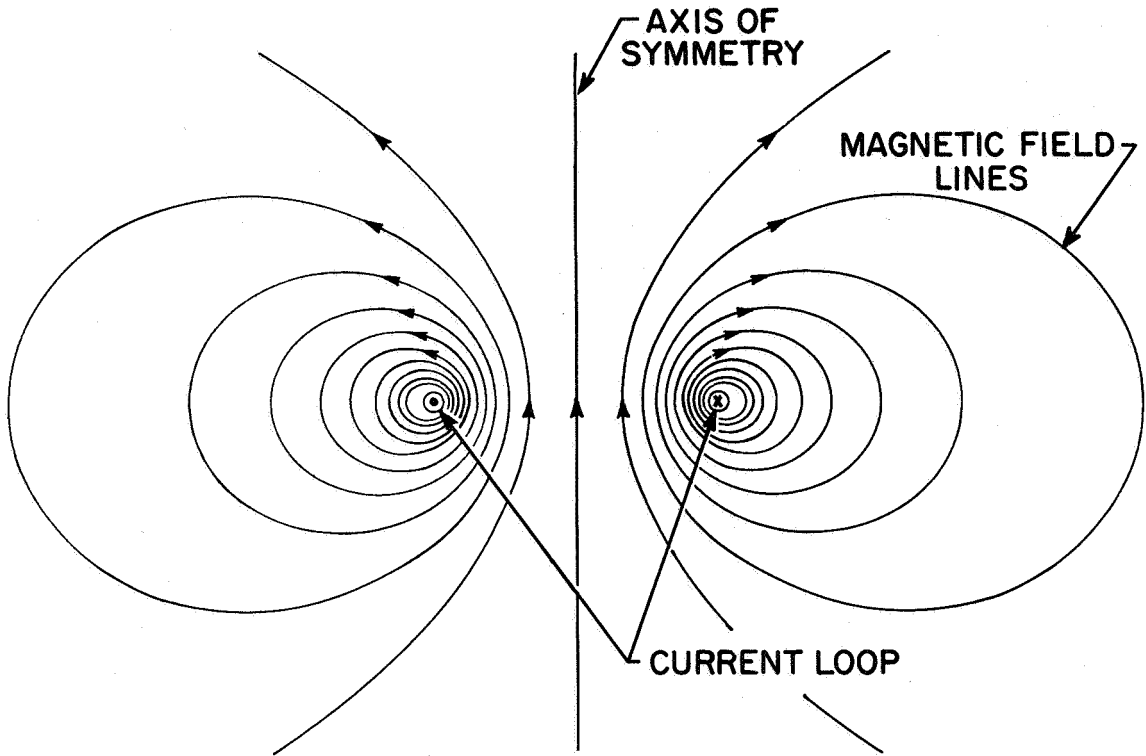


Fig. 3.2 A loop current is the simplest form of magnet giving a field shape satisfying the requirements of the Plasma Radiation Shield. This illustration shows the general shape of the magnetic field lines surrounding such a loop.

in favor of a topological torus. The condition that a space vehicle utilizing the Plasma Radiation Shield be a topological torus is on examination not as restrictive as one might suppose, although it does rule out direct adaptation of shapes not satisfying this condition. There are an unlimited number of ways in which a topological torus can be deformed; two examples are shown in Figs. 3.3 and 3.4. Of these two, the first represents a more substantial departure from current thinking about the shape of space vehicles than the second. Several other possibilities are discussed in Section 5 under the general heading of Vehicle Configuration Possibilities. For the present, we note that the configuration of Fig. 3.4 may have important advantages, although, pending further study, these remain uncertain. A brief discussion of these advantages is given in Section 3.6.

A second observation of considerable importance also follows directly from the form of the expression ($\underline{v} \times \underline{B}$) for the force exerted on an electron by a magnetic field. That is that the force is zero when the electron is stationary. But since a force is obviously required to counteract the electric field, the electrons must be (on the average) in motion. Thus, we are seeking a dynamic rather than a static equilibrium. The electron cloud must be permanently in motion of a rather complicated kind, and this motion must be so accurately perpendicular to the electric field that the electrons do not reach the space vehicle in a time comparable to the duration of a solar flare (i. e., about 48 hours). The nature and present state of understanding of this dynamic equilibrium are briefly discussed in Section 3.4 and in the Appendix. For the present we note only that the dynamics of the electron cloud poses many problems concerning which our present knowledge is incomplete.

One further conclusion to be reached on the basis of the force expression is quantitative. The magnitude of the magnetic force is evB . The electric force which this is supposed to counterbalance is eE . Equating these yields

$$B = E/v = \frac{E}{\beta c} , \text{ where } \beta = v/c \quad (3.3.1)$$

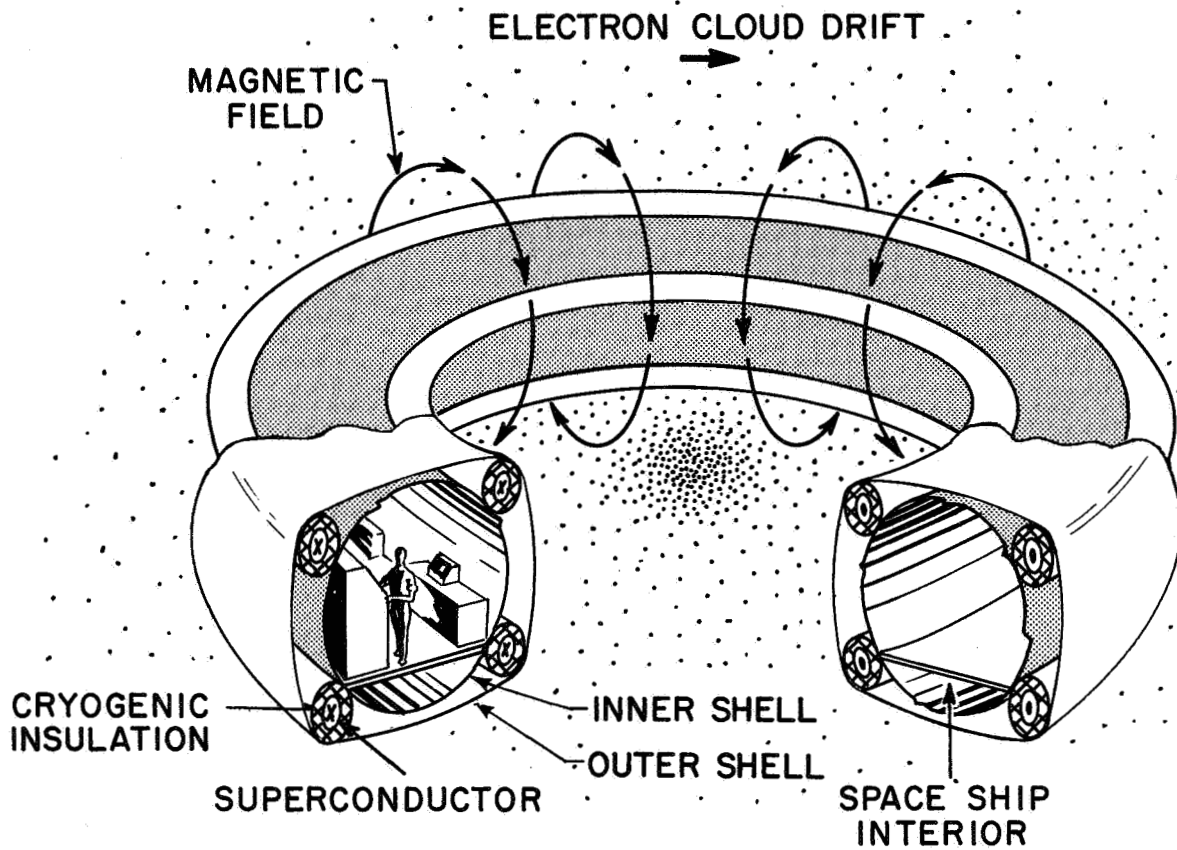


Fig. 3.3 Shows how the simple loop current shown in Fig. 3.2 can be adapted to a space vehicle. In this particular realization, the vehicle is symmetric in azimuth around the axis of the loop. Also shown are the electron cloud with its associated direction of drift, and a possible 4-coil arrangement for the superconducting magnet. The double-walled construction is discussed in Section 7. Of the many other realizations of the Plasma Radiation Shield that are possible, one more is shown in Fig. 3.4

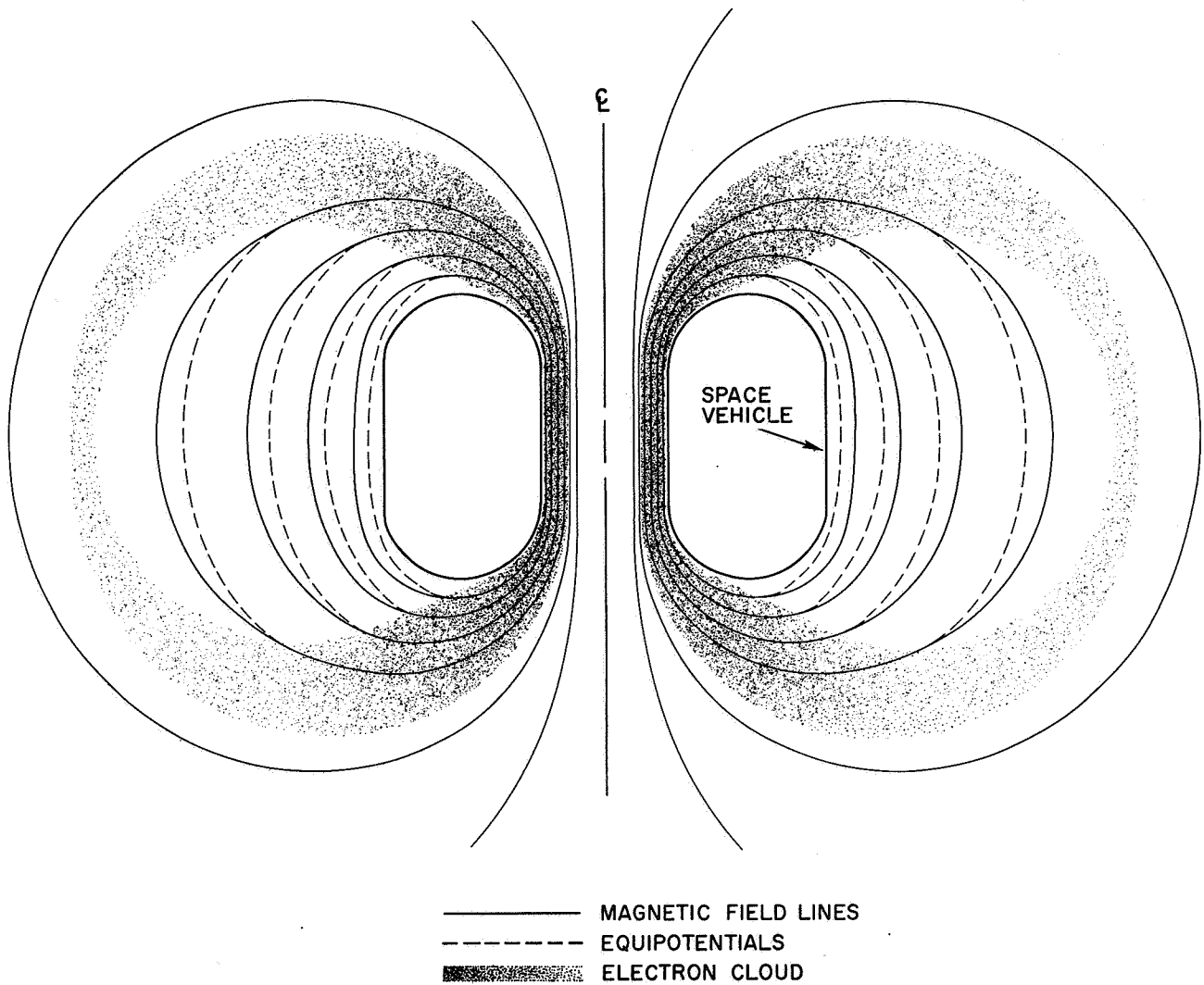


Fig. 3.4 Possible alternate conceptual configuration for a Plasma Radiation Shielded space vehicle. This speculative configuration could utilize a cylindrical launch vehicle. The relative merits of this approach are discussed in Section 3.6. The equipotentials follow magnetic field lines in the interior of the electron cloud, but are distinct outside of the cloud.

and if we knew v this would determine B since E is fixed by the electrostatics of the situation. But an absolute upper limit to v is given (by the theory of relativity) as the speed of light $c = 3 \times 10^8$ m/sec. Using the value of $E = 5 \times 10^7$ volts/m and assuming that the electron velocity can be one-half of its maximum value (i. e., $\beta = 1/2$), we find a characteristic magnetic field of .33 webers/m², or 3.3 k gauss. This magnetic field is far below what would be required for a pure magnetic radiation shield. Note also that it depends directly on our assumption about the electron velocity. Here again is a case where necessary basic knowledge is lacking; in this case if the β chosen to be 1/2 had been in fact 1/10, the magnetic field would have been 5 times more intense than the 3.3 k gauss quoted. This would give a magnetic field comparable in strength to that required for a pure magnetic shield, and we already know that the weight of these devices makes them unattractive. On the other hand, it may be permissible to go the other way; perhaps β can be as high as 0.9, giving a magnetic field of only 1.9 k gauss. This large uncertainty has a considerable effect on the calculated weight of the Plasma Radiation Shield, since the superconducting magnetic field coil (with its structure, insulation, power supply, controls, etc.) is the only massive item in the Plasma Radiation Shield. Up to the present, it has been guessed that $\beta = 1/2$ and all estimates have been based on this guess. The factors that determine the largest achievable $\beta (< 1)$ are not yet fully understood.

A final point to consider in connection with the magnitude of the magnetic field is the following: although low values of the mean magnetic field appear attainable, this by itself does not necessarily represent an optimum design. A more meaningful quantity is the total magnitude of the magnetic field energy. Now this total energy varies as the square of the mean magnetic field, and the cube of some linear dimension. It may very well turn out to be desirable to utilize larger mean magnetic fields over smaller volumes. Study of this trade-off is likely to be an important element in a deeper systems study of the Plasma Radiation Shield. In particular, the configuration illustrated in Fig. 3.4 (and briefly discussed in Section 3.6) would probably operate with rather substantial fields

(10-30 k gauss) in the relatively small interior volume. The most important unknown in this trade-off is the way in which the shielded volume varies with magnetic field energy.

3.4 Containment of the Electron Cloud

The fundamental idea underlying the concept of the Plasma Radiation Shield is certainly sound in principle. However, although a magnetic field as described is capable of holding the electron cloud in place, many difficult problems must be solved before it can be stated with assurance that this capability can actually be realized. The basic problem is that the electron cloud has a strong tendency to collapse onto the Plasma Radiation Shield; from the thermodynamic point of view this tendency is due to the very large free energy associated with the electric field. The Plasma Radiation Shield will work if it turns out that all the means available to the electron cloud of giving up its free energy operate at acceptably low rates.

The quantitative definition of "acceptably low" turns out to be very restrictive. Specifically, the electrons in the cloud are held at a distance from the space vehicle by the magnetic field; various mechanisms will allow the electrons to cross the magnetic field at appropriate speeds, and to fall into the space vehicle. Such motion constitutes a loss current. Plainly, this loss current must be extremely small if all the electrons (and hence the protective electric field) are not to be lost in a time short in comparison with the duration of a solar flare. If we take this time to be 2 days $\approx 2 \times 10^5$ seconds, and take the total charge in the cloud to be .022 coulombs, the loss current due to all losses should be substantially less than $.11\mu$ amps. A current of this magnitude crossing a voltage of 5×10^7 volts yields a maximum acceptable loss power of 5.5 watts. Put somewhat differently, at a speed of $1/2c$, an electron will drift around the Plasma Radiation Shield in a time of about $.1\mu$ secs. Thus the mean direction of drift must be perpendicular to the magnetic field to an accuracy of roughly 1 part in 10^{12} (or 10^5 secs/ $.1\mu$ secs).

3.4.1 Instabilities

By far the most dangerous possibility is that the electron cloud would be unstable. By this we mean that some collective effect in the

electron cloud could cause the cloud to fall across the magnetic field on a large scale. But the times associated with inherent instabilities of the usual kind would be expected to correspond to the inherent time scales of the electron cloud. These time scales are typically on the order of the time it takes an electron to drift around the device (i. e., $.1\mu$ sec), or, even shorter, the electron plasma period, or even the electron cyclotron period. These times are so extremely short that it is vital for the success of the concept that the electron cloud be exceedingly stable. It is a fortunate fact that prolonged and careful study of the question of stability has yielded consistently encouraging results. The details of these studies are given in Ref. 48 to 53; but a summary of the results suggests that if the inner edge of the electron cloud is maintained very close to the surface of the space vehicle, stability can be attained. There is also empirical evidence that a small-scale device (the Vac-Ion Pump)⁵⁴ which is closely related to the Plasma Radiation Shield is successful only because electron clouds of our type are in fact very stable. Our own experiments have also suggested the same, but there is an important proviso: no experiments have been done in the geometry demanded by the Plasma Radiation Shield concept. Since certain possible modes of instability are strongly dependent on geometrical factors, it will ultimately be necessary to test the stability of the Plasma Radiation Shield in a direct manner. At present, all that we can say is that experimental, empirical, and theoretical evidences are all sufficiently encouraging to proceed to other (generally slower) forms of loss on the assumption that the hoped for stability is in fact present. The question of stability is discussed in somewhat greater detail in the Appendix.

3.4.2 Classical Diffusion

These other, slower forms of loss come generally under the heading of "classical diffusion" caused by close collisions of the electrons with (1) other electrons; (2) ions; (3) neutral atoms and (4) particulate matter. We deal with these possibilities in order.

- (1) Electron-electron collisions. Collisions between like particles cause only a very weak form of diffusion, when there is a gradient of density or temperature. Calculations indicate that losses from this source are less than 0.1 watts, and are

therefore well within the allowable maximum diffusion rate.

- (2) Electron-ion collisions. These are no problem in the Plasma Radiation Shield for the following reasons: positive ions are strongly expelled from the electron cloud by the electric field and are sufficiently massive that the magnetic field cannot restrain them. The residence time for a typical ion in this field is on the order of 10^{-7} seconds, and this time is so short that the ion will generally have no close collisions with electrons of the cloud. This is true of the solar flare ions, and also of any other ions that from time to time might be present in the system. In particular, ions coming from outside the cloud (i. e., from space) are reflected elastically by the electric field with no net exchange of energy.
- (3) Electron-neutral collisions. Due to solar UV radiation and other effects, the ambient density of neutral atoms in deep space is negligible, but there will be atoms coming out of the space vehicle due to leaks from the pressurized cabin, and to outgassing from exposed surfaces. The Plasma Radiation Shield concept puts a very severe restriction on the flux of these atoms, for the following reasons: an atom coming off the space vehicle will generally be moving at a speed corresponding to the temperature of the surface from which it came. These speeds are generally moderate, and the atom is at once exposed to the circulating flux of electrons in the cloud. If these electrons have a density of $10^8/\text{cm}^3$, and a speed of 10^{10} cm/sec, and if we take the cross section for ionization as 10^{-18}cm^2 , the length of time that elapses before the atom is ionized will generally be about 1 sec. This suggests that a non-negligible fraction of the neutral atoms coming off the space vehicle will be ionized during their passage across the electron cloud. Now, after ionization an electron and a positive ion are formed; the electron will become just part of the electron cloud, but the ion, unrestrained by the magnetic field on account of its greater

mass, will be ejected into deep space by the electric field in the time 10^{-7} seconds previously quoted. But the transport of a positive ion from some point near the surface of the space vehicle to infinity is just as much a loss as is the transport of electrons from the outer regions of the cloud to the surface of the space vehicle. In the worst case, all the ions are formed right at the surface of the space vehicle and subsequently ejected across the full 5×10^7 volts. In this case the limit on the current of ions is about $.1\mu$ amps. This represents a maximum allowable number of such ions on the order of 10^{12} /sec, and this is also the maximum allowable rate of escape of neutral atoms from the active space vehicle. If this is a leak of oxygen from the cabin, it corresponds to an allowable leak rate of about 10^{-6} grams of oxygen in two days! In fact, the mean potential at which neutrals are ionized can be considerably lower than 5×10^7 volts, since in the 1 sec mean free time estimated above the neutrals would cover a distance like 100 m. or more. Suppose, for instance, that the mean potential of ionization is only 1% of the full voltage, or 5×10^5 volts. The tolerable current is then 10μ amps corresponding to a flux of 10^{14} /sec, or 10^{-4} gms in 2 days. However, even with these figures, it is obvious that the cabin pressure vessel must be a high quality vacuum vessel; if it is double-walled, however, this low leak rate should be attainable. There is also a severe restriction on the amount of outgassing of the whole surface that can be permitted; this corresponds roughly to a pressure over the surface of about 10^{-12} mm Hg, again a very low but not unattainable level. It must be remembered that ample time is generally available to bake and thoroughly clean all exposed surfaces before activation of the Plasma Radiation Shield. We shall return to this question in Section 7.

- (4) Particulate matter. If the surface of the Plasma Radiation Shield is clean, no dust particles should be present on it;

preliminary activation of the electric field should help to achieve the required degree of cleanliness. There remains, then, the flux of micrometeorites from space. If, as is believed,⁵⁵ this flux is less than 10^{-8} gm/cm²/year outside the immediate neighborhood of the earth, there should be no problem from this source. A large meteorite might shut off the electric field, and reactivation would take perhaps an hour or less, but the probability of such an event coinciding with a solar flare is reasonably low.

This completes our discussion of problems of classical diffusion; by far the most important difficulty to have arisen is the control of leakage and outgassing. Although difficult, it cannot be stated that this problem is insuperable; the actual constraints that it is likely to impose are reviewed in Section 7.

3.5 Achievement of Very High Voltages

It was mentioned in Section 2 (in connection with electrostatic shielding) that the required voltages are higher than any yet achieved on earth, and the same comment applies to the Plasma Radiation Shield. It is natural to ask, in these circumstances, how it is that we can contemplate reaching these voltages in the Plasma Radiation Shield. At this stage we can do no more than explain why the effects that limit the voltage in present-day machines do not apply to the Plasma Radiation Shield. This lack of applicability of known limitations is encouraging, but is obviously not a guarantee that the required voltages can be reached. This is an area in which there can be no substitute for an experiment.

In general, the achievement of high voltages in the laboratory has been limited by problems of breakdown.⁵⁶⁻⁶⁴ The particular breakdown experiments which are most relevant are those having to do with breakdown between parallel electrodes in high vacuum conditions. It seems that the best available theory⁵⁶ of how this occurs is as follows: at the negative electrode (or cathode) the electric field points in such a direction as to draw electrons out of the surface. A current is actually drawn by the quantum-mechanical mechanism known as field emission. This current depends

exponentially on the electric field and is therefore concentrated at microscopic projections on the cathode where the electric field is intensified. Next, the current through these projections heats them by Ohmic dissipation. At a certain field strength this heating is sufficient to evaporate the projections altogether; breakdown then occurs in the gas thus formed. Now, if this is indeed the true mechanism of breakdown, there is reason to be optimistic where the Plasma Radiation Shield is concerned, for in our case, there is no material cathode at which field emission can occur. The only material electrode is the space vehicle itself, and this is the anode (positive electrode); that is the direction of the electric field is such that it tries to extract positive ions. From a quantum-mechanical viewpoint, the extraction of positive ions by field emission is virtually impossible. The evidence as regards anode field strength limitations is from the working of the positive ion microscope,⁶⁵ a device in which a large cathode and a tiny anode produce an enormous electric field at the surface of the latter. This device draws a satisfactory ion current only when the electric field is on the order of 100 million volts/cm, a field some 100 times greater than that contemplated for the Plasma Radiation Shield. Furthermore, this field strength produces electrostatic forces on the order of 3,000 atmospheres, that is, on the order of the yield strength of most materials. Microscopically, it is 1 volt/angstrom. Taking 1 angstrom as a typical spacing between ions in a lattice, and 1 volt as a typical binding energy, it is again plain why an ion current can be drawn by an electric field of this strength. To sum up this subject, the Plasma Radiation Shield should not be subject to high vacuum breakdown as it is presently understood, and should not lose appreciable ions at the field strengths contemplated. As stated before, these hopes can only be proved sound by an appropriate experiment.

3.6 Possibilities for the Configuration of Fig. 3.4

The configuration of Fig. 3.4 may turn out to be very advantageous. The reasons for this possibility must for the moment be regarded as speculative, but nevertheless it is worthwhile to offer herewith some discussion of these reasons. This discussion accomplishes two purposes, of which the first is specific and the second general. The first purpose is that if the

anticipated advantages of this configuration hold up under further study, the Plasma Radiation Shield will be substantially simpler to achieve than might otherwise have been the case. The second purpose is to show, by means of an example, that there is still a large amount of room for the application of imaginative ideas to the Plasma Radiation Shield. The concept is still far from complete definition; further study on a broad front can still be expected to yield large as well as small changes in its overall desirability.

It was stated in Section 3.2 that magnetic field lines on which there were electrons must be equipotentials. This statement may not be strictly true, for the following reasons: in axially symmetric magnetic fields (as, for instance, that shown in Fig. 3.2) magnetic field lines that pass close to the axis of symmetry (say, at a radial distance r_{small}) close at a very large radial distance, roughly $r_{\text{large}} = \sqrt{V/(2\pi r_{\text{small}}^2)}$, where V is a representative volume of the magnet. But since the electrons of the cloud are attracted to the positive charge on the space vehicle, the electrons may not wish to locate themselves quite so far away from the vehicle as r_{large} . This suggests that the electron cloud might be confined to some region near the space vehicle, of characteristic volume V , and that the remainder of the magnetic field is largely, or even entirely, free of electrons. The interpretation of the statement in Section 3.3 about magnetic field lines being equipotentials is then as follows: throughout the electron cloud, magnetic field lines are indeed equipotentials, but in regions of the magnetic field where there are no electrons, there is no such requirement. Thus, it is possible to imagine that the equipotentials follow the magnetic field lines in the region near the axis of the magnetic field, but that outside of some contour defining the boundary of the electron cloud, the electrostatic potential satisfies Laplace's equation. In this case the equipotentials would fall inside the magnetic field lines in the vacuum region, but would become tangent to the magnetic field at the boundary of the electron cloud. This situation would not affect the basic shielding properties of the configuration.

It is not known for sure whether such an electron cloud is possible, but, on the assumption that it is, the configuration of Fig. 3.4 would have important advantages, as follows:

1. The shape of the magnetic field is roughly that of a long solenoid; in such a magnetic field, the field lines close at larger distances than they would, say, for the loop current of Fig. 3.2. Thus, the electron cloud should be substantially confined to the interior of the solenoid.
2. The general shape of the space vehicle is cylindrical, in accordance with many current ideas about such vehicles; such a shape is naturally compatible with launching rockets.
3. The construction of a solenoidal magnet is a simpler task structurally than the construction of the four-coil magnet of Fig. 3.3. Also, the stray magnetic fields in the shielded volume would be very small indeed.
4. Since there is essentially no electron cloud outside the vehicle, gas atoms coming from the vehicle will not be ionized, and will therefore constitute no electrical loss. Thus, the vacuum problem (discussed briefly in Section 3.4.2, and in detail in Section 7) would be confined to the relatively small area of the space vehicle facing the electron cloud. In particular, ports, doors, antennas, etc. could be located on the exterior surface without the necessity for special sealing.
5. The electric field on the outside of the space vehicle would be quite low. Thus protuberances of various sorts could easily be tolerated, and would have essentially no effect on the electron cloud.
6. The injection of the electrons could be accomplished in the low field region outside the vehicle; these electrons would then quite naturally proceed to the high magnetic field region inside the solenoid. Such an injection procedure might be extremely simple.

In conclusion, we must emphasize that the existence of the type of equilibrium we are considering has not yet been demonstrated. Even less is known about possible instabilities of such equilibrium configurations. In particular, we do not yet know how to calculate the shielded volume

associated with such a configuration, i. e., what outer radius of the space vehicle can be tolerated. An important effect of this ignorance is that calculations of the weight of such a Plasma Radiation Shield are irrelevant to the extent that we cannot associate them with definite values of the shielded volume. Lastly, the extent of these uncertainties can be taken as a rough measure of the present degree of definition of the Plasma Radiation Shielding concept.

3.7 Basic Design Parameters

The most basic design parameters of the Plasma Radiation Shield are, first, the size and shape, and second, the overall voltage. The voltage is set by considering such questions as the actual frequency and spectra of solar flares, and allowable radiation doses to the crew. This subject is discussed in some detail in Section 4. The size is set fundamentally by the nature of the mission to be undertaken, especially the crew size and the mission duration, but the shape is set (as discussed in Section 3.3) by the requirement that the Plasma Radiation Shield be essentially toroidal. Two possible configurations are shown in Figs. 3.3 and 3.4, but these suggestions are far from exhausting the possibilities.

Now a principal object of any analysis of the possibilities inherent in the Plasma Radiation Shield must be a curve showing the relation between the shielded volume and the systems weight. However, we are not yet in a position to calculate either of these quantities with any precision. The uncertainty associated with the shielded volume was discussed briefly in Section 3.6 in connection with the configuration of Fig. 3.4, but stems basically from lack of definition of the overall configuration of the space vehicle, magnetic field and electron cloud. The uncertainty associated with the systems weight stems basically from a lack of definition of the attainable value of β (Eq. 3.3.1), since this parameter determines the level of the required magnetic field. The weight of a Plasma Radiation Shield resides primarily in the superconducting coil. The weight of the superconductor itself is proportional to β^{-1} , while the weight of its power supply and structure scale with β^{-2} . The weight of the cryogenic system (including refrigerator) depends strongly on the coil configuration. Lack of certainty

about the configuration also makes it difficult to assign a weight to other components of the system, such as penalties associated with vacuum requirements.

The net result of these considerations is that it is not possible, at the present time, to calculate the weight of a Plasma Radiation Shield with any more precision than was done in Ref. 44. The curve of weight vs. shielded volume of that paper is reproduced here, as Fig. 3.5, and indicates clearly the advantages that may be possible with a Plasma Radiation Shield. Since this curve was drawn, the physical basis for the concept has been placed in a much sounder framework. Thus it is now possible to take up again the question of systems integration; as stated in the Preface (Section 1), it is the purpose of this paper to lay the basis for such a systems study, rather than to accomplish it. This being the case, in calculating system weights, we leave our results for the most part as formulas, showing the dependence of the weights of different components on characteristic parameters such as the magnet current. In particular, we do not attempt to establish a sample design for which weights can be calculated, as this does not seem presently to be justified.

3.8 Summary

To sum up, the basic features of the Plasma Radiation Shield are as follows:

1. A cloud of electrons of total charge $-Q$ is held away from the space vehicle (which has a positive charge $+Q$) by a magnetic field. The magnitude of Q is determined roughly by a knowledge of the required voltage of the space vehicle and its size and shape, and (to a smaller extent) by the details of the distribution of the electron cloud. Potentials from 10 to, say, 200 million volts are considered. Characteristic electric fields are on the order of 1 million volts/cm.
2. The space vehicle is necessarily toroidal; it carries a large current (generally several million ampere turns) around its major radius, and its shape in the meridional section must coincide with some line of force of the magnetic field.

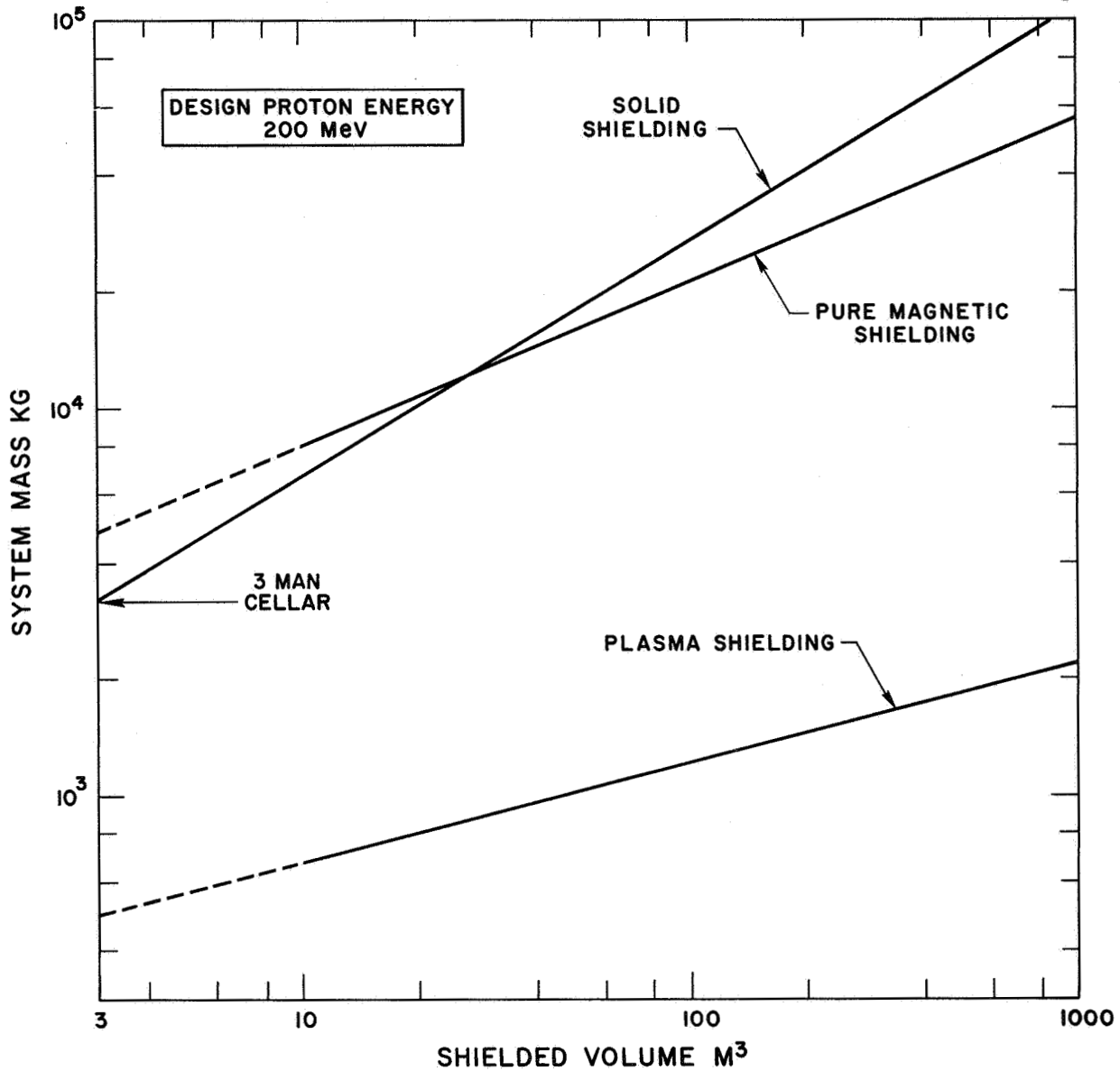


Fig. 3.5 The weight of a Plasma Radiation Shield as a function of the shielded volume. This curve, reproduced from Ref. 44, remains the most reasonable estimate of the weight of a Plasma Radiation Shield, pending more detailed systems studies. Thus it must be regarded as subject to large uncertainties. Shown for comparison are estimated weights for solid and pure magnetic shields, for 200 MeV design energy.

Magnetic fields required are on the order of several thousands of gauss.

The whole concept of Plasma Radiation Shielding is associated with two large unknowns; these are as follows:

1. It is not certain that under any conditions the electron cloud around the Plasma Radiation Shield will function satisfactorily, although there are at present grounds for being guardedly optimistic on this score. Some of the questions that arise, and the reasons for our guarded optimism are discussed later in the paper, and especially in the Appendix.
2. Even if all the questions that arise under the above topic are satisfactorily resolved, it will still remain true that to incorporate a Plasma Radiation Shield in an actual space vehicle would involve very far reaching design "boundary conditions" affecting the space vehicle as a whole. Whether these conditions are acceptable or not will certainly be a question of balancing in detail all the various pro's and con's. In particular, it is important to know exactly what concessions in terms of weight would be demanded by the provision of adequate solid shielding. If the weights are large, it could well be worthwhile to adapt the over-all space vehicle design to the demands of the Plasma Radiation Shielding concept. We are not yet ready to undertake a detailed study of the relative advantages of this concept; however, we are in a position to be fairly specific about the demands of the Plasma Radiation Shield. To the extent presently possible, these demands are discussed in the following sections.

4. VOLTAGE SELECTION IN THE PLASMA RADIATION SHIELD

The two most basic parameters of the Plasma Radiation Shield are the over-all size and shape, and the magnitude of the voltage. In this section we discuss the considerations which enter into the selection of the voltage.

The starting point is a consideration of the maximum permissible dose to which the crew may be subjected. In Table 8 of Ref. 30 are listed the biological doses sustained behind various bulk shielding configurations for all the principal solar flare events from February 1956 to October 1962. If one stipulates some sort of dose tolerance criterion — e. g., a maximum acute dose or a maximum cumulative dose over some time period — one can then determine the thickness of bulk shielding that will just satisfy this criterion. One can then enter proton range-energy tables, such as Ref. 66, and determine the maximum energy of proton that is stopped by this thickness. As a first approximation we may consider that a Plasma Radiation Shielding system should be capable of stopping this same proton. For example, Ref. 30 shows that the maximum surface dose behind 10 gm/cm² of aluminum for any single event (actually three separate events in one week) was 66 rad. Also, the same source shows that the maximum cumulative dose during any two-year period for the same shielding configuration was 151 rad. If it is assumed that these dose figures are tolerable, then the required bulk shielding thickness is 10 gm/cm² of aluminum. Reference to range-energy tables⁶⁶ shows that this thickness is adequate to stop 100 Mev protons.

Now, the rate of loss of energy of fast particles in matter is a strongly decreasing function of energy. Thus, at high energy, the use of solids to stop protons is relatively wasteful. Conversely, at low energy, the use of solid shielding is relatively efficient. Further, any space vehicle configuration will possess a certain amount of solid shielding in the form of its skin and other equipment. This shielding may be estimated roughly at

2-4 gm/cm² aluminum.* Suppose, for example, that it is required to stop 100 MeV protons. If the skin thickness is 2 gm/cm², reference to the range-energy tables shows that this thickness will just stop a 40 MeV proton. It is therefore only necessary to provide 60 million volts of potential in the Plasma Radiation Shield in order to achieve the desired effect. The incident 100 MeV proton crosses the Plasma Radiation Shield voltage, losing 60 MeV. The remaining 40 MeV are then absorbed in the 2 gm/cm² of skin. If the skin thickness is 4 gm/cm², reference to the range-energy tables shows that this thickness will stop a 60 MeV proton. Thus a 40 MV Plasma Radiation Shield outside of 4 gm/cm² of skin would also suffice to stop 100 MeV incident protons. Proceeding in this way, one can, using the range-energy tables, construct a graph showing the different combinations of Plasma Radiation Shield voltage and solid shielding thickness that will stop a given proton. This graph is presented in Fig. 4.1. From it we can, by looking along the line marked "Proton Energy 100 MeV," find the two examples just discussed of a vehicle skin of 2 or 4 gms/cm², with Plasma Radiation Shield voltages of 60 and 40 million volts respectively. Another way to look at Fig. 4.1 is to consider the relative effectiveness of, say, a 40 million volts Plasma Radiation Shield against protons of various energies. For example, to stop a 100 MeV proton requires 10 gm/cm² of solid shielding. But we saw above that 40 MV Plasma Radiation Shielding ahead of 4 gm/cm² of skin will also stop a 100 MeV proton. In a sense, the 40 MV Plasma Radiation Shield is the equivalent of 6 gm/cm² of solid shielding. Again, to stop a 150 MeV proton requires 19 gm/cm² of solid shielding. But a 40 MV Plasma Radiation Shield will cut a 150 MeV proton down to 110 MeV, and to stop a 110 MeV proton requires only 12 gm/cm². At this level, the 40 MV Plasma Radiation Shield is the equivalent of 7 gm/cm² of solid shielding.

We have assumed that one need only determine the total stopping power of any shielding combination in order to calculate its shielding

* For a space vehicle having a surface area of $4 \times 10^6 \text{ cm}^2$, 2-4 gm/cm² corresponds to total weights of 8,000 and 16,000 kg respectively.

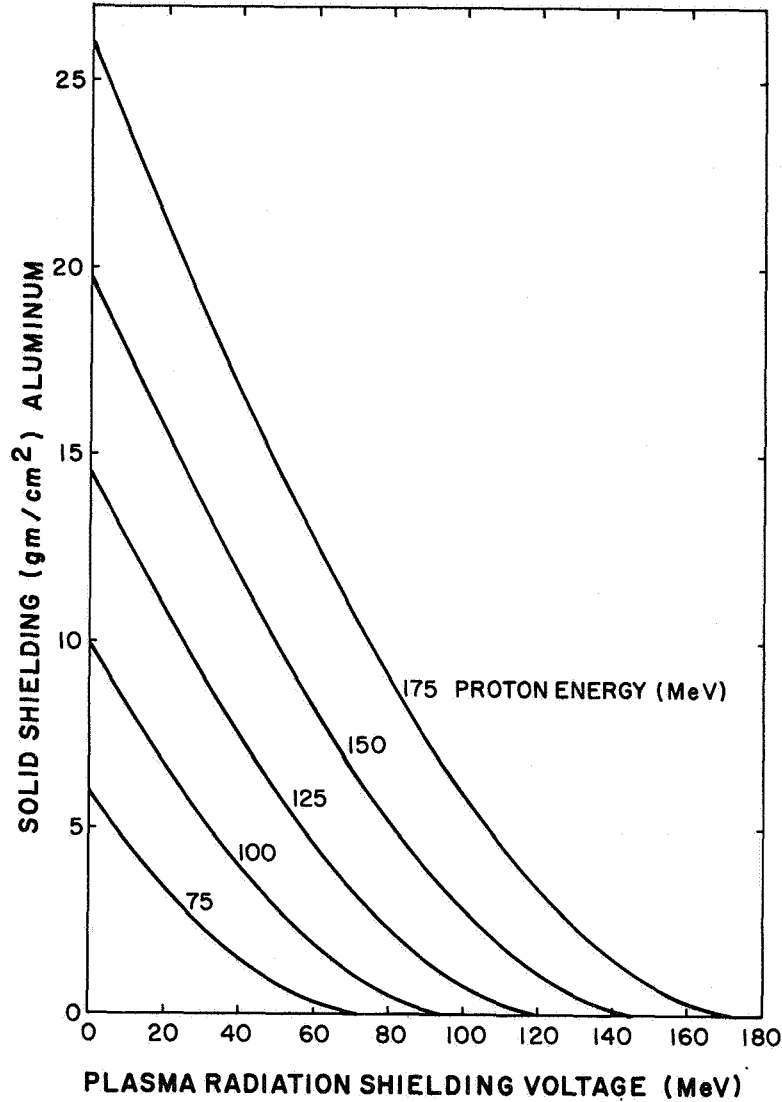


Fig. 4.1 "Range-Energy Tables" appropriate to a combination of electrostatic and solid shielding. Following the curves corresponding to a given proton energy, one may read off the different proportions of the two shielding components required to stop the proton. Note the great relative advantage of the first 20 or 30 MV of electrostatic shielding. Note also that the graph assumes the electrostatic potential is outside the solid matter. Reversing the order of the shields greatly reduces the effectiveness of a given combination.

effectiveness. This will, in general, be true where the incident spectrum is soft, because in this case nearly all the dose delivered at any point is given (since the spectrum is soft) by those particles which just arrive. However, it is not strictly true since different shielding combinations will differently affect the spectra of protons above the cut-off energy. This effect is exhibited in Fig. 4.2, and in Table 4.1. We consider, for example, a 60 MV Plasma Radiation Shield ahead of 2 gm/cm^2 of aluminum. Both these shields just stop 100 MeV protons; their different effects on more energetic protons are listed in Table 4.1. At energies above 100 MeV the composite shield removes more energy from the incident protons than the solid shield, but this effect is relatively small for very high energies.

To make these considerations more specific, consider an incident flux of protons having an integral spectrum in free space given by

$$I_0(> E_0) = I_{\text{REF}} \left[\frac{E_{\text{REF}}}{E_0} \right]^n \quad (4.1)$$

E_{REF} is any convenient reference energy (in MeV), and I_{REF} is the integrated flux of particles per sq. cm^2 having energies greater than E_{REF} . Later on, for a specific case, we shall choose $E_{\text{REF}} = 100 \text{ MeV}$, and $I_{\text{REF}} = 10^8 \text{ protons/cm}^2$, but these choices have no special validity.

The flux of particles in free space having energies between E_0 and $E_0 + dE_0$ is

$$- \frac{dI_0}{dE_0} dE_0 = n I_{\text{REF}} \left[\frac{E_{\text{REF}}}{E_0} \right]^{n+1} \frac{dE_0}{E_{\text{REF}}} \quad (4.2)$$

Let the Plasma Radiation Shield have a voltage V . There will then be no flux of particles behind the Plasma Radiation Shield whose energy E_0 in free space was less than V . The simplest model would be to consider the flux of particles with energy E_1 , behind the Plasma Radiation Shield, to

TABLE 4.1

Comparison of Shield Effectiveness

| | Shield I | | Shield II |
|--------------|--------------|--------------|--------------|
| E_2 Mev | E_1 Mev | E_0 Mev | E_0 Mev |
| 0 | 40 | 100 | 100 |
| 20 | 47 | 107 | 102 |
| 50 | 67 | 127 | 115 |
| 100 | 110 | 170 | 149 |
| 150 | 158 | 218 | 190 |
| 200 | 206 | 266 | 232 |
| 500 | 502 | 562 | 522 |
| 1000 | 1001 | 1061 | 1020 |

equal the flux of particles with energy $(E_1 + V)$ in free space. However, this approach would yield a finite flux of particles with low energy behind the Plasma Radiation Shield and does not do justice to the properties of the electrostatic shield. Particles having an energy just greater than V in free space will be strongly deflected by the electric field, and can only penetrate it if their initial motion is accurately parallel to some electric field line. An estimate of the strength of this effect is that the flux of particles of energy $E_0 (> V)$ is reduced by the factor $(E_0 - V)/E_0$ in passing through the field. This factor is strictly correct for simple geometries and is probably at least representative for more complicated ones. It has the right general trend of emphasizing the deflection, or scattering phenomenon for particles with free space energy E_0 just greater than V . When E_0 is much greater than V , the deflection is insignificant, and the factor goes to unity. Use of this factor yields a differential flux behind the Plasma Radiation Shield given by:

$$- \frac{dI_1(E_1)}{dE_1} dE_1 = n I_{REF} \left[\frac{E_{REF}}{E_1 + V} \right]^{n+2} \frac{E_1 dE_1}{E_{REF}^2} \quad (4.3)$$

For the present purposes we can roughly simulate the loss of energy of protons in matter by the equation

$$- \frac{dE}{dx} = \frac{k}{E} \quad (4.4)$$

where x is in gm/cm^2 . k is a constant, representative of the stopping material, and having the dimensions $(\text{MeV})^2 \text{cm}^2/\text{gm}$. If the thickness of the solid shield in the composite arrangement is x_1 , it will just stop protons of energy $E_1 = \sqrt{2kx_1}$. If E_1 is higher than this, the energy E_2 on emerging from the solid shield is $E_2 = \sqrt{E_1^2 - 2kx_1}$. The total stopping power of the arrangement is $V + \sqrt{2kx_1}$. The spectrum of energies

emerging from the solid shield is:

$$-\frac{dI_2(E_2)}{dE_2} dE_2 = n I_{REF} \left[\frac{E_{REF}}{\sqrt{E_2^2 + 2kx_I} + V} \right]^{n+2} \frac{E_2 dE_2}{E_{REF}^2} \quad (4.5)$$

If the thickness of Shield II is x_{II} gms/cm², the differential spectrum behind it is

$$-\frac{dI_2(E_2)}{dE_2} dE_2 = n I_{REF} \left[\frac{E_{REF}}{\sqrt{E_2^2 + 2kx_{II}}} \right]^{n+2} \frac{E_2 dE_2}{E_{REF}^2} \quad (4.6)$$

and the shields are comparable if

$$V + \sqrt{2kx_I} = \sqrt{2kx_{II}} \quad (4.7)$$

Choosing for Shield I $\sqrt{2kx_I} = 40$ MeV and $V = 60$ MeV, and for Shield II $\sqrt{2kx_{II}} = 100$ MeV, the differential spectra (4.5) and (4.6) are shown in Fig. 4.3. We have chosen two values of n , $n = 2$ (a hard spectrum), and $n = 4$ (a soft spectrum). We have also shown the differential spectrum (4.2) in free space. All these spectra are normalized to the quantity I_{REF}/E_{REF} , and we have chosen $E_{REF} = 100$ MeV, so that I_{REF} is the total flux of particles in free space with energies greater than 100 MeV. We observe that the composite shield passes less flux than the solid shield at all energies, and that the effect is more pronounced for the softer flare. This is because the electrostatic scattering factor $(E_0 - V)/E_0$ is more effective for the softer flare.

These flux calculations can also be converted into dose calculations if we neglect the variation of the RBE with energy. Using the assumption

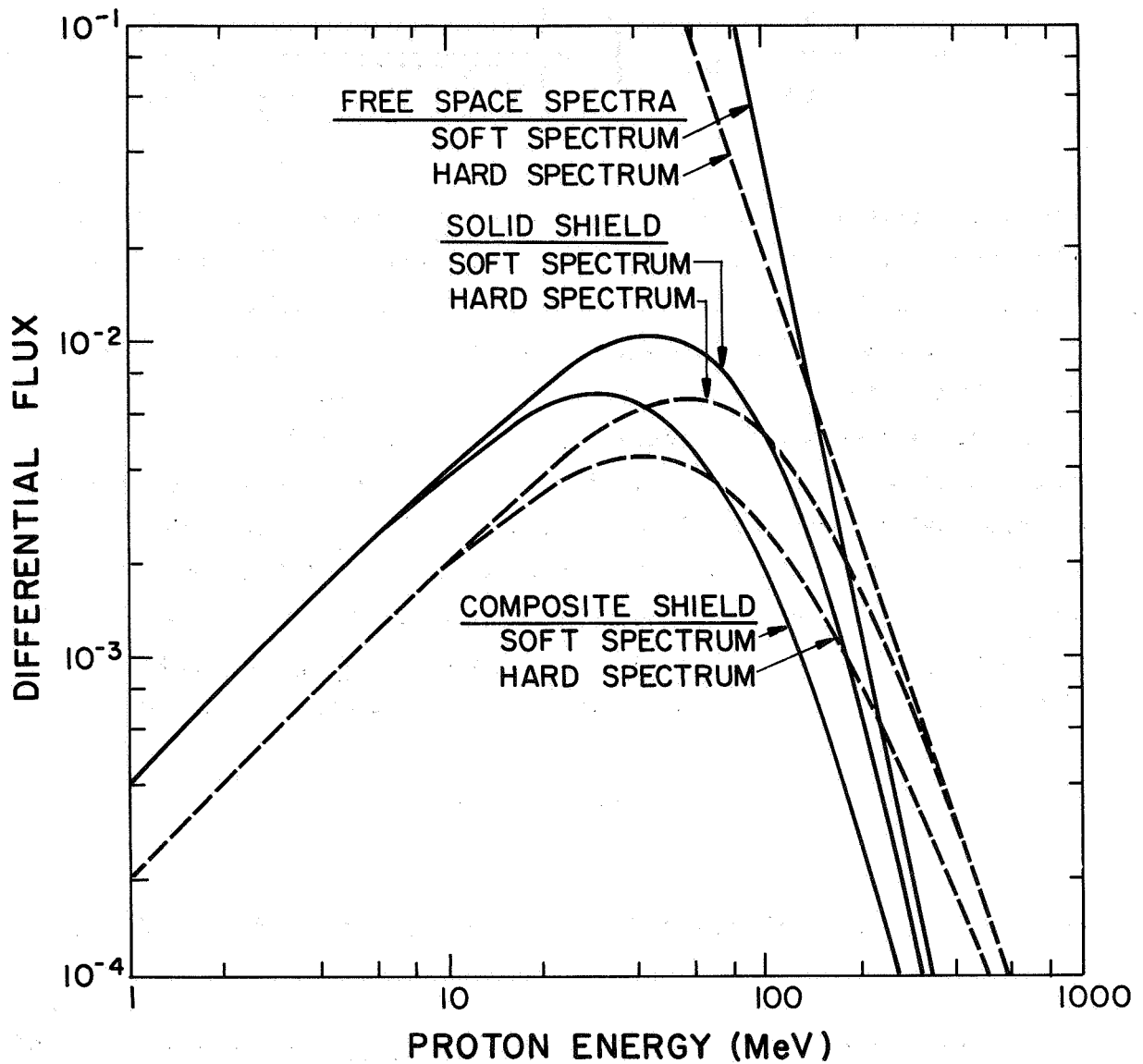


Fig. 4.3 Differential flux spectra behind the two shields illustrated in Fig. 4.2. The units of flux are protons/cm²/MeV divided by the total flux of particles I_{REF} above 100 MeV. Two free space spectra are considered, a soft spectrum having $I(>E) \propto E^{-4}$ and a hard spectrum having $I(>E) \propto E^{-2}$. Both spectra are assumed to have the same total flux above 100 MeV.

(4.4) on the rate of energy loss of the protons, the total energy deposition per unit mass at the back of Shield I (composite) is just:

$$D = \frac{k}{E_{REF}} I_{REF} \int_0^{\infty} n \left[\frac{E_{REF}}{\sqrt{E_2^2 + 2kx_I + V}} \right]^{n+2} \frac{dE_2}{E_{REF}} \quad (4.8)$$

Doses calculated in this way can be shown to be the point dose at the center of a sphere of radius x_I , and charged to a potential V , provided the flux in space is isotropic, with intensity $I_0/4\pi$ per steradian.

The energy deposition per unit mass of equation (4.8) is (owing to the units in which k is defined) in units of MeV/gm. However, this is easily converted, first to ergs/gm, and thence to rads, so that D is a measure of the radiation dose. To give an idea of the magnitude of the dimensional factor in Eq. (4.8) we can take $E_{REF} = 100$ MeV, I_{REF} (which is the number of protons above 100 MeV) = 10^8 protons/cm², and k appropriate to the range of 100 MeV protons in aluminum, i. e., 500 MeV² cm²/gm. In this case the dimensional factor kI_{REF}/E_{REF} is, after changing units, approximately 8 rads. We introduce the notation

$$\sqrt{2kx_I} = E \quad (4.9)$$

so that E is the thickness of the solid shield measured in MeV, we find:

$$\frac{D}{(kI_{REF}/E_{REF})} = n \int_0^{\infty} \frac{dy}{\left[\sqrt{y^2 + (E/E_{REF})^2 + V/E_{REF}} \right]^{n+2}} \quad (4.10)$$

Using this formula, we have calculated the dose as a function of E/E_{REF} , V/E_{REF} , and n . E_{REF} is just an arbitrary normalizing constant, so that the true parameters are E (the equivalent thickness, in

TABLE 4.2

| $D/(k I_{REF}/E_{REF})$ | E/E_{REF} | V/E_{REF} | $(E + V)/E_{REF}$ |
|----------------------------|-------------|-------------|-------------------|
| <u>n=2 (Hard Spectrum)</u> | | | |
| .021 | 0 | 3.175 | 3.175 |
| .021 | 1.941 | 1.941 | 3.882 |
| .021 | 4.225 | 0 | 4.225 |
| .167 | 0 | 1.587 | 1.587 |
| .167 | 0.971 | 0.971 | 1.941 |
| .167 | 2.112 | 0 | 2.112 |
| 1.33 | 0 | 0.794 | 0.794 |
| 1.33 | 0.485 | 0.485 | 0.791 |
| 1.33 | 1.056 | 0 | 1.056 |
| <u>n=4 (Soft Spectrum)</u> | | | |
| .005 | 0 | 2.737 | 2.737 |
| .005 | 1.605 | 1.605 | 3.209 |
| .005 | 3.397 | 0 | 3.397 |
| .167 | 0 | 1.369 | 1.369 |
| .167 | 0.802 | 0.802 | 1.605 |
| .167 | 1.699 | 0 | 1.699 |
| 5.33 | 0 | 0.684 | 0.684 |
| 5.33 | 0.401 | 0.401 | 0.802 |
| 5.33 | 0.849 | 0 | 0.849 |

energy terms, of the solid absorber part of a composite shield), V (the voltage of the Plasma Radiation Shield part of a composite shield), and n , the spectrum index. As indicated at the beginning of this section, the most important parameter of any shield is the energy of the particle it will just stop. In our case, the composite shield will just stop a proton of initial energy $(E + V)$ MeV. We have therefore shown, in Fig. 4.4, contours of constant dose D (non-dimensionalized as indicated in Eq. 4.10), on axes representing the total stopping power of the shield $(E + V)$, and the Plasma Radiation Shield voltage V . On such a graph straight lines can be drawn to indicate constant values of the ratio of E to V . When $E \gg V$, the solid shield is thick and the Plasma Radiation Shield voltage is low, and vice-versa.

As expected, the dose is overwhelmingly a function of $E + V$, and only to lesser extent is it affected by the proportions of E and V going to make up $E + V$. Thus, for the soft spectrum ($n = 4$), a factor of 2 change in $E + V$ yields a factor of 32 change in D . For the hard spectrum ($n = 2$), a factor of 2 change in $E + V$ yields a factor of 8 change in D . In spite of this basic dependence on $E + V$, however, there is a distinct reduction in the dose if, at constant $E + V$, the Plasma Radiation Shield voltage is raised and the solid shielding thickness reduced. Thus, for the soft spectrum at constant $E + V$, the dose for pure Plasma Radiation Shielding is 66% lower than the dose for pure solid shielding. But, since the skin of the vehicle is not negligible, this is an extreme case. If, instead of going to pure Plasma Radiation Shielding ($E = 0$) we go only as far as $E = V$, the dose is only 25% below the pure solid ($V = 0$) case — always at constant $E + V$. For the harder spectrum, these percentages are respectively 58% and 22%. But for the harder spectrum, the dose is not quite such a strong function of $(E + V)$, so that these differences can be more significant. The differences are chiefly of importance in evaluating the skin dose just behind the skin of the space vehicle. The dose to organs located deep in the body is likely to correspond to $E \gg V$, so that the total stopping power $(E + V)$ of the shield is the only parameter of significance. Some of the numbers calculated from Eq. (4.10) are listed in Table 4.2.

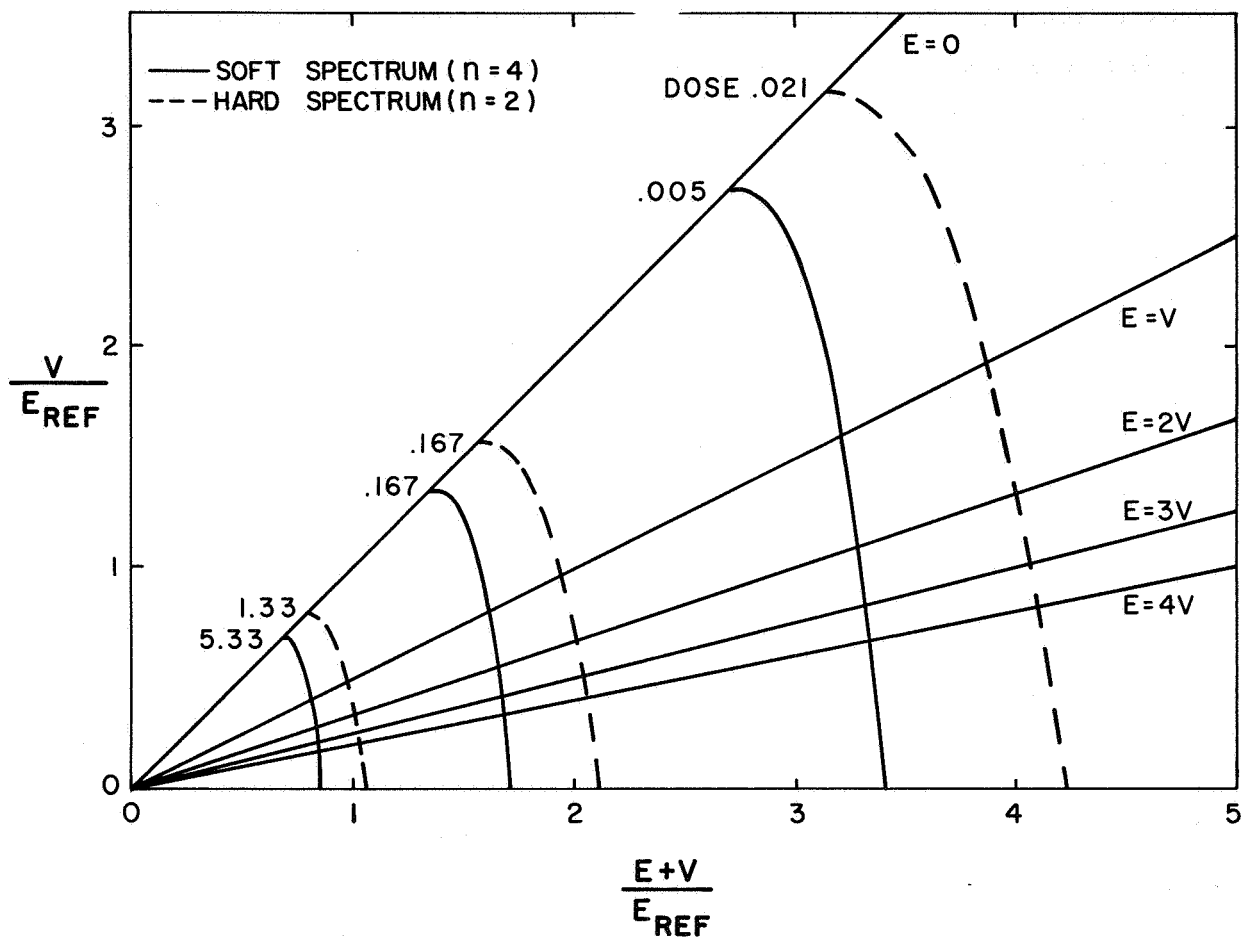


Fig. 4.4 Contours of constant dose behind shields having varying proportions of Plasma Radiation Shielding (at voltage V) and absorber (measured by the energy E of the proton which it will just stop). The doses are given in arbitrary units, which depend on the choice of a reference energy (E_{REF}) and a reference integrated flux (I_{REF}) of protons $> E_{REF}$. For $E_{REF} = 100$ MeV, $I_{REF} = 10^8 / \text{cm}^2$, the unit of dose is roughly 8 rads. The two spectra used have the same total flux of particles above the energy E_{REF} . The dose is principally determined by the total stopping power ($E + V$) of the combination, but this is truer for the soft spectrum than for the hard one. The straight lines represent constant proportions of Plasma Radiation Shielding voltage V and absorber thickness E .

A point of unknown importance is the effect of the Plasma Radiation Shield on the production of secondary radiations. Although the efficiency with which energetic protons produce secondaries is a strongly increasing function of energy, the steep spectra associated with solar flares are thought to result in the lower energy particles producing the bulk of the secondaries. If this is true, the Plasma Radiation Shield will exhibit a further advantage, since the low energy protons will be deflected electrostatically and have no opportunity to produce secondaries. The relative magnitude of the dose due to secondaries in solid shields has been estimated⁷ at 10% of the direct dose for thick shields.

Another factor whose importance remains to be evaluated is the effect on the flux of protons of the magnetic field. There may be a further reduction of the flux of particles of energy just greater than V due to this effect, but the magnitude of this reduction will depend on the configuration, and is presently unknown.

In conclusion, we have attempted to bring out the principal factors governing the choice of Plasma Radiation Shielding voltage. By far the most important parameter, from the dose point of view, is the total stopping power $(E + V)$ of the shielding system, including the vehicle skin. Final selection of the voltage must involve consideration of the total weight of a shielding system of given $(E + V)$, as E and V vary. It is likely that an optimum combination will be found, but it is too early to be precise about its location. In numbers our conclusion from Fig. 4.1 is that voltages in the general range 30-60 MV are likely to be attractive for shielding purposes.

5. CONFIGURATION RESTRICTIONS

As previously discussed, conditions on the magnetic field dictate that the shape of a space vehicle that utilizes the Plasma Radiation Shielding concept be a topological torus. However, this requirement is not as restrictive as one would initially suppose, and we will discuss some possible approaches that may be explored to satisfy this requirement. It should be borne in mind that the following discussion is intended to be heuristic rather than definitive, and it is hoped that this brief exposition will stimulate further ideas in this area.

Shown in Figs. 5.1A to F are some possible spacecraft designs that would satisfy the configuration requirements. It should be noted that their common feature is that they all contain a hole someplace. Fig. 5.1A shows a single element toroidal vehicle that is suitable for a small space station or interplanetary vehicle. Such a vehicle could have a maximum diameter of about 33 feet to fit the diameter of a Saturn S-II stage. This type of vehicle could be made from rigid material, with a minimum number of joints, and checked out for leaks on the ground. These last considerations are of particular importance for the Plasma Radiation Shielding concept for, as will be discussed in Section 7, the need for an extremely tight pressure vessel favors configurations with a minimum number of joints and a low wall porosity.

The maximum allowable size for the vehicle should not be limited by the diameter of the launch vehicle. One way of attaining growth potential while still retaining the basic toroidal shape is to use an inflatable torus that can be packaged into a small volume and deployed in orbit. Such a device, however, is probably not too practical as it would lack the requisite structural strength and rigidity, as well as probably being prone to leakage. A second way of attaining growth potential that appears more attractive is to use rigid modules to construct a large vehicle. One such possibility is illustrated in Fig. 5.1B which shows a larger space vehicle constructed from two rigid toroidal modules. The modules could be stacked up, for instance, on a

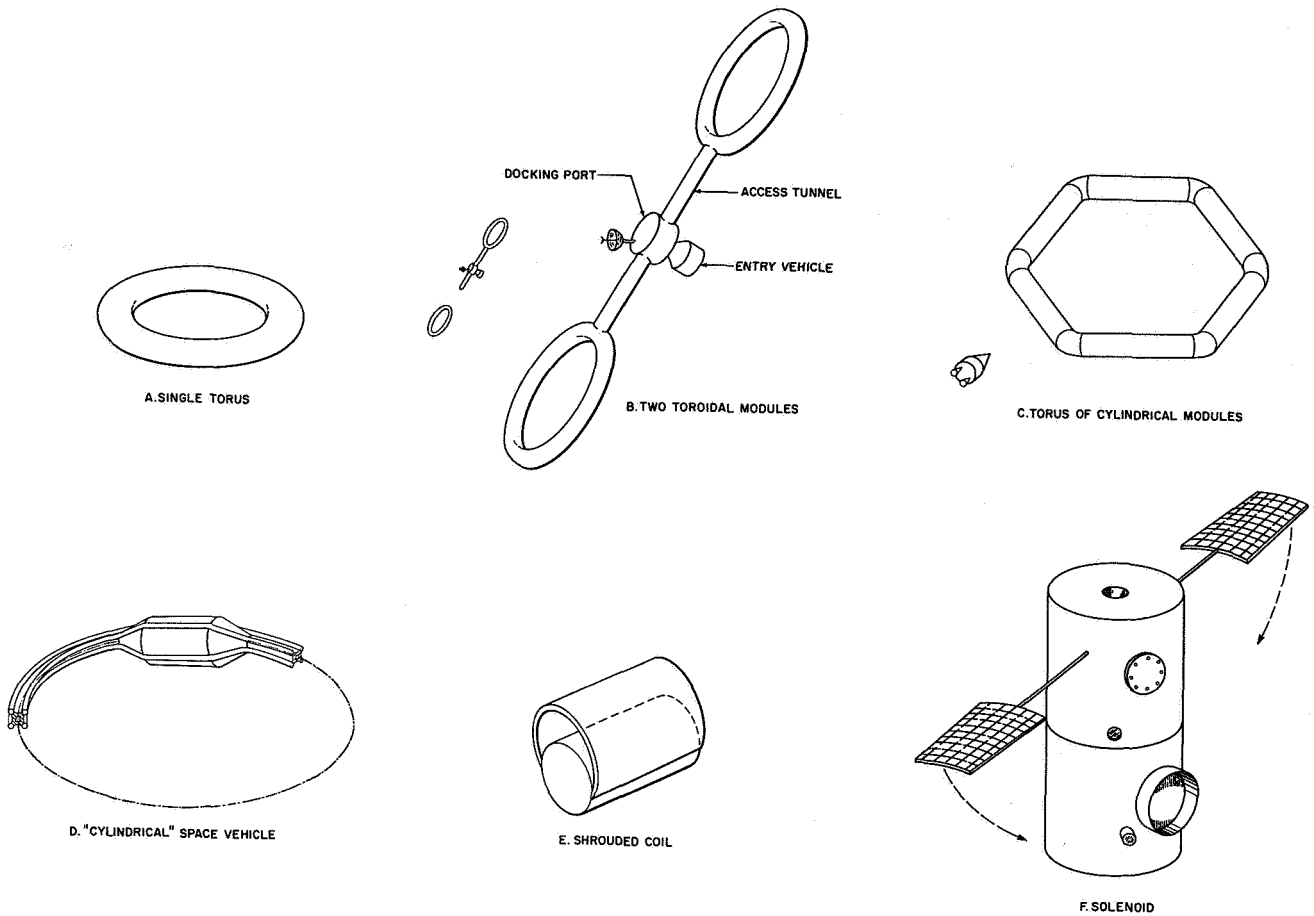


Fig. 5.1 Some possible configurations of spacecraft that utilize the Plasma Radiation Shield concept. In 'A' is shown the basic toroidal shape that may be most appropriate for small vehicles. In 'B' and 'C' are shown growth versions that may find application for intermediate and very large size vehicles. Configurations that are not geometrical toruses but which are acceptable from a topological point of view are shown in 'D' through 'F'. In 'D' is shown a design that utilizes a cylindrical vehicle with a coil that can be deployed in orbit, while in 'E' is shown a cylindrical vehicle with a coil contained in a rigid shroud-like structure. Illustrated in 'F' is a vehicle that utilizes the solenoid principle discussed in Section 3. 6; such a configuration, if feasible, offers several potential design advantages.

Saturn S-II and assembled in orbit. The docking port and access tunnels could be of conventional construction, and detached from the systems when the Plasma Radiation Shield is activated. This configuration has the same advantages as the single module shown in Fig. 5.1A, with the additional advantage of a redundant shelter for crew safety in the event of a failure in one of the modules. If it is desired to use the system for a high altitude, earth-orbiting station, this configuration would provide some gravity gradient stabilization.

Another version of the multi-module approach is shown in Fig. 5.1C which shows several cylindrical elements joined together to form a six-sided torus. The cylindrical elements could be launch vehicle upper stages, and this configuration could serve as a very large space station. It may be noted that the vehicle in Fig. 5.1C is not too different from several designs that have previously been suggested, with the exception that the latter have generally included a central docking hub and access spokes to the toroid. However, because of the requirement that no magnetic field lines intersect the vehicle, such a variant is unacceptable here. The vehicle shown in Fig. 5.1C has the ability to provide a measure of artificial gravity for the crew by rotation about its axis.

There are also allowable spacecraft configurations that do not look like conventional toruses but still meet the requirements imposed by the Plasma Radiation Shielding concept. Three of these are shown in Figs. 5.1D to F. In Fig. 5.1D is shown a cylindrical type spacecraft with a field coil deployed from it. Such a coil could be deployed in orbit from a vehicle that may be similar to proposed MOL or Apollo Applications-type vehicles. Such an approach, however, presents several difficult problems in storing and erecting the coil in space, as well as in adequately supporting it once it is erected. This concept also does not make the most effective use of the field. The vehicle shown in Fig. 5.1E is a variation of that shown in Fig. 5.1D, with a shrouded coil replacing the deployable coil. This design eliminates the coil storage and deployment problems, and provides better support for the coil.

An interesting possibility is illustrated in Fig. 5.1F where the vehicle has many of the characteristics of a solenoid. (See also Fig. 3.4.)

The feature of this design is that the preponderance of electrons are concentrated in a relatively small hole through the center of the vehicle. Because of the low density of electrons along the field lines exterior to the vehicle, the outer surface may have less stringent requirements for leak prevention and protuberance control. Thus, as shown in Fig. 5.1F, the outer surface could contain solar panels, antennas, hatches, docking ports, telescopes, etc., and be of more conventional construction. The inner surface, however, would still require careful control of its leakage characteristics and surface smoothness. Although this approach has many attractive features, it should be emphasized that it is speculative, being dependent on the unproven assumption of electron concentration in the hole.

It has been mentioned above that the outer surfaces of the vehicles (with the possible exception of that shown in Fig. 5.1F) should be relatively smooth and free of protuberances. Just what constitutes an acceptable degree of smoothness requires further study, and this criteria might well strongly influence vehicle design and construction. Also influencing the configuration is the requirement for a structure to resist the magnetic field forces (a topic that will be discussed in Section 6).

6. SUPERCONDUCTING COIL SYSTEM

It is clear that our whole concept depends on the hope that large scale superconducting coils can be operated in space. It is easily demonstrated that the power requirements of any room temperature or cryogenic (not superconducting) electromagnet would be prohibitive for our application. Superconductors, however, have the property of dissipating no heat at all through resistive losses but they must be maintained at very low temperatures. To achieve very high magnetic fields, it is desirable to work at 4.2°K (boiling point of liquid helium). But the Plasma Radiation Shield may be operated with relatively small fields over relatively large volumes. In this case it might be adequate to operate around 13°K^* and use liquid hydrogen. It is quite possible that a space vehicle would have a liquid hydrogen system in connection with its propulsion. Thus this possibility may be quite attractive.

In the absence of ohmic dissipation in the field coils, the only requirement for power arises from the necessity of removing the heat that leaks through the thermal insulation. These powers are generally low, but since heat must be removed at very low temperatures and rejected at almost room temperature, refrigeration efficiencies are low. Notice, however, that the Carnot efficiency of a refrigerating cycle operating between 13°K and room temperature is three times greater than the efficiency of a cycle operating from 4.2°K .

The current that must be carried by the coil is proportional to the required level of the magnetic field B , times a characteristic radius R of the magnet. From Eq. (3.3.1) the magnetic field intensity B is proportional to E/β . But the voltage V of the Plasma Radiation Shield is a more basic parameter than the level of the electric field, and scales as

*For example, Niobium-Tin has a critical temperature of over 18°K .

ER . Thus

$$I \propto \frac{BR}{\mu_0} \propto \frac{ER}{\mu_0 \beta c} \propto \frac{V}{\mu_0 \beta c} \quad (6.1)$$

and in a first approximation the current is independent of the size of the vehicle, although there is a dependence on the shape which it is not yet possible to calculate with much precision. For $V = 50 \times 10^6$ volts and $\beta = 1/2$, Eq. (6.1) yields a current of 3×10^5 amperes, but the actual current required might be several times this value. In particular, the attainable value of β is quite uncertain. In the rest of this section we shall use a total current of 3×10^6 ampere turns as a typical value, allowing a factor of 10 for the various uncertainties in Eq. (6.1).

Present-day superconductors are characterized by maximum current densities of about 10^4 amp/cm², but this figure has been increasing as a result of technical progress. If it is assumed that by the time the Plasma Radiation Shield is built current densities of the order of 10^5 amp/cm² will be available, then the cross-sectional area of superconductor required, $A_{s.c.}$, will be $10^{-5} I \text{cm}^2$. If $I = 3 \times 10^6$ amps, $A_{s.c.} = 30 \text{cm}^2$. The associated mass of superconductor, $M_{s.c.}$, is then

$$M_{s.c.} = 2 \pi R \rho_{s.c.} A_{s.c.} \quad (6.2)$$

$\rho_{s.c.}$ is the density of the superconducting material, and may be taken as 10gms/cm^3 . The value of R depends on the coil configuration but will probably be in the neighborhood of 5 meters. Thus $M_{s.c.} \approx 930 \text{kg.}$, subject to the uncertainty in I . The characteristic magnetic fields are several thousands of gauss.

The weight of the cryogenic system (insulation, refrigeration machinery, power supply and waste heat radiator) is directly proportional to the coil surface area, and inversely proportional to the absolute

operating temperature. For a single turn coil (Fig. 3.2), the area of the cryogenic surface is

$$A_{\text{cry}} = .7R(I/10^6)^{1/2} \text{ m}^2 \quad (6.3)$$

For $I = 3 \times 10^6$ amps, $R = 5$ m. this is 6.6 m^2 , and is less sensitive to the uncertainty in I than $M_{\text{s.c.}}$. The four-coil arrangement of Fig. 3.3, having one quarter the current in each of four coils, would have twice the cryogenic area, about 13.2 m^2 . If the configuration of Fig. 3.4 used a winding distributed along the length of the solenoid, A_{cry} might be as much as 50 m^2 . For a system operating at 4.2°K , the mass of the cryogenic system and the refrigerator power may be estimated from data presented in Fig. 6.1 (based on Ref. 36). From this figure it is seen that if $A_{\text{cry}} = 50 \text{ m}^2$, the power required is 42 kw, and the mass of the system 750 kg. The weight of the power supply has been estimated using a figure of about 10 kg/kw. Operating at 13°K , the same system would require a power of 8 kw, and would weigh about 250 kg.

The third component in the superconducting magnet system, in addition to the superconducting coil and the cryogenic components, is the support structure necessary to contain the energy stored in the coil. The structural mass is determined by requirements to resist both tangential (or hoop) and meridional stresses in the torus (Ref. 36). The magnitude of the characteristic magnetic field has a strong influence on the structural weight since the weight varies as the square of the field strength. The stress level in the magnet is approximately equal to the magnetic pressure $B^2/2\mu_0$. For a magnetic field strength of about 3300 gauss, such as considered herein, the equivalent magnetic pressure is about 5 psi. Since this pressure is of the same order of magnitude as the cabin atmosphere pressure, the required structural problems are not contemplated to be severe. The actual stress pattern in a configuration like that of Fig. 3.3 would be quite complex and it is difficult to arrive at an accurate estimate for the structural weight. The structure of the solenoidal field coil

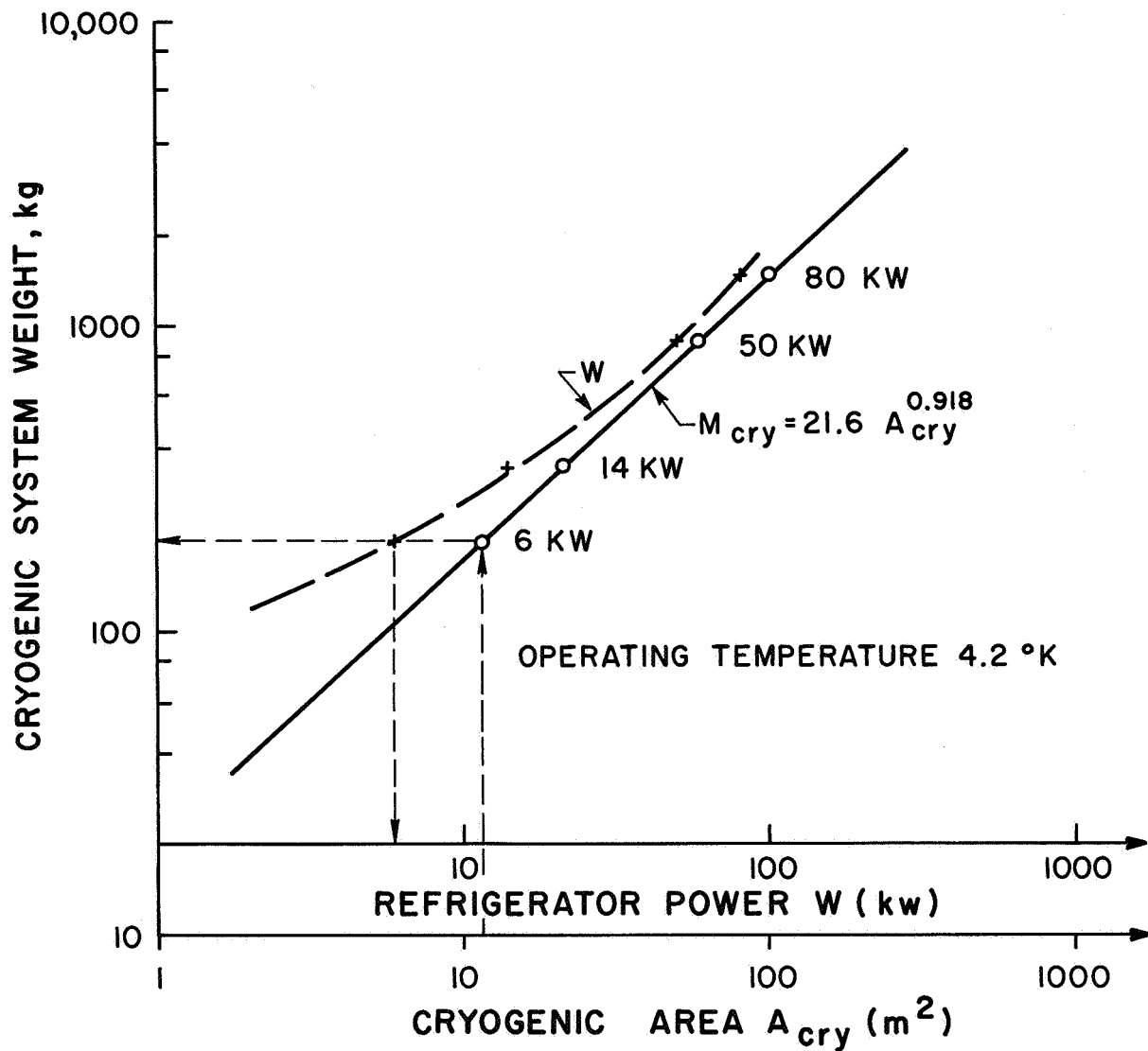


Fig. 6.1 Mass and require power for a cryogenic system comprising insulation, refrigerator, power supply and waste heat radiator. The weight of the last two was estimated using a conversion figure of about 10 kg/kw. The graph is for an operating temperature of 4.2°K. At 13°K, all powers and weights would be reduced by a factor of about 3. The data is based on Ref. 36. As an example, suppose $A_{cry} = 10.2 m^2$. The solid line then indicates a system weight of 200 kg. Also, reading horizontally to the dashed line, and then down, the room temperature refrigerator power required is 7 kw.

associated with the configuration of Fig. 3.4 would be relatively simple. Only a small amount of work has been carried out in this area and much more remains to be done.

One last problem needs to be mentioned in connection with the design of the magnetic field. In general, one would like to design the coils so that the vast majority of the magnetic flux is where it is needed, that is, in the electron cloud and hence outside the space vehicle. In general, however, any particular coil design will have a certain level for the stray fields inside the space vehicle. These stray fields must be kept at low levels if they are not to interfere with the function of equipment sensitive to magnetic fields within the space vehicle; such things as cathode ray tubes, magnetic tape recorders and ferrites come to mind. The need to keep stray fields low would tend to produce a diffused coil design, such as the four-coil scheme shown in Fig. 3.3 or the solenoid of Fig. 3.4. Such designs, however, would entail a penalty in surface area (and hence refrigeration).

7. VACUUM REQUIREMENTS

It was pointed out in Section 3 that the ionization of neutral atoms by the electron cloud can constitute a serious source of loss; control of this source of loss requires that the outward flow of neutral gas originating in the space vehicle must be held to extremely low levels. The two primary sources of such gas are: 1) Outgassing from the outer surface of the space vehicle, and 2) Leaks from the interior. In this section we discuss first the factors determining allowable loss rates, and second, the effect of these rates on the design of the Plasma Radiation Shield.

7.1 Factors Controlling Allowable Leak Rates

In Section 3 we made a preliminary estimate of the allowable leak rate, but this was based on the most pessimistic assumption, namely, that each neutral emitted by the space vehicle was ionized right at the wall. When this happens, the ion thus formed carries away an energy corresponding to the full voltage of the Plasma Radiation Shield. On the other hand, our estimate of the mean free time of the neutral before ionization was 1 second; in this time the neutral is capable of crossing the electron cloud many times. For example, let the speed of the neutral be 10^5 cm/sec and let the size of the electron cloud be 10^3 cm. In this case, the mean potential at ionization will be on the order of 1% of the full potential; this results in a vacuum requirement 100 times less stringent than the most pessimistic case discussed above. To resolve the uncertainties arising in this way, it is necessary to take account of a number of factors. These factors are listed below, but, except for the last one (influence of the overall geometry), it is felt that the individual uncertainties are not very large. Later on, in the interest of offering definite numbers, we shall guess that the combined effect of all the factors does not amount to more than an order of magnitude, but additional work is required to justify this guess. The factors are:

1. The actual velocity of the neutrals. Here it is reasonable to assume that the neutrals leave the surface of the space vehicle with a Maxwellian distribution of velocities corresponding to the temperature of the surface. If the temperature of the surface is $15^{\circ}\text{C} = 288^{\circ}\text{K}$, the mean value of the velocity component normal to the surface for some typical gases is:

| | |
|----------------|----------------------------------|
| H | $1.2 \times 10^5 \text{ cm/sec}$ |
| H ₂ | $.87 \times 10^5$ |
| He | $.60 \times 10^5$ |
| N | $.32 \times 10^5$ |
| N ₂ | $.23 \times 10^5$ |
| O | $.3 \times 10^5$ |
| O ₂ | $.21 \times 10^5$ |

2. The spatial distribution of the electrons. The mean free time of 1 sec quoted above was a very rough average. In order to calculate this time correctly, we require (among other things) to know whether the electrons are in a dense layer near the space vehicle, or spread out over a considerable distance. The ratio of the size of the electron cloud x to the mean free path of the neutrals is roughly $xn\sigma_e/v_n$ where the symbols stand for the size of the electron cloud, the electron number density, the ionization cross section, the electron velocity, and the neutral velocity. But xn_e is roughly proportional to the electric field at the wall of the vehicle, and this in turn is roughly proportional to ϕ_0/x , where ϕ_0 is the potential of the Plasma Radiation Shield. For a given potential, the ratio in question is smaller when x is relatively large. A more important ratio is that of the mean potential at ionization to the potential ϕ_0 . However, to a first approximation, this ratio is similar to the ratio of lengths calculated above.

3. The distribution of electron velocities. This quantity has an important effect on the product $\sigma_e v_e$ which occurs in these calculations.

For electrons having kinetic energies significantly large compared to the ionization energy, the product σv_e varies roughly as

$$\sigma v_e \propto \frac{1}{v_e I} \ln \frac{\frac{1}{2} m v_e^2}{eI}$$

where I is an appropriate ionization energy. In general, the electron energies will be well above the ionization energy so that

$$\sigma v_e \propto \frac{1}{v_e}$$

roughly. Hotter electrons are therefore less efficient producers of ionization, and hence more desirable from our point of view. To a first approximation, the electron velocity is simply E/B , but superposed on this drift motion there is likely to be a "thermal" distribution at an unknown temperature. This thermal component is likely to be especially important near the outer edge of the electron cloud, where E/B is low. However, the effect of ionizations which occur near the outer edge is also low. Its magnitude is at present quite uncertain; this lack of knowledge may eventually require experimental study.

4. The species of neutral. This not only affects the expected neutral velocity, but also the ionization cross-section through the quantity I occurring in the above formula. In general, the heavier gases not only move more slowly through the electron cloud, but also have larger ionization cross-sections. However, it is easier to control the leakage of the heavier gases.

5. The overall geometry. The electric and magnetic field, the potential and the electron density have characteristic values, but can also vary quite widely as a function of position around the space vehicle. For

example, the electric field and the number density on the outside of the Plasma Radiation Shield (facing away from the axis) are substantially lower than those on the inside (facing towards the axis). The extreme possibility here is the solenoidal configuration of Fig. 3.4. If, as we hope, it turns out that the electron cloud is entirely confined to the region inside the solenoid, the whole vacuum problem becomes very much easier. For leaks from those parts of the surface not facing the electron cloud (i. e., the outer surface) are of no consequence, and we only have to restrict leakage from the inside of the solenoid. Thus, one would place all access doors, antennas and other protuberances on the outside. As stated in Section 3.6, the existence of this type of confined electron cloud has not yet been demonstrated.

The factors discussed above are not likely to achieve substantially better definition in the immediate future. It is therefore appropriate, in the spirit of this paper, to consider the effects of our rough estimates of allowable leak rates on the design of the Plasma Radiation Shield.

The allowable leak rates were estimated in Section 3, on the basis of two different assumptions, as the equivalent of 10^{-6} and 10^{-4} gms of oxygen in two days. Except for the configuration of Fig. 3.4, it is probably not reasonable to imagine that more than a further factor of 10 could come out of detailed consideration of the various factors enumerated above. This could give an upper limit to the leak rate of 10^{-3} gms in two days. To appreciate the magnitude of these figures let us compare them with comparable figures for past and planned manned vehicles. The Mercury vehicles experienced a leak rate of 2.24 lb/day = 1 kg/day (of air at 5 psia).⁶⁷ The internal volume of the Mercury vehicles was small, about 30 ft³ (.85 m³), so the leak rate per unit volume was about 7.5×10^{-2} lb/day/ft³ (1.2 kg/day/m³). It is anticipated that the latter figure for the Apollo vehicles will be improved by an order of magnitude to about 7.5×10^{-3} lb/day/ft³^{68, 69} (.12 kg/day/m³). However, this vehicle will have a much larger internal volume so that the leak rate itself will not be an order of magnitude less than Mercury's. Clearly the Mercury-Apollo type construction would yield leak rates that are many orders of magnitude too large for the application in mind. However, for these vehicles no

particular attempt was made in the design to obtain low leak rates, for the principal penalty was to carry along a few extra pounds of air. At the very least it is obviously unreasonable to contemplate losses on the order of 1 kg/day for missions lasting several hundred days. Current thinking indicates that it is possible to obtain much lower leak rates than those quoted through careful design and a pre-launch program of leak detection.

7.2 Outgassing

If we suppose that the principal source of neutrals near the space vehicle is due to outgassing from the walls, then we can estimate an allowable effective pressure over the walls. The permitted current of atoms may be in the range 10^{12} to 10^{15} atoms/sec. Assuming a surface area of 3×10^6 cm², this gives a mean allowed flux of from 10^6 to 10^9 atoms/cm²sec. By way of example, these fluxes correspond to a partial pressure of oxygen of 10^{-15} to 10^{-12} mm Hg at 15°C. These levels imply that it will be necessary to apply very high quality vacuum technology to the design of the Plasma Radiation Shield. However, there are certain factors which make the environment in deep space exceptionally suitable for the application of this technology. There will, for example, be ample time to clean the surface thoroughly in the hard vacuum of outer space. This could be accomplished by baking out the entire surface while in space, to above 400°C. On the basis of present knowledge, these procedures, if applied in space, should be extremely effective and should indeed result in outgassing rates of the right order of magnitude. Many metal materials are compatible with bakeout procedures of this type, and bakeout of the outer metal wall could be accomplished in earth orbit, before departure for deep space. It could also be accomplished before the vehicle was manned, although there need be no requirement for the temperature inside the vehicle to reach the bakeout temperature. Hydrocarbon or teflon seals cannot be baked to 400°C, but ceramic seals can. It would be desirable to have more information on the achievement of very clean, outgassed surfaces in the space environment, but preliminary ideas suggest that this environment is uniquely suitable to our purposes.

7.3 Leaks from the Interior

At room temperature and pressure, the flux of oxygen through a small plane hole into a vacuum is roughly $10 \text{ gms/cm}^2 \text{ sec}$ or $1.7 \times 10^6 \text{ gm/cm}^2$ in two days. On this simple-minded basis, it would appear necessary to restrict leaks to a total area of 10^{-12} to 10^{-9} cm^2 , but several factors render this estimate unreasonably pessimistic. Principally, leaks generally involve long and narrow paths which offer considerable resistance to any flow. Possibly more important is the fact that the use of high quality seals and good high vacuum techniques should result in an essential elimination of leaks.

In spite of these possibilities it seems that it would be highly desirable to use a double-walled construction technique for the space vehicle. The inner wall would contain the atmosphere in which the crew would live, while the space between the two walls could be evacuated to a rather low pressure, say between 10^{-6} and 10^{-9} mm Hg . With pressures of this order in the space between the two walls, the leak through an aperture in the outer wall would be reduced to $2.3 \times 10^{-3} \text{ gm/cm}^2$ to $2.3 \times 10^{-6} \text{ gms/cm}^2$ in a period of two days. Thus, in the best case (allowable loss of 10^{-3} gms , and an inter-wall pressure of 10^{-9} mm Hg), it would be permissible to have holes in the outer vessel amounting to 1000 cm^2 ! In the worst case (allowable loss of 10^{-6} gms , and an inter-wall pressure of 10^{-6} mm Hg), plane holes in the outer vessel should not exceed 10^{-3} cm^2 . The comment above on long, narrow leakage paths also applies here.

The double-walled construction suggested above has several very attractive features:

1. Double-walled construction is highly favored as a protection against puncture of the pressure vessel by large micrometeorites. In addition to contributing materially to the stopping power of the wall, the construction provides some degree of fail-safe protection of the cabin atmosphere.
2. Pumping in the space between the walls to maintain a low pressure in this region would in any event not be difficult. It is particularly assisted in the present case by the presence of the cryogenic system associated with the superconducting coils. This system normally comprises

a liquid nitrogen container surrounding the liquid helium; surfaces at liquid nitrogen temperatures should effectively trap all the heavy gases leaking out through the inner wall, and reduce the pressure of all other gases that might be present.

3. Double-walled construction with inter-wall pumping relieves the problem of leaks to such an extent that the use of standard polymer or teflon seals should be quite satisfactory for the inner vacuum barrier.

Although any form of high vacuum pump could be used to keep the pressure low between the walls, a particularly attractive prospect might be to utilize the existing magnetic field to turn part of the space between the walls into a sort of Vac-Ion Pump. This would involve maintaining a moderate electric potential between a cathode and an anode, and using a circulating electron beam to ionize and pump any residual neutrals. A particularly attractive possibility associated with the configuration of Fig. 3.4 is that the outer wall need only cover that part of the surface facing the electron cloud, i. e., the interior. Thus, if the outer wall were not continued on the outside part of the surface, the infinite pump of outer space would be available to pump from the inter-wall region on the inside surface.

7.4 Summary

The Plasma Radiation Shield will require a clean outgassed outer surface and a double-walled pressure vessel with a pressure of roughly 10^{-6} to 10^{-9} mm Hg in the space between the walls. The exact requirements cannot yet be stated with much precision, but do not appear excessively difficult. The space environment is especially favorable to the achievement of clean surfaces and high vacuum, and the double-walled construction has subsidiary advantages. On the other hand, this construction presents many novel design problems to the space vehicle designer. The requirements for low permeability walls and ground detection of leaks indicate that a welded, metal construction will be necessary. Such a construction is rigid and places limitations on packaging within the launch vehicle as well as on the manner in which the system can grow. It will also require careful consideration of the placement and design of cutouts in the pressure vessel

walls, and in the design and selection of material for the seals around these cutouts.

In addition to the prevention and careful control of leaks, care must be exercised in allowing no other type of exhalations from the vehicle during a solar flare. This has ramifications in design of such systems as power supply, attitude control, propulsion, life support, etc. Such systems should either be chosen to not have an exhaust or, if they do, to be inoperative during a solar flare. A possible exception to these considerations is the configuration of Fig. 3.4.

A preliminary conception of the double-walled construction is shown in Fig. 7.1.

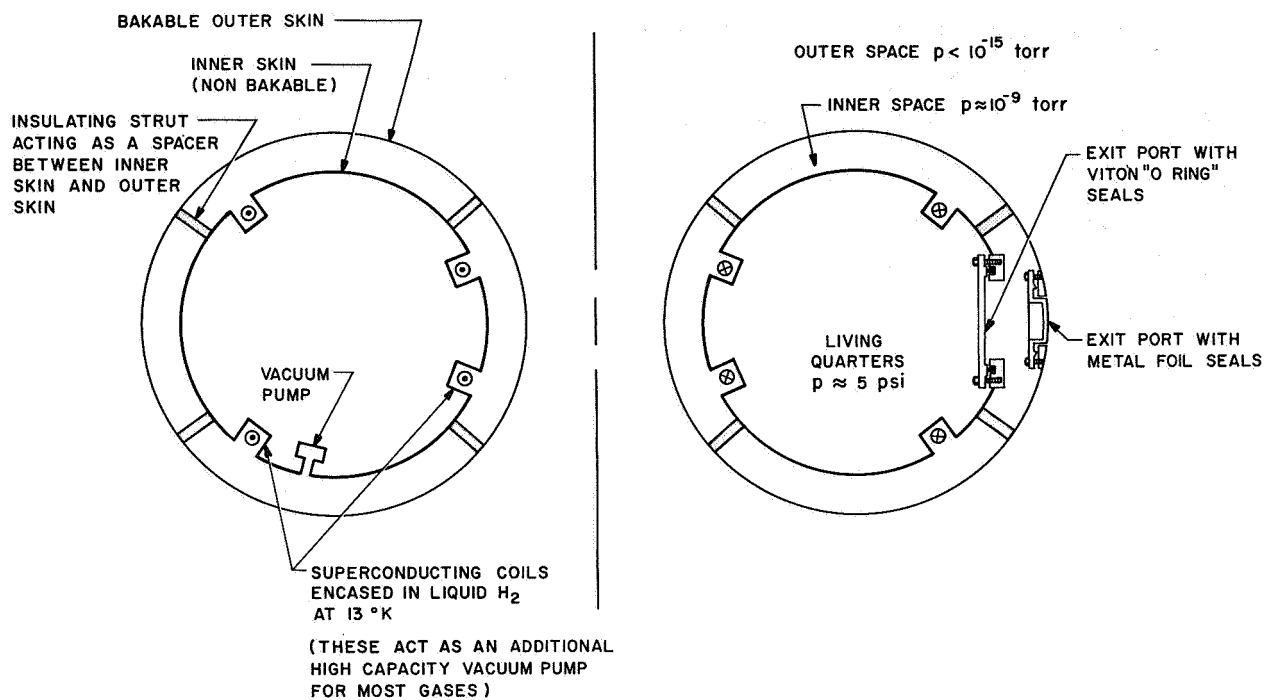


Fig. 7.1 Shows schematically one out of the many possible ways in which the double-wall concept could be applied to a toroidal space vehicle using a Plasma Radiation Shield. The space between the walls is kept at a pressure like 10^{-9} torr by a combination of vacuum pumps pumping into the interior and the low temperature environment of the superconducting coils.

8. OTHER SYSTEMS CONSIDERATIONS

The design of other subsystems that go into the total spacecraft system will also be influenced by the requirements imposed by the Plasma Radiation Shield. Several of these systems that are most obviously influenced will now be discussed, and possible design approaches suggested.

8.1 Magnet Charging Power Supply

The total electric field energy is $\frac{1}{2} CV^2$ where C is the effective capacity of the space vehicle and electron cloud. If we guess that C is 10^{-9} farads, the stored electric energy at 50×10^6 volts is 1.25×10^6 joules. The magnetic energy is larger than this by roughly β^{-2} , so that if $\beta = \frac{1}{2}$ the magnetic energy is 5×10^6 joules. These total figures are subject to considerable uncertainty both as regards the capacity and the value of β . We shall suppose, for purposes of illustration, that the uncertainty is a factor of ten, and take a representative magnetic field energy as 50×10^6 joules.

The maximum time allowable to energize these fields is of the order of the time interval between first detection of the flare and the first arrival of appreciable particle flux. If this time is taken as 1-1/2 hr, the power that must be supplied during this time is about 10 kw for a 50 MV 50 M joule system. (This figure is in addition to steady power requirements for the cryogenic system, and typically about 5 to 10 kw for other spacecraft needs.) The power source for field energization must be operative during every major solar flare (maybe ten times during a mission) and must not (except possibly in the configuration of Fig. 3.4) vent exhaust gases to the exterior during its operation. The latter requirement rules out several otherwise likely candidates, and a very large solar cell array is ruled out because it would cut through magnetic field lines. A class of power sources that meet these requirements and can be available in the time period of interest is the fuel cell. Two types of fuel cells may be considered for the application discussed here — the hydrogen-oxygen and the lithium-chlorine

types. The hydrogen-oxygen fuel cell is currently available for powers of a few kilowatts. These devices give off easily-storable water as a by-product of the reaction, and operate optimally at a relatively low temperature (90°C). A 2 kw unit will soon be available that weighs 146 lbs.⁷⁰

If more power is necessary, the power supply should have a lower specific weight. Taking hydrogen and oxygen consumption rates of 0.1 and 0.8 lb/kw-hr, respectively, the weight of the fuel cell reactants for the mission is then

$$w_f = (0.1 + 0.8) \frac{\text{lb.}}{\text{kw.hr.}} \times 1.5 \text{ hr} \times 10 \text{ kw} \times 10 \text{ applications} = 135 \text{ lbs.}$$

Including the tankage, the total weight of the power supply using hydrogen-oxygen fuel cells should be around 1500 lbs for the 10 kw level, and would scale roughly as the field energy. Lithium-chlorine fuel cells are still in development but offer the promise of high power levels for short times at low weight. Aside from their present unavailability, a disadvantage to this type of fuel cell is their high operating temperature, 650°C. A reasonable energy density figure to be expected from these cells for a 10 kw system with an operating time of 1-1/2 hr is about 200 w-hr/lb.^{71,72} Using 10 of these units for the mission would result in a total power supply system weight of about

$$W = \frac{10,000 \text{ w} \times 1-1/2 \text{ hr}}{200 \text{ w-hr/lb}} \times 10 \text{ applications} = 750 \text{ lbs.}$$

In summary, it appears feasible to use hydrogen-oxygen or lithium-chlorine fuel cells for the power supply with system weights of less than 1500 lbs. Integration of the magnet charging power supply with the general spacecraft power system would result in a lower weight assignable directly to the Plasma Radiation Shield, because the specific weight of such power systems is smaller for larger powers.

8.2 Communications

It is very desirable, if not essential, for the crew to be able to communicate with the outside while the Plasma Radiation Shield is in operation. With the exception of the configuration of Fig. 3.4, this must be accomplished by transmission through the electron cloud that surrounds the space vehicle, and without the use of lengthy antennas. To do this in the radio range requires a frequency above the plasma frequency, ν_0 , given by $\nu_0 = 9 \times 10^{-3} (n_e)^{1/2}$ with ν_0 expressed in megacycles per second, and n_e , the electron density, in electrons per cubic centimeter. For $n_e = 2.1 \times 10^8$ per cm^3 (Section 3.2), the plasma frequency is 130 Mc/s. Thus, transmissions at higher frequencies (such as commonly-used S-band) would be possible. Another means of communication that could be considered is by laser beam, since it is anticipated that this type of communication, with its promised high data rate, will be available in the time period of interest.

8.3 Attitude Control and Propulsion

The attitude control and the propulsion systems are constrained not to have an exhaust while the Plasma Radiation Shield is in operation. If it is necessary to change vehicle attitude during a solar flare, such a change could possibly be affected by the use of devices such as momentum wheels. If chemical or nuclear rockets are used as the main propulsion system on the space vehicle, it would seem that the probability of having to fire them during a solar flare would be somewhat small. If, however, the propulsion unit is a system that depends on attaining a desired impulse by a small thrust applied over a long time, the system would be required to be shut down while the Plasma Radiation Shield is in operation.

8.4 Life Support

In regard to the crew and their life support, the ecological system must be of the closed-cycle type, at least for the duration of the flare. Although the Plasma Radiation Shield concept requires the magnetic field to be external to the spacecraft, it is fairly certain that some stray, extraneous fields are bound to exist within the spacecraft interior. While the level of these stray fields can be reduced arbitrarily, stringent requirements on the allowable level will cause the magnet weight to rise. It is therefore

worthwhile to examine the effects of these fields on the crew and on internal equipment.

Medical evidence has been negative as to the effects of magnetic fields, at least of the magnitudes anticipated in the spacecraft, on human beings.⁷³ The effects of magnetic field gradients are somewhat more obscure but it is felt that gradients of the magnitude occurring in the spacecraft will also be safe for humans.

8.5 Effect of Stray Magnetic Fields on Electronic Equipment

With respect to the effects of these stray magnetic fields on internal electronic devices, the situation is not so optimistic. It is anticipated that field strengths could conceivably be strong enough to require shielding or careful positioning of devices such as tape recorders and oscilloscopes.

9. CONCLUSIONS

We have reviewed in some detail the various features of the Plasma Radiation Shield concept likely to be important in any systems analysis of a space vehicle using the Plasma Radiation Shield. In summing up our findings, the point of departure must be the following observation: there still remains a wide range of opinions on the magnitude of the threat posed by solar flare protons to astronauts. Our premise is that a substantial problem exists. Since estimates of the solid shielding required are high, the possibility of reducing shielding weight by using the Plasma Radiation Shield is attractive.

Pending the satisfactory resolution of several questions, the possibility of realizing the advantages offered by the Plasma Radiation Shield must remain in doubt. The outstanding questions fall into two distinct categories:

- 1) Questions associated with the fundamentals of the concept itself, such as the attainability of very high voltages, and the stability of the electron cloud.

- 2) Questions associated with the integration of a Plasma Radiation Shield into a space vehicle. The Plasma Radiation Shield makes demands on the vehicle design in areas of overall configuration, power supply, and leak control, to name only the most important.

At this point, it is possible to be guardedly optimistic about the questions in the first category. No insuperable difficulties have been found, but affirmative statements cannot be made without further experimental and theoretical studies. It is particularly important to establish the maximum permissible value of $\beta = E/cB$, since this parameter determines the strength of the magnetic field and hence the weight of the magnet. In estimating the weight of a Plasma Radiation Shield, the magnet is by far the most important component.

As regards the second category of questions, these reduce to definite quantitative requirements which must be met by any space vehicle incorporating the Plasma Radiation Shield. The most important questions are those of overall configuration, and control of leaks.

It was stated in the preface that this paper was regarded as preliminary to a deeper systems analysis of the Plasma Radiation Shield. It is therefore appropriate to make some remarks here on the basic problems likely to be encountered in such an analysis. Now a primary goal of such a systems analysis will be a reliable graph of weight vs. shielded volume. This is because unless such a graph can be developed, the advantages of the Plasma Radiation Shield over solid shielding cannot be exhibited in a quantitative manner. It was explained above that the weight will remain uncertain until the allowable value of β can be established. However, it is also true that the shielded volume of different configurations cannot yet be given with much accuracy; it is even more true that for a given configuration, the dimensions cannot be optimized to yield a minimum magnet weight per unit shielded volume. We are now in a position to calculate the shielded volume for a variety of configurations, but the calculations are difficult and have not yet been undertaken. Clearly, such calculations must constitute the first step in a detailed systems analysis.

In summary, the Plasma Radiation Shield still appears to offer the promise of substantial reductions in shielding weight. More work in several areas will be required in order to show that these reductions can be realized.

10. ACKNOWLEDGMENTS

It is a pleasure to acknowledge the assistance of G. S. Janes and J. D. Daugherty in connection with several parts of this paper. We are indebted to Dr. John C. Helmer of Varian Associates, Palo Alto, California for permission to use Figs. A.1 and A.2, and to Mr. A. Reetz of NASA, Washington, D. C. for supplying the figures appearing in Table 2.1.

Appendix

Status of Work on the Electron Cloud

A.1. Introduction

The current status of work on the electron cloud is as follows:

1. Theoretical work⁴⁷⁻⁵³ has thus far failed to find any reason why a stable dynamic equilibrium for the electron cloud should not exist. This "double negative" statement is the best that can be made, since, in a problem as complicated as that of the electron cloud, a positive theoretical proof of stability is virtually impossible. There have, nevertheless, appeared certain conditions that the electron cloud must satisfy if it is to be stable. The most important of these are:

- a) the number density n of the electrons, and the magnetic field strength B must satisfy the condition

$$\frac{ne}{\epsilon_0 B^2} \lesssim \frac{1}{30} \quad (\text{A. 1. 1})$$

- b) the inner edge of the electron cloud must be rather close to the surface of the Plasma Radiation Shield.

2. It has been observed that the electron cloud in the Plasma Radiation Shield closely resembles the electron cloud in a high vacuum pump (the Vac-Ion Pump). Encouraging conclusions may be drawn from the apparent stability of the electron cloud in this pump.

3. Several experiments^{49, 74} have been performed to study the electron cloud, although none has been in the geometry of the Plasma Radiation Shield. One of the objects of these experiments has been the demonstration of high voltages using the inductive charging system. In an electron cloud 10 cm. in radius, voltages in excess of 80,000 have been

demonstrated; the achievement of higher voltages presently awaits development of the means to measure them.

A.2 Theoretical Work

It is a relatively easy matter to find dynamic equilibria for the electron cloud under the assumption that the motions of the electrons are adequately represented by the "guiding center" approximation:

$$\underline{v}_e = \underline{E} \times \underline{B} / B^2 . \quad (\text{A.2.1})$$

In configurations with axial symmetry, both the electric and magnetic field vectors lie in the meridional plane, so that the velocity vector is in the azimuthal direction. Then, if the number density of electrons is independent of the azimuth (the symmetrical situation) the condition

$$\text{div } \underline{j} = - \text{div } n_e e \underline{v}_e \quad (\text{A.2.2})$$

on the current is trivially satisfied. It is necessary, however, to require that the electric potential be such that the magnetic field lines are equipotentials. This can be done as follows: since $\text{div } \underline{B} = 0$ we can write (in r, θ, z coordinates)

$$B_r = \frac{1}{r} \frac{\partial \psi}{\partial z} \quad B_z = - \frac{1}{r} \frac{\partial \psi}{\partial r} \quad (\text{A.2.3})$$

the surfaces $\psi(r, z) = \text{constant}$ are then the field lines since along such a surface

$$0 = d\psi = \frac{\partial \psi}{\partial r} dr + \frac{\partial \psi}{\partial z} dz = -r [B_z dr - B_r dz] \quad (\text{A.2.4})$$

or

$$\frac{B_r}{B_z} = \frac{dr}{dz} \quad . \quad (\text{A. 2. 5})$$

If we then require the potential $\phi(r, z)$ to have the form

$$\phi(r, z) = F[\psi(r, z)] \quad (\text{A. 2. 6})$$

where F is an arbitrary function, all the necessary conditions are satisfied. The number density can be obtained from (A. 2. 6) through Poisson's equation. It is then only necessary to restrict the range of functions F by the condition that the number density be everywhere positive.

Inasmuch as the equation (A. 2. 1) is a very good approximation to the electron dynamics in the Plasma Radiation Shield, it is expected that equilibria derived by the method just described will be very close to true equilibria of the whole electron cloud.

Having exhibited the possibility of equilibria, we turn next to the much more difficult problem of stability. As stated in the introduction, stability analysis can in general only arrive at negative statements. Thus, one can prove that such and such a mode is stable, but, in complicated systems, one can never be sure that all the important modes have in fact been dealt with. With these reservations, we can make the following general statements: In general, we expect stability trouble to occur at or near characteristic frequencies of the medium. For our electron plasma there are three such frequencies, namely, the electron gyro frequency

$$\omega_c = eB/m \quad (\text{A. 2. 7})$$

the electron plasma frequency

$$\omega_p = (ne^2/\epsilon_0 m)^{1/2} \quad (\text{A.2.8})$$

and the frequency with which the electrons circulate around the space vehicle

$$\omega_0 = E/BR \quad (\text{A.2.9})$$

In view of the connection between the electron number density and the electric field, these frequencies are related by the following approximate formula:

$$\omega_p^2 = \omega_0 \omega_c \quad (\text{A.2.10})$$

A convenient non-dimensional number is the ratio

$$q = \frac{\omega_p^2}{\omega_c^2} = \frac{nm}{\epsilon_0 B^2} \quad (\text{A.2.11})$$

In terms of this ratio, our frequencies can be ordered as follows:

$$\omega_0 : \omega_p : \omega_c \equiv q : \sqrt{q} : 1 \quad (\text{A.2.12})$$

Now for the Plasma Radiation Shield q is a small number, on the order of 10^{-3} . It follows that the frequencies listed in (A.2.12) are in ascending order, with a factor ~ 30 between each pair.

All these frequencies are high, however, ω_0 being in the range of 3Mc/sec or so. Hence any instability having a growth rate of even a fairly

small fraction of these frequencies would be disastrous.

Our findings for the three frequency ranges are as follows:

- a) The gyro frequency: Here there is apparently always an instability. However, the growth rate of this instability is on the order of $\omega_0 \cdot e^{-2/q}$. For $q = 10^{-3}$ and $\omega_0/2\pi = 3 \text{ Mc/sec.}$, this gives an exponentiating time longer by far than the age of the universe! This is not a "fairly" small fraction of ω_0 and represents a growth so slow as to be quite unreasonable. This instability is of interest only for $q \gtrsim 1/30$.
- b) The plasma frequency: Analysis in this region is not yet complete, but it appears that there is no important instability here.
- c) The frequency $\omega_0 = \omega_p^2/\omega_c$: The instability that is important in this range is called the "diocotron instability." It appears, on the basis of a considerable amount of work, that this instability can be avoided in the Plasma Radiation Shield configuration provided that there is not too large a gap between the inner edge of the electron beam and the conducting wall of the Plasma Radiation Shield.

Thus, the results of our stability analysis, while not conclusive, are encouraging. We turn next to the empirical and experimental evidence in favor of the stability of low- q crossed-field electron beams.

A.3 Empirical Evidence

Two important devices depend upon crossed-field electron beams — the microwave magnetron and the low density Penning discharge as applied, say, in the Vac-Ion Pump.^{54,75} These devices are geometrically rather similar: both have cylindrical anodes and axial magnetic fields. It is a striking fact that while both devices are thoroughly successful, the magnetron works because an inherent instability of the electron beam makes it possible to extract considerable microwave power, while the Vac-Ion Pump works because the beam is extremely stable; this stability results in long containment times for the electrons which are therefore quite effective at pumping.

It can be shown that the principal difference between these devices are the value of q . For the magnetron, q is characteristically a few tenths.

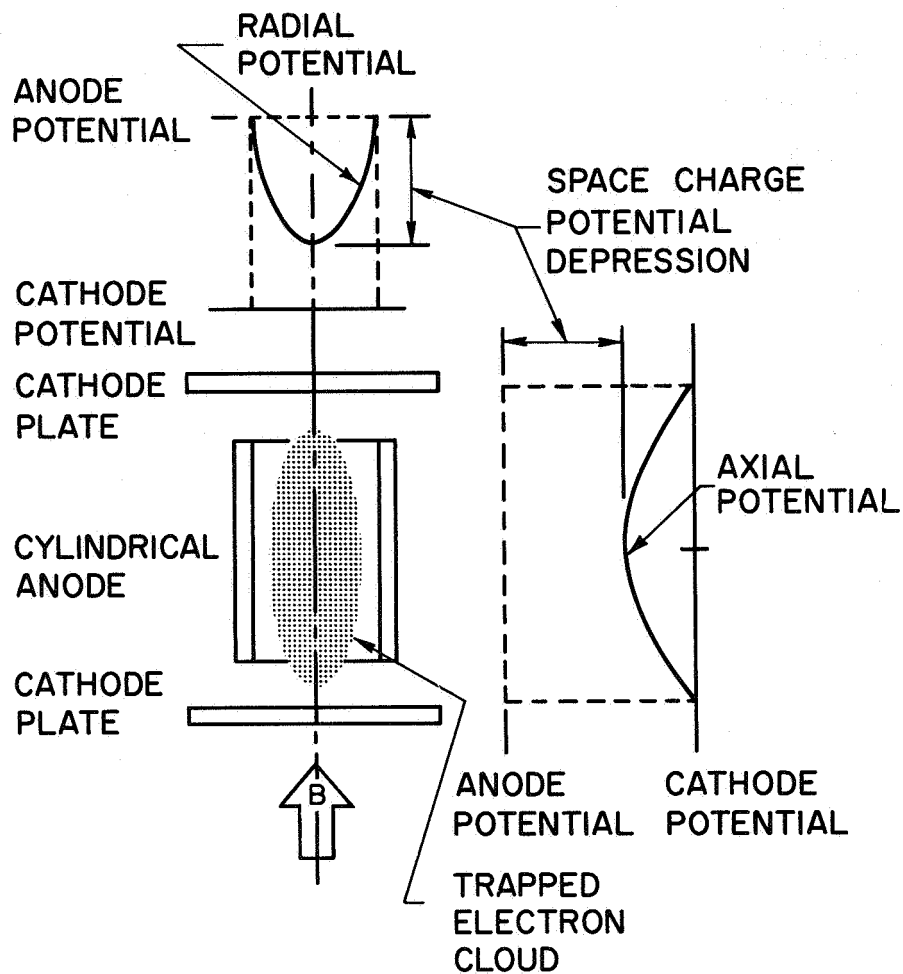
For the Vac-Ion Pump, q is generally $\sim .07$ or less. The instability described in the previous section having a growth rate $\omega_0 e^{-2/q}$ is of the utmost importance for the magnetron and is altogether negligible for the Vac-Ion Pump. Naturally, at still smaller values of q this instability is "even more negligible." It appears that the Plasma Radiation Shield can be considered as a scaled-up Vac-Ion Pump. As such, it may be hoped that it will exhibit the same remarkable degree of stability.

Fig. A.1 is a schematic drawing of the Vac-Ion Pump, taken from an article by Helmer and Jepsen.⁵⁴ Fig. A.2 is characteristic of the calibration curves associated with these pumps. The most striking feature of Fig. A.2 is the roughly linear relationship existing between the gas pressure in the device and the current drawn. This linear relationship is an indication that nothing other than classical diffusion of the electrons by collisions with the neutrals is taking place. Knowing the voltage applied across the device and its characteristic size, it is possible to estimate the total number of electrons contained in it. Then, on dividing by the current, one obtains an estimate for the containment time. At a pressure 10^{-6} mm Hg, this containment time is approximately 10^{-3} secs. For the Plasma Radiation Shield, in the vacuum of space, a pressure of 10^{-14} mm should lead to the required containment time of 10^5 secs, or about a day.

A.4 Experimental Work

A number of experiments related to the Plasma Radiation Shield have been carried out. However, none of these has been in the geometrical shape of the Plasma Radiation Shield, for the following reason: the topology of the Plasma Radiation Shield (see, for example, Fig. 3.3) cannot be used in a simple way in a laboratory experiment, since the supporting strut which must necessarily be used is certain to interrupt the drift of the electron cloud.

The first experiments on the containment of electron clouds are described in Refs. 49 and 74. Here, we shall give a very brief description of the most recent experiment. This is an "inside out" torus, shown schematically in Fig. A.3, and photographically in Fig. A.4. The object of the experiment is to exhibit the containment of electron plasmas for



J.C. HELMER
R.L. JEPSEN

Fig. A.1 Schematic diagram of a Vac-Ion Pump taken from Ref. 54. The dynamics of the electron cloud in this device are very similar to the dynamics of the electron cloud in the Plasma Radiation Shield, since the value of $q = \omega_p^2 / \omega_c^2 \approx 1/30$. The stability of the electron cloud in this device is clearly implied by the calibration curve shown in Fig. A.2.

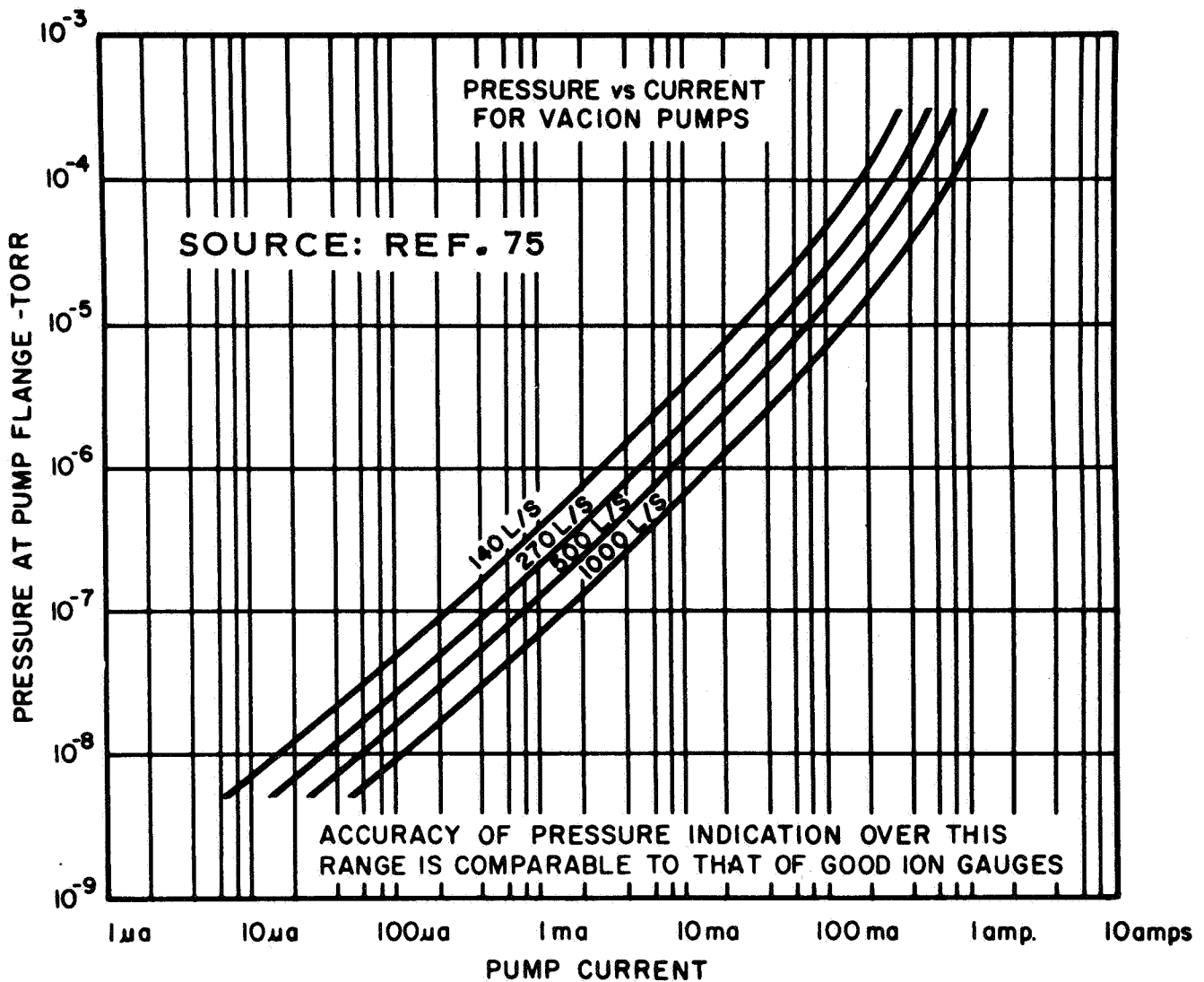


Fig. A. 2 Calibration curve of a Vac-Ion Pump taken from a Varian catalog (Ref. 75). Note the roughly linear relationship between the pressure and the output current over a very wide range of the variables. This linear relationship can only be the result of classical diffusion of the electrons to the anode by means of collisions with the neutrals. Other pumps of this character have operated down to pressures like 10^{-12} mm Hg. An estimate of the electron confinement time at this pressure is 1000 secs.

HEAVY ION PLASMA ACCELERATOR

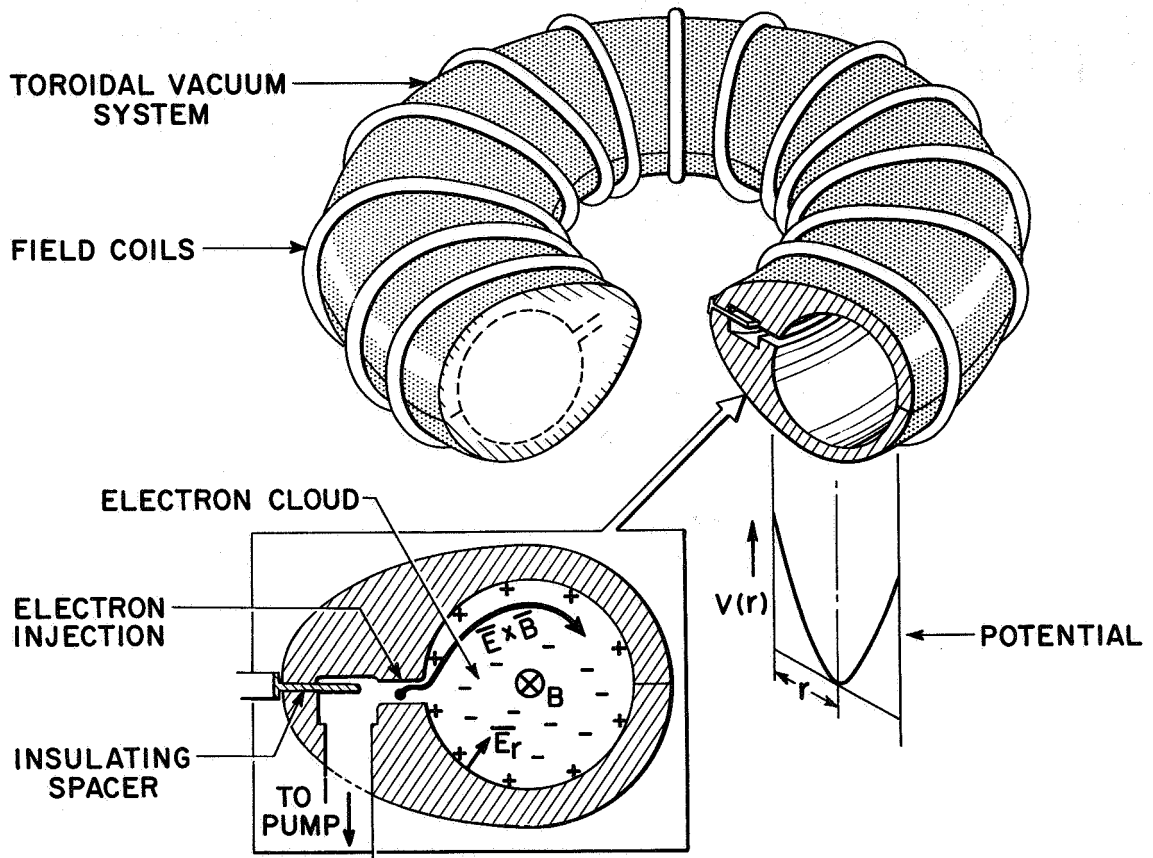


Fig. A. 3 Schematic of toroidal electron plasma experiment. Electrons are introduced into the torus from a filament in the slot, compressed by a rising magnetic field, and create a potential depression along the circular axis of the device.

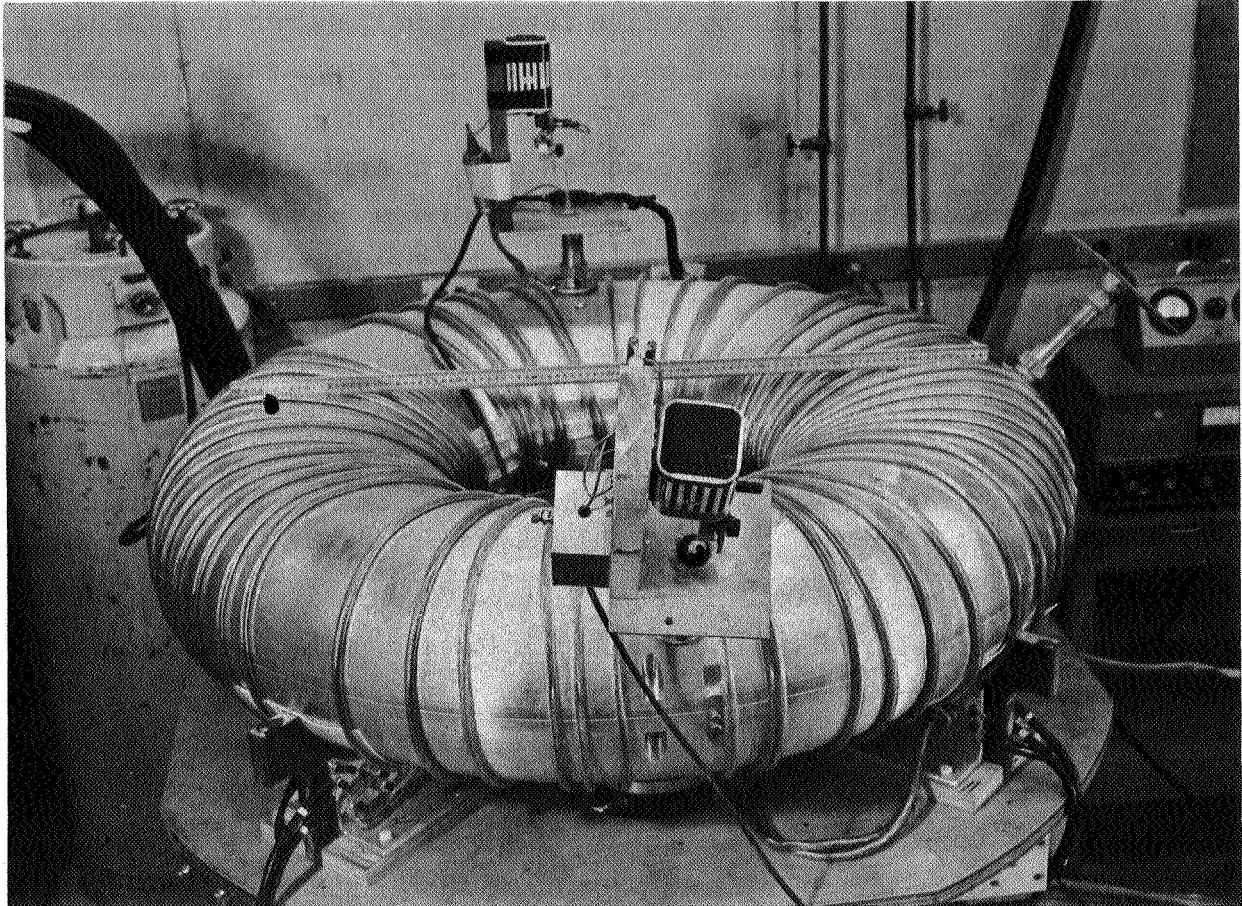


Fig. A. 4 Photograph of the apparatus shown in Fig. A. 3. Note the meter rule across the device.

short times (~ 1 msec.), and the achievement of high voltages by compressing the electron cloud with a rising magnetic field. Containment times longer than 1 msec. cannot be achieved with this apparatus since a) the magnetic field is aligned by image currents in the aluminum torus; these currents decay after about 1 msec., and b) the apparatus cannot be pumped down below pressures of a few $\times 10^{-8}$ mm Hg. The residual gas at this pressure will discharge the electron cloud in approximately 1 msec.

Electrons are injected into the apparatus from the heated circular filament shown in Fig. A.3. The rising magnetic field then carries these electrons in towards the middle of the device, where they generate a potential depression or well. The depth of the well is measured by electrostatic probes. When the magnetic field reaches its peak value, it is "crowbarred," and decays in about 1 msec.

The experiment has a minor radius of 10 cm and a major radius of 50 cm. Approximately .02 webers of magnetic flux are introduced in a rise time of about 20μ sec, giving an induced voltage of about 1 kV. This voltage appears across the slot where the filament is located. The peak magnetic field is about 5 k gauss.

An experimental oscillogram is shown in Fig. A.5, and data from several runs is plotted in Fig. A.6. Peak well depths in excess of 80,000 volts have been observed, and our ability to generate higher voltages is limited at present by lack of means to measure them, since the electrostatic probes cannot be operated much beyond this figure.

The well depth generated appears to scale roughly with the voltage induced across the gap by the rising magnetic field, the amplification factor (or gain), being in the range 50-100.

So far as they go, these experiments may be regarded as satisfactory. Current work is directed at improving the gain to a number on the order of several hundred; it is hoped that this can be done through better control of the details of the injection process. Another objective is the development of diagnostic techniques capable of recording voltages above 100 kV. When these techniques become available, it should be possible to operate the experiment at generally higher levels of power, voltage, etc.

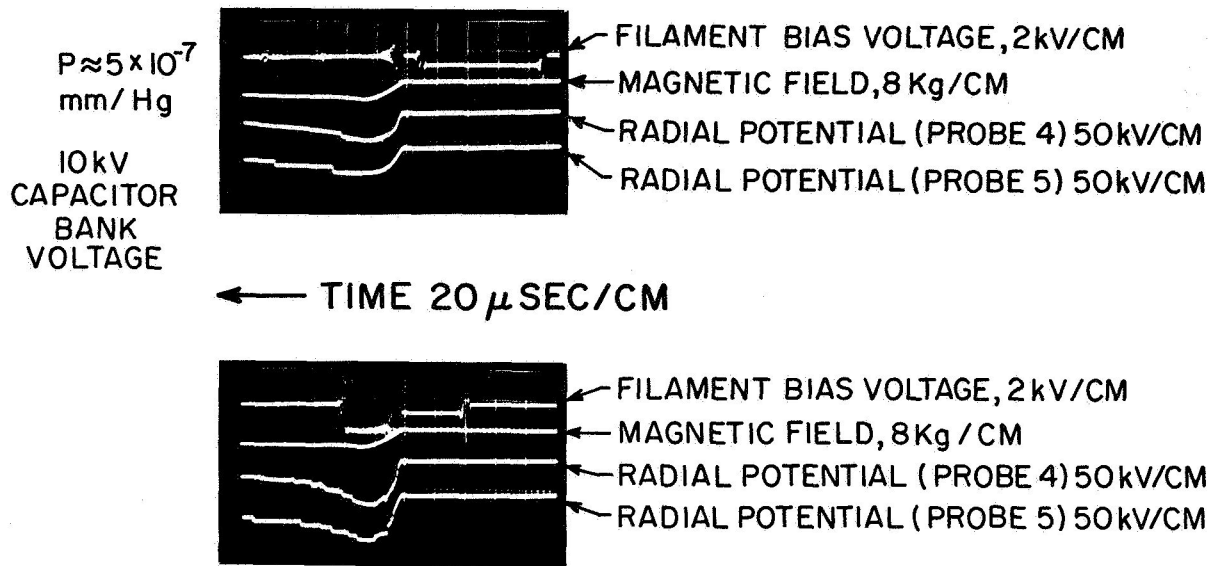


Fig. A. 5 Data obtained with the apparatus of Figs. A. 3 and A. 4. Note the favorable effect of biasing the filament in the second oscillogram. The peak potential is 80,000 volts, when the magnetic field is about 5 k gauss.

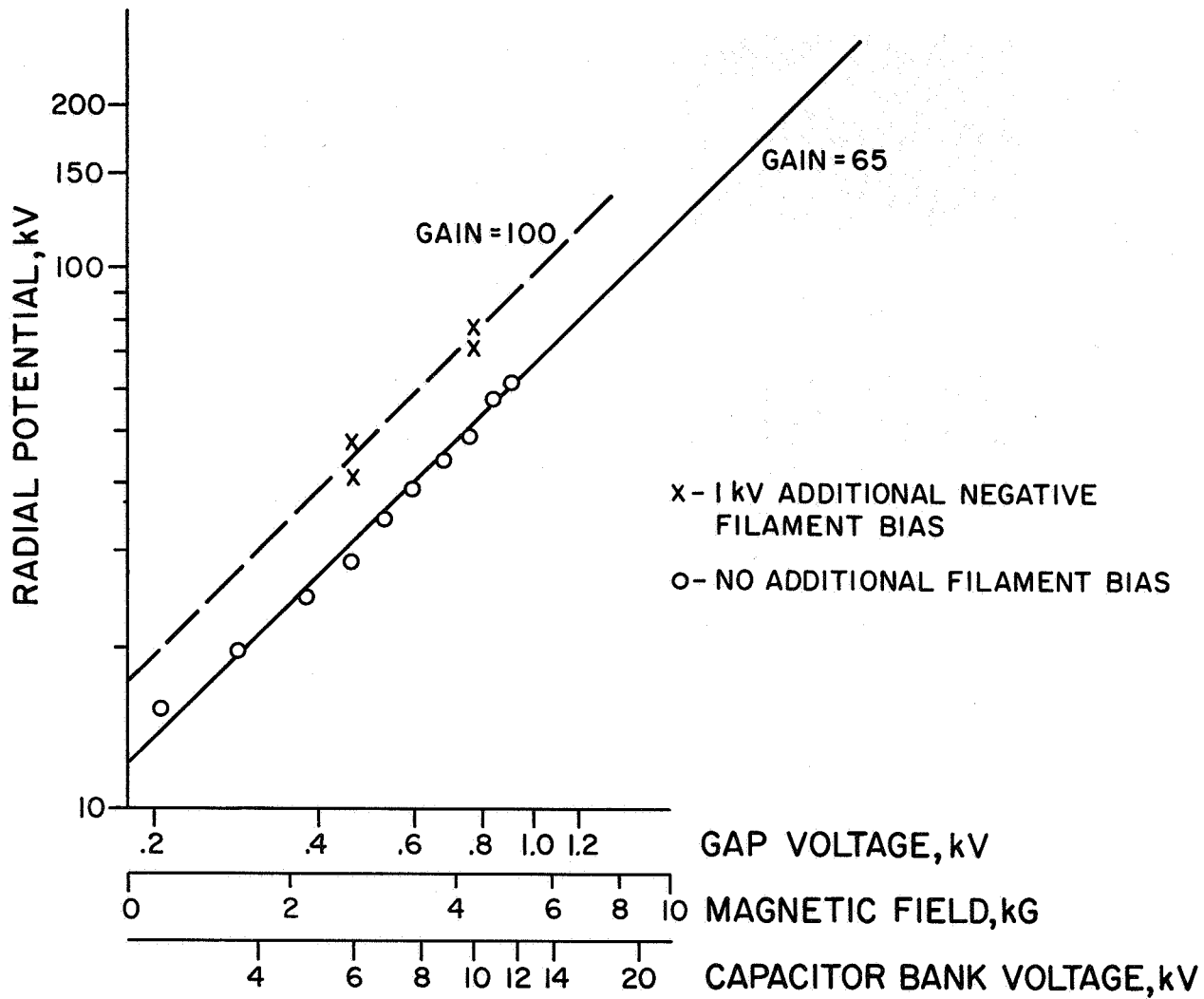


Fig. A. 6 Cross plot of data from the apparatus of Figs. A. 3 and A. 4. Note the linear relationship between the depth of the potential well and the gap voltage.

Under consideration is a new experiment designed to extend our capabilities in the direction of longer containment times. In this area, the primary requirement is the use of superior vacuum techniques.

A.5. Summary

Experimental and theoretical work on a wide front has failed to produce any fundamental obstacle to the realization of the Plasma Radiation Shield; on the other hand, the highest voltage exhibited falls short of that required for the Plasma Radiation Shield by a factor of several hundred, and containment times at these voltages fall short of the Plasma Radiation Shield requirements by a factor of 10^8 .

With regard to the absolute voltage level, however, for a given electron number density this scales with the square of a suitable linear dimension. As a full scale device would certainly be ten times the size of the existing experiment, the short fall in voltage level appears quite reasonable. As regards the containment time, the Vac-Ion Pump shows that in devices of this kind very long containment times are possible, and that these times depend only on the pressure of the residual gas. Thus, while further experimental and theoretical work is obviously required, it is reasonable to interpret optimistically the data obtained so far.

REFERENCES

1. Second Symposium on Protection Against Radiations in Space, National Aeronautics and Space Administration, SP-71, Gatlinburg, Tennessee, October 1964.
2. Burrell, M. O., Wright, J. J. and Watts, J. W., "A Preliminary Report on Energetic Space Radiation and Dose Rate Analysis," National Aeronautics and Space Administration Technical Memorandum X-53531, October 31, 1966.
3. Hilberg, R. H., "Solar Cosmic Ray Events," Bellcomm, Inc., Report No. TR-65-340-1, November 1, 1965.
4. Hilberg, R. H., "Radiation Shielding Needed for Extended Interplanetary Missions - Case 103-2," Bellcomm, Inc., August 11, 1966.
5. Burrell, M. O., "Space Radiation Doses During Planetary Missions," National Aeronautics and Space Administration Technical Memorandum X-53190, January 20, 1965.
6. Anderson, K. A., "Preliminary Study of Prediction Aspects of Solar Cosmic Ray Events," National Aeronautics and Space Administration TN D-700, April 1961.
7. French, F. W. and Hansen, K. F., "Radiation Shielding Requirements for Manned Satellites," J. Spacecraft and Rockets 2, 931 (1965).
8. Keller, J. W., "Long-Range NASA Shielding Requirements," Symposium on the Protection Against Radiation Hazards in Space, Gatlinburg, Tennessee, November 1962.

9. Abel, J., "Radiation Considerations for Lunar Missions," AAS Preprint 62-37, January 1962.
10. Bailey, D. K., "Time Variations of the Energy Spectrum of Solar Cosmic Rays in Relation to the Radiation Hazard in Space," J. Geophys. Res. 67, 391-396 (January 1962).
11. Ehricke, K. A., "A Study of Early Manned Interplanetary Missions (Empire Follow-On)," General Dynamics/Astronautics, GD/A-AOK 64-002, January 1964.
12. "Manned Mars Exploration in the Unfavorable (1975-1985) Time Period," Vol. II, Summary, Douglas Report SM-45576, January 1964.
13. Sanders, H. C., "The Effects of Man on the Weight of a Manned Space Vehicle," AAS Preprint 62-12, January 1962.
14. "Manned Interplanetary Missions," Lockheed Missiles and Space Company, Vol. I, Summary, 8-32-63-4, January 1964.
15. Langham, W. H., "Some Radiation Problems of Space Conquest," Astron. Sci. Rev. 2, 9 (October-December 1960).
16. Proceedings of Conference on Radiation Problems in Manned Space Flight, National Aeronautics and Space Administration TN D-588, June 1960.
17. Barnes, T. G., Finkelman, E. M. and Barazotti, A. L., "Radiation Shielding of Lunar Spacecraft," Astron. Sci. Rev. 3, 11 (January-March 1961).
18. Tobias, C. A., "Radiation Hazards in Space Flight," University of California, RAD Laboratory Report UCRL 8115, January 1958.

19. Schaefer, H. J., "Radiation Danger in Space," *Astron.* 5, 36 (1960).
20. Schaefer, H. J., "Proton Radiation Hazards in Space," *Astron.* 6, 39 (1961).
21. Foelsche, T., "Protection Against Solar Flare Protons," 7th Annual Meeting, American Astronautical Society, Dallas, Texas, January 1961.
22. Babinsky, A. D., Del Duca, M. G. and Bond, A. F., "The Radiation Problem in Low Thrust Space Travel," presented at the ARS 14th Annual Meeting, Washington, D. C., November 16-20, 1959, ARS Report 989-59.
23. Robey, D. H., "Radiation Shield Requirements for Two Large Solar Flares," *Astronautica Acta* 6, 206 (1960).
24. Barbieri, L. J. and Lampert, S., "The Interdependence of Manned Spacecraft Design and Radiation Shielding," *Aerospace Eng.* 20, 14 (1961).
25. Anderson, K. A. and Fichtel, C. E., "Discussions of Solar Proton Events and Manned Space Flight," National Aeronautics and Space Administration TN D-671, March 1961.
26. Savin, R. C., Deerwester, J. M., and Masey, A. C., "Sensitivity of Manned Planetary Spacecraft Design to Radiation Uncertainties," *J. Spacecraft* 4, 249 (1967).
27. French, F. W., "Radiation Shielding of Manned Mars Vehicles," presented at AIAA "Stepping Stones to Mars Meeting" at Baltimore, Maryland, March 1966.

28. Saylor, W. P., Winter, D. E., Eiwien, C. J. and Coriker, A. W., "Space Radiation Guide," Aerospace Medical Division Report AMRL-TDR-62-86, p. 25, 1962.
29. Webber, W. R., "An Evaluation of the Radiation Hazard Due to Solar-Particle Events," Boeing Company Report D2-90469, December 1963.
30. Snyder, J. W., "Radiation Hazard to Man from Solar Proton Events," *J. Spacecraft Rockets* 4, 826 (1967).
31. "Radiation Biology and Space Environmental Parameters in Manned Spacecraft Design and Operations," *Aerospace Medicine* 36 (February 1965).
32. *Cosmic Rays, Handbuch d. Phys.* 46 (1961).
33. Levy, R. H., "Radiation Shielding of Space Vehicles by Means of Superconducting Coils," *ARS J.* 31, 1568 (1961).
34. Brown, G., "Magnetic Radiation Shielding," Proceedings of the International Conference on High Magnetic Fields, M.I.T., November 1961; also Wiley, 1962, pp. 370-378.
35. Dow, N. F., "Structural Implications of the Ionizing Radiation in Space," Proceedings of the Manned Space Stations Symposium, Los Angeles, California, April 1960.
36. Bernert, R. E. and Stekly, Z. J. J., "Magnetic Radiation Shielding Systems Analysis," Avco Everett Research Laboratory Report AMP 134, July 1964.
37. Levy, R. H., "Prospects of Active Shielding," presented at Symposium on the Protection Against Radiation Hazards in Space, Gatlinburg, Tennessee, November 1962.
38. Tooper, R. F. and Davies, W. O., "Electromagnetic Shielding of Space Vehicles," IAS Paper No. 62-156, June 1962.

39. Tooper, R. F., "Electromagnetic Shielding Feasibility Study," Armour Research Foundation Technical Documentary Report No. ASD-TDR-63-194, May 1963.
40. Kash, S. W., "Magnetic Space Shields," AIAA Paper No. 65-629, August 1965.
41. Levine, S. H., Bhattacharjie, A. and Lepper, R., "Forbidden Regions Produced by Two Parallel Dipoles," AIAA J. 4, 654 (1966).
42. Prescott, Urban and Shelton, "The Application of the Liouville Theorem to Partially Shielded Regions," Paper presented at Second Symposium on Protection Against Radiation Hazards in Space, Gatlinburg, Tennessee, October 1964.
43. Bhattacharjie, A. and Michael, I., "Mass and Magnetic Dipole Shielding Against Electrons of the Artificial Radiation Belt," AIAA J. 2, 2198 (1964).
44. Levy, R. H., Comment on "Mass and Magnetic Dipole Shielding Against Electrons on the Artificial Radiation Belt," AIAA J. 3, 988 (1965).
45. Felten, J. E., "Feasibility of Electrostatic Systems for Space Vehicle Radiation Shielding," J. Astron. Sci. 11, 16 (1964).
46. Levy, R. H. and Janes, G. S., "Plasma Radiation Shielding," AIAA J. 2, 1835 (1964).
47. Levy, R. H. and Janes, G. S., "Plasma Radiation Shielding," Space/Aeronautics 45, 106 (1966).
48. Levy, R. H., "The Diocotron Instability in a Cylindrical Geometry," Phys. Fluids 8, 1288 (1965).
49. Levy, R. H., "The Effect of Coherent Radiation on the Stability of a Crossed-Field Electron Beam," J. Appl. Phys. 37, 119 (1966).

50. Levy, R. H. and Janes, G. S., "The Electron Plasma: Experiment, Theory and Applications," AIAA Paper No. 65-538 (1965).
51. Janes, G. S., "Experiments on Magnetically Produced and Confined Electron Clouds," Phys. Rev. Letters 15, 135 (1965).
52. Levy, R. H. and Callen, J. D., "The Diocotron Instability in a Quasi-Toroidal Geometry," Phys. Fluids 8, 2298 (1965).
53. Buneman, O., Levy, R. H. and Linson, L., "The Stability of Crossed-Field Electron Beams," J. Appl. Phys. 37, 3203 (1966).
54. Helmer, J. C. and Jepsen, R. L., "Electrical Characteristics of a Penning Discharge," Proc. IRE 49, 1920 (1961).
55. Alexander, W. M., "Cosmic Dust," Science 138, 1098 (1962).
56. Alpert, D., Lee, D. A., Lyman, E. M. and Tomaschke, H. E., "Initiation of Electrical Breakdown in Ultrahigh Vacuum," J. of Vacuum Science & Technology 1, November/December 1964.
57. Dyke, W. P. and Trolan, J. K., "Field Emission: Large Current Densities, Space Charge and the Vacuum Arc," Phys. Rev. 89, 799 (1953).
58. Dyke, W. P., Trolan, J. K., Martin, E. E. and Barbour, J. P., "The Field Emission Initiated Vacuum Arc. I. Experiments on Arc Initiation," Phys. Rev. 91, 1043 (1953).
59. Dolan, W. W., Dyke, W. P. and Trolan, J. K., "The Field Emission Initiated Vacuum Arc. II. The Resistively Heated Emitter," Phys. Rev. 91, 1054 (1953).
60. Fowler, R. H. and Nordheim, L., "Electron Emission in Intense Electric Fields," Proc. Roy. Soc. (London) A119, 173 (1928).

61. Van Atta, L. C., Van De Graaff, R. J. and Barton, H. A., "A New Design for a High-Voltage Discharge Tube," *Phys. Rev.* 43, 158 (1933).
62. Cranberg, L., "Initiation of Electrical Breakdown in Vacuum," *J. Appl. Phys.* 23, 518 (1952).
63. Bennett, W. H., "Magnetically Self-Focusing Streams," *Phys. Rev.* 45, 890 (1934).
64. Boyle, W. S., Kisliuk, P. and Germer, L. H., "Electrical Breakdown in High Vacuum," *J. Appl. Phys.* 26, 720 (1955).
65. Muller, E. W., "Field Ionization and Field Ion Microscopy," *Advances in Electronics and Electron Physics*, Vol. XIII (1960).
66. Rich, M. and Madey, R., "Range-Energy Tables," University of California Radiation Laboratory Report No. 2301, March 1954.
67. "Environmental Control Systems and Selection for Manned Space Vehicles," ASD-TDR-61-240, Part I, December 1961.
68. Lin, H., "Structures and Materials in the Long-Duration Manned Spacecraft," *Astron. and Aeron.* 4, 37 (March 1966).
69. Thomas, R. S., "Choice of an Atmosphere for an Extended Space Mission," *Proceedings of the First Space Vehicle Thermal and Atmospheric Control Symposium*, ASD-TDR-63-260, April 1963, pp. 735-759.
70. Hibben, R. D., "Allis-Chalmers Pushes Fuel Cell Efforts," *Aviat. Wk.* 86, 65 (1967).
71. "First Quarterly Technical Progress Report, Thermal Battery, 1 July - 30 September 1966," Contract AF 33(615)-5343, Allison Division of General Motors, October 1966.

72. Hietbrink, E. H. , Private communication, Allison Division of General Motors, Indianapolis, Indiana, 1967.
73. Beischer, D. E. , "Human Tolerance to Magnetic Fields," Astron. 7, 24-25, 46-48 (March 1962).
74. Quarterly Progress Report, Contract NAS8-20310, National Aeronautics and Space Administration, Office of Advanced Research and Technology, December 1966.
75. Vac-Ion Pump 140, 270, 500 and 1000 L/S Data Study, Varian Vacuum Division, Palo Alto, California.



THE QUASI-HOLLOW CONDUCTOR MAGNET
AS A SPACE SHIELD AGAINST ELECTRONS*By: S. H. Levine and R. Lepper
Nortronics Applied Research Department

INTRODUCTION

There are missions for which electrons are the principal hazard to manned operations in space. Either large superconducting magnets or material shields can be utilized to provide protection against this hazard during these operations.¹ Active or superconducting magnetic shields produce a totally forbidden region into which charged particles having momentum less than some specified value cannot penetrate. By appropriately designing the magnet, this totally forbidden region can be used to shield space vehicles from the radiation in space.

Analytical studies by Levy,² Tooper,³ and Brown⁴ have compared the mass of superconducting active shields with equivalent material shields for protecting toroidally shaped vehicles against solar flare protons. More recently, Bhattacharjie and Michael¹ have similarly compared the mass of a superconducting solenoid shield with an aluminum-lead material shield for protecting against the trapped electrons in space. In all cases, the active shields compared favorably by providing greater protection with a reduction in total shield mass. For electrons the situation is particularly promising in that the active shield prevents production of hazardous bremsstrahlung, an effect which can

*This program has been supported by the Air Force Avionics Laboratory under Contract No. AF 33(615)-1220, Leo Krautman, Project Monitor.

incur heavy-weight penalties to the material shield.

These analytical studies utilize, in most cases, approximations to obtain the shape of the protective regions because exact solutions are extremely difficult to obtain.⁵ For this reason, the authors have built and developed, during the past several years, a magnetic shield simulator (MAGSIM) to measure experimentally the protective region produced by magnets having a complex geometric configuration^{6,7,8} and have utilized this information for designing active shield systems.

A superconducting active shield system consists of the superconductor, a cryogenic refrigerator and its power supply, the structure, and equipment for integrating the system into the spacecraft. The structure is the most massive component of an active shield system for protecting against the high energy protons (~ 100 Mev or greater) whereas the mass of the cryogenic cooling system dominates when the much lighter electrons (1 to 10 Mev) are considered. Since the exposed area of the superconductor is directly related⁹ to the mass of the cryogenic refrigerator, large savings in the total mass of the active shield for electrons can be accrued by reducing the exposed area. This condition is achieved for protecting toroidally shaped vehicles by replacing a hollow conductor magnet (HC) with individual coils suitably positioned around the vehicle - a design called the quasi-hollow conductor (QHC). This concept does induce magnetic fields inside the space vehicle, but such fields can be kept well below 500 gauss throughout most of the space vehicle, eliminating any serious problem in this respect.¹⁰

In this paper we will consider a QHC configuration, studied in the MAGSIM, that provides a protective region appropriately shaped for enclosing a

relatively small volume toroidal vehicle.⁸ A small volume toroid is constrained to have a large ratio of cross sectional diameter to the radius of the toroid, a configuration which produces for the HC an outward displacement of the protective volume from the center of the vehicle. By redistributing the current in the QHC design, this displacement has been nullified. The data is scaled to protect a 10-foot diameter (3.2 meters) space cabin (420 meter³ volume) against space electrons and the results utilized to compute the magnetic fields about the vehicle and the total mass of the active shield system.

MAGSIM DATA

The MAGSIM is an analogue device in which the forbidden volume produced by externally deflecting magnets is measured. It employs an electron gun, a phosphor coated grid, support assembly for the magnet and grid, power supplies, vacuum chamber, and photographic equipment properly positioned for accurate measurements as shown in Figure 1. The two parallel, point dipole magnets used to study a complex magnet configuration⁷ are shown suspended in the screen grid. The forbidden areas are defined by the outline of the illuminated areas on the screen grid and photographs taken through the camera ports permit an accurate determination of these regions. Figure 2 shows a seven-coil QHC model used in the MAGSIM together with a representative data picture taken with the model.

The MAGSIM data can be scaled, for studying large active shields that will protect manned space vehicles from the high energy charged particle radiation in space, by transforming all measurements into Storer units, C_{st} , where

$$C_{st} = \sqrt{\frac{Mq}{cp}} \quad (1)$$

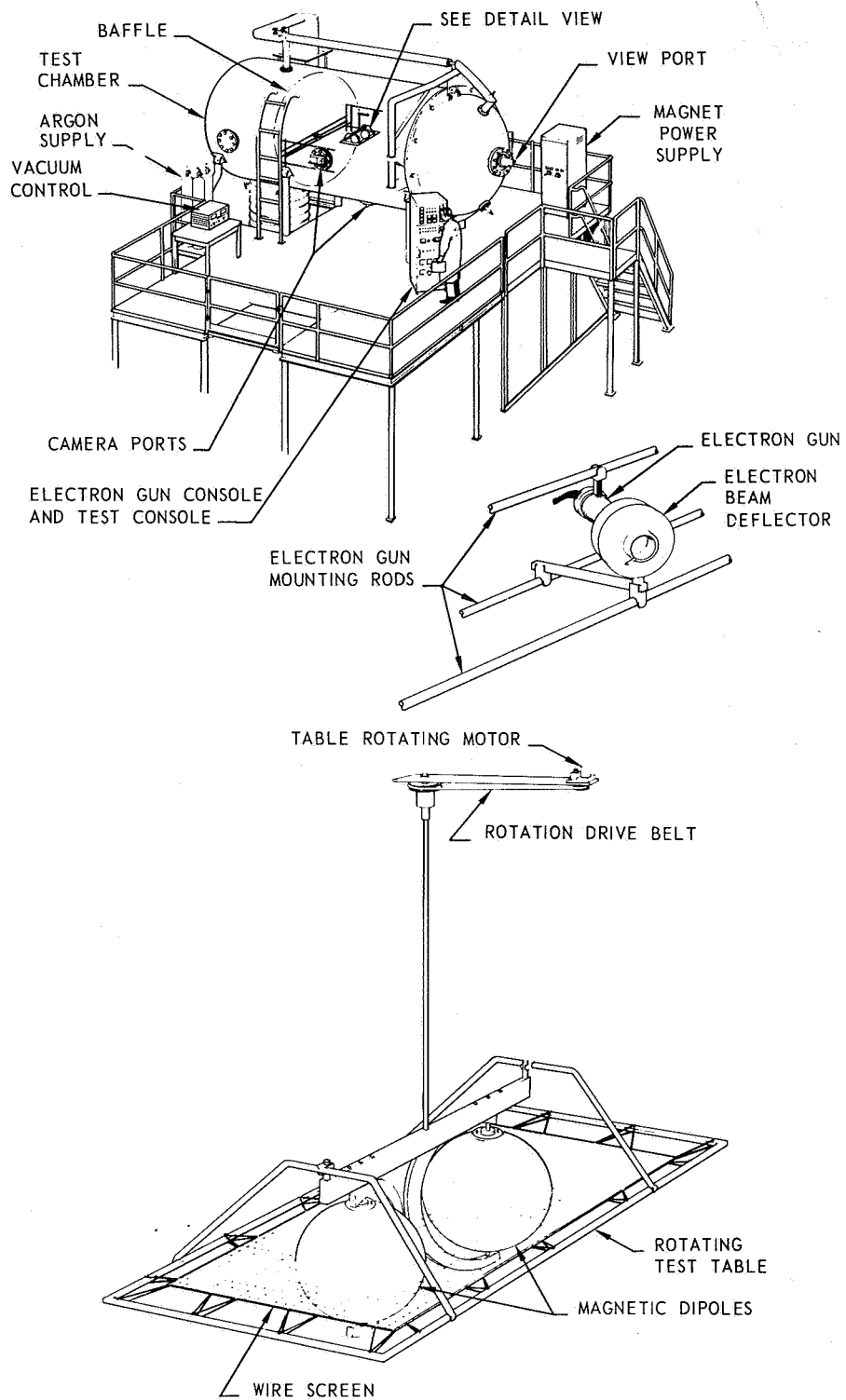


FIGURE 1 NORTHROP SPACE LABORATORY MAGSIM

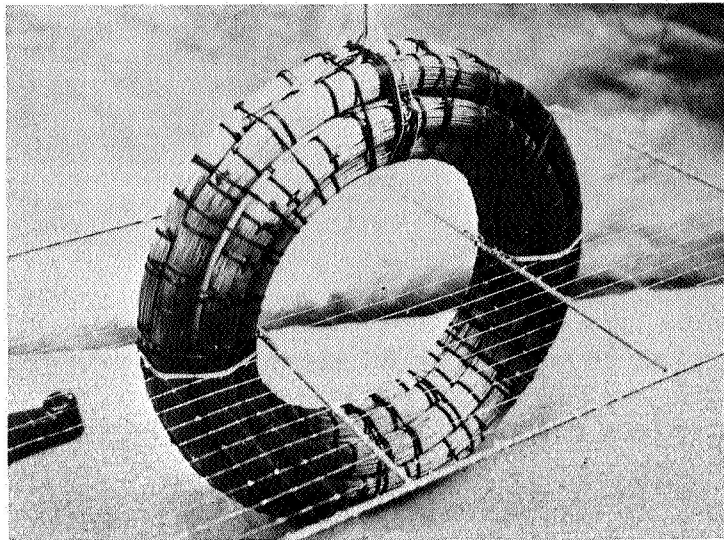


FIGURE 2a SEVEN TURN QUASI-HOLLOW CONDUCTOR COIL

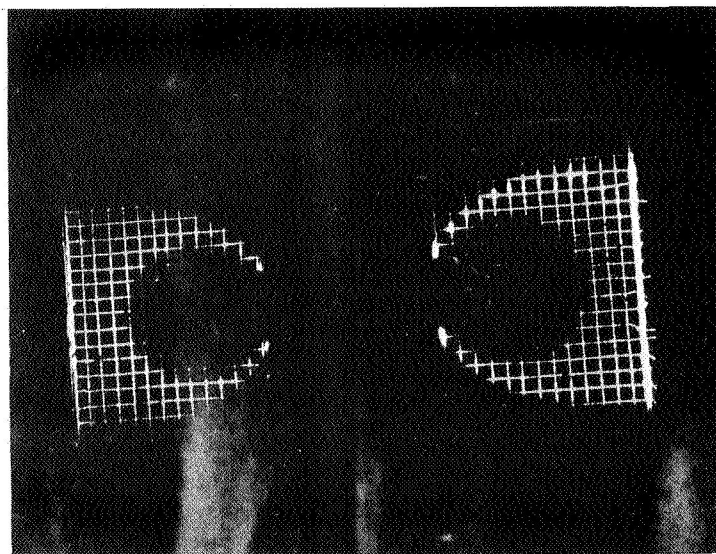


FIGURE 2b DATA PICTURE USING SEVEN TURN QUASI-HOLLOW CONDUCTOR COIL WITH 2.0 AMPS IN EACH SET OF COILS AND A 350-VOLT ELECTRON BEAM

and

M = the magnetic moment of the magnet

q = the electrical charge of the particle

c = the velocity of light

p = the linear momentum of the particle

(All units are e.s.u. units.)

It has also been used to study the HC magnet first proposed by Levy² as a shield against solar flare protons. On analyzing this concept for protecting against space electrons, it becomes advantageous to replace the hollow conductor with individual current loops to minimize the exposed area of the superconductor and to permit redistributing the current around the vehicle for shaping the protective region to enclose the vehicle in an optimum manner.

Two non-dimensional parameters

$$\Delta s = \frac{2 r_0}{a} \quad (2)$$

and

$$\lambda = a/C_{st} \quad (3)$$

are used to scale the MAGSIM data to both large vehicles and high energy electrons where the parameters a and r_0 are defined in Figure 3. For the small volume toroidally shaped vehicles, (a few hundred meters³), the ratio of the cross sectional diameter to the radius of the toroid, Δs , is relatively large since the vehicle is constrained to provide ample height for the astronauts. When the shield has a Δs of 0.1 or greater, the center of the

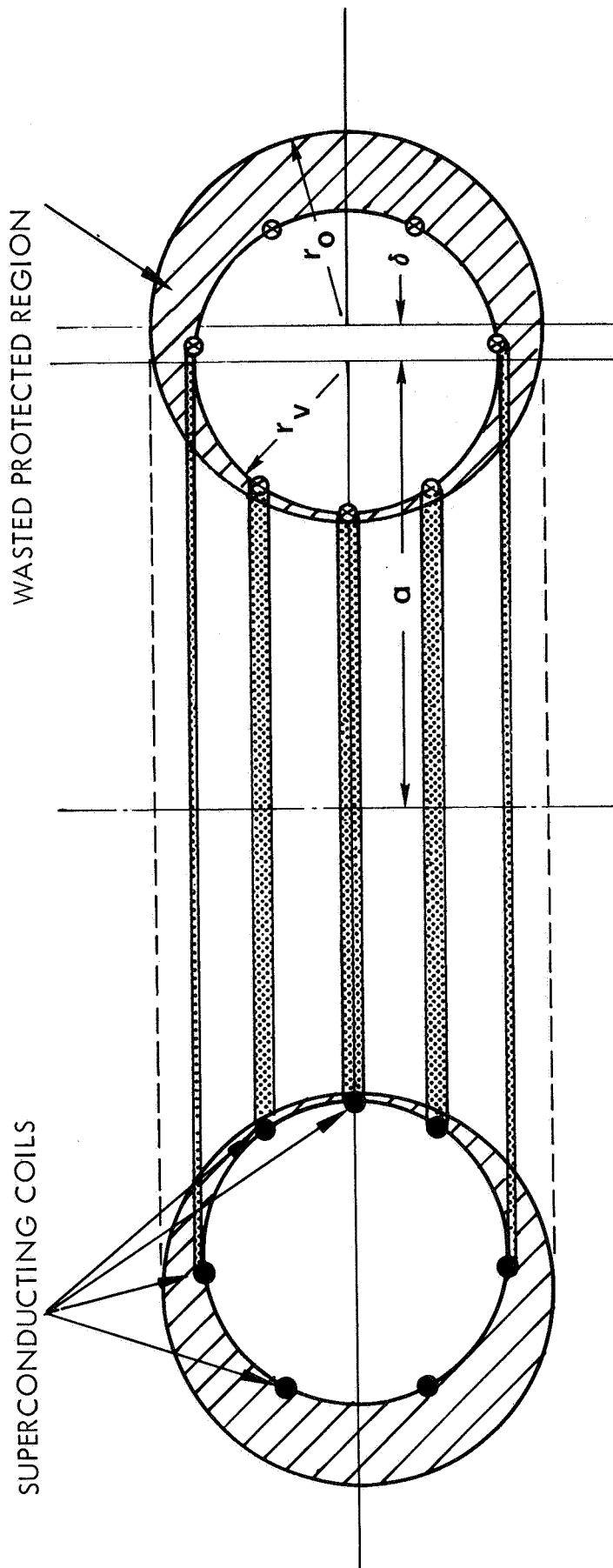


FIGURE 3 CUT-AWAY VIEW OF QUASI-HOLLOW CONDUCTOR CONFIGURATION

protective region is displaced outward from the center of the vehicle, an effect which must be nullified. This condition has been achieved in the MAGSIM with the seven coil model magnet shown in Figure 2. This model magnet has a radius, a , of 4.22 inches and a cross sectional radius of 0.8 inches resulting in a $\Delta s = 0.38$. Each of the seven coils has 250 turns and they are spaced about the model as shown schematically in Figure 3.

By effecting 188 ampere turns in each of the three inner coils and 275 ampere-turns in the two adjacent coils, the shape of the protective region coincided with that of the model.⁸ A 350 volt electron beam was employed in the measurements. Thus, only five coils are needed in this QHC configuration.

These data are scaled to large volume vehicles and high energy charged particles consistent with a configuration having a $\Delta s = 0.38$. Consequently, the volume of the vehicle is arbitrary; only the ratio $\frac{2 r_o}{a}$ is of importance. The ratio, Δs , together with the cross sectional diameter, $2 r_o$, determines the toroidal radius, a , and the volume of the vehicle. A practical minimum volume toroid vehicle is constrained to a diameter $2 r_o$ of approximately 3.2 meter (10 ft) to provide the necessary height for the astronauts. This constraint results in a scaled up vehicle based upon the five coil QHC model having an $a = 8.4$ meter and a volume, $V = 420$ meter³.

The method used here to scale the MAGSIM data to the large vehicle situation is based on the functional relation between λ and Δs for defining the totally forbidden volume produced by the hollow conductor.² Utilizing this relationship, it is found that a Δs of 0.38 corresponds to a λ of 0.452.

Equation (3) can be also expressed as

$$\lambda = \left(\frac{\pi e}{cp} \right)^{\frac{1}{2}} (I)^{-\frac{1}{2}} \quad (4)$$

to show explicitly the relationship between λ , p , and I , the ampere turns. Consequently, once λ and the electron momentum, p , are established, I is also determined and its value is independent of the volume of the vehicle. Equation (4) defines the ampere turns that will protect a totally forbidden volume, associated with the corresponding Δs , from electrons having momentum or energy below the specified value. This upper electron energy is referred to as the E_{cutoff} , and it is a function of the electron flux and energy spectrum encountered by the vehicle while orbiting the earth.

The energy spectra of the trapped electrons about the earth are complex functions of the vehicle orbit altitude and inclination; however, all such spectra exhibit a steep drop in intensity with increase in energy. Using Vette's model environment,¹¹ reasonable E_{cutoff} values are estimated to be 7 Mev and 2 Mev for protecting against the lower altitude electrons and outer zone electrons, respectively.

Equation (4) is used to determine the ampere turns of a hollow conductor magnet required to protect a toroidal vehicle that has a $\lambda = 0.452$ ($\Delta s = 0.38$) from 2 Mev and 7 Mev electrons, neglecting any displacement of the protective region. Under this assumption

$$I = 1.28 \times 10^5 \text{ ampere turns for 2 Mev electrons}$$

and

$$I = 3.28 \times 10^5 \text{ ampere turns for 7 Mev electrons}$$

For the 350 volt electron beam employed in the MAGSIM, $I = 990$ amp-turns.

This information is sufficient to scale up the MAGSIM data.

If the ampere turns utilized by the five coil QHC is totaled, the result is $I = 1110$ ampere turns - a factor 1.12 greater than that required by the HC to produce the same volume vehicle. However, the HC forbidden volume is displaced outward from the vehicle leaving portions of the vehicle exposed to the radiation. Thus, it is interesting to make comparisons between HC and QHC shields concerning ampere turn requirements and protective regions. First, the protective region produced by a hollow conductor having a $\Delta s = 0.38$ is displaced a significant amount so that electrons would impinge on the inner ring of the vehicle and the bremsstrahlung generated by these electrons would present a hazard to the personnel inside the vehicle. By increasing the hollow conductor current, the protective region can be enlarged until the inner ring of the vehicle is protected, but the total forbidden region is much larger than the vehicle itself as shown schematically in Figure 3. For a $\Delta s = 0.38$, a protective volume increased to just include the inner radius of a toroidal vehicle becomes approximately 2.5 times larger than the vehicle itself. Thus, a significant reduction in the ampere turns required to shield the total vehicle is gained when protecting against electrons by redistributing the current about the vehicle.

Second, the radii of the five coils of the shield are all less than the radius of the vehicle. Therefore, the mass of the shield is less than that which would be required if the total ampere turns were assumed to be concentrated at the center of the space vehicle. In fact, it will be shown that for the five coil configuration utilized in this study, the reduction in effective coil radius of the magnet almost cancels any increase in active shield mass that would be expected from increasing the ampere turns by the 1.12 factor.

MAGNETIC FIELD CALCULATIONS

The magnetic field intensity produced by a circular loop is well known, being axially symmetric and having only the radial, H_ρ , and axial, H_z components.^{1,2} The magnetic field at a point due to any number of co-axial coils can be determined by summing the vector components associated with each coil. For a coil radius a_i and current I_i whose center is on the z axis at z_i , we have

$$H_\rho = \frac{0.2 I_i (z - z_i)}{\rho [(a_i + \rho)^2 + (z - z_i)^2]^{\frac{1}{2}}} \left[-K(k_i) + \frac{a_i^2 + \rho^2 + (z - z_i)^2}{(a_i - \rho)^2 + (z - z_i)^2} E(k_i) \right] \quad (5)$$

$$H_{zi} = \frac{0.1 I_i}{[a_i + \rho]^2 + (z - z_i)^2]^{\frac{1}{2}}} \left[K(k_i) + \frac{a_i^2 - \rho^2 - (z - z_i)^2}{(a_i - \rho)^2 + (z - z_i)^2} E(k_i) \right] \quad (6)$$

where

$$k_i = \frac{4 a_i \rho}{(a_i + \rho)^2 + (z - z_i)^2} \quad (7)$$

Letting $\xi_i = \rho/a_i$, the above equation can be written as

$$H_{\rho i}(\rho, z) = \frac{I_i}{a_i} \beta_\rho(\xi_i, \rho, z) \quad (8)$$

$$H_{zi}(\rho, z) = \frac{I_i}{a_i} \beta_z(\xi_i, \rho, z)$$

The total magnetic field at a point $P(\rho, z)$ is, therefore,

$$H_\rho = \sum_i H_{\rho i} \quad (9)$$

$$H_z = \sum_i H_{zi}$$

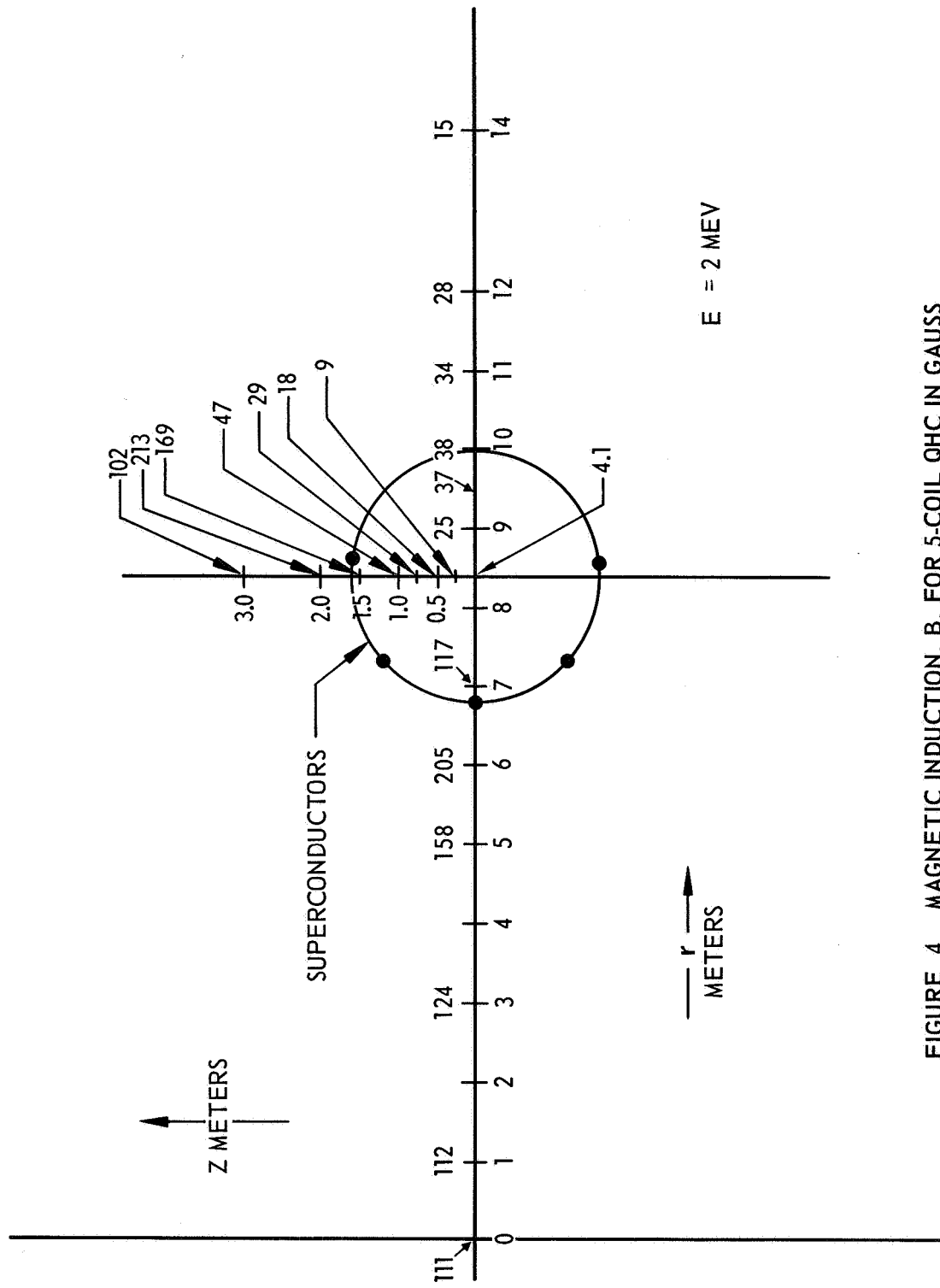
and

$$H = \left(H_\rho^2 + H_z^2 \right)^{\frac{1}{2}} \quad (10)$$

These equations have been programmed on the digital computer with flexibility in the code to allow for handling 20 coils, each carrying a different current.

The magnetic field produced by five coil QHC configuration for the 8.4 meter radius vehicle has been determined utilizing this code and the results presented in Figure 4 for the 2 Mev shield. Since the magnetic induction, B , is the entity of intensity,¹³ and for our study $B = H$ (i.e., $\mu = 1$), the quantities are given in units of gauss. Magnetic fields associated with a QHC shield designed to protect against 7 Mev electrons can be obtained from Figure 4 by increasing the values there by 300%.

It can be observed that inside the vehicle the fields generated by the individual coils tend to cancel each other and that fields above 100 gauss for the 2 Mev shield and 300 gauss for the 7 Mev shield are encountered in regions near the coils. The magnetic fields outside the vehicle are also of reasonable magnitudes particularly on the outer rim of the vehicle. The strengths of these magnetic fields are sufficiently low that they should not preclude utilizing this type shield.



$E = 2 \text{ MEV}$

FIGURE 4 MAGNETIC INDUCTION, B, FOR 5-COIL QHC IN GAUSS

MASS CALCULATIONS

The mass of an active shield, M_T , consists of the mass of the superconductor, M_C , the mass of the structure, M_S , the mass of the cryogenic cooling system, M_{CRY} , and the mass of equipment used to integrate the shield into the spacecraft, M_E . Thus,

$$M_T = M_C + M_S + M_{CRY} + M_E \quad (11)$$

We will proceed to calculate the total mass, M_T , recognizing that it will be several years at least before such a shield might be utilized. Also, a few of the subsystems such as the cryogenic cooling system are now being developed and will not be available for a few more years. It is, therefore, necessary in some cases to utilize technology that has been extrapolated to a few years hence. Under this supposition, we will assume that long Nb_3Sn superconducting wire or some similar superconducting material can be fabricated that will support a current density of 2.5×10^5 amps/cm² at 10°K. Short samples of this material have been fabricated which support a practical current density of 2×10^5 amps/cm² at approximately 10°K in a 4 kilogauss external magnetic field.¹⁴ Using this current density and the 8 gm/cm³ density of Nb_3Sn the mass of the superconductor, M_C , for the QHC is obtained from the relation

$$M_C = \sum_{i=1}^5 2 \pi a_i \rho_C I_i / j \quad (12)$$

where

a_i = radius of the i^{th} coil in the QHC

I_i = ampere turns in the i^{th} coil

j = current density

ρ_C = density of the superconductor

The M_C so obtained is 23 kg and 68.5 kg for QHC shields designed to protect the 8.4 meter radius vehicle from 2 Mev and 7 Mev electrons, respectively.

Each superconducting coil will be enclosed in a small titanium alloy tube to support the superconductor and to contain the helium coolant which flows around the superconductor to maintain its temperature below 10°k . The inner radius of the support tube, R_1 , is chosen sufficiently large to permit unrestrained flow of helium through the tubes. The tube thickness, $R_2 - R_1$, is made large enough to withstand the force exerted on it by the superconductor. A detailed design would consider the exact force components acting on each coil and integrate the shield system into the structure of the vehicle to minimize the total mass involved. Since our design is of a more general nature, we will design the tubes in a more uniform manner, employing reasonable assumptions. For instance, the cross-sectional radius of the i^{th} coil, R_{oi} , is

$$R_{oi} = \left(\frac{I_i}{\pi j} \right)^{\frac{1}{2}} \quad (13)$$

Since the two outer coils have the largest such radii, their R_o will be assumed to exist for all coils of the same shield - a conservative assumption. Maximum cross sectional radii are given in Table I for QHC shields designed to protect against 2 Mev and 7 Mev electrons. Setting $R_1 = 0.5$ cm and 0.6 cm for 2 Mev and 7 Mev shields, respectively, adequate space for unrestrained flow through the tubes is provided.

TABLE I
FIVE COIL QHC ACTIVE SHIELD PARAMETERS ($V = 420 \text{ m}^3$)

| E | R_o | R_1 | R_2 | R_3 | M_c | M_s | M_I | M_{CRY} | M_E | M_T | Power |
|-----|-------|-------|-------|-------|-------|-------|-------|-----------|-------|-------|-------|
| Mev | cm | cm | cm | cm | kg | kg | kg | kg | kg | kg | kw |
| 2 | 0.21 | 0.5 | 0.6 | 6 | 23 | 37 | 53 | 350 | 40 | 450 | 3.3 |
| 7 | 0.37 | 0.6 | 0.7 | 7 | 68.5 | 44 | 72 | 369 | 48 | 530 | 3.3 |

There are two sources for inducing forces on the conductor which are then transmitted to the support tube. The first is that due to the magnetic induction, B , generated by the adjacent coils interacting with the coil current producing a force per unit length, f_1 , where

$$\underline{f}_1 = \underline{I} \times \underline{B} \quad (14)$$

The second force is a self-induced radial force,

$$\underline{f}_{r^2} = \frac{I^2}{a} \left[\ln \frac{8a}{R_o} - \frac{3}{4} \right] \quad (15)$$

tending to expand the wire. The vector force, \underline{f}_1 , can be resolved into radial and axial force components, the radial force being directed outward to add to the self-induced force. The resultant total radial force induces a tensile force, F_t , defined by

$$F_t = f_r a \quad (16)$$

on the conductor. By employing equations (14), (15), and (16), the total tensile force, F_t , on the inner coil of the 7 Mev shield is 2180 kg and on the outermost coil, 1570 kg. Applying a safety factor of 1.5, the titanium tube need only have a maximum wall thickness of 0.05 cm to safely contain the superconductor. Titanium alloys having a tensile ultimate of 17,600 kg/cm² (250,000 psi) and a density of 4.44 gm/cm³ are utilized in this analysis. For convenience, the tubes are all given a 0.1 cm wall thickness resulting in the R_s values given in Table I. The mass of the structure is assumed to be integrated into the structure so that containment of the axial force is attained without the need of additional structural support. Thus, M_s is the mass of the tube for which values are also given in Table I. It should be mentioned that the forces on

the coils of the 2 Mev shield are reduced by a factor of 9 from that of the 7 Mev shield although we have not taken advantage of this in our analysis.

The mass of the cryogenic system, M_{CRY} , includes the mass of the insulation, refrigerator equipment, the mass of the radiator, and the mass of the power supply. The two pertinent parameters that determine M_{CRY} are the superconductor temperature, T_0 , and the heat leakage into the helium coolant, Q , expressed per unit length as

$$\frac{Q}{L_1} = \frac{2\pi K_e \Delta T_1}{\ln R_3/R_2} \quad (17)$$

where K_e = effective thermal conductivity

L_1 = Total length of insulation.

R_2 = Superinsulation inside radius.

R_3 = Superinsulation outside radius.

ΔT_1 = Temperature drop across insulation where $\Delta T_1 = T_1 - T_0$.

T_0 = Superconductor wire temperature and

T_1 = average temperature on outer surface of insulation.

Equation (17) can be written

$$Q/L_i = \frac{3.13 \times 10^{-4} \Delta T}{\ln R_3/R_2}$$

where $K_e = 5 \times 10^{-5}$ Btu/hr-ft-F⁰ has been used. The external temperature T_1 on the outer surface of the insulation is

$$T_1 \cong \frac{500 + 400 + 530 + 0}{4} = 360^\circ R \text{ (200}^\circ K)$$

where the temperatures

- Equilibrium temperature in sunlight = 500°R
- Equilibrium temperature in earth albedo = 400°R
- Space equilibrium temperature = 0°R
- Thermal radiation from vehicle external skin = 530°R

are used to determine T_1 .

Equation (11) pertains to the ideal geometrical configuration shown in Figure 5. However, it is not feasible to utilize any detailed design since the heat leakage will vary as a function of the actual configuration in a complicated manner. Therefore, for this investigation, the effect of the structure and other sources for reducing the thermal conductivity in equation (11) will be approximated by increasing K_e by 250%. Thus, equation (11) reduces to

$$Q/L_1 = 0.045 \text{ watts/meter} \quad (18)$$

where

$$\Delta T = 190^{\circ}\text{K}$$

$$K_e = 8.66 \times 10^{-5} \text{ watts/meter-}^{\circ}\text{K} \quad (5 \times 10^{-5} \text{ Btu/hr-ft-}^{\circ}\text{R})$$

and

$$\frac{R_3}{R_2} = 10$$

The outer radii of the insulator are 6 cm and 7 cm for the two QHC shields considered. These values have been chosen somewhat arbitrarily; however, the function $\ln R_3/R_2$ is a slowly varying function and to reduce $\frac{Q}{L_1}$ further by a significant amount will require a substantial increase in R_3 . Thus, a ratio R_3/R_2 of 10 was chosen as a reasonable value for this study.

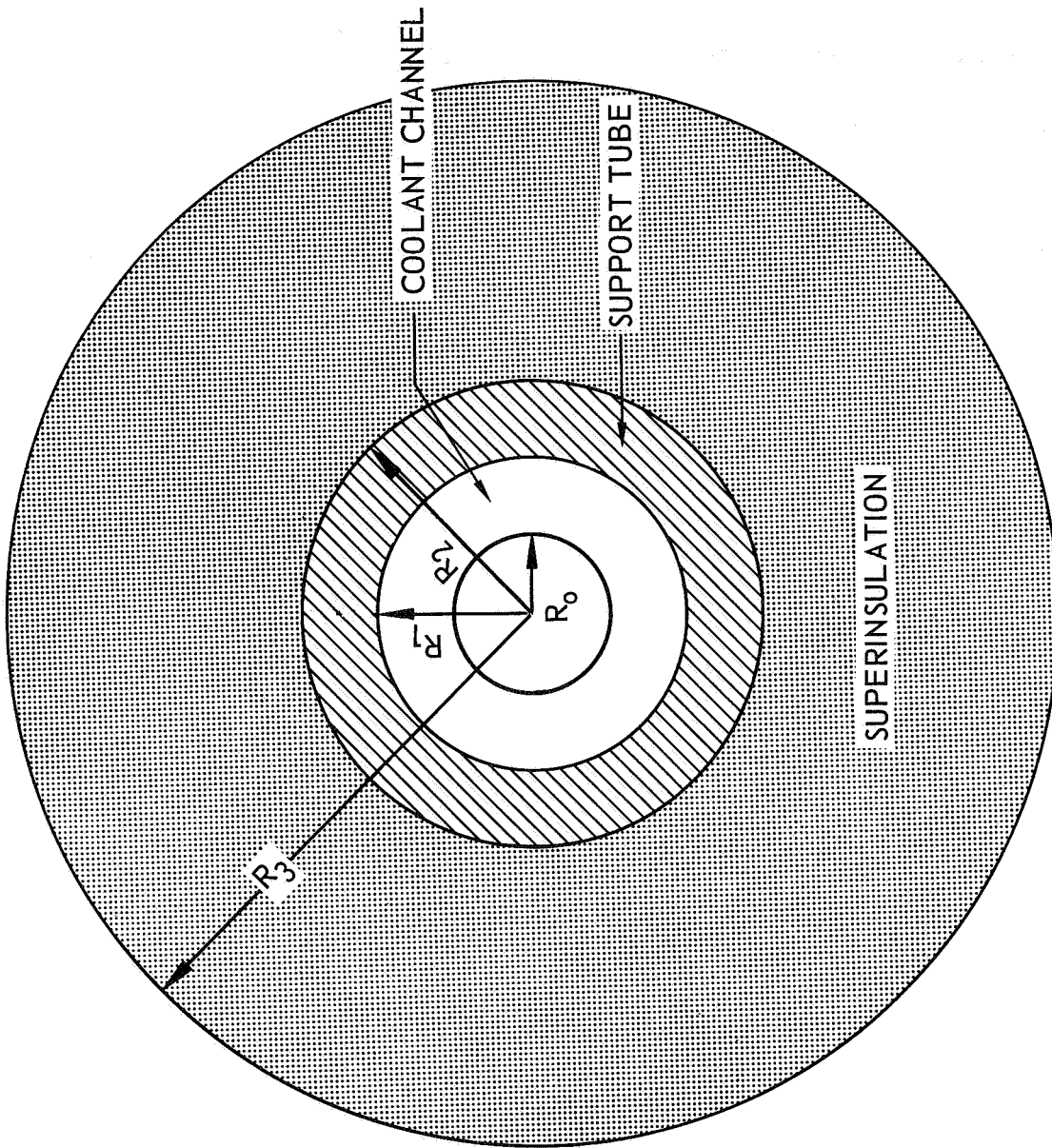


FIGURE 5 SUPERCONDUCTING WIRE CONFIGURATION

Dimplar superinsulation which has a density of 16.1 kg/m^3 is employed in the design. Increasing this density by 20% to account for the more dense insulator materials needed to attach the superinsulation to the tubes, the mass of the insulation, M_I , is computed and the results are given in Table 1.

The total heat leakage into the superconductor is, using equation (18), 11 watts for both shields. This is a modest cooling requirement for the size of the vehicle considered here. Arthur D. Little is currently developing a 1 watt, 3.6°k , 100 lb rotary stroking refrigerator for satellite purposes.¹⁵ Utilizing their extrapolated state-of-the-art data (5 years hence), the weight requirements for the refrigerator machinery and radiator are 124 kg and 20 kg, respectively. The power required to operate this equipment, maintaining a cryogenic temperature of 10°K , is 3.3 kilowatts. Using a value of 45 kg/kw (100 lbs/kw) the mass of the power supply becomes 153 kg. Adding the mass of the refrigerator equipment, the mass of the radiator, and the mass of the power supply to that of the insulator, the M_{CRY} is determined and the results are given in Table 1. The masses of all subsystems are now totaled and 10% of this total mass is assumed to be required for integrating the active shield into the satellite. The total mass of the active shield is then determined using equation (5), and the results are presented in Table 1.

CONCLUSION

The QHC shield presented in this report with its relatively low mass provides another highly promising concept for utilizing active shields in space. The projected operational characteristics of the components for this active shield are all close to the state-of-the-art so that the concept is feasible and the results attainable. It may be possible to further reduce the mass of the QHC active shield since our analysis does not include any optimization procedure; it only considers a set of favorable conditions for demonstrating the potential of this type active shield.

The most massive component of the QHC active shield is the cryogenic cooling system, M_{CRY} , and, consequently, any significant reduction in M_{CRY} will correspondingly affect the total system mass, M_T . Thus a significant reduction in the mass of the active shield could be achieved by reducing the heat load and/or increasing the critical temperature of the superconductor provided there is no large decrease in the critical current density resulting in much heavier and larger superconductor coils. A large increase in R_0 will not only increase M_C , but will also cause all of the other cross sectional radii, R_1 , R_2 , and R_3 , to be correspondingly increased, offsetting the decrease in $(M_{CRY} - M_I)$. The current density can be decreased by 50% without significantly affecting R_1 ; however, the mass of $(M_{CRY} - M_I)$ is sensitive to small changes in the critical temperature, $10^{\circ}K$, chosen for the study. An increase of 20% in the allowed superconductor operational temperature will reduce the $(M_{CRY} - M_I)$ by approximately 20% and, in general, increasing T_0 is the direction to take. The steep drop in critical current density above $10^{\circ}K$ for Nb_3Sn precluded our using a higher temperature.

Several other sources for reducing M_{CRY} may become available in the future, but they will depend on the development of new materials. More effective and lighter insulators and superconductor materials having high current densities at temperatures above $10^{\circ}K$ are two such advancements. However, reducing the heat load by increasing the insulation thickness will not reduce M_{CRY} abruptly, since M_I is proportional to R_3^2 and Q is a slowly varying function of R_3 . As R_3 is increased beyond its present size, its contribution to M_{CRY} will increase significantly and it will also become more difficult to integrate into the spacecraft.

Assigning a nuclear power supply to the vehicle and utilizing only the additional mass of the power supply needed to increase its basic output capacity by 3.3 kw will reduce the mass of the QHC active shield significantly. The 45 kg/kw specific mass for the power supply assumed in our analysis is realistic but results in a power supply weighing 153 kg - almost 30% of the total mass of the 7 Mev shield. If the space vehicle employs a nuclear power supply, the additional mass required to add 3.3 kw to the vehicle power station will be small if Stekly's data⁹ is utilized.

The structural mass, on the other hand, is less than 10% of the total mass since the induced forces are easily counteracted with the titanium alloy tube. The small radial and axial forces exerted on the conductor in the 2 Mev shield are increased by a factor of nine when the energy cutoff is raised to 7 Mev; however, even at this higher electron energy, no special structural considerations are necessary. Increasing currents by another factor of 30 or more to shield space protons increases the forces on the conductor by three orders of magnitude and, consequently, M_s becomes the dominant mass component of the proton active shield.

We may best compare the QHC electron shield with an equal mass aluminum shield using the material shield to protect a 420m^3 sphere - an optimum configuration for a material shield. For this configuration, a thin spherical shell of aluminum 0.072cm thick (0.194 gm/cm^2), which is equal to the range of 0.45 Mev electrons, will weigh 530 kg . To effectively stop 7 Mev electrons from penetrating the material shield will require 4 gm/cm^2 or a total shield mass, M_T , of approximately $11,000\text{ kg}$. Even with this excessive weight, the bremsstrahlung produced in the aluminum penetrates the shield with little attenuation and this clearly demonstrates the advantage the active shield holds over the material shield in protecting against electrons.

The magnetic induction, produced by the QHC currents, inside the 420m^3 vehicle is relatively small except within a few centimeters of the coils where it increases above 100 gauss and 300 gauss for the 2 Mev and 7 Mev shields, respectively. At the center of the vehicle, B is approximately 4 gauss for the 2 Mev shield and 12 gauss for the 7 Mev shield. Thus, B is of nominal magnitude throughout most of the vehicle so that its presence in the spacecraft does not compromise the practicality of the QHC concept. Increasing the volume of the vehicle and corresponding active shield without increasing the cross sectional radius of the toroid, r_0 , or electron cutoff energies will reduce the magnetic field from that of Figure 4. In general, increasing the radius, a , of the toroid will reduce the magnetic field, all other quantities remaining the same. Also, there is an upper limit on the values of Δs that can successfully utilize a QHC shield. A $\Delta s = 0.38$ is already of sufficient magnitude that the ampere turns are almost all concentrated on the inner half of the toroid as seen in Figure 3. Increasing Δs further will increase this concentration and, consequently, the magnetic field inside the vehicle. Conversely, reducing Δs will have the opposite effect.

One phenomenon not mentioned in this paper concerns the orientation of the vehicle during its mission. The QHC will align its axis with the earth's magnetic field lines providing a strong stable platform - an effect which must be considered in planning a mission. For low latitude or synchronous orbits, this may be an advantage, but for polar orbits, this may be a problem. However, the low mass of the QHC shield and its potential for further improvements makes it an attractive concept for the future.

The authors would like to thank Mr. G. D. Duckworth for performing the computer calculations associated with determining the magnetic field, and Mr. G. Sherman for his help in obtaining information on the cryogenic cooling system.

REFERENCES

1. A. Bhattacharjie and I. Michael, "Mass and Magnetic Dipole Shielding Against Electrons of the Artificial Radiation Belt," Vol. 2, No. 12, pp. 2198-2201, AIAA Journal (December 1964).
2. R. H. Levy, "Radiation Shielding of Space Vehicles by Means of Superconducting Coils, Vol. 31, pp 1568, ARS Journal (1961).
3. R. F. Tooper, "Electromagnetic Shielding Feasibility Study," ASD-TDR-63-194, Aeronautical Systems Division (1963).
4. G. V. Brown, in High Magnetic Fields, Kolm et al., ed., pp. 370, MIT/Wiley, New York.
5. C. Stormer, "The Polar Aurora," Oxford Press (1955).
6. S. H. Levine and R. Lepper, "Magnetic Shield Simulator," pp 401, 1965 Annual Technical Meeting Proceedings, Institute of Environmental Sciences' (1965).
7. S. H. Levine, A. Bhattacharjie and R. Lepper, "Forbidden Regions Produced by Two Parallel Dipoles," Vol. 4, No. 4, pp 654, AIAA Journal (April 1966).
8. S. H. Levine and R. Lepper, "Analogue Studies of Magnetic Shields," AIAA Journal (to be published).
9. R. E. Bernett and Z. J. J. Stekly, "Systems Analysis of Superconducting Magnets for Space Radiation Shielding," Contract No. NAS 8-5278, Avco Everett Research Laboratory (1964).

REFERENCES (CONTINUED)

10. J. B. Cladis, et al, "Feasibility of Magnetic Orbital Shielding System," Technical Report 8-94-64-2, Lockheed Missile and Space Company (1964).
11. J. I. Vette, "Models of the Trapped Radiation Environment," Volume I: Inner Zone Protons and Electrons and Volume II: Inner and Outer Zone Electrons, NASA SP-3024 (1966).
12. W. R. Smythe, "Static and Dynamic Electricity," McGraw-Hill, Inc. (1950).
13. A. Sommerfeld, Electrodynamic Lectures on Theoretical Physics, Vol. III, pp. 11, Academic Press Inc., New York (1952).
14. R. Hecht and C. M. Harper, "Study of Properties of High-Field Superconductors at Elevated Temperatures," Contract NAS 8-11272, RCA (1965).
15. W. Breckenridge, "Exploratory Development of a 3.6^oK Rotary Stroking Refrigerator," RTD PR NR 20534, Arthur D. Little (1966).

ELECTRON BREMSSTRAHLUNG CROSS-SECTION MEASUREMENTS^a

D. H. Rester and W. E. Dance

N 68-26137

LTV Research Center, Ling-Temco-Vought, Inc.
Dallas, Texas

Differential cross sections for the production of bremsstrahlung have been measured for Al and Au at electron bombarding energies of 0.2, 1.0, 1.7, and 2.5 MeV and in addition for Cu and Sn at 0.2 and 1.0 MeV. At each energy measurements were made at photon angles ranging from 0 deg to the largest angle which allowed a reasonable signal-to-background ratio. At 0.2 MeV the present experimental results are higher than the values predicted by the Born approximation except in the region below 75 keV. At higher bombarding energies the measured values are closer to the predicted values, reaching good agreement for $Z = 13$ at 1.7 MeV. At all four energies the difference between the measured values and the Born-approximation values increases with atomic number. At 1.0 MeV the present results for Al are below those reported by Motz at 10 and 30 deg for photon energies less than 800 keV. The present results for Au at 1.0 MeV are also below those of Motz for 0, 20, and 30 deg, but are in agreement with Motz's values at 90 deg at this energy. Comparison of the present results for Al and Au at 2.5 MeV show agreement within the experimental errors with the results of Starfelt and Koch at 2.72 MeV. At each energy comparison of the integrated cross-sections differential in photon energy with the Born-approximation values exhibit increasing hardness with atomic number as compared with the theory.

^a Work performed under National Aeronautics and Space Administration Contracts NASW-1385 and NAS8-21055

INTRODUCTION

Measurements of bremsstrahlung production cross sections due to electrons in the intermediate energy range, i.e. between 0.1 and about 4.0 MeV, have been relatively few. J. W. Motz (1) reported measurements at 0.5 and 1.0 MeV for targets of Al and Au at angles between 0 and 90 deg and at 1.0 MeV on Be. N. Starfelt and H. W. Koch (2) reported measurements for the same target materials at 2.72 MeV at angles of 0 and 6.03 deg. Comparison of these experimental results, which, however, are limited to only small angles at 2.72 MeV, to the Born-approximation theory indicates that the experimental cross section values are generally well above the theory at 0.5 and 1.0 MeV and in agreement with or below the theory at 2.72 MeV. Between these energies no previous measurements have been reported.

The measurements reported in the present study were carried out on targets of Al, Cu, Sn, and Au at incident electron energies of 0.2 and 1.0 MeV and on targets of Al and Au at energies of 1.7 and 2.5 MeV.^b At each incident electron energy measurements were made in the region from 0 deg to the largest angle at which the target photons could be separated from the background. Since the bremsstrahlung cross sections are predicted to vary as Z^2 , it was generally possible to extend the measurements to larger angles for Sn and Au at a given incident energy. Measurements were limited to smaller angles as the incident energy was increased due to the energy dependence of the angular distribution. For example, at 2.5 MeV measurements were confined to the region from 0 to 30 deg, while at 0.2 MeV measurements were made in the region from 0 to 105 deg. Cross sections from the present

^b The results of cross-section measurements at 1.0, 1.7, and 2.5 MeV, as well as additional results at 1.7 and 2.5 MeV, are to be published in The Physical Review.

measurements are compared to those reported by Motz and by Starfelt and Koch. Comparisons are also made to the unscreened Born-approximation theory. It is not expected for any of the measurements that this theory would adequately predict the cross sections in the photon energy region near the high energy limit.

EXPERIMENTAL PROCEDURE

The electron beams were provided by a 3-MeV Van de Graaff accelerator at 1.0 MeV and higher incident energies and by a Cockcroft-Walton accelerator at 0.2 MeV. Energy calibration of the accelerators was carried out by observing the scattered beam with a Si(Li) detector. The error in the energy determination and the energy fluctuation during the bremsstrahlung measurements were estimated to be less than 1% of the incident energy.

The bremsstrahlung detector for the 200-keV spectra was a 2 x 2-inch, thin window NaI(Tl) scintillation detector. At higher energies a NaI(Tl) anticoincidence spectrometer of the type used by Trail and Raboy (3) was found to give the best response while allowing backgrounds to be limited to low levels. The response of this spectrometer is approximated by a Gaussian full-energy peak plus a simple low-energy tail portion which is constant in amplitude with pulse height. The detector response and efficiency as a function of energy were determined from a series of measurements of gamma-ray lines in the region of interest.

Self-supporting targets were prepared by the standard vacuum evaporation technique. At each energy target thicknesses were chosen so that effects due

to multiple scattering were negligible. Only for the measurements at 0.20 MeV on Au and Sn was it necessary to use composite targets. These targets were made by evaporating the metals onto thin VYNS backings. The contribution to the bremsstrahlung spectra due to the VYNS was determined to be less than 3%.

Since a typical pulse height distribution due to bremsstrahlung ranges over two or three orders of magnitude downward from low photon energy to the high-energy end, in many cases a second measurement was made with a lead "beam hardener" inserted between the target and the detector. The hardener reduced the high count rate at low pulse height, while reducing the rate for photons with energies above 70% of the end point value by less than 15%. This method allowed improved statistical accuracy near the spectral end-points to be obtained in reasonable data accumulation periods, without introducing pulse pile-up effects. In many cases the spectra, therefore, are composites of spectra taken without the hardener, joined at about 70% of the end-point energy to the spectra from the hardener runs corrected for photon attenuation in the hardener material.

Background bremsstrahlung, largely generated by stopping the incident beam, was reduced by shielding the Faraday cup with 6 in. of lead. The bremsstrahlung detector itself was enclosed in a 3-inch thick lead cylinder and surrounded by the NaI annulus. Background effects still present, mostly attributed to the target-scattered beam, were removed from the pulse height spectra by inserting a tantalum photon absorber between the target and detector with the target in place and subtracting the resulting spectrum from that taken without the absorber. The shape of the absorber was such that it

blanked out to the detector only an area on the target slightly larger than the beam spot, leaving the background-producing areas exposed.

DATA REDUCTION

Several methods of removing the spectrometer response from the pulse height spectra were investigated. However, the relatively simple response of the spectrometer to monoenergetic photons allowed an accurate correction for the response to be made without applying elaborate iterative techniques or inverting the spectrometer response matrix. The method of removing the response from the measured pulse height data normalized with respect to the number of incident electrons and the solid angle subtended by the spectrometer consisted of the following operations:

1. Pulse height spectra were hand smoothed out to the photon energy corresponding to the incident electron energy. Beyond this point the data were set to zero. The hand-smoothed spectra were smeared by multiplying them by the spectrometer response matrix.
2. The smoothed pulse height spectra were ratioed to the smeared spectra.
3. The original unsmoothed pulse height spectra were multiplied by their appropriate sets of ratios.
4. The response-corrected spectra were corrected for spectrometer efficiency.

The correction factors derived in the above manner are essentially efficiency corrections at photon energies below approximately 85% of the end-point energy due to the simple response below the full energy peak. Above

this photon energy, the combined corrections vary more rapidly, reflecting the correction for the Gaussian response of the spectrometer. The corrections at 1.0 MeV electron energy for Au at 0 deg, are typical of the corrections made to most of the pulse height distributions. For example, the combined correction increases from 1.0 at 0.2 MeV to 1.6 at 0.85 MeV and the more rapidly to 2.7 at 1.0 MeV. The Al correction factors, on the other hand, are considerably different near the end-point energy. The correction factors for Al at 1.0 MeV bombarding energy and 0 deg increase from 1.6 at 0.85 MeV to only 1.85 at 1.0 MeV. This difference is a result of the difference in the shapes of the spectra from about 70% of the spectral end point. Most of the spectra fall off sharply at the high energy end; however, Al and Cu spectra at 0 and 4 deg decrease less rapidly near the end point. This method of response removal was shown by use of test spectra to have an accuracy to within a few percent in the photon energy interval below 90% of the end point. In the region above 95% of the end point it was necessary to apply an additional 15% correction.

EXPERIMENTAL RESULTS

The estimated average experimental error in the cross sections in the photon energy interval below 90% of the high energy limit is about 15%. At the smaller angles, 0 and 4 deg, the average error is estimated to be about 7% in this energy interval. At the larger angles additional uncertainty arises from the angular uncertainty of 0.3 deg and the strong dependence of the photon yield on angle at angles greater than 10 deg. The extent to which the accuracy is affected by the bremsstrahlung angular distribution increases with increasing incident energy. In the photon energy region greater than 90% of the end point additional uncertainty arises due to increased statistical

error and the spectrometer response removal from the pulse height spectra. At the largest angle for each incident energy the total error in the region of photon energy greater than 90% of the end-point increases to about 30-50%.

The measured cross sections are shown in Figs. 1 through 21. The spectral shapes are, of course, similar at each energy. However, it is of interest to observe at each incident energy the trend of the data with atomic number relative to the Born-approximation theory. As expected it is generally true that the experimental values for the higher Z materials show the larger discrepancy. Also for each atomic number the trend with energy is apparent, namely that the experimental values become closer to the theoretical values as the incident energy is increased. Figure 1 shows the measured cross sections at 0.2 MeV for Al. The experimental results exceed the theoretical values at every angle in the photon energy region above 75 keV. The experimental cross section at 0 deg and a photon energy of 150 keV is a factor of 2.5 greater than the theoretical prediction. The experimental values at larger angles exceed the theory to about the same extent. Figure 2 shows a similar comparison at 1.0 MeV. At this energy it is clear that the experimental results are much closer to the theory than at 0.2 MeV. The measured values at 0 deg cross the values at 10 deg as predicted by the theory. Below about 400 keV at 0 deg the experimental values fall 15% below the theory due to the effect of screening, which has not been included in the theory. Figure 3 shows the results of measurements on Cu targets at an incident energy of 0.2 MeV. The comparison is similar to that for Al at this energy except that the experimental values are somewhat greater relative to the theory than those

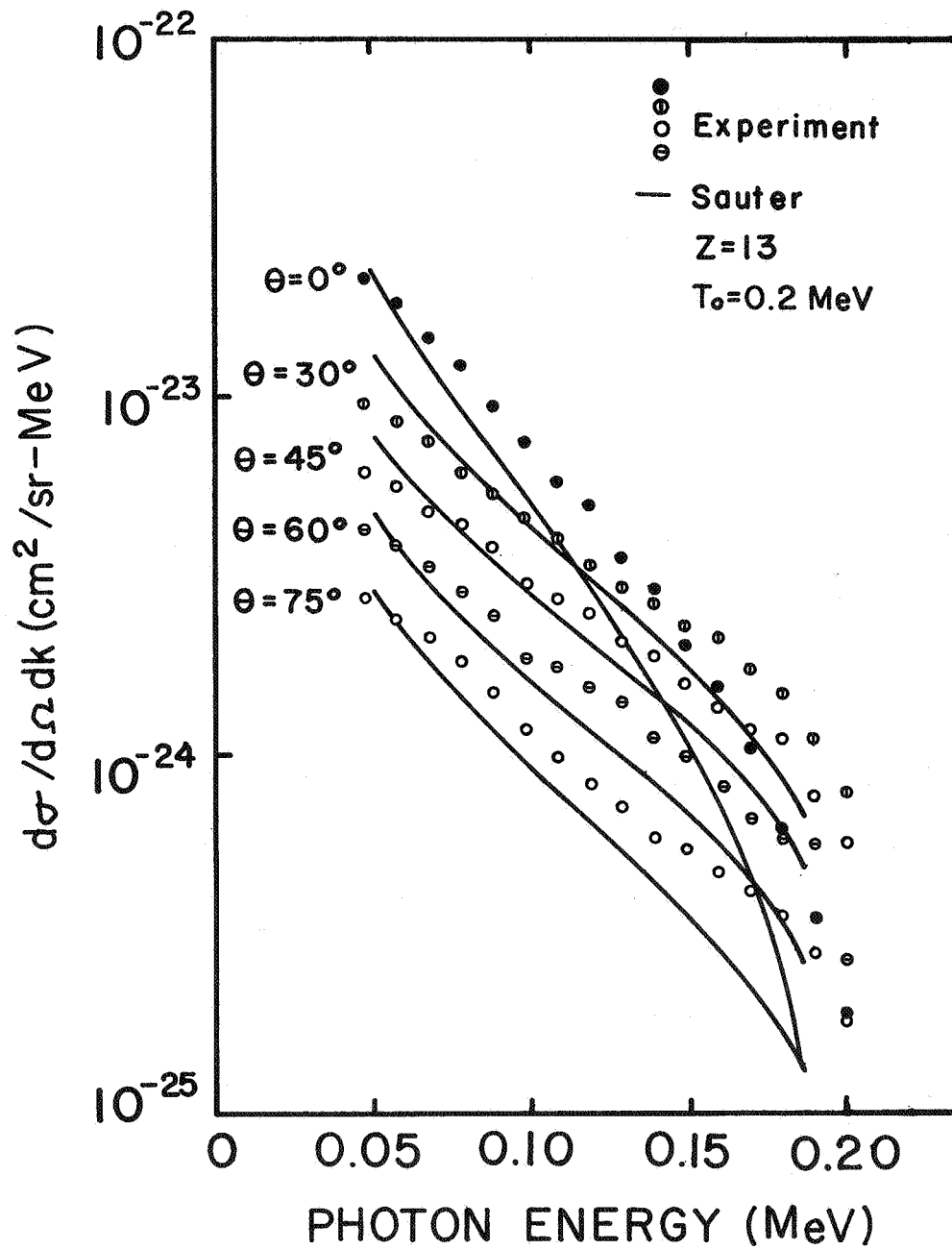


Fig. 1. Cross sections differential in photon energy and solid angle for production of bremsstrahlung by 0.2-MeV electrons incident on an Al target. Comparison is made to the Born-approximation values (evaluated by Sauter).

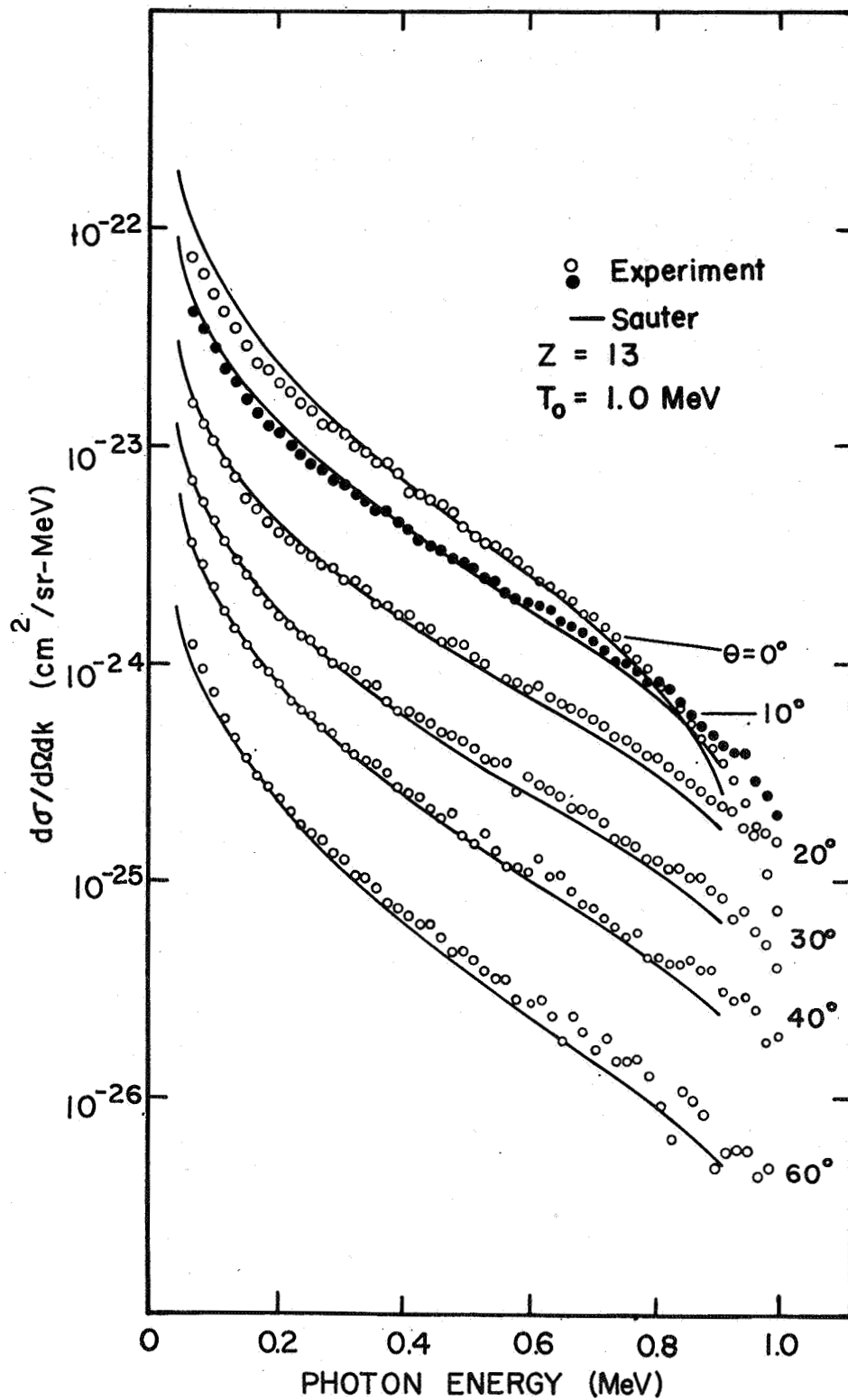


Fig. 2. Bremsstrahlung differential cross sections for 1.0-MeV electrons on Al.

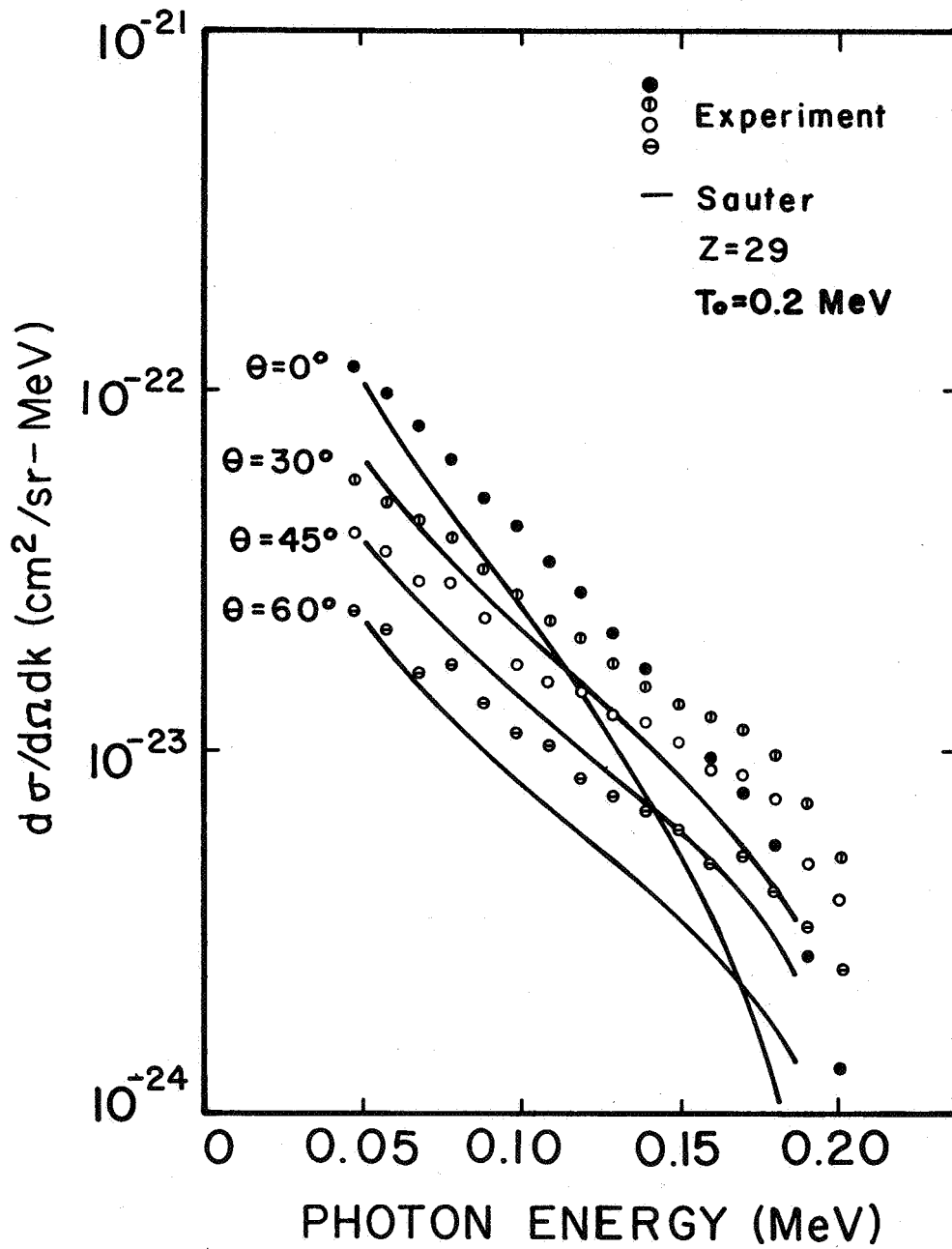


Fig. 3. Bremsstrahlung differential cross sections for 0.2-MeV electrons on Cu.

for Al. Figure 4 is a comparison of the experiment on Sn to the theory. In this case the experimental values exceed the theoretical values at 0 deg and 150 keV by a factor of 4. Thus at 0 deg the measurements at 150 keV are relatively 1.6 times greater than those for Al. Figure 5 shows the results for Au at 0.2 MeV. The values here are again even higher relative to the theory. The characteristic x ray at 70 keV due to K-shell ionization has been removed from the spectra. Its contribution was apparent at all angles but was most significant at large angles. Figure 6 shows the measurements at 10 and 20 deg for Al, Cu, Sn, and Au. These are presented separately for clearness, since the data at these angles cross the values for neighboring angles. However, the plot for all four materials makes it possible to see the effect of the Z dependence of the cross sections at 0.2 MeV bombarding energy. Figure 7 shows the results of the measurements on Cu at 1.0 MeV. As for Al, the values measured for Cu are closer to the theory than at 0.2 MeV. However, at 1.0 MeV the measured values for Cu are still above the theory and relatively greater than those of Al at this energy. Figure 8 shows the 1.0-MeV data for Sn. Figure 9 shows the data for Au at this energy. The cross sections at 120 deg are included for Au although the experimental values at 120 deg have crossed over the theoretical values for 90 deg. The increase of the measured values relative to the theory in the high photon interval below the end point is most apparent for Au. Also the effect of screening is large with the values at 0 deg falling 30 to 40% below the theory at a photon energy of 200 keV. Figure 10 shows the measurements at 4 deg for all atomic numbers. This angle has been plotted separately for clearness. The Z dependence of the cross section is easily seen. The effect attributed to screening is most pronounced for Au. Increased hardening of the spectra

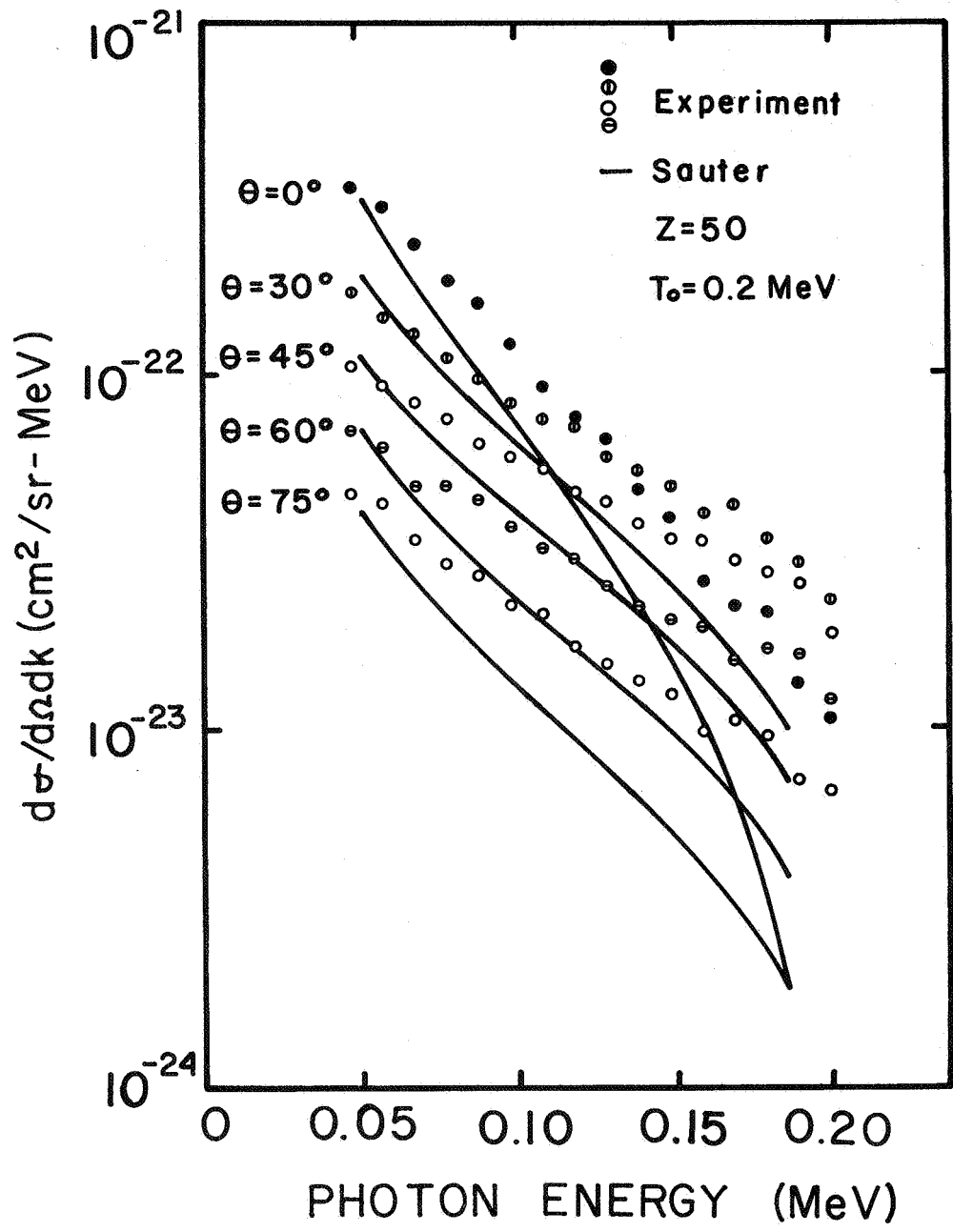


Fig. 4. Bremsstrahlung differential cross sections for 0.2-MeV electrons on Sn.

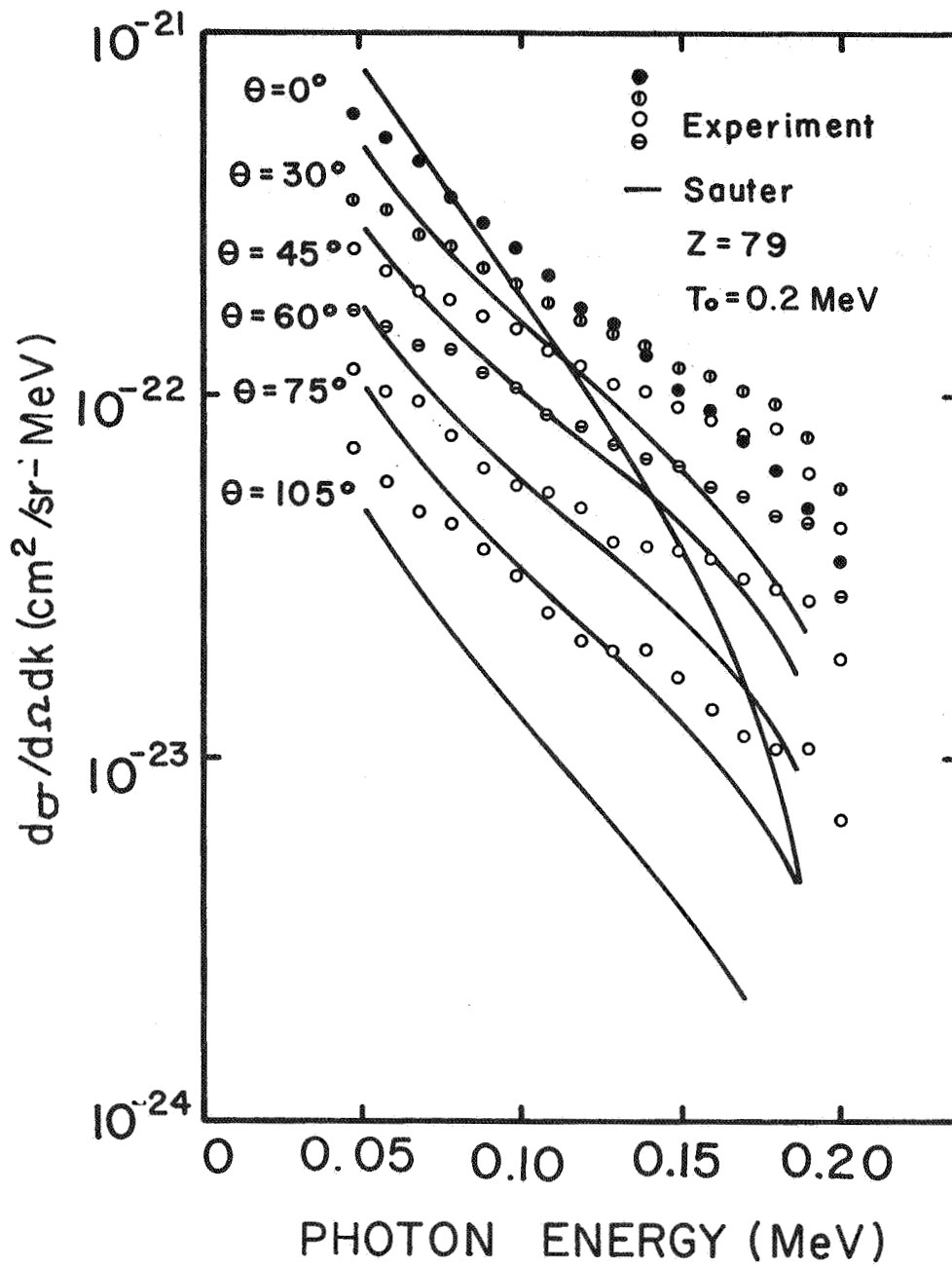


Fig. 5. Bremsstrahlung differential cross sections for 0.2-MeV electrons on Au.

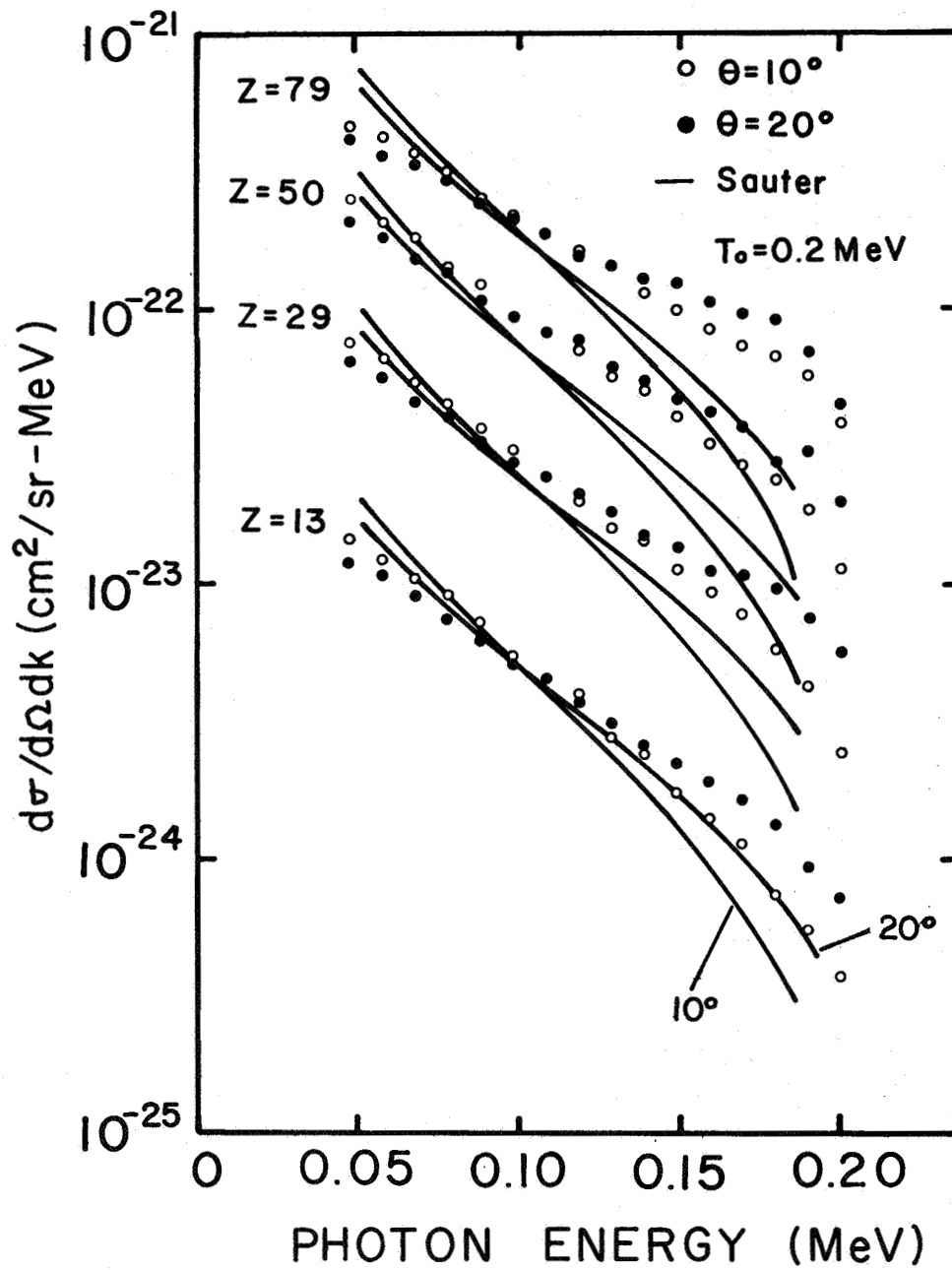


Fig. 6. Bremsstrahlung differential cross sections for 0.2-MeV electrons on Al, Cu, Sn, and Au at photon angles of 10 and 20 deg.

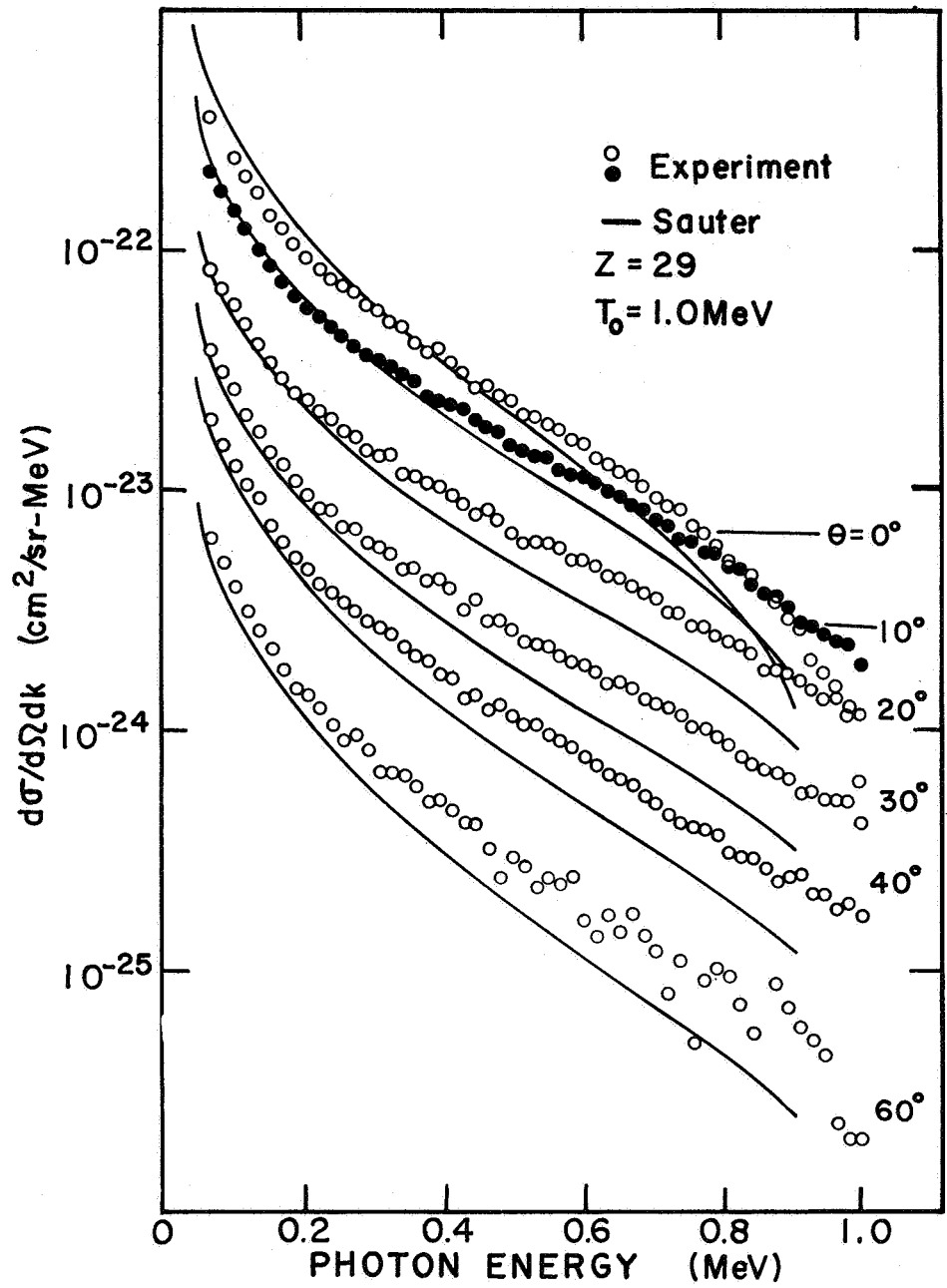


Fig. 7. Bremsstrahlung differential cross sections for 1.0-MeV electrons on Cu.

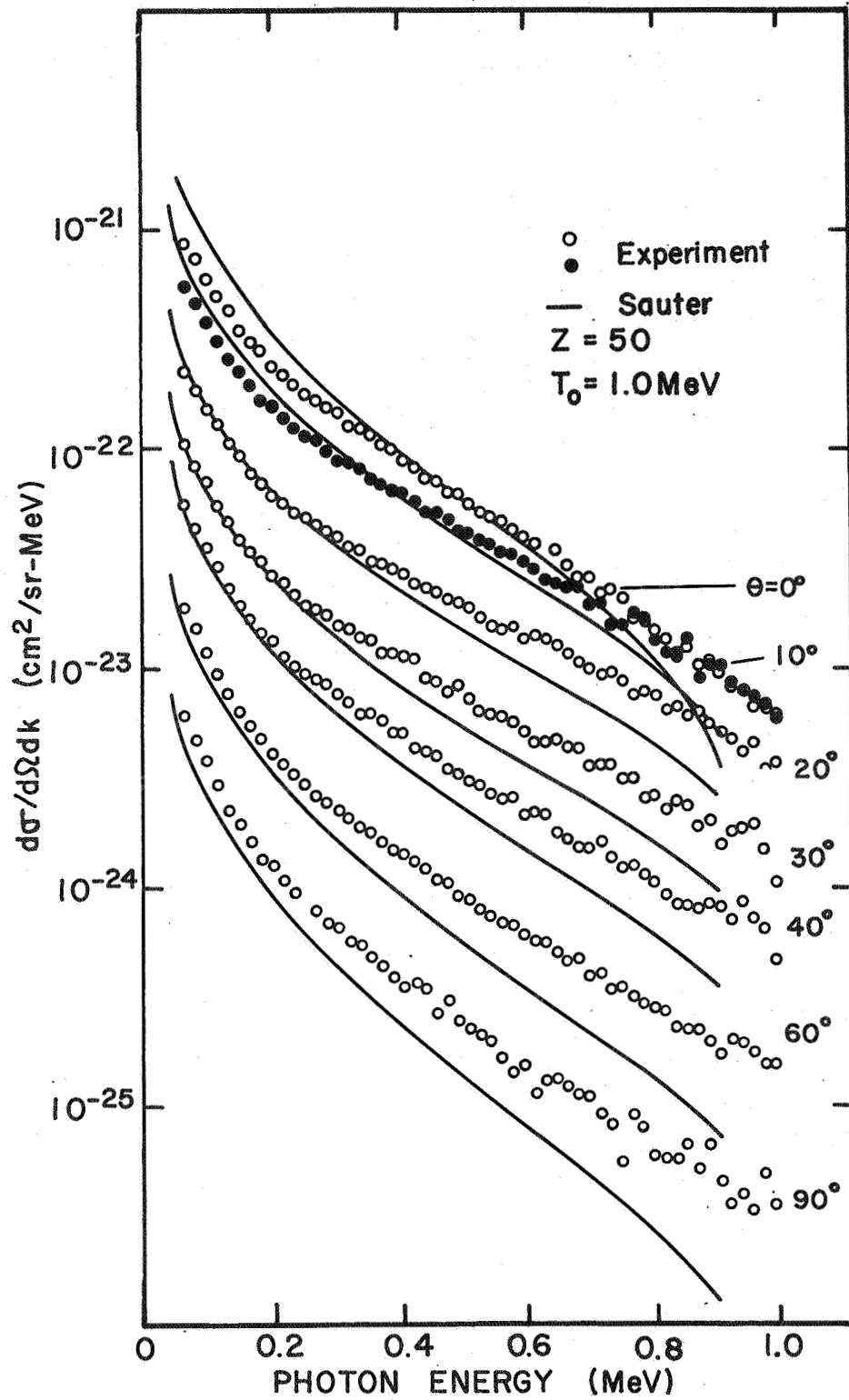


Fig. 8. Bremsstrahlung differential cross sections for 1.0-MeV electrons on Sn.

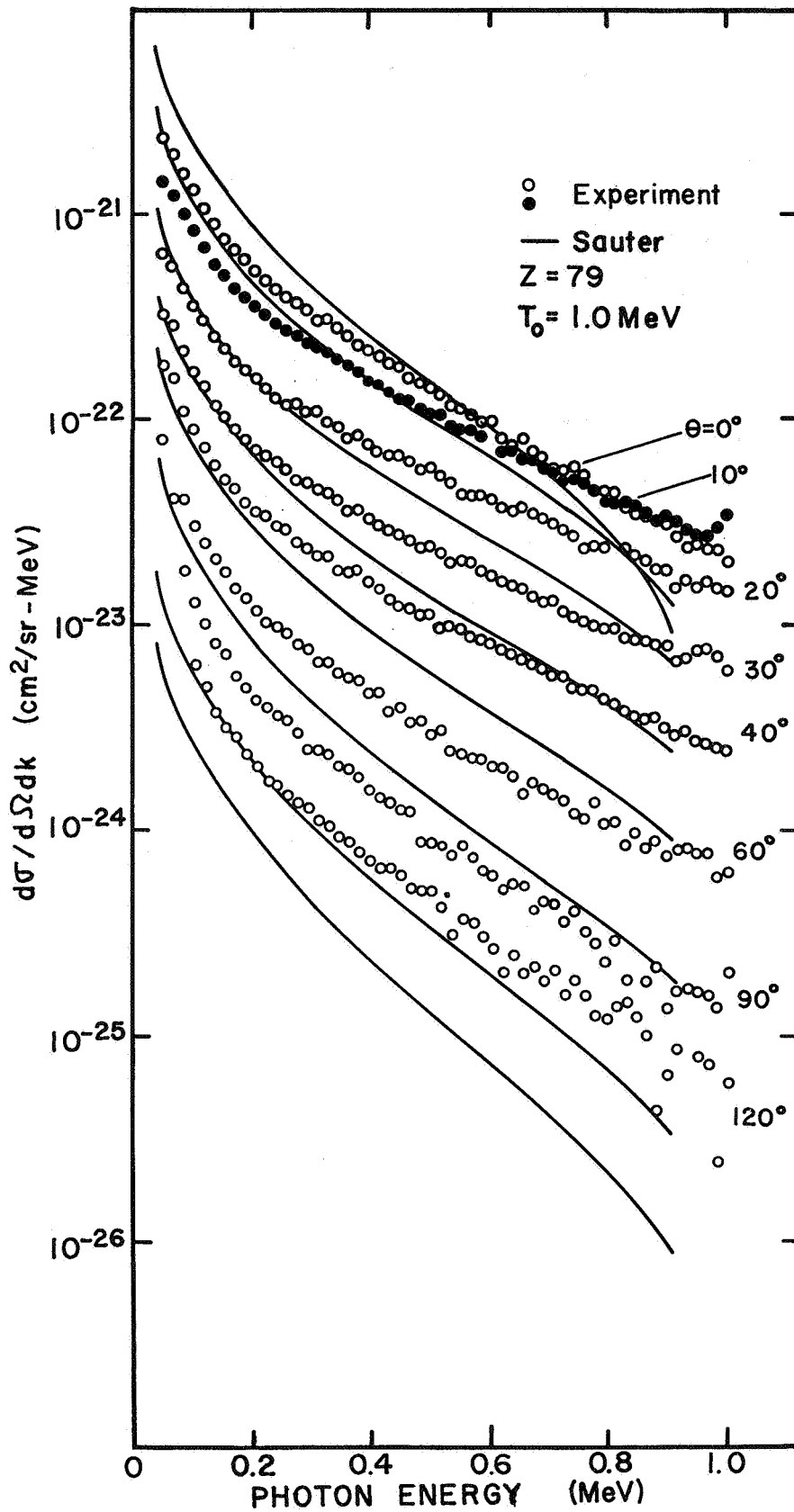


Fig. 9. Bremsstrahlung differential cross sections for 1.0-MeV electrons on Au.

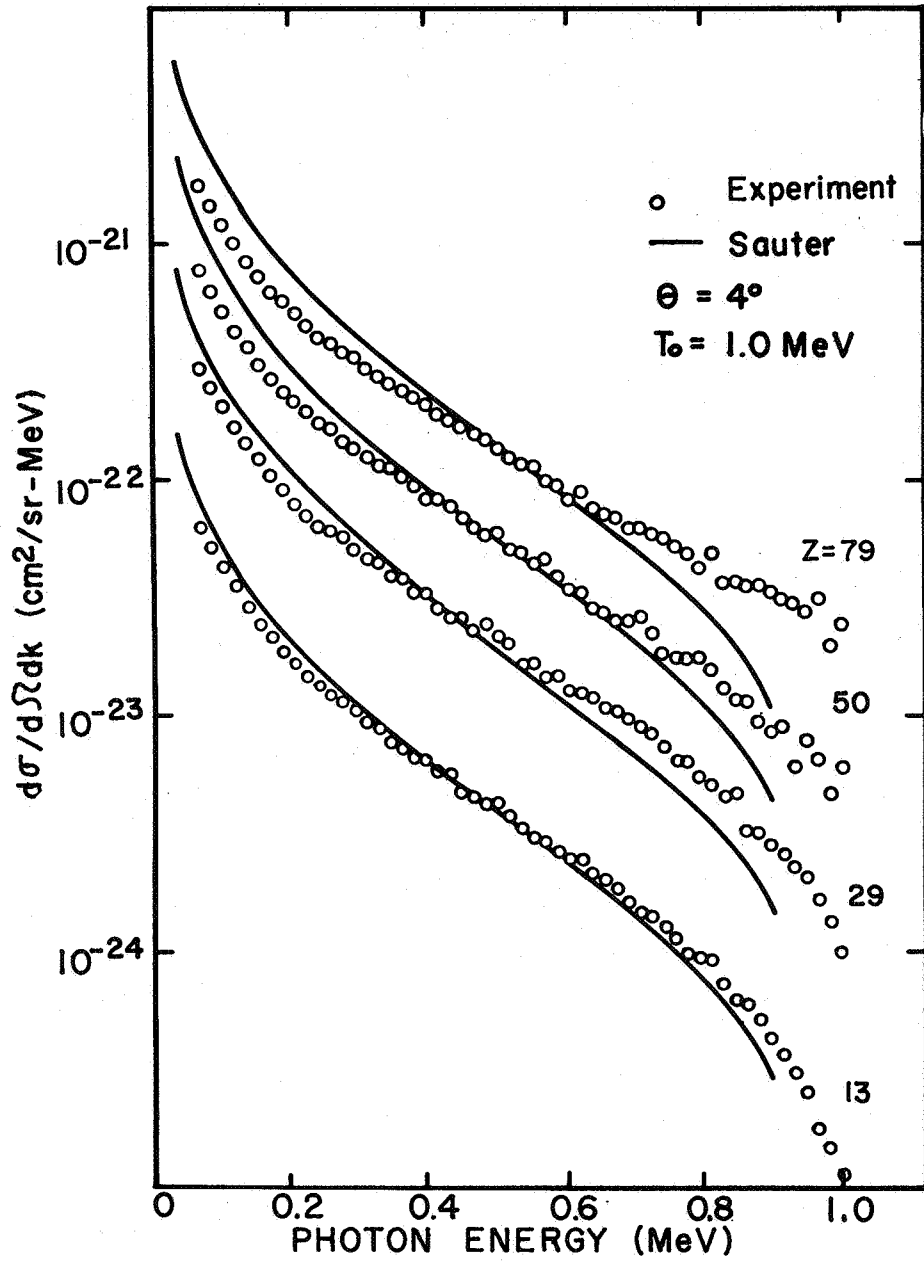


Fig. 10. Bremsstrahlung differential cross sections, $\theta = 4$ deg, for 1.0-MeV electrons on Al, Cu, Sn, and Au.

with atomic number is also observed. Figure 11 is a comparison of the present measurements, open circles, to those reported by Motz also at 1.0 MeV for Al, at 10 and 30 deg. The data at 10 deg from the present measurements are 60% below those of Motz at a photon energy of 200 keV and become closer by about 800 keV. At 30 deg on the average the experimental results are closer, but are still outside the stated experimental errors below a photon energy of 400 keV. Figure 12 shows a similar comparison of the cross sections for Au at 0, 20, 30 and 90 deg. While the two experiments are in disagreement at low photon energy at 0 deg, they become closer at 20 and 30 deg and at 90 deg are in agreement. Figure 13 shows the experimental results at 1.7 MeV for Al. The measurements here are very close to the theory at all angles. Figure 14 shows the results for Au at 1.7 MeV. The experimental values are closer to the theory here than at 1.0 MeV. At 0 deg the measurements fall below the theory out to nearly 1.3 MeV. Likewise the 4-deg values are well below the theory in this region. At larger angles the measured spectra are greater than the predictions of the theory, with increasing discrepancy with larger angle. At 2.5 MeV Fig. 15 shows the measurements on Al at 0, 4, 10, and 20 deg. Measurements at larger angles were prohibited by the rapid decrease in yield with angle. At 1.5 MeV photon energy the yield is reduced by a factor of 7 between 10 and 20 deg. Figure 16 shows the measurements on Au at 2.5 MeV. While the measured values at 0 and 4 deg are well below the theory, the data at 10 deg is quite close to the theory from 200 keV to about 1.8 MeV. At 20 and 30 deg the measurements are generally above the theory, but closer than at 1.0 or 1.7 MeV. Figure 17 shows the comparison of the present measurements at an incident energy of 2.5 MeV on Al and Au at

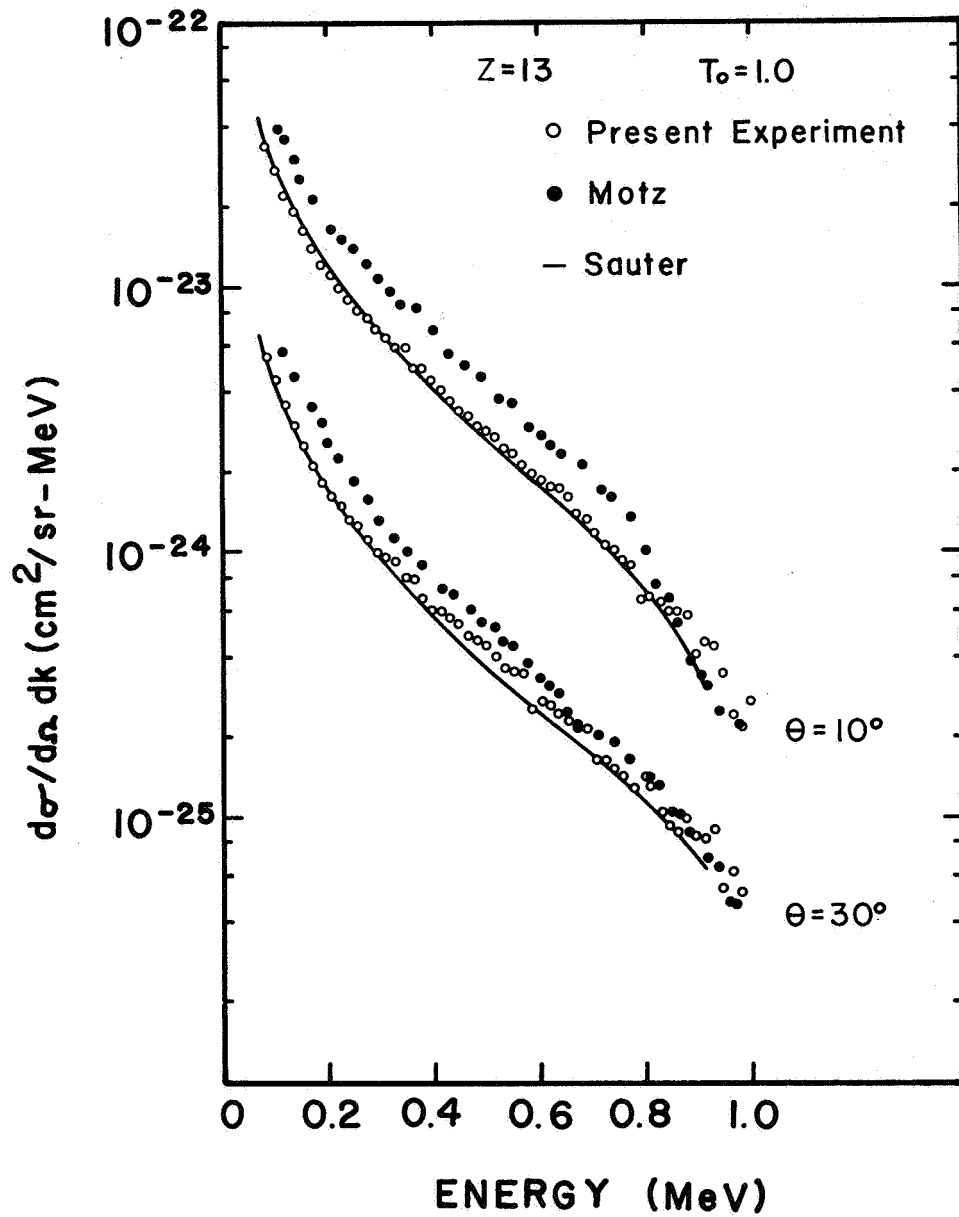


Fig. 11. Comparison of bremsstrahlung cross sections from the present experiment with those reported by Motz for 1.0-MeV electrons on Al, $\theta = 10$ and 30 deg.

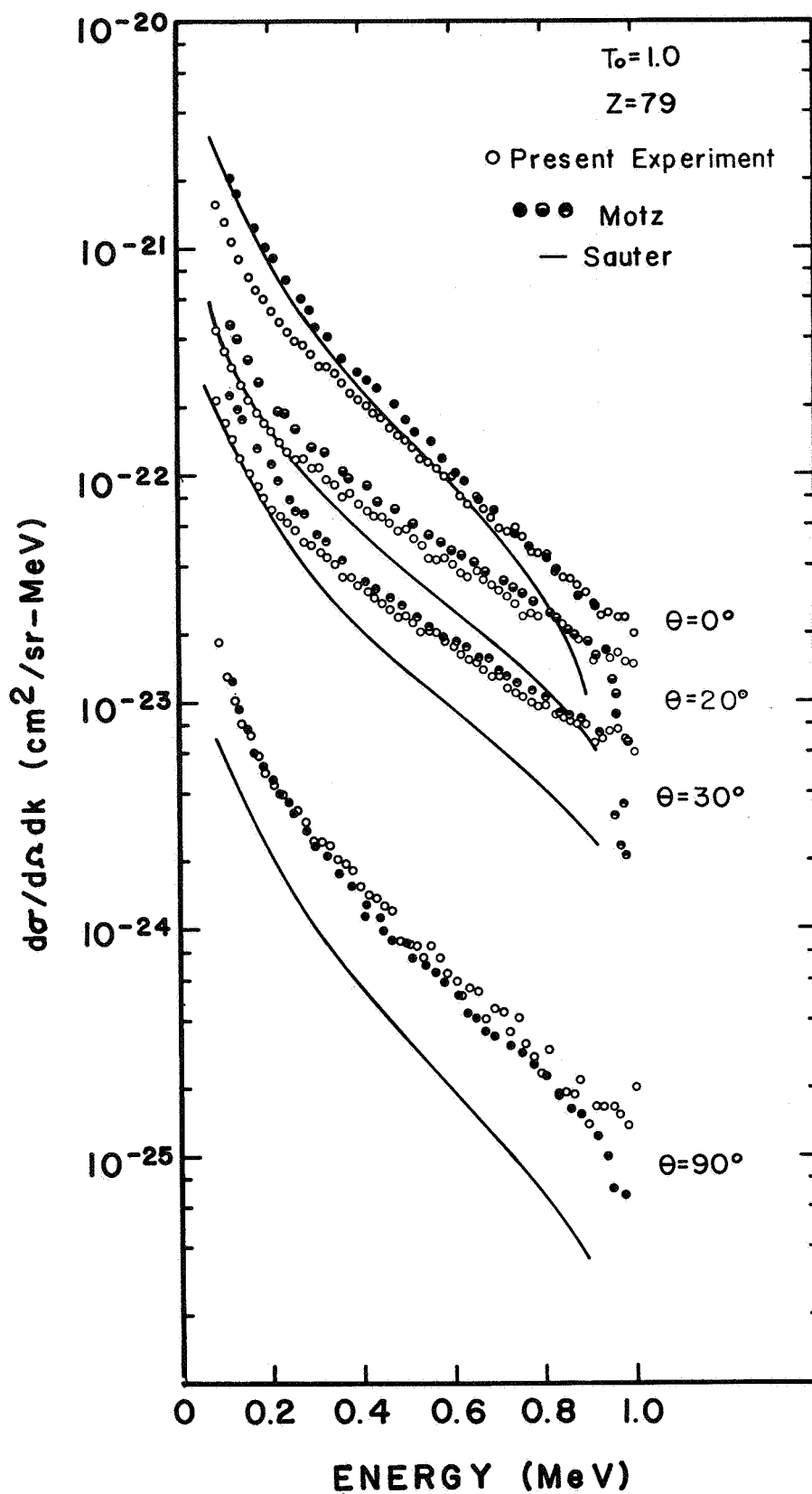


Fig. 12. Comparison of bremsstrahlung cross sections from the present experiment with those of Motz for 1.0-MeV electrons on Au, $\theta = 0, 20, 30,$ and 90 deg.

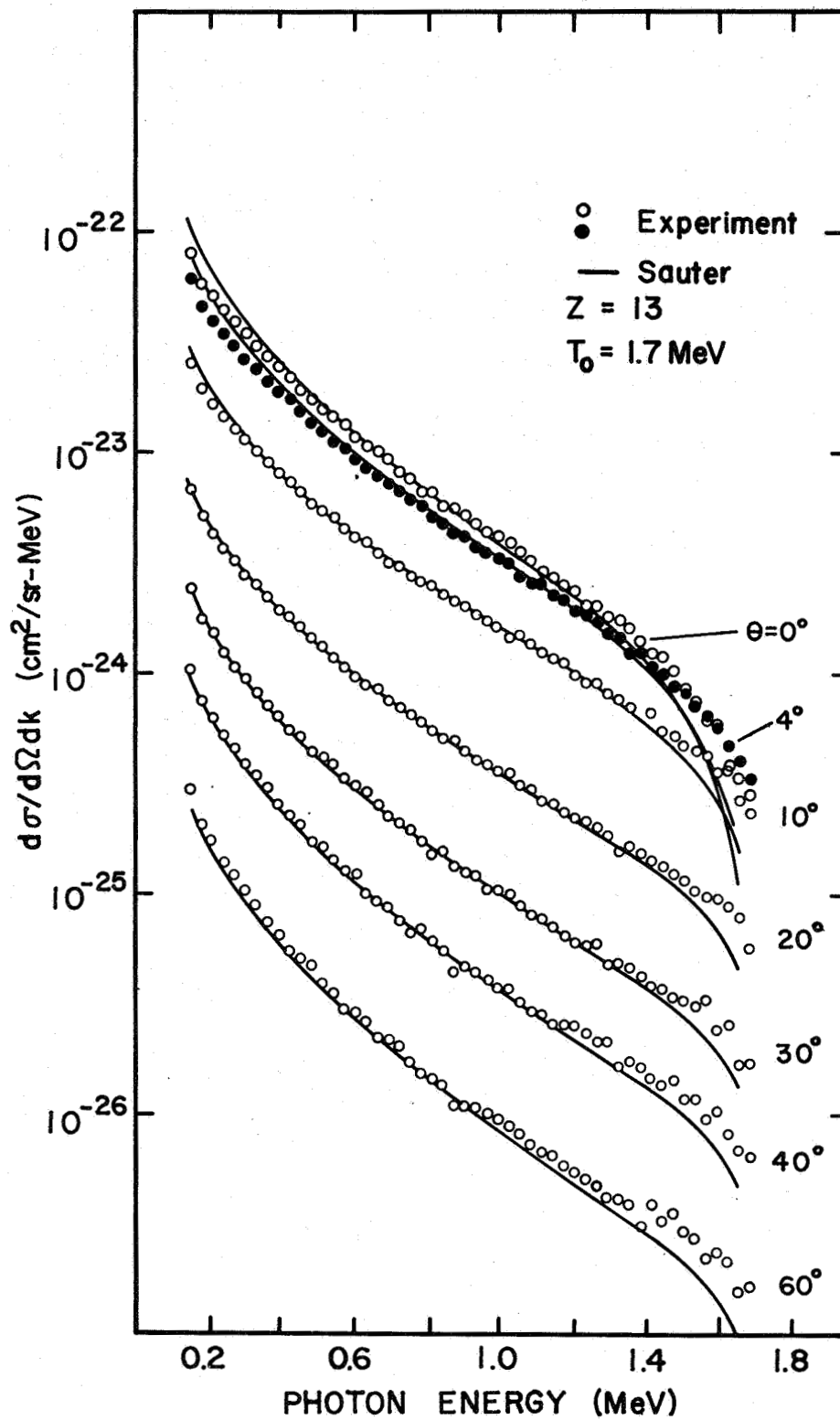


Fig. 13. Bremsstrahlung differential cross sections for 1.7-MeV electrons on Al.

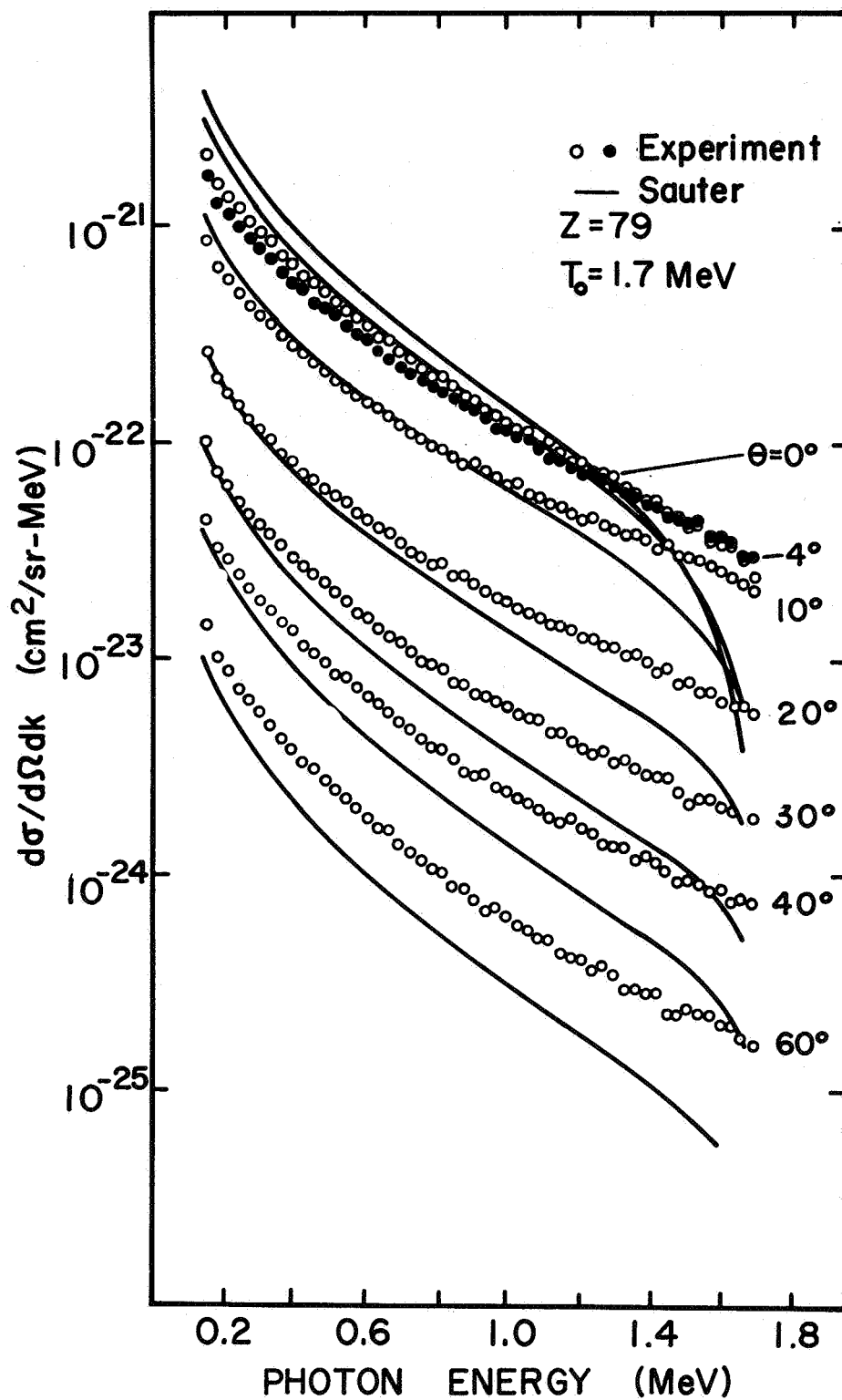


Fig. 14. Bremsstrahlung differential cross sections for 1.7-MeV electrons on Au.

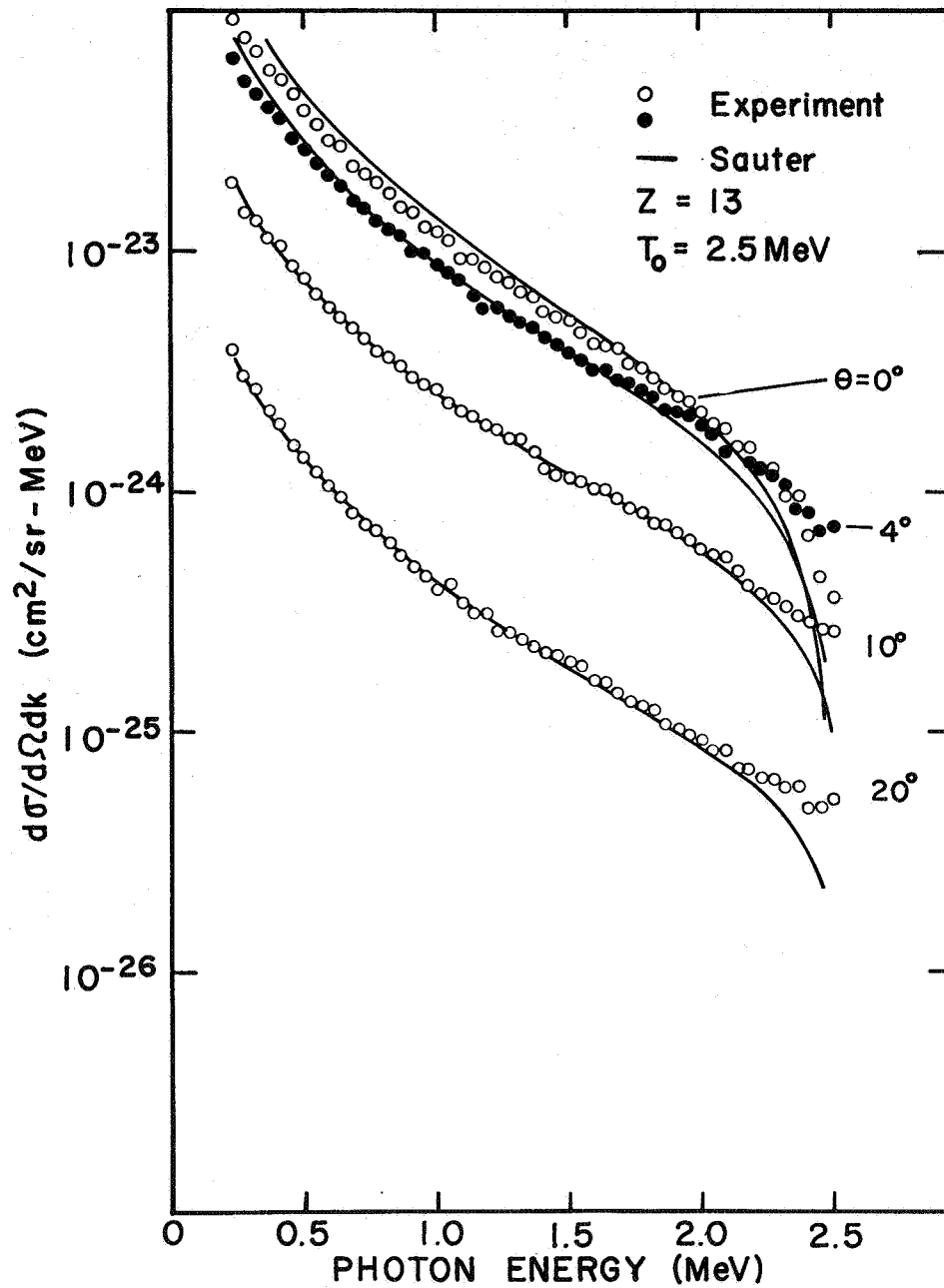


Fig. 15. Bremsstrahlung differential cross sections for 2.5-MeV electrons on Al.

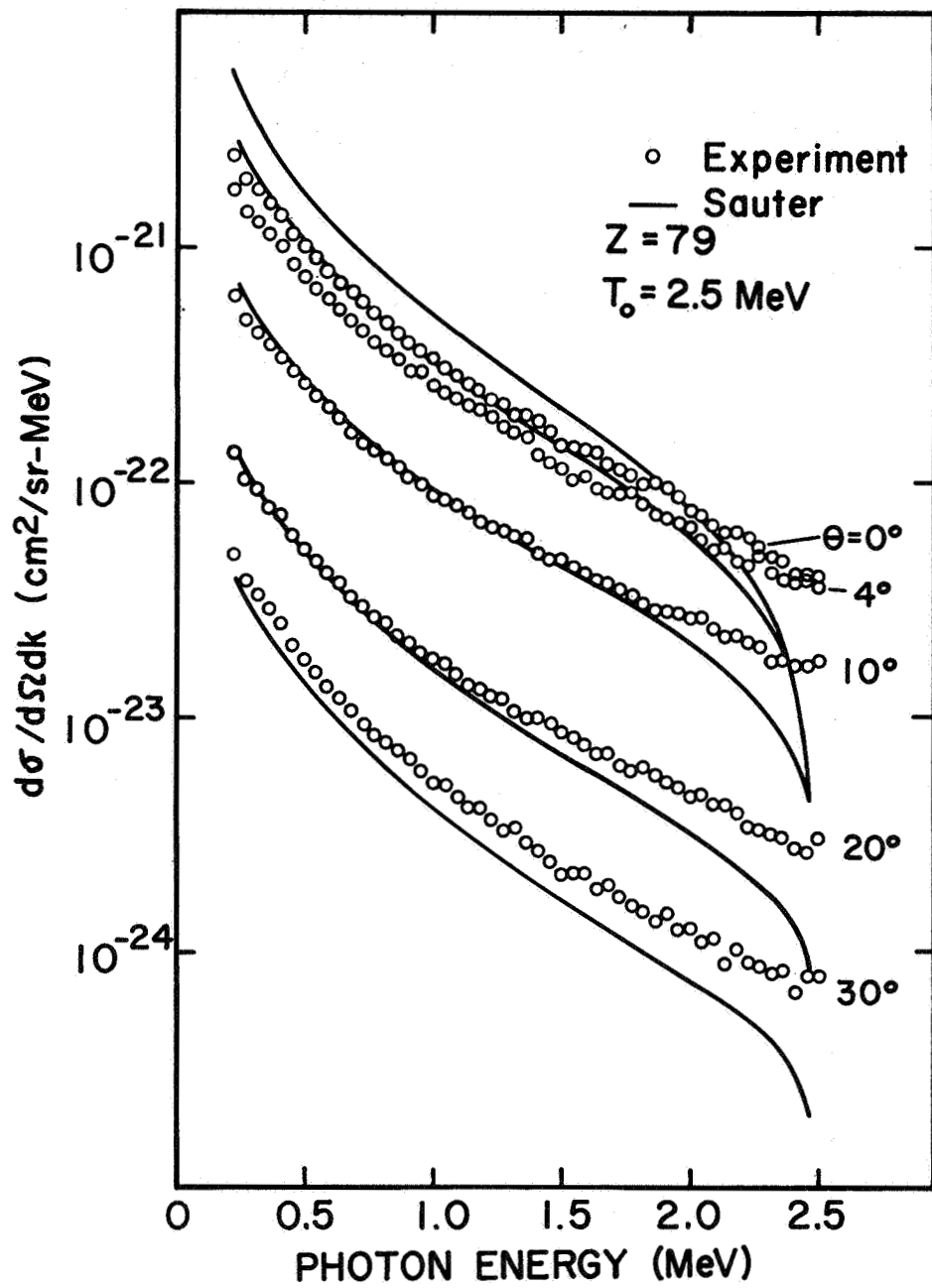


Fig. 16. Bremsstrahlung differential cross sections for 2.5-MeV electrons on Au.

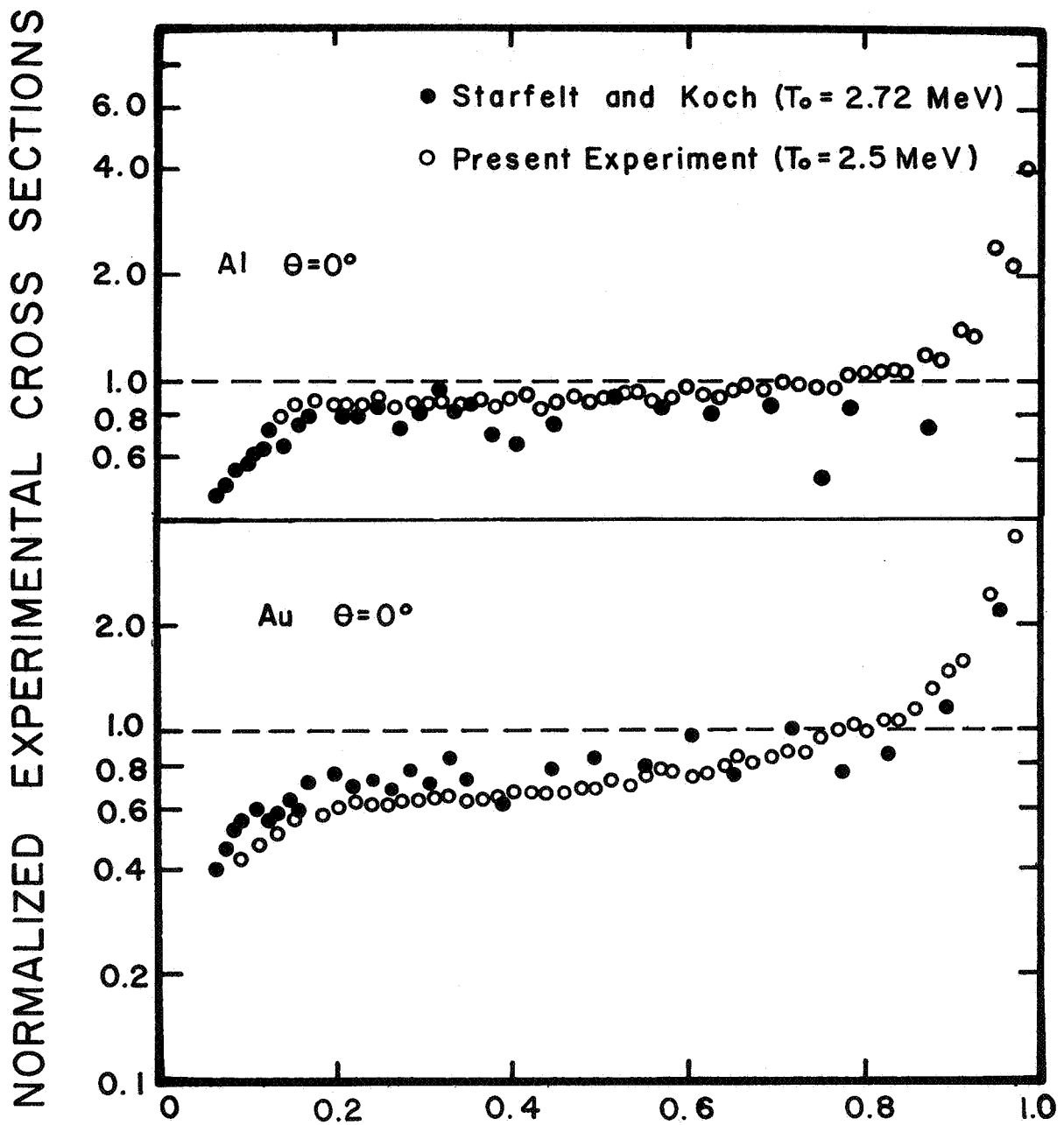


Fig. 17. Comparison of bremsstrahlung cross sections normalized to the Born-Approximation values for 2.5-MeV electrons on Al and Au at 0 deg to those reported by Starfelt and Koch at 2.72 MeV.

0 deg to those of Starfelt and Koch at 2.72 MeV. Both sets of experimental cross sections are normalized to the Born-approximation theory. The horizontal axis is the ratio of the photon energy to the incident electron energy. The agreement between the two measurements is within the experimental error.

Figure 18 shows the cross sections differential in energy only, i.e. after integrating the previous spectra over solid angle for the four elements at 0.2 MeV. The solid lines are the Born-approximation values. The values derived from the measurements are shown as circles. The uncertainty in the integrated cross sections is estimated to be 15% at photon energies less than 90% of the high-energy end point and about 30% in the region greater than 90% of the end point. As for the values at the various angles the measurements exhibit increasing hardness with atomic number as compared with the theory. The dashed line shows the Born-approximation theory corrected for the Coulomb effect by the Elwert factors. For Al the corrected theoretical and the experimental values are in agreement. However for Au the experimental values are still significantly larger. Figure 19 shows the integrated cross sections for Al, Cu, Sn, and Au at 1.0 MeV from the present measurements and the integrated values reported by Motz for Al and Au. The experimental cross sections are normalized to the Born-approximation values. The present values, open circles, are close to the Born-approximation values for Al, although below 300 keV photon energy they drop 10-15% below. The value at 1.0 MeV is in agreement with the corrected Sauter-Fano (4) values of the cross section at the incident electron energy. The values reported by Motz for Al are indicated by closed circles. The comparison of the two experiments reveals significant discrepancies below about 800 keV in photon energy.

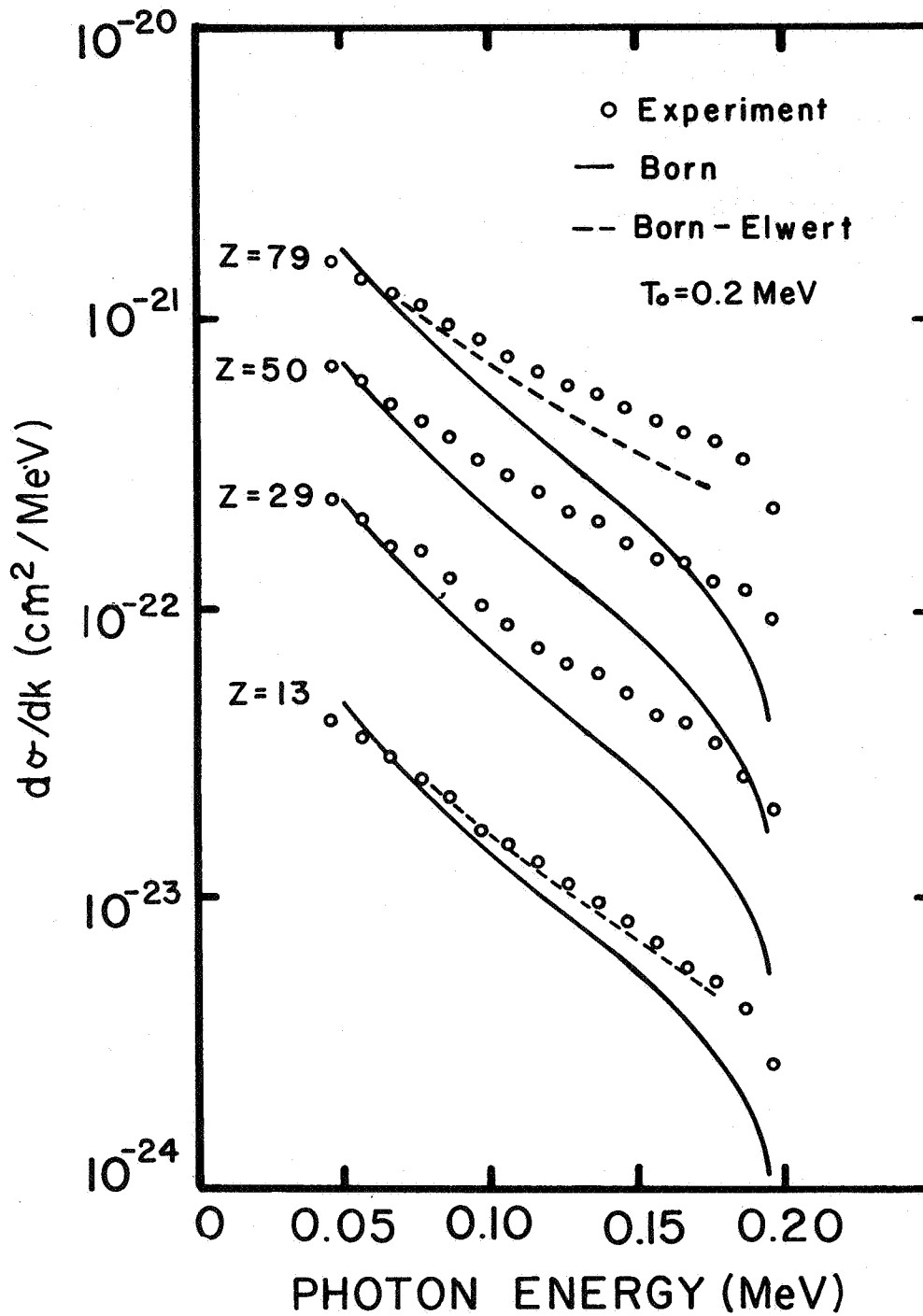


Fig. 18. Bremsstrahlung cross sections differential in photon energy for 0.2-MeV electrons on Al, Cu, Sn, and Au, resulting from integrating the data over solid angle.

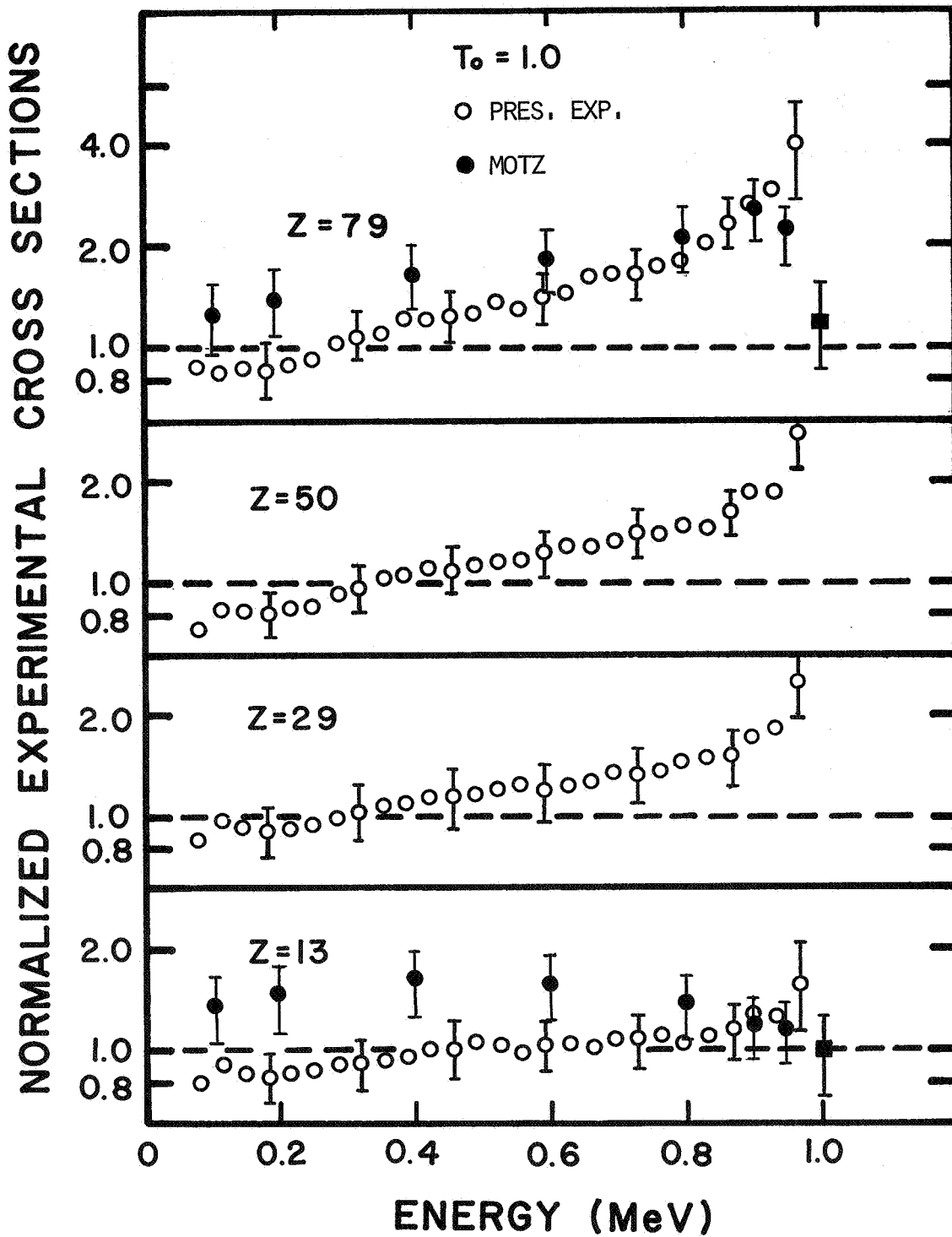


Fig. 19. Normalized integrated cross sections for bremsstrahlung production by 1.0-MeV electrons. The solid squares at 1.0-MeV photon energy are ratios to the corrected Sauter-Fano values.

However above this energy the experimental values converge. A similar comparison of the two experiments is shown for Au. In the photon energy region above 400 keV the two experiments are within the experimental errors. Below 400 keV the measurements are just outside the experimental errors. Figure 20 shows the cross sections for Al and Au, differential in energy at 1.7 MeV bombarding energy. At 1.7 MeV the experimental values for Al are in agreement with the theory. The values for Au are above the theory in the photon energy region greater than 500 keV. Figure 21 contains plots of the cross sections for Al and Au differential in energy at an incident energy of 2.5 MeV. At this energy the experimental values for Al are approximately 8% below the theory. A somewhat larger shift for the case of Au was observed as compared to the data at 1.7 MeV. The experimental values for Au are about 15% below the theory at 1.0 MeV and cross the theory at 1.7 MeV.

NORMALIZED EXPERIMENTAL CROSS SECTIONS

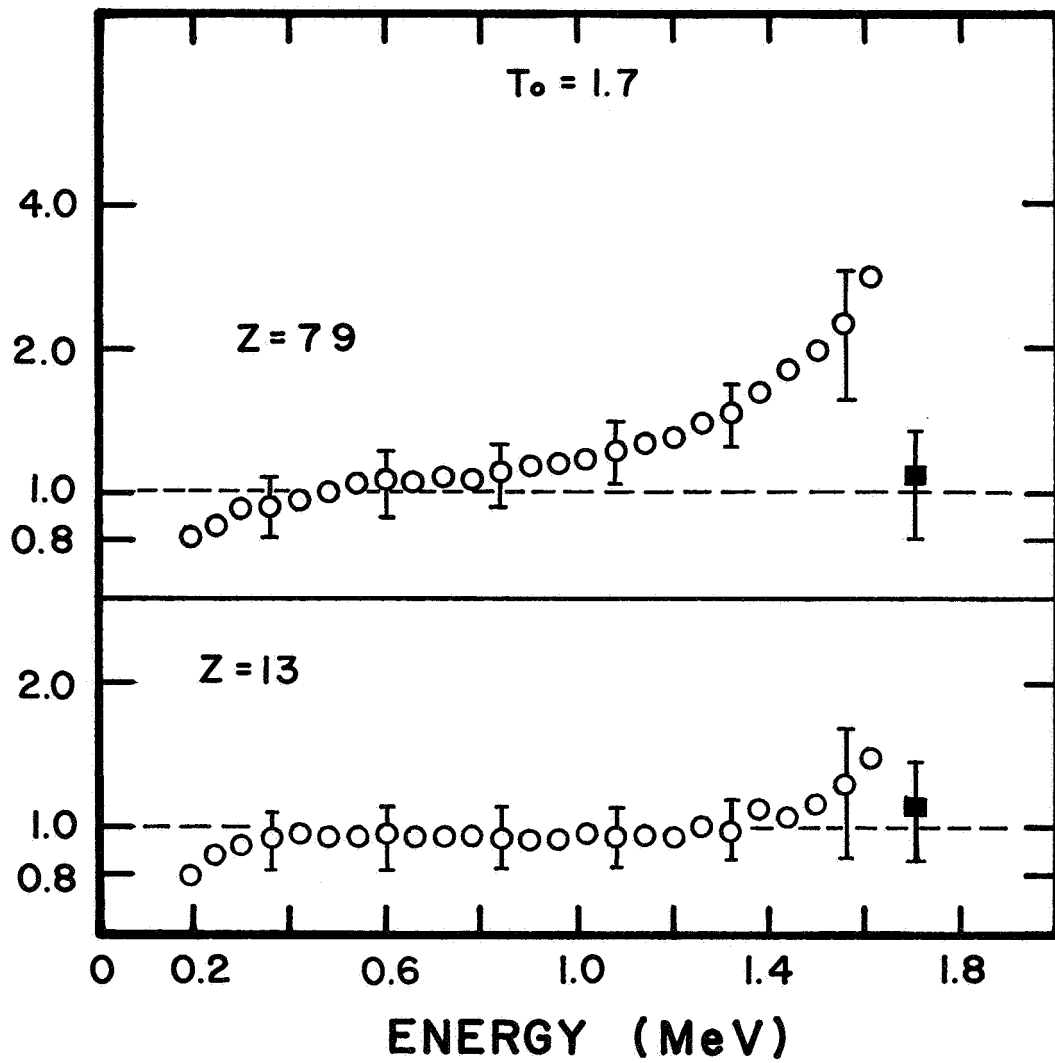


Fig. 20. Normalized integrated cross sections at 1.7 MeV bombarding energy. The solid squares at 1.7 MeV photon energy are ratios to the corrected Sauter-Fano values.

NORMALIZED EXPERIMENTAL CROSS SECTIONS

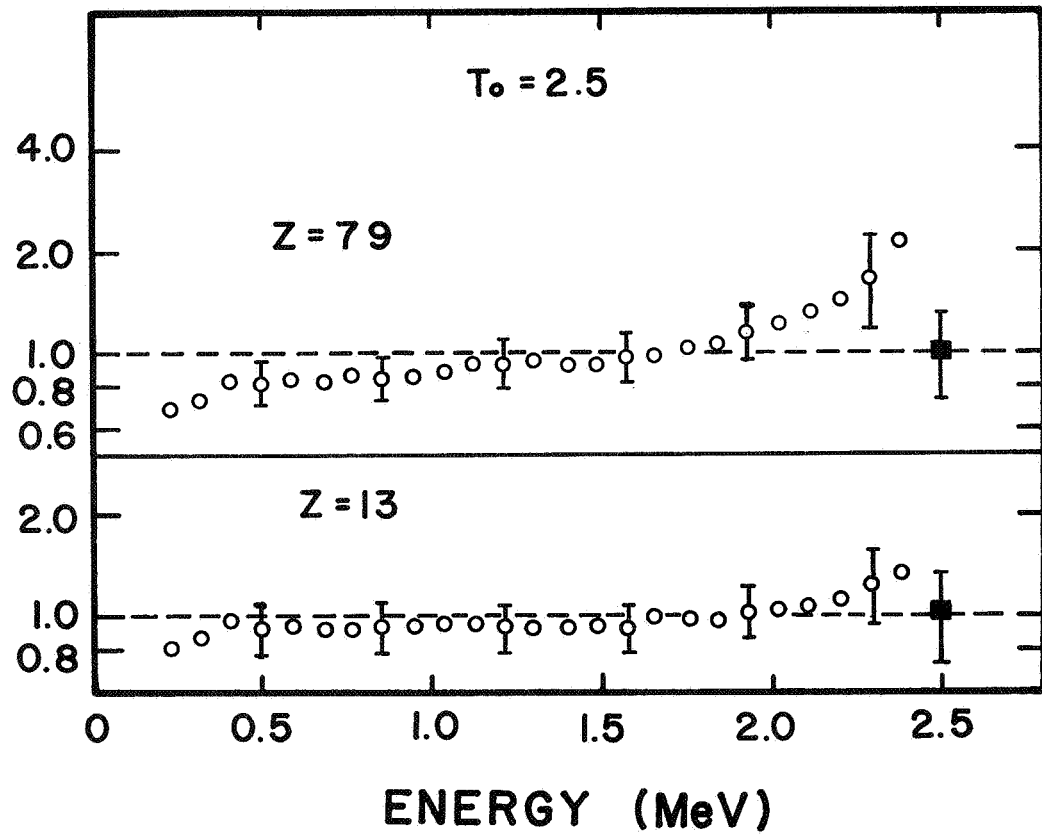


Fig. 21. Normalized integrated cross sections at 2.5 MeV bombarding energy. The solid squares at 2.5 MeV photon energy are the ratios to the corrected Sauter-Fano values.

1. J. W. Motz, Phys. Rev. 100, 1560 (1955).
2. N. Starfelt and H. W. Koch, Phys. Rev. 102, 1598 (1956).
3. C. C. Trail and Sol Raboy, Rev. Sci. Instr. 30, 425 (1959).
4. U. Fano, H. W. Koch, and J. W. Motz, Phys. Rev. 112, 1679 (1958).



AN EXPERIMENTAL STUDY OF THE TRANSPORT
OF ELECTRONS THROUGH THICK TARGETS^{*†}

C. P. Jupiter, J. A. Lonergan and G. Merkel[‡]

General Atomic Division
General Dynamics Corporation

1. INTRODUCTION

Experimental results and methods used in a general study of the transport of electrons in thick targets are described here; this is an extension of earlier preliminary work^(1, 2) performed at General Atomic. The purpose of this continuing program was to provide a comprehensive body of experimental data which could be used to validate analytical methods employed in determining the transport of electrons through shield materials - with particular emphasis on determining the shielding effectiveness of spacecraft components. Measurements were made of the electron transport for incident electron energies of 4.0 MeV and 8.0 MeV to provide data in the energy range where radiation penetration by magnetically trapped electrons in the Van Allen belt is most pronounced. Bremsstrahlung measurements were also performed for an incident electron energy of 10.0 MeV. A stringent test of existing analytical methods (including transport and Monte Carlo techniques) is made possible by an accurate determination of measurable parameters such as the incident

* Work sponsored by National Aeronautics and Space Administration

† Invited paper

‡ Present address: Office of Naval Research, Washington, D. C.

electron energy E_0 , the atomic number of the target, the target thickness t , the angle θ of the transmitted electron or photon and the energy spectra of emitted straggled electrons and bremsstrahlung.

A magnetic spectrometer was employed in determining the electron energy spectra for emission angles ranging between 0° and 80° in order to define completely the energy transport in the forward direction. Bremsstrahlung spectra were measured for emission angles up to 40° using a large NaI (Tl) crystal spectrometer. Target materials included aluminum and beryllium of various thicknesses corresponding to 0.2, 0.5 and 0.7 times the range⁽³⁾ of the incident electrons.

Measured spectra and angular distributions are compared with the Monte Carlo results of Berger and Seltzer.⁽⁴⁾

2. EXPERIMENTAL APPARATUS AND METHODS

The source of electrons used in these studies was an L-band traveling wave electron linear accelerator (LINAC). This machine was operated at energies of 4 MeV, 8 MeV and 10 MeV; the pulse rate was 720 pulses per second and the pulse width was typically 0.5 μ second. After passing through a 0.25 inch diameter collimator, the electrons from the LINAC were analyzed in energy by the "incident beam analyzing magnets" shown in Fig. 1. These comprise an achromatic system⁽⁵⁾ and focus the electron beam on a target at the center of the 24-inch diameter scattering chamber with less than 10 per cent distortion in the beam spot size and a divergence of less than 10^{-3} radians. The energy resolution of the magnet system was less than 2 per cent (full width at half maximum). A number of exit ports in the scattering chamber allowed various observations to be made. These ports included a beam monitor port at -40° which allowed a measurement of the intensity of electrons scattered into a fixed solid angle and was used to normalize other measurements to the electron

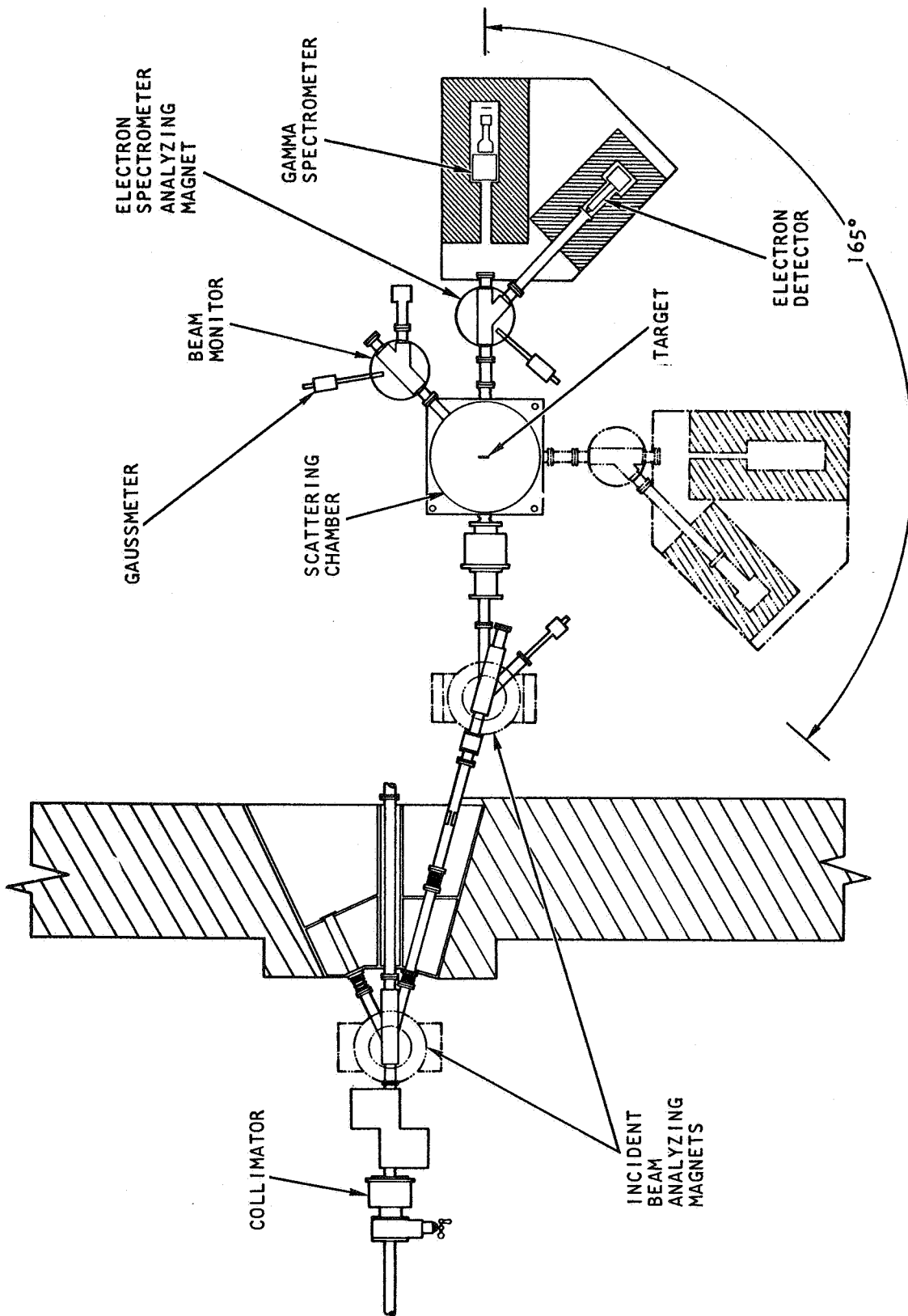


Fig. 1 -- Experimental apparatus for electron transport studies

beam current incident on the target. Magnetic analysis was employed to reduce the gamma background and alleviate uncertainties in the low energy electron counts due to small fluctuations in the gain of the detection system electronics. After magnetic analysis, the electrons were detected by a thin anthracene crystal.

Both the electron and gamma spectrometers were mounted on a rotatable platform which moved in a circular arc between 0° and 120° with the target position at the center of the arc. The movable exit port on the scattering chamber which connected the vacuum system of the chamber to that of the detector system was built into a 0.012 inch thick stainless steel sliding vacuum seal which covered an arc-shaped slot in the side of the scattering chamber. Some of the details of the chamber construction may be observed in the photograph of Fig. 2. Bremsstrahlung spectra were measured using a 5-inch diameter, 6-inch long NaI (Tl) crystal spectrometer which was housed in lead shielding. The electrons emitted from the target were swept aside by the spectrometer magnet and analyzed in energy before being counted by the electron detector which consisted of a thin anthracene crystal observed by a photomultiplier. The energy resolution of the magnetic spectrometer was $\sim 7\%$. The energy of the analyzed electrons for the various magnets was determined by using a rotating coil gaussmeter to monitor the magnetic field between the pole tips. An independent energy calibration of this system was performed by direct comparison of the analyzed electron beam in a second spectrometer calibrated by determining the magnetic field associated with the electron energy at the 15.1 MeV resonance fluorescence gamma-ray line for carbon; this spectrometer employed a nuclear magnetic resonance gaussmeter. The absolute calibration of the electron spectrometer used in these measurements was determined by measuring the fraction of incident electrons emerging from the target in the forward direction. The total number of electrons, integrated over all forward angles, as measured

with the spectrometer was set equal to this fraction; thus, the flux of electrons emitted from the target was normalized to the incident electron current.

The relative number of incident electrons emitted in the forward direction was determined from a measurement of the ratio of charge deposited in the target to the charge leaving the target. To make this measurement an aluminum chamber having 0.5-inch thick walls (thicker than the range of the transmitted electrons) was placed inside and insulated from the scattering chamber. This inner chamber was 20 inches in diameter and completely surrounded the target except for several holes which were small enough that the chamber could be considered a 4π -collector with only a negligible error. One of the holes served as the incident electron beam entrance port; others served as exit ports for the electron spectrometer and for a monitor which observed scattered electrons through a small cone at -40° . The charge deposited on the 4π -collector and the charge remaining in the target (which was electrically isolated) were measured in a series of experimental runs in which the total counts of the monitor were related to the measured charge.

The collected charge was integrated by a circuit shown schematically in Fig. 3. The current was passed through a picoammeter that operated as a preamplifier; its 0 to 3 volt output was used to drive the signal cable from the experimental area to the data room. The current was then integrated by a current integrator; the charge Q collected was determined by the expression:

$$Q = (R \times I_{fs} / 3) VC \quad (1)$$

Here R is the value of the precision resistance, I_{fs} is the full-scale reading of the picoammeter on the scale used, V and C are recorded by the current integrator. In this instrument the charge entering it is in essence, collected on a capacitor of capacitance C giving rise to a voltage V , across the capacitor.

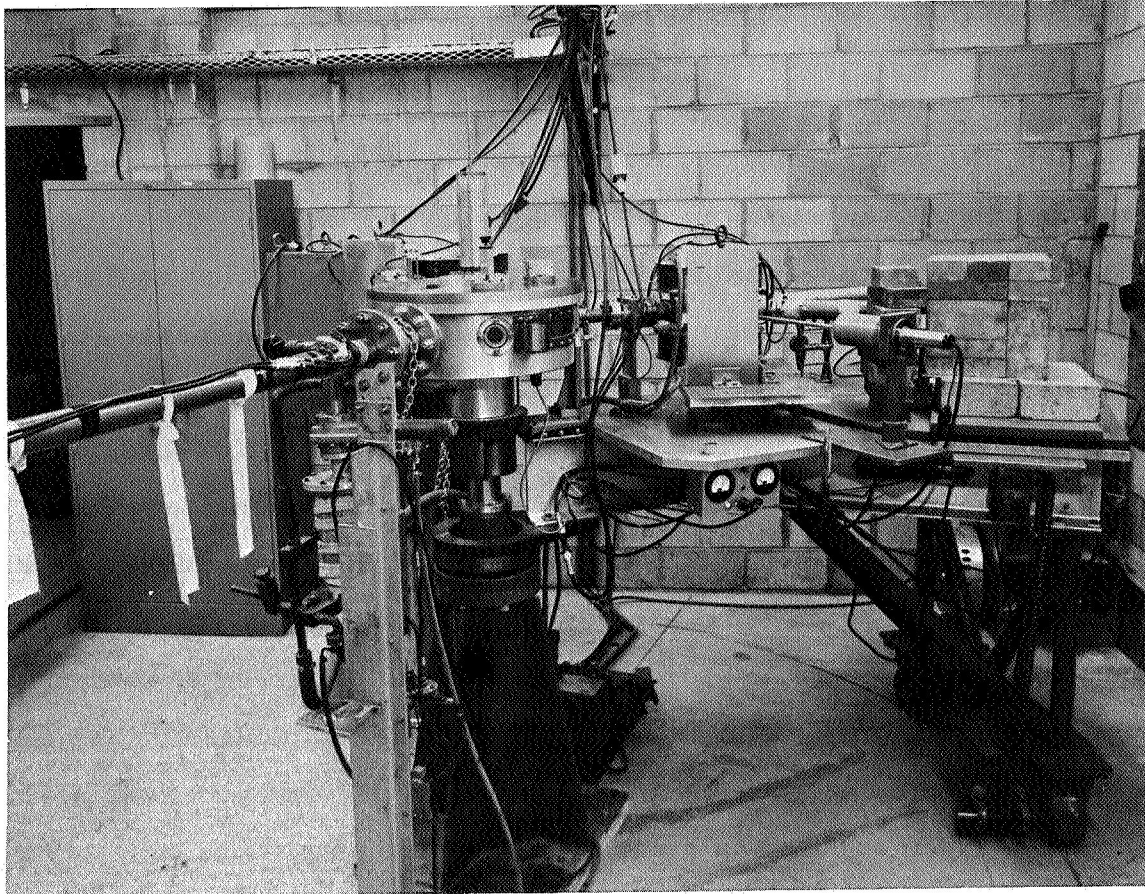


Fig. 2--Electron scattering chamber and associated apparatus

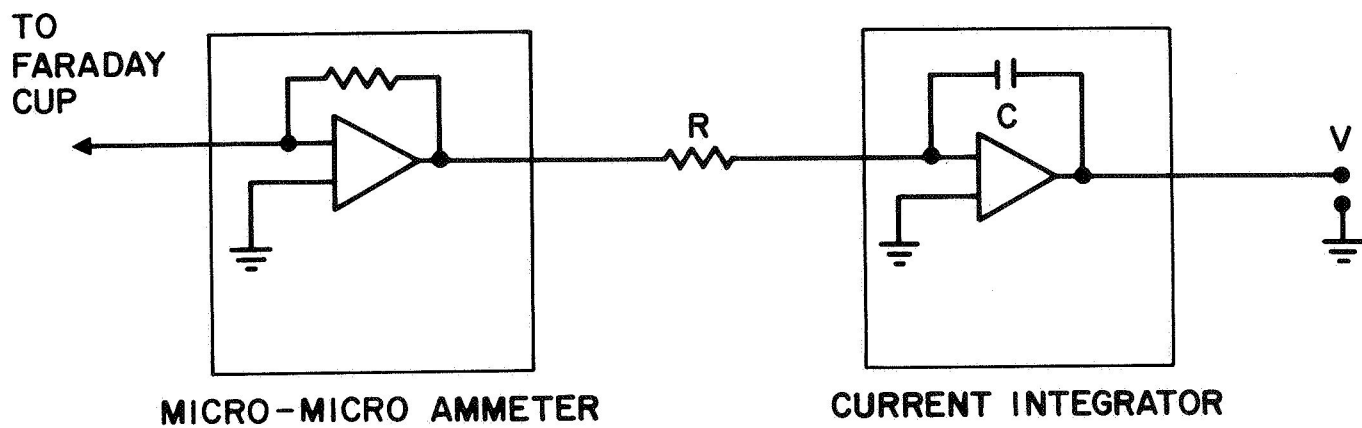


Fig. 3--Current integrating circuit

The fraction of incident electrons leaving the target in the forward hemisphere was determined by subtracting those that were backscattered from the total emitted flux. For the case studied here (i. e., 8.0 MeV electrons incident on a 2.38 g/cm^2 thick slab of aluminum) the back-scattered electron flux was estimated to be 2.7% of the incident electron flux; ⁽⁶⁾ the fraction of electrons leaving the target was measured to be 80% so that 77.3% of the incident electrons emerge in the forward hemisphere. This number was related to the integrated area under the measured angular distribution to yield the proper normalization.

3. METHODS OF DATA ANALYSIS

3.1 ELECTRON SPECTRA

The relationship of the parameters measured in these experiments may be expressed in the following form:

$$C(H, \theta) = KP(E_0, E, \theta)\Delta E(H)\Delta\Omega \quad (2)$$

where $C(H, \theta)$ is the number of electrons observed in the spectrometer per electron observed in the monitor. The spectrometer subtends a solid angle $\Delta\Omega$ at the target and accepts electrons in the energy interval $\Delta E(H)$ about an energy value $E(H)$, where both quantities are dependent on the analyzing field, H . The constant K is determined by calibrating the monitor with respect to the incident beam flux. From knowing K , ΔE and $\Delta\Omega$ and measuring $C(H, \theta)$ we have determined $P(E_0, E, \theta)$ which is the probability that an electron of energy E_0 will be emitted from the target at an angle θ to its incident direction with an energy E (per MeV - steradian). The solid angle interval $\Delta\Omega$ is determined by directly measuring the geometric acceptance of the electron analyzer. The energy bin accepted by the spectrometer ΔE is a function of all physical parameters

of the spectrometer. A calculation following the method of Penner⁽⁷⁾ was made to determine that $\Delta E/E = 0.07$. The value of K was determined from the fraction F of incident electrons that emerge in the forward hemisphere in the manner described above. That procedure can be summarized in the following expression

$$KF = K \int_{\theta'=0}^{\theta'=\pi/2} d\Omega' \int_0^{E'_{\max}} dE' P(\theta', E') = \int_{\theta'=0}^{\theta'=\pi/2} d\Omega' \int_0^{E'_{\max}} dE' \frac{C(\theta', E')}{\Delta\Omega\Delta E} \quad (3)$$

where the parameters associated with the emerging electrons are distinguished with a prime from those associated with the spectrometer.

3.2 BREMSSTRAHLUNG SPECTRA

The pulse height spectra of bremsstrahlung were converted to photon energy spectra using the iterative unfolding procedure of Smith and Scofield.⁽⁹⁾ The response function used to make the unfolding was an extrapolation of the response matrix given by Hubbel.⁽¹⁰⁾ A correction was inserted to account for the greater efficiency of our 5-inch diameter, 6-inch long NaI(Tl) crystal.

The bremsstrahlung photon spectrum N_i was calculated from the spectrometer pulse height spectrum P_j by

$$N_i = \sum_{j=1}^n m_{ij}^{-1} P_j$$

where m_{ij} is the response function matrix for the spectrometer and i and j refer to photon energy bins and voltage pulse height bins, respectively. These bremsstrahlung data were collected at a relatively low

count rate so that pile-up effects would be kept to a few per cent or less. The spectrum of double pulses $P''(\epsilon)$ in the data was analytically estimated using the formulation of Starfelt and Koch⁽¹¹⁾ as shown below:

$$P''(\epsilon) = p \frac{\int_0^{\epsilon} P(\epsilon_i) P(\epsilon - \epsilon_i) d\epsilon_i}{\int_0^{\epsilon_{\max}} P(\epsilon_i) d\epsilon_i} \quad (4)$$

Here, $P(\epsilon_i)$ is the spectrum of single pulses and p is the ratio of the probability of recording two photons in the same LINAC burst to the probability of recording one photon. $P''(\epsilon)$ can be calculated by successive approximations.

3.3 RESULTS AND COMPARISON

3.3.1 Electrons

Electron spectra and angular distributions were measured at several angles and energies and for several targets. These data are summarized in Table 1 and displayed in Figs. 4 through 20. The data taken for a 2.38 g/cm² thick aluminum target and 8.0 MeV incident electrons have been normalized by the procedure described earlier to give the absolute number of emitted electrons per (MeV-steradian-incident electron). It was found that 77.3% of the electrons were transmitted in the forward direction for this case. This number is in good agreement with the 78.9% value measured by Ebert.⁽⁸⁾ These spectra were compared with spectra calculated by Berger and Seltzer.⁽⁴⁾ The areas under these curves were calculated and compared in the angular distribution displayed in Fig. 4. The agreement is generally good between the Monte Carlo angular distribution and the measured data. The

Table 1
SUMMARY OF RESULTS

| E_o | Target | | Angles | Figure No. |
|-------|----------|-----------------------------------|------------------------|------------|
| | Material | Thickness (g/cm ²) | | |
| 8.0 | Al | 2.38 | Angular distribution | 4 |
| 8.0 | Al | 2.38 | 0° | 5 |
| 8.0 | Al | 2.38 | 10° | 6 |
| 8.0 | Al | 2.38 | 20° | 7 |
| 8.0 | Al | 2.38 | 30° | 8 |
| 8.0 | Al | 2.38 | 40° | 9 |
| 8.0 | Al | 2.38 | 50° | 10 |
| 8.0 | Al | 2.38 | 60° | 11 |
| 8.0 | Al | 2.38 | 70° | 12 |
| 8.0 | Al | 2.38 | 80° | 13 |
| 8.0 | Al | 2.38 | 0°, 20°, 40°, 60°, 80° | 14 |
| 8.0 | Al | 0.952 | Angular distribution | 15 |
| 8.0 | Al | 0.952 | 10°, 20°, 40°, 60° | 16 |
| 8.0 | Be | 2.52 | Angular distribution | 17 |
| 8.0 | Be | 2.52 | 0°, 20°, 40° | 18 |
| 4.0 | Al | 1.238 | Angular distribution | 19 |
| 4.0 | Al | 1.238 | 0°, 10°, 30°, 50°, 70° | 20 |

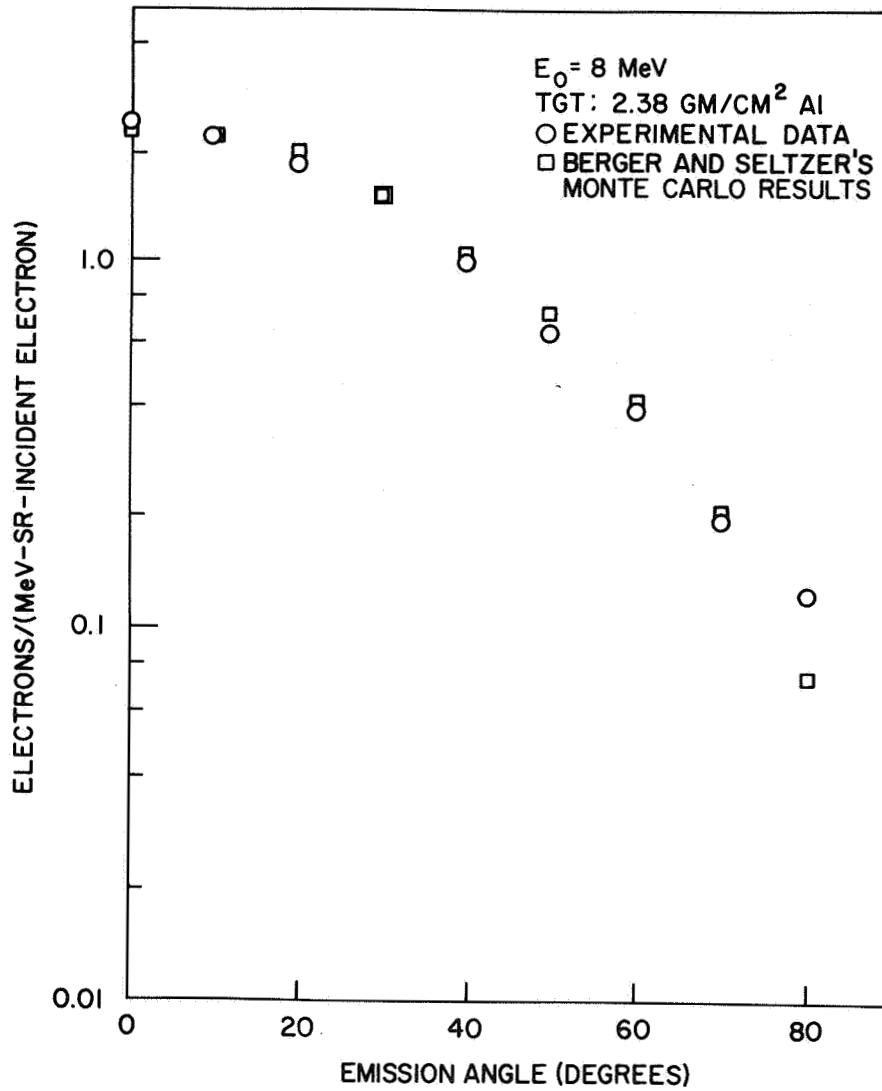


Fig. 4--Angular distribution of electrons emitted from a 2.38 g/cm^2 aluminum target bombarded by 8 MeV electrons. The open circles represent experimental data; crosses represent the Monte Carlo results of Berger and Seltzer.

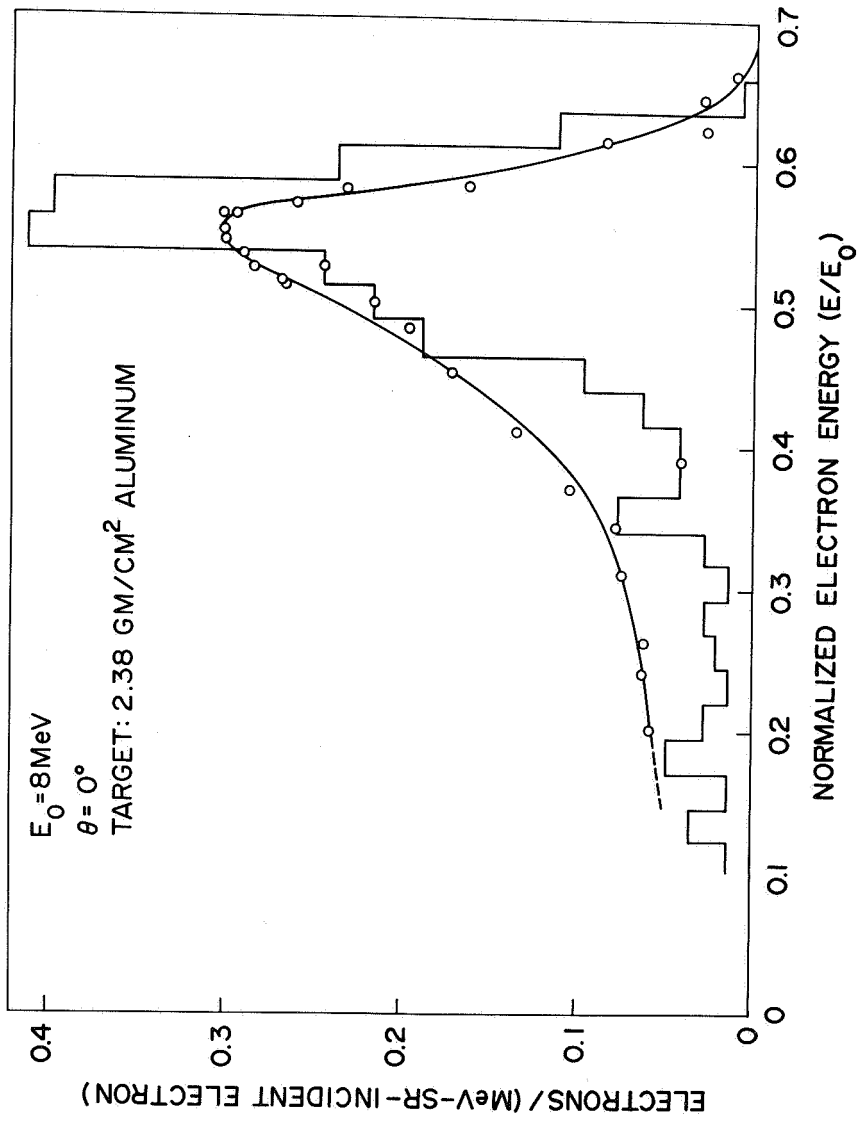


Fig. 5--Spectrum of straggled electrons emitted at 0° from a 2.38 g/cm² aluminum target bombarded by 8 MeV electrons. The open circles represent experimental data, while the histogram represents the Monte Carlo results of Berger and Seltzer.

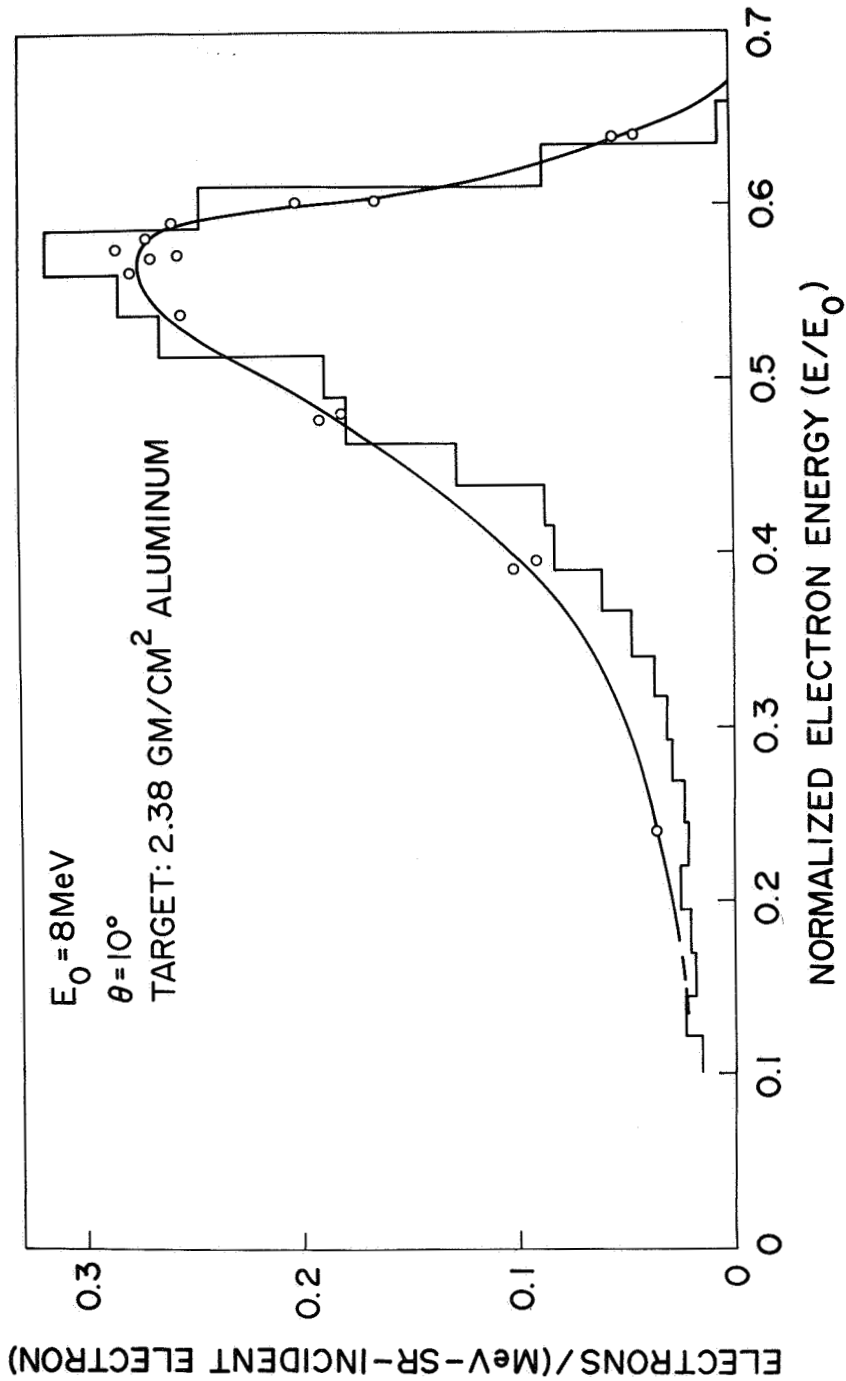


Fig. 6--Spectrum of straggled electrons emitted at 10° from a 2.38 g/cm^2 aluminum target bombarded by 8 MeV electrons. The open circles represent experimental data, while the histogram represents the Monte Carlo results of Berger and Seltzer.

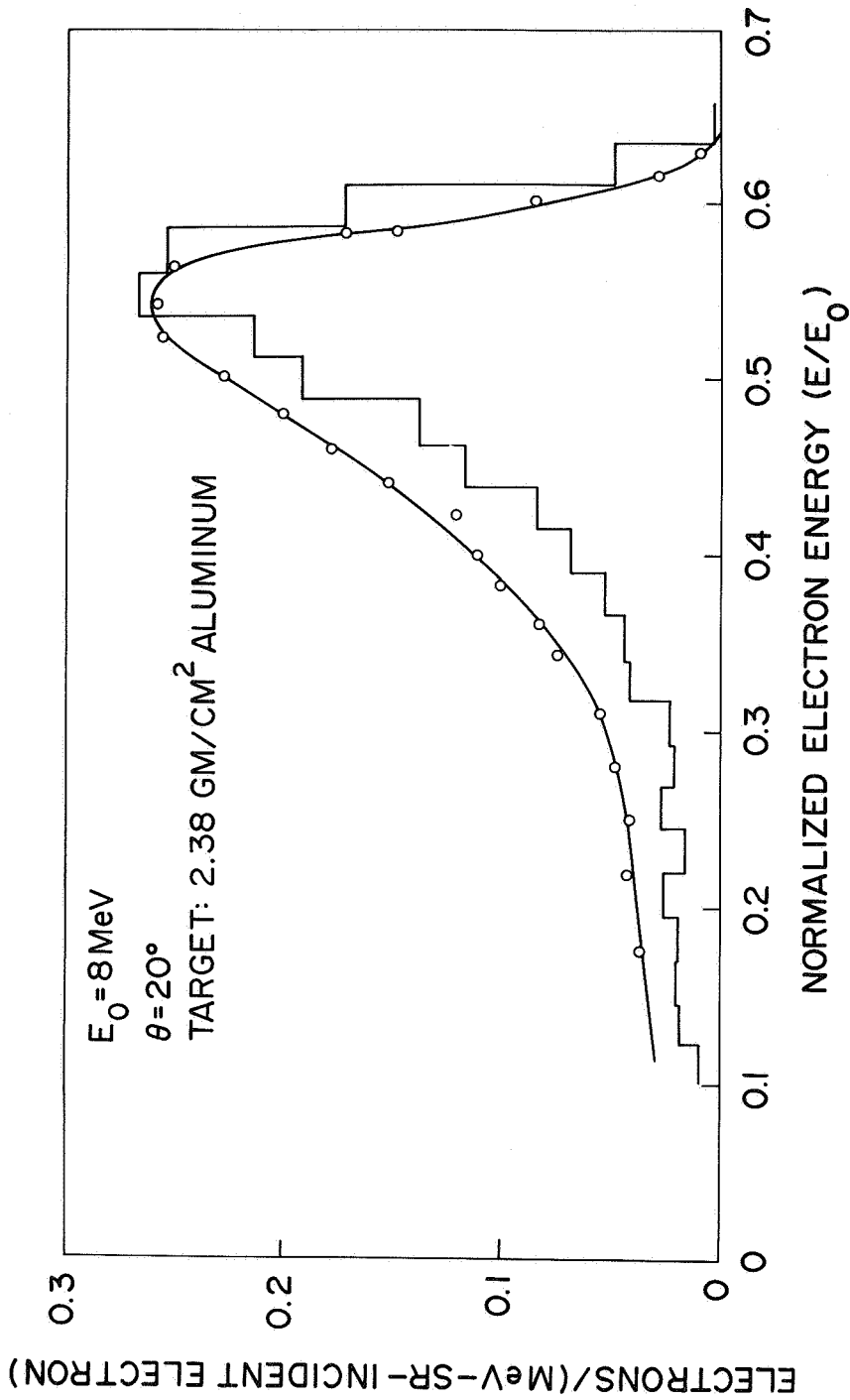


Fig. 7--Spectrum of straggled electrons emitted at 20° from a 2.38 g/cm² aluminum target bombarded by 8 MeV electrons. The open circles represent experimental data, while the histogram represents the Monte Carlo results of Berger and Seltzer.

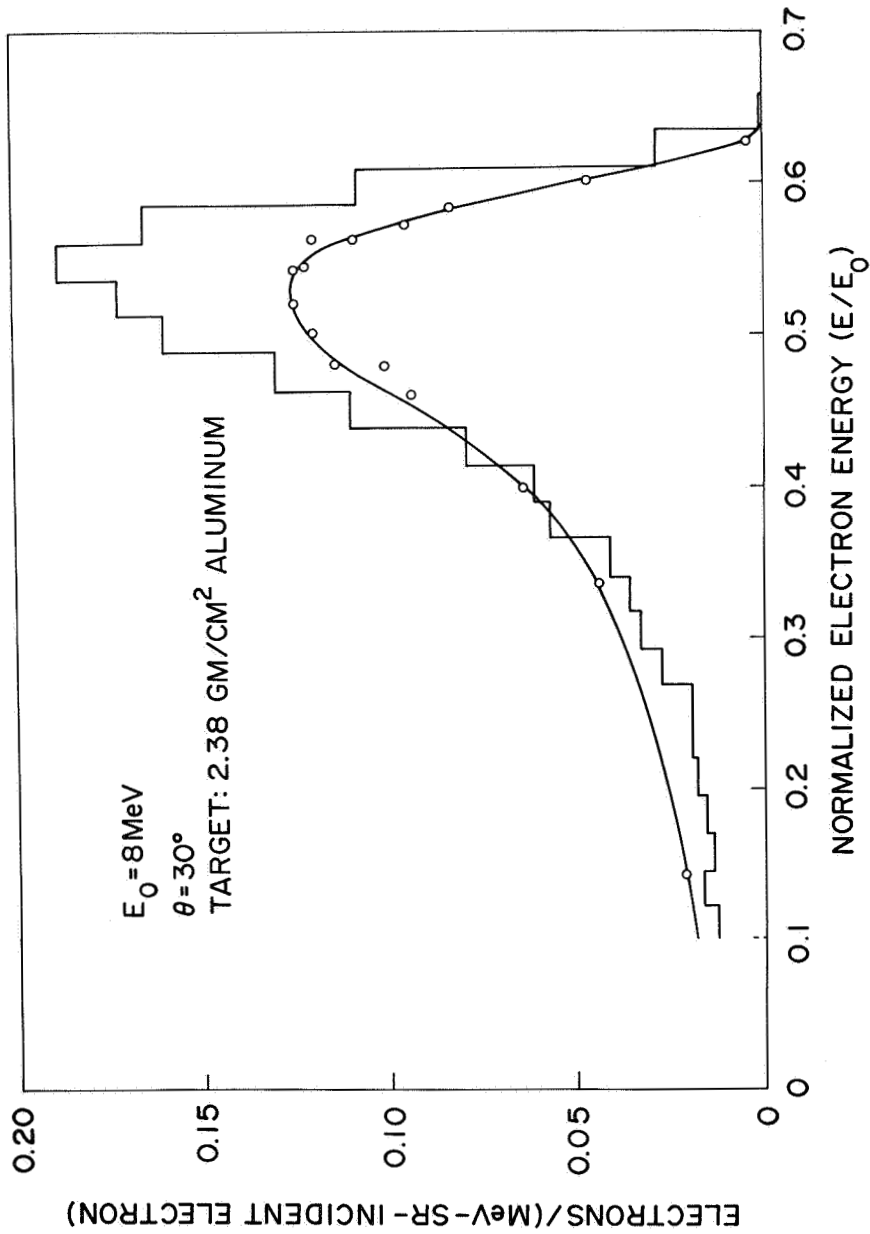


Fig. 8--Spectrum of straggled electrons emitted at 30° from a 2.38 g/cm² aluminum target bombarded by 8 MeV electrons. The open circles represent experimental data, while the histogram represents the Monte Carlo results of Berger and Seltzer.

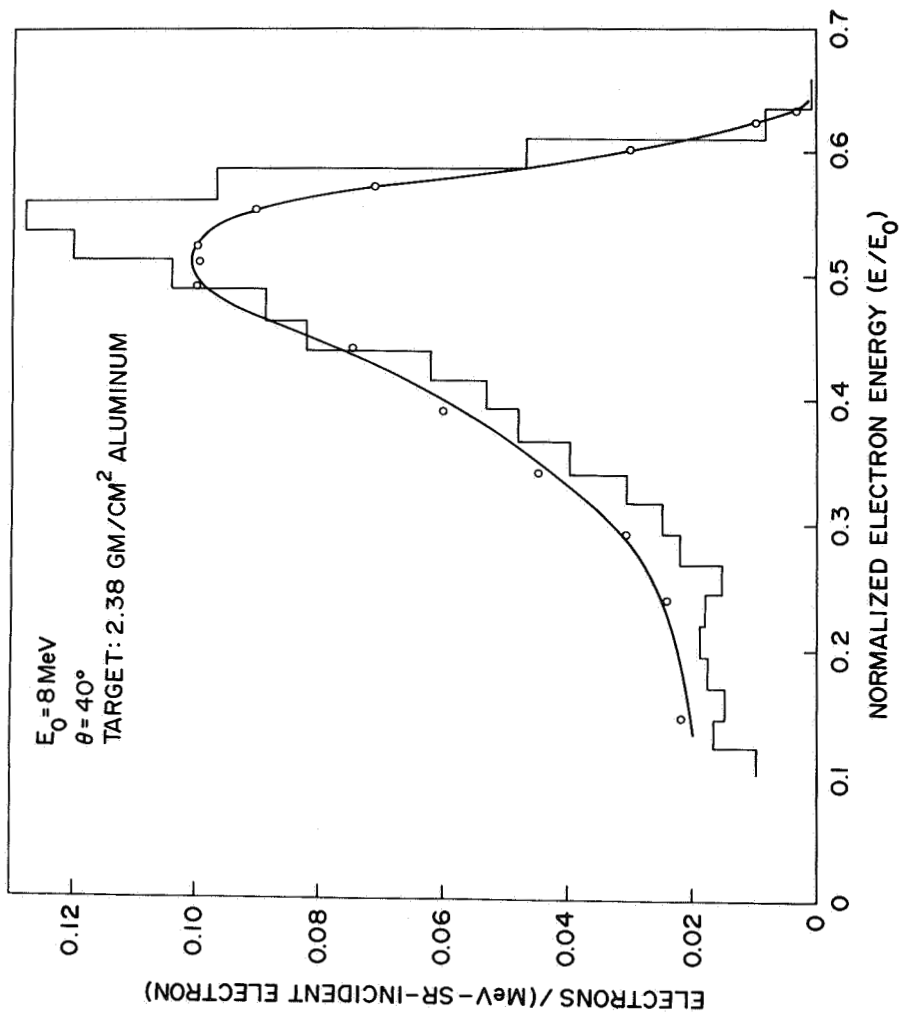


Fig. 9--Spectrum of straggled electrons emitted at 40° from a 2.38 g/cm² aluminum target bombarded by 8 MeV electrons. The open circles represent experimental data, while the histogram represents the Monte Carlo results of Berger and Seltzer.

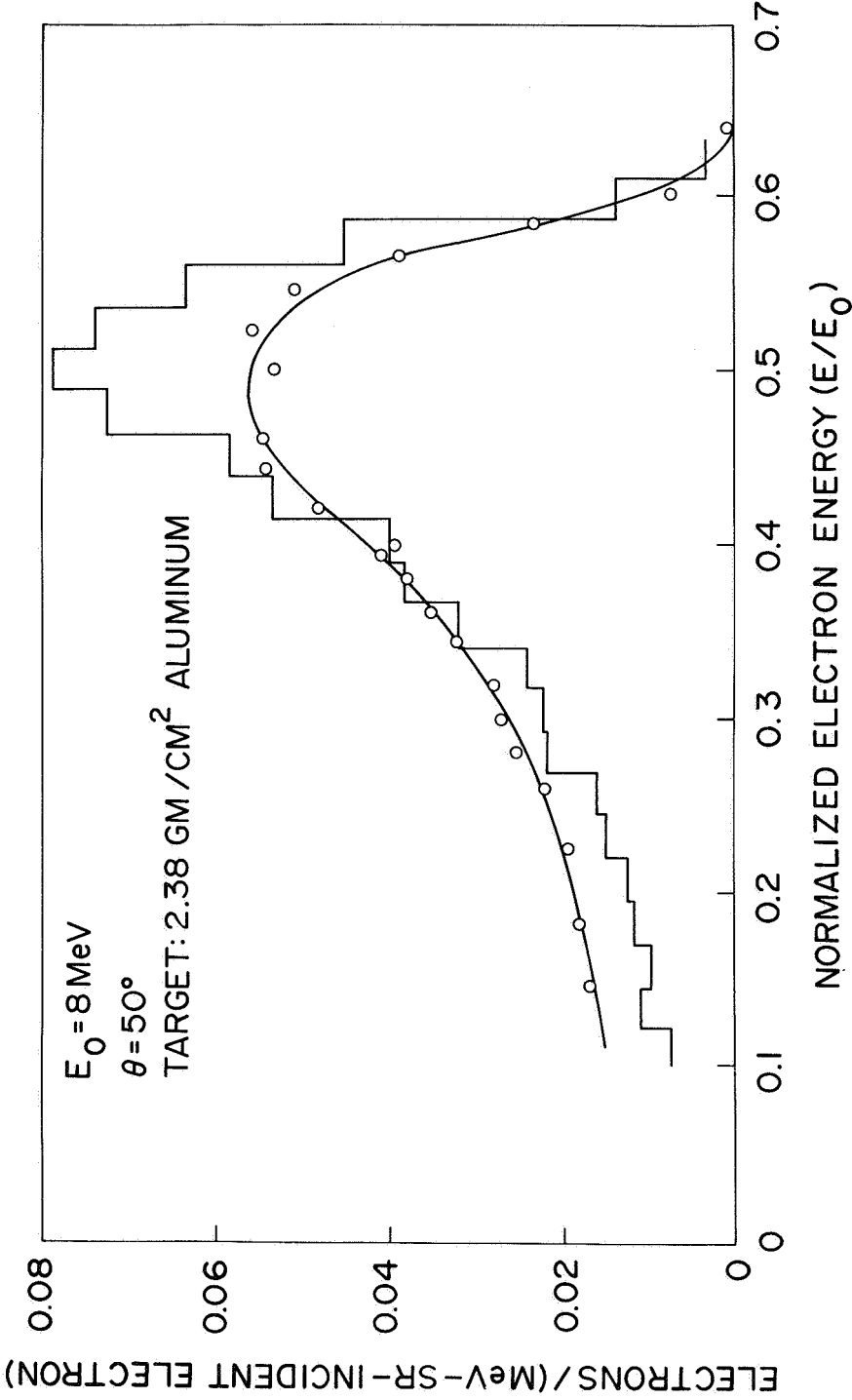


Fig. 10--Spectrum of straggled electrons emitted at 50° from a 2.38 g/cm² aluminum target bombarded by 8 MeV electrons. The open circles represent experimental data, while the histogram represents the Monte Carlo results of Berger and Seltzer.

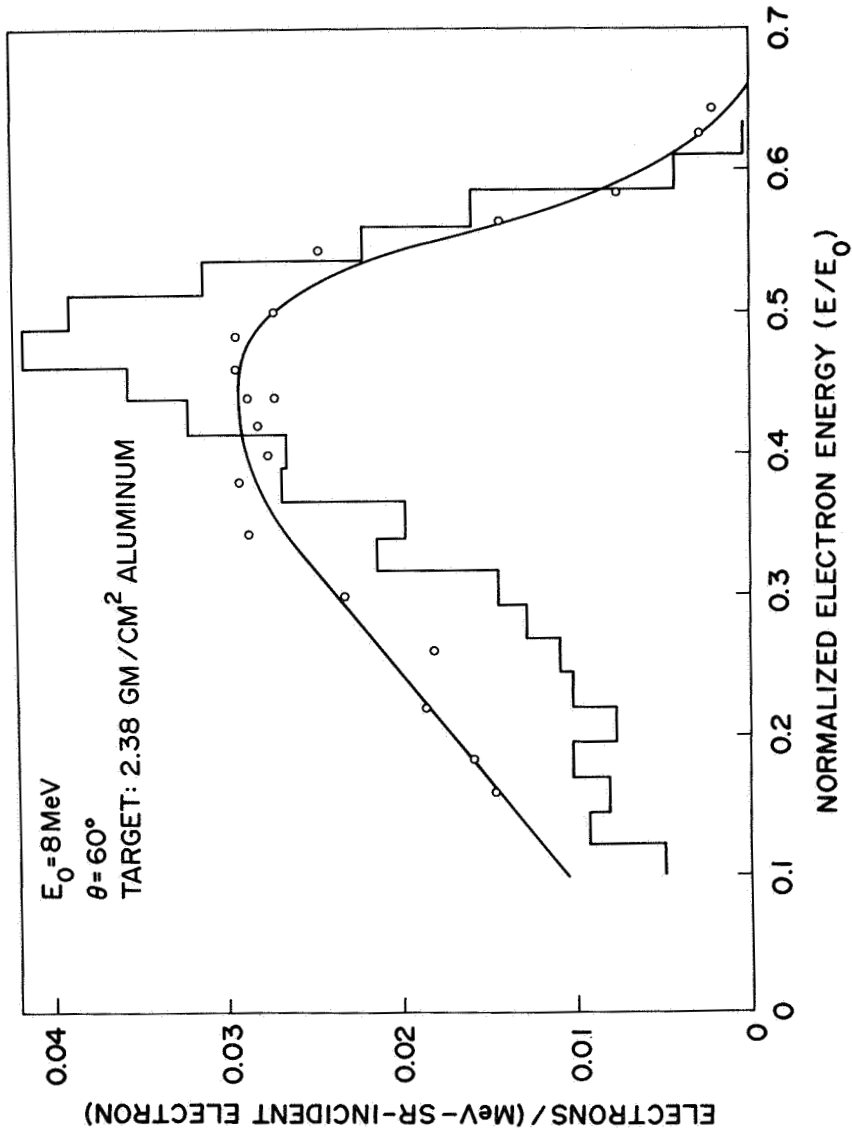


Fig. 11--Spectrum of straggled electrons emitted at 60° from a 2.38 g/cm² aluminum target bombarded by 8 MeV electrons. The open circles represent experimental data, while the histogram represents the Monte Carlo results of Berger and Seltzer.

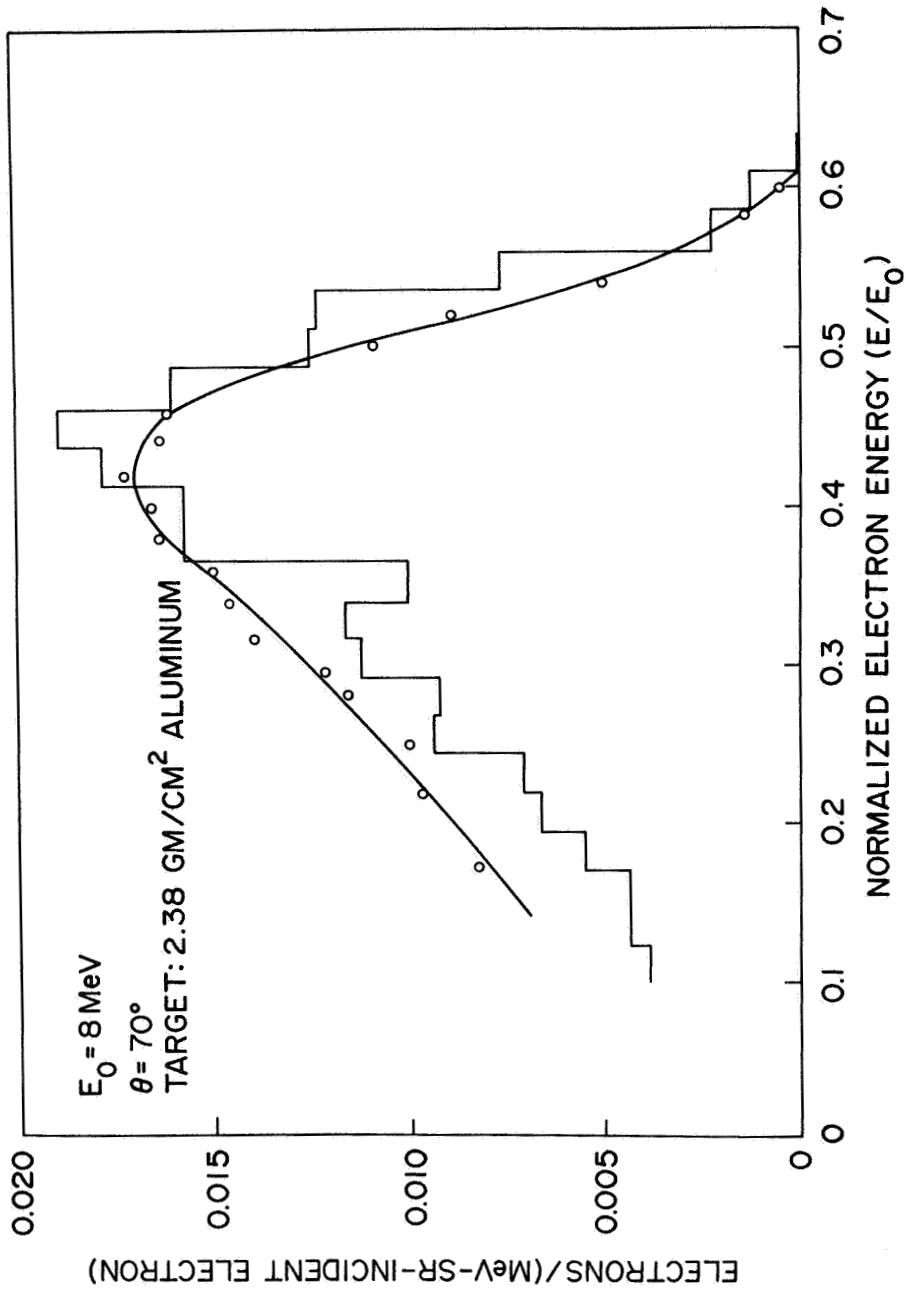


Fig. 12--Spectrum of straggled electrons emitted at 70° from a 2.38 g/cm^2 aluminum target bombarded by 8 MeV electrons. The open circles represent experimental data, while the histogram represents the Monte Carlo results of Berger and Seltzer.

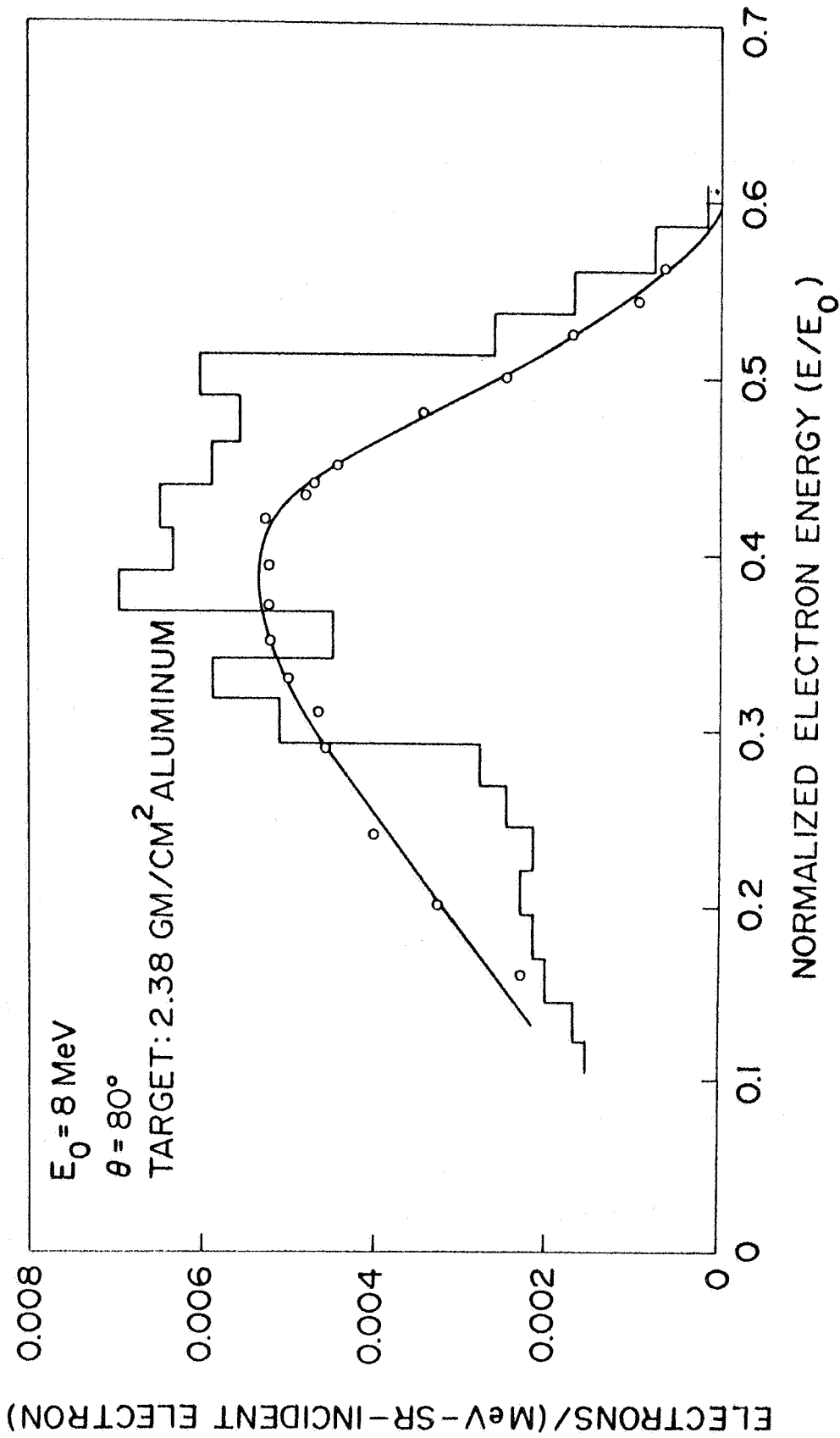


Fig. 13--Spectrum of straggled electrons emitted at 80° from a 2.38 g/cm² aluminum target bombarded by 8 MeV electrons. The open circles represent experimental data, while the histogram represents the Monte Carlo results of Berger and Seltzer.

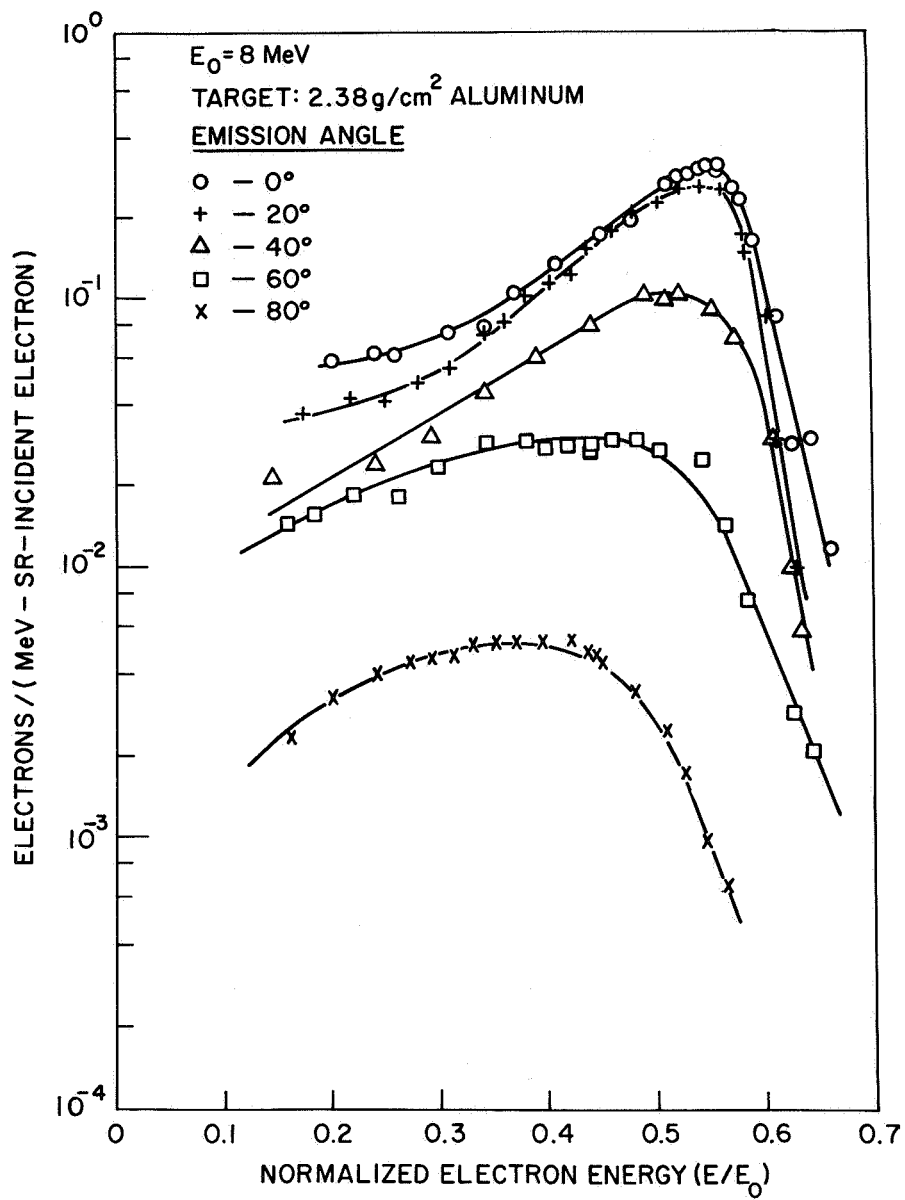


Fig. 14--Spectra of straggled electrons emitted from a 2.38 g/cm^2 thick aluminum target bombarded by 8 MeV electrons

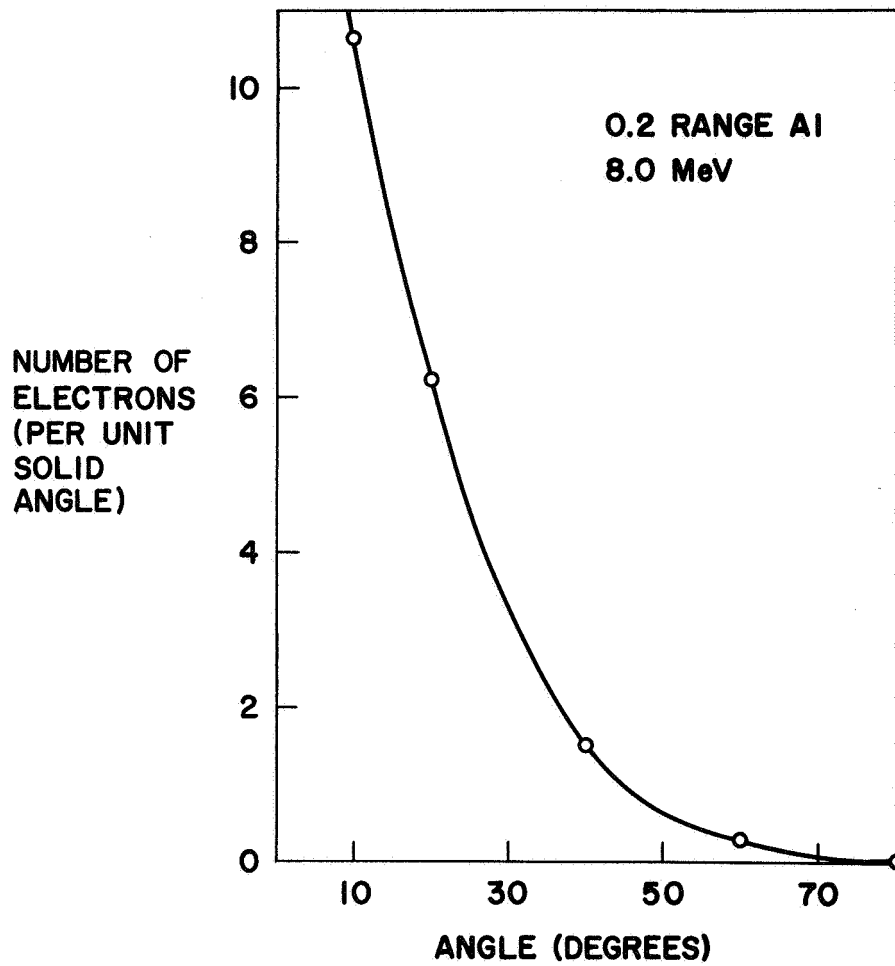


Fig. 15--Spectra of straggled electrons emitted from a 0.952 g/cm^2 thick aluminum target bombarded by 8 MeV electrons

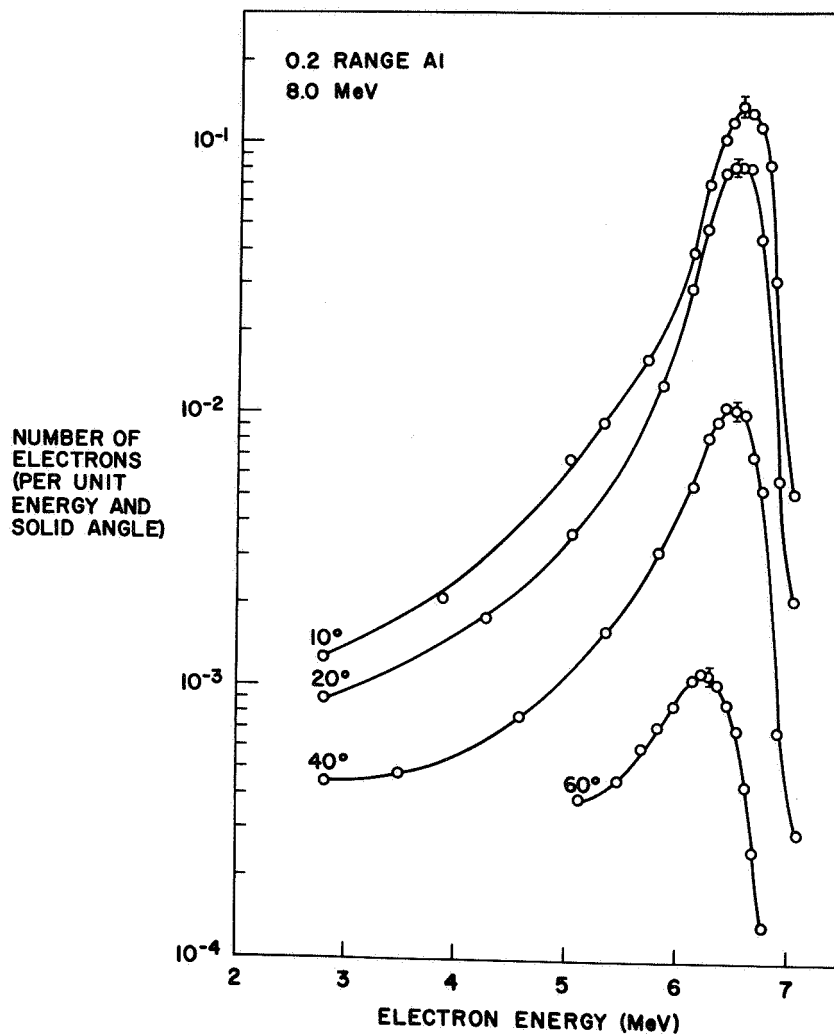


Fig. 16--Spectra of straggled electrons emitted from a 0.952 g/cm^2 thick aluminum target bombarded by 8 MeV electrons

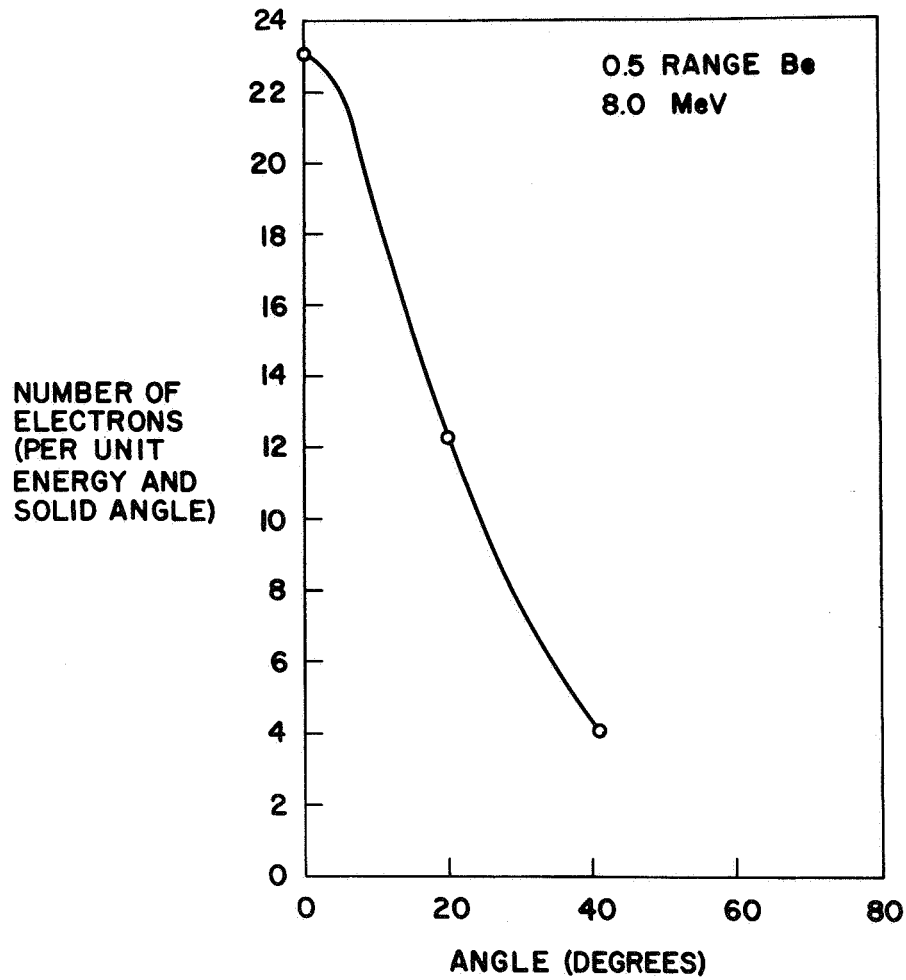


Fig. 17--Angular distribution of electrons emitted from a 2.52 g/cm^2 beryllium target bombarded by 8 MeV electrons

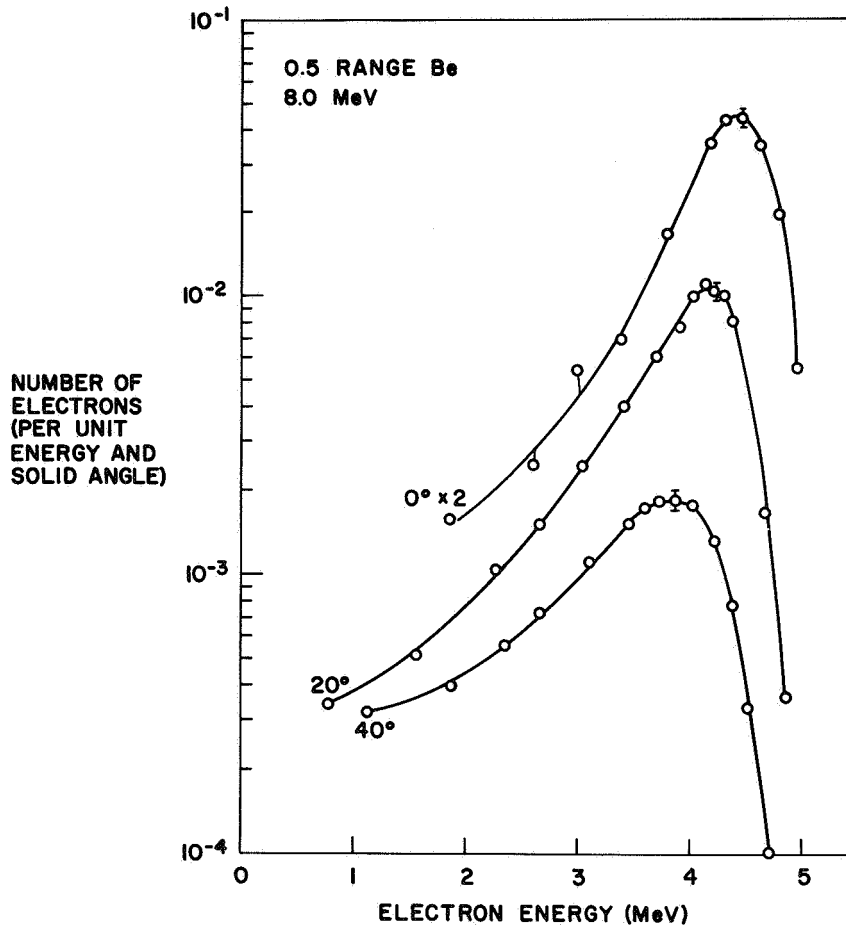


Fig. 18--Spectra of straggled electrons emitted from a 25.2 g/cm^2 beryllium target bombarded by 8 MeV electrons

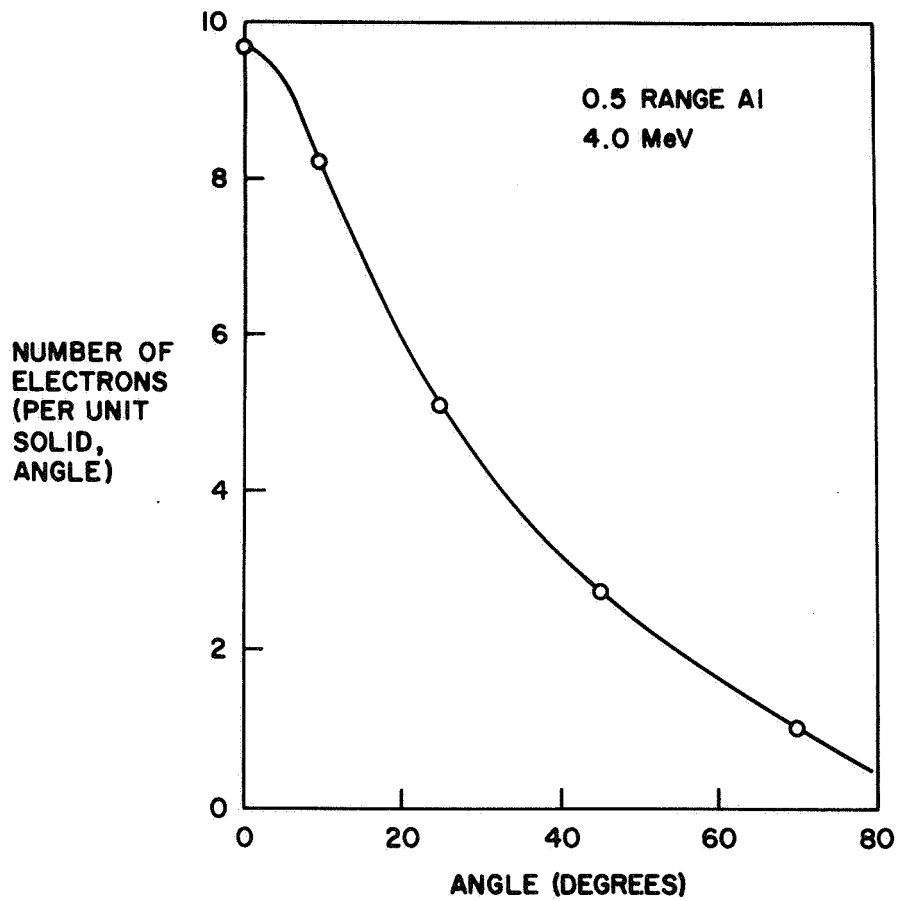


Fig. 19--Angular distribution of electrons emitted from a 1.238 g/cm^2 aluminum target bombarded by 4 MeV electrons

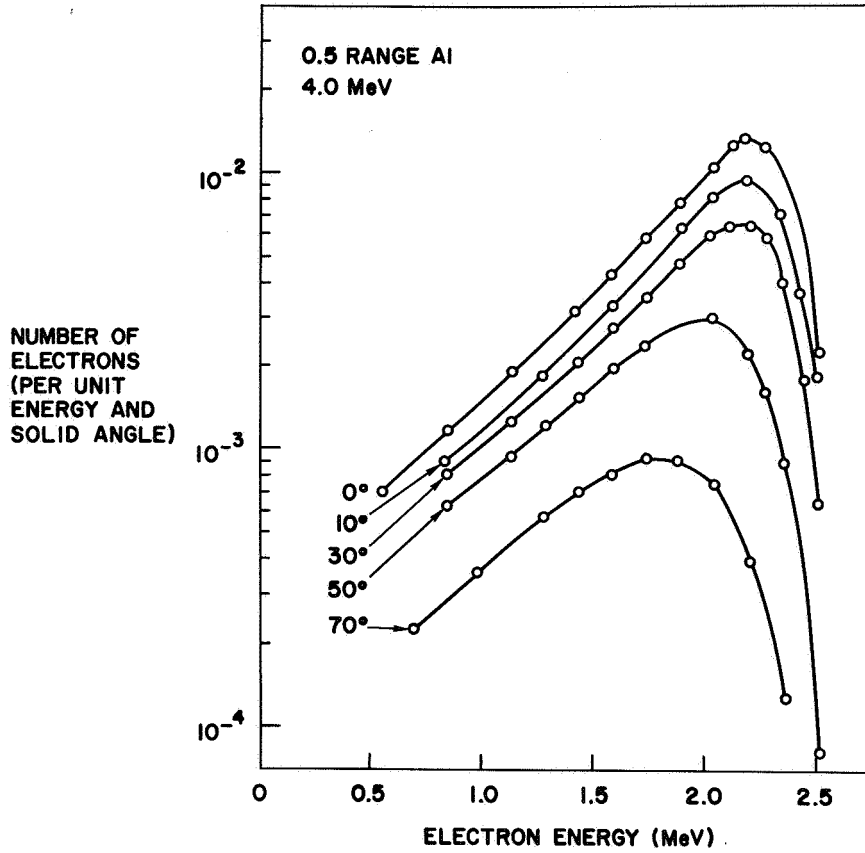


Fig. 20--Spectra of straggled electrons emitted from a 1.238 g/cm² aluminum target bombarded by 4 MeV electrons

analytically derived spectra have been compared individually with the experimental spectra. The experiments and calculations agree as to the most probable energy of emerging electrons but the experimental peaks seem to be slightly broader than the calculated peaks. The experimental resolution of the spectrometer was not unfolded from the data; it was about $\sim 7\%$ which is comparable with the $\sim 5\%$ resolution of the histogram corresponding to the Monte Carlo calculations. Since this resolution could only account for a few percent of the peak width, it does not account for the discrepancies in the widths.

Monte Carlo data for the other targets and energies were not available so experimental data were plotted in condensed form; the electron intensity is shown in arbitrary units. Note that the data corresponding to 8.0 MeV electron incident on a 2.38 g/cm^2 aluminum target is plotted on a linear scale, while the others are plotted on semi-log paper. From these data it is seen that the most probable energy decreases with angle as one would expect because of the longer average path, although the maximum energy is independent of angle, since the minimum path length through the target is the same for all angles. Also as expected the straggled electron spectra broadens with increasing angle. In drawing the smooth curves through the plotted angular distributions we made use of the fact that the slope must be zero at 0° . These angular distributions are in agreement with what one would generally expect.

3.3.2 Bremsstrahlung

Bremsstrahlung spectra were measured for 10 MeV electrons incident on a 4.67 gm/cm^2 thick aluminum target, corresponding to 0.7 times the range of the incident electrons. Data was taken for emission angles of 0° , 10° , 20° , 30° and 40° . The pulse height spectra from the NaI (Tl) crystal spectrometer were unfolded to produce the

photon spectra shown by the dashed line in Figs. 21 through 25. Corrections for the spectrum of double pulses were made using the formulation of Starfelt and Koch as mentioned earlier. The presence of some photon counts (appreciably less than 10^{-3} of the total) above the high energy tip at 10 MeV is due to inaccuracies in estimating the spectrum of double pulses probably because of a modulation of the electron beam from the LINAC. The shape of the experimental results were compared to the Monte Carlo data of Berger and Seltzer (the solid line) by adjusting the amplitude by a constant factor for a best fit along the entire range of energy. Agreement is fair, having an average deviation of less than 20% over most of the data. However, it is recognized that a better comparison using more accurate data is desirable to validate analytical methods. This experimental work is being repeated; the accumulation of data will be carried out separately for the high energy and the low energy portions of the spectrum (using a low Z filter to suppress high counting rates in the low energy portion when collecting high energy pulse height spectra) so that the statistical accuracy will be more uniform over the energy range studied.

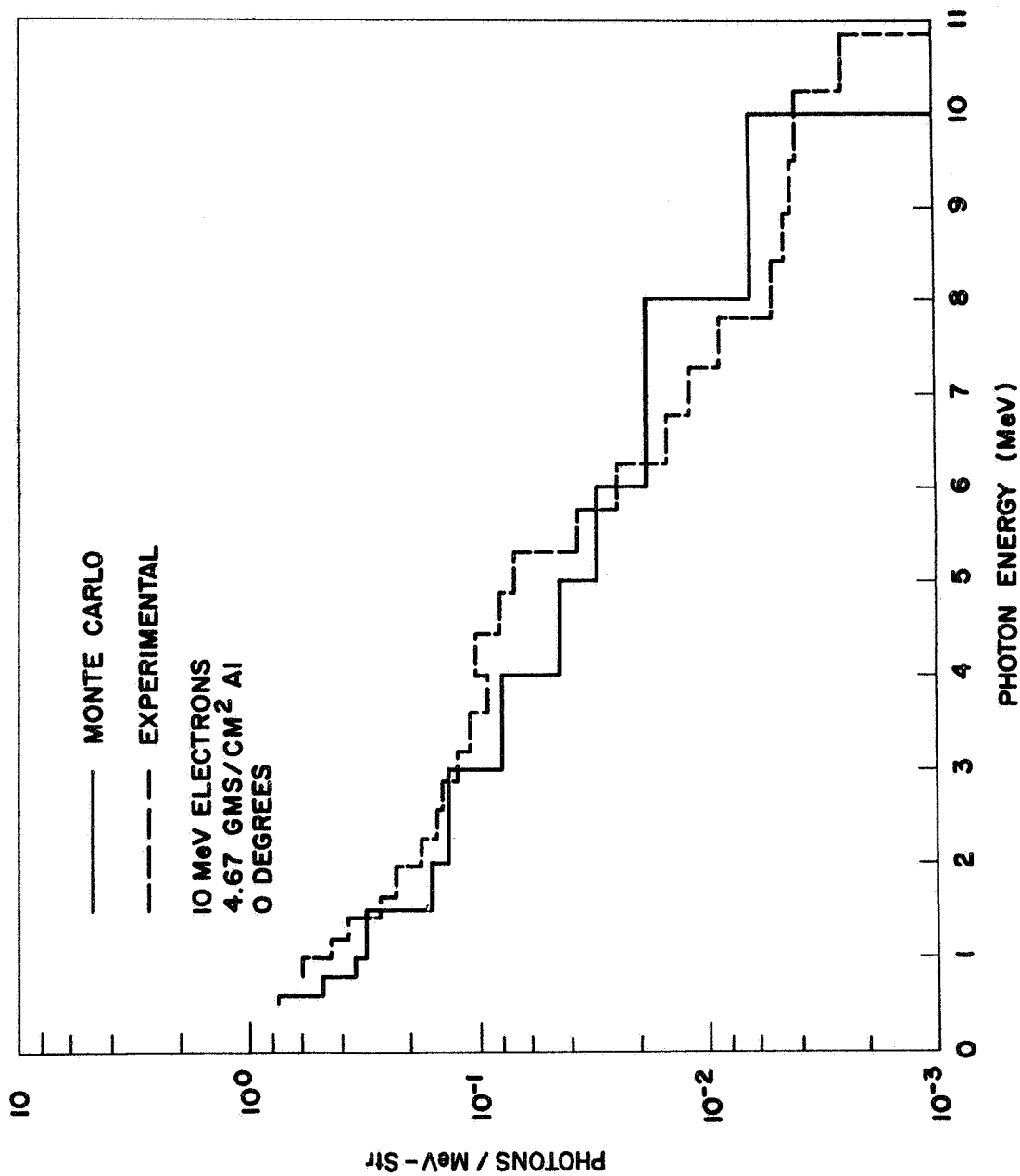


Fig. 21--Experimental and theoretical bremsstrahlung photon spectra
 for 8.2 MeV electrons incident on a 4.67 g/cm aluminum target.
 Emission angle = 0°

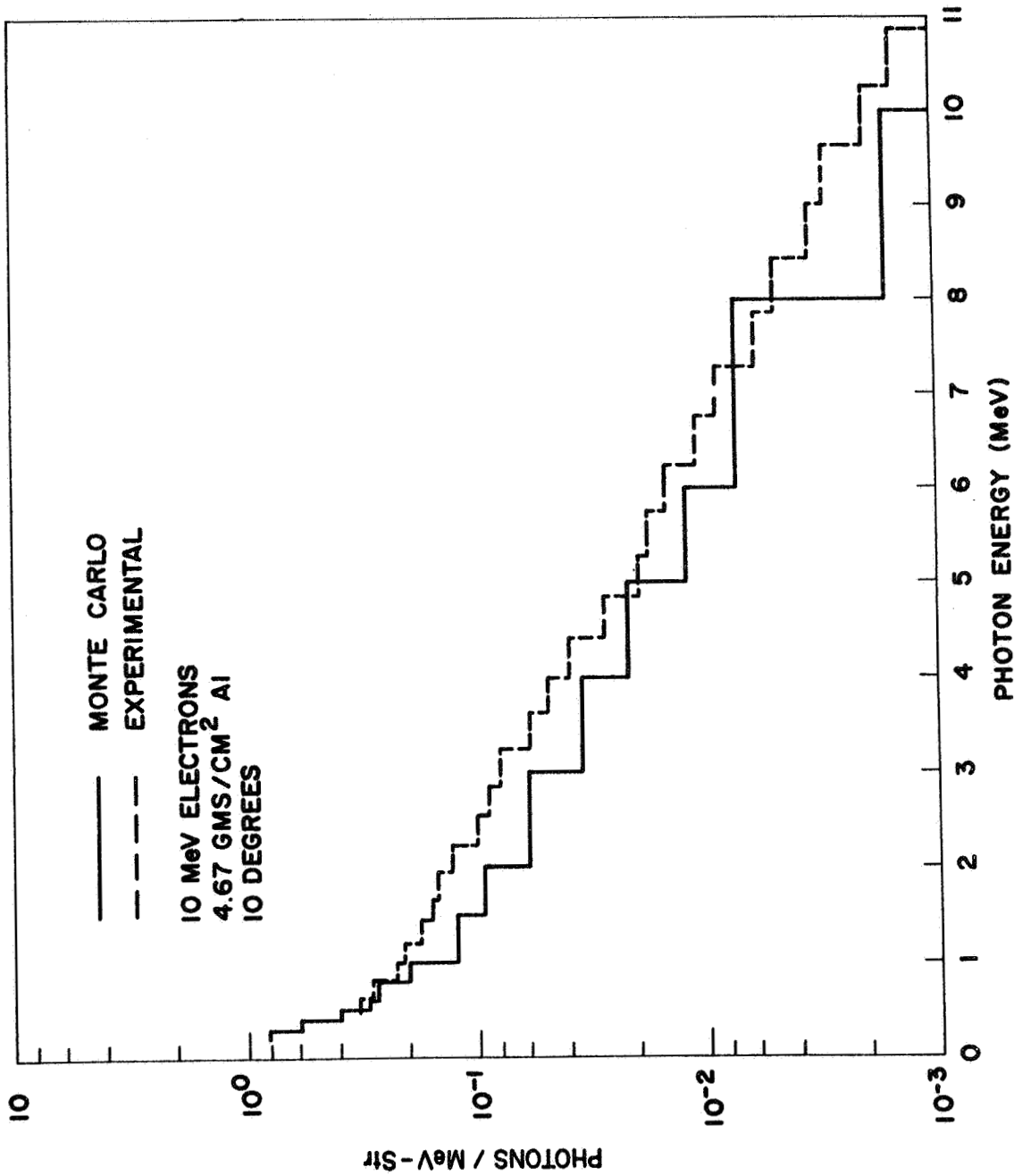


Fig. 22--Experimental and theoretical bremsstrahlung photon spectra
 for 8.2 MeV electrons incident on a 4.67 g/cm aluminum target.
 Emission angle = 10°

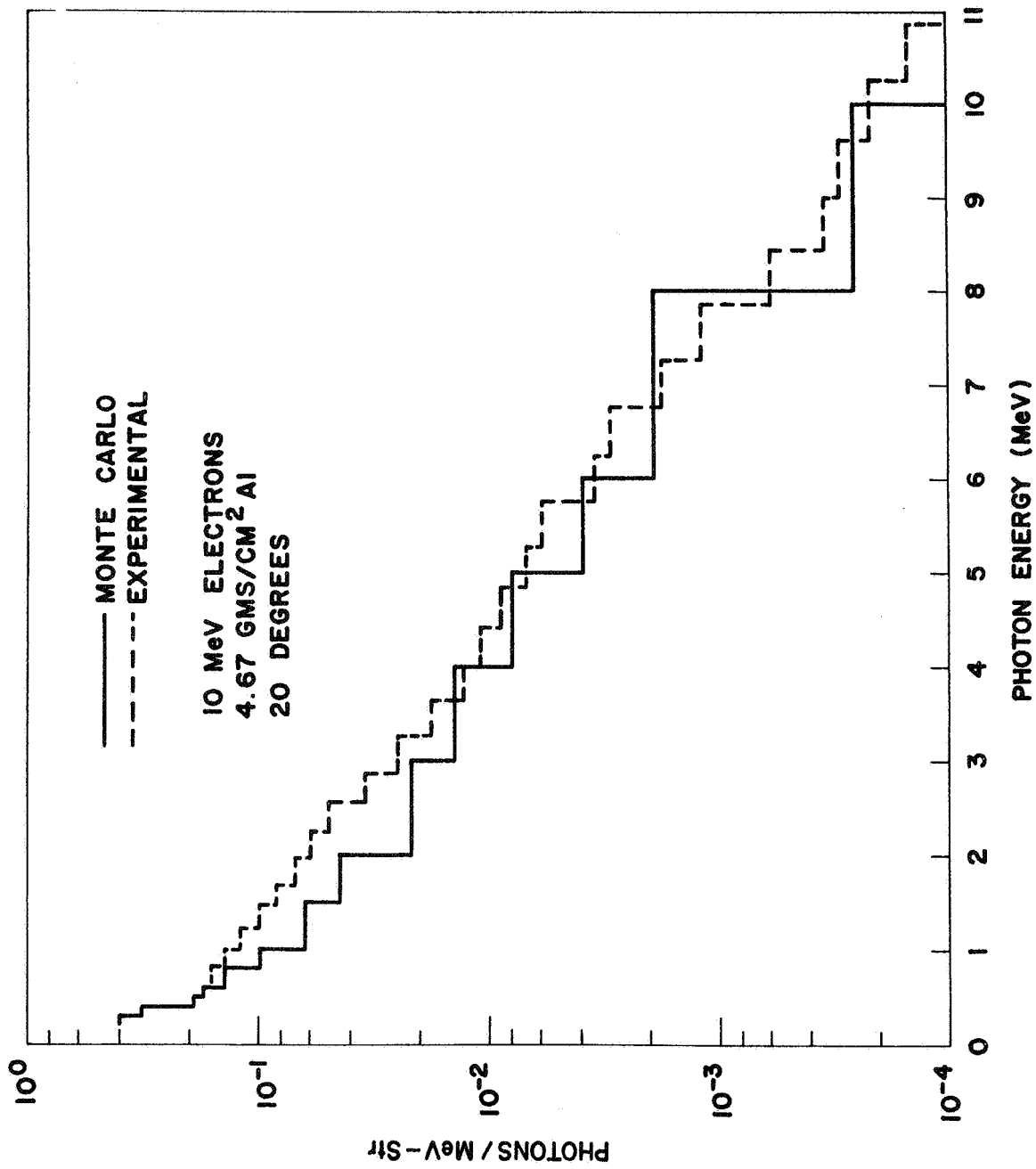


Fig. 23--Experimental and theoretical bremsstrahlung photon spectra for 8.2 MeV electrons incident on a 4.67 g/cm aluminum target. Emission angle = 20°

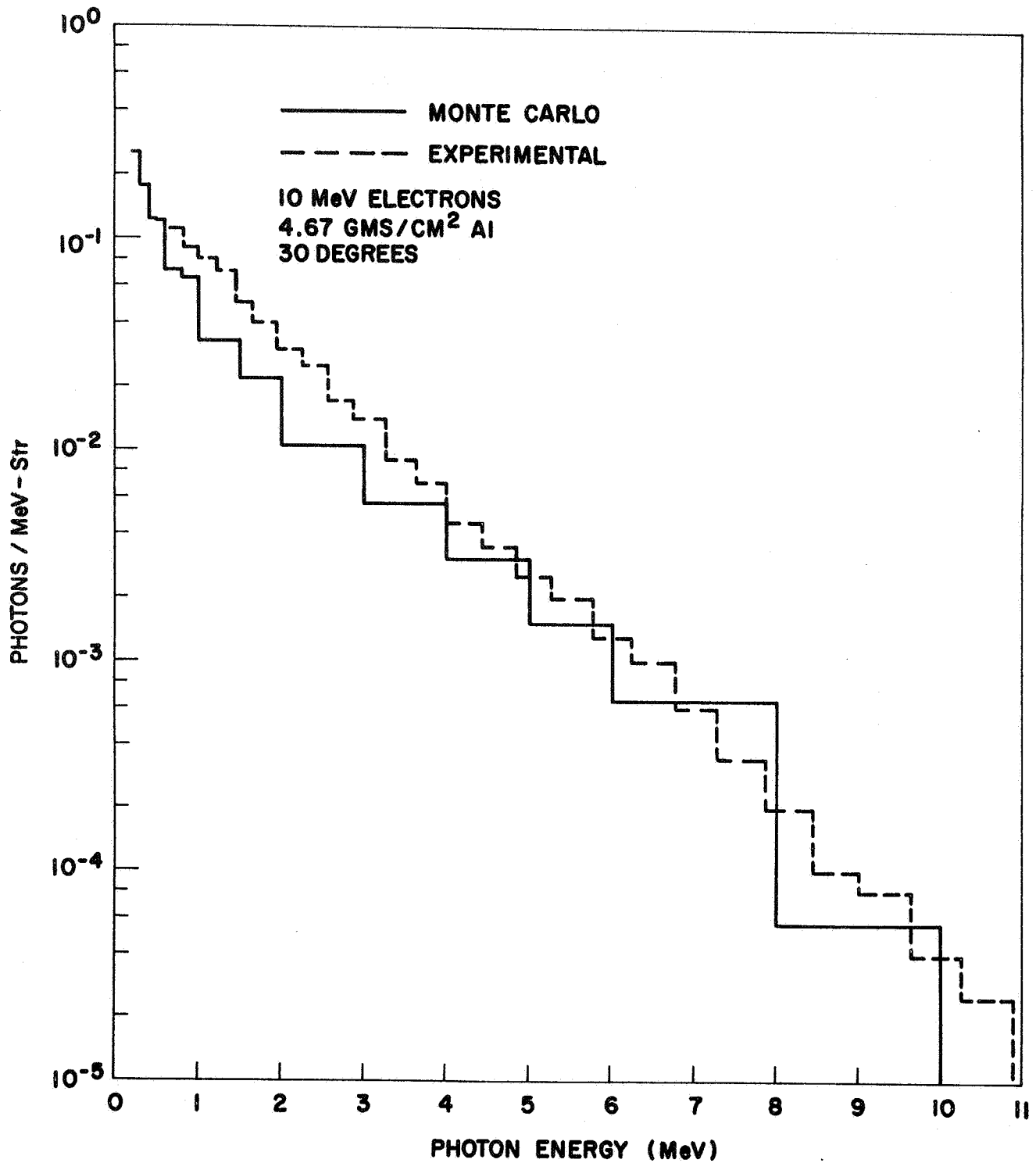


Fig. 24--Experimental and theoretical bremsstrahlung photon spectra
 for 8.2 MeV electrons incident on a 4.67 g/cm aluminum target.
 Emission angle = 30°

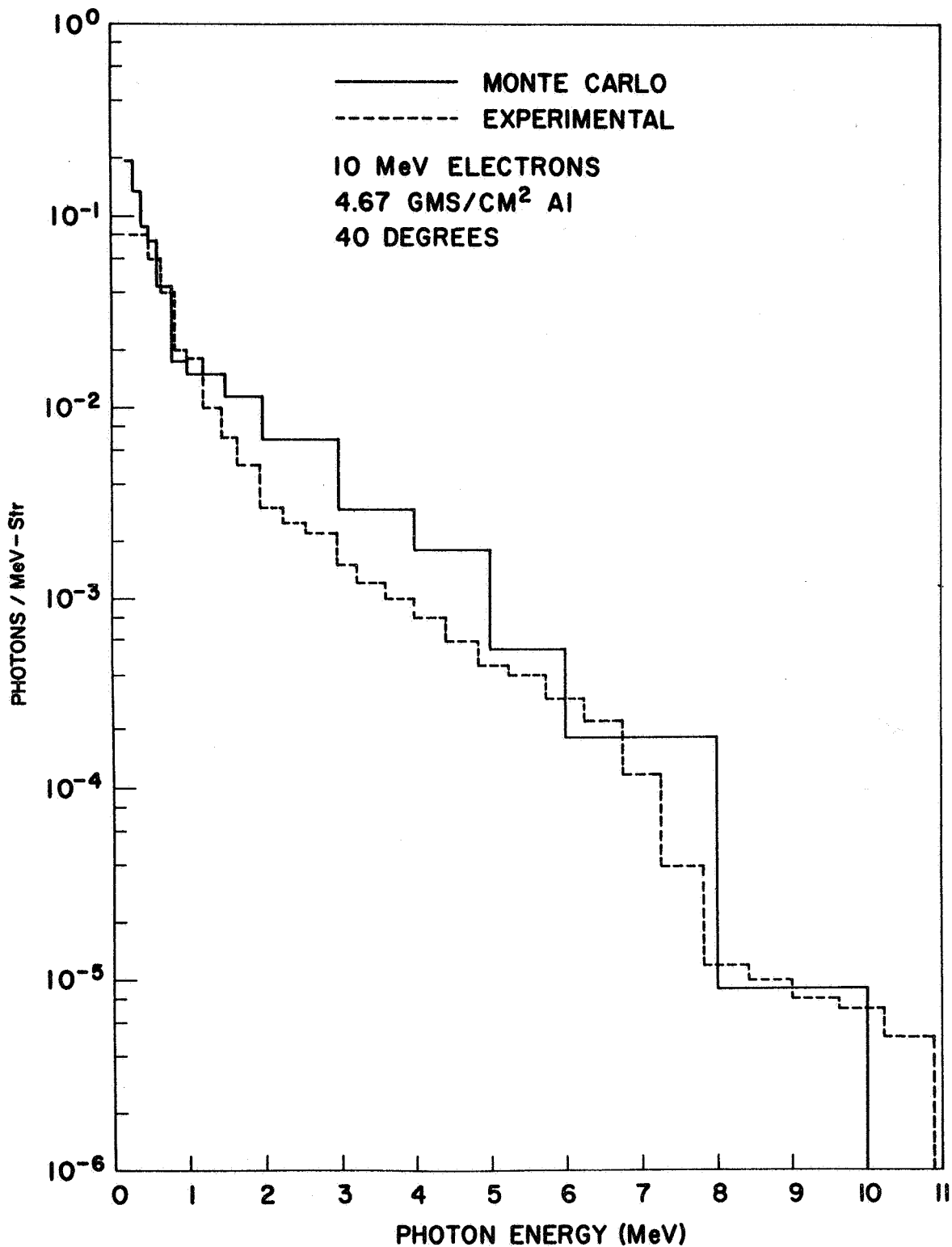


Fig. 25--Experimental and theoretical bremsstrahlung photon spectra
 for 8.2 MeV electrons incident on a 4.67 g/cm aluminum target.
 Emission angle = 40°

REFERENCES

1. C. P. Jupiter, G. Merkel and J. Perez, "Measurement of Energy Straggling of 8-MeV Electrons in Aluminum," Bull. Amer. Phys. Soc., Series II, 10, 6, 726 (1965).
2. C. P. Jupiter and G. Merkel, "Measurement of Thick Al Target Bremsstrahlung Spectra Produced with 10-MeV Electrons," Bull. Amer. Phys. Soc., Series II, 11, 5, 745 (1966).
3. Berger and Seltzer, "Tables of Energy Losses and Ranges of Electrons and Positrons," NASA SP-3012.
4. M. Berger and S. Seltzer (Private communication).
5. K. L. Brown, "Achromatic Beam Translation System for Linear Accelerators," Rev. Sci. Instr. 27 No. 12, 959 (1956).
6. R. W. Dressel, "Retrofugal Electron Flux from Massive Targets Irradiated with a Monoenergetic Primary Beam," Phys. Rev. 144, 1, 332 (1966).
7. S. Penner, "Calculations of Properties of Magnetic Deflection Systems," Rev. Sci. Instr. 32, 150 (1961).
8. P. J. Ebert, A. F. Lauzon, E. M. Lent and R. G. Der, "Transmission and Backscatter of 3.6- to 12-MeV Electrons in Various Elements," Bull. Amer. Phys. Soc. Series II, Vol. 11, No. 7 (1966).
9. C. V. Smith and N. E. Schofield, USNRDL-TR-829, March 5, 1965.
10. J. H. Hubble, "Response of a Large NaI Detector to High Energy X-Rays," Rev. Sci. Instr. 29, 65, (1958).
11. N. Starfelt and N. W. Koch, "Differential Cross Section Measurements of Thin-Target Bremsstrahlung Produced by 2.7 to 9.7 MeV Electrons," Phys. Rev. 102, (1958, 1956).



PRECEDING PAGE BLANK NOT FILMED.

Penetration of Electrons and Associated Bremsstrahlung
through Aluminum Targets*

M. J. Berger and S. M. Seltzer
National Bureau of Standards
Washington, D. C.

This paper contains a brief description of Monte Carlo programs designed to calculate the transport of fast electrons and associated bremsstrahlung through extended media. Two applications are discussed: (1) transmission of electrons through plane-parallel targets, and (2) emergence of secondary bremsstrahlung from such targets. It is shown that the predicted results are in reasonably good agreement with recent experiments for electron beams with energies up to 8 Mev incident normally on aluminum targets. Extensive new calculated data for transmission and thick-target bremsstrahlung production are presented for aluminum targets exposed to an isotropic electron flux.

* Work supported by National Aeronautics and Space Administration under Contract R-80.

1. Introduction

This paper has two purposes: (1) to review the status of electron and photon transport calculations that have been done in recent years at the National Bureau of Standards under the sponsorship of the National Aeronautics and Space Administration; and (2) to present results on the transmission of electrons through aluminum and on the production of thick-target bremsstrahlung in such targets. Comparisons are made with recent experimental data for electron beams incident perpendicularly on the target. In addition, extensive information is presented for a situation of practical importance for which direct experimental data are lacking, namely, aluminum targets exposed to an isotropic electron flux.

The assumed source-medium configuration has been kept simple. It involves a broad incident electron beam, and a plane-parallel target that is finite in one dimension and unbounded in the other two. Results for such a simple configuration provide an understanding of the essential features of electron transport in extended matter, and allow for convenient direct comparison with corresponding experiments. They also provide reference data which may be used to check the validity of more approximate calculational procedures that may have to be used for the solution of complex engineering problems.

The computer programs that have been developed provide information about: (1) transmission and reflection of electrons; (2) production of bremsstrahlung photons in targets of arbitrary thickness, and the emergence of these photons from the target; (3) deposition of energy and charge by the incident electron beam in the target; (4) the energy spectrum of the electron flux (both primary and secondary) as a function of the depth in the medium. In the earlier stages of our work, a number of different programs were developed which treated these problems separately. With the availability of ever larger computer memories the trend has been to combine these into one master program. In the present paper, information of types (1) and (2) only is presented. Preliminary results for items (3) and (4) will be presented elsewhere.^{1/}

2. Method of Calculation

The required task is to solve an electron-photon cascade problem in which each type of radiation acts as a source for the other. The determination of the photon component of the cascade is done by conventional random sampling imitating the physical processes of photoelectric absorption, Compton scattering and pair production. Electron collisions (elastic as well as inelastic) are too numerous to be followed individually. Electron tracks are therefore sampled by

letting the electrons carry out a random walk with transition probabilities derived from analytical multiple scattering theories. Calculations according to such a random-walk model have been carried out already by several authors.^{2-9/} The procedures used by us appear to be more detailed than most others in the literature, and are an elaboration of those described earlier in Ref. 6.

We shall now describe the sampling rules used in our most up-to-date Monte Carlo program (ETRAN 15). Some of the results to be given below were obtained with earlier programs which in some cases have lesser generality and make more approximations. A comparison of these programs is given in Table 1.

2.1. Division of Electron Track into Segments. Each track is divided into many major segments which we call steps. In an aluminum medium the step-size is chosen so that the electron energy, on the average, decreases by a factor 2^{-8} per step. Each step is in turn subdivided into four equal subdivisions which are called short steps. The choice of step sizes is determined by the conditions of validity of the multiple scattering theories used and by the requirement that a further decrease of the step size should not change the final results significantly.

| | ETRAN 5 | ETRAN 9 | THICKBREM | ETRAN 15 |
|---|---------|---------|-----------|----------|
| <u>Processes taken into account</u> | | | | |
| Mean energy loss by collision (continuous slowing down approximation) | No | No | Yes | No (*) |
| Collision energy loss straggling | Yes | Yes | No | No (*) |
| Mean energy loss by bremsstrahlung | Yes | No | Yes | Yes (*) |
| Bremsstrahlung energy loss straggling | No | Yes | No | Yes (*) |
| Histories of secondary bremsstrahlung photons followed | No | No | Yes | Yes (*) |
| Histories of secondary knock-on electrons followed | No | No | No | Yes (*) |
| Histories of secondary electrons due to bremsstrahlung followed | No | No | Yes | Yes (*) |
| <u>Output Information</u> | | | | |
| Electron transmission and reflection (differential in energy and angle) | Yes | Yes | No | Yes |
| Electron transmission and reflection coefficients | Yes | Yes | Yes | Yes |
| Thick-target bremsstrahlung (differential in energy and angle) | No | No | Yes | Yes |
| Charge deposition in target | No | No | No | Yes |
| Energy deposition in target | No | No | Yes | Yes |
| Electron flux as function of depth in target (differential in energy) | No | No | No | Yes |

Table 1. Comparison of various Monte Carlo models. Program 15 is flexible and the options accompanied by an asterisk can be changed from no to yes and vice versa.

2.2. Multiple Elastic Scattering by Atoms. At the end of each short step the direction of the electron is allowed to change in conformity with the net multiple scattering angular deflection sampled from the Goudsmit-Saunderson distribution. This distribution has the form of a long Legendre series whose coefficients are determined by the Mott single-scattering cross section. Screening effects are taken into account in the same manner as in the multiple scattering theory of Molière.

2.3. Multiple Inelastic Scattering by Atomic Electrons. The energy loss resulting from the cumulative effect of many inelastic collisions in each step is sampled from the Landau distribution (modified in the manner of Blunck and Leisegang to take into account binding effects).*

* In some of the simpler Monte Carlo models, based on the so-called continuous slowing down approximation, the collision energy loss is taken to be the product of the mean loss (given by the Bethe stopping power formula) and the length of the step.

2.4. Knock-on Electrons. The production of secondary electrons (with energies greater than some chosen cut-off value) is sampled from a probability distribution derived from the Møller cross section.*

* This cross section applies only to the scattering of electrons by free electrons and does not take into account binding effects. It can therefore be used only for primary electron energies that are a good deal larger than the atomic binding energies involved (1.56 keV for aluminum). Reliable information about electron-electron scattering with binding effects is not available.

The histories of the secondary electrons are followed in turn. Eventually all required generations of knock-on electrons are included.

2.5. Bremsstrahlung. The production of bremsstrahlung quanta is sampled from a probability distribution derived from the best available theoretical bremsstrahlung cross sections (Bethe-Heitler theory plus refinements). We have used a cross section package essentially equivalent with that recommended in a review article by Koch and Motz^{10/} which includes, at least approximately, the effects of screening, the Coulomb correction, and the exact high-frequency limit. Koch and Motz also suggest multiplication of the cross section by empirical correction factor that depends on the energy of the electron before the bremsstrahlung

event. For aluminum this correction factor differs from unity most at an energy of 0.5 Mev where it has the value 1.3. We have used this correction factor in some but not in all of our calculations.

The energy given to a bremsstrahlung photon is subtracted from the energy of the electron.* The history of the photons

* In some of the simpler Monte Carlo models we have not sampled the occurrence of bremsstrahlung events, but have simply subtracted the mean radiative energy loss in each short step from the electron energy.

is followed in turn, as are the histories of the photo-electrons, Compton electrons and electron-positron pairs resulting from photon interactions with the medium. In the present version of the program positrons are treated as if they were electrons. A more refined treatment is planned which will take into account electron-positron differences in energy loss, knock-on production and multiple elastic scattering.

2.6. Boundary Crossings. The program is set up so as to treat simultaneously many slab targets with different thicknesses. Boundary crossings (transmission or reflection) of electrons usually occur in the middle of a short step. The energy and direction at the time of crossing are determined by the energy and direction at the beginning of this short step modified in two ways: 1) by a small additional energy loss in the fraction of the step to the boundary (sampled again from the Landau distribution), 2) by a small additional deflection sampled from an exponential approximation to the Goudsmit-Saunderson distribution. The assumption is built into this procedure that the path of the electron is rectilinear in each short step, the entire trajectory having the form of a polygon. Numerical experimentation indicated to us that with the step-size finally chosen the error introduced by this approximation was not significant. For the evaluation of the emergence of the photons from the target such an approximation is not needed. For each sampled photon scattering we compute the probability that the photon, after the collision, will escape from the target without any further interaction. The average value of this probability then provides an estimate of the emergent number of photons.

2.7. Approximations. Certain simplifications are introduced into the Monte Carlo model which involve mainly the neglect of correlations. The electrons are not allowed to be deflected as the result of bremsstrahlung events; this type of deflection is assumed to be included in the large-angle tail of the Goudsmit-Saunderson multiple scattering distribution. Thus we neglect the correlation of sudden large deflections and large bremsstrahlung losses. Similarly, inelastic collisions resulting in the appearance of knock-on electrons are not allowed to result in a deflection of the primary electron; this type of deflection is taken into account approximately by an inelastic scattering due to Fano which is incorporated into the Goudsmit-Saunderson distribution.* Thus the correlation between

* We do not regard our present procedures for treating inelastic scattering as entirely satisfactory, and are working on improvements.

large energy losses and deflections in inelastic scattering events is neglected. The energy of a secondary knock-on electron is not subtracted from the energy of the primary electron producing it; the energy loss of the primary is determined entirely by the Landau distribution. This implies neglect of the correlation between the occurrence of large energy losses of primary electrons and the appearance of energetic delta rays.

In the sampling of the production of bremsstrahlung photons and knock-on electrons the energy of the primary electron at any point within a step is taken to be weighted average of the energies at the beginning and at the end of the step. In other words, energy-loss straggling is allowed only at the end of each step, but within a step the continuous-slowing-down approximation is used.

We were reluctant to introduce these approximations but were finally led to adopt them because they considerably simplify and shorten the calculations, which already are lengthy enough. We convinced ourselves by trial calculations with various models that the errors resulting from the approximations are likely to be small. Our program certainly could be improved in various respects if one wanted to take the trouble, but we think it is sufficiently accurate for many applications in space science and technology, and commensurate in its detail with the precision of the available input cross sections.

2.8. Preparation of Input Data. The sampling procedures outlined above require as input the values of many cross sections and multiple scattering distributions at a large number of energies and

angles. Numerical experimentation indicates that the Monte Carlo results depend quite sensitively on most of the input information, so that approximation of the input by crude and simple formulas is not appropriate. Because of the repetitive nature of the Monte Carlo computations it would be prohibitively time-consuming to evaluate the data every time when needed. We have therefore gone to great lengths to tabulate all the input data once and for all in a form convenient for table look-up. The evaluation and pre-digestion of input data is carried on in a program called DATAPAC which generates typically on the order of 20,000 words of information and stores them on magnetic tape for later use by ETRAN 15. Even DATAPAC does not compute all cross sections and other data from scratch but makes use of an extensive tape library with cross section information for approximately fifty elements, compounds and mixtures.

3. Comparisons of Calculated and Measured Results

3.1. Scaling. When presenting transmission and thick-target bremsstrahlung data as function of the target thickness, we find it convenient to use the scaled thickness z/r_0 , where z is the actual thickness, and r_0 the mean electron range at the source energy T_0 . By this choice of variable the dependence of the results on the source energy is greatly reduced so that interpolation with respect to T_0 is much easier. A short list of r_0 -values for aluminum

is given in Table 2. These values were obtained by integrating the reciprocal of the mean energy loss by collision and radiation, i.e. $r_0 = - \int_0^{T_0} (dE/dx)^{-1} dT$.

3.2. Electron Transmission (Perpendicular Incidence). Figures 1 and 2 contain comparisons between Monte Carlo results and recent experiments by Jupiter, Merkel and Lonergan^{11/} (source energy 8.2 Mev) and by Rester and Dance^{12/} (source energy 1 Mev) on the transmission of electrons through aluminum targets. The Monte Carlo results, obtained with the computer program ETRAN 9, are in each case based on a sample of 30,000 electron histories. Comparisons are made for the energy spectra of the transmitted electrons emerging at various angles with respect to the direction of incidence. On the whole there is a reasonably good agreement between the calculated and measured spectra but there are discrepancies which indicate a possible need for further work. The further study of the location and particularly the width of the peak of the spectrum would be of interest. There is a tendency for the experimental width to be somewhat greater than the calculated width. Experimentally one can think of a few effects that might broaden the spectrum, e.g. the energy spread of the incident beam around the nominal source energy, a possible angular divergence of the incident beam, etc.

| T_0 (Mev) | r_0 (g/cm ²) | T_0 (Mev) | r_0 (g/cm ²) |
|-------------|----------------------------|-------------|----------------------------|
| 0.5 | 0.224 | 2.5 | 1.54 |
| 0.55 | 0.255 | 3.0 | 1.86 |
| 0.6 | 0.287 | 3.5 | 2.17 |
| 0.7 | 0.351 | 4.0 | 2.48 |
| 0.8 | 0.417 | 4.5 | 2.78 |
| 0.9 | 0.483 | 5.0 | 3.08 |
| 1.0 | 0.549 | 5.5 | 3.37 |
| 1.2 | 0.683 | 6.0 | 3.66 |
| 1.4 | 0.816 | 7.0 | 4.23 |
| 1.6 | 0.949 | 8.0 | 4.78 |
| 1.8 | 1.08 | 9.0 | 5.32 |
| 2.0 | 1.21 | 10.0 | 5.84 |

Table 2. Electron Mean Ranges in Aluminum

Comparisons with other experimental results are now in progress. We show one of them in Fig. 3, with an experiment by Van Kamp^{13/} designed to measure the transmission spectrum in the forward direction with great accuracy in the vicinity of the spectral peak. In this case, for relatively thin aluminum targets and a source energy of 3.66 Mev, the agreement with the Monte Carlo results is rather close.

3.3. Thick-target Bremsstrahlung (Perpendicular Incidence).

Figures 4-6 contain comparisons, for source energies up to 2 Mev, between calculated and experimental results for the distribution in energy and angle of bremsstrahlung photons emerging from thick targets. The Monte Carlo results shown were obtained with the program THICKBREM which employs the continuous-slowng-down approximation. Recent trial calculations with the program ETRAN 15 indicate that the inclusion of energy-loss straggling raises the amount of bremsstrahlung from an aluminum target by only 1-2 percent for a source energy of 2 Mev.*

* The straggling effect in aluminum increases with source energy and is estimated to raise the bremsstrahlung yield by 5-6 percent at 5 Mev and by 7-8 percent at 10 Mev.

Figures 4 and 5 contain comparisons with the experimental results of Dance and Baggerly,^{14/} mainly for aluminum but also for iron and gold. The corresponding Monte Carlo results are based on a sample of 2,500 electron histories and 125,000 photon histories for each case.* For aluminum and iron, a bremsstrahlung

* The number of bremsstrahlung photons per electron was artificially increased to obtain better statistical accuracy, and this increase was compensated by giving the photons appropriate small weight factors.

cross section package without the Koch-Motz empirical correction factor was used, whereas for gold this factor was included. This choice was made to get the best agreement with the experimental results. We have made other calculations that indicate that the inclusion of the correction factor leaves the shape of the bremsstrahlung spectrum essentially unchanged but alters the normalization. For aluminum the spectral values were found to be increased by 28%, 34% and 31% for source energies of 2, 1 and 0.5 Mev, Respectively. Conversely, the omission of the correction factor for gold lowered the spectrum by 42% for a source energy of 2 Mev.

Inspection of Figs. 4 and 5 shows good agreement between calculated and measured results in regard to spectral shape, for various source energies, target thicknesses and directions of emergence.

The absolute normalization can be brought into agreement through the use of a suitable empirical correction factor, depending on the electron energy only, that multiplies the bremsstrahlung cross section. However, there is an inconsistency between the value of the correction factor that one would extract from the cross section measurements reviewed by Koch and Motz, and the value derived from the thick-target experiment of Dance and Baggerly. It should be kept in mind that the experimental uncertainty of the Koch-Motz data in the energy region of interest is estimated to be 20% so that the discrepancy may be more apparent than real, and could very well be resolved by further measurements of the bremsstrahlung cross section. In this connection new measurements by Rester and Dance^{15/} may be of help.

In Fig. 6, further comparisons for low source energies are made between thick-target bremsstrahlung spectra calculated with the program THICKBREM (based on samples of 1,000 electron histories and 25,000 photon histories) with corresponding measurements by Placious.^{16/} The calculations include the Koch-Motz correction factor. Agreement between calculated and measured spectra is good. Attention should be called to the low-energy peak of the

spectrum for tin between 10 and 20 kev, as well as to the peak for the spectra at 70 kev from gold targets in Fig. 6. These peaks are caused by the presence of characteristic x-ray production.

4. Results for Cosine-law Sources

4.1. Definition of Cosine-law Source. The extent to which electrons penetrate through a thick target depends on their direction of incidence. In detailed shielding calculations for spacecraft one must therefore take into account the orientation of the vehicle, and the characteristics of the radiation field, at each point along the trajectory. A simplifying approximation is often made in which the electron flux is assumed to be isotropic. This approximation is justified to the extent that the time-average of the electron flux is isotropic in a coordinate system attached to the shield, and to the extent that the perturbation of the flux by the shield can be disregarded. If the shield has the shape of a plane-parallel plate, the number of electrons entering a unit area of the shield is then proportional to the cosine of the angle between the normal to the shield and the incident-velocity vector, and we speak of a cosine-law source.

4.2. Electron Transmission. Extensive calculation of electron transmission, based on Monte Carlo samples on the order of 100,000 histories per case, have been carried out by M. Lopez^{17/} at NASA (Houston MSC), using the computer program ETRAN 5. They provide the most detailed set of available calculated data. We present here some excerpts from them, taken from a computer print-out put at our disposal.

Table 3 gives a list of number and energy transmission coefficients for various target thicknesses, as well as corresponding reflection coefficients for a semi-infinite medium, all for aluminum and seven source energies between 0.5 Mev and 6.0 Mev. One interesting feature of this table is that the transmission coefficients as functions of the scaled target thickness z/r_0 are rather slowly varying function of the source energy. This is a phenomenon which has previously been found in calculations based on the continuous-slowing-down approximation; the scaling of the transmission curves appears to be preserved to a large extent when energy-loss straggling is taken into account. Fig. 7, for a 2-Mev source, shows the energy spectra of transmitted electrons emerging at various directions. In Fig. 8 corresponding spectra are shown that result from an integration over all forward direction and correspond to the reading of a 2π -detector. The Monte Carlo histograms were smoothed out by eye to obtain spectra curves. It can be seen that the spectra for thin targets

| | | | | | | | |
|----------------------------|---|-------|-------|-------|-------|-------|-------|
| T_0 (Mev) | 0.50 | 1.00 | 2.00 | 3.00 | 4.00 | 5.04 | 5.99 |
| r_0 (g/cm ²) | 0.224 | 0.549 | 1.21 | 1.85 | 2.48 | 3.10 | 3.65 |
| z/r_0 | | | | | | | |
| | <u>Number Transmission Coefficient</u> | | | | | | |
| 0.1 | 0.841 | 0.853 | 0.875 | 0.889 | 0.899 | 0.906 | 0.914 |
| 0.2 | 0.708 | 0.732 | 0.766 | 0.789 | 0.807 | 0.819 | 0.831 |
| 0.3 | 0.555 | 0.587 | 0.634 | 0.667 | 0.692 | 0.711 | 0.725 |
| 0.4 | 0.394 | 0.428 | 0.484 | 0.522 | 0.555 | 0.577 | 0.593 |
| 0.5 | 0.241 | 0.271 | 0.322 | 0.363 | 0.399 | 0.425 | 0.441 |
| 0.6 | 0.119 | 0.146 | 0.181 | 0.218 | 0.250 | 0.276 | 0.290 |
| 0.7 | 0.042 | 0.051 | 0.068 | 0.090 | 0.109 | 0.127 | 0.135 |
| | <u>Energy Transmission Coefficient</u> | | | | | | |
| 0.1 | 0.736 | 0.735 | 0.741 | 0.746 | 0.751 | 0.753 | 0.757 |
| 0.2 | 0.530 | 0.533 | 0.542 | 0.550 | 0.558 | 0.562 | 0.567 |
| 0.3 | 0.356 | 0.360 | 0.373 | 0.384 | 0.394 | 0.400 | 0.405 |
| 0.4 | 0.214 | 0.220 | 0.233 | 0.246 | 0.257 | 0.264 | 0.268 |
| 0.5 | 0.110 | 0.115 | 0.126 | 0.137 | 0.147 | 0.155 | 0.159 |
| 0.6 | 0.045 | 0.048 | 0.057 | 0.065 | 0.072 | 0.077 | 0.079 |
| 0.7 | 0.013 | 0.014 | 0.016 | 0.020 | 0.024 | 0.027 | 0.028 |
| | <u>Reflection Coefficients for Semi-infinite Medium</u> | | | | | | |
| Number | 0.273 | 0.251 | 0.216 | 0.193 | 0.172 | 0.158 | 0.145 |
| | 0.176 | 0.153 | 0.122 | 0.103 | 0.088 | 0.078 | 0.070 |

Table 3. Transmission and Reflection Coefficients for Aluminum Targets,
for a Cosine-law Source.

are characterized by rather sharp peaks which then broaden with increasing target thickness. The spectra at a given scaled target thickness z/r_0 , when plotted as function of ratio T/T_0 of the spectral energy to the source energy, have a shape that depends rather insensitively on the source energy. This facilitates interpolation to source energies other than those for which calculations have been made. Figure 9 shows angular distributions of transmitted photons, integrated over all spectral energies, for various target thicknesses. For a very thin target, the distribution is given very nearly by a cosine-law, which means that the incident angular distribution is still preserved. For thicker targets, the angular distribution is concentrated more strongly in the forward direction than would be the case for a cosine-law.

4.3. Thick-target Bremsstrahlung. Very recently we have carried out thick-target bremsstrahlung calculations for aluminum targets with program ETRAN 15, using a bremsstrahlung cross section package including the Koch-Motz correction factor. Just as in the case of the Houston transmission results, the bremsstrahlung results are much too voluminous to be reproduced here, and we have merely selected for presentation some typical cases. Figure 10

shows spectra, for various source energies and a target thickness equal to r_0 , for photons emerging in the forward direction ($0-10^\circ$) and at an oblique angle ($55-65^\circ$). The shape of the spectra does not seem to depend very strongly on the source energy or on the direction of emergence. Starting from the top energy T_0 the spectra rapidly increase; in the absence of photon absorption the spectra would tend to rise indefinitely as the spectral energy becomes lower; in fact the spectra have a definite peak at some energy between 30 to 50 Kev whose position depends somewhat on the angle of emergence, and below which the spectral curve falls off rapidly.

Corresponding results of the bremsstrahlung spectra integrated over all forward directions (2π geometry) are shown in Fig. 11 for various target thicknesses. An interesting feature of the spectra can be noted for the highest source energy shown; at 5 Mev, for targets with thicknesses equal to r_0 or $2r_0$, the low-energy part of the spectrum (between 10 and 20 kev) show a sudden increase. By looking at various stages of the electron-photon cascade we have convinced ourselves that this phenomenon is not a numerical fluke but quite real, and must be attributed to photons of the fourth or higher stages of the cascade which happen to be produced by secondary electrons very close to the exit surface.

Another interesting quantity is the forward bremsstrahlung efficiency by which we mean the fraction of the incident electron energy that leaves the target in the forward direction in the form of bremsstrahlung. A plot of the efficiency vs. target thickness for different source energies is given in Fig. 12. It can be seen that after a rapid buildup the efficiency reaches a peak at a target thickness approximately equal to $0.6 r_0$. As the target thickness is further increased, a small decrease of the efficiency occurs due to photon absorption within the target. It is convenient to represent the forward efficiency by a formula*

$$Y = 10^{-4} a Z T_0$$

* A similar formula is often used to describe the conversion of electron kinetic energy to bremsstrahlung energy in an unbounded medium, without regard to geometric factors. It should be kept in mind that our parameter a pertains to a specific situation, namely, a cosine-law source and a plane-parallel target of finite thickness, and takes into account scattering and absorption of the photons within the target.

where Z is the atomic number, T_0 the source energy and a is a proportionality constant that is usually taken to be a constant. Actually, a is somewhat dependent on the source energy and to a greater extent on the target thickness, as can be seen in detail in Table 4.

Acknowledgments

The authors would like to express their thanks for the hospitality accorded to them by the Laboratory for Theoretical Studies at the Goddard Space Flight Center on whose computer some of the calculations were carried out. They would also like to thank M. Lopez and his colleagues of the NASA Manned Spaceflight Center in Houston for their collaboration in the electron transmission calculations.

| T_0 (Mev) \ z/r_0 | 10 | 5 | 2 | 1 | 0.5 |
|-----------------------|-----|-----|-----|-----|-----|
| 0.2 | 3.0 | 3.0 | 2.8 | 2.8 | 2.6 |
| 0.4 | 4.1 | 4.2 | 4.1 | 4.0 | 4.0 |
| 0.6 | 4.4 | 4.5 | 4.4 | 4.3 | 4.3 |
| 0.8 | 4.2 | 4.4 | 4.3 | 4.2 | 4.3 |
| 1.0 | 3.9 | 4.2 | 4.2 | 4.1 | 4.2 |
| 1.2 | 3.7 | 4.0 | 4.0 | 4.0 | 4.1 |
| 1.4 | 3.5 | 3.8 | 3.9 | 3.9 | 4.0 |
| 1.6 | 3.3 | 3.7 | 3.8 | 3.8 | 3.9 |
| 1.8 | 3.1 | 3.5 | 3.7 | 3.7 | 3.8 |
| 2.0 | 3.0 | 3.4 | 3.6 | 3.6 | 3.8 |

Table 4. Value of the parameter \underline{a} in the formula $Y = 10^{-4} a Z T_0$ for the forward bremsstrahlung efficiency (cosine-law source, aluminum target).

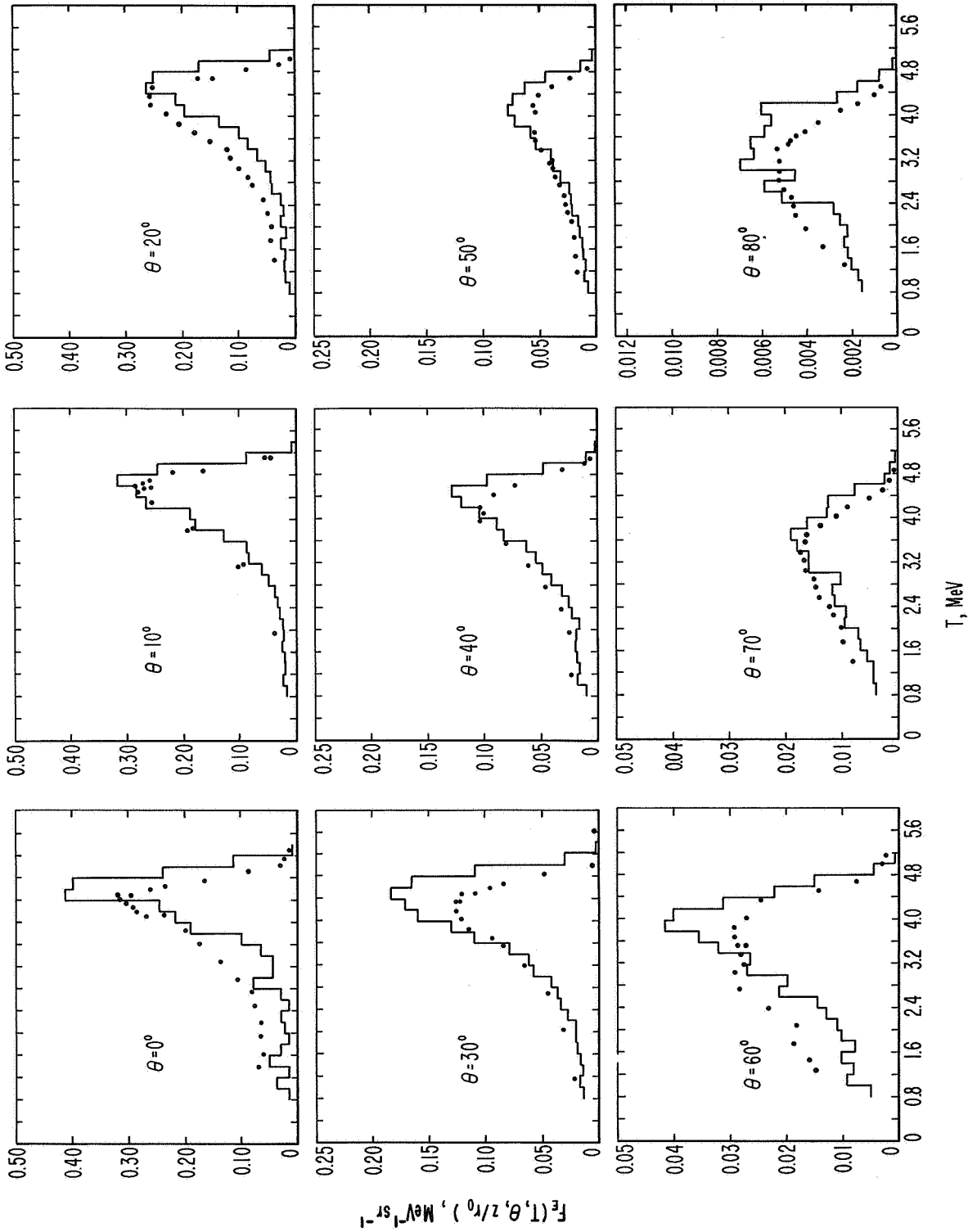


Figure 1. Energy spectra of transmitted electrons emerging in various directions from an aluminum target bombarded with 8.2-Mev electrons. Normal incidence, target thickness 2.38 g/cm² (=0.491 r₀). Points are from experiment by Jupiter, Lonergan and Merkel. Histograms were obtained with Monte Carlo program ETRAN 9.

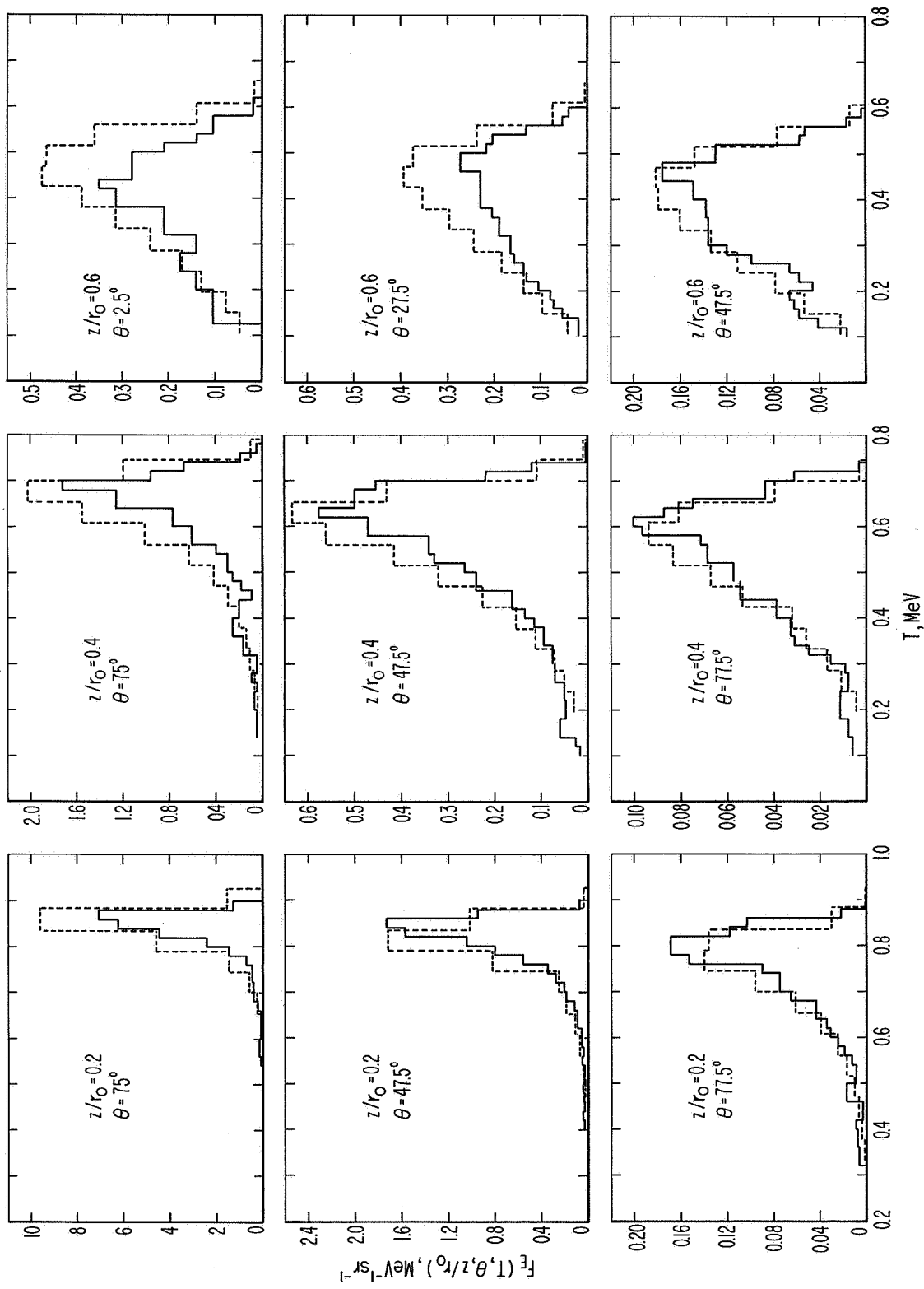


Figure 2. Energy spectra of transmitted electrons emerging in various directions from aluminum targets bombarded with 1-Mev electrons. Normal incidence; target thicknesses are 0.11 g/cm² (=0.2 r₀), 0.22 g/cm² (=0.4 r₀) and 0.33 g/cm² (=0.6 r₀). Dashed histograms represent experimental results of Rester and Rainwater. Solid histograms were calculated with Monte Carlo program ETRAN 9.

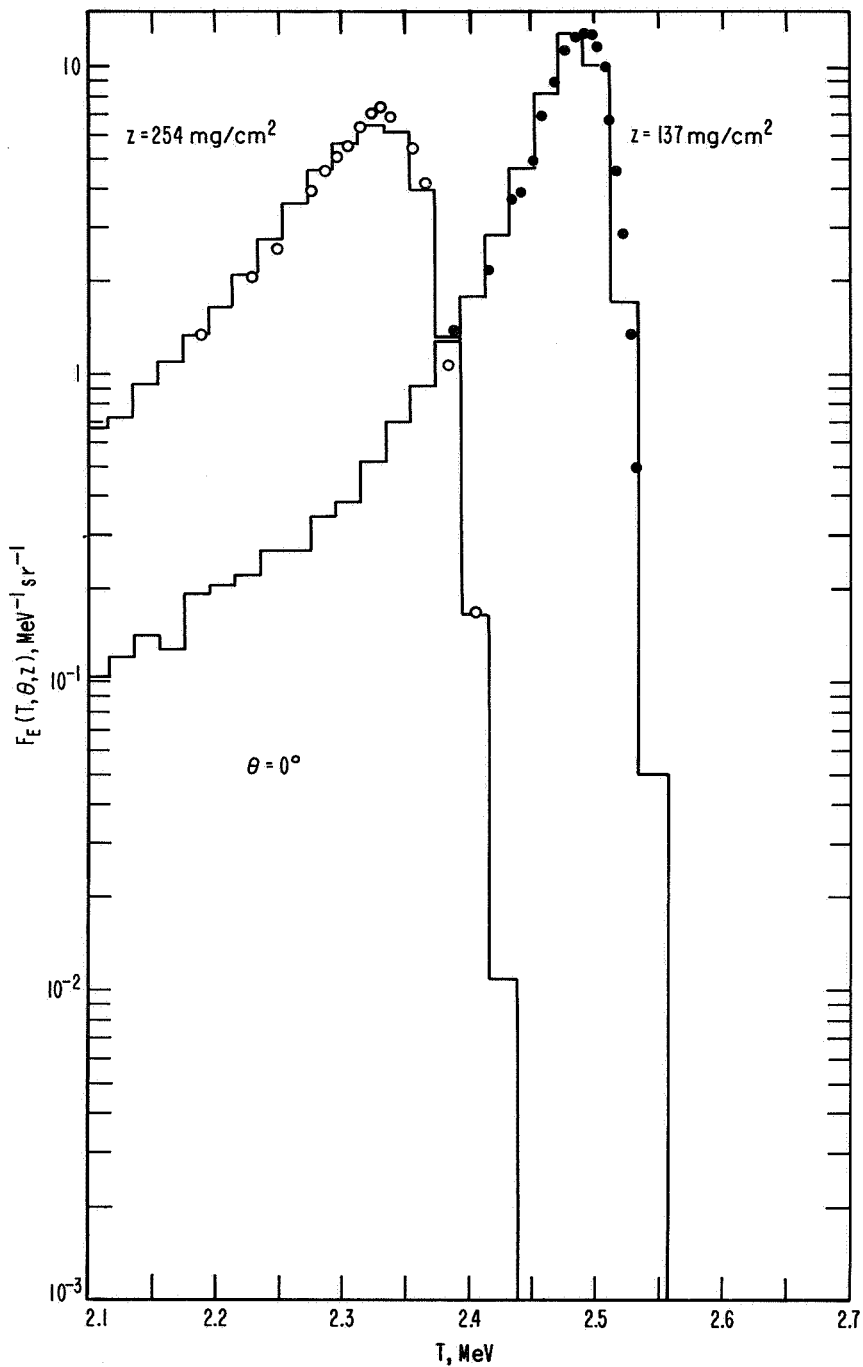


Figure 3. Energy spectra of transmitted electrons emerging in forward direction from aluminum target bombarded with 2.66-Mev electrons. Normal incidence. Target thicknesses are 0.137 g/cm^2 ($=0.084 r_0$) and 0.254 g/cm^2 ($=0.15 r_0$). Points are from an experiment by Van Camp and Vanhuyse. Histograms were obtained with Monte Carlo program ETRAN 15.

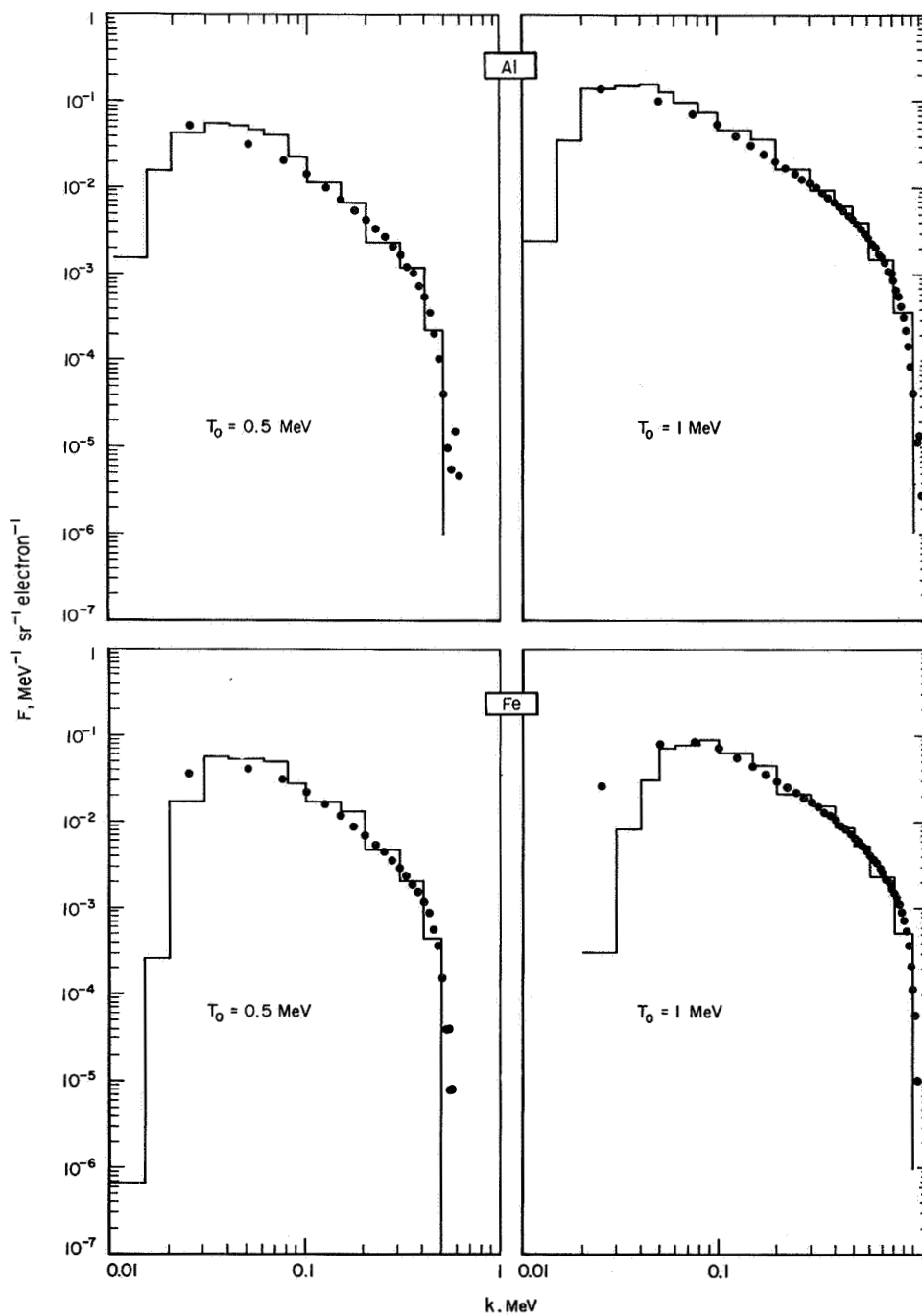


Figure 4. Energy spectra of bremsstrahlung emerging in forward direction (0 degrees). Normal incidence. Aluminum targets with thickness of 0.548 g/cm^2 ($=2.44 r_0$) for $T_0 = 0.5 \text{ MeV}$ and 0.707 g/cm^2 ($=1.29 r_0$) for $T_0 = 1 \text{ MeV}$. Iron targets with thickness of 0.248 g/cm^2 ($=1.0 r_0$) for $T_0 = 0.5 \text{ MeV}$ and 0.870 g/cm^2 ($=1.44 r_0$) for $T_0 = 1 \text{ MeV}$. Points are from experiment of Dance and Baggerly. Histograms were calculated with Monte Carlo program THICKBREM.

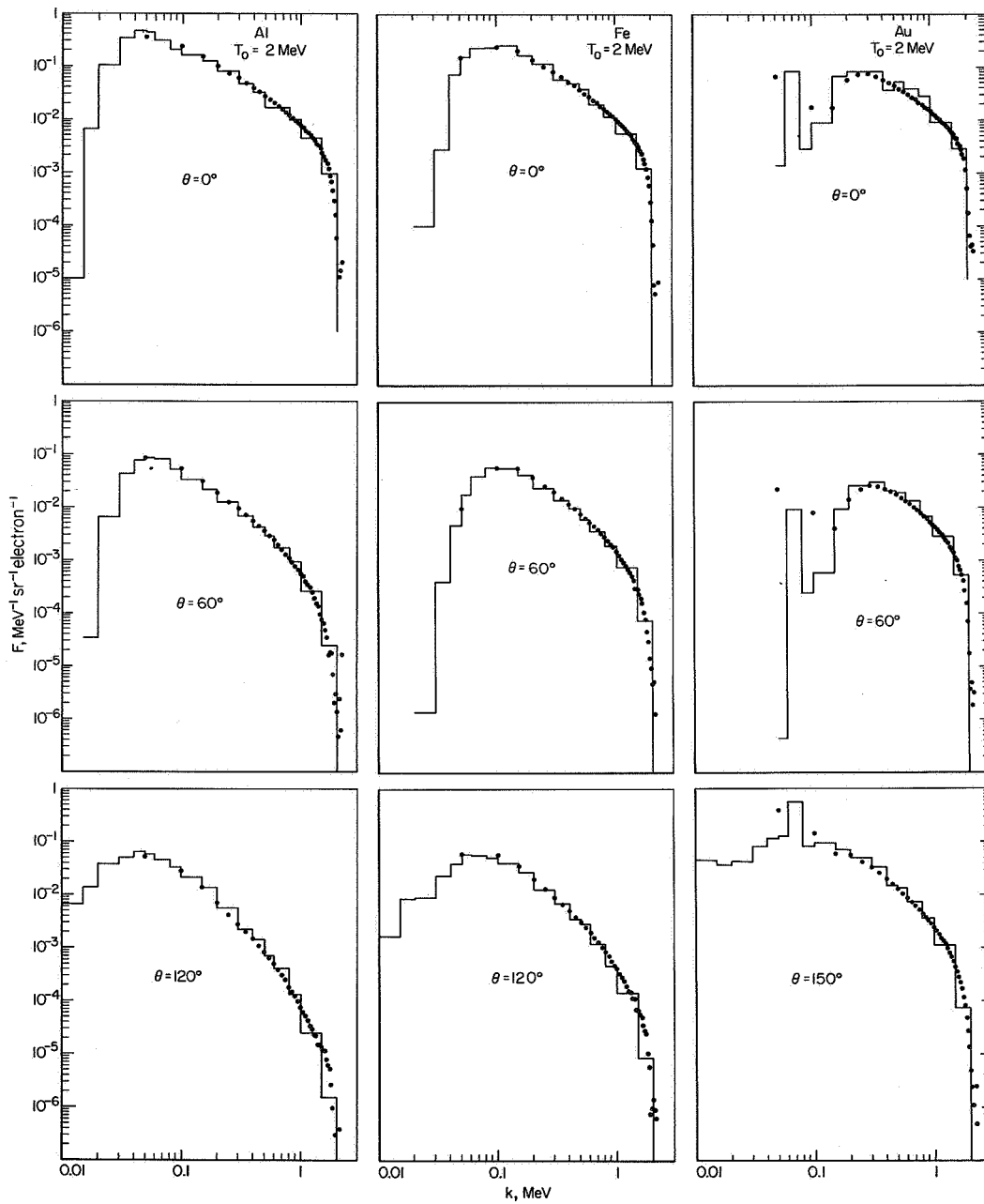


Figure 5. Energy spectra of bremsstrahlung emerging in various directions from thick targets bombarded by 2-Mev electrons. Normal incidence. Target thicknesses are 1.74 g/cm^2 ($=1.43 r_0$) aluminum, 1.30 g/cm^2 ($=0.986 r_0$) iron, and 1.62 g/cm^2 ($=1.04 r_0$) gold. Points from the experiment by Dance and Baggerly. Histograms were calculated with Monte Carlo program THICKBREM.

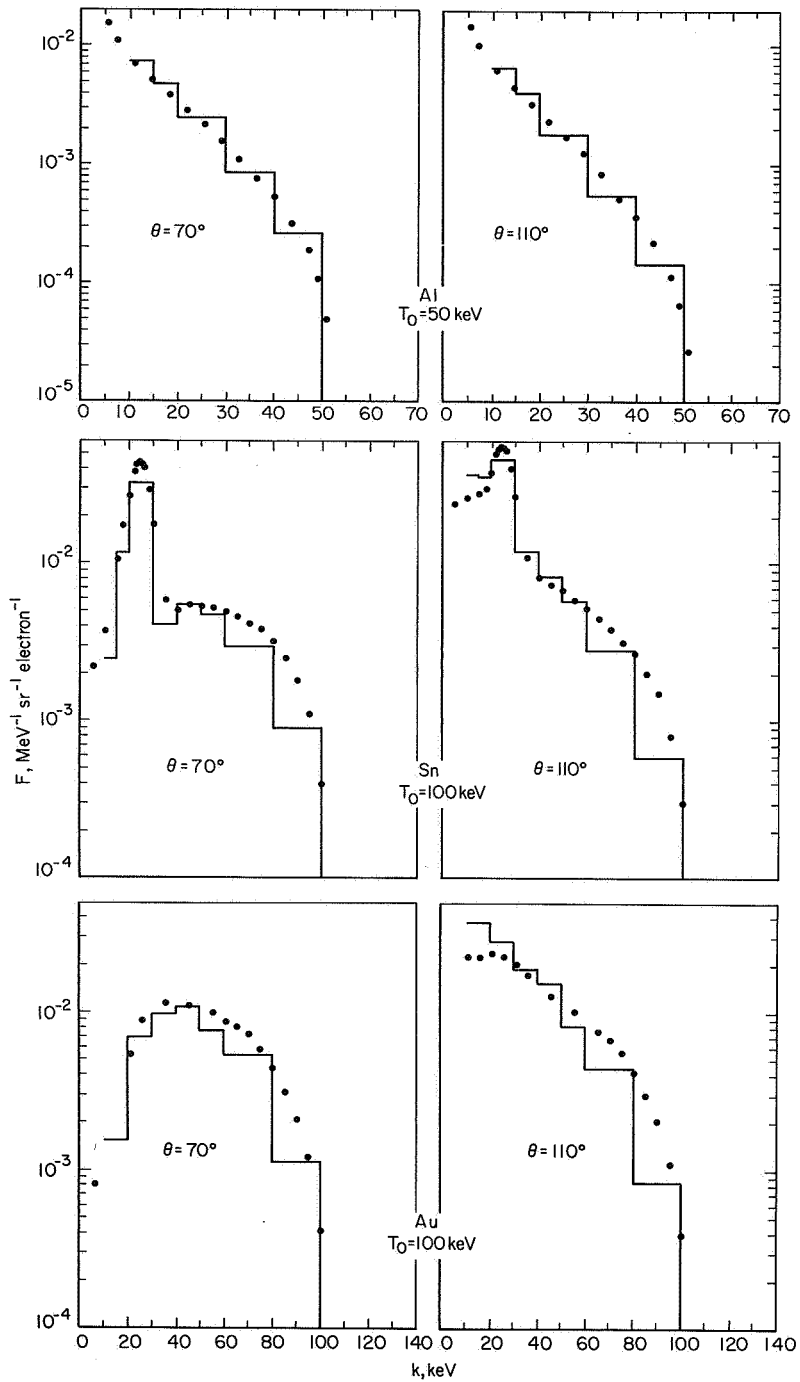


Figure 6. Energy spectra of bremsstrahlung emerging in forward and backward directions from thick targets. Normal incidence. Target thicknesses are 3.8 mg/cm^2 ($=0.67 r_0$) aluminum for $T_0 = 50 \text{ keV}$, 21.6 mg/cm^2 ($=0.82 r_0$) tin for $T_0 = 100 \text{ keV}$, and 19.3 mg/cm^2 ($=0.64 r_0$) gold for $T_0 = 100 \text{ keV}$. Points are from an experiment by Placious. Histograms were calculated with Monte Carlo program THICKBREM.

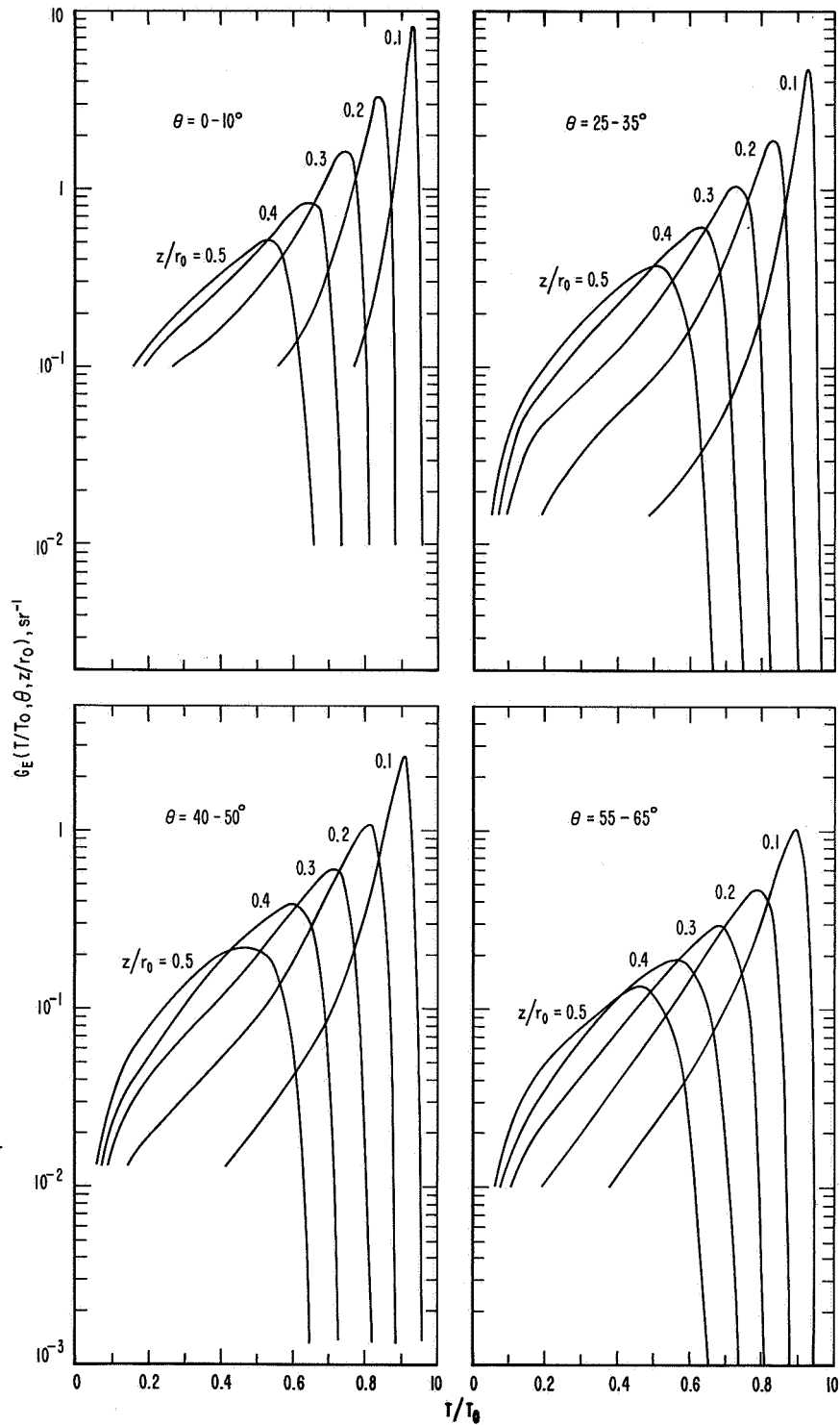


Figure 7. Energy spectra of transmitted electrons emerging in various directions from aluminum targets. Source energy 2 Mev, cosine-law source. Calculated by M. Lopez with Monte Carlo program ETRAN 5.

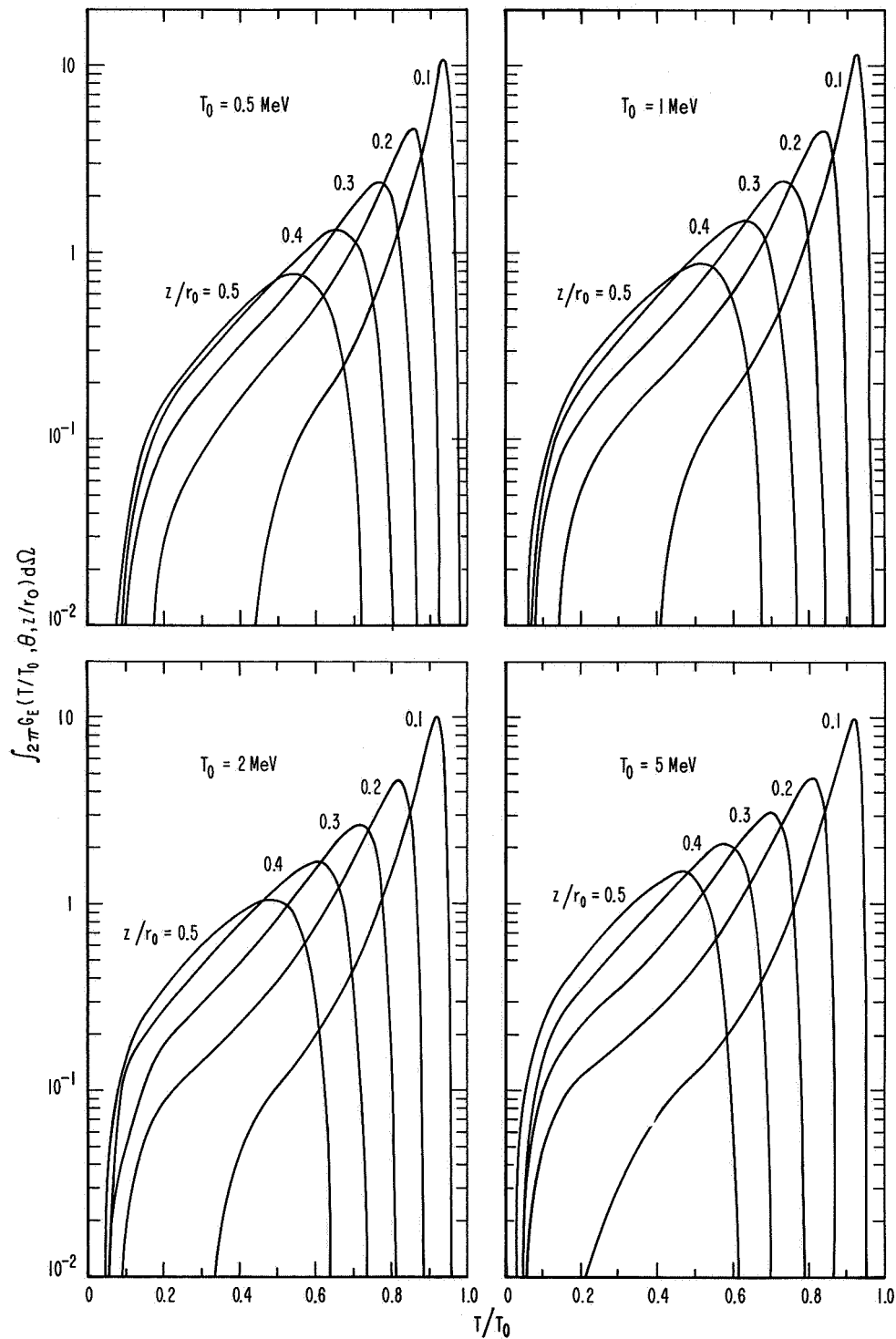


Figure 8. Energy spectra of electrons transmitted through aluminum. Spectra are integrated over all forward directions. Cosine-law source. Calculated by M. Lopez with Monte Carlo program ETRAN 5.

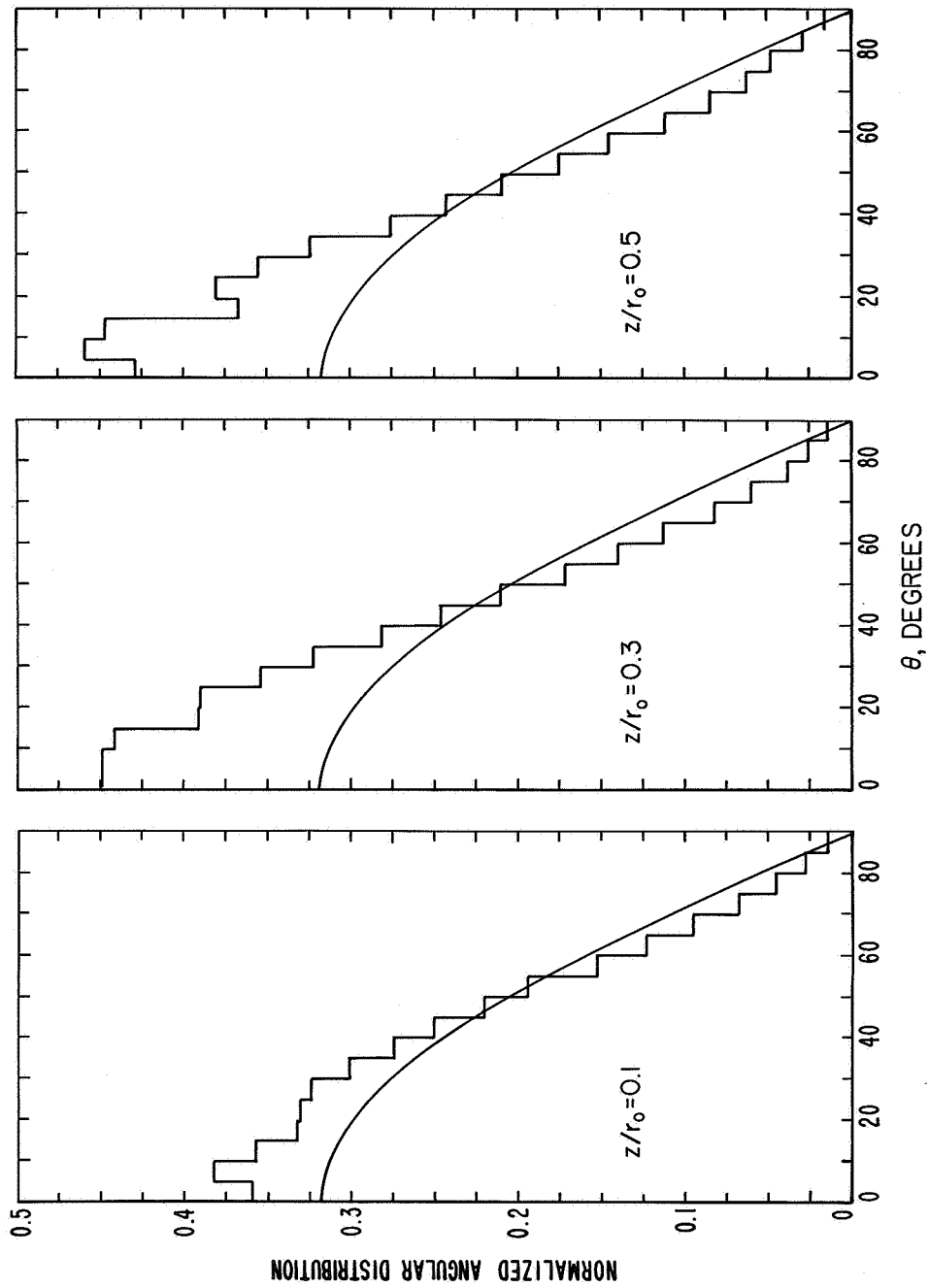


Figure 9. Angular distribution of electrons transmitted through aluminum. Distributions are normalized to unity. $T_0 = 2$ Mev, cosine-law source. Histograms are Monte Carlo results obtained by M. Lopez with program ETRAN 5. The curves represent the distribution $(1/\pi)\cos\theta$.

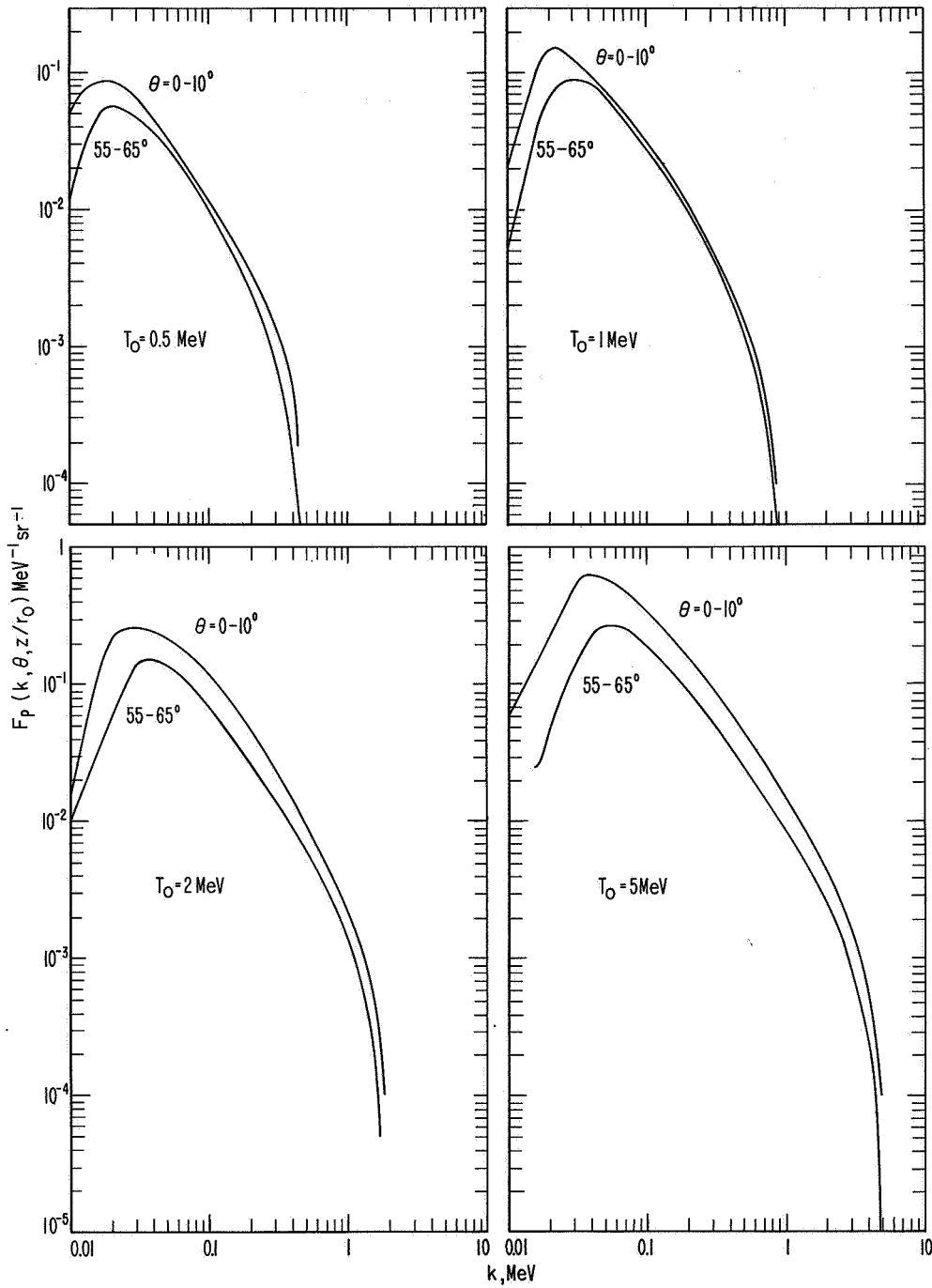


Figure 10. Energy spectra of bremsstrahlung emerging in various directions from thick aluminum targets. Cosine law source, target thickness $0.6 r_0$. Calculated with Monte Carlo program ETRAN 15.

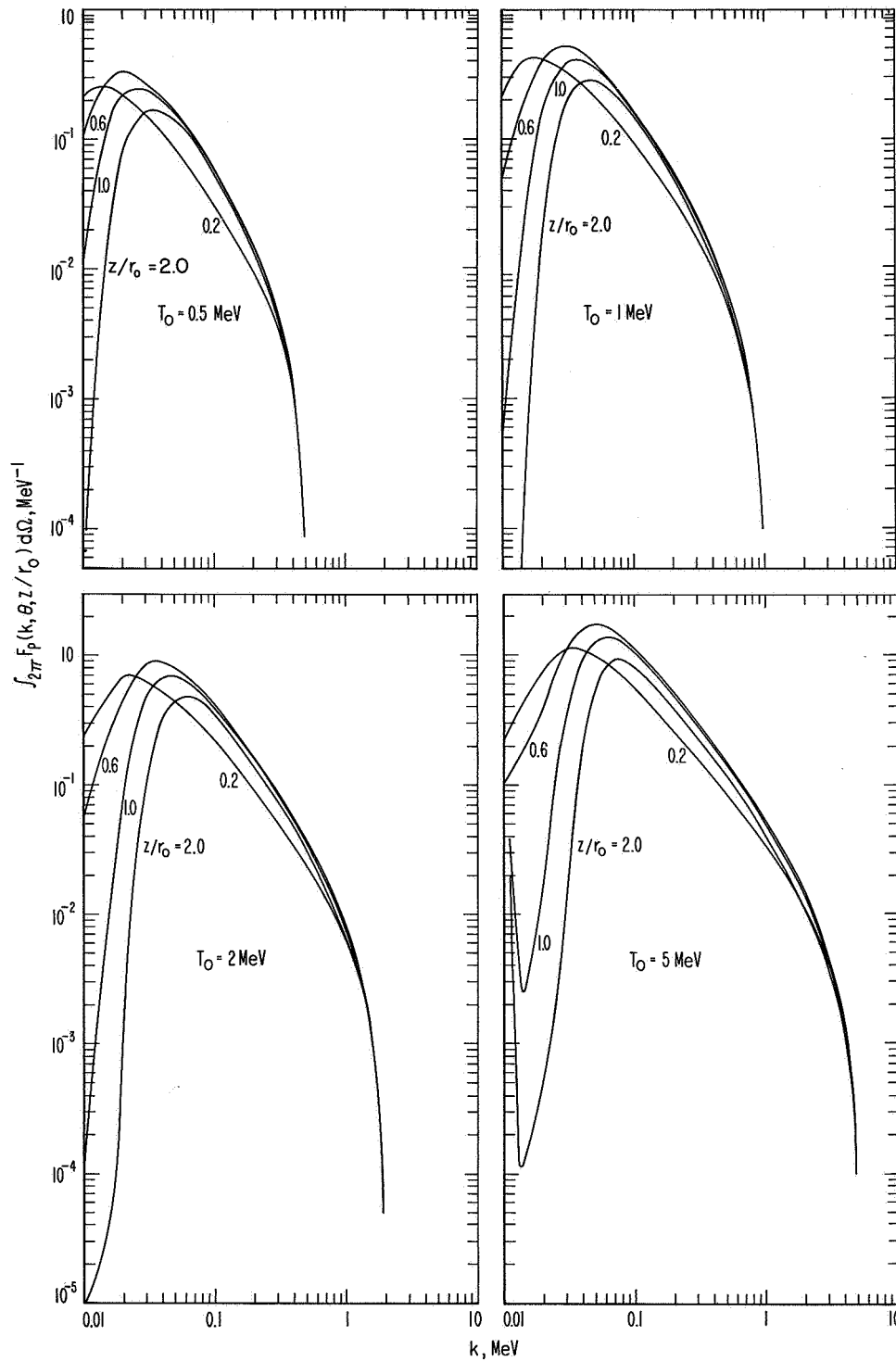


Figure 11. Energy spectra, integrated over all forward directions of bremsstrahlung emerging from thick targets. Cosine law source. Calculated with Monte Carlo program ETRAN 15.

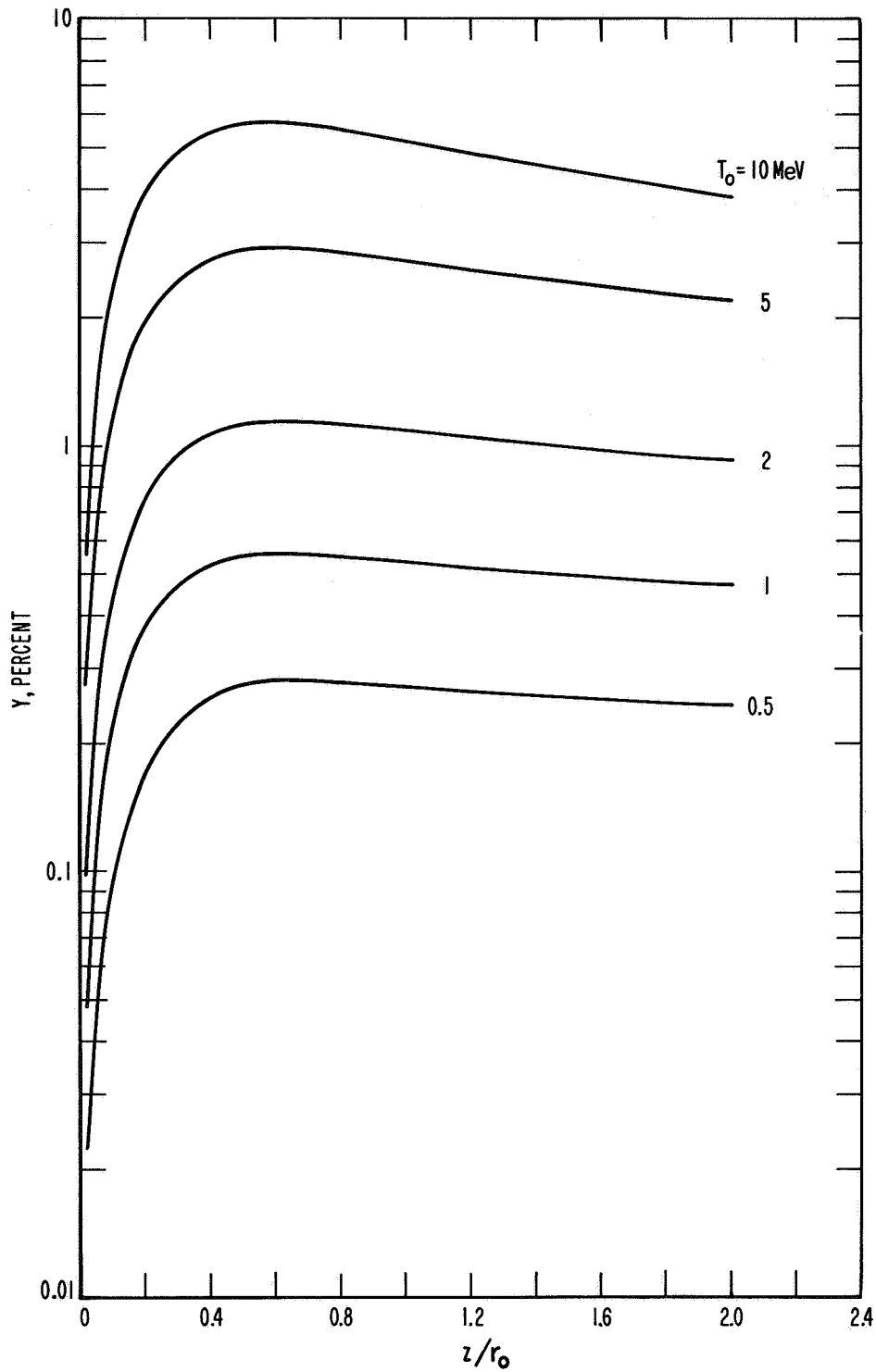


Figure 12. Forward bremsstrahlung efficiency for aluminum, as function of target thickness, for a cosine law source. Calculated with Monte Carlo program ETRAN 15.

References

1. M. J. Berger and S. M. Seltzer, NBS Report 9566, July 1967 (unpublished); to be published in the Proceedings of a Conference on High-Energy Radiation Therapy Dosimetry, N. Y. Academy of Sciences and Am. Assoc. of Physicists in Medicine, New York, June 1967.
2. D. V. Hebbard and P. R. Wilson, Australian J. Physics 8, 90 (1955).
3. T. Sidei, T. Higashimura and K. Kinoshita, Mem. Fac. Eng. Kyoto Univ. 19, 22 (1957).
4. J. E. Leiss, S. Penner and C. S. Robinson, Phys. Rev. 107, 1544 (1957).
5. J. F. Perkins, Phys. Rev. 126, 1781 (1962).
6. M. J. Berger, Methods in Computational Physics, Vol. I, Academic Press, N. Y. (1963).
7. G. Meissner, Zeitschr. f. Naturf. 19a, 269 (1964).
8. D. Harder, Durchgang schneller Elektronen durch dicke Materieschichten, Habilitationsschrift, University of Würzburg, Germany, (January 1965).
9. B. W. Mar, Nucl. Sci. Eng. 24, 193 (1966).
10. H. W. Koch and J. W. Motz, Rev. Mod. Phys. 31, 920 (1959).
11. G. P. Jupiter, J. A. Lonergan and G. Merkel, private communication; also Trans. Am. Nuclear Soc. 10, 379 (1967).
12. D. H. Rester and W. J. Rainwater, Jr., "Investigations of Electron Scattering in Aluminum", Rep. 0-71000/5R-12, LTV Research Center (May 1965).
13. K. J. Van Camp, V. J. Vanhuyse, private communication; see also Phys. Letters 19, 504 (1965).
14. W. E. Dance and L. L. Baggerly, Bremsstrahlung Production in Aluminum and Iron, Rep. 0-71000/5R-13, LTV Research Center (May 1965).
15. R. Placious, J. Appl. Physics 38, 2030 (1967).
16. D. H. Rester, W. E. Dance, Trans. Am. Nuclear Soc. 10, 378 (1967).
17. A. C. Hardy, M. D. Lopez, and T. T. White, Trans. Am. Nuclear Soc. 10, 383 (1967).

THE THEORY OF THE TRANSPORT OF RELATIVISTIC ELECTRONS

Richard Scalettar

Gulf General Atomic
San Diego, California

I. INTRODUCTION

We shall in this paper describe a generalization of a procedure, due to Bethe, Rose, and Smith,⁽¹⁾ for calculating the transport of relativistic electrons through matter. The primary improvements over the method of Bethe, et al., is the consequent inclusion of inelastic scattering and a correction for large angle scattering so that a complete treatment of the coupled spatial, angular, and energy straggling distributions is attained. As we shall see, the form for our solution of the transport equation is a superposition of energy straggling distributions, analogous to (but not identical with) Blunck-Leisegang⁽²⁾ distributions, appropriately weighted in position and angle. It is to be emphasized, as shown in detail in Section II, that the rapid increase of the eigenvalues associated with the generalized Bethe eigenfunction expansion makes for a good convergence of the series expansion for the flux. This result is suitable not only for computational purposes but also enables one to obtain a clearer picture of the transition from thin foil scattering to deep penetration.

The problem of electron penetration of condensed materials has, of course, been the subject of intense theoretical study for many years. Useful

(1) H. A. Bethe, M. E. Rose, L. P. Smith, Proc. Amer. Phil. Soc., 71, 573 (1938).

(2) J. Blunck and S. Leisegang, Ztsch. f. Phys., 128, 500, (1950).

general surveys of early work have been given by Bohr⁽³⁾ and Bethe and Ashkin⁽⁴⁾. A clear qualitative analysis of the relative importance of various physical effects and the relation between a classical and quantum mechanical treatment was presented by Williams;⁽⁵⁾ however, his discussions reflect the limitations of understanding of relativistic and field theoretic effects at the time. A more complete quantitative analysis was also given by Williams⁽⁶⁾ who first derived the Gaussian angular distribution. A treatment by Landau,⁽⁷⁾ based on a version of the transport equation from which all angular dependence had been deleted, yielded an energy straggling distribution applicable to thin foils; the treatment of the energy loss cross-sections was approximate and was improved by Blunck and Leisegang⁽²⁾. It is characteristic of these early attempts, as well as of most of the subsequent attacks on this problem, that discussions of spatial, angular, and energy dependence of the flux were carried out separately or in a partially unified fashion; thus a complete description of the solution of the problem was lacking. Goudsmit and Saunderson⁽⁸⁾ analyzed the angular distribution without reference either to discrete energy loss or spatial dependence. A modification of the Goudsmit-Saunderson treatment was

(3) N. Bohr, Det. Kgl. Danske Vid. Selskab., Mat-Fys. Medd., 18, 1, (1948).

(4) H. A. Bethe and J. Ashkin, "Passage of Radiations Through Matter" in E. Segre, "Experimental Nuclear Physics," Vol. I, Wiley, (1953).

(5) E. J. Williams, Science Progress, 121, 14, (1936).

(6) E. J. Williams, Proc. Roy. Soc. (London), A 159, 531, (1939).

(7) L. Landau, Journ. of Phys. USSR, 8, 201, (1944).

(8) S. Goudsmit and J. L. Saunderson, Phys. Rev. 57, 24, (1940) and Phys. Rev. 58, 36, (1940).

carried out by Lewis⁽⁹⁾ who also utilized a continuous slowing down approximation and was restricted to a discussion of the infinite medium problem. It is to be emphasized, in connection with the treatment by these authors of the angular distribution problem that their discussions of the Bethe, Rose, Smith approximation is invariably coupled with an additional small angle approximation. It is characteristic of our own analysis that a small angle approximation is not made, although the fact that the cross-sections themselves are highly peaked in the incident direction (not necessarily the forward direction deep in the material) is utilized. In addition a perturbation-type correction for large-angle single scattering is made in our complete discussion; we have not, due to limitations of space, included the details in this report. An improved version of the early theories, in the sense that it is applicable to all scattering cross-sections and yields an analytical result, was made by Moliere⁽¹⁰⁾ and a simplified derivation as well as a critical comparison of his with earlier results was carried out by Bethe⁽¹¹⁾. It remains the case that the Moliere treatment is based on a continuous slowing down approximation in which the distinction between energy and position is lost and that a small-angle approximation is made. An interesting series of papers by Spencer⁽¹²⁾ and his co-workers investigated the problem further but they still included the above approximations. Useful

(9) H. W. Lewis, Phys. Rev. 78, 526, (1950).

(10) G. Moliere, Ztsch. f. Naturforsch; 39, 78, (1948).

(11) H. A. Bethe, Phys. Rev. 89, 1256, (1953).

(12) L. V. Spencer and J. Coyne, Phys. Rev. 128, 2230 (1962). The earlier Spencer papers may be traced from this reference. A pre-print of a recent work appears to avoid certain of the previous limitations.

calculations based on Monte Carlo methods but utilizing the Goudsmit-Saunders angular distributions and the Blunck-Leisegang energy straggling distributions, have been carried out by Berger and co-workers⁽¹³⁾.

Before entering into the quantitative aspects of our treatment we wish to comment briefly on certain deeper questions concerning the description of electron transport. The electron energies with which we shall deal are ~ 10 Mev. so that a complete treatment of a cascade shower⁽¹⁴⁾ is not envisioned. Nonetheless for such energies the motion of the electron is relativistic and our description must be in concord with the laws of quantum electrodynamics. The cross-sections for the relevant processes-atomic excitation and ionization, bremsstrahlung, pair production, etc. - were derived long ago,⁽¹⁵⁾ but treatments from a recent point of view are by and large incomplete. In particular in the case of heavy atoms, for which the binding energy of the inner electrons is a substantial fraction of the rest energy, a relativistic description of the atomic electrons is also indicated. Self-consistent field treatments by Swirles⁽¹⁶⁾ and Grant⁽¹⁷⁾ fail to take proper account of virtual pair production and radiation effects and indeed this is not really possible in an unambiguous way in the old-fashioned

(13) M. J. Berger and M. S. Seltzer, NAS Nat. Res. Council, Pub. 1133.

(14) S. L. Belenkii and T. P. Ivanenko, Soviet Physics Uspekhi, 2, 912, (1960).

(15) For a summary of these early results see H. A. Bethe, "Quantenmechanik der Ein und Zwei-Elektronen Probleme," Handbuch der Physik, Vol. 24/1, Springer (1933). For a more recent, but less complete as to scattering problems, treatment see H. A. Bethe and E. E. Salpeter "Quantum Mechanics of the One and Two Electron Problems," Academic Press, (1957).

(16) B. Swirles, Proc. Roy. Soc. A152, 625, (1935).

(17) I. P. Grant, Proc. Roy. Soc., A 261, 555, (1962).

theories. A major advance in the correct relativistic description of bound state problems was the formulation of the Bethe-Salpeter Equation.⁽¹⁸⁾ Subsequently this equation was derived directly from quantum field theory⁽¹⁹⁾ and at least its formal generalization to the multiparticle case accomplished. Important steps in the clarification of the physical interpretation of the Bethe-Salpeter wave functions were made by Wick⁽²⁰⁾ and Mandelstam,⁽²¹⁾ the latter of whom showed how scattering transition amplitudes involving composite particles could, in principle at least, be calculated from the Bethe-Salpeter wave functions and the n-particle Green's functions. The problem was further clarified from a formal point of view by Nishijima⁽²²⁾ who established the connection between these results, the Schwinger equations⁽²³⁾ for the Green's functions, and time-independent scattering theory in terms of the T-matrix.⁽²⁴⁾ The net result of these investigations has been to provide a correct framework for a completely relativistic calculation of cross-sections involving bound electrons.

Equally important with the possibility of obtaining corrections to the cross-sections associated with binding effects is the fact that the formal similarity of the final equations⁽²²⁾ to those of non-relativistic scattering

(18) E. E. Salpeter and H. A. Bethe, Phys. Rev. 84, 1232, (1951).

(19) M. Gell-Mann and F. Low, Phys. Rev. 84, 350, (1951).

(20) G. C. Wick, Phys. Rev. 96, 1124, (1954).

(21) S. Mandelstam, Proc. Roy. Soc. (London), A 233, 248, (1955).

(22) K. Nishijima, Prog. Theor. Physics (Japan), 17, 765, (1958).

(23) J. Schwinger, Proc. Nat. Acad. of Sciences (U.S.A.), 37, 452, (1951).

(24) H. Ekstein, Phys. Rev. 101, 880, (1956).

theory makes possible the extension of the Foldy⁽²⁵⁾ and Watson⁽²⁶⁾ procedure for the treatment of the multiple scattering problems to the relativistic case. We have thus been able to obtain an exact relativistic generalization of the coupled Foldy-Watson integral equations, which describe the production of an effective field by scattering from other atoms in the solid and its role in the generation of the scattered wave. Following Foldy and Lax,⁽²⁷⁾ in averaging over the positions of the particles in the scatterer, we obtain the equations for the propagation of the coherent wave and the latter serves as a source in the integral equations for the wave intensity (density matrix). Finally, the introduction of the Wigner density⁽²⁸⁾ leads to the relativistic generalization of the coupled transport equations which exhibit certain corrections in the effective cross-sections governing the over-all description of particle conservation. It is to be emphasized that the numerical results to be presented subsequently do not embody fully the corrections associated with the above treatment, since this analysis has been completed in parallel with the development of the above mentioned generalization of the Bethe, Rose, Smith treatment of the conventional transport equation.

We shall in this paper focus attention on the latter problem and shall now outline our method for the solution of the transport equation. Full details will be presented in papers to be published elsewhere.

(25) L.L. Foldy, Phys. Rev. 67, 107, (1945).

(26) M. L. Goldberger and K. M. Watson, "Collision Theory," Ch. 11, Wiley, (1964).

(27) M. Lax, Rev. Mod. Phys., 23, 287, (1951).

(28) E. P. Wigner, Phys. Rev. 40, 749, (1932).

II. THE SOLUTION OF THE TRANSPORT EQUATION

We shall now describe the numerical and analytical technique developed for solving the electron transport equation. In order to fix the notation we shall first write the latter in a standard form, discretized in the energy variable

$$\vec{\Omega} \cdot \frac{\partial f_g(\vec{x}, E, \vec{\Omega})}{\partial \vec{x}} = \sum_{g'=0}^{\infty} \int d\vec{\Omega}' \int_{E_g}^{E_{g+1}} dE' \sigma_{gg'}(\vec{\Omega}, \vec{\Omega}') f_{g'}(\vec{x}, E', \vec{\Omega}') - \sigma_g f_g(\vec{x}, E, \vec{\Omega}) + S_g(\vec{x}, E, \vec{\Omega}) \quad (1)$$

Here f_g is the number of electrons in the g^{th} energy group at position \vec{x} traveling in the direction of the unit vector, $\vec{\Omega}$, with energy E , per unit range in each of the variables. $\sigma_{gg'}(\vec{\Omega}, \vec{\Omega}')$ is the (corrected) cross-section for scattering from energy group, g' , to g and direction $\vec{\Omega}'$ to $\vec{\Omega}$; this cross-section includes ionization and bremsstrahlung effects to be modified in accordance with the discussion in the Introduction. $S_g(\vec{x}, E, \vec{\Omega})$ is an effective source term which includes the coupling with the photons. A small bit of algebra enables us to write (1) in the form

$$\vec{\Omega} \cdot \frac{\partial f_g(\vec{x}, E, \vec{\Omega})}{\partial \vec{x}} = \int_{E_g}^{E_{g+1}} dE' \int d\vec{\Omega}' \sigma_g(E'-E; \vec{\Omega}, \vec{\Omega}') f_g(\vec{x}, E', \vec{\Omega}') - \sigma_g f_g(\vec{x}, E, \vec{\Omega}) + Q_g(\vec{x}, E, \vec{\Omega}) \quad (2)$$

where the down-scattering from higher energies is now included in the modified source term, Ω_g .

A Fourier transformation of (2) yields, with the definition,

$$\gamma_g(\tau, \Omega, \Omega') = \int_0^{\infty} dK \sigma_g(K; \Omega, \Omega') e^{i\tau K} \quad (3)$$

the equation

$$\begin{aligned} \vec{\Omega} \cdot \frac{\partial \tilde{f}_g(\vec{x}, \tau, \vec{\Omega})}{\partial \vec{x}} &= \int d\vec{\Omega}' \gamma_g(\tau, \vec{\Omega}, \vec{\Omega}') \tilde{f}_g(\vec{x}, \tau, \vec{\Omega}') \\ &\quad - \sigma_g \tilde{f}_g(\vec{x}, \tau, \vec{\Omega}) + \tilde{Q}_g(\vec{x}, \tau, \vec{\Omega}) \end{aligned} \quad (4)$$

in the transformed variables \tilde{f}_g and \tilde{Q}_g . At this point we introduce an approximation based on the highly peaked angular dependence of the cross-sections in our range of energies; it may be shown that if $\sigma(\vec{u} \cdot \vec{v})$ is large for $\vec{u} \cdot \vec{v} \sim 1$ (\vec{u} and \vec{v} unit vectors) then⁽²⁹⁾

$$I(\vec{u}) = \int \sigma(\vec{u} \cdot \vec{v}) [f(\vec{v}) - f(\vec{u})] d\vec{v} \quad (5)$$

is, to a good approximation, given by

$$I(\vec{u}) = \frac{\sigma_{tr}}{2} \left\{ \frac{1}{\sin \theta} \frac{\partial}{\partial \theta} (\sin \theta) \frac{\partial f}{\partial \theta} + \frac{1}{\sin^2 \theta} \frac{\partial^2 f}{\partial \varphi^2} \right\} \quad (6)$$

where $\vec{u} = (\sin \theta \cos \varphi, \sin \theta \sin \varphi, \cos \theta)$ and $\sigma_{tr} = \pi \int_{-1}^{+1} (1-\mu)\sigma(\mu)d\mu$.

Introducing this result into Eq. 4 and noting that the suppressed energy

variable in (6) must be Laplace transformed, we obtain, assuming a one-dimensional spatial dependence and azimuthal symmetry of the flux, the equation ($\mu = \cos \theta$)

$$\mu \frac{d\tilde{f}_g(x, \tau, \mu)}{dx} = \alpha_g^{(1)}(\tau) \left\{ \frac{d}{d\mu} \left[(1-\mu^2) \frac{d\tilde{f}_g(x, \tau, \mu)}{d\mu} \right] + \beta_g(\tau) \tilde{f}_g(x, \tau, \mu) \right\} + \tilde{Q}_g \quad (7)$$

where

$$\alpha_g^{(0)}(\tau) = 2\pi \int_{-1}^{+1} d\mu \gamma_g(\tau, \mu) \quad (8)$$

$$\alpha_g^{(1)}(\tau) = \pi \int_{-1}^{+1} d\mu (1-\mu) \gamma_g(\tau, \mu) \quad (9)$$

$$\beta_g(\tau) = \frac{\alpha_g^{(0)}(\tau) - \sigma_g}{\alpha_g^{(1)}(\tau)} \quad (10)$$

We note that $\alpha_g^{(0)}(\tau)$ and $\alpha_g^{(1)}(\tau)$ are the Fourier transforms of the total cross-sections and the transport cross-sections respectively. Defining the generalized Bethe eigenvalue problem⁽²⁹⁾ (we suppress the subscripts) by

$$\frac{d}{d\mu} \left[(1-\mu^2) \frac{d\psi_n}{d\mu} \right] + \beta \psi_n(\mu) = -\lambda_n \mu \psi_n(\mu) \quad (11)$$

(29) Corrections to the approximation (6) to include large angle scattering have been made by a modified definition of the eigenvalue problem (11). Full details of the procedure will be described in later publications.

we find for the solution of Eq. 7

$$\tilde{f}_g^{(\pm)}(x, \mu, \tau) = \sum_n \tilde{C}_n^{(g)(\pm)}(x, \tau) \tilde{\psi}_n^{(g)}(\mu, \tau) \quad (12)$$

where

$$\begin{aligned} \tilde{C}_n^{(g)(+)}(x, \tau) &= \tilde{C}_n^{(g)(+)}(0, \tau) e^{-\alpha_g^{(1)}(\tau) \lambda_n^{(g)} x} \\ &+ \int_0^x e^{-\alpha_g^{(1)}(\tau) \lambda_n^{(g)} (x-x')} \tilde{Q}_n^{(g)(+)}(x', \tau) dx' \end{aligned} \quad (13)$$

$$\begin{aligned} \tilde{C}_n^{(g)(-)}(x, \tau) &= \tilde{C}_n^{(g)(-)}(L, \tau) e^{-\alpha_g^{(1)}(\tau) \lambda_n^{(g)} (x-L)} \\ &+ \int_L^x e^{-\alpha_g^{(1)}(\tau) \lambda_n^{(g)} (x-x')} \tilde{Q}_n^{(g)(-)}(x', \tau) dx' \end{aligned} \quad (14)$$

Here h^\pm for any $h(\mu)$ is defined by $h^\pm(\mu) = h(\mu) Y(\pm\mu)$ when $Y(\mu)$ is the step function. In the usual experimental situation $C_n^{(g)(-)}(L, \tau) = 0$ and $C_n^{(g)(-)}(0, \tau)$ determines the reflection coefficients. The first two eigenfunctions and the associated eigenvalues for $\beta = 0$ are depicted in Figs. 1 and 2. A detailed mathematical investigation of the solutions to the Bethe eigenvalue problem Eq. 11 has been carried out utilizing the results of Kamke⁽³⁰⁾ and Dorodnitsyn;⁽³¹⁾ however, we can not enter into the details

(30) E. Kamke, I Math. Ztsch., 45, 759, (1939); II Math. Ztsch., 46, 231, (1940); III Math. Ztsch., 46, 251, (1940).

(31) A. A. Dorodnitsyn, Uspekhi Mat. Nauk, SSSR, 6, (1952).

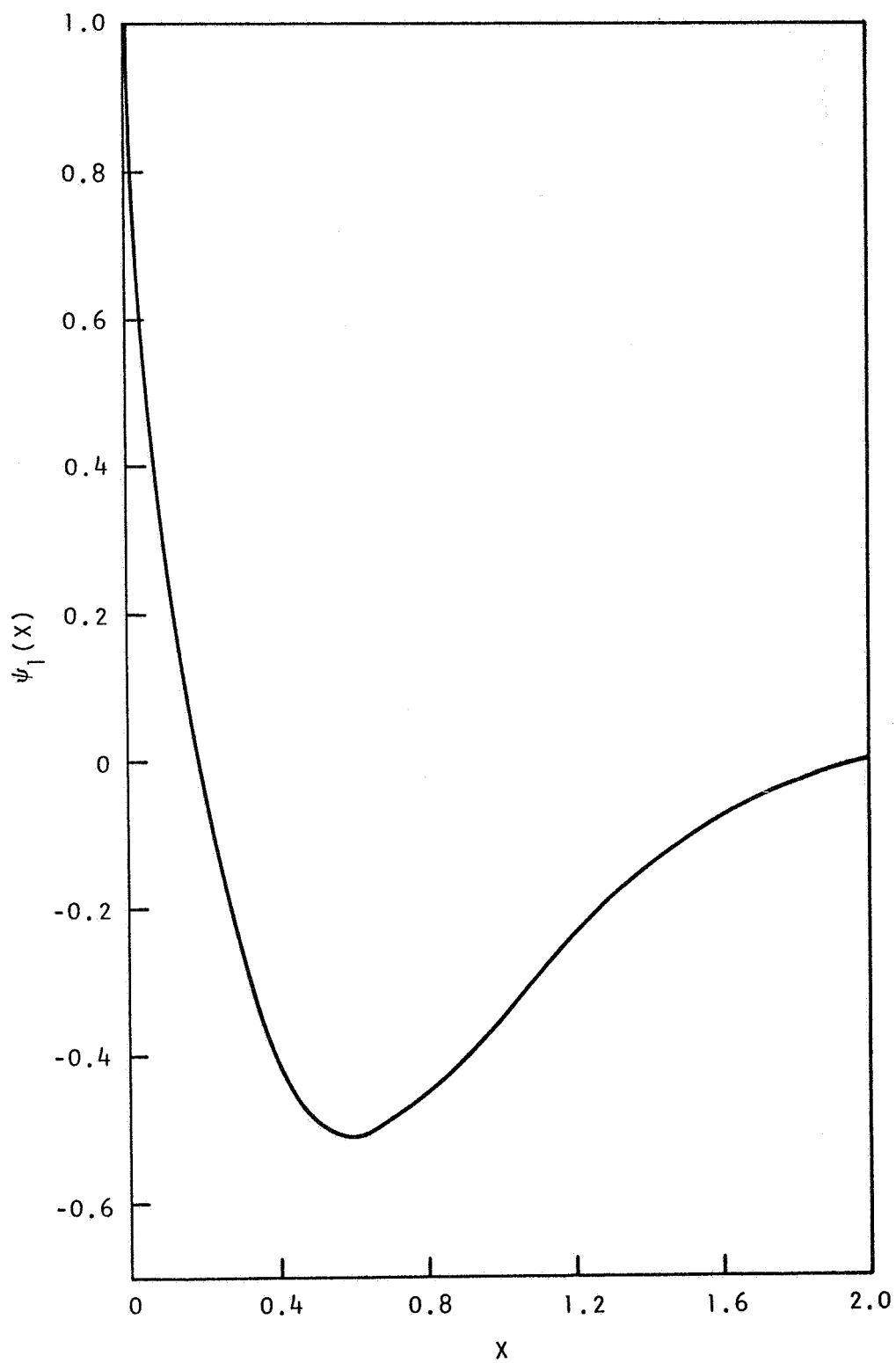


Fig. 1 The Bethe eigenfunction for $k_1 = 14.527$

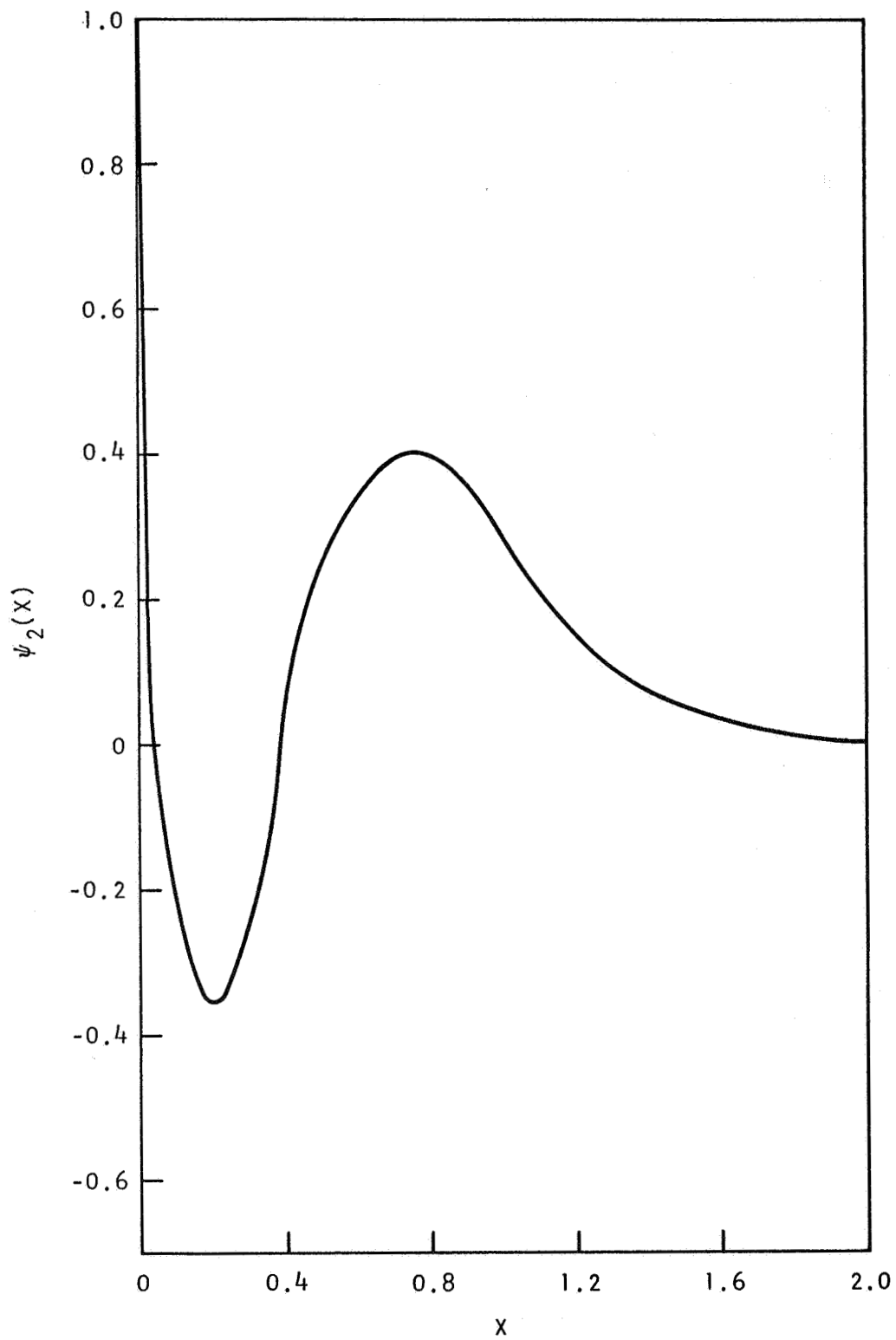


Fig. 2 The Bethe eigenfunction for $k_2 = 42.04$

here. The important point to notice as emphasized in the Introduction is that the rapid increase of the eigenvalues make for good convergence of the series expansion.

By inversion of the Fourier transformation we find

$$f_g^{(+)}(x, \mu, E) = \int dE' \int d\epsilon \sum_n \left\{ G_n^{(g)}(x, E', \epsilon) C_n^{(g,+)}(0, E') + \int_0^x dx' G_n^{(g)}(x-x', E', \epsilon) Q_n^{(g,+)}(x', E') \right\} \psi_n^{(g)}(\mu, \epsilon) \quad (15)$$

where the Green's function

$$G_n^{(g)}(x, E', \epsilon) = \frac{1}{2\pi} \int_{-\infty}^{+\infty} d\tau \exp[-i\tau(E', \epsilon) + H_n^{(g)}(x, \tau)] \quad (16)$$

with

$$H_n^{(g)}(x, \tau) = -\sigma_g^{(tr, e)} \lambda_n' + x \epsilon_n^{(g)} \bar{K}_g i\tau + x \epsilon_n^{(g)} \int_0^{E_0} dK \sigma_g^{(i)}(K) [e^{i\tau K} - 1 - i\tau K] \quad (17)$$

where the mean energy loss

$$K_g = \int_0^{E_0} dK K \sigma_g^{(\mu)}(K) \quad (18)$$

Using approximate expressions for the cross-sections⁽³²⁾ we find that in

(32) R. D. Birkhoff, "The Passage of Fast Electrons Through Matter" Encyclopedia of Physics, Vol. 34, 53, Springer (1958).

the limit of thin slabs we recapture the Landau^{(33) (2)} result. For intermediate thicknesses Eq. 15 must be evaluated numerically but fortunately in the deep penetration region the Green's function may be expressed in terms of the tabulated Airy functions. In Figs. 3-6 we give the results of calculations for the energy straggling for several thicknesses and angles; the experimental points are those of Jupiter, Lonergan, Merkel, et al.⁽³⁴⁾ It is seen that the agreement is reasonably satisfactory. It is our intention to incorporate the modifications described in the Introduction, as well as certain improvements in the analysis, into our calculations and compare with more recently obtained experimental results. However the computational procedure here outlined appears to provide a sound basis for the description of the deep penetration of electrons of intermediate relativistic energies.

(33) L. Landau, J. Phys. U.S.S.R., 8, 201, 1944.

(34) C. Jupiter, J. Lonergan, G. Merkel, private communication.

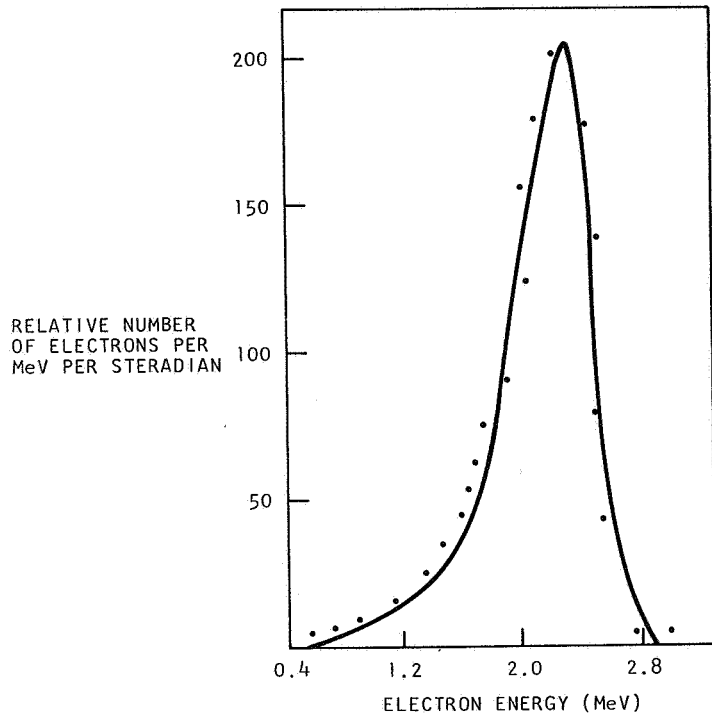


Fig. 3 Energy straggling of 4 MeV electrons through 0.181 in. Al at 0°

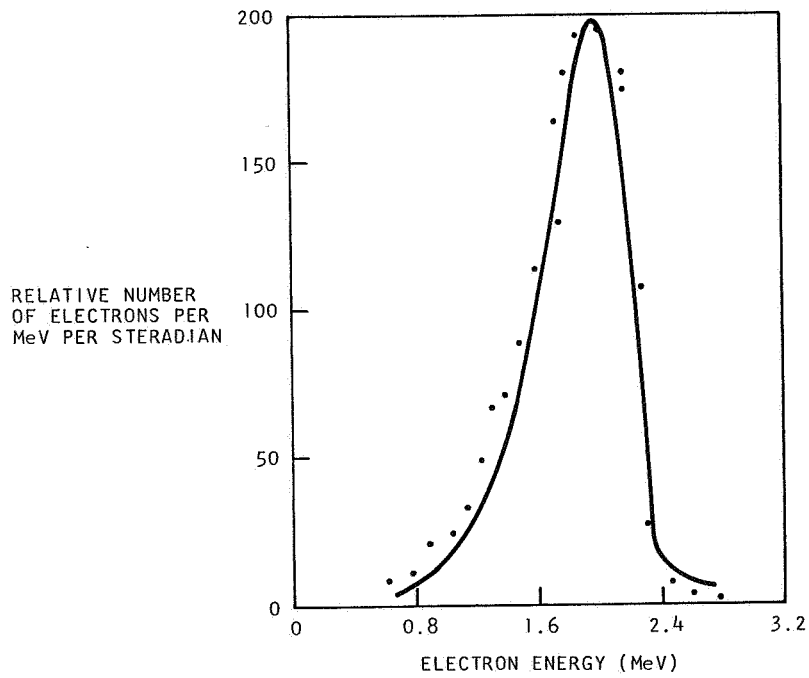


Fig. 4 Energy straggling of 4 MeV electrons through 0.181 in. Al at 30°

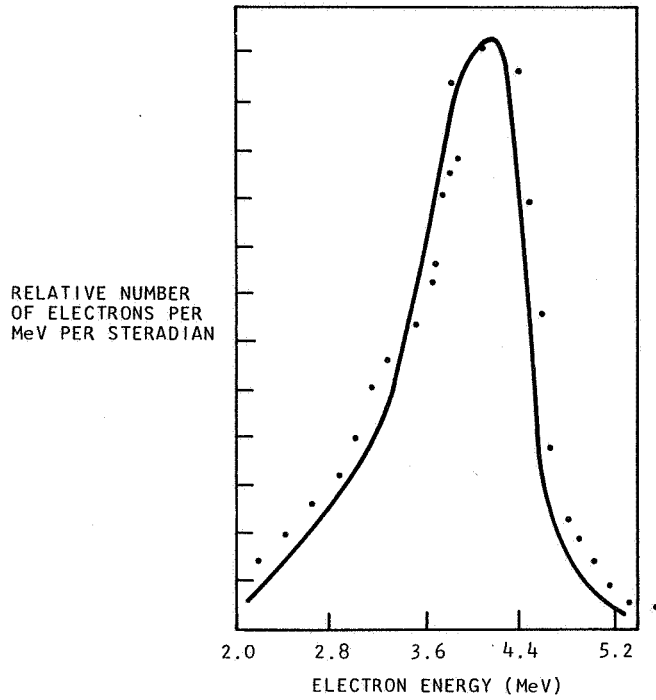


Fig. 5 Energy straggling of 8.2 MeV electrons through 0.35 in. Al at 0°

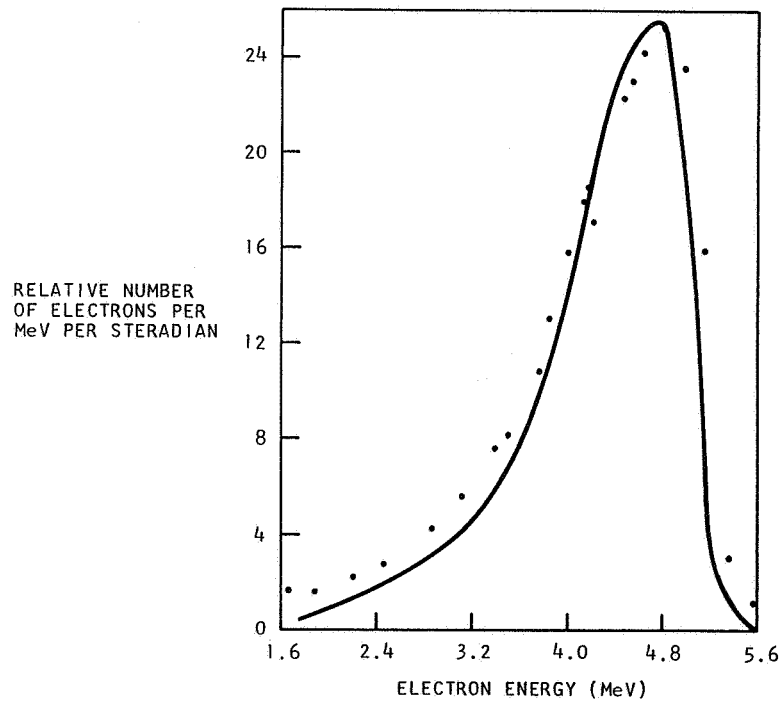


Fig. 6 Energy straggling of 8.2 MeV electrons through 0.35 in. Al at 30°

ANGULAR DISTRIBUTIONS OF THICK TARGET
BREMSSTRAHLUNG COMPARED WITH EXPERIMENT

W. WAYNE SCOTT

Chattanooga State Technical Institute, Chattanooga, Tennessee

A theoretical analysis for predicting the spectrum of bremsstrahlung which includes multiple electron scatterings as described by a random-walk procedure has previously been presented as a thesis (1965) at the College of William and Mary. At the time of the thesis presentation, there was a scarcity of experimental data, however, recent experiments conducted by the Ling-Tempco-Vought Research Center have made available data for the comparisons included within this report. Also, a semi-empirical relation to account for the discrepancy of the Bethe-Heitler equation is presented for inclusion in the thick-target relation.

INTRODUCTION

Electrons that exist in the radiation belt¹ surrounding the earth present a radiation hazard to man and equipment in space explorations. This hazard to manned space vehicles from electrons is primarily in the form of penetrating secondary radiation produced by the energy degradation of electrons in the space-vehicle wall. The radiation, designated as bremsstrahlung, results from interactions of the incoming electrons with the charged particles (nuclei or electrons) of which the vehicle wall is composed.

A vehicle wall could be treated as a thin target if, while traversing the

wall, the incident electron has only one radiative collision, suffers no significant elastic deflection, and loses no appreciable energy by ionization. However, in practice, these conditions seldom exist. Generally a space vehicle wall will be representative of a thick-target; that is, the wall will be of such a thickness that the majority of the incident electrons will lose sufficient energy to be stopped. For this case, the description of the bremsstrahlung field behind the target is a difficult problem, complicated by multiple electron scatterings, electron energy losses, photon absorption, and shower production.

Previous estimates of the bremsstrahlung spectra from thick targets for electrons with energies of the order of the rest-mass energy (0.511 MeV) have depended upon the theory developed by Kramers². However, the validity of Kramers' theory is limited in that the theory estimates the photon energy distribution integrated over all directions of the emitted photons and the theory is nonrelativistic. Estimates have also been made by Wilson³, the author of the present paper⁴, and others, but these results are also in the form of an average over the direction of photon emission and no attempt is made to account for multiple electron scattering within the target.

The recent thesis⁵ by the author was intended to provide a basic formula for approximating, with a reasonable degree of accuracy, the thick-target spectrum. This approximating capability is considered important for shielding studies since experimental data are scarce and there is a need for theoretical data over a wide electron energy and material range.

The procedure for computing the bremsstrahlung spectra is programmed in the FORTRAN (FORMula TRANslation) IV language for the IBM 7094 electronic data processing system.

THEORY OF A THICK-TARGET ANALYSIS

For a monoenergetic, monodirectional beam of electrons incident on a thick-target, a random-walk computer program for the analysis of thick-target bremsstrahlung has been generated⁵. This analysis takes into account various aspects of electron penetration and diffusion: angular deflection, energy losses, spatial propagation, and the radiative process of scattering. The large number of interactions (running into the tens of thousands) which an electron may undergo in a thick-target makes it necessary to resort to a sophisticated scheme in which many successive collisions are grouped into a single step of an artificial random-walk. The scattering probabilities for the random-walk are then obtained from pertinent analytical multiple electron scattering theories⁶ governing angular deflections and energy losses.

The random-walk scheme must provide, for each step of the random-walk, a rule for selecting an energy-loss increment $E_i - E_{i+1}$, a step length $r_i - r_{i+1}$, a change of electron direction from $(\epsilon_\alpha, \psi_\gamma)$ to $(\epsilon_{\alpha+1}, \psi_{\gamma+1})$ and a spatial displacement $\bar{r}_i - \bar{r}_{i+1}$. A great variety of schemes are possible, which differ with regard to the input parameters and the necessary amount of computing time. The rules used for the random-walk sampling presented herein have been discussed in some detail by Berger⁷.

For this analysis a continuous slowing-down approximation is used to select a constant electron energy loss $\Delta E = E_i - E_{i+1}$; that is, the thick target is subdivided into a number of thin strips in each of which an electron energy loss ΔE occurs. For example, one may consider a target whose thickness corresponds to the range of a 1-MeV electron (approximately 0.5 g/cm^2 of aluminum). The arbitrary selection can be made to subdivide the target into 20 thin targets each of which corresponds to an energy loss of 0.05 MeV.

The length t_i in each thin target is a function of the energy-loss increment according to the following relation

$$|t_i - t_{i+1}| = \int_{E_i}^{E_{i+1}} \frac{dE}{\frac{1}{\rho} \frac{dE}{dt}} \quad (1)$$

where $\frac{dE}{dt}$ is the energy loss per centimeter of path length in the target.

A simplifying assumption is made for the spatial displacement $\bar{r}_i - \bar{r}_{i+1}$. Essentially the spatial displacement parameter \bar{r} will be reduced from three dimensions to one dimension; for example, the spatial position of the electron is considered to be along the projected path of the initially incident electron at all times and no lateral deflection in position is to be considered at each scattering. This assumption is reasonable since the total path length of the electron within the target is itself relatively small in comparison with the distance between the target and detector position. Thus, only a change of direction from $(\epsilon_\alpha, \psi_\gamma)$ to $(\epsilon_{\alpha+1}, \psi_{\gamma+1})$ is considered to influence the bremsstrahlung spectrum.

The present analysis differs from the usual random-walk method. The random-walk method consists of sampling many electron trajectories (called case histories), starting each electron with initial energy E_0 , and following it until it comes to rest. In the present analysis, the electrons are forced to assume predetermined or preset directions (different combinations of polar angles $\epsilon_\alpha, \psi_\gamma$). Along each of the electron trajectories the change in the polar angles, at each scattering, is chosen by some arbitrary (unweighted) technique. Having chosen the polar angles, the result is then multiplied by the appropriate scattering probability for this chosen direction. It is in this particular sense of scoring that the present analysis differs from the usual random-walk method. The appropriate probability

for the electron being scattered at each set of polar angles will be determined by the use of the Goudsmit-Saunderson theory.

In summary of the previous discussion, it can be said that the electron is presumed to be normally incident on the first of a series of thin targets with energy E_0 . The bremsstrahlung production in the first thin target is then calculated. The electron direction is then changed and the bremsstrahlung production is again determined for the given parameters. The changing of electron direction and the calculation of bremsstrahlung production is continued until all the predetermined angles have been assumed. The electron is then considered to be entering into the second thin strip at a normal angle of incidence with an energy of $E_0 - \Delta E$. This procedure of changing the angles and calculating the bremsstrahlung production is again repeated. This sequence of events (random-walk steps) is continued until the electron has been brought to rest. The thick-target spectrum is then considered to be the sum of the radiation contributions from each thin strip.

DERIVATION OF THE THICK-TARGET EQUATION

It is possible to approximate the angular distribution of bremsstrahlung behind a thick-target by the superpositioning of several complex processes. These processes are: (1) Radiation of electrons in thin targets as predicted by the Bethe Heitler theory⁸ ($d\sigma/dk d\Omega$), (2) Electron penetration into a medium which includes: (a) multiple-electron scattering as predicted by Goudsmit-Saunderson⁶ (P_e), (b) electron backscatter out of the target ($1-W$), (c) nonlinear electron energy losses⁹ (dE/dx), (d) electron-electron bremsstrahlung [$Z(Z+1)$], (3) The absorption and buildup of photons in the target [$B \exp(-\mu x / \cos \phi)$] and (4) a semi-empirical correction (ξ).

Consider an electron of normal incidence on a thick-target where the target has been subdivided into thin strips as shown in figure 1. Within each thin target the electron will travel in some direction defined by the two polar angles ϵ and ψ . A schematic representation of a radiative scattering in any slab i is shown in figure 2. In this figure, ϵ is the angle between the electron velocity vector in the i th slab and the preceding electron direction. The angle θ_0 is the angle between the electron velocity vector and the emitted photon. Note that only photons traveling at an angle ϕ_d with respect to the incident electron direction will reach the detector.

For a thick target which consists of many thin targets there will occur a scattering, typical of the scattering shown in figure 3, in each thin target. Figure 3 is representative of the present analysis of the multiple electron scatterings that occur in a thick target. Again as in figure 2, ϵ and ψ are the polar angles with ϵ representing the angle between the incident electron direction and the electron velocity vector in the i th slab. Recall that the assumption is made that the lateral displacement of the electron within the target is very small compared with the distance between the target and detector and has negligible effect on the thick-target spectrum. Thus the multiple scattering is considered to influence the spectrum only through changes in the electron direction with respect to the initially incident electron direction.

The path shown in figure 3 is certainly not unique. In other words, the path of the electron in the target is random; therefore, it is necessary to consider all directions of electron scattering in each slab relative to the initial electron direction. Within each slab all possible combinations of ϵ and ψ (fig. 3) are to be considered along with the representative probability of the electron having each particular combination of angles.

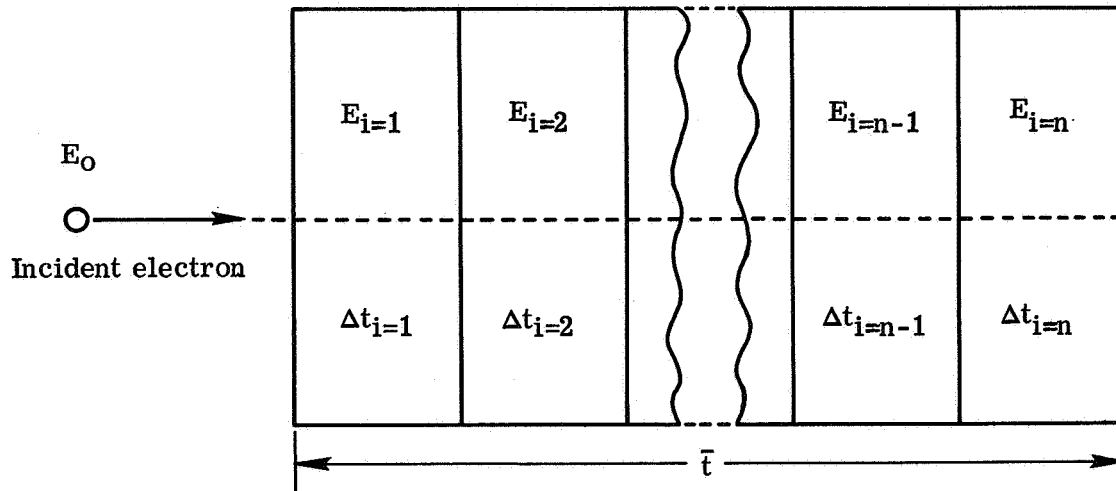


Fig. 1 Thick-target subdivision

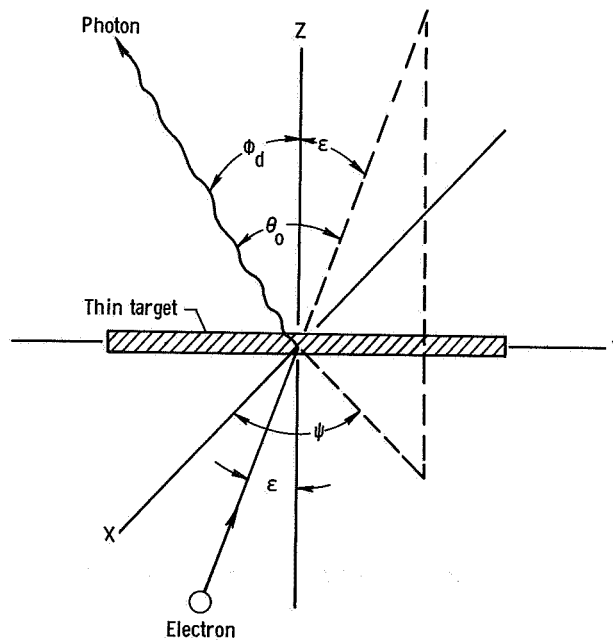


Fig. 2 General radiative scattering in thick-target

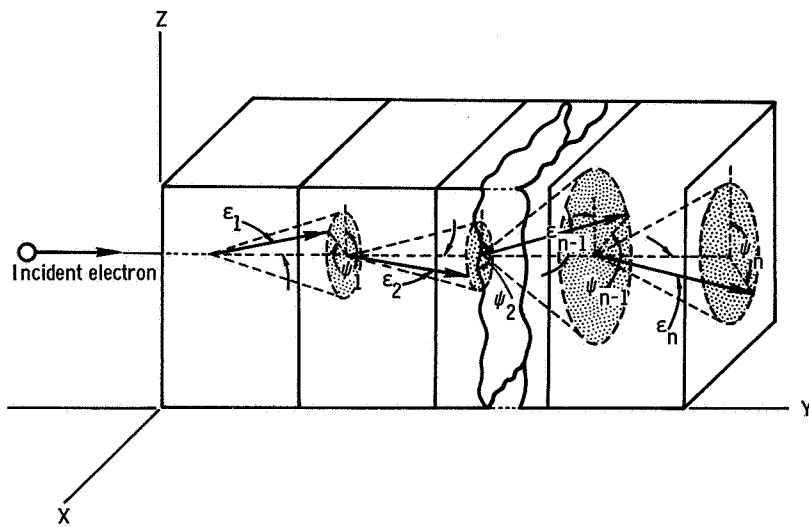


Fig. 3 Multiple electron scattering in thick-target

Now consider for each thin target a cylindrical differential element of volume dV having a normal unit area and length Δt (slab thickness) relative to the initial electron direction. The total probability for the emission of a photon of energy k in the direction θ_0 in each thin strip for a specified

ϵ_α , ψ_γ , and ϕ_d is

$$\left[\frac{d\sigma}{dk d\Omega}(E_i, k, \theta_0) \Delta t N_a \right]_i \quad (2)$$

where N_a is the number of atoms/cm³. The photon energy release is dependent upon the angles ϵ , ψ , and ϕ_d , where these angles are related by the equation

$$\cos \theta_0 = \cos \epsilon_\alpha \cos \phi_d + \sin \epsilon_\alpha \sin \phi_d \cos \psi_\gamma \quad (3)$$

Expression (2) is an unweighted function with respect to the electron direction. The probability of the photon energy release must be correlated with the probability (weighted function) of the electron having the specific values of ϵ_α and ψ_γ . This scattering probability P_ϵ is expressed as

$$P_\epsilon = \sum_{l=0}^{\infty} \left(l + \frac{1}{2} \right) \exp \left[- \int_0^t G_l(t') dt' \right] P_l(\cos \epsilon) \quad (4)$$

where

$$G_l(t') = 2\pi N \int_0^\pi \sigma(\theta, t') \left[1 - P_l(\cos \theta) \right] \sin \theta d\theta \quad (5)$$

and

- N number of atoms per unit volume
- t path length traversed by electron
- $\sigma(\theta, t')$ single-scattering cross section, whose dependence on the electron energy is expressed in the continuous slowing-down approximation, through the path length t

Hence,

$$P_{\epsilon} = \left[P_{\epsilon}(E_i, \epsilon_{\alpha}) \right]_i \quad (6)$$

Thus for one electron direction of ϵ_{α} and ψ_{γ} the probability of the generation of a photon of energy k that will reach the detector at an angle Φ_d is the product of the two probabilities

$$\left[\frac{d\sigma}{dk d\Omega}(E_i, k, \theta_0) \Delta t N_a P_{\epsilon}(E_i, \epsilon_{\alpha}) \right]_i \quad (7)$$

For all angles of electron direction within each slab, that is, for ϵ varying from 0 to π and ψ varying from 0 to 2π , the total radiative probabilities in slab i are

$$\left(\frac{d\sigma}{dk d\Omega} \right)_i = \sum_{\alpha=0}^{\beta} \sum_{\gamma=0}^{\delta} \left[\frac{d\sigma}{dk d\Omega}(E_i, k, \theta_0) \Delta t N_a P_{\epsilon}(E_i, \epsilon_{\alpha}) \sin \frac{\alpha\pi}{\beta} \frac{\pi}{\beta} \frac{2\pi}{\delta} \right]_i \quad (8)$$

where

$\alpha, \beta, \gamma, \delta$ integers

$$\epsilon_{\alpha} = \frac{\alpha\pi}{\beta}$$

$$\Delta\epsilon = \frac{\pi}{\beta}$$

$$\Delta\psi = \frac{2\pi}{\delta}$$

It is now necessary to sum these probabilities over the electron energy (or the corresponding thickness of the target necessary to bring the electron to rest.) In theory it is possible to determine the differential path length of an electron within an absorber with the aid of the electron energy loss per unit path length equation (dE/dt). The differential path length is expressed as

$$dt = \frac{dE}{\frac{dE}{dt}} \quad (9)$$

or

$$\Delta t = \frac{\Delta E}{\frac{dE}{dt}} \quad (10)$$

where

$$\Delta E = \frac{E_0}{n} \quad (11)$$

Substituting equation (10) into equation (8) and summing over i slabs in terms of the electron energy give

$$\left(\frac{d\sigma}{dk d\Omega} \right)_{\text{thick target}} = \sum_{i=1}^n \sum_{\alpha=0}^{\beta} \sum_{\gamma=0}^{\delta} \left(\frac{d\sigma}{dk d\Omega} \right)_{\text{thin target}} (E_i, k, \theta_0) \frac{N_a}{\frac{dE}{dt}} P_{\epsilon}(E_i, \epsilon, \alpha) \sin \frac{\alpha\pi}{\beta} \frac{\pi}{\beta} \frac{2\pi}{\delta} \frac{E_0}{n} \quad (12)$$

Only electrons with energies greater than k can create photons of energy k ; thus, a lower limit is placed on the energy summation. Rewriting and regrouping equation (12) and expressing the electron energy in terms of the total electron energy give

$$\left(\frac{d\sigma}{dk d\Omega} \right)_{\text{thick target}} = N_a \int_{k+m_0c^2}^{E_0} \frac{dE}{dt} \int_0^{2\pi} \int_0^{\pi} \left(\frac{d\sigma}{dk d\Omega} \right)_{\text{thin target}} P_{\epsilon} \sin \epsilon d\epsilon d\psi \quad (13)$$

The additional processes of photon absorption and buildup, electron-electron bremsstrahlung, and backscattering can now be included in equation (13) as follows:

$$\left(\frac{d\sigma}{dk d\Omega}\right)_{\text{thick target}} = \xi N_a Z(Z+1)(1-W) \int_{k+m_0c^2}^{E_0} \left[\frac{e^{-\mu_m t_x / \cos \phi_d}}{Be} \frac{1}{\frac{dE}{dt}} dE \int_0^{2\pi} \int_0^\pi \left(\frac{1}{Z^2} \frac{d\sigma}{dk d\Omega}\right)_{\text{thin target}} P_\epsilon \sin \epsilon d\epsilon d\psi \right] \quad (14)$$

where

$e^{-\mu_m t_x / \cos \phi_d}$ photon absorption in target

B photon buildup

$Z(Z+1)$ approximate correction for electron-electron bremsstrahlung

$1 - W$ correction for electron backscattering out of target

ξ semi-empirical correction (to be discussed later in report)

Intensity is now defined as the photon energy k multiplied by the number of photons

$\left(\frac{d\sigma}{dk d\Omega}\right)_{\text{thick target}}$ with energy k . Thus, expressing equation (14) in terms of intensity

and replacing N_a by $N_A \rho / A$ give

$$\left(k \frac{d\sigma}{dk d\Omega}\right)_{\text{thick target}} = \xi \frac{N_A}{A} Z(Z+1)(1-W) \int_{k+1}^{E_0} \left[\frac{e^{-\mu_m t_x / \cos \phi_d}}{Be} \frac{1}{\frac{dE}{\rho dt}} dE \int_0^{2\pi} \int_0^\pi \left(\frac{k}{Z^2} \frac{d\sigma}{dk d\Omega}\right)_{\text{thin target}} P_\epsilon \sin \epsilon d\epsilon d\psi \right] \quad (15)$$

where the integration

$$\int_0^{2\pi} \int_0^\pi P_\epsilon \sin \epsilon d\epsilon d\psi$$

is normalized to one in each slab. Equation (15) now represents an expression for approximating the angular distribution of bremsstrahlung behind a thick target.

RESULTS AND DISCUSSION

Because there exists a scarcity of experimental thick-target data, a complete comparison between theory and experiment over a wide range of electron energies and materials cannot be made. However, some experimental data for thick aluminum and iron targets have been obtained by the LTV Research Center¹⁰ and are used herein for comparison with theoretical calculations.

The comparisons of the theoretically predicted results (eq.(15)) with the experimental data for aluminum and iron targets and electron energies of 0.5 and 1.0 MeV are shown in figures 4-7. These figures represent the general trend of all the comparisons made. Model one refers to having used equation (15) without the semiempirical correction ξ and model two is with the semiempirical correction included.

The discrepancy that exists between model one results and experimental data is expected, inasmuch as the Born approximation technique is used in the theoretical thick-target model. Since no exact analytic expression exists for the thin-target cross section, the logical approach is to correct for the discrepancy in the Bethe-Heitler relation with a semiempirical correction.

A semiempirical relation of the form

$$\xi(k, T_0, \theta_0) = \exp \left\{ (k/T_0 - 0.4) \left| \frac{\theta_0 - 10}{\theta_0} \right| \right\}$$

was obtained by the trial and error method by many comparisons of model one results and experimental data. The correction factor (ξ) is the function that best adjusts model one results to fit the experimental data over a wide range of energies and angles. It is anticipated that this correction will hold true over an extended range of materials and energies.

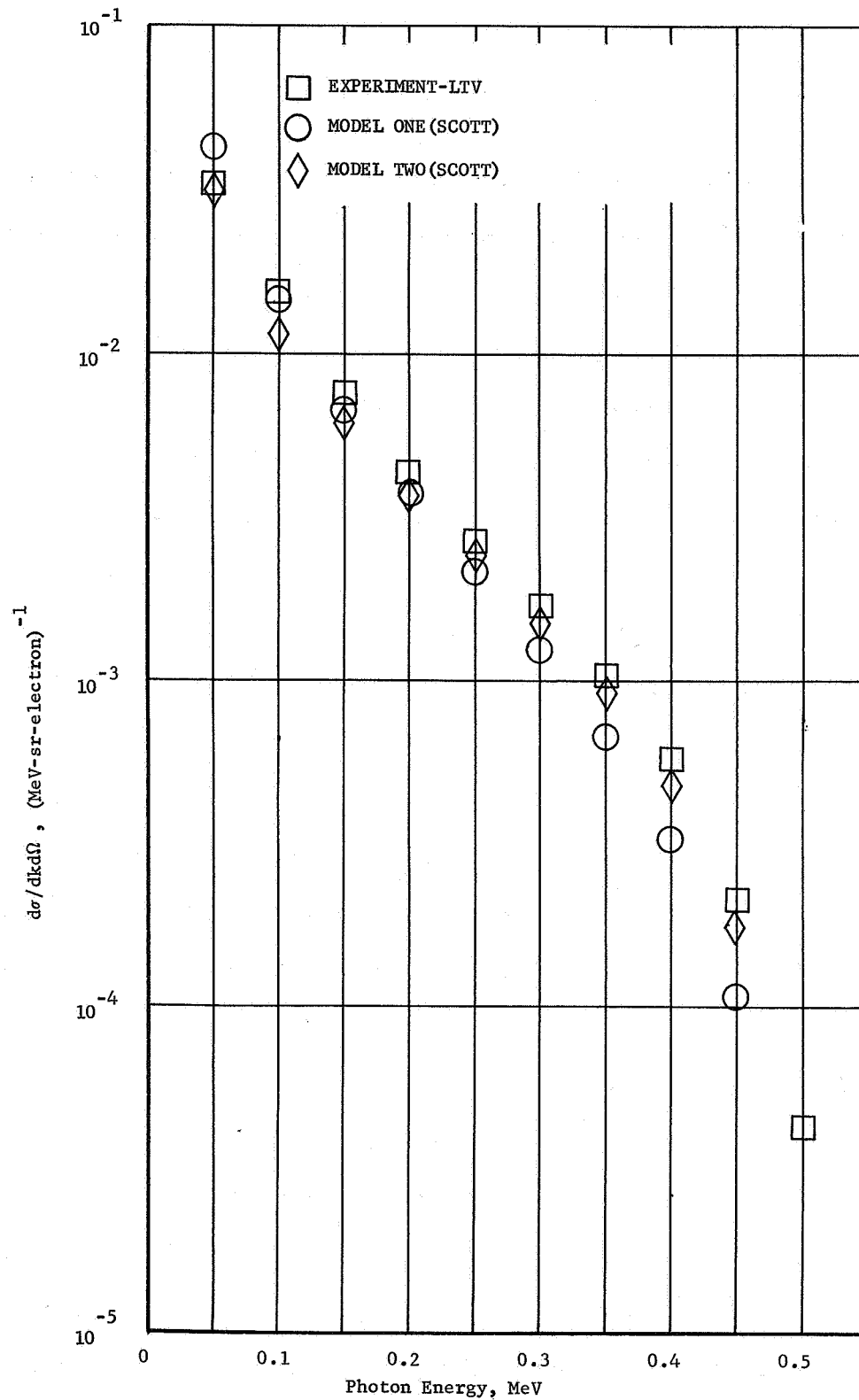


Fig. 4 Thick-target Bremsstrahlung Spectrum in aluminum for an incident electron energy of 0.5 MeV and photon emission angle of 0 degrees

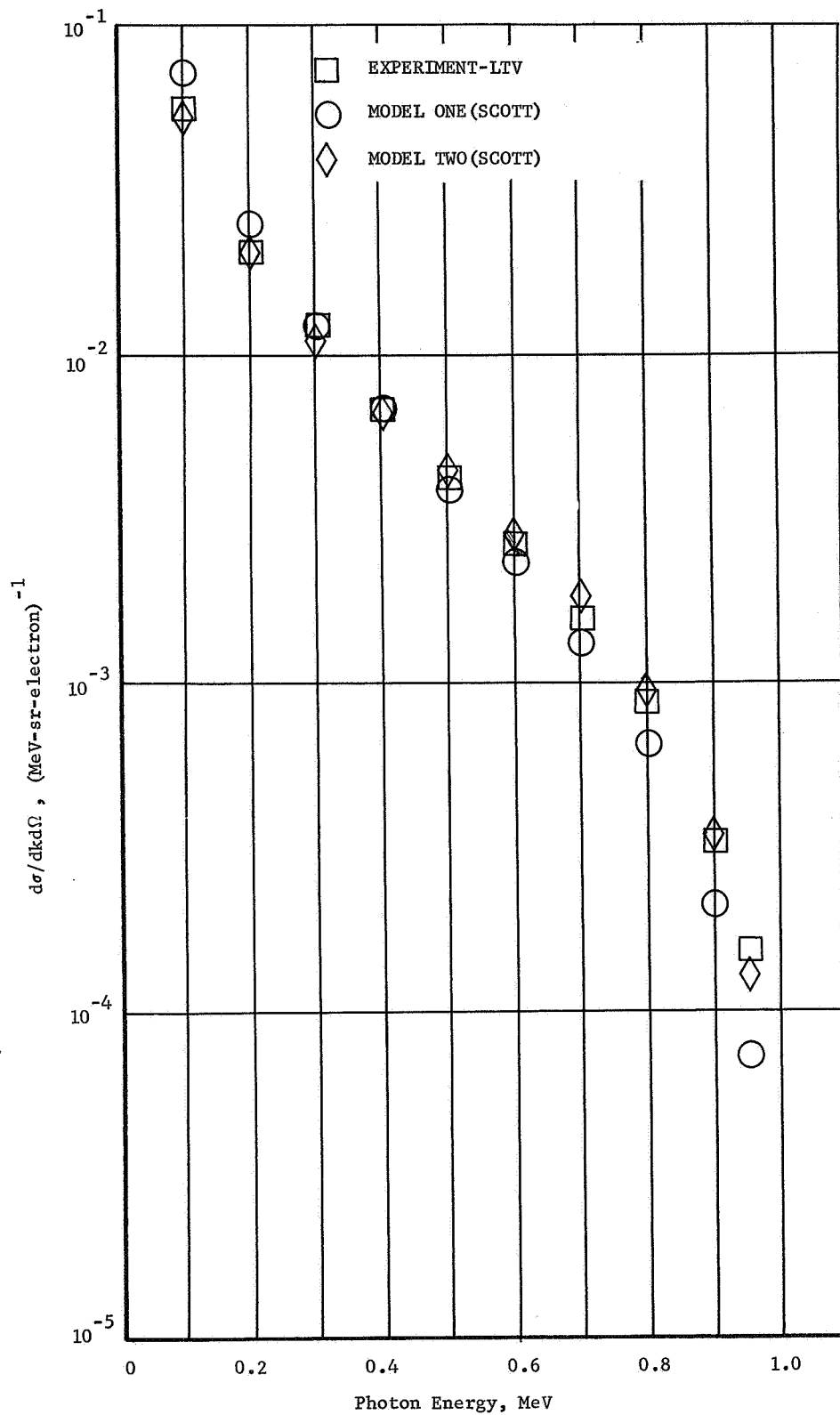


Fig. 5 Thick-target Bremsstrahlung Spectrum in aluminum for an incident electron energy of 1.0 MeV and photon emission angle of 0 degrees

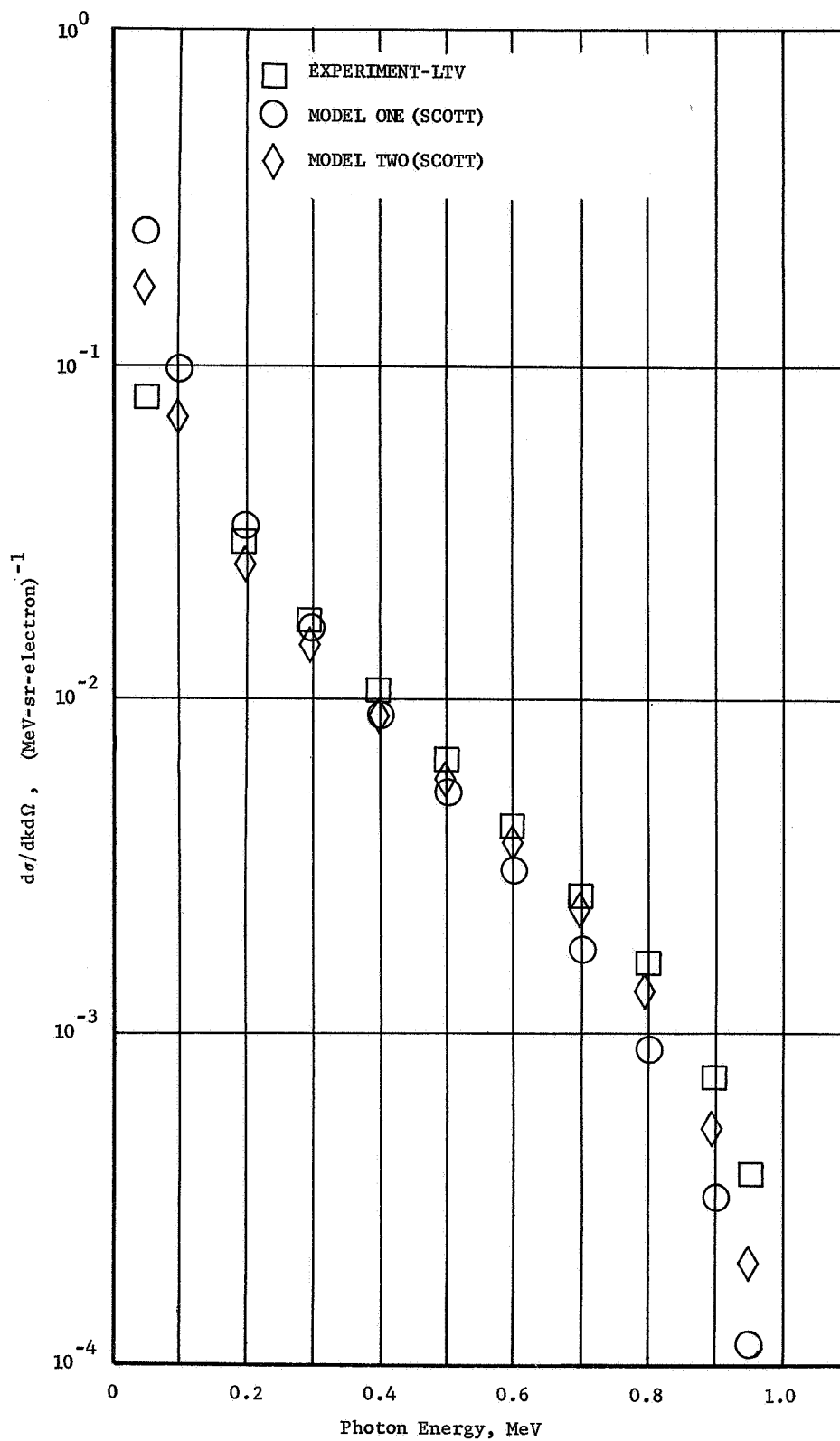


Fig. 6 Thick-target Bremsstrahlung Spectrum in iron for an incident electron energy of 1.0 MeV and photon emission angle of 0 degrees

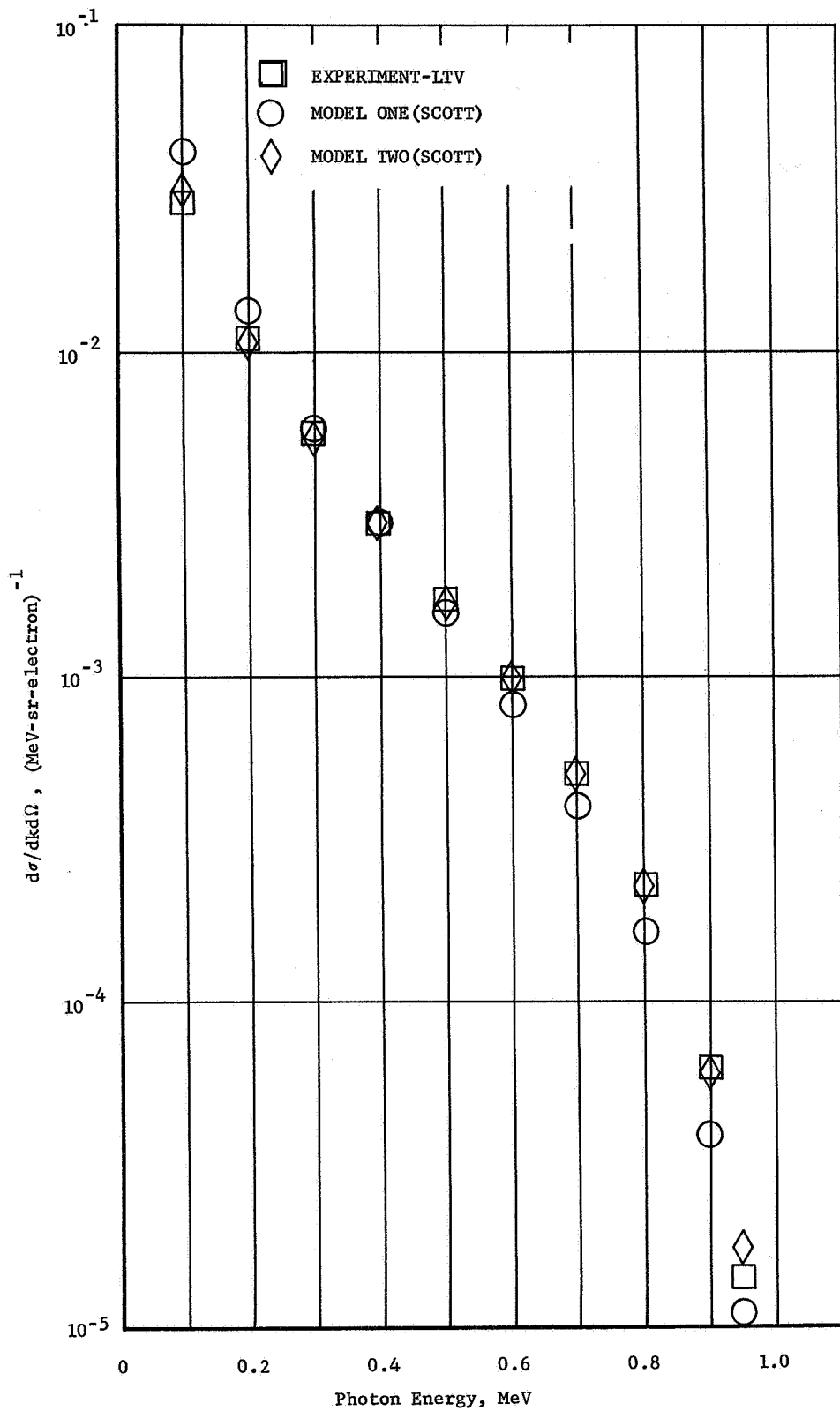


Fig. 7 Thick-target Bremsstrahlung Spectrum in iron for an incident electron energy of 1.0 MeV and photon emission angle of 60 degrees

CONCLUDING REMARKS

The complication of multiple electron scattering within a thick absorber makes a rigorous analytical solution difficult for the prediction of the angular distribution of bremsstrahlung from completely stopped electrons. Therefore, an approximating formula has been presented for predicting the thick-target spectrum which is differential both in photon energy and angle of emission. This approximation is derived from the summation of the contribution from successive thin strips into which the absorber is divided. The use of the thin target Born approximation cross section for deriving the thick-target expression introduces an error that is presently unavoidable.

The comparisons between the results obtained from the theory derived herein and experimental data are favorable; thus, it can be concluded that the approximating formula for the angular distribution of electron bremsstrahlung in thick-targets is valid and is an improvement over the usual straight-through theory.

REFERENCES

- (1) Hess, W. N.: The Artificial Radiation Belt Made on July 9, 1962. *J. Geophys. Res.*, vol. 68, no. 3, Feb. 1, 1963, pp. 667-683.
- (2) Kramers, H. A.: On the Theory of X-Ray Absorption and of the Continuous X-Ray Spectrum. *Phil. Mag.*, vol. 46, No. 275, Nov. 1923, pp. 836-871.
- (3) Wilson, Richard: A Formula for Thick Target Bremsstrahlung. *Proc. Phys. Soc. (London)*, vol. 66, pt. 7, no. 403 A, July 1, 1953, pp. 638-644.
- (4) Scott, W. Wayne: Electron-Bremsstrahlung Differential Cross Sections for Thin and Thick Targets. NASA TN D-2659, 1965.
- (5) Scott, W. Wayne: A Formula for Predicting the Angular Distribution of Thick-Target Bremsstrahlung. Thesis. The College of William and Mary in Virginia, 1965.
- (6) Goudsmit, S.; and Saunderson, J. L.: Multiple Scattering of Electrons. *Phys. Rev., Second ser.*, vol. 57, no. 1, Jan. 1, 1940, pp. 24-29.
- (7) Berger, Martin J.: Monte Carlo Calculation of the Penetration and Diffusion of Fast Charged Particles. *Methods in Computational Physics, Vol. 1--Statistical Physics*, Berni Alder, Sidney Fernbach, and Manuel Rotenberg, eds., Academic Press, 1963, pp. 135-215.
- (8) Heitler, W.: *The Quantum Theory of Radiation*. Third ed., Clarendon Press (Oxford), 1954, pp. 242-256 and 418.

(9) Bethe, Hans A.; and Ashkin, Julius: Passage of Radiations Through Matter. Experimental Nuclear Physics, Vol. I, E. Segre, ed., John Wiley and Sons, Inc., c. 1953, pp. 166-357.

(10) Dance, William E.; Baggerly, Leo L.; Rester, David H.; and Rainwater, Walter J., Jr.: Investigations of Electron Interactions With Matter. NASA CR-334, 1965.

Electron Distribution in a
Slowing-Down Medium

Dong H. Nguyen
Nuclear Engineering Program
The University of Texas
Austin, Texas

Lawrence M. Grossman
Department of Nuclear Engineering
University of California
Berkeley, California

This paper presents a novel method of solution to the Lewis' transport equation of the multiple scattering problem. (1) In particular, we undertake to obtain the electron distribution in space, energy and direction of motion resulting from a monoenergetic isotropic plane source in an infinite and homogeneous medium. The knowledge of the detailed electron distribution would yield several physical quantities of interest. For example, the range is obtained as the deepest penetration at which this distribution vanishes; the space-energy distribution results from the integration over all directions of motion; multiplying the space-energy distribution by the stopping power and integrating the result over all energies yield the space-dependent energy deposition by the penetrating electrons; finally, the ion production rate by slowing down electrons can be calculated by dividing the energy deposition by their w -value. The objective of the present paper is to present our method of solution and to demonstrate its validity in the calculation of the electron range-energy relationship.

Prior to 1950, few attempts were made to calculate electron

detailed distribution taking into account both energy loss and direction changes. Instead, simpler situations were studied, in which one or another effect was neglected. A discussion of these partial problems has been undertaken by Fano (2) and Spencer (3). When H. W. Lewis (1) proposed his electron transport equation in 1950, he provided a basis for the systematic theoretical treatment of the electron penetration taking into account both effects of scattering and slowing down. The first attempt (3) to construct spatial distributions from the knowledge of the first few moments met with failure, due to the dependence of the deep penetration trend on higher order moments, which were difficult to obtain. In 1955, Spencer (3) combined arguments connected with the Wick-type asymptotic calculation and a "function-fitting" technique similar to those used in x-ray penetration problems, to successfully construct the electron spatial distribution for an infinite medium. Later, Spencer (4) used a better device to treat the deep penetration problem, by deriving a second order differential equation governing the spatial dependence of the higher order moments. In 1957, Meister (5) studied the problem of electron transmission and self-absorption in metallic foils. Essentially, Meister distinguished two slowing-down regions: in the first, angular deflections by scattering were neglected, thereby removing the "scattering integral" in the transport equation; in the second, the slowing down was assumed to be a diffusion process, for which the distribution was weakly dependent on angle and the age-diffusion approximation might be used.

Our method of solution makes use of the small scattering angle approximation to reduce the Lewis' equation into a first order partial differential equation in three variables, which can be solved by the method of "characteristics." The small angle ap-

proximation is utilized here in a different way than in Snyder and Scott's work (6), not only in mathematical techniques but also in our inclusion of the effect of slowing down. The solution thus obtained is a detailed distribution in energy, space and directions of motion, which yields an energy-range relationship in excellent agreement with measurements for aluminum.

1. The Electron Transport Equation and Nuclear Scattering Cross Sections

In a plane geometry with azimuthal symmetry about the coordinate z , the Lewis' equation becomes (3,7)

$$-\frac{\partial f(x, \mu, t)}{\partial t} + \mu \frac{\partial f}{\partial x} = \int_{-1}^1 d\mu' \int_0^{2\pi} d\varphi' K(t, \mu_0) [f(x, \mu', t) - f(x, \mu, t)] + S(x, \mu, t) \quad (1)$$

where the following definitions have been used:

t = reduced residual path length, i.e., residual path length of an electron of energy T , $s(T)$, measured in units of total path length s_0 .

$$= s(T)/s_0 \quad (2)$$

$$s(T) = \int_0^T \frac{dT'}{(dT'/ds)} \quad (3)$$

dT'/ds = the energy loss per unit length, or stopping power.

x = the spatial coordinate measured in units of s_0
 $= z/s_0$.

μ', μ = cosines of the angles made between the initial and final electron directions of motion and the z-axis, respectively.

$2\pi f(x, \mu, t) d\mu dt$ = the electron distribution at a point x , with reduced residual path lengths lying in dt about t and with directions of motion lying in the differential solid angle $2\pi d\mu$ about direction $\theta = \cos^{-1} \mu$.

$S(x, \mu, t)$ = an external source.

$K(t, \mu_0)$ = the scattering kernel
 $= s_0 N \sigma(t, \mu_0)$

N = atomic density of the scattering medium.

$\sigma(t, \mu_0)$ = the nuclear scattering cross section per atom for deflecting an electron with residual path length t from an initial direction (μ', φ') to a final direction (μ, φ) through an angle whose cosine is $\mu_0(\mu, \varphi; \mu', \varphi')$.

$$\mu_0(\mu, \varphi; \mu', \varphi') = \mu\mu' + (1-\mu^2)^{\frac{1}{2}}(1-\mu'^2)^{\frac{1}{2}}\cos(\varphi-\varphi')$$

Eq. (1) takes into account the energy loss by simply regarding the energy of the particle as a function of its residual path length. This is achieved through the definition (3) which establishes a relation between the residual path length and the kinetic energy of the electrons, assuming that the latter lose their energy continuously. For light stopping materials and for electrons having kinetic energy of a few Mev, the radiation loss is negligible

and the stopping power is due mainly to electron-electron inelastic collisions described by the Bethe-Block equation

$$-\frac{dT}{ds} = \frac{2\pi Ze^4}{mv^2} N \left\{ \ln \frac{mv^2 T}{2I^2 (1-\beta^2)} - \ln 2 (2\sqrt{1-\beta^2} - 1 + \beta^2) + \frac{1}{8} (1 - \sqrt{1-\beta^2})^2 + 1 - \beta^2 \right\}; \quad (4)$$

$$\beta = v/c$$

where Z and N are the atomic number and atomic density of the stopping material, respectively and I is the average excitation potential.

The calculation of electron nuclear scattering cross sections without atomic or nuclear excitation has been reviewed by Motz, Olsen and Koch (8). The most accurate theoretical scattering cross section by "point nuclei" is given by the Mott-exact formula, which has been calculated by Dogget and Spencer (9) and Sherman (10). Their results are tabulated in the form of the ratio $B(Z, T, \mu_0)$ of Mott-to-Rutherford cross sections for various atomic numbers Z , initial energy T and scattering angle $\theta_0 = \cos^{-1} \mu_0$, i.e.

$$B(Z, T, \mu_0) = \frac{\sigma(T, \mu_0)}{\sigma_R(T, \mu_0)} \quad (5)$$

where

$$\sigma_R(T, \mu_0) = \frac{Z^2 e^4}{m^2 c^4} \frac{(1-\beta^2)}{\beta^4} \frac{1}{(1-\mu_0)^2} \quad (6)$$

is the Rutherford cross section. With the screening factor $\eta(T)$ included, the nuclear scattering cross section can be written as:

$$\sigma(T, \mu_0) = \frac{Z^2 e^4}{m^2 c^4} \frac{(1-\beta^2)}{\beta^4} \frac{B(Z, T, \mu_0)}{[1-\mu_0+2\eta(T)]^2} \quad (7)$$

Based on the Thomas-Fermi model of the atomic structure, we have

$$\eta(T) = \frac{1}{4} \frac{Z^{1/3}}{.885 \times 137} \frac{(mc^2)^2}{T(T+2mc^2)} \left\{ 1.13 + 3.76 \left(\frac{Z}{137} \right)^2 \frac{(T+mc^2)^2}{T(T+2mc^2)} \right\} \quad (8)$$

Because the exact formula (7) does not readily lend itself to analytic calculations, a simpler representation for the nuclear scattering cross section will be introduced. This can be done satisfactorily for small scattering angles for which the Mott-exact cross section is known to approach the Rutheford formula, so that the ratio $B(Z, T, \mu_0)$ approaches unity. We rewrite Eq. (7) as

$$\sigma(T, \mu_0) = \frac{Z(Z+1)}{4\pi} \frac{(1-\beta^2)}{\beta^4} \frac{B(Z, T, \mu_0)}{[1-\mu_0+2\eta(T)]^2} \quad (\text{barns}) \quad (9)$$

where the factor $Z(Z+1)$ replaces Z^2 in attempt to account for the scattering by atomic electrons and where we have used the definition $\frac{4\pi e^4}{m^2 c^4} = 1$ barn. We now approximate Eq. (9) by the expression:

$$\tilde{\sigma}[t(T), \mu_0] = \frac{Z(Z+1)}{4\pi} \frac{\bar{C}}{t} \frac{B(Z, T, \mu_0)}{[1 - \mu_0 + 2\bar{\eta}]^2} \quad (10)$$

where the parameters \bar{C} and $\bar{\eta}$ are to be adjusted so that Eq. (10) best approximates Eq. (9) as follows. $\bar{\eta}$ is first evaluated from Eq. (8) at an average energy, \bar{T} , so chosen as to obtain the best results for cross sections in the energy range of interest. Table I shows that \bar{T} decreases weakly with increasing Z for the electron energy up to a few Mev. The parameter \bar{C} can be next calculated by a more systematic way. Essentially we would like to achieve the equality between Eq. (9) and Eq. (10), so that exactly:

$$C(T, \mu_0) = \frac{(1-\beta^2)}{\beta^4} t(T) \frac{(1-\mu_0 + 2\bar{\eta})^2}{(1-\mu_0 + 2\eta(T))^2}$$

A plot of C versus T for small scattering angles yields a slowly-varying curve for $T > 0.1$ Mev and so, the approximation (10) is effected by taking an average \bar{C} .

We shall not attempt to justify theoretically the approximation procedure described above. Instead, we compare Eq. (10) with Eq. (9) for small-angle scattering in several slowing down media (Gold, Aluminum, Argon; Figs. 1 through 3). For Gold, we have also used the results of Lin's calculations (11) of the Mott-exact formula with screened nuclei.

Table I
The Parameters \bar{C} and \bar{T} in Eq. (10)

| Materials | Atomic Number Z | \bar{T} (Mev) ^(a) | \bar{C} ^(a) |
|-----------|-----------------|--------------------------------|--------------------------|
| Neon | 10 | .6 | .1318 |
| Argon | 18 | .6 | .1220 |
| Aluminum | 13 | .55 | .1318 |
| Copper | 29 | .55 | .1283 |
| Gold | 79 | .5 | .1143 |
| Uranium | 92 | .5 | .1000 |

(a) Electron initial energy: 1.3 Mev.

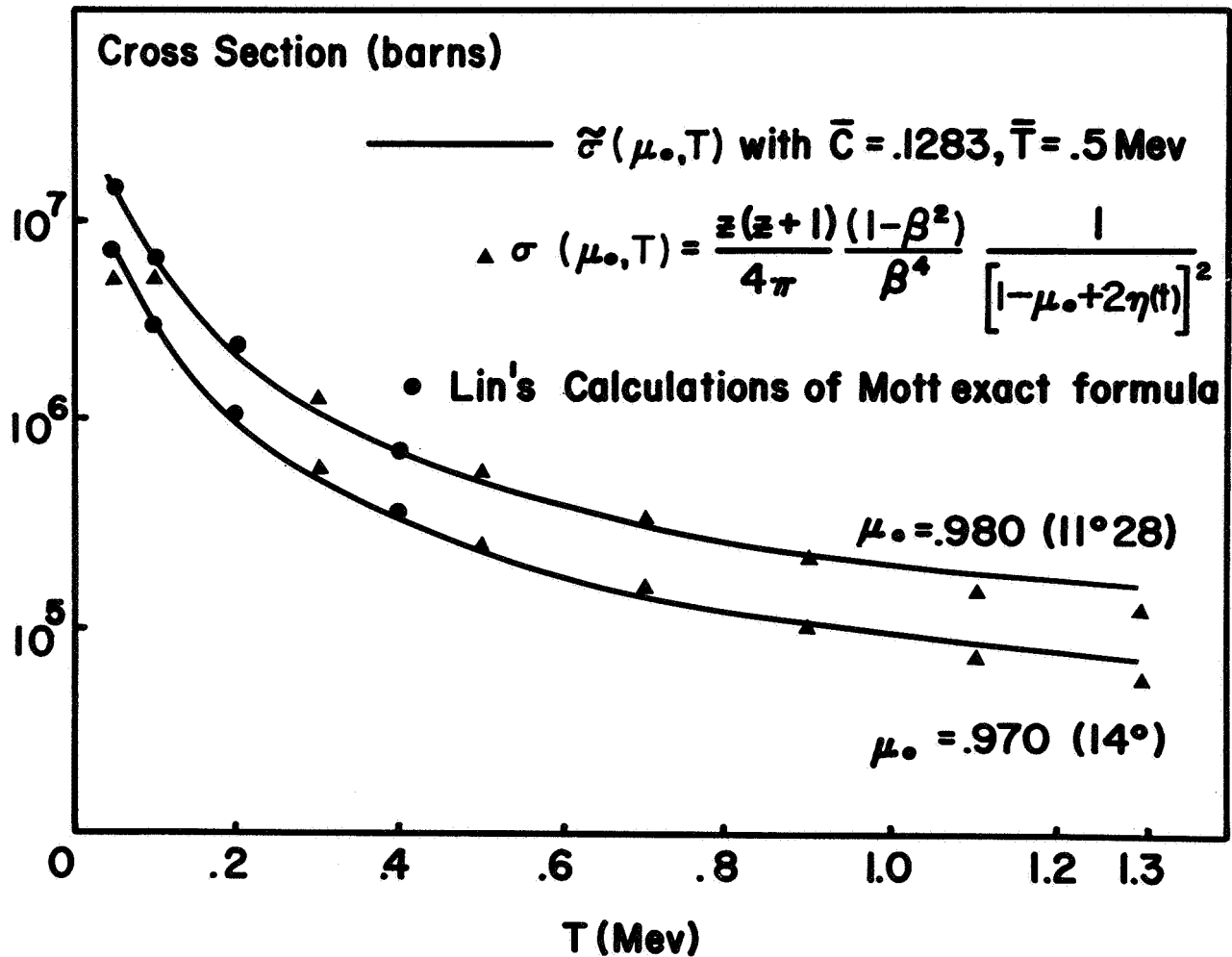


Figure 1. Nuclear scattering cross section for Gold

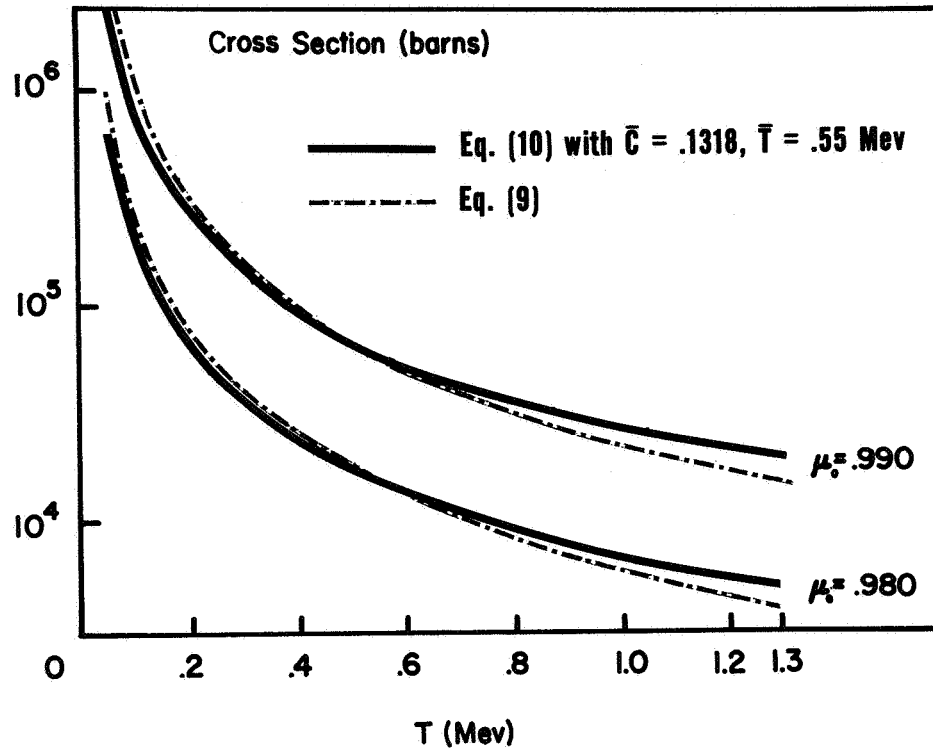


Fig. 2 Nuclear scattering cross section for Aluminum

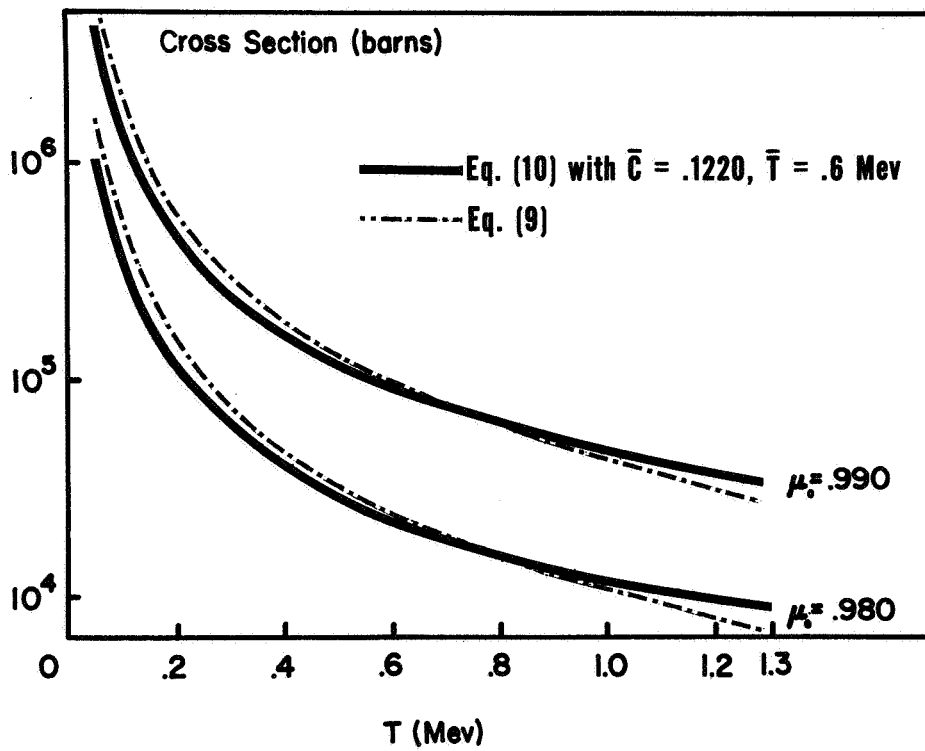


Fig. 3 Nuclear scattering cross section for Argon

2. Reduction of the Transport Equation to a Linear First-Order Partial Differential Equation

The exact scattering kernel in Eq. (1) is

$$K(t, \mu_0) = \frac{S_0 NZ(Z+1)}{4\pi} \frac{(1-\beta^2)}{\beta^4} \frac{B(Z, t, \mu_0)}{[1-\mu_0+2\eta(t)]^2} \quad (11)$$

where the Mott-exact cross section (9) has been used. With the aid of Eq. (10), the kernel (11) reduces to the approximate kernel $\tilde{K}(t, \mu_0)$:

$$\tilde{K}(t, \mu_0) = \frac{S_0 NZ(Z+1)}{4\pi} \frac{\bar{c}}{t} \frac{B(Z, t, \mu_0)}{[1-\mu_0+2\eta]^2} \quad (12)$$

which will be used henceforth in Eq. (1).

By expanding $f(x, \mu', t)$ into a Taylor's series about μ ,

$$f(x, \mu', t) = \sum_{n=0}^{\infty} \frac{(\mu' - \mu)^n}{n!} \frac{\partial^n}{\partial \mu^n} f(x, \mu, t) \quad (13)$$

and substituting it in Eq. (1), it is obtained

$$-\frac{\partial f}{\partial t} + \mu \frac{\partial f}{\partial x} = \sum_{n=1}^{\infty} M^n(\mu, t) \frac{\partial^n}{\partial \mu^n} f(x, \mu, t) + S(x, \mu, t) \quad (14)$$

where $M^n(\mu, t)$ are the moments of the scattering kernel $\tilde{K}(t, \mu_0)$:

$$M^n(\mu, t) = \frac{S_0 NZ(Z+1)}{4\pi} \frac{\bar{c}}{t} \int_{-1}^1 d\mu' \int_0^{2\pi} d\varphi' \frac{(\mu' - \mu)^n}{n!} \frac{B(Z, t, \mu_0)}{[1 + 2\bar{\eta} - \mu_0(\mu', \varphi'; \mu, \varphi)]^2} \quad (15)$$

The nuclear scattering of electrons is predominantly forward. Since only small-angle scattering is important, the contribution to the "scattering-in" integral in Eq. (1) largely comes from those collisions at directions μ' in the vicinity of μ . In addition, we assume the angular variation of the distribution $f(x, \mu, t)$ is sufficiently smooth so that the collision density $\tilde{K}(t, \mu_0) f(x, \mu, t)$ always yields a predominantly forward contribution. The expansion (13) is thus terminated after the first two terms, thereby reducing Eq. (14) to a linear first order partial differential equation in three variables:

$$-M^1(\mu, t) \frac{\partial f}{\partial \mu} + \mu \frac{\partial f}{\partial x} - \frac{\partial f}{\partial t} = S(x, \mu, t) \quad (16)$$

where the first moment $M^1(\mu, t)$ becomes:

$$M^1(\mu, t) = \frac{S_0 NZ(Z+1)}{4\pi} \frac{\bar{c}}{t} \int_{x_1(\mu)}^{x_2(\mu)} d\mu' \int_0^{2\pi} d\varphi' \frac{(\mu' - \mu)}{[1 + 2\bar{\eta} - \mu_0(\mu', \varphi'; \mu, \varphi)]^2} \quad (17)$$

In Eq. (17), for convenience of analytical calculations, we have made use of the fact that for small-angle scattering, the ratio $B(Z,t,\mu_0)$ approaches unity. Of course, if a numerical integration is desired, the actual ratio $B(Z,t,\mu_0)$ may be used. $X_1(\mu)$ and $X_2(\mu)$ are the limits of integration on μ' , so determined as to be consistent with the small-angle approximation implied in (16). These limits are obtained by referring to Fig. 4. Here, x represents the abscissa in a one-dimensional geometry; θ' , θ are the initial and final directions of electron motions, respectively; φ' , φ are the corresponding azimuthal angles; $\theta_0(\mu',\mu)$ is the scattering angle between the initial and final directions of motion. We shall integrate φ' over 2π , but for θ' we introduce a cut-off angle θ_c beyond which, scattering is assumed to contribute nothing to the final direction $\theta = \cos^{-1}\mu$. Thus we integrate θ' from $(\theta-\theta_c)$ to $(\theta+\theta_c)$, thereby defining the limits $X_1(\mu)$ and $X_2(\mu)$ in Eq. (17) as follows:

$$\begin{aligned} X_1(\mu) &= \cos(\theta+\theta_c) \\ &= \mu\cos\theta_c - (1-\mu^2)^{\frac{1}{2}}\sin\theta_c \end{aligned} \tag{18-a}$$

$$\begin{aligned} X_2(\mu) &= \cos(\theta-\theta_c) \\ &= \mu\cos\theta_c + (1-\mu^2)^{\frac{1}{2}}\sin\theta_c \end{aligned} \tag{18-b}$$

If $\theta_c = 15^\circ$,

$$\begin{aligned} X_1(\mu) &= .9659\mu - .2588(1-\mu^2)^{\frac{1}{2}} \\ X_2(\mu) &= .9659\mu + .2588(1-\mu^2)^{\frac{1}{2}} \end{aligned}$$

For convenience, Eq. (17) is rewritten as:

$$M^1(\mu, t) = \frac{S_0 NZ(Z+1)}{4\pi} \frac{\bar{C}}{t} I(\mu) \quad (19)$$

where $I(\mu)$ is clearly the integral contained in Eq. (17).

The integration of $I(\mu)$ is lengthy but straightforward. For $-1 < \mu < 1$, we found:

$$\begin{aligned} \frac{I(\mu)}{2\pi} = & + \frac{PX_1 + \mu^2(2b^2-4a)X_1^2}{(4a-b^2)(a+bX_1+X_1^2)^{\frac{1}{2}}} \\ & - \frac{PX_2 + \mu^2(2b^2-4a)X_2^2}{(4a-b^2)(a+bX_2+X_2^2)^{\frac{1}{2}}} \\ & - \left[\frac{3}{2}b\mu^2 + 2\mu(1+2\bar{\eta}-\mu^2) \right] [L_1 - L_2] \\ & - \frac{\mu^2(2b^2-4a)}{(4a-b^2)} \left[(a+bX_1+X_1^2)^{\frac{1}{2}} - (a+bX_2+X_2^2)^{\frac{1}{2}} \right] \\ & + \frac{1}{2}\mu^2 \left\{ \left[(2X_1+b)^2 + 4a-b^2 \right]^{\frac{1}{2}} - \left[(2X_2+b)^2 + 4a-b^2 \right]^{\frac{1}{2}} \right\} \end{aligned} \quad (20)$$

where

$$P = -4a(1+2\bar{\eta}-\mu^2)(1+2\bar{\eta}+b\mu-\mu^2) - [2b(1+2\bar{\eta}-\mu^2)^2 + 2\mu(1+2\bar{\eta}-\mu^2)(2b^2-4a) - 2ab\mu^2]$$

$$L_1 = \log \left[(a+bX_1+X_1^2)^{\frac{1}{2}} + X_1 + \frac{b}{2} \right]$$

$$L_2 = \log \left[(a+bX_2+X_2^2)^{\frac{1}{2}} + X_2 + \frac{b}{2} \right]$$

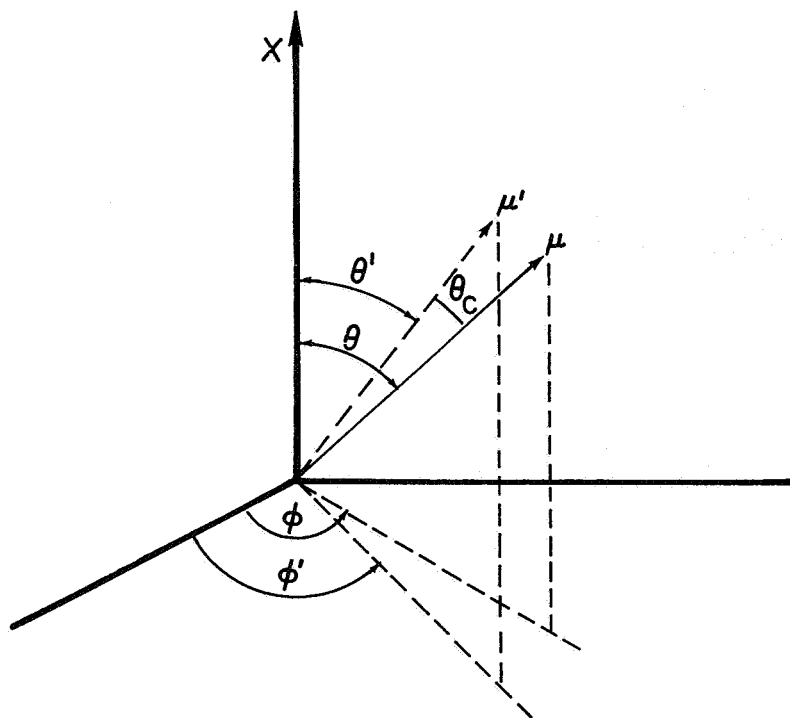


Fig. 4 Coordinates for scattering angles

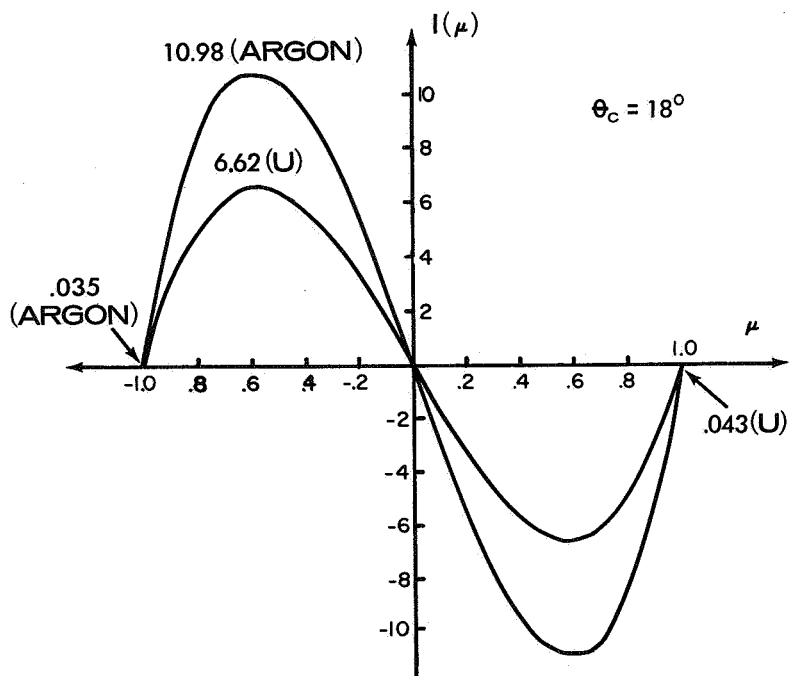


Fig. 5 The integral $I(\mu)$ in the first moment of the scattering kernel for Uranium and Argon

$$a = 4\bar{\eta}(1 + \bar{\eta} - \mu^2)$$

$$b = -4\bar{\eta}\mu$$

At $\mu = \pm 1$, $(4a-b^2) = 0$, the integral $I(\mu)$ must be treated separately. We found

$$I(\pm 1) = 2\pi \left[\pm \cos\theta_c \mp 1 \mp 2\bar{\eta} \ln \frac{2\bar{\eta}}{(1+2\bar{\eta}) - \cos\theta_c} \right] \quad (21)$$

$I(\mu)$, as defined by Eqs. (20) and (21) is antisymmetric in μ as shown in Fig. 5 for uranium and argon and for $\theta_c = 18^\circ$. It can be accurately represented by a simple expression:

$$I(\mu) = 2\pi A\mu(\mu^2 - a) \quad (22)$$

where "A" and "a" are constants. "A" is determined by the maximum of $I(\mu)$, while "a" is the "zero" of the curve and can be determined accurately by combining Eq. (21) and Eq. (22). Their values for several materials are shown in Table II.

Using Eq. (22) in Eq. (17), we have

$$M^1(\mu, t) = \frac{D}{t} \mu(\mu^2 - a) \quad (23)$$

where

$$D = \frac{S_0 NZ(Z+1)}{2} \frac{-}{CA} \quad (24)$$

Table II
Physical Quantities for the Calculation of Electron Ranges

| Substances | Argon | Aluminum | Copper | Gold | Uranium |
|---|------------------------|----------|---------|---------|---------|
| gm/cm ³ | 1.784 10 ⁻³ | 2.702 | 8.92 | 19.3 | 18.7 |
| Z | 18 | 13 | 29 | 79 | 92 |
| Molecular Weight | 40 | 26.98 | 63.54 | 197. | 235. |
| I (Mev) | | .00015 | .000276 | .000695 | .000811 |
| A($\theta_c = 18^\circ$) | 10.984 | 11.209 | 9.865 | 6.842 | 6.618 |
| D | 2.992 | 2.357 | 4.664 | 8.722 | 8.787 |
| a | 1.0032 | 1.0031 | 1.0036 | 1.0060 | 1.0066 |
| b | 1.674 | 2.105 | 1.556 | 1.289 | 1.277 |
| c | 1.160 | 1.733 | .879 | .460 | .445 |
| d | .0570 | .0494 | .0113 | .0041 | .0053 |
| S ₀ (cm) (a) | 464.27 | .2766 | .0954 | .0569 | .0616 |
| M=max h(μ, t) _{$\mu=1$} | .608 | .602 | .436 | .265 | .261 |

(a) Electron initial energy: 1.3 Mev.

Finally, putting Eq. (23) in Eq. (16), we obtain

$$-\frac{D_{\mu}(\mu^2-a)}{t} \frac{\partial}{\partial \mu} f(x, \mu, t) + \mu \frac{\partial f}{\partial t} - \frac{\partial f}{\partial t} = S(x, \mu, t) \quad (25)$$

In the following section, this equation will be solved by the method of "characteristics."

3. Detailed Electron Distribution for a Monoenergetic Isotropic Plane Source.

For this case, the source is:

$$S(x, \mu, t) = \frac{1}{4\pi} \delta(x) \delta(t-1) \quad (26)$$

For $t < 1$, we have

$$-\frac{D_{\mu}(\mu^2-a)}{t} \frac{\partial}{\partial \mu} f(x, \mu, t) + \mu \frac{\partial f}{\partial x} - \frac{\partial f}{\partial t} = 0; \quad (27)$$

$$t < 1$$

The source term will be used as an initial condition. The three ordinary differential equations associated with Eq. (27) are:

$$\frac{d_{\mu}}{-D_{\mu}(\mu^2-a)/t} = \frac{dx}{\mu} = -\frac{dt}{1} = \frac{df}{0} \quad (28)$$

which admit as independent solutions the following complete integrals:

$$U_1(\mu, t) = \left[\frac{\mu^2}{a-\mu^2} \right] \frac{1}{2Da} t = C_1 \quad (29)$$

$$U_2(x, \mu, t) = x - \frac{C_1}{D} \int \left[\frac{a-\mu^2}{\mu^2} \right] \frac{1}{2Da} \frac{d\mu}{(a-\mu^2)} = C_2(C_1) \quad (30)$$

$$U_3(f, x, \mu, t) = f(x, \mu, t) = C_3 \quad (31)$$

where C_1, C_2, C_3 are independent constants. Any surface given by a functional of the form (12)

$$F[U_1(\mu, t), U_2(x, \mu, t), U_3(f, x, \mu, t)] = 0 \quad (32)$$

or equivalently,

$$U_3(f, x, \mu, t) = \mathcal{F}[U_2(x, \mu, t), U_1(\mu, t)] = f(x, \mu, t)$$

will be an integral surface of Eq. (27); the last equality follows from Eq. (31). In other words, Eqs. (29) through (31) represent families of integral surfaces of Eq. (27) and the solution is the locus of the intersection of those surfaces in a manner prescribed by Eq. (32), i.e., the solution is constituted of "characteristic

curves." Furthermore, Eq. (31) implies that along the "characteristic curves", the distribution $f(x, \mu, t)$ is a constant.

To progress further toward an analytic solution, we digress to consider the evaluation of the integral in Eq. (30). Because "a" is always slightly greater than unity, for sufficiently large D (of order $D > 1$), the quantity $\left[\frac{a-\mu^2}{\mu^2} \right] \frac{1}{2Da}$ is a slowly-varying function over a large range of μ , compared to the quantity $\frac{1}{(a-\mu^2)}$, except near $\mu = 0$. For $0 < |\mu| \leq 1$, the integrand

$\left[\frac{a-\mu^2}{\mu^2} \right] \frac{1}{2Da} \frac{1}{(a-\mu^2)}$ is dominated by the quantity $\frac{1}{(a-\mu^2)}$, the more

so for larger D. Table II shows that D is larger than unity for $\theta_c \approx 18^\circ$, being larger for heavier materials, so that the above property is observed for common materials. Since the quantity

$\left[\frac{a-\mu^2}{\mu^2} \right] \frac{1}{2Da}$, symmetric with respect to the line $\mu=0$, is a comparatively slowly-varying function over a large range of μ , we introduce the representation

$$\left[\frac{a-\mu^2}{\mu^2} \right] \frac{1}{2Da} \simeq \begin{cases} d/\mu + b - c\mu & \text{for } \mu > 0 \\ -d/\mu + b + c\mu & \text{for } \mu < 0 \end{cases} \quad (33)$$

where the parameters b, c, d can be easily found by least-square fitting (see Table II). The representation (33) was found to be quite satisfactory. Using Eq. (33) and Eq. (29) in Eq. (30), we obtain

$$U_2(x, \mu, t) = C_2(C_1)$$

$$= C_2 \left\{ \left(\frac{\mu^2}{a - \mu^2} \right)^{n_1} t \right\}$$

(34)

$$= x - \frac{t}{D} \left(\frac{\mu^2}{a - \mu^2} \right)^{n_1} \ln \left\{ \left(\frac{\sqrt{a+\mu}}{\sqrt{a-\mu}} \right)^{n_2} (a - \mu^2)^{\pm n_4} \mu^{\pm n_3} \right\}$$

$$\begin{cases} + & \text{for } \mu \geq 0 \\ - & \text{for } \mu < 0 \end{cases}$$

where for convenience, we have defined:

$$n_1 = \frac{1}{2Da}$$

$$n_2 = \frac{b}{2/a}$$

$$n_3 = d/a$$

$$n_4 = \frac{1}{2}(c-d/a)$$

(35)

The values of these constants for several materials are included in Table II.

In Appendix A, we show that

$$\lim_{\mu \rightarrow 0} I(\mu) = \lim_{\mu \rightarrow 0} \int \left[\frac{a - \mu^2}{\mu^2} \right]^{n_1} \frac{d\mu}{(a - \mu^2)} = 0$$

For μ near zero, the second term in the RHS of Eq. (34) varies as $\pm t \mu^{2n_1} \ln \mu^2$, which by l'Hôpital's rule, vanishes as $\mu \rightarrow 0$ for any $n_1 > 0$. Thus, Eq. (34) takes on the correct value at $\mu = 0$, although it approaches this value more slowly than in the exact case.

We return now to the solution of Eq. (27). The source term (26) is used as an initial condition as follows:

- a) Source electrons of initial residual path length $t = 1$ are introduced only at $x = 0$, so that

$$\text{for } t = 1, x = 0 \quad (36-a)$$

- b) The source is isotropic and its strength is $\frac{1}{4\pi}$:

$$\text{for } t = 1, \text{ and } x = 0, \quad f = \frac{1}{4\pi} \left(\frac{\text{electrons}}{\text{cm}^2 \text{sec}} \right) \quad (36-b)$$

The determination of the functional \mathcal{F} in the general solution (32) is equivalent to the determination of a functional relationship between C_1 , C_2 , and C_3 defined by Eqs. (29), (30) and (31) such that (32) and (36) are compatible. Applying condition (36-a) to Eq. (34), we have

$$C_2 \left\{ \left(\frac{\mu^2}{a-\mu^2} \right)^{n_1} \right\} = - \frac{1}{D} \left(\frac{\mu^2}{a-\mu^2} \right)^{n_1} \ln \left\{ \left(\frac{\sqrt{a+\mu}}{\sqrt{a-\mu}} \right)^{n_2} (a-\mu^2)^{\pm n_4 \pm n_3} \right\} \quad (37)$$

Introducing the new variable

$$u = \left(\frac{\mu^2}{a-\mu^2} \right)^{n_1}$$

Eq. (37) becomes

$$C_2(u) = -\frac{u}{D} \ln \left\{ \left(\frac{a^{\frac{1}{2}} + [g(u)]^{\frac{1}{2}}}{a^{\frac{1}{2}} - [g(u)]^{\frac{1}{2}}} \right)^{n_2} (a-g(u))^{\pm n_4} (g(u))^{\pm \frac{n_3}{2}} \right\} \quad (38)$$

where

$$g(u) = \frac{a^{\frac{1}{2}}}{[1 + u^{-\frac{1}{n_1}}]^{\frac{1}{2}}}$$

By substituting ut for u , and returning to the variable μ , it is obtained:

$$C_2 \left\{ \left(\frac{\mu^2}{a-\mu^2} \right)^{n_1} t \right\} = -\frac{t}{D} \left(\frac{\mu^2}{a-\mu^2} \right)^{n_1} \ln \left\{ \left(\frac{y(\mu) + \mu}{y(\mu) - \mu} \right)^{n_2} \frac{a^{\pm (\frac{n_3}{2} + n_4)} \mu^{\pm n_3} (a-\mu^2)^{\pm n_4} \left(\frac{1}{t} \right)^{\pm \frac{n_4}{n_1}}}{[y(\mu)]^{\pm (\frac{n_3}{2} + n_4)}} \right\} \quad (39)$$

where

$$y(\mu) = [\mu^2 + (a-\mu^2)t^{-\frac{1}{n_1}}]^{\frac{1}{2}} \quad (40)$$

Combining (39) with (34) yields the "characteristic curves":

$$x = -[h^\pm(\mu, t)] \quad \left\{ \begin{array}{l} + \text{ for } 0 \leq \mu \leq 1 \\ - \text{ for } -1 < \mu < 0 \\ \text{all } t : 0 \leq t \leq 1 \end{array} \right. \quad (41)$$

where

$$h^\pm(\mu, t) = \frac{t}{D} \left(\frac{\mu^2}{a - \mu^2} \right)^{n_1} \ln \left\{ \left(\frac{Y(\mu) + \mu}{Y(\mu) - \mu} \right)^{n_2} \cdot \frac{a^{\pm \frac{1}{2} - \mu} \left(\frac{1}{t} \right)^{\pm n_4 / n_1}}{[Y(\mu)]^{\pm \frac{(n_3 + n_4)}{2}}} \right\} \quad (42)$$

Fig. 6 shows the characteristic curves in the forward direction ($\mu=1$) for several materials.

According to Eq. (31), the distribution $f(x, \mu, t)$ is constant along the characteristic curves. The condition (36-b) requires this constant to be $\frac{1}{4\pi}$ on the initial curve $t = 1, x = 0$. Since the characteristic curves pass through this initial curve (because when $t = 1, h(\mu, t)$ vanishes), f must be equal to $\frac{1}{4\pi}$ along the characteristic curves, i.e.:

$$f(x, \mu, t) = \frac{1}{4\pi} \delta[x + h^\pm(\mu, t)] \quad \frac{\text{electrons}}{\text{cm}^2 \text{ sec}} \quad (43)$$

We note in passing that the solution (43) may be considered as the Green's function for a monoenergetic, isotropic plane source of unit strength.

4. The Electron Range-Energy Relationship.

One should distinguish between the range $R(T)$, which is the deepest penetration of an electron of energy T , and the total path length $S(T)$, defined by Eq. (3). Because of scattering, the total path length is larger than the range. Figs. 7, 8 show the path length versus energy in several materials. For the case of a monoenergetic, isotropic plane source, the range is given by the distance z from the source at which the distribution vanishes. This deepest penetration is achieved by those electrons moving in the forward direction ($\mu = 1$). According to (43), the distribution vanishes as soon as $|x|$ becomes larger than $|h(\mu, t)|$.

Let

$$M = \max_{\mu=1} |h(\mu, t)|$$

then, because x is measured in units of total path length $S(T)$ of an electron with energy T , i.e.

$$x = \frac{z}{S(T)}$$

the range of that electron can be obtained as

$$\begin{aligned} R(T) &= M S(T) \\ &= M \int_0^T \frac{dT'}{(dT'/ds)} \end{aligned} \quad (44)$$

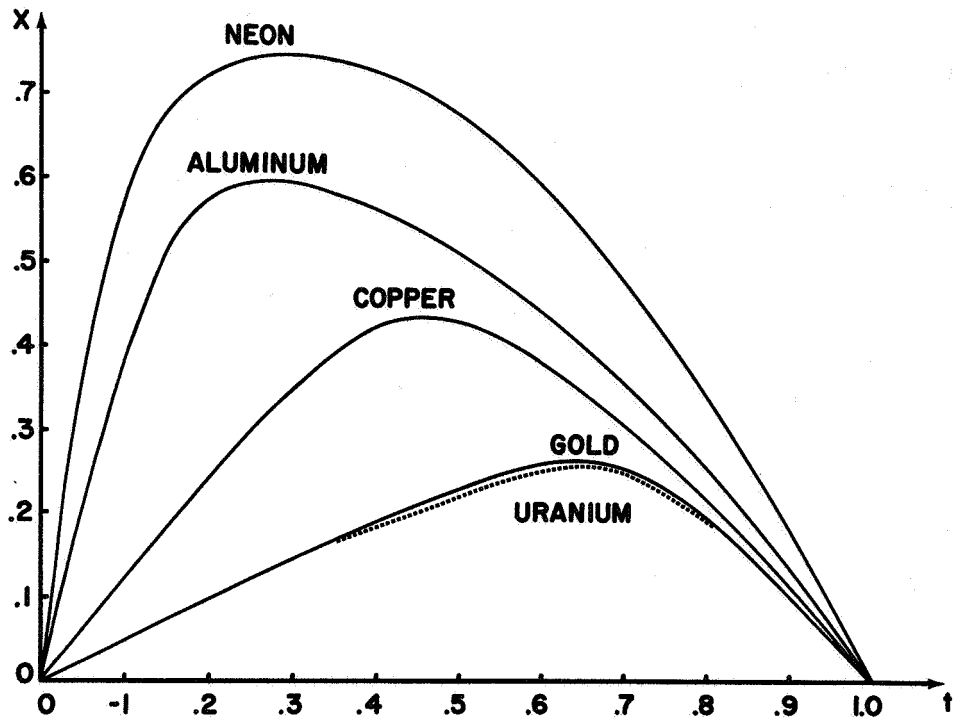


Fig. 6 Characteristic curves in the forward direction for a monoenergetic, isotropic plane source

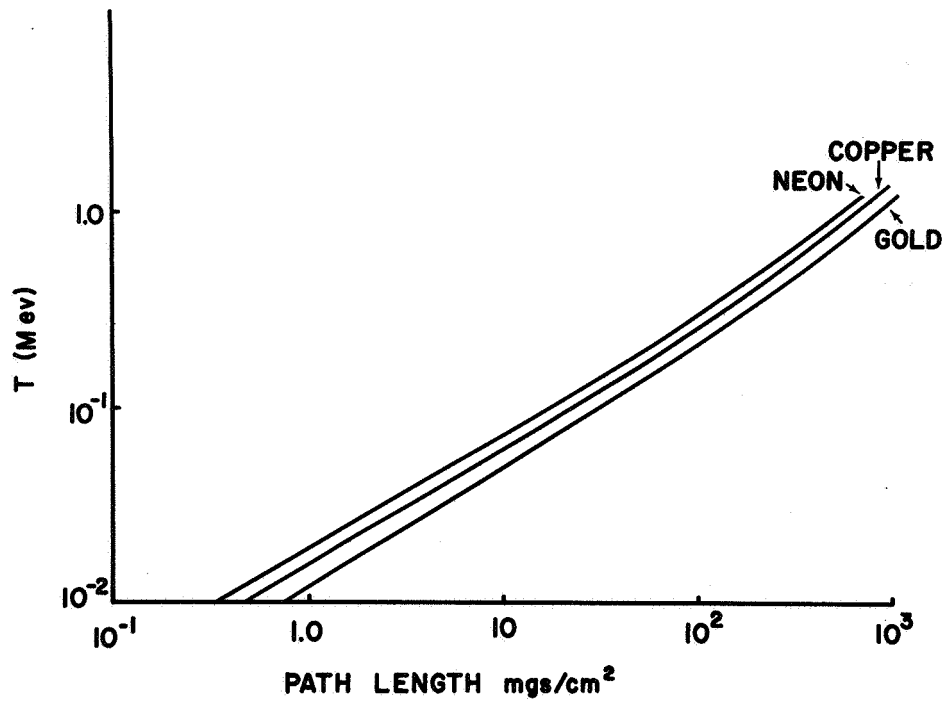


Fig. 7 Electron path length versus energy

This range-energy relationship yields results in excellent agreement with measurements in aluminum as shown in Fig. 9. It is seen also that the electrons ranges in units of (mgs/cm²) for different slowing down media may deviate appreciably from their ranges in aluminum.

5. Remarks. The Lewis' equation (Eq. (1)) is valid for electrons of energies below the critical energy of the shower region. The bremsstrahlung effect could be included satisfactorily in Eq. (1) by making use of the ratio of radiative-to-ionization losses, which depends on the electron energy and the atomic number of the medium.

The method presented here can be applied to the two-medium problem in which electrons produced in one medium escape and slow down in an adjacent medium. This will be the topic of a subsequent paper. The method is not limited to an isotropic or spatially uniform source, although it is expected that an anisotropic or space-dependent source would complicate the determination of the explicit form of the characteristic curves.

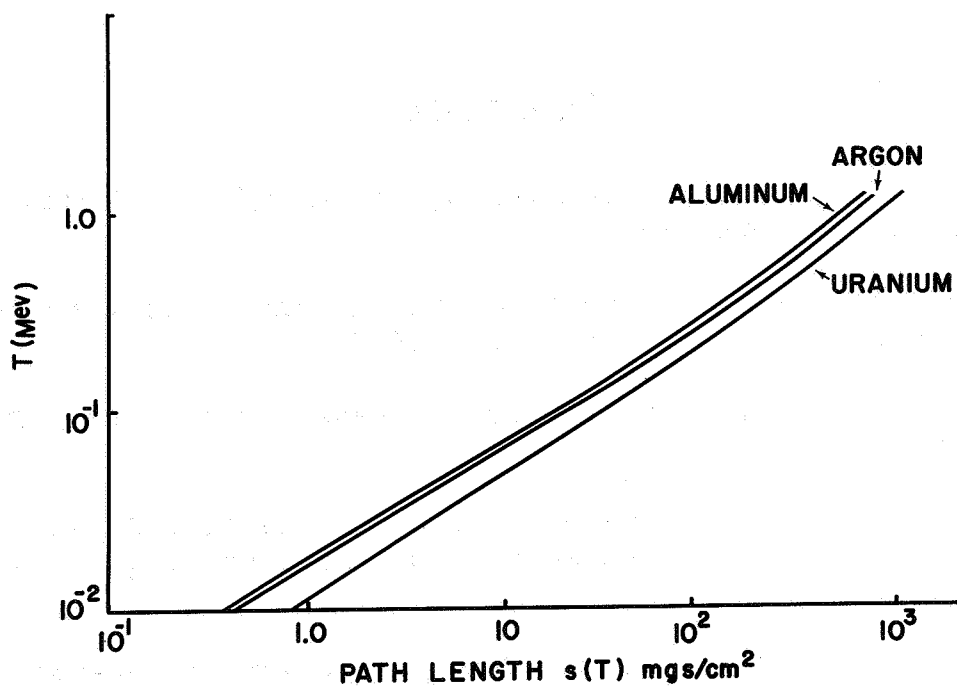


Fig. 8 Electron path length versus energy

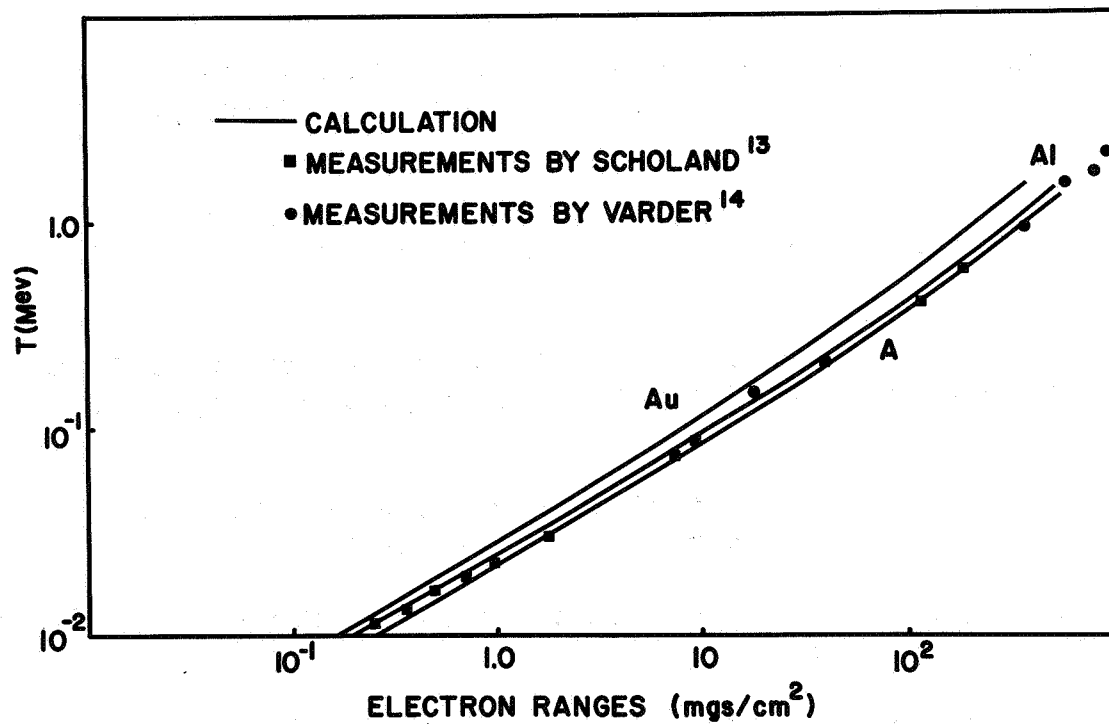


Fig. 9 Electron range versus energy

References

1. H. W. Lewis, "Multiple Scattering in an Infinite Medium," *Phy. Rev.*, 78, 526 (1950).
2. V. Fano, "Degradation and Range Straggling of High-Energy Radiations," *Phy. Rev.*, 92, 328 (1953).
3. L. V. Spencer, "Theory of Electron Penetration," *Phy. Rev.*, 98, 1597 (1955).
4. L. V. Spencer and J. Coyne, "Theory of the Deep Penetration of Electrons and Charged Particles," *Phy. Rev.*, 128, 2230 (1962).
5. Von H. Meister, "Zur Theorie der Absorption monoenergetischer Elektronen in metallischen Folien," *Z. Naturforschg.*, 13-a, 809 (1958).
6. H. S. Snyder and W. T. Scott, "Multiple Scattering of Fast Charged Particles," *Phy. Rev.*, 76, 220 (1949).
7. Dong H. Nguyen, "Ionization by Fission Fragments and Decay Electrons," Ph.D. Thesis, the University of California, Berkeley, 1965.
8. J. W. Motz, H. Olsen and H. W. Koch, "Electron Scattering without Atomic or Nuclear Excitation," *Rev. Mod. Phys.*, 36, 881 (1964).
9. J. A. Dogget and L. V. Spencer, "Elastic Scattering of Electrons and Positrons by Point Nuclei," *Phy. Rev.*, 103, 1597 (1956).
10. N. Sherman, "Coulomb Scattering of Relativistic Electrons by Point Nuclei," *Phy. Rev.*, 103, 1601 (1956).
11. Shin R. Lin, "Elastic Electron Scattering by Screened Nuclei," *Phy. Rev.*, 133, A965 (1964).
12. R. Courant and D. Hilbert, Methods of Mathematical Physics, V. II., Chapter 2, Interscience Publishers, New York, London, (1962).

13. From R. D. Evans, The Atomic Nucleus, p. 624, McGraw-Hill Book Company, Inc., New York, 1955.
14. Ibid.

Appendix A

We wish to show that

$$\lim_{\mu \rightarrow 0} I(\mu) = \lim_{\mu \rightarrow 0} \int \left[\frac{a-\mu^2}{\mu^2} \right]^{n_1} \frac{d\mu}{(a-\mu^2)} = 0 \quad (\text{A-1})$$

where

$$n_1 = \frac{1}{2Da}$$

Rewrite the integral as

$$I(\mu) = \int \frac{G(\mu)}{\mu^{2n_1}} d\mu \quad (\text{A-2})$$

where $G(\mu) = (a-\mu^2)^{n_1-1}$. Expand $G(\mu)$ in a MacLaurin's Series:

$$\begin{aligned} G(\mu) &= G(0) + \mu G'(0) + \frac{\mu^2}{2} G''(0) + \dots \\ &= a^{n_1-1} - (n-1)\mu^2 a^{n_1-2} + \text{terms with higher power in } \mu. \end{aligned} \quad (\text{A-3})$$

Substitute this result in A-2:

$$I(\mu) = \int \left[\frac{a^{(n_1-1)}}{\mu^{2n_1}} - (n-1) a^{(n_1-2)} \mu^{(2-2n_1)} + \text{terms with higher power in } \mu \right] d\mu$$

(A-4)

$$= \frac{a^{(n_1-1)} \mu^{1-2n_1}}{(1-2n_1)} - \frac{(n-1) a^{(n_1-2)} \mu^{3-2n_1}}{(3-2n_1)} + \text{terms with higher power in } \mu.$$

From the last result,

$$\lim_{\mu \rightarrow 0} I(\mu) = 0 \quad \text{if } 2n_1 < 1 \quad \text{(A-5)}$$

Given $D > 1$ and $a > 1$, this condition is always satisfied.



A PARAMETRIC TECHNIQUE OF COMPUTING

PRIMARY ELECTRON DOSE

By Alva C. Hardy, Manuel D. Lopez,
and Timothy T. White
Space Physics Division
NASA Manned Spacecraft Center
Houston, Texas

The requirement to support the manned space-flight program with an evaluation of the radiation environment has necessitated the development of a calculational procedure to determine interactions of electrons with complex shielding configurations. This procedure enables rapid calculation of the primary dose component from fluxes of omnidirectional incident electrons without time-consuming references to transmission data or shielding descriptions.

Presented at the
Thirteenth Annual American Nuclear Society Meeting
San Diego, California
June 12, 1967

INTRODUCTION

An evaluation of the effect of radiation environments — specifically, high energy electrons trapped in the earth's magnetic field — is of importance for manned space flight. For such an evaluation, a calculational procedure is needed to determine how electrons interact with complex shielding configurations. The procedure, to be useful in mission planning and support, should provide rapid calculation of the primary dose component from fluxes of omnidirectional incident electrons without time-consuming references to transmission data or shielding descriptions. This paper reports the development of such a procedure.

INTERACTION OF ELECTRONS WITH MATTER

As electrons pass through matter, their energy is lost by ionization and by radiative collisions.^a Each of these interactions may cause

^aRadiative energy losses (bremsstrahlung) contribute a significant component of the total dose when thick shields and high fluxes of energetic incident electrons (8 MeV) are present. This paper will be concerned only with the dose contributions of those electrons reaching the dose point, and not with bremsstrahlung production and its resultant dose.

the electrons to suffer significant path deflections. Also, elastic scattering causes a large number of deflections. These interactions result in attenuation of the energy of the electrons along very erratic paths as the electrons pass through the absorbing medium. These complex interactions pose the greatest difficulty in calculating primary electron dose, that is, determining the number, direction, and energy of electrons transported through the shielding.

Berger and Seltzer (Ref. 1) have developed a Monte Carlo transport code which uses a random number generator to simulate the complex interactions of electrons in matter. Extensive runs of this code have been made at the Manned Spacecraft Center to synthesize a cosine-law source of monoenergetic electrons incident on aluminum slab shields. A cosine-law source of electrons incident on a slab shield corresponds to an omnidirectional flux of electrons. Up to 100 000 Monte Carlo histories were investigated so that statistically significant data could be obtained for thick shields and for penetrations near the shield normal. Figure 1 shows the result of 100 000 histories for 2-MeV incident electrons. The data are presented as a normalized differential transmission coefficient versus degraded energy for various shield thicknesses. The normalized differential transmission coefficient is defined as the relative degraded energy distribution for monoenergetic incident electrons transmitted through slab shields of given thicknesses. For simplicity, it is assumed that only those particles exiting normal to a shield are incident on the dose point. This is a good approximation when the solid angle subtended

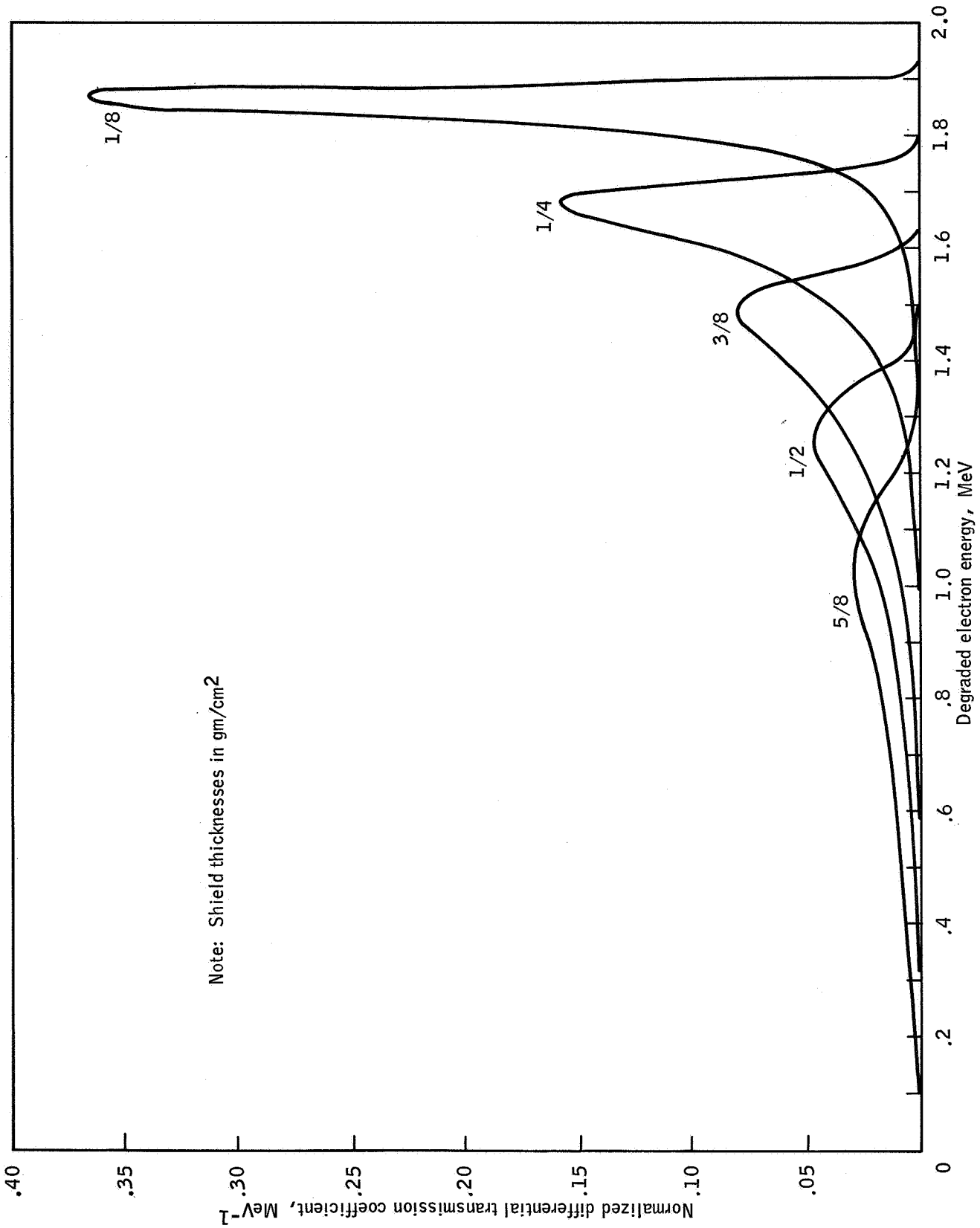


Fig. 1 Differential transmission coefficient versus degraded energy of 2-MeV incident for various shield thicknesses.

by the shield is less than 0.1 steradian, and is slightly conservative for larger solid angles. To improve the statistical reliability of the data, the number of particles exiting normal to the shield is taken to be the average of the number transmitted within 10 degrees of the normal.

PRIMARY ELECTRON DOSE CALCULATION

Using transmission data as described, the electron dose within a vehicle whose shielding description is defined in equivalent thicknesses of aluminum may be obtained from the relationship

$$D(t_i, E, E') = \frac{C}{W} \int_{E_{co}}^{E_{max}} \frac{dN}{dE} \sum_{i=1}^N S_i \int_0^{E'_{max}} \frac{dT(t_i, E, E')}{dE'} \frac{dE'}{dX} dE' dE \quad (1)$$

where

| | |
|-----------------|---|
| $D(t_i, E, E')$ | dose or dose rate, rem or rem/unit time |
| C | 1.6×10^{-8} (dose conversion factor from MeV/gm to rad) |
| W | cone of acceptance for transmission data, ster |
| E_{max} | maximum incident energy considered, MeV |
| E_{co} | minimum incident electron energy sufficient to reach dose point, MeV |
| $\frac{dN}{dE}$ | differential isotropically incident electron energy spectrum, electrons/cm ² -MeV for dose and electrons/cm ² -MeV-time for dose rate |
| N | number of solid angles in the vehicle shielding description |
| S_i | solid angle subtended by the shield (from the dose point), ster |

E'_{\max} maximum energy of transmitted electrons, MeV

$\frac{dT(t_i, E, E')}{dE'}$ normalized transmitted electron differential energy spectrum (transmission data are a function of the incident energy E , the degraded energy E' , and thickness t of shield as seen by the dose point for the i th solid angle)

$\frac{dE'}{dX}$ linear energy transfer for electron in tissue as a function of the energy at the dose point, $\text{MeV-cm}^2/\text{gm}$ (Ref. 2)

E' degraded energy after shielding interactions, MeV

E incident energy of electrons, MeV

The cutoff energy E_{co} is defined as the mean or average energy an electron must have to traverse the shield thickness being considered (Ref. 2).

PARAMETRIC TECHNIQUE OF COMPUTING

PRIMARY ELECTRON DOSE

The solution of Eq. (1) is involved and time consuming. Since the incident electron energy spectrum dN/dE is the only variable which is changed frequently, a new parameter incorporating all the variables except dN/dE is desired. The first step in generating this parameter is to eliminate the transmission data and the linear energy transfer function, which are functionally dependent on the transmitted electron energy E' . This is done by numerically integrating the following equation for each thickness and incident energy

$$D'(E, t_i) = 1.6 \times 10^{-8} \text{ rad-gm/MeV} \int_0^{E'_{\max}} \frac{dT}{dE'}(E, t_i, E') \frac{dE'}{dX} dE' \quad (2)$$

The result of this integration is the dose per unit flux deposited in tissue due to an electron of a given energy incident on the i th slab of thickness t . Figure 2 shows the dose versus incident electron energy for different thicknesses of aluminum. With the elimination of the variable E' , the solution of the dose equation now requires only that the incident electron energy spectrum and the vehicle shielding be specified. This simplified dose equation is

$$D(E, t_i) = \frac{1}{W} \int_{E_{co}}^{E_{max}} \frac{dN}{dE} \sum_{i=1}^N S_i D'(E, t_i) dE \quad (3)$$

The next step in simplifying the calculation is to evaluate the effect of the shielding. This is done through the following equation

$$D''(E) = \frac{1}{W} \sum_{i=1}^N S_i D'(E, t_i) \quad (4)$$

The value of D' for the thickness associated with the i th solid angle is taken from the data in Fig. 2. This desired parameter D'' is the dose per unit flux in tissue at a point inside a vehicle due to electrons of given energies which are omnidirectionally incident on the vehicle. Figure 3 shows curves of D'' for the Apollo command module and lunar module and for Gemini spacecraft as a function of incident electron energies.

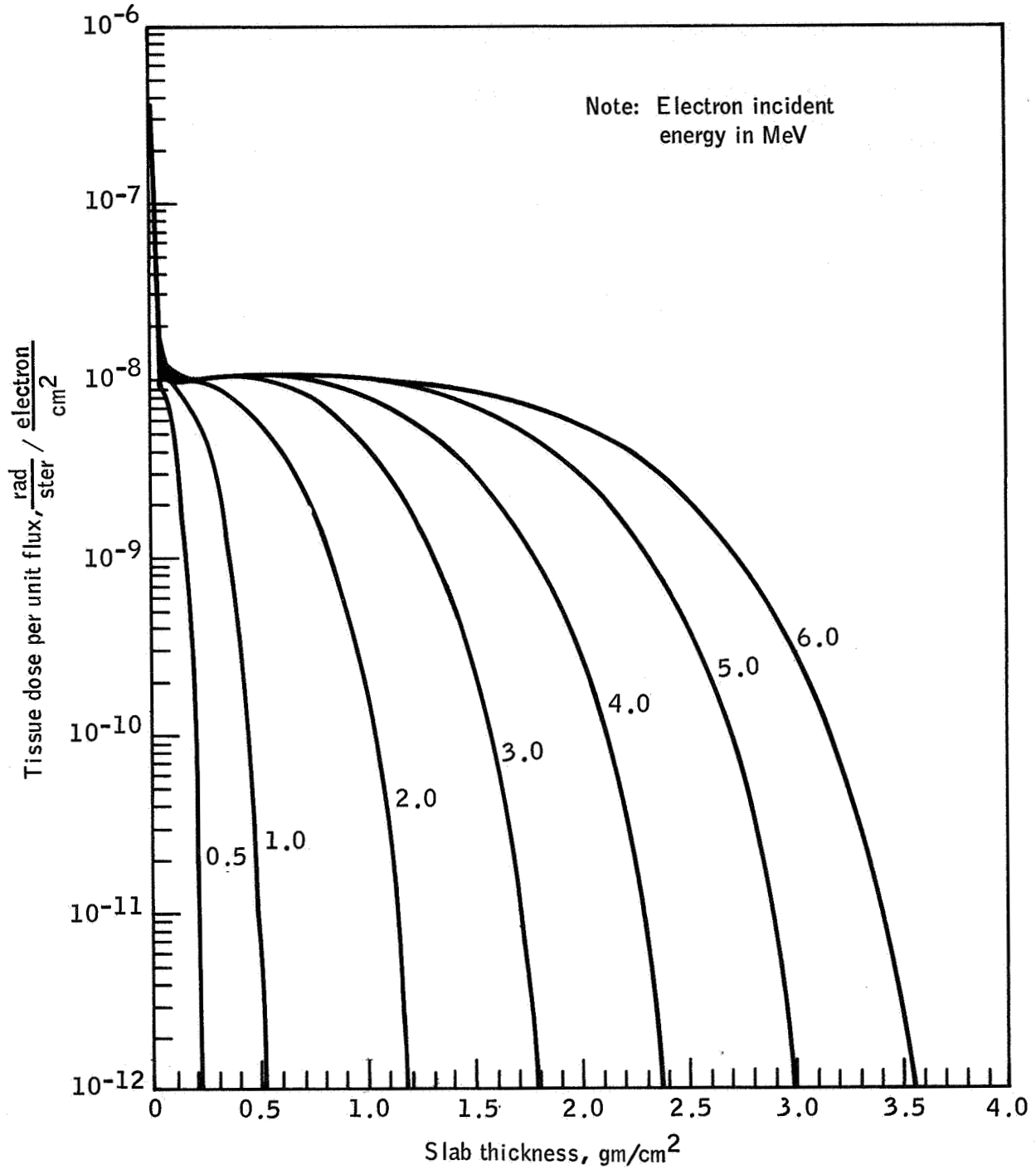


Fig. 2 Dose per unit flux as a function of slab thickness of aluminum for various incident energies.

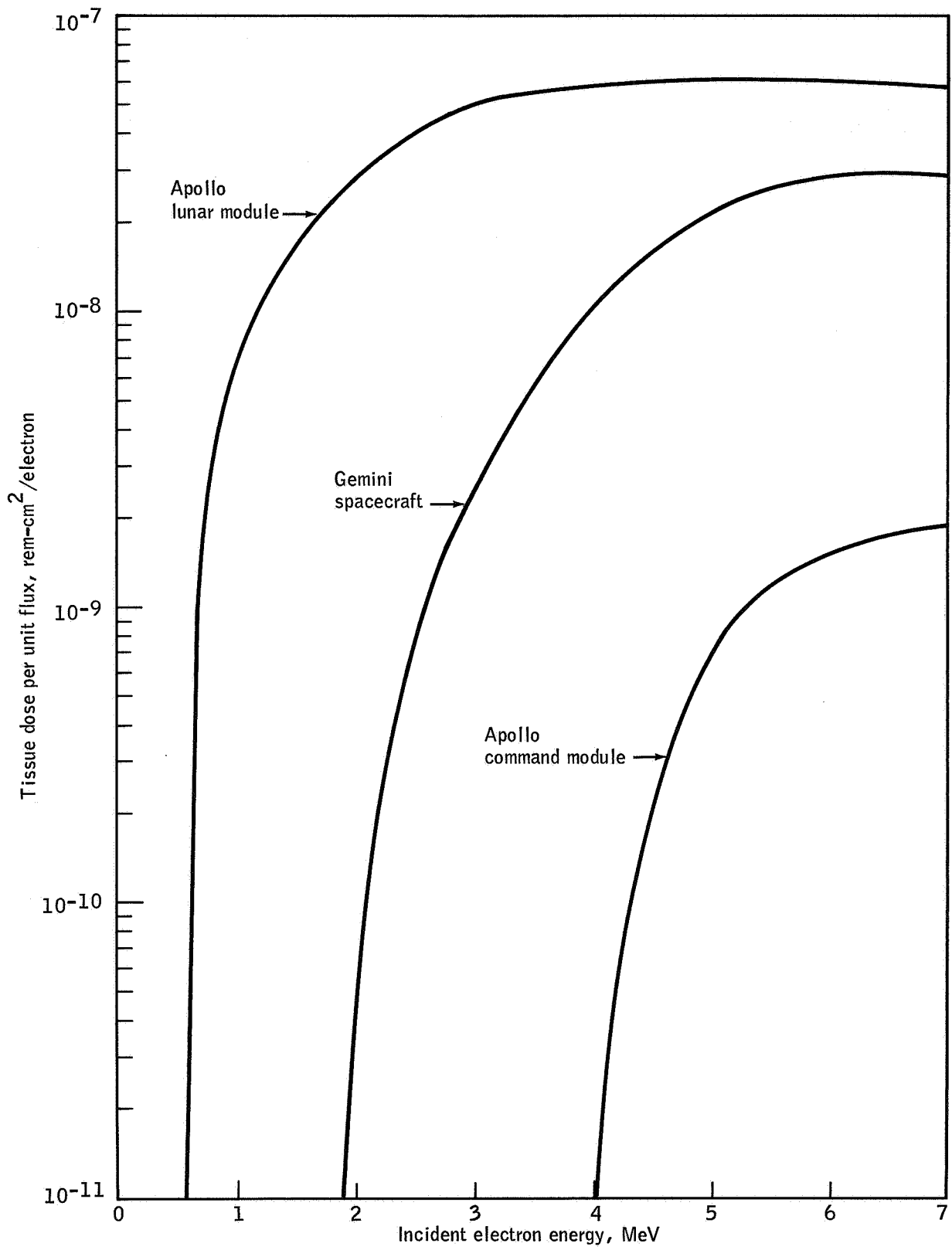


Fig. 3 Dose per unit flux versus energy for various spacecraft.

The electron dose can now be calculated dependent only on the incident omnidirectional electron spectra. The equation is as follows

$$D = \int_{E_{co}}^{E_{max}} D''(E) \frac{dN}{dE} dE \quad (5)$$

where $D''(E)$ is provided by Fig. 3 or, in practice, as a tabulated function for the shield configuration under consideration.

CONCLUSIONS

The parametric technique for computing primary electron dose inside complex vehicle shielding requires a minimum of computer logic and calculation time. This technique has wide application in the planning of manned space missions or where analysis of real-time data will not permit time-consuming references to electron transport data and vehicle shielding descriptions.

ACKNOWLEDGMENTS

The authors are indebted to M. J. Berger and S. M. Seltzer of the National Bureau of Standards (NBS) for their cooperation in providing MSC with a copy of the Monte Carlo Electron Transport Code ETRAN5E.

REFERENCES

1. M. J. BERGER and S. M. SELTZER, "Results of Some Recent Transport Calculations for Electrons and Bremsstrahlung," Second Symposium on Protection Against Radiations in Space, NASA SP-71 (1965).
2. M. J. BERGER and S. M. SELTZER, "Tables of Energy Losses and Ranges of Electrons and Positrons," NASA SP-3012 (1964).



HIGH-ENERGY NUCLEON TRANSPORT*

N 68-26144

R. G. Alsmiller, Jr.

Oak Ridge National Laboratory
Oak Ridge, Tennessee

In this paper the recent work on the transport of high-energy nucleons through dense matter is reviewed. The application of this transport to space-shielding studies is emphasized so the discussion is restricted to low and intermediate energies (≤ 1 GeV) and to relatively thin shields. A review article on this subject has recently been published¹ and therefore the discussion here is, in the main, concerned with work which has become available since this review.**

The accuracy of transport calculations must be determined by comparison with experimental measurements made on thick targets, and I shall therefore begin by discussing two such comparisons that have recently been made.

J. S. Fraser et al.² have measured the thermal neutron flux produced when large targets of Be, Sn, Pb, and depleted uranium are bombarded by high-energy (0.5 to 2 GeV) protons. A schematic diagram of the experimental arrangement for the case of a lead target is shown in Fig. 1. In the experiment a narrow proton beam was incident on one face of a thick target which was surrounded by a large water bath, and the thermal neutron flux was measured as a function of position in the water. W. A. Coleman,³ using the nucleon transport code written by W. E. Kinney,⁴ has calculated this thermal flux for the case of 540-MeV protons on a lead target (see Fig. 1)

*Research sponsored by the National Aeronautics and Space Administration under Union Carbide Corporation's contract with the U. S. Atomic Energy Commission.

**Much of the work that will be described is unpublished. I thank all of the investigators involved for making their work available to me prior to its publication.

CYLINDRICAL SYMMETRY ABOUT BEAM AXIS

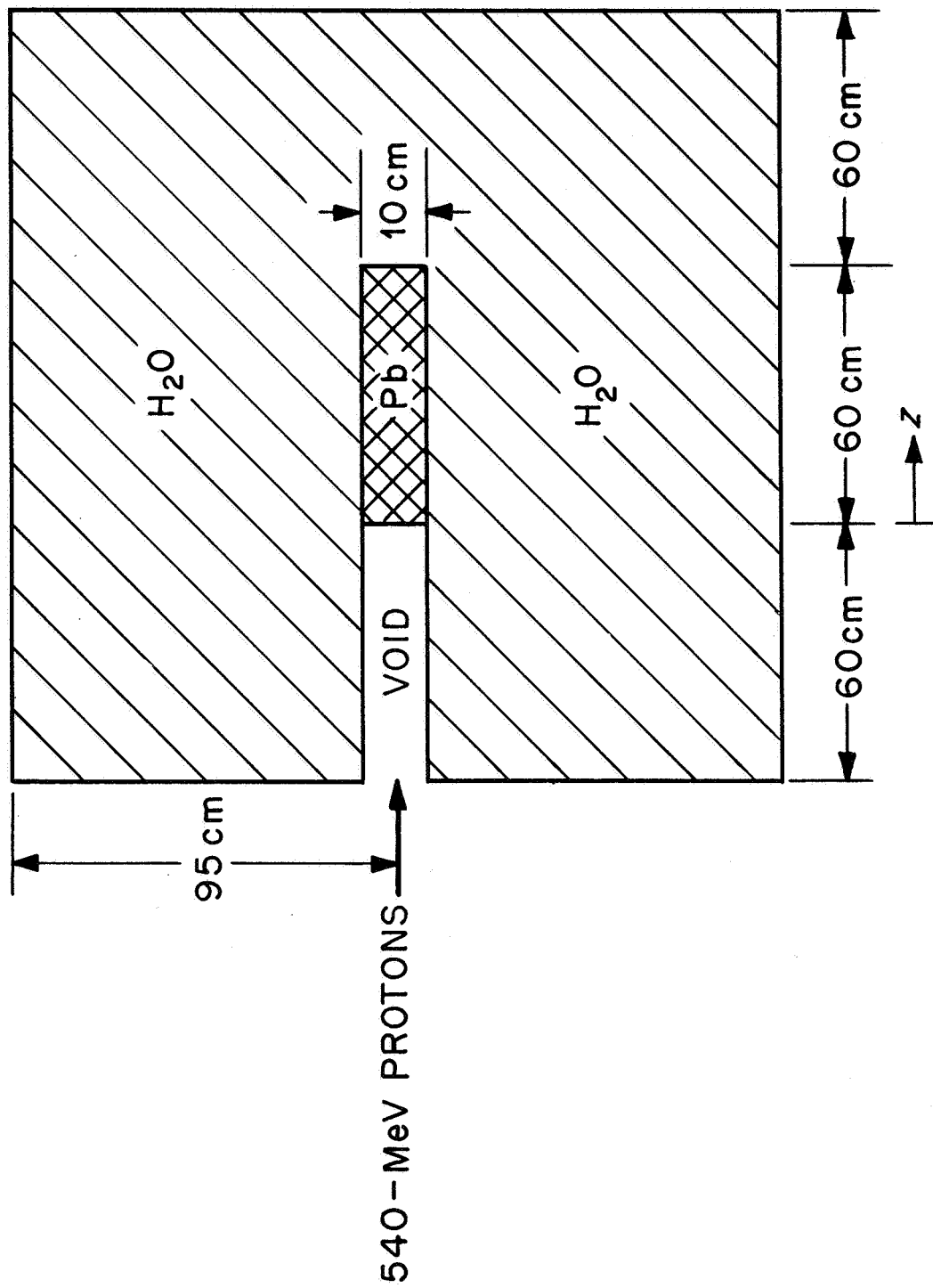


Fig. 1 Schematic of intense neutron generator (ING) experiment

and made comparisons with the experimental measurements. This transport code uses Monte Carlo methods and treats particle production from high-energy (> 50 MeV) nuclear reaction by means of an intranuclear-cascade code written by H. W. Bertini.⁵ Below 50 MeV nonelastic collisions are treated by using an evaporation code written by L. Dresner,⁶ and elastic collisions are treated using experimental data. In the calculations of Coleman, the geometry was the same as that shown in Fig. 1, and the thermal flux was calculated assuming a single velocity for neutrons with an energy of less than 0.5 eV.

The comparisons between the calculated and measured values are shown in Figs. 2 and 3. In the figures the thermal flux is plotted as a function of radius at depths of -11.5 cm and 34 cm, respectively. These depths (see Fig. 1) are measured from the front face of the lead target. The histograms show the calculated values while the plotted points correspond to the experimental measurements. The dashed curve is drawn through the experimental points for comparison purposes. The numerical values in the histogram give the percent standard deviation obtained in the Monte Carlo calculations. The experimental and calculated results are in very good agreement at all radii at both of the depths considered. These comparisons are important from the point of view of shielding because they represent the first definitive test of the ability of the Kinney code using the Bertini data to calculate accurately the low-energy neutrons. Of course the intranuclear-cascade calculations are expected to be more accurate for heavy nuclei such as lead than for light nuclei, so the good agreement in Figs. 2 and 3 cannot be taken to indicate that similar agreement will be obtained with lighter nuclei. Comparisons of calculations with the experimental measurements made using a Be target are in progress but they are not yet available.

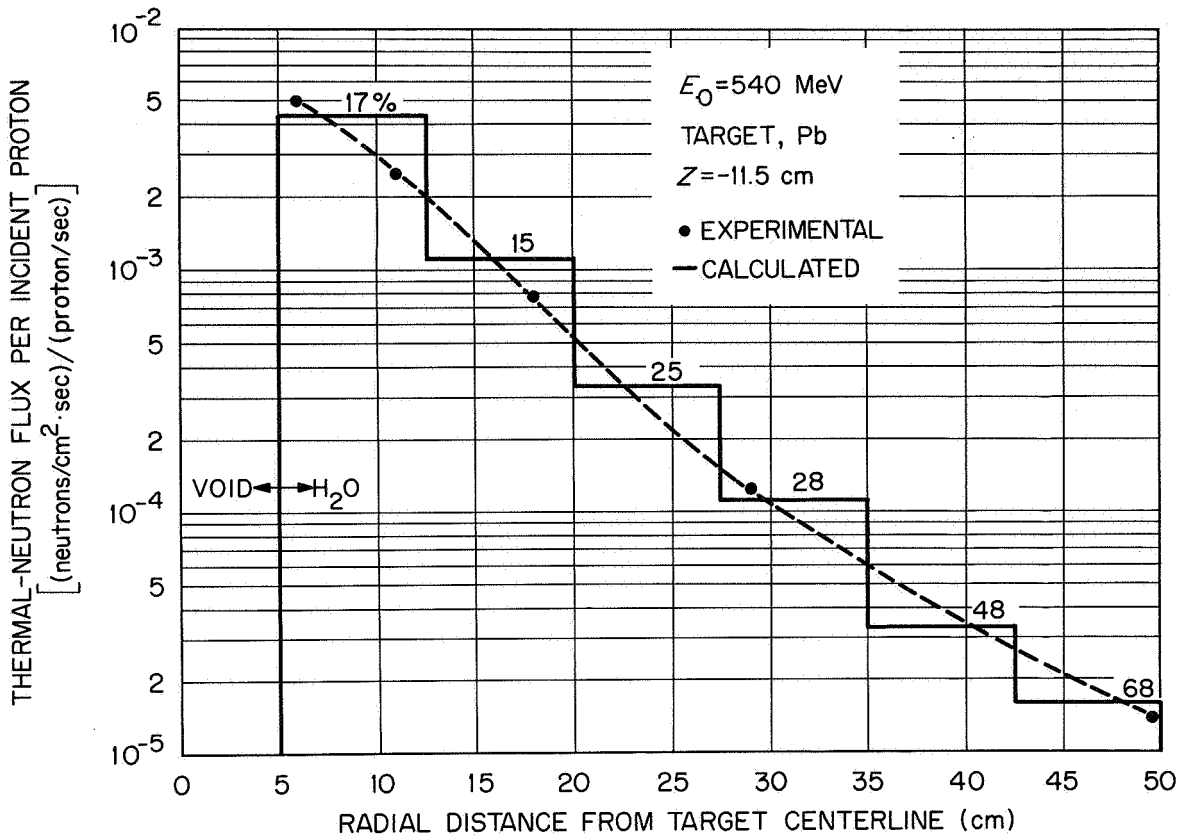


Fig. 2 Thermal neutron flux distribution in ING experiment

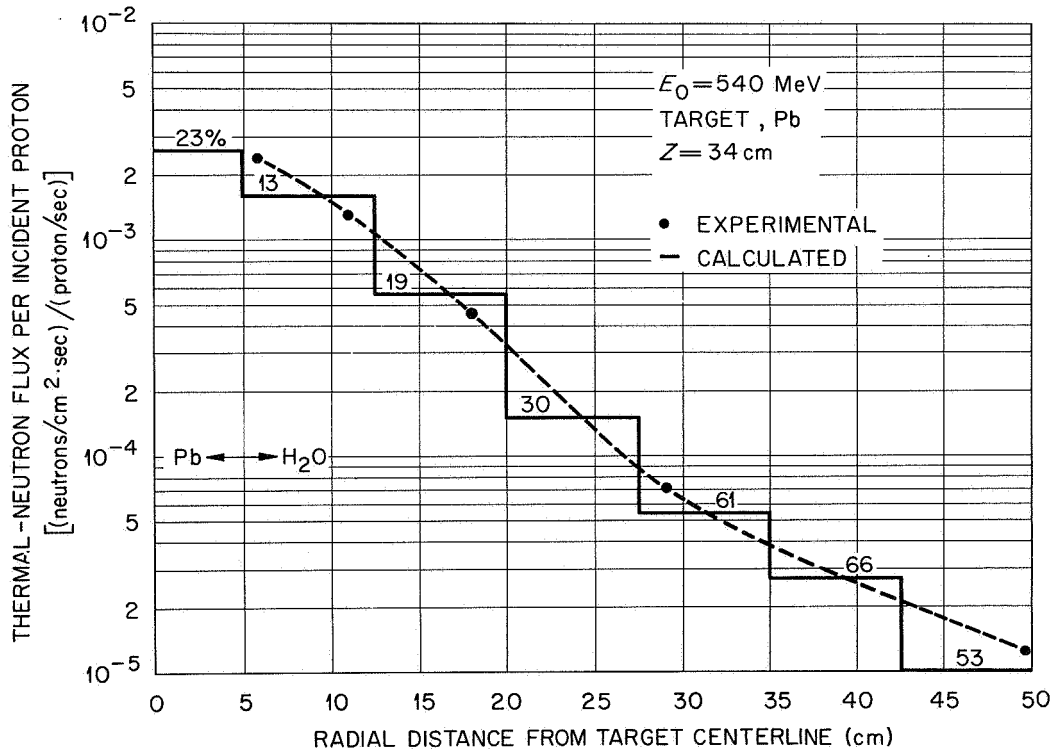


Fig. 3 Thermal neutron flux distribution in ING experiment

Comparisons of the calculated and measured particle fluxes emerging from thick targets provide a definitive test of the transport calculations, but such comparisons do not give a very good indication of the error to be associated with calculation of integral quantities such as dose. A series of experimental measurements of the dose as a function of depth in a spherical phantom placed at a variety of positions with respect to a target irradiated by 160-MeV protons has been carried out by T. V. Blosser et al.⁷ The geometrical arrangement used in this set of experiments is shown in Fig. 4. For a variety of target materials and thicknesses and for various values of the parameters α , β , θ , and d , the energy deposition, i.e., the dose, was measured as a function of depth in the water phantom. It should be noted that except in the very special case when α , β , and θ are all equal to zero the experimental arrangement is such that the measured dose is due entirely to secondary particles, or, more precisely, to secondary particles and primary particles which have undergone large-angle and multiple small-angle Coulomb scattering.

B. Liley and A. G. Duneer, Jr.⁸ have carried out dose calculations and made comparisons with these experimental data. In these calculations which are carried out using Monte Carlo methods, first-generation secondary particles are calculated explicitly and then treated using attenuation factors. The details of the calculations will be published shortly and will not be discussed here. There is, however, one feature of the method employed which I think should be noted. The angular distribution of the first-generation secondary cascade particles is included in the calculations by using an interesting approximation. If $F_{ij}(E', E, \vec{\Omega}', \vec{\Omega})$ is the number of cascade particles

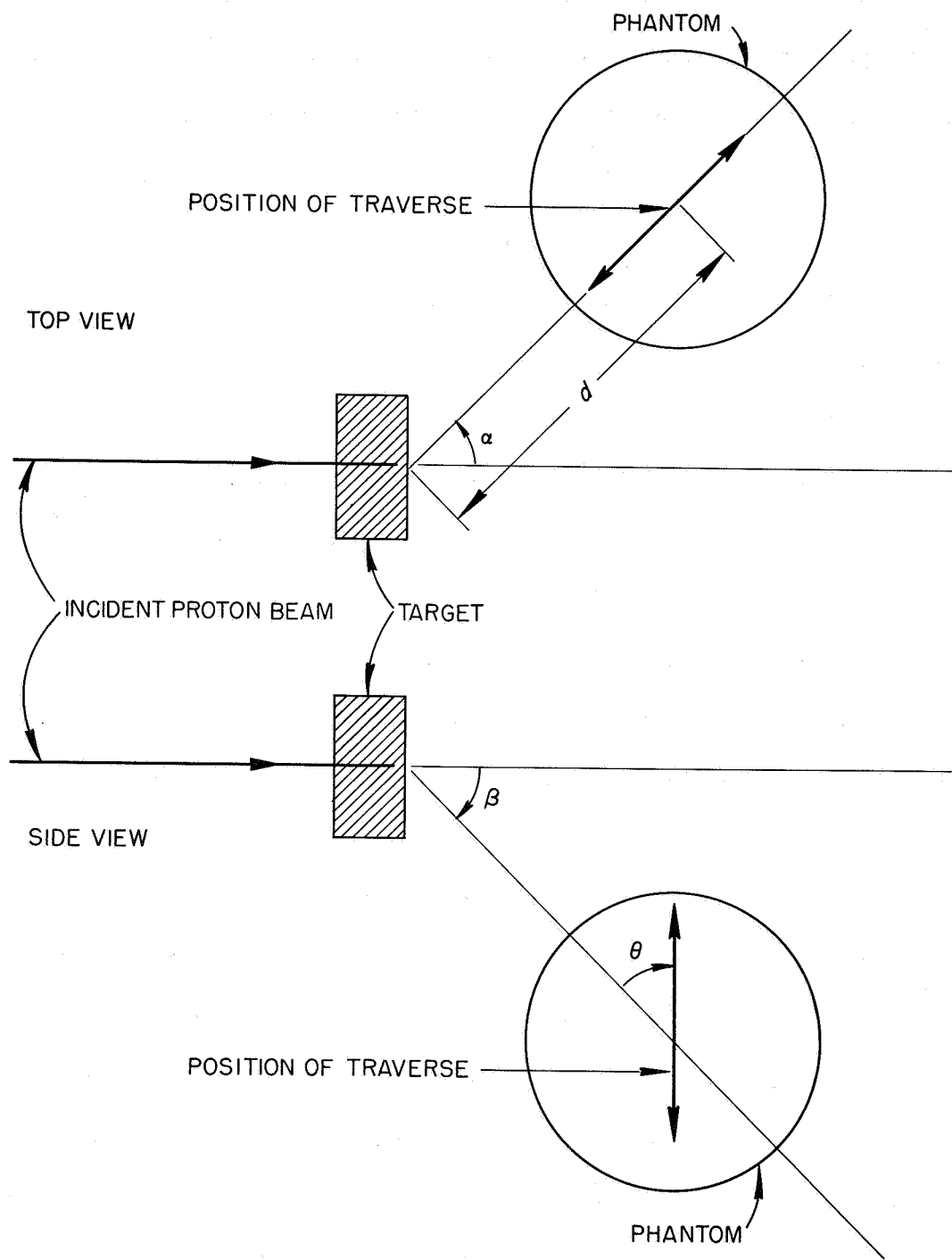


Fig. 4 Schematic of water-filled spherical phantom experiment of T. V. Blosser et. al.

of type i per unit energy about E per unit solid angle about $\vec{\Omega}$ which arises from the nonelastic nuclear collision of a particle of type j with energy E' going in the direction $\vec{\Omega}'$, the assumption is made that

$$F_{ij}(E', E, \vec{\Omega}' \cdot \vec{\Omega}) = f_{ij}(E', E) g_{ij}(E', \vec{\Omega}' \cdot \vec{\Omega}) ,$$

where

$$f_{ij}(E', E) = \int_{4\pi} F_{ij}(E', E, \vec{\Omega}' \cdot \vec{\Omega}) d\Omega$$

$$g_{ij}(E', \vec{\Omega}' \cdot \vec{\Omega}) = \frac{\int_0^{E'} F_{ij}(E', E, \vec{\Omega}' \cdot \vec{\Omega}) dE}{\int_0^{E'} \int_{4\pi} F_{ij}(E', E, \vec{\Omega}' \cdot \vec{\Omega}) d\Omega dE} ;$$

that is, it is assumed that there is no correlation between the energy of emission and the angle of emission but all of the angular dependence is not omitted. This approximation is interesting because it is in a sense intermediate between using the complete angular dependence and using the often-employed straightahead approximation in which g_{ij} is approximated by $1/2\pi \delta(1 - \vec{\Omega}' \cdot \vec{\Omega})$. In their calculations Liley and Duneer have used the analytic expressions for g_{ij} obtained by H. Alter.⁹ The expressions were obtained by fitting the Monte Carlo data of Bertini⁵ by the method of least squares. The angular distribution, g_{pp} , of protons emitted from 150-MeV protons on aluminum obtained by Alter is shown in Fig. 5. In the figure $2\pi g_{pp}$ is called SIGMA and MU is used for $\vec{\Omega}' \cdot \vec{\Omega}$. The plotted points show the data obtained from Bertini and the solid curve is the least-square fit. The distribution is peaked forward, but there is, of course, particle emission at angles other than zero.

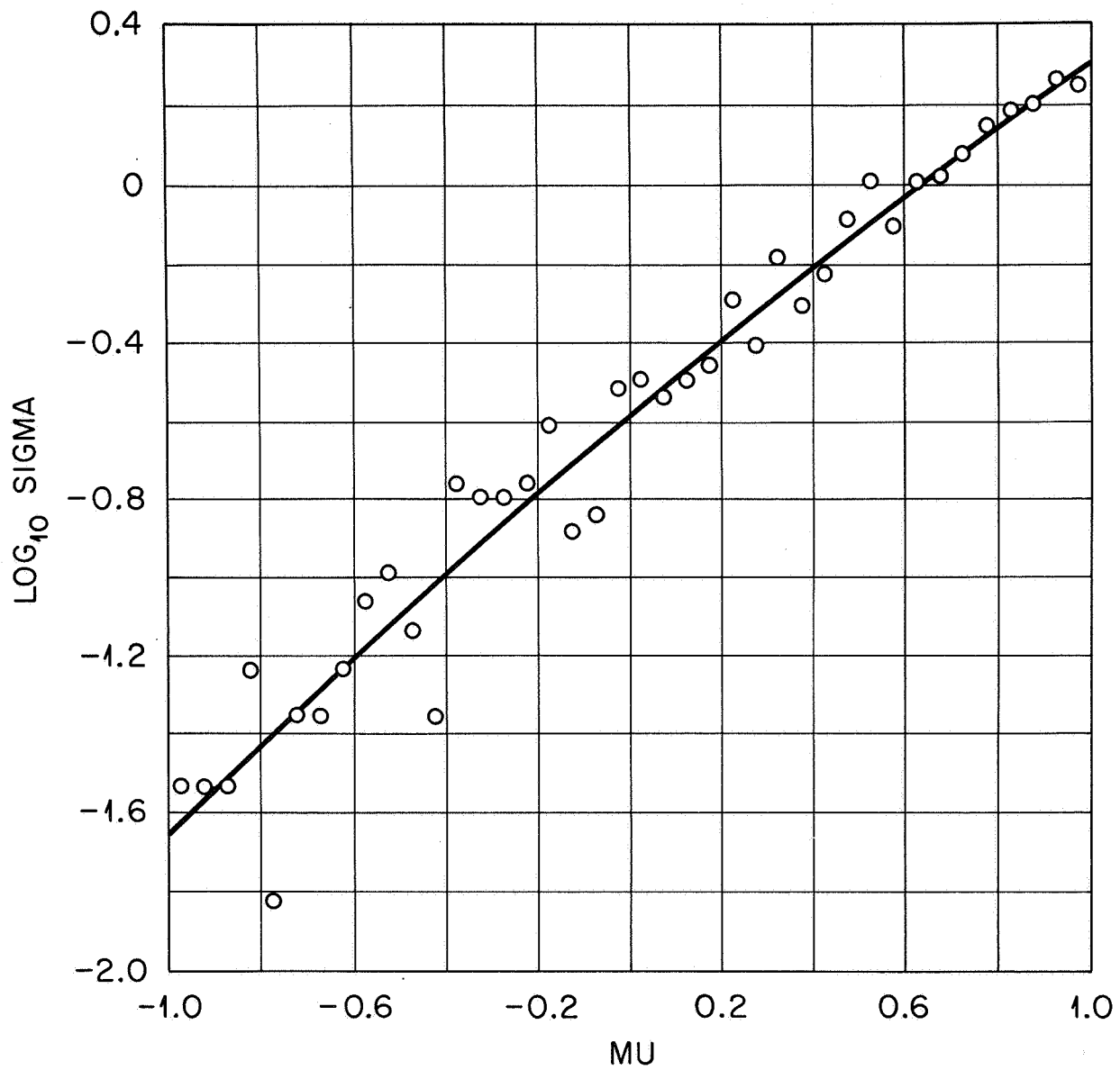


Fig. 5 Cascade proton angular distribution; E = 150 MeV, ²⁷Al.

The comparison between the calculations and the measurements for the case of 160-MeV protons incident on an aluminum target of 26.9 g/cm^2 thickness and $\alpha = \beta = 45^\circ$, $\theta = 0^\circ$, $d = 53.7 \text{ cm}$ (see Fig. 4) is shown in Fig. 6. The calculations are systematically high compared with the experimental values. In considering this comparison, it must be remembered that the entire contribution to the dose in this case is coming from the secondary particles, and thus the calculational error is not indicative of that which would be obtained in a typical space shielding calculation where the primary particles contribute a large fraction of the dose.

Using Monte Carlo methods, it is feasible to solve the transport equations without approximation. In general, however, to obtain such solutions a large amount of computing time is required, and it is very desirable for design purposes to have methods for obtaining adequate, readily calculable approximate solutions. One such method that is often used employs the straightahead approximation. In this approximation it is assumed that when a nucleon-nucleus collision occurs the secondary particles are emitted in the direction of the incident particle. In a previous paper, the validity of this approximation was tested by comparing exact* calculations with calculations carried out using the approximation for the case of monoenergetic protons isotropically incident on slab shields followed by tissue.¹⁰ A further test of the approximation has now been obtained by making similar comparisons for the case of a typical flare proton spectrum normally incident on a slab shield followed by tissue.¹¹ For isotropic incidence the angular distribution of the primary particles tends to de-emphasize the angular

*"Exact" is used here to mean calculations in which the angular distribution of the secondary particles is taken into account without approximation. The use of this term is not meant to imply anything about the physical validity of the calculations.

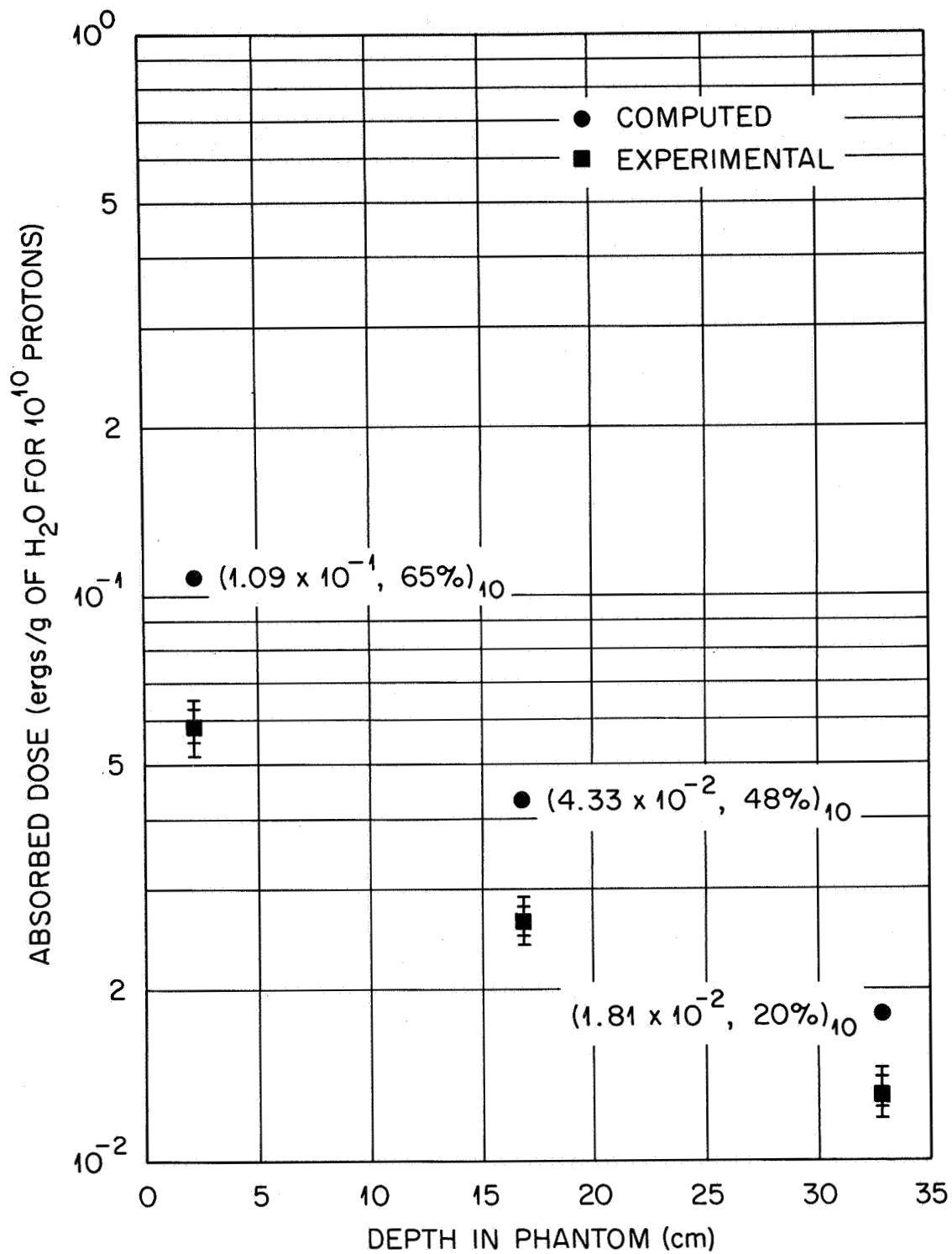
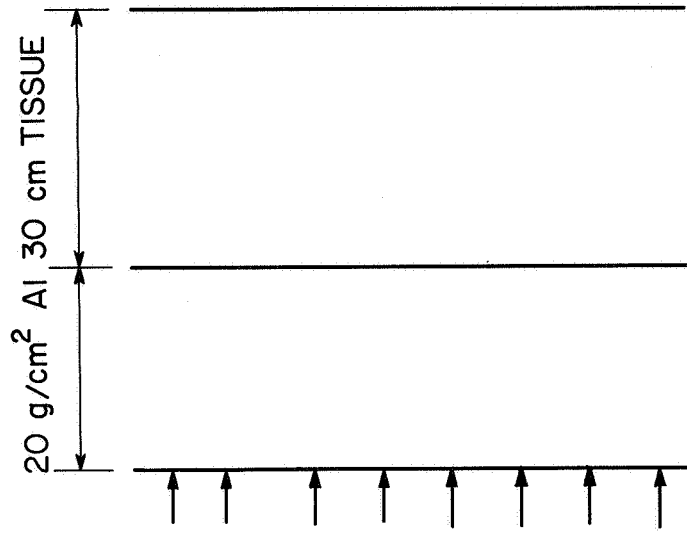


Fig. 6 Absorbed dose versus depth; comparison of experimental and calculated results

distribution of the secondary particles so the case of normal incidence provides a more stringent test of the approximation than does the case of isotropic incidence.

In order to insure that any differences in the results are due to the approximation being tested and not to such things as differences in nuclear data, both the exact and the straightahead calculations were carried out using the transport code written by W. E. Kinney.⁴ The straightahead approximation as used here applies to all particles emitted from nuclear collisions. In both the exact and approximate calculations, the primary protons are assumed to travel in a straight line and continuously lose energy. When a nuclear collision occurs, all of the emitted particles, both evaporation and cascade, are assumed to go in the direction of the incident particle, i.e., no attempt is made to discriminate against particles emitted at large angles as is sometimes done in using the approximation. The flare spectrum used was taken to be exponential in rigidity with a characteristic rigidity of 100 MV and was arbitrarily normalized to 10^9 protons/cm² with energy greater than 30 MeV. In the calculations only particles with energy less than 400 MeV were considered. The form of the flare spectrum and the geometry are shown schematically in Fig. 7. The dose calculations in the tissue were carried out as described previously and, in particular, the quality factors used in obtaining the dose in rem are the same as those used previously.¹²

Comparisons between the exact and approximate calculations for the flare spectrum normally incident on 20 g/cm² of aluminum (see Fig. 7) are shown in Figs. 8, 9, and 10. In Fig. 8 the exact and approximate secondary proton and neutron currents at the aluminum-tissue interface are compared. The straight-ahead approximation overestimates the low-energy secondary neutron current and



$$J_p(>E) = K e^{P(30)/P_0} e^{-P(E)/P_0} \quad (E < 400 \text{ MeV})$$

$$P(E) = \frac{1}{e} [E(E + 2M_p)]^{1/2}$$

$$K = 10^9 \text{ protons/cm}^2$$

$$P_0 = 100 \text{ MV}$$

Fig. 7 Schematic of geometry for flare spectrum normally incident on a slab

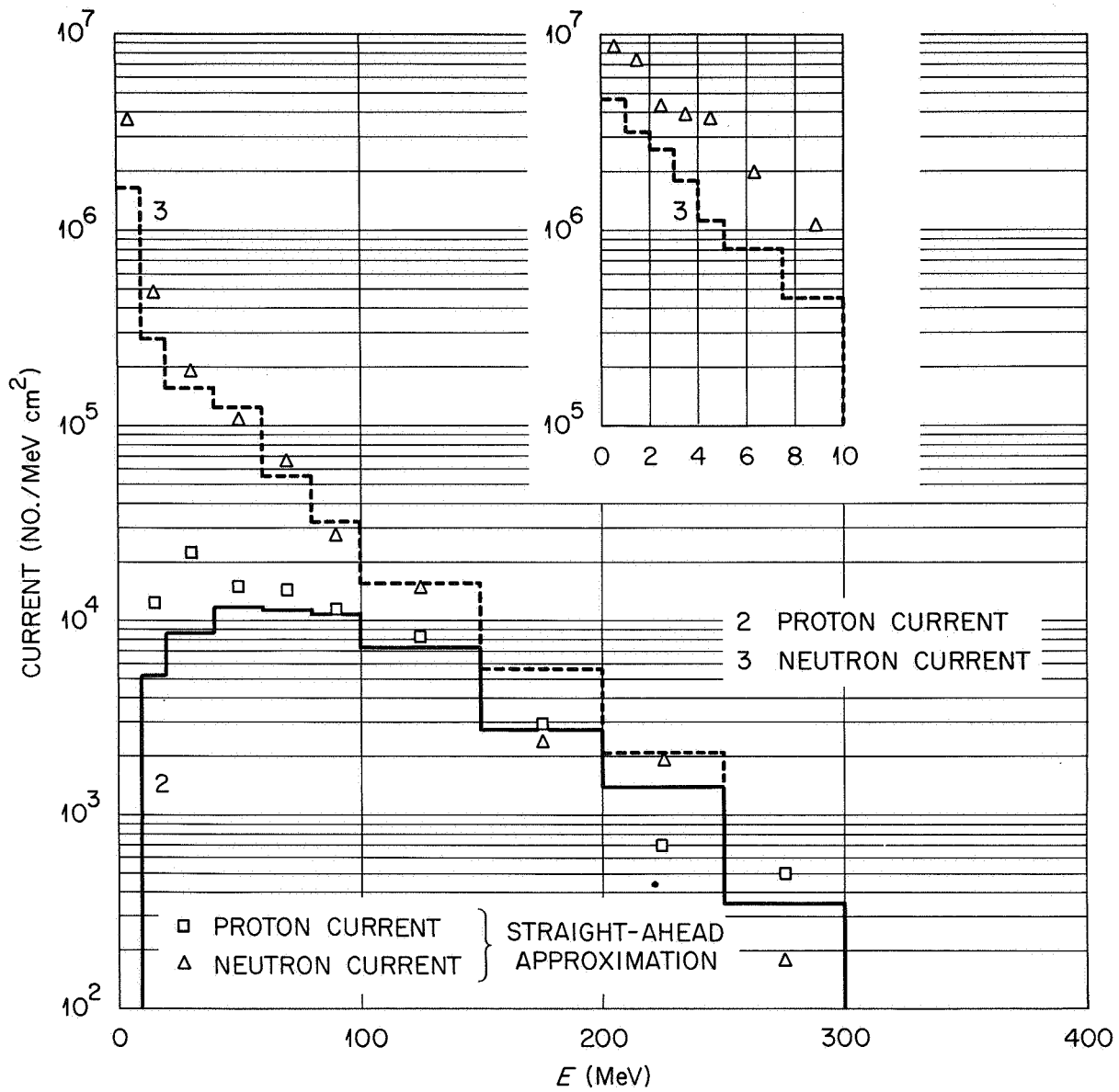


Fig. 8 Secondary particle current at aluminum-tissue interface; flare spectrum ($B_0 = 100$ MV) normally incident on 20 g/cm^2 of Al followed by tissue

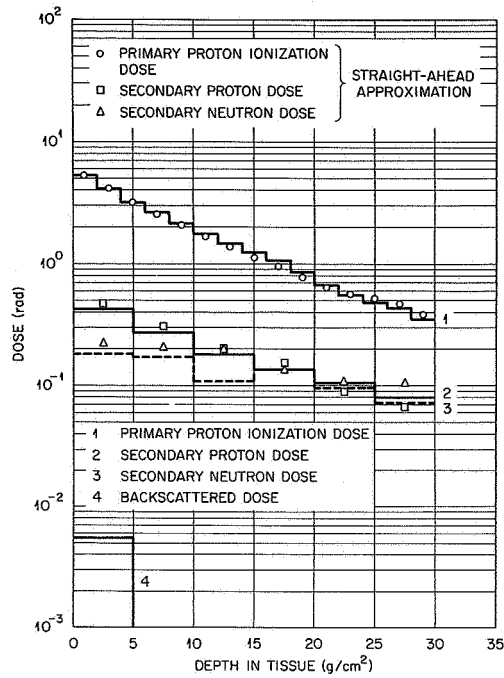


Fig. 9 Tissue dose (rad) vs depth; flare spectrum ($P_0 = 100$ MV) normally incident on 20 g/cm^2 of Al followed by tissue

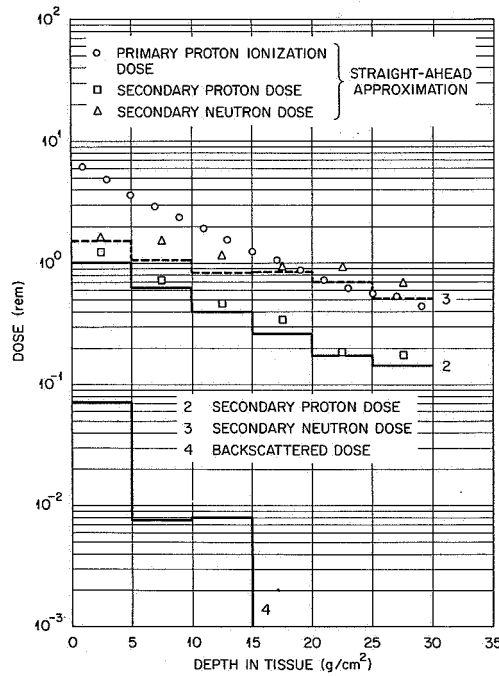


Fig. 10 Tissue dose (rem) vs depth; flare spectrum ($P_0 = 100$ MV) normally incident on 20 g/cm^2 of Al followed by tissue

the low-energy secondary proton current. At high energies (> 100 MeV or so) the statistical fluctuations are large, and the differences between the exact and approximate currents are probably to be ascribed to poor statistics rather than to any failure of the straightahead approximation.

In Figs. 9 and 10 the exact and approximate doses as a function of depth in the tissue in rad and rem, respectively, are shown. For comparison purposes, the total dose has been divided into four parts: primary proton-ionization dose, secondary proton dose, secondary neutron dose, and backscattered dose. The primary proton-ionization dose is the dose from those incident protons which have undergone neither elastic nor nonelastic nuclear collisions. The primary proton-ionization dose is by definition the same in the exact and approximate calculations. Since this is the case, the exact primary proton-ionization dose has not been shown in Fig. 10. The secondary proton dose is the dose from all charged particles that are produced by primary or secondary protons. The secondary neutron dose is the dose from all charged particles produced by secondary neutrons. It should be noted that the secondary proton dose and secondary neutron dose include contributions from particles produced both in the shield and in the tissue. In addition to the contribution from protons, the secondary doses also include a contribution from charged evaporation particles with mass greater than that of a proton and from recoil nuclei. The backscattered dose is the dose from all particles and their progeny which cross from the tissue into the aluminum. This backscattered dose is by definition zero in the straightahead approximation. The agreement between the exact and approximate secondary doses in both Figs. 9 and 10 is quite good at all tissue depths. The straightahead approximation overestimates the secondary doses, particularly in rem, but in the present instance at least the error does not seem excessive from the point of view of shielding. Finally,

it should be noted that while the secondary dose in Fig. 9 is small compared to the primary dose this is not the case in Fig. 10. The quality factors used in the calculations and consequently the dose calculations in rem must be considered to be very approximate. The calculations do serve to indicate, however, that the importance of secondary particles in space vehicle shielding is dependent on the quality factors which are found to be applicable.

At the present time the code collection of the Radiation Shielding Information Center of the Oak Ridge National Laboratory contains five proton penetration codes, written in various approximations, which were designed for doing space shielding calculations. To test the consistency of these codes, W. W. Scott and R. G. Alsmiller, Jr.¹³ have compared the results given by each code to a typical sample problem.

The codes which have been considered are those written by W. E. Kinney⁴ at the Oak Ridge National Laboratory, by R. P. Moshofsky¹⁴ at The Boeing Company, by C. W. Hill et al.¹⁵ at the Lockheed-Georgia Company, by J. R. Lilley and W. R. Yucker^{16*} at the Douglas Aircraft Company, and by R. I. Hildebrand and H. E. Renkel¹⁷ at the Lewis Research Center. An extensive discussion of the data and method of calculation used in each of these codes is given in the listed reference, and therefore only a very brief discussion will be given here. The code written by Kinney is the only one of the codes which solves the complete transport equations. The codes written by Hill et al. and by Hildebrand and Renkel employ the straightahead approximation and include a calculation of the higher generation secondary particles. The codes by Moshofsky and by Lilley and Yucker employ the straightahead approximation, calculate explicitly only

*The code by Lilley and Yucker was not available at the time reference 13 was written and therefore the results from this code presented here are not included in reference 13.

first-generation secondary particles, and utilize attenuation factors to treat the higher generations. The codes by Kinney and by Hildebrand and Renkel use the particle-production data generated by Bertini, while the other codes rely on the older, more approximate data.

The sample problem used in the comparison is that shown in Fig. 7: i.e., a proton flare spectrum, taken to be exponential in rigidity with $P_0 = 100$ MV, normally incident on a slab of aluminum of thickness 20 g/cm^2 followed by a 30-cm slab of tissue. The doses as a function of depth in the tissue from primary protons, secondary protons, and secondary neutrons are compared in Figs. 11, 12, and 13, respectively.

The primary proton doses from the various codes shown in Fig. 11 are in reasonable agreement. This is to be expected since there is little uncertainty in the data, and this dose is relatively easy to calculate. In Fig. 12 where the secondary proton doses are compared, all of the results are in reasonable agreement except those given by the Boeing code.* In Fig. 13 the secondary neutron doses are compared. The Boeing results are somewhat higher than those given by the other codes. The Lockheed-Georgia results appear to be high in the first few centimeters of the tissue but thereafter agree with the results given by the Lewis and Douglas codes. The statistical uncertainty in the ORNL results are rather large, but in general these results are lower than those given by the Lewis and Douglas codes. This difference may be attributed at least to some extent to the straightahead approximation used in the Lewis and Douglas codes.

*M. Wilkinson of Boeing has informed me that he has revised the Boeing code and now obtains results which are in substantial agreement with the other codes. This revised code is not, however, at this time available from the Radiation Shielding Information Center.

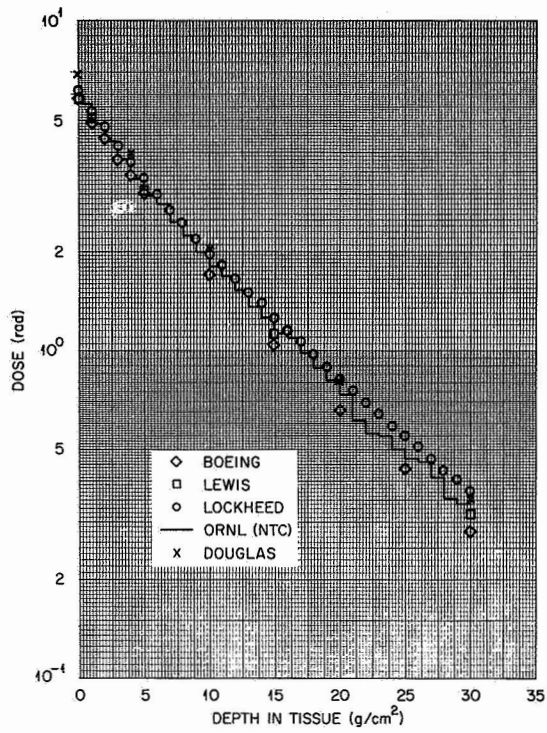


Fig. 11 Primary proton dose vs depth in tissue

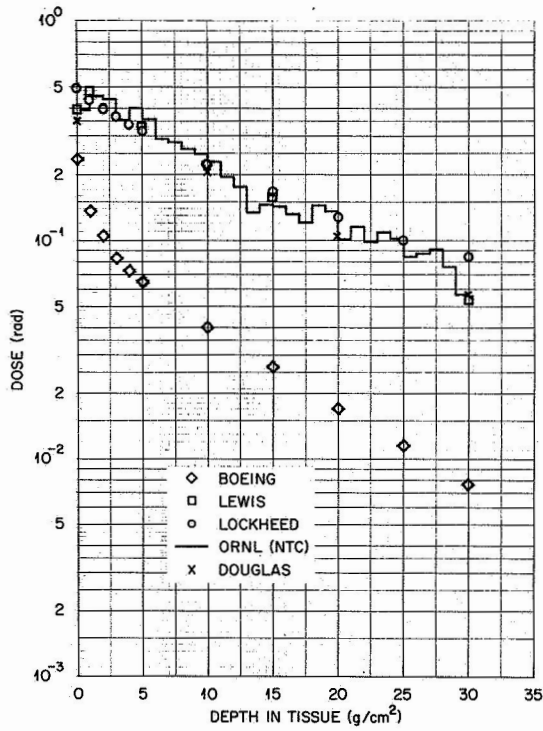


Fig. 12 Secondary proton dose vs depth in tissue

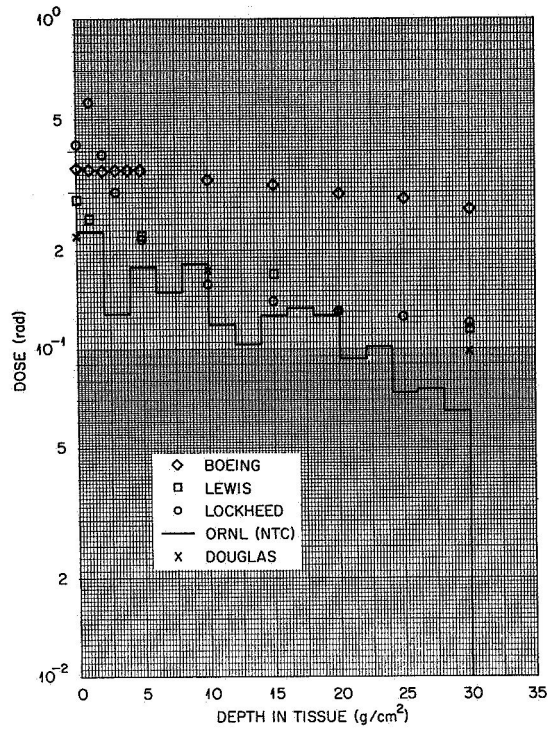


Fig. 13 Secondary neutron dose vs depth in tissue

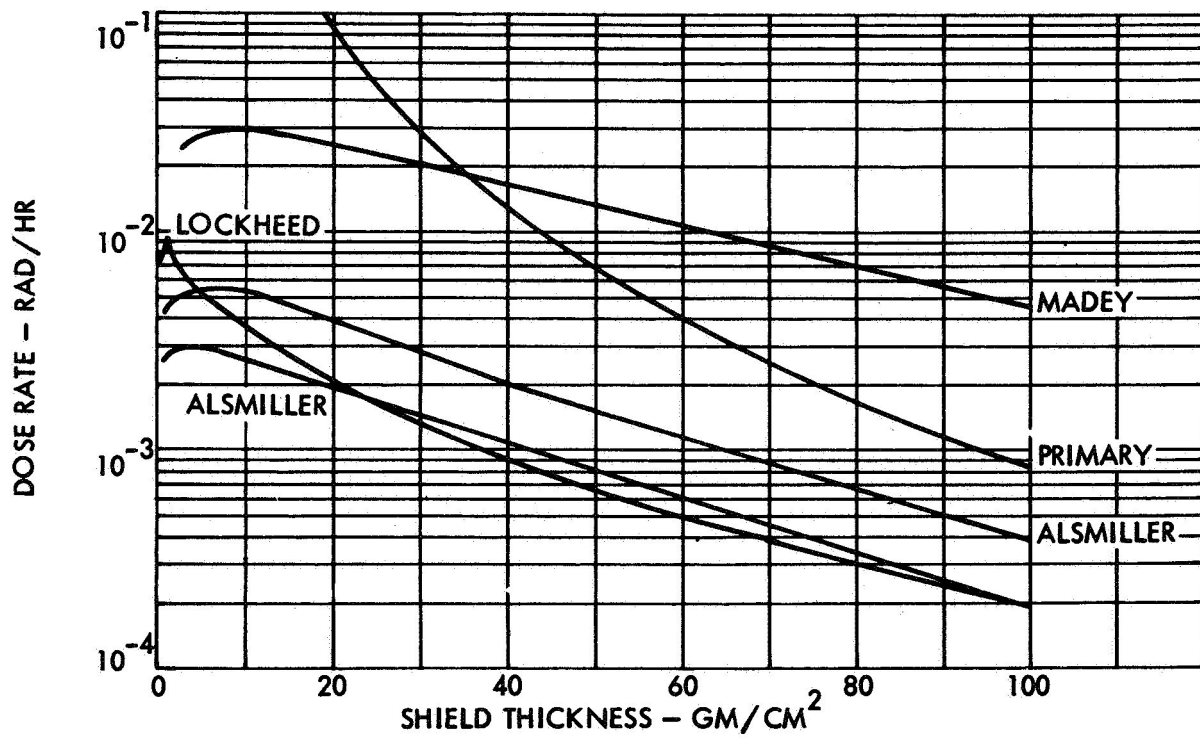


Fig. 14 Primary proton and gamma dose rate; aluminum shield

None of the comparisons mentioned above include a contribution from the gamma rays. Calculations have been carried out for gamma rays with the straight-ahead approximation by Madey et al.,¹⁸ Dye,¹⁹ and Alsmiller et al.²⁰ Gamma-ray calculations have also been performed by Hill et al.,^{15,21} who used a model which accounts for the angular distribution of the produced gamma ray and is applicable to a slab shield. In the first three calculations, only gamma-ray production by incident protons was considered; in the last calculation, gamma-ray production by all of the secondary nucleons, as well as the incident protons, is included. Madey et al. and Dye obtained gamma-ray production data by extrapolating from a very limited amount of experimental data. Alsmiller et al. obtained their data by applying crude Coulomb corrections to the theoretical data of Troubetskoy²² for gamma-ray production by neutrons. These data extended to only 22 MeV. It was assumed that the 22-MeV data applied to protons of energy up to 50 MeV. Hill et al. used the model of Troubetskoy with Coulomb corrections and calculated gamma-emission data at the higher energies.

A comparison of the Madey, Alsmiller, and Hill calculations, due to Hill and Simpson,²¹ is shown in Fig. 14. The results shown are the primary proton and gamma-ray doses at the center of a spherical-shell aluminum shield as a function of shield thickness. The form of the incident spectrum considered may be found in Madey et al.¹⁸ and Alsmiller et al.²⁰ The two Alsmiller curves were obtained using different gamma-ray production data. In obtaining the lower curve, it was assumed that protons with energy greater than 22 MeV could not produce gamma rays; in obtaining the upper curve, gamma-ray production from all protons of energy less than 50 MeV was included. Because of the crude extrapolation used in obtaining the gamma-ray production data, the upper curve is probably an overestimate.

The Alsmiller et al. and the Hill et al. calculations are in reasonably good agreement except for thin shields. The reason for the thin-shield difference is not known, but probably can be attributed to a difference in the assumed gamma-ray production data for very low energy incident protons. The calculation by Madey et al. is much larger than the other two because of the very different production data used. Experimental information on gamma-ray production from proton-nucleus collisions has recently become available,^{23,24} and it is now possible to draw a few tentative conclusions about the validity of the calculations.

In Fig. 15 the interaction cross section multiplied by the number of emitted photons, when a proton collides with an aluminum nucleus, and the interaction cross section multiplied by the total energy of all emitted photons, when a proton collides with an aluminum nucleus, are plotted as a function of incident proton energy. The solid and the dashed curves are obtained from the data used in the calculations of Alsmiller et al., shown in Fig. 14.* If only the solid curves in Fig. 15 are used, then the lower curve labeled Alsmiller in Fig. 14 is obtained. If both the solid and the dashed curves are used, then the upper curve labeled Alsmiller in Fig. 14 is obtained. The plotted points are the experimental points of W. Zobel et al.^{23,24} The experimental points have been obtained by integrating the measured differential cross section for photon production and the differential cross section for photon production multiplied by photon energy over all emitted photon energies greater than 600 keV. Hopefully but not certainly the contribution to the integrals from photons of energy less than 600 keV is small.

The upper dashed line in Fig. 15 overestimates considerably the energy emitted in the form of photons multiplied by the cross section between 22 MeV and 50 MeV while the lower dashed line is in very rough agreement with the cross section

*The analogous data used in the calculations of Hill et al. are not given in reference 21, and therefore comparisons with these data cannot be made.

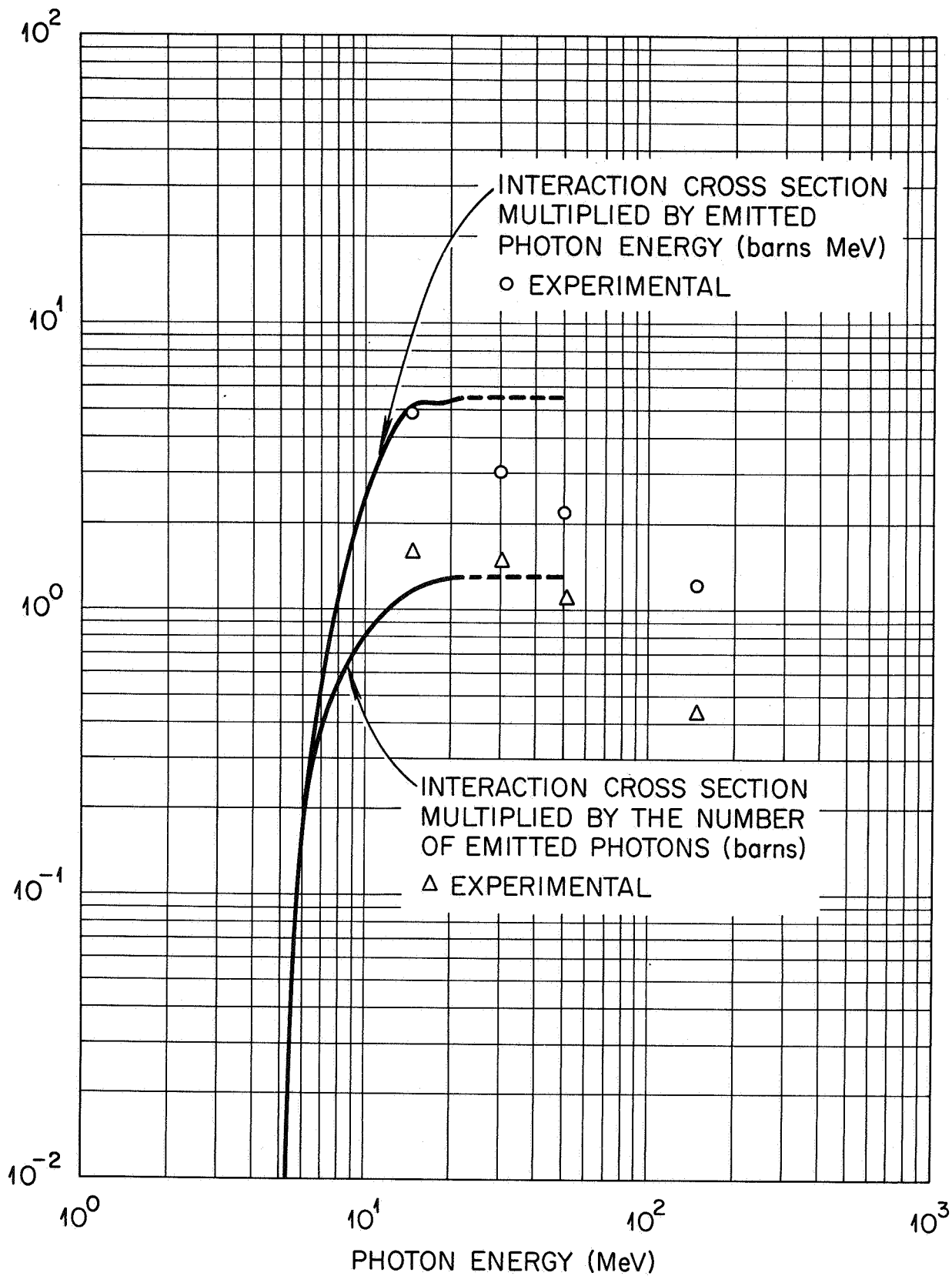


Fig. 15 Photons from protons incident on aluminum

multiplied by the photon multiplicity in this energy region. This means of course that the upper curve in Fig. 14 labeled Alsmiller is too high. In the energy region from 14.6 MeV to 22 MeV the solid curves underestimate the experimental data on cross section times multiplicity and overestimate slightly the experimental data on emitted photon energy times cross section. On the basis of the comparison shown in Fig. 15, there seems to be no reason to expect that the lower Alsmiller curve in Fig. 14 is greatly in error. Of course the actual photon emission spectrum has not been compared and there may be some changes due to this. Of even more importance, however, is the fact that there are no experimental data for proton energies of less than 14.6 MeV. This energy region is important from the standpoint of gamma-ray production because of the large number of low-energy protons in a typical solar-flare spectrum. If the rapid decrease with decreasing energy of the solid curves in Fig. 15 should be in error, it is still possible that the estimates of the secondary photon contribution to the dose could change appreciably. In this regard, it should also be noted that while secondary nucleon production is a high-energy phenomenon in the sense that the higher energy incident protons (≥ 100 MeV in a typical flare spectrum) tend to be important in their production, this is not the case with secondary gamma rays. All of the calculations, particularly the work of Hill et al.,²¹ indicate that the gamma rays produced by very low energy flare protons produce most of the gamma-ray dose even for moderately thick shields. Thus, if the low-energy portion of the flare spectrum, which is not well known, should be much larger than that assumed in the calculations, the gamma dose could increase considerably while the primary proton and secondary nucleon doses remain essentially unchanged.

REFERENCES

1. R. G. ALSMILLER, JR., "High-Energy Nucleon Transport and Space Vehicle Shielding," Nucl. Sci. Eng., 27, 158 (1967).
2. J. S. FRASER et al., "Neutron Production in Thick Targets Bombarded by High-Energy Protons," Phys. Can., 21, No. 2, 17 (1965).
3. W. A. COLEMAN, Oak Ridge National Laboratory, private communication.
4. W. E. KINNEY, "The Nucleon Transport Code, NTC," ORNL-3610, Oak Ridge National Laboratory (1964).
5. H. W. BERTINI, "Low-Energy Intranuclear-Cascade Calculations," Phys. Rev. 131, 180 (1963); with erratum, Phys. Rev., 138, AB2 (1965).
6. L. DRESNER, "EVAP - A FORTRAN Program for Calculating the Evaporation of Various Particles from Excited Compound Nuclei," ORNL-TM-196, Oak Ridge National Laboratory (1961).
7. T. V. BLOSSER, F. C. MAIENSCHHEIN, and R. M. FREESTONE, JR., "The Energy Deposition in a Water-Filled Spherical Phantom by Secondaries from High-Energy Protons and by Neutrons," Health Phys., 10, 743 (1964).
8. B. LILEY and A. G. DUNEER, JR., "Secondary-Dose Equivalent Model and Comparison of 160-MeV Proton-Induced Neutron and Proton Dose with a Comprehensive Experiment," Space and Information Systems Division, North American Aviation, Inc. (submitted to Nuclear Science and Engineering).
9. H. ALTER, "Basic Microscopic Data for Space Shielding Analysis," AI-Memo-8853, Atomics International, North American Aviation, Inc. (1963).

10. R. G. ALSMILLER, JR., D. C. IRVING, and H. S. MORAN, "The Validity of the Straightahead Approximation in Space Vehicle Shielding Studies," Second Symposium on Protection Against Radiations in Space, Gatlinburg, Tenn., Oct. 12-14, 1964, NASA SP-71, p. 177, National Aeronautics and Space Administration (1965).
11. This work was carried out by R. G. ALSMILLER, JR., D. C. IRVING, and H. S. MORAN at the Oak Ridge National Laboratory.
12. C. D. ZERBY and W. E. KINNEY, "Calculated Tissue Current-to-Dose Conversion Factors for Nucleons Below 400 MeV," Nucl. Instr. Meth., 36, 125 (1965).
13. W. W. SCOTT and R. G. ALSMILLER, JR., "Comparison of Results Obtained with Several Proton Penetration Codes," RSIC-17, Oak Ridge National Laboratory (1967).
14. R. P. MOSHOFSKY, "Computer Codes for the Evaluation of Space Radiation Hazards. Vol. 8: Space Radiation Doses from Protons and their Secondary Radiations," D2-90418-8 (NASA-CR-58299), Aerospace Div., The Boeing Company (1964).
15. C. W. HILL et al., "Computer Programs for Shielding Problems in Manned Space Vehicles," ER-6643 (NASA Contract NAS8-5180), The Lockheed-Georgia Company (1964).
16. J. R. LILLEY and W. R. YUCKER, "Charge, A Space Radiation Shielding Code," SM-46335, Douglas Missile and Space Systems Division, Douglas Aircraft Company (1965).
17. R. I. HILDEBRAND and H. E. RENKEL, "The Lewis Proton Shielding Code," NASA TM X-52166, Lewis Research Center (1966).

18. R. MADEY et al., "Gamma Dose from Solar Flare Protons Incident on an Aluminum Shield," Trans. Am. Nucl. Soc., 5, 1, 213 (1962).
19. D. L. DYE, "Space Proton Dose at Points Within the Human Body," DZ-90106, The Boeing Company (1962).
20. F. S. ALSMILLER, R. G. ALSMILLER, JR., and D. K. TRUBEY, "Comparison of Primary Proton Dose with the Dose from Gamma Rays Produced by Inelastic Scattering of Solar Flare Protons," Proc. Symposium on Protection Against Radiation Hazards in Space, Gatlinburg, Tenn., Nov. 5-7, 1962, TID-7652, Division of Technical Information Extension, USAEC (1962).
21. C. W. HILL and K. M. SIMPSON, JR., "Calculation of Proton Induced Gamma-Ray Spectrum and Comparison with Experiment," Proc. Second Symposium on Protection Against Radiations in Space, Gatlinburg, Tenn., Oct. 12-14, 1964, NASA SP-71, p. 189, National Aeronautics and Space Administration (1965).
22. E. S. TROUBETSKOY, "Fast Neutron Cross Sections of Iron, Silicon, Aluminum, and Oxygen," NDA-2111-3, Vol. C, Nuclear Development Associates, Inc. (1959).
23. W. ZOBEL, F. C. MAIENSCHNEIN, and R. J. SCROGGS, "Spectra of Gamma Rays Produced by the Interaction of ~160-MeV Protons with Be, C, O, Al, Co, and Bi," ORNL-3506, Oak Ridge National Laboratory (1965).
24. W. ZOBEL, Oak Ridge National Laboratory, private communication.

NUCLEAR REACTION CROSS SECTIONS FOR SPACECRAFT SHIELD DESIGN^a

R. W. Peelle

Oak Ridge National Laboratory

Oak Ridge, Tennessee

N 68-26145

Spherical shield geometry is adequate for studying the contribution of nuclear reactions to the dose received by spacecraft occupants. Very high energy incident protons produce in the shield an essentially isotropic volume source proportional to the angle-integrated production cross section. Protons with range too short to penetrate the shield produce a yield dependent upon the current into the shield, with the importance of cross sections at a given energy being dependent on the incident spectrum and the inverse of the stopping power. Protons of intermediate energy penetrate the shield and stop in the pilot, and so are important for primary rather than for secondary dose. If the shield is not too thick, the secondary dose inside the cavity is rather independent of position in both the high- and low-incident energy limits. Therefore, calculations can be made for the dose at the center of the sphere, where the secondary flux from an isotropic primary flux is equal to that obtained in a modified straight-ahead approximation for monodirectional primary protons incident on a slab.

Widely available intranuclear cascade-plus-evaporation calculations give secondary nucleon cross sections which agree fairly well with experiments using incident protons. New data is presented to illustrate that the present model has some limited validity even for incident proton energies as low as 20 MeV. Computational models are not known to have yielded generally valid cross sections for secondary gamma rays or for secondary neutrons from alpha particles.

^aResearch funded by the National Aeronautics and Space Administration, under Union Carbide Corporation's contract with the U. S. Atomic Energy Commission.

I. THE INFLUENCE OF SPACECRAFT GEOMETRY ON THE RELATIVE IMPORTANCE OF NUCLEAR SECONDARY CROSS SECTIONS

When we wish to think in a simple way about the influence of secondary nuclear radiations on the shield design of a spacecraft, we can think of the cabin as a one-dimensional sphere with the pilot conveniently huddled in the center as illustrated in Fig. 1. The incident protons and alpha particles, averaged over the flight, are assumed to be isotropic in the absence of the vehicle. We are concerned with any influence that nuclear reactions in the shield may have on the dose to the pilot. The shield is thin enough, in terms of the interaction length of the secondary neutrons and gamma rays, that multiple collisions cannot dominate. We are also concerned with how the reactions of primary (or secondary) particles in the pilot may affect him. This discussion aims to help clarify which cross sections are important.

The sphere geometry seems crude, but it is adequate for the present purpose. The broad angular distribution of secondary radiations allows us a simple shield representation even for cases that seem to demand great geometric complexity for estimation of the dose from degraded primaries. If we ever become ready to abandon our sphere, at worst only a few simply shaped shield regions will be needed. (Pathlengths through the various gross regions may be preserved from primary dose calculations to allow good secondary source strength estimations.) On the other hand, precise nuclear calculations will be needed for the simpler geometries so that we will not be misguided about complex multiple-collision effects or the influence of detailed spectra.

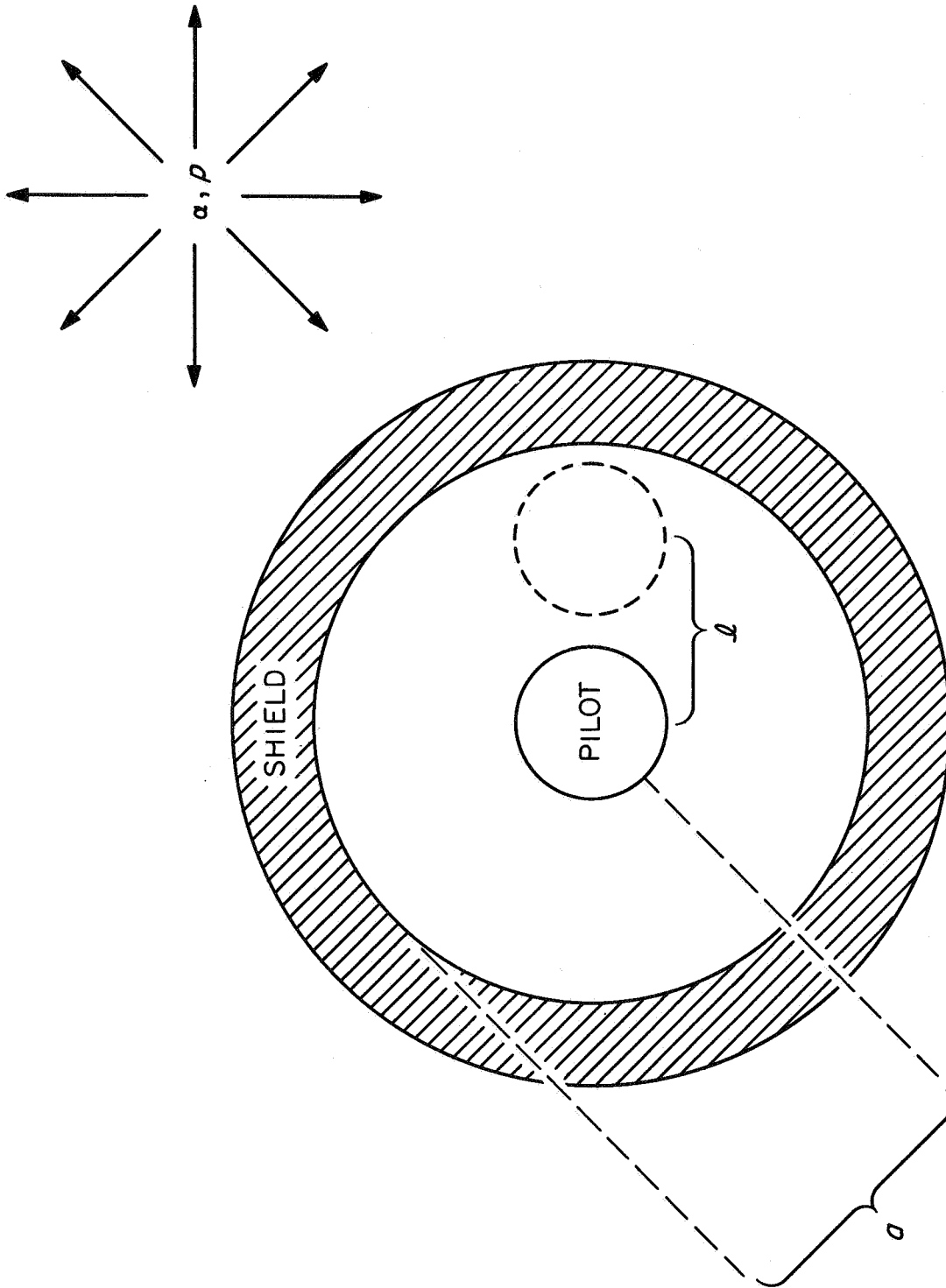


Fig. 1 An adequate geometry to represent a spacecraft cabin for studying the effects of nuclear secondaries

How can we decide whether a primary proton of given energy E will damage the pilot directly or by way of secondary particles? The relation of shield thickness to incident-particle range distinguishes three cases:

a) Primaries so energetic that they pass completely through the cabin and its occupants lose little enough energy in their continuous slowing-down process that secondary reactions can well compete. The slow energy dependence of the relevant cross sections implies that there is produced in this case an isotropic volume source of secondaries throughout the shield, independent of the angle variations of the differential cross sections. Ignoring details of secondary particle type and energy spectrum, the strength (cm^{-3}) of this volume source V is

$$V = \int_{E_a}^{\infty} \phi(E) \Sigma(E) dE , \quad (1)$$

where $\phi(E)$ is the incident flux integrated over all solid angle, and Σ is the macroscopic cross section at energy E for production of the secondaries being considered. Σ includes the multiplicity.

b) Less energetic primaries which penetrate the shield but stop in the pilot contribute the dominant share of the primary dose, so secondaries in this case are relatively unimportant. (For a 5-g/cm^2 shield we are talking about proton energies between 70 and 200 MeV). For simplified calculations the temptation should be overwhelming to treat secondary production by these primaries as if Eq. (1) were valid.

c) Low-energy charged primaries cannot penetrate the shield, but their secondary neutrons and gamma rays can. The current of low-energy particles into the spacecraft skin produces a surface secondary source of strength

S (cm⁻²) given by

$$S = \frac{1}{4} \int_0^{E_c} dE' \phi(E') \int_0^{E'} \frac{\Sigma(E) dE}{|dE/dx|} \quad (2)$$

The stopping power enters in the denominator because to find the yield one must integrate over the path of each primary from its original energy down to zero. Unlike the volume source produced by the high-energy primaries, the surface source strength usually has an angular distribution relative to the shield normal. Equation (2) is in the proper form if input data is to be cast as thick-target yields for stopping a primary of energy E'. The order of integration is reversed to employ the cross section at a given energy and the integral flux $\Delta\phi^i(E)$ up to the cutoff E_c at which the range equals the shield thickness; that is,

$$\begin{aligned} S &= \frac{1}{4} \int_0^{E_c} \frac{dE \Sigma(E)}{|dE/dx|} \int_E^{E_c} \phi(E') dE' \\ &= \frac{1}{4} \int_0^{E_c} \frac{dE \Sigma(E) \Delta\phi^i(E)}{|dE/dx|} \end{aligned} \quad (2a)$$

I think that plausible assessment of the importance of this surface source of gamma rays and neutrons is the most obviously unsolved problem in space shielding. We can already say something in the case of gamma rays. Integrated preliminary data of Zobel, Maienschein, and Scroggs¹ suggest that the gamma-ray production cross section for incident protons on aluminum behaves with energy between 15 and 150 MeV almost like the proton stopping power, allowing a quick estimation of the secondary surface source using Eq. (2). The result is that the surface source of gamma rays produced

in aluminum would be about 2×10^{-3} times the incident proton energy current into the shield (less ~ 15 MeV/proton). With flare spectra which are quite soft, i.e., for a rigidity parameter less than 50 megavolts, it appears that the gamma rays might contribute significantly for shields greater than 10 g/cm^2 thick. For harder flare spectra, aluminum gamma rays cannot produce a significant contribution. Neutron production cross sections behave differently with energy, so a less stringent rule probably applies.

Now let us return to our sphere model. You may question whether it was fair for me to draw the man in the center. Does the sphere integrate so well that this is a good approximation? I have in Fig. 2 a rough answer for the case of an isotropic volume source within the shield. The secondary flux at a point in the interior is estimated as a function of radial position for a sphere 5% as thick as its radius ($t/a = 0.05$). With no attenuation of secondaries the flux rises with radius to 20% above the central value at $2/3$ the capsule radius and to about 55% above at 0.9. As secondary attenuation (no scattering) is introduced to the extent of $\Sigma_s t$ mean free paths along the radial direction, the distribution becomes flatter. For present purposes it seems just barely fair to call the central point representative. At the sphere center the secondary flux is

$$F = Vt[1 - \exp(-\Sigma_s t)]/\Sigma_s t \quad . \quad (3)$$

Equation (3) reduces to $F = Vt$ for small $\Sigma_s t$, and to $F = V/\Sigma_s$ for large $\Sigma_s t$. This is the same estimate one would obtain in the straightahead approximation! As stated by Wallace et al.,² the straightahead approximation for the spherical shell in an isotropic flux, viewed at the sphere center, gives the same numerical result as the same approximation gives for a slab of

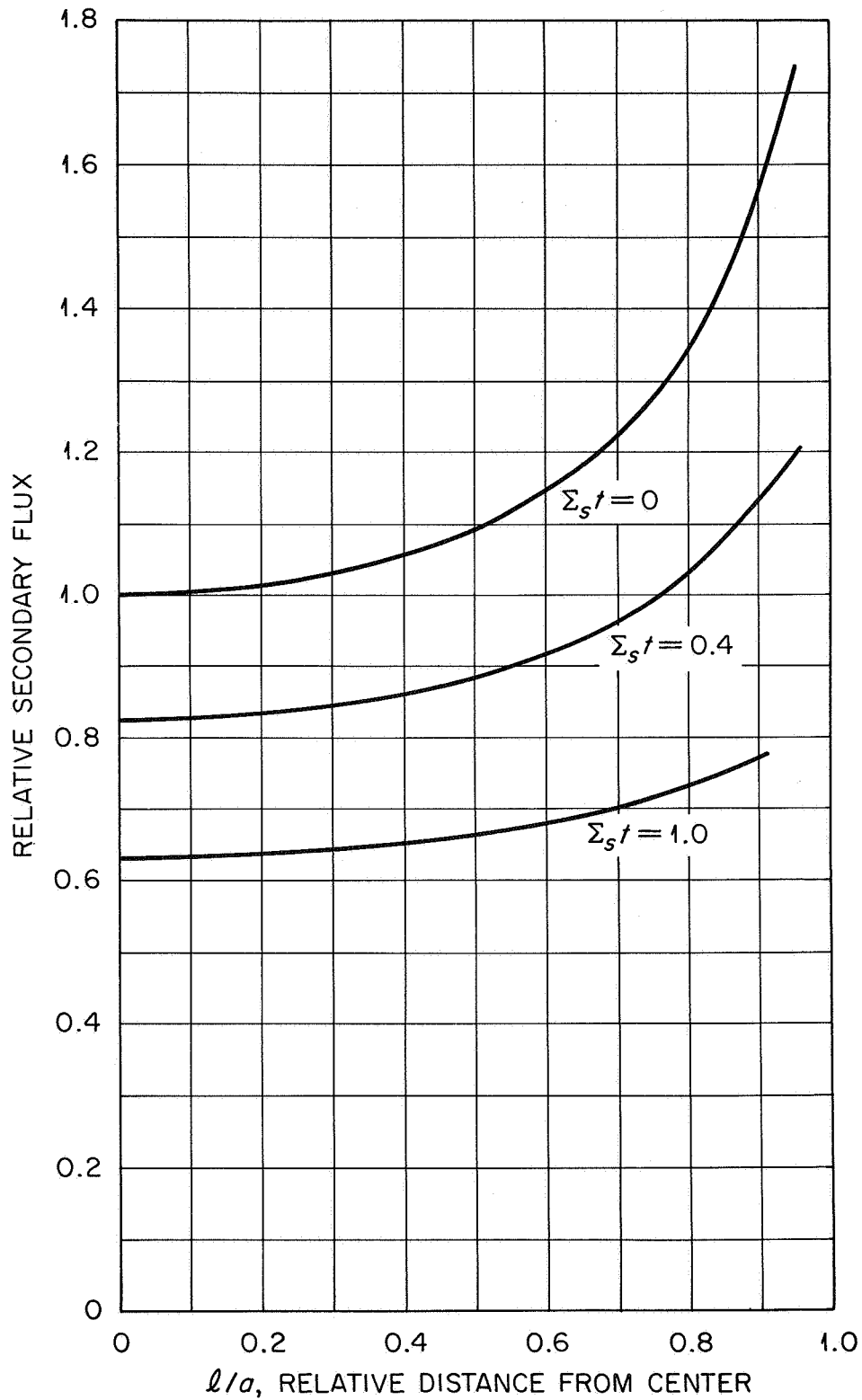


Fig. 2 Interior flux vs. radial position for a spherical shell volume source of thickness t equal to 5% of the radius. Σ_s is the macroscopic cross section for the secondary radiation.

the same thickness with normally incident (not isotropic) flux. Recall that the volume source strength V has an energy spectrum but contains only the angle-integrated differential cross sections.

A similar approach was made to the problem of secondaries from the low-energy primaries which cannot penetrate the shield. The current rather than the flux is important, so the surface source strength is a function of angle unless the cross sections for secondary production are isotropic. Using the (assumed isotropic) integral primary flux $\Delta\Phi^i$ defined in Eq. (2a), the contribution to the angle-differential surface source strength ($\text{cm}^{-2} \text{sr}^{-1} \text{MeV}^{-1}$) from the differential macroscopic cross sections $\Sigma(E, \alpha)$ is

$$S(E, \Psi) = \frac{\Delta\Phi^i(E)}{4\pi|dE/dx|} \int_{\Omega} d\Omega \cos\beta \Sigma(E, \alpha) , \quad (4)$$

where β and Ψ are respectively the angles relative to the shield normal of the primary and secondary particles, and α is the angle between the two particles. For a detector at the center of the sphere, $\Psi = 0$ and $\beta = \alpha$, and the angular distributions as expected occur weighted by the cosine of the scattering angle. When the differential cross section is expressed in a Legendre expansion with coefficients $\Sigma_{\ell}(E)$, i.e.,

$$\Sigma(E, \alpha) = \frac{1}{4\pi} \sum_{\ell} \Sigma_{\ell}(E) P_{\ell}(\cos\alpha) , \quad (5)$$

the integral in Eq. (5) may be performed to give the differential surface source:

$$S(E, \Psi) = \frac{\Delta\Phi^i(E)}{16\pi|dE/dx|} \sum_{\ell} A_{\ell} \Sigma_{\ell}(E) P_{\ell}(\cos\Psi) . \quad (6)$$

The A_ℓ 's may be obtained by applying the addition theorem for spherical harmonics to Eq. (4) using the expansion (5). The resulting integral is known,³ leading to the results tabulated below.

| ℓ | A_ℓ | ℓ | A_ℓ |
|--------|----------|--------------|----------|
| 0 | 1 | 3, 5, 7, ... | |
| 1 | 2/3 | 4 | -1/24 |
| 2 | 1/4 | 6 | 1/192 |

$$A_\ell = \pi^{1/2} \left[4\Gamma\left(\frac{3-\ell}{2}\right) \Gamma\left(\frac{5+\ell}{2}\right) \right]^{-1}$$

The expression (6) for $S(E, \Psi)$ leads to prediction of the radial dependence of the secondary flux within the cavity, illustrated in Fig. 3. Again it seems provisionally adequate to confine attention to the center of the sphere. If we ignore the detail that all secondaries are not produced just on the skin, the flux at the center is given by

$$\begin{aligned}
 F &= 4\pi e^{-\Sigma_s t} \int_0^{E_c} S(E, 0) dE \\
 &= \frac{\exp(-\Sigma_s t)}{4} \sum_{\ell} A_\ell \int_0^{E_c} \frac{\Sigma_\ell(E)}{|dE/dx|} \Delta\Phi^i(E) dE \quad . \quad (7)
 \end{aligned}$$

This is the result which would be given by the straightahead approximation using modified production cross sections equal to $\frac{1}{4} \sum_{\ell} A_\ell \Sigma_\ell$ rather than the

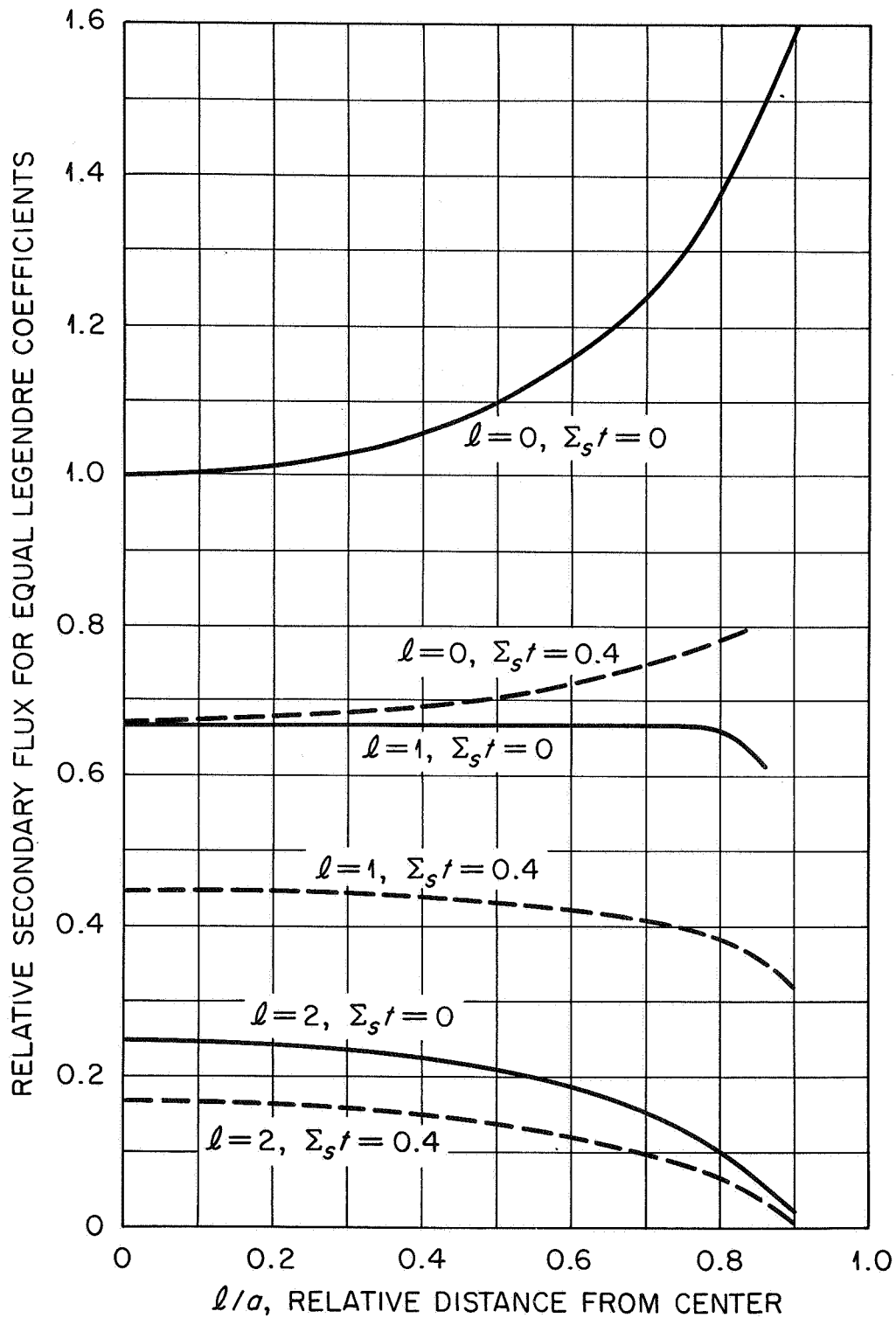


Fig. 3 Interior flux as a function of radius for a spherical surface source produced by secondaries from stopped charged particles. The contributions from the first three Legendre coefficients of the differential yield are shown for two values of the normal attenuation thickness $\Sigma_s t$.

customary Σ_0 . Again this time, by using the modified cross section, the spherical problem may be adequately transformed to a slab problem with normally incident flux.^b

To summarize, it appears that our cabin can revert from sphere to slab, that high-energy cross sections are important in a form integrated over angle and weighted by the differential primary flux, and that low-energy cross sections are important integrated over angle, with roughly a $\cos\alpha$ weighting, and weighted by the integral flux over the stopping power.

II. CROSS SECTIONS FOR SECONDARY NUCLEON PRODUCTION

Now consider what knowledge of nuclear cross sections has been made readily applicable to shield design. Generally, it seems preferable to use computed cross sections or interpolations among them, since experiments have not produced results at sufficiently regular energy and angle intervals. This approach is now workable for neutrons (or protons) produced by incident protons from at least 800 MeV down to some nebulous threshold below 100 MeV. By contrast, there is yet little valid guidance from calculations on how to handle neutrons produced by alpha particles.

Every serious shielding effort I have read tries to use nucleon-nucleus cross sections based upon the intranuclear cascade model results of

^b Those who have codes in slab geometry which operate with isotropic incident fluxes and which already contain information on the energy spectra of secondary particles may wish to consider use of the normal emission approximation, in which all secondaries penetrate the shield along the shortest path. This approximation does fairly well conceptually in the high-energy limit, and at low energies yields the appropriate result without the use of modified cross sections. (Isotropic flux on a slab does not transform properly for the primary flux, however.)

Metropolis et al.⁴ or the more recent ones of Bertini et al.,⁵ though several other similar computations have been made. Bertini's are now available in fitted form⁶ and on magnetic tape.⁷ These Monte Carlo estimation procedures are based on the idea that, for incident nucleons above perhaps 100 MeV, interactions with the nucleus are dominated by sequential microscopic two-body nucleon-nucleon scattering events for which free-particle cross sections apply. The resulting estimated cross sections are slow functions of angle, incident energy, and target mass, as are experimentally observed cross sections. Figure 4 shows sample differential cross sections at 10, 30, and 45 deg for 160-MeV protons on aluminum. The broad peak at the high-energy end of each spectrum moves with angle almost as it would for billiard-ball cross sections. This peak is a reflection of the use of free-particle kinematics for the microevents, blurred by the momentum distribution assigned to target nucleons and by the occurrence of intranuclear cascades. I have superposed a predicted cross section for Bi at 160 MeV and an appropriately scaled one for Fe at 60 MeV to show how invariant is the predicted differential cross section.

Each intranuclear cascade Monte Carlo history is terminated when no particle has enough energy inside the model nuclear potential to leave the nucleus with more than a specified (low) cutoff energy. The residual excitation energy can be very large; for example, the average excitation energy ranges from 35 to 110 MeV for incident 50- to 400-MeV nucleons on a heavy nucleus like tantalum. This excitation energy is usually handled by assuming that nucleons and heavier fragments "boil off" in variable evaporation chain processes similar to that described and programmed in Monte Carlo by Dostrovsky et al.⁸ This evaporation process produces a high (presumably) isotropic contribution at low energies which is not

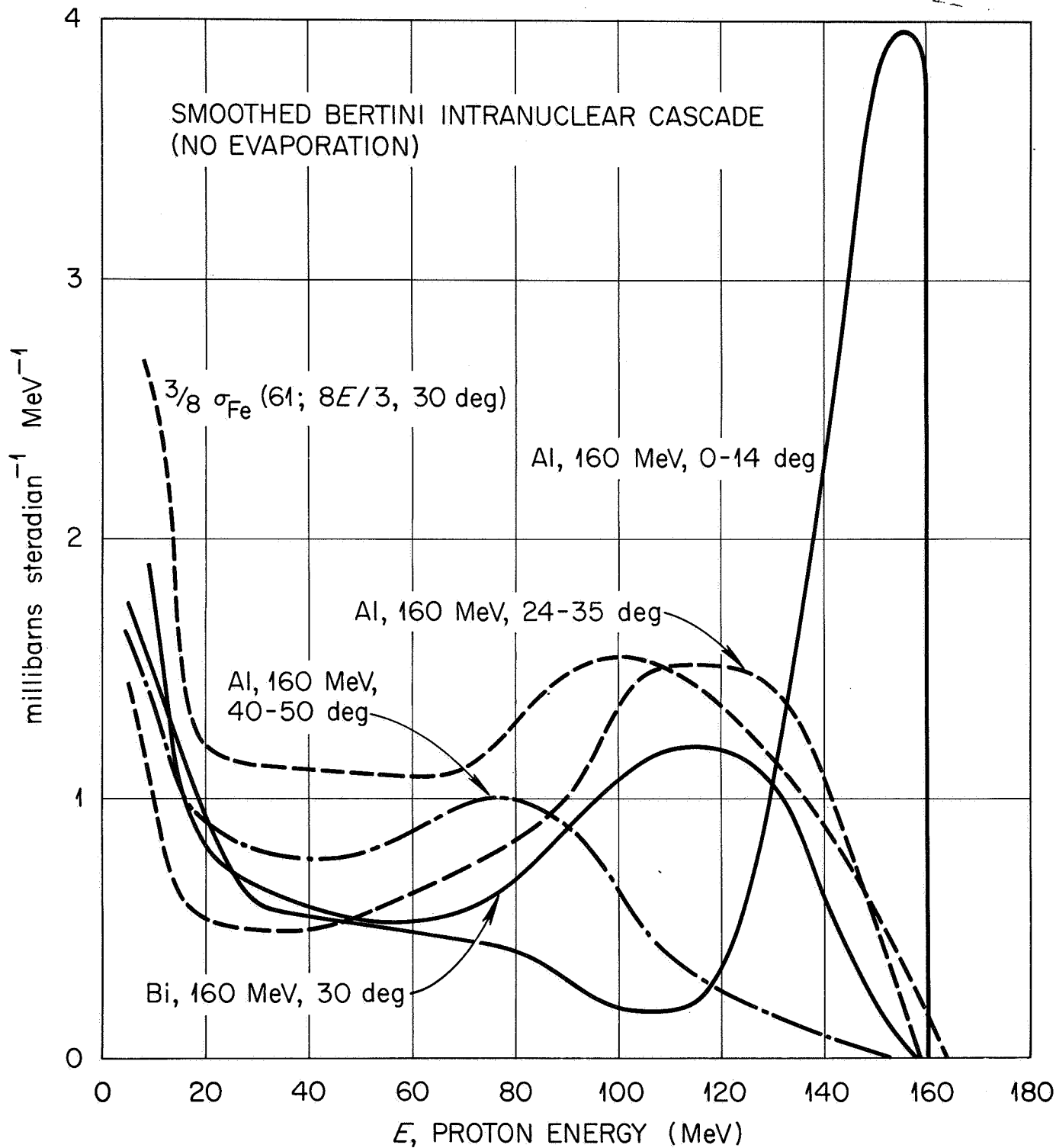


Fig. 4 Hand-smoothed differential cross sections from the Bertini intranuclear cascade calculation. The cross section for 61-MeV protons on iron has been stretched to preserve constant area.

included in Fig. 4. Estimated cross sections for neutrons look very similar to this figure except that the predicted (largely unmeasured) quasifree scattering peaks are less pronounced, and except that for heavy elements the predicted evaporation yields are quite high.

How valid are the cross sections obtained from the cascade model? They are remarkably so, though as an experimentalist I enjoy dwelling on residual difficulties. For instance, though the works of Wall and Roos⁹ and of Genin et al.¹⁰ support the marked quasifree peak in the 45 deg region, our work,¹¹ the recent results of Brun et al.,¹² and perhaps the 185-MeV data of Dahlgren¹³ all tend to require that quasifree scattering be less apparent. Figure 5 shows that at 60 deg Bertini predicts cross sections for 160-MeV protons on Al which are in accord (on an absolute basis, no free parameters) with the experiments of Wachter et al.¹⁴ and myself¹¹ but not quite with those of Roos and Wall.⁹ Neutrons from 140-MeV protons have been studied by Bowen¹⁵ at forward angles, where they characteristically disagree with calculation in the manner shown in Fig. 6; the predicted peak is always too intense and the tail too weak, though the situation does vary a little with target mass number. For a comparison at higher energy, Bertini has recently shown results from a new program which includes meson production.¹⁶ Figure 7 compares his estimates for 660-MeV protons on Cu with the experiment of Azhgirey et al.¹⁷ The new code is final but the cross-section parameters are yet subject to improvement.

Since I have emphasized cross sections integrated over angle, I would like to encourage comparisons on that basis. Figure 8, from the Orsay work of Brun et al.,¹² illustrates that cascade calculations can give fits within 20% to angle-integrated spectra for 156-MeV protons on silver.

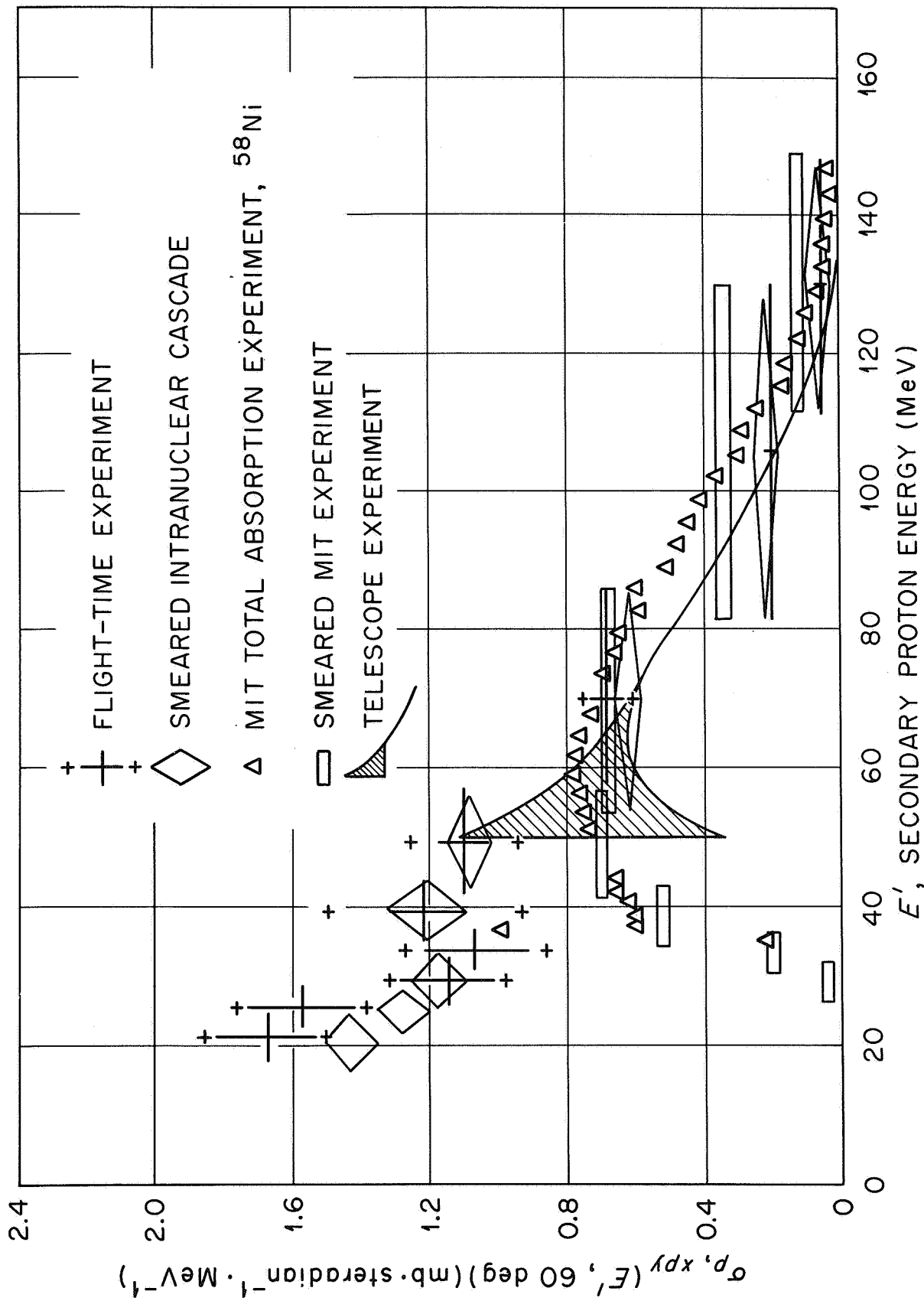


Fig. 5 Differential cross sections at 60 deg from 160-MeV protons on cobalt. Results from the Bertini calculations and from the MIT experiment of Wall and Roos are shown with and without smearing appropriate to the author's flight-time experiment.

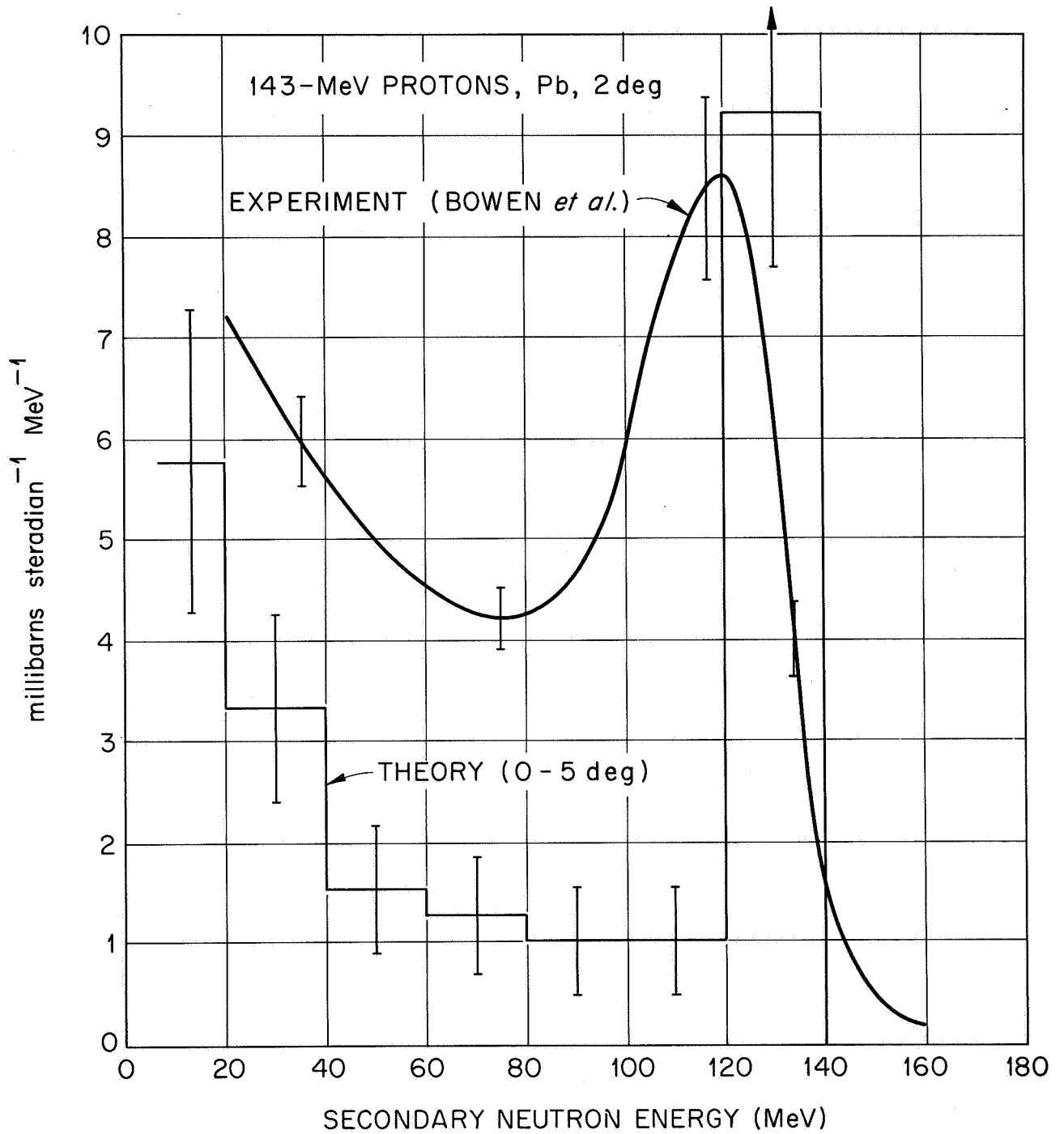


Fig. 6 Comparison of the Bertini intranuclear cascade calculation against experiment for secondary neutrons at 2 deg from 143-MeV protons on lead.

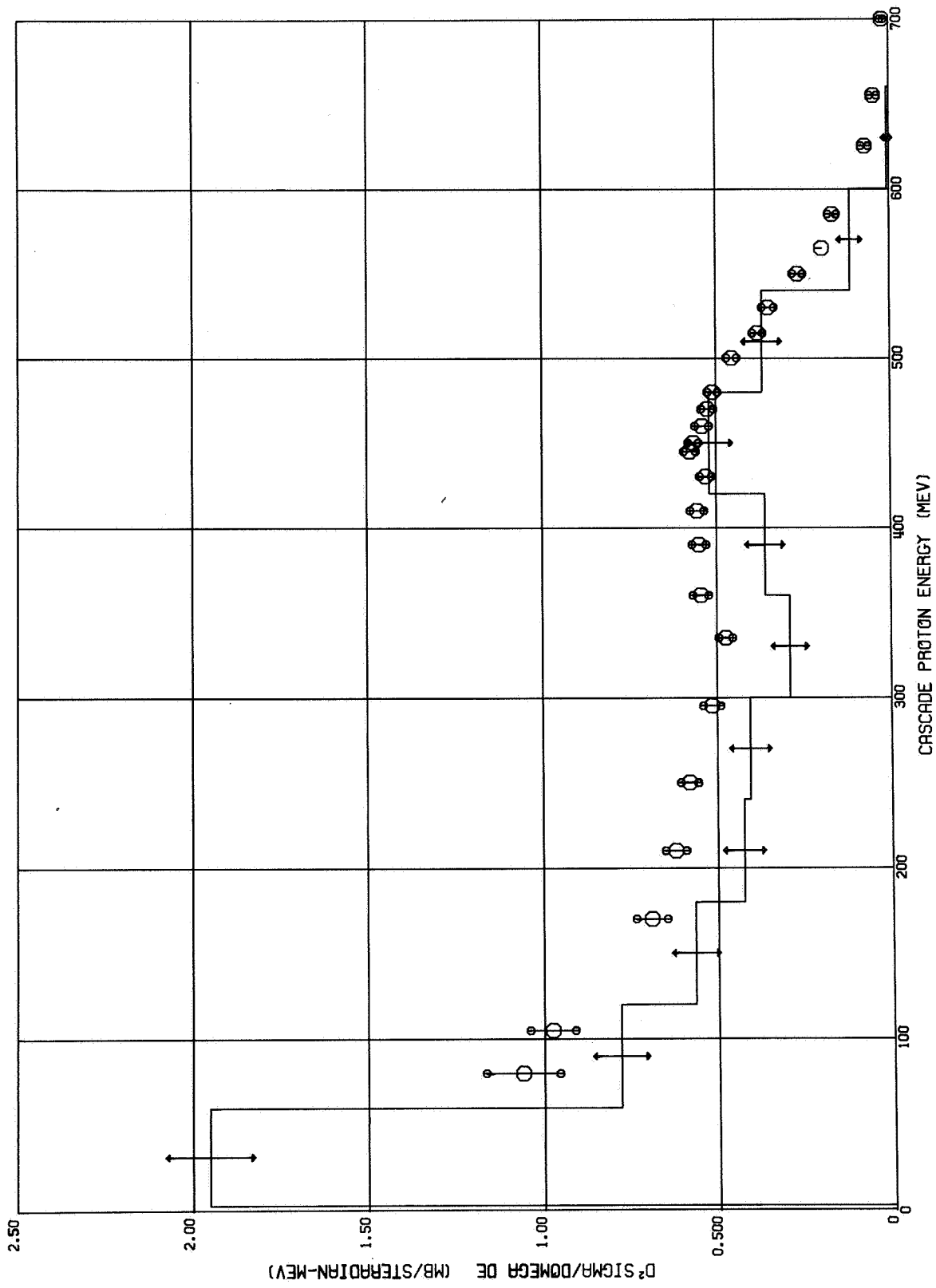


Fig. 7 Secondary protons at 30 deg from 660-MeV protons on ^{65}Cu . The high-energy intranuclear cascade predictions of Bertini are compared against the experiment of Azhgirey et al.

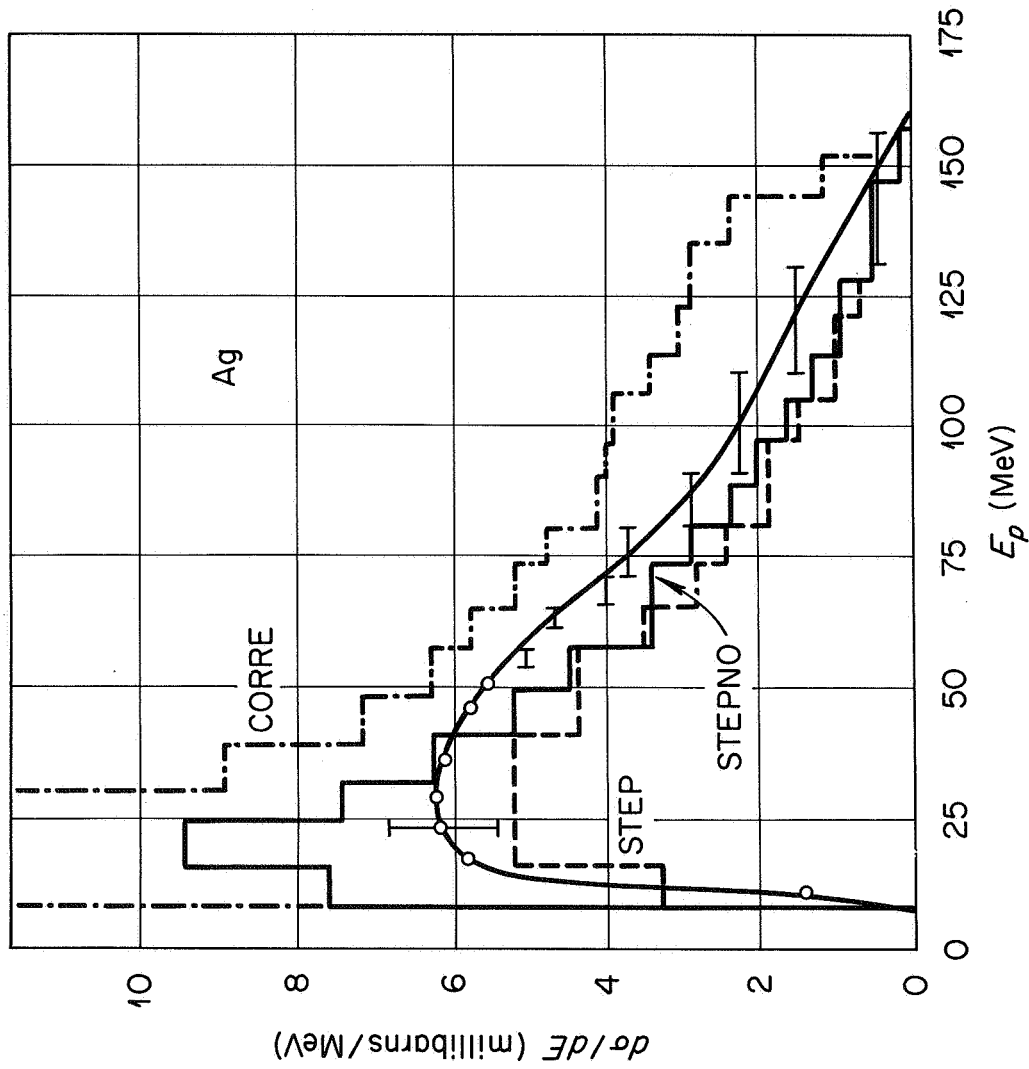


Fig. 8 A comparison from C. Brun et al. for the angle-integrated "direct reaction" proton spectrum from 156-MeV protons on silver. Protons believed to have originated from nucleon evaporation have been subtracted prior to comparison against his three intranuclear cascade calculations. (Courtesy Nuclear Physics.)

The cascade model was originally intended for use with rather high incident energies. What should be used for calculations on the soft flares which are apt to be important for secondary production? Figure 9 shows some recent data of Bertrand et al.¹⁸ at 30 deg for incident 60-MeV protons on ^{54}Fe . Below the region of marked group structure the Bertini model fits well, except that the evaporation proton yield from the associated treatment of nucleon evaporation is twice too large. (I refuse to show the 20-deg data, which fits perfectly in the high-energy region.) The poor fit in the evaporation region is sensitive to nuclear details - the predicted spectrum for ^{56}Fe fits the data! In all these measurements the deuteron cross section at the higher energies is about 1/10 of the proton cross section, though emerging deuterons cannot be predicted by the present cascade model. Deuterons and heavier particles are predicted to compete in the evaporation process, and Fig. 10 at 60 deg for the same target and energy includes comparisons for five particle types. For protons this case shows a less favorable comparison with calculation; the predicted cross section does not hold up well at energies over 40 MeV. In these figures the experimental data are shown as a smooth curve below the near-elastic region, though they were obtained in a thousand individual channels. In the smoothed regions the data have been shown to be statistically consistent with a smooth curve. Figures 11 and 12 show similar comparisons for 61-MeV protons on Bi. At 30 deg the calculation fits the proton cross sections only at high energies; at 60 deg there is no agreement. The failure of the model to predict a reasonably shaped spectrum for Bi may be related to the model's neglect of fission.

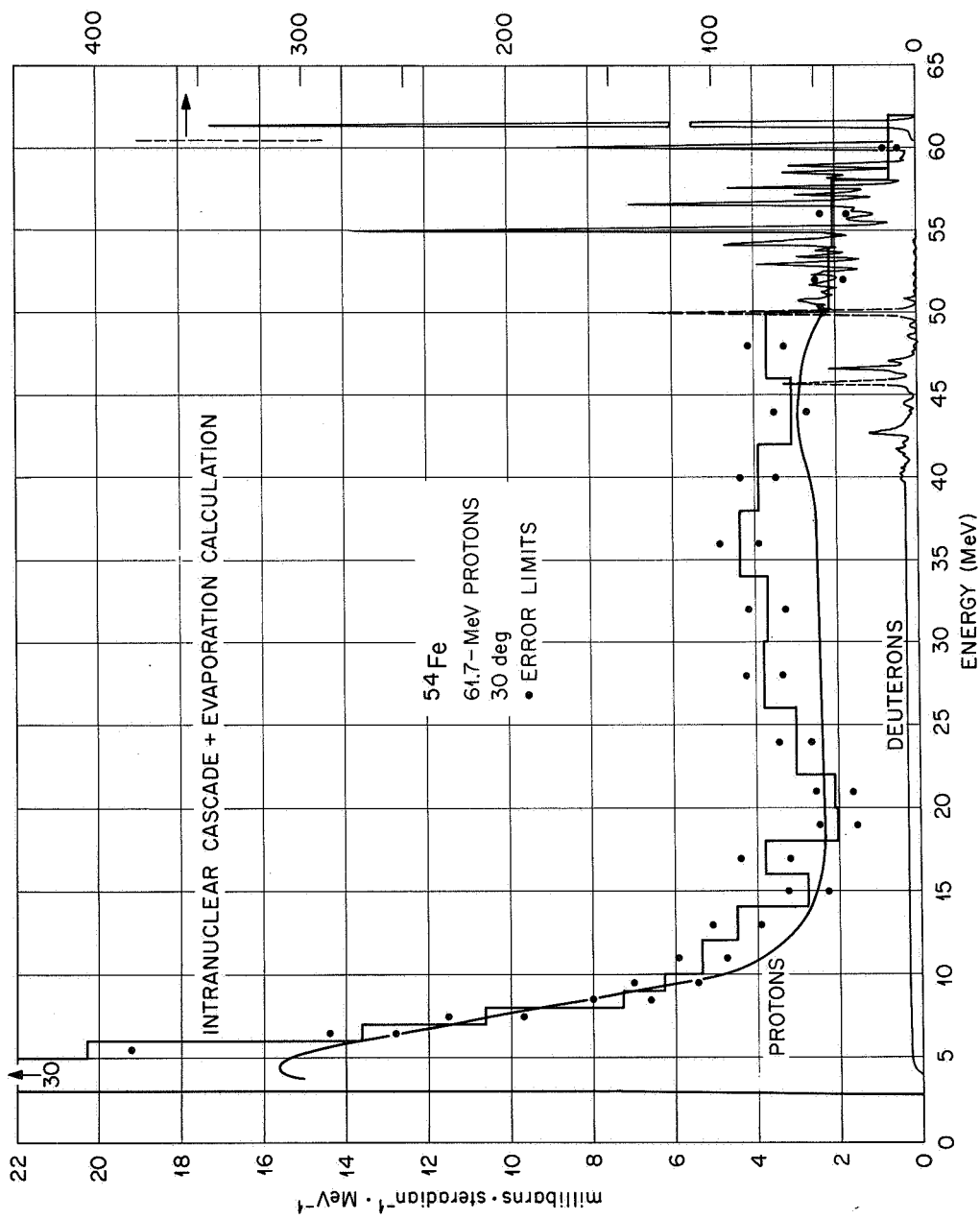


Fig. 9 Differential cross sections for secondary protons and deuterons at 30 deg from 61-MeV protons on ^{54}Fe . The experiment of Bertrand *et al.* is compared against intranuclear cascade-plus-evaporation calculations using the program of Bertini.

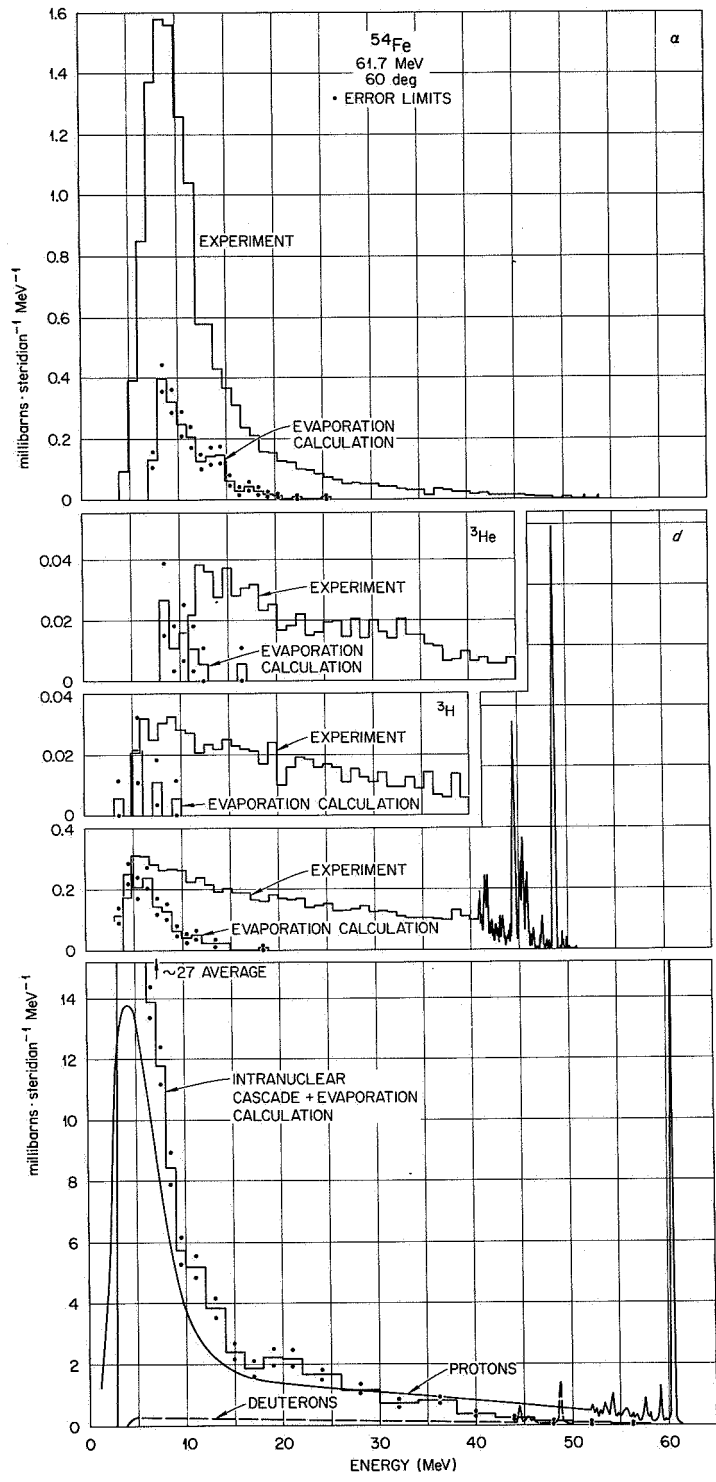


Fig. 10 Differential cross sections for secondary p, d, t, ^3He , and ^4He ions at 60 deg from 61-MeV protons on ^{54}Fe compared against the intranuclear cascade-plus-evaporation model.

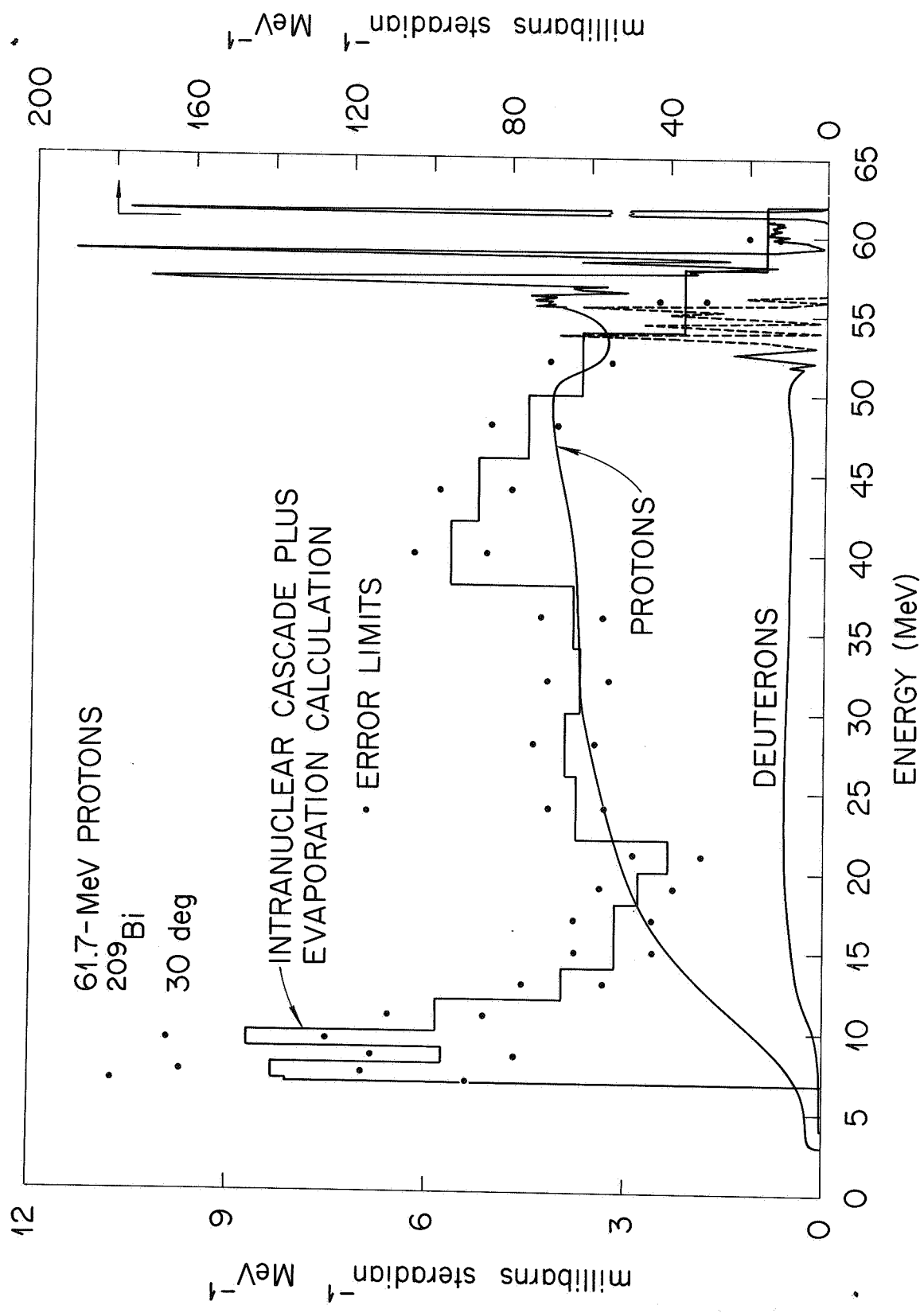


Fig. 11 Differential cross sections for secondary protons and deuterons at 30 deg from 61-MeV protons on ^{209}Bi compared against the intranuclear cascade-plus-evaporation model.

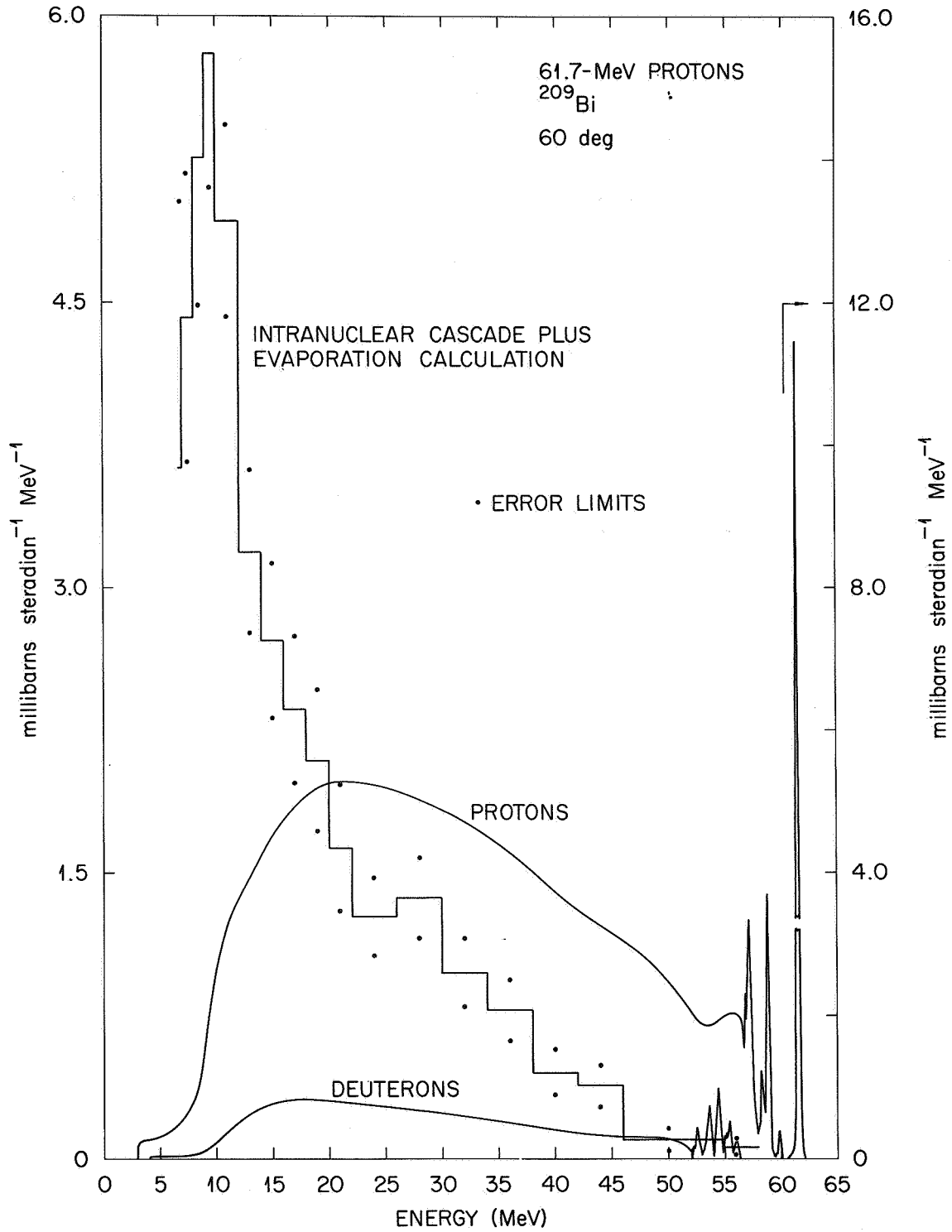


Fig. 12 Differential cross sections for secondary protons and deuterons at 60 deg from 61-MeV protons on ^{209}Bi , compared against the intranuclear cascade-plus-evaporation model.

When this work is completed we should have some picture of the validity of the cascade model for incident 60-MeV protons and emerging charged particles, with some few runs for incident 40-MeV protons and some for alpha particles. The 40-MeV proton data shows continuum regions similar to those at 60 MeV, but of course it becomes harder and harder to ignore the excitation of definite final states. Alpha particles do give substantial numbers of energetic secondary protons. Because of the importance of charged-particle reactions in dose calculations when the quality factor is given consideration, we will try to get data on C and O targets.

The lower energy limit for intranuclear cascade calculations can be pressed even more by looking at the new cross sections of Verbinski and Burrus¹⁹ at 15 to 18 MeV for (p,n) reactions on several elements. The observed cross sections for elements as heavy as Fe show energy group structure and at the higher energies a definite angular distribution.

Figure 13 shows the cross sections $^{27}\text{Al}(p,n)$ integrated over solid angle. I have shown for each of two energies a comparison of experiment with a Monte Carlo evaporation theory of the Dostrovsky⁸ type and with the cascade plus evaporation theory of Bertini. The evaporation-only calculations assume that all the incident energy is absorbed into a compound nucleus with an arbitrary 500-mb reaction cross section. Though imperfect, the Bertini estimate is the better though he is slightly shocked by our use of his program at these energies. Whether the agreement is satisfactory, and whether it can easily be improved upon, await further analysis. At least two problems other than the residual shape error arise in routinely applying the presently available cascade programs to this energy range. The calculated and observed spectra have high-energy end-points quite out of line when the (p,n) Q-value is far different from the zero estimate made in Bertini's

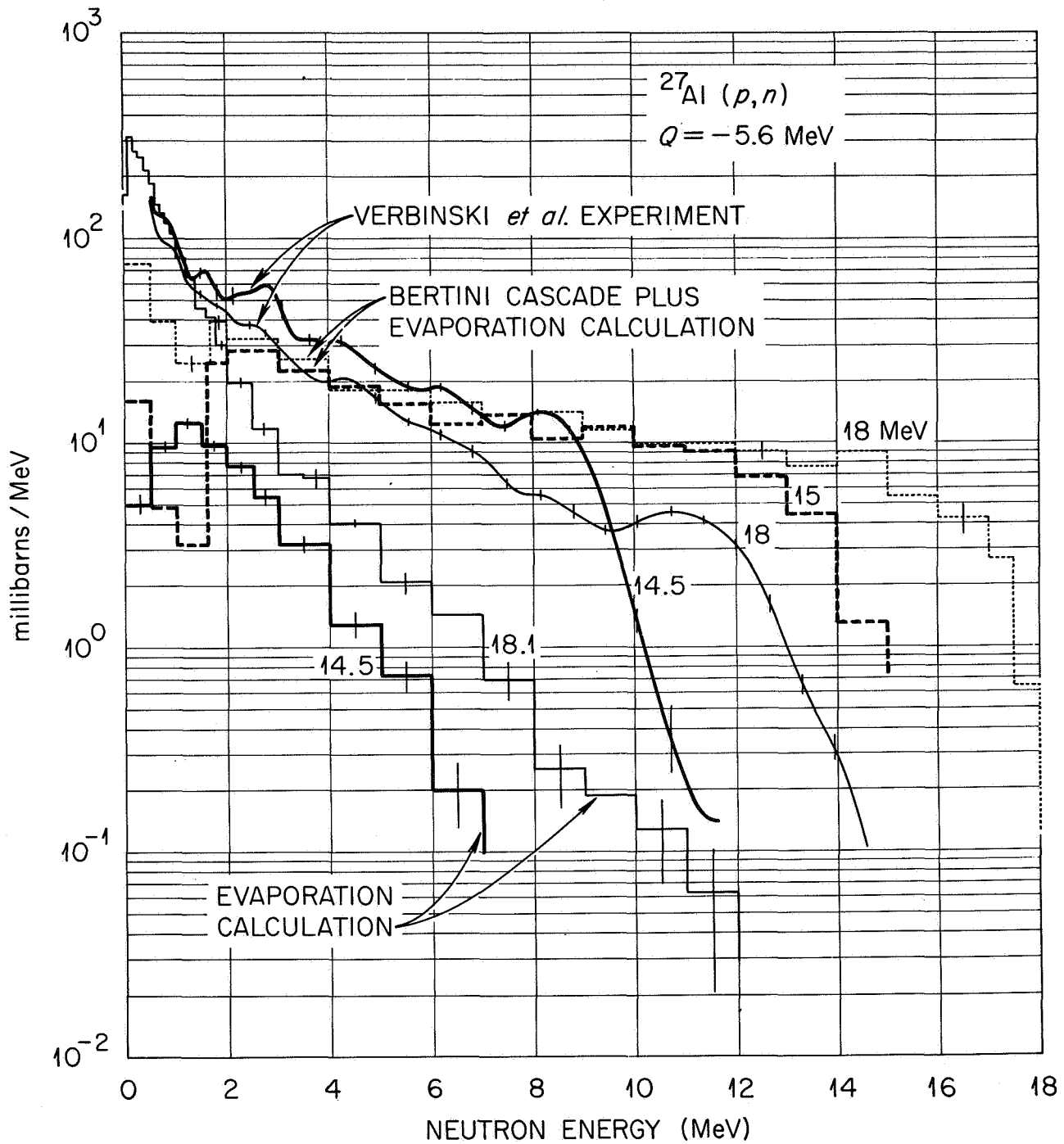


Fig. 13 Angle-integrated energy spectra from 14.5- and 18-MeV protons on Al. The experiment of Verbinski and Burrus is compared with cascade-plus-evaporation calculations and with "pure" evaporation calculations.

cascade program. This effect is apparent in Fig. 13. Also, as emphasized in Fig. 14 for Ta, the cutoff energy which customarily terminates the model cascade reactions produces a nonphysical kink in the predicted energy distributions. Lowering the cutoff from 6.6 to 2 MeV improved the behavior of the spectrum but markedly increased the computer running time. The evaporation-only model gives the same shape as the low-energy data shown for the 6.6-MeV cutoff, but 25% more intense if the same nonelastic cross section is used.

I have little to report on neutron production by alpha particles, except to observe that in the case of the ${}^9\text{Be}(\alpha, n)$ reaction the cross section is large, between 400 and 700 mb for alpha particles between 5 and 10 MeV, and the energy spectrum does not much resemble an evaporation spectrum. This integrated cross section is as large as the geometrical cross section of sulphur, and if it remains so large at higher energies it would imply that about 4% of the 60-MeV alpha particles stopping in a Be shield would produce neutrons. Figure 15 illustrates the angle-integrated neutron spectra obtained by Verbinski²⁰ for two incident energies, illustrating that even at low resolution there is definite character to the spectra. The angular distributions are also marked. It may always be necessary to take this type of data from experiment.

III. CROSS SECTIONS FOR SECONDARY GAMMA RAYS

Finally there is the problem of secondary gamma rays. As I indicated earlier, conclusions await the implications of the spectra that Zobel, Maienschein, and Scroggs¹ have obtained at incident energies from 14 to 160 MeV, and the developing information concerning the intensity of soft

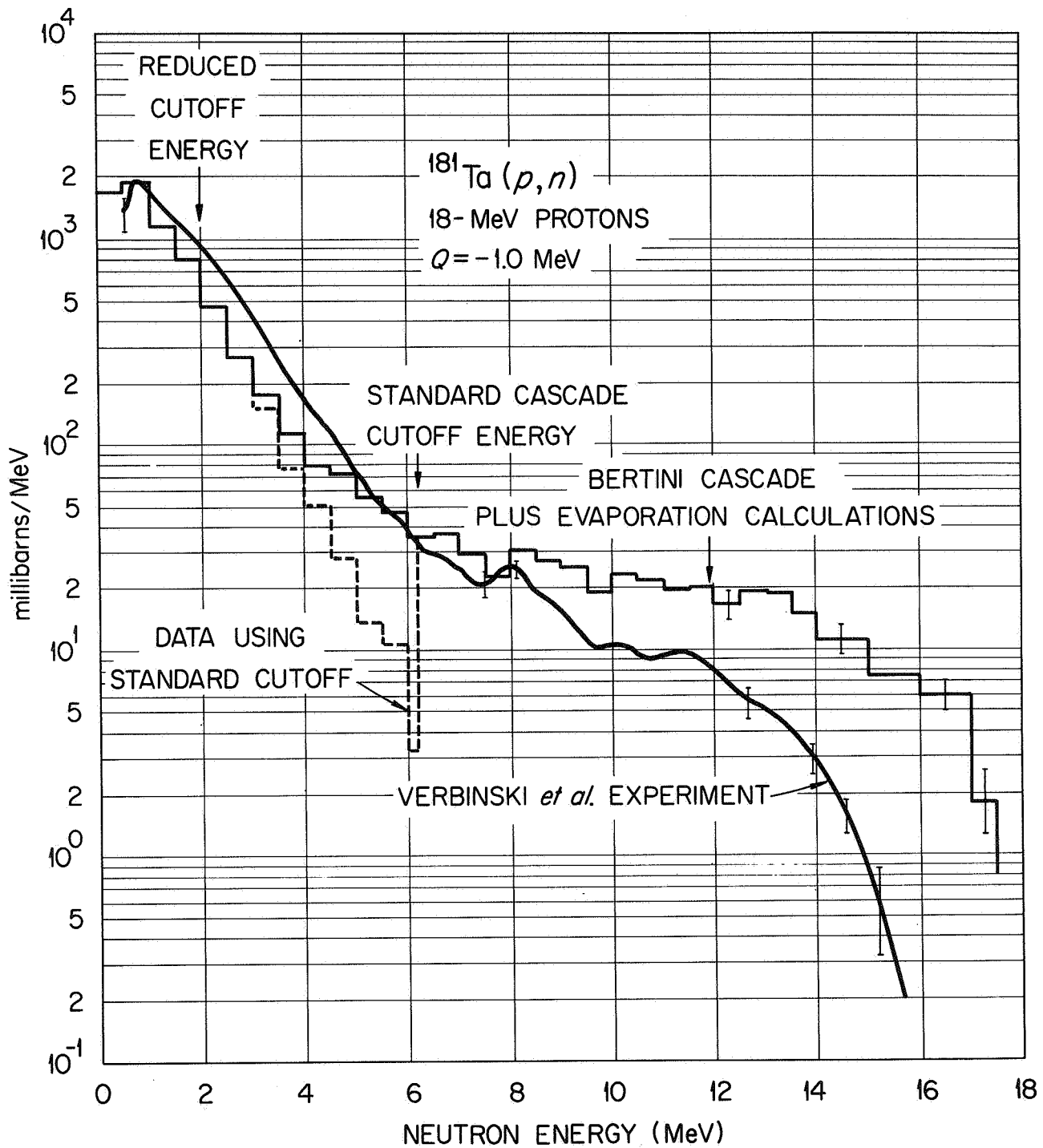


Fig. 14 Angle-integrated energy spectra from 18-MeV protons on ^{181}Ta . The experiment of Verbinski and Burrus is compared with cascade-plus-evaporation calculations.

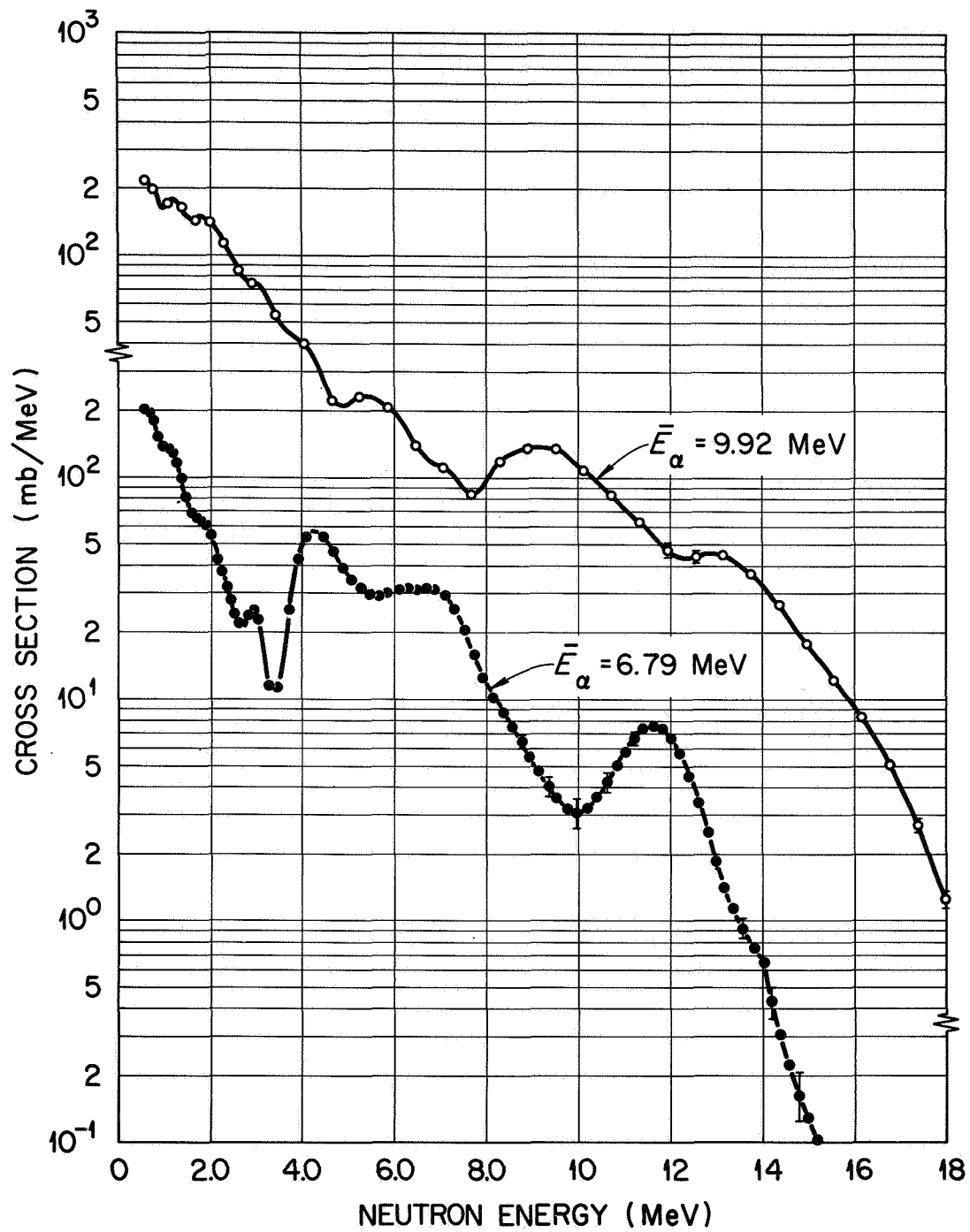


Fig. 15 Angle-integrated neutron spectra from the ${}^9\text{Be}(\alpha, n)$ reaction for 6.8- and 9.9-MeV incident alpha particles. From the experiments of Verbinski.

flares. Figure 16, showing gamma rays from 33-MeV protons on H₂O, serves to remind us that such gamma rays are real.

IV. CONCLUSIONS

To summarize, I believe our course should be to use the cascade plus evaporation data, made widely available by Bertini et al., at even very low energies. We must however search for an effective way to join this system with a type of cross-section system more suitable for the lower energies. We must devise suitable cross-section estimators for incident helium ions and for secondary gamma rays.

Once the energies of incident particles become so low that their ranges are short compared to shield thicknesses and to the attenuation lengths of secondaries, precalculated secondary yields as a function of incident energy would be helpful to shield computations. The difficulties of spacecraft geometry should not inhibit ever-improving estimations of secondary effects based on the simplest geometries. Finally, in considering secondaries, soft flares must receive the main attention.

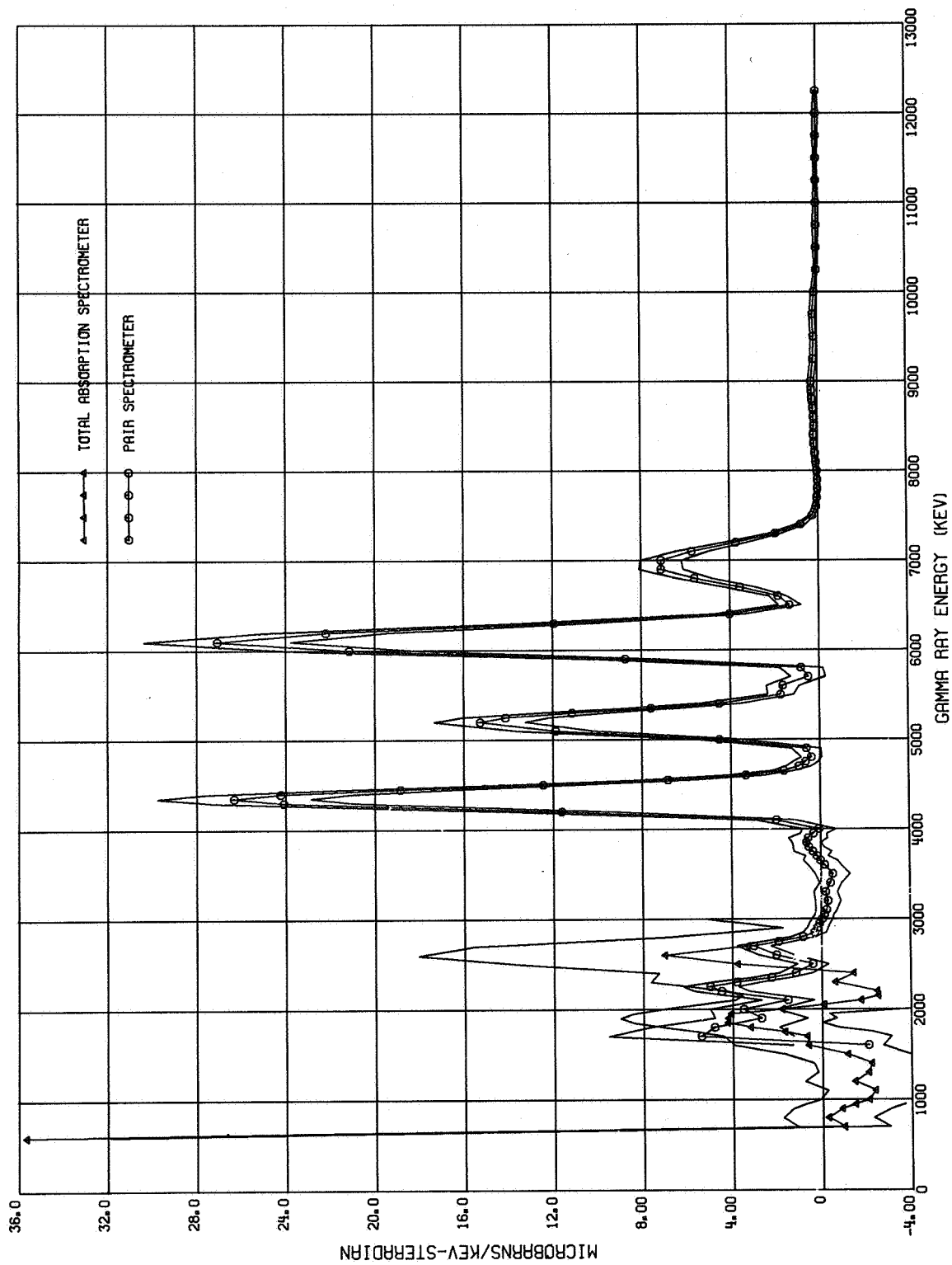


Fig. 16 Gamma-ray differential cross section observed by Zobel and Maienschein at 135 deg from 33-MeV protons on water.

REFERENCES

1. W. ZOBEL, F. C. MAIENSCHEIN, and R. J. SCROGGS, "Spectra of Gamma Rays Produced by the Interaction of ~ 160 -MeV Protons with Be, C, O, Al, Co, and Bi," ORNL-3506, Oak Ridge National Laboratory (April 1965);
W. ZOBEL et al., "Secondary Gamma Rays from Proton Bombardment of ${}^7\text{Li}$, Be, ${}^{11}\text{B}$, C, O, Mg, Al, and Fe," in ORNL-3838, Vol. II, Oak Ridge National Laboratory (November 1965).
2. R. WALLACE, P. G. STEWARD, and C. SONDHAUS, "Primary- and Secondary-Proton Dose Rates in Spheres and Slabs of Tissue," Second Symposium on Protection Against Radiations in Space, NASA SP-71, Gatlinburg, Tennessee (October 1964).
3. Handbook of Mathematical Functions, M. Abramowitz and I. Stegun, eds., National Bureau of Standards Applied Mathematics Series 55 (1964);
Formula 8.14.15.
4. N. METROPOLIS et al., "Monte Carlo Calculations on Intranuclear Cascades. I. Low-Energy Studies," Phys. Rev. 110, 185 (1958); "Monte Carlo Calculations on Intranuclear Cascades. II. High-Energy Studies and Pion Processes," Phys. Rev. 110, 204 (1958).
5. H. W. BERTINI, "Low-Energy Intranuclear Cascade Calculation," Phys. Rev. 131, 1801 (1963), with erratum Phys. Rev. 138, AB2 (1965); "Monte Carlo Calculations on the Intranuclear Cascades," ORNL-3383, Oak Ridge National Laboratory (April 23, 1963); "Description of Printed Output from Intranuclear Cascade Calculation," ORNL-3433, Oak Ridge National Laboratory (May 14, 1963).

6. R. G. ALSMILLER, JR., M. LEIMDORFER, and J. BARISH, "Analytic Representation of Nonelastic Cross Sections and Particle-Emission Spectra from Nucleon-Nucleus Collisions in the Energy Range 25 to 400 MeV," ORNL-4046, Oak Ridge National Laboratory (April 1967).
7. H. W. BERTINI, "Results from Low-Energy Intranuclear-Cascade Calculation," ORNL-TM-1225, Oak Ridge National Laboratory (September 1965).
8. I. DOSTROVSKY, Z. FRAENKEL, and G. FRIEDLANDER, "Monte Carlo Calculations of Nuclear Evaporation Processes. III. Applications to Low-Energy Reactions," Phys. Rev. 116, 683 (1959); I. DOSTROVSKY, Z. FRAENKEL, and L. WINSBERG, "Monte Carlo Calculations of Nuclear Evaporation Processes. IV. Spectra of Neutrons and Charged Particles from Nuclear Reactions," Phys. Rev. 118, 781 (1960).
9. N. S. WALL and P. R. ROOS, "Quasifree Scattering of 160-MeV Protons from Nuclei," Phys. Rev. 150, 811 (1966).
10. J. GENIN et al., "Protons, Deutons, Tritons, et Noyaux d'Hélium Démis par ^{197}Au sous l'Action de Protons de 154 MeV," J. Phys. Radium 22, 615 (1961); "Etude des Deutons et des Triton Emis lors du Bombardement de Noyaux de Carbone par des Protons de 155 MeV," J. Phys. Radium 21, 322 (1960).
11. R. W. PEELLE et al., "Differential Cross Sections for the Production of Protons in the Reactions of 160-MeV Protons on Complex Nuclei," ORNL-3887, Oak Ridge National Laboratory (September 1966).

12. C. BRUN et al., "Direct Interaction Protons Emitted from Ag and Au Targets Bombarded by 156 MeV and 91 MeV Protons," Nucl. Phys. A95, 337 (1967).
13. S. DAHLGREN et al., "A Study of the Large-Angle Emission of Charged Particle from Nuclei Bombarded by 186-MeV Protons," Arkiv Fysik 32, 510 (1964).
14. J. W. WACHTER, W. R. BURRUS, and W. A. GIBSON, "Neutron and Proton Spectra from Targets Bombarded by 160-MeV Protons," ORNL-TM-1781, Oak Ridge National Laboratory (1967).
15. P. H. BOWEN et al., "Neutrons Emitted at 0° from Nuclei Bombarded by 143-MeV Protons," Nucl. Phys. 30, 475 (1962).
16. H. W. BERTINI, "Intermediate-Energy Intranuclear-Cascade Calculation," Bulletin of the American Physical Society, 1967 Spring Meeting at Washington, D. C., April 24-27, 1967; also to be published in the Neutron Physics Division Annual Progress Report for period ending April 30, 1967, ORNL-4134, Oak Ridge National Laboratory.
17. L. S. AZHGIREY et al., "Nuclear Interactions of 660-MeV Protons and the Momentum Distribution of Nucleons in Nuclei," Nucl. Phys. 13, 258 (1959).

18. F. E. BERTRAND et al., "The Mass and Energy Spectra of Charged Reaction Particles from Targets Bombarded by 60-MeV Protons," Neutron Physics Division Annual Progress Report for Period Ending April 30, 1967, ORNL-4134, Oak Ridge National Laboratory.
19. V. V. VERBINSKI, Oak Ridge National Laboratory, personal communication (May 1967).
20. V. V. VERBINSKI et al., "Neutrons from ${}^9\text{Be}(\alpha, n)$ Reactions at 6-10 MeV," Oak Ridge National Laboratory (to be published).

SECONDARY-DOSE EQUIVALENT MODEL AND
COMPARISON OF 160-MEV PROTON-INDUCED NEUTRON
AND PROTON DOSE WITH A COMPREHENSIVE
EXPERIMENT*

Bobby Liley

and

Arthur G. Duneer, Jr.

Space and Information Systems Division

North American Aviation, Inc.

A secondary-dose equivalent model for calculating secondary proton and neutron doses in arbitrary geometries is described. The random position of origin of the secondary nucleon, primary proton residual kinetic energy and secondary nucleon kinetic energy, and survival weight at the point of generation of the secondary particles are determined by random sampling techniques. Results from this model are compared with the experiment of Maienschein and Blosser which measured the dose from a 160-Mev proton beam incident on an aluminum slab. The agreement is generally better than the state-of-the-art accuracy for secondary-dose calculations.

*Published previously in Nuclear Science and Engineering, Vol. 29, 1967, pp. 189-197.

INTRODUCTION

Several papers have described analytical methods of computing secondary proton and neutron dose generated by nonelastic reactions of primary protons with aluminum slabs. However, a literature search revealed no comparisons of such analytical results with an experiment designed to validate the theoretical secondary analysis. ^(1 - 4) A comprehensive experiment (Maienschein and Blosser) ⁽⁵⁾ for 160-Mev primary protons was compared with the results of the computational model. This experiment provides a stringent test of the model's ability to represent secondary particle production, transport, and energy deposition for a complex geometry. A complete description of the secondary model is presented. This relatively simple computational model generates state-of-the-art secondary computational accuracy without extensive computations.

SECONDARY NEUTRON AND PROTON MODEL PHYSICS

Although the model to be presented is specifically for the Maienschein and Blosser experiment, ⁽⁵⁾ the computer program is sufficiently general to accommodate interplanetary or lunar spacecraft. The following aspects of the physical equivalent model are discussed:

1. Primary proton attenuation and secondary-generation effective source strength
2. Position of secondary generation
3. Secondary energy
4. Differential scattering
5. Attenuation of secondary nucleons
6. Buildup and flux to dose conversion factors
7. Normalization of dose

The secondary dose calculation is executed with Monte Carlo techniques.

PRIMARY ATTENUATION AND SECONDARY PRODUCTION

Figure 1 will be used to facilitate discussions in this section. $W(E)$ represents the incident flux if the incident spectrum is mono-energetic or the spectral weight for a generalized spectrum. The weight of the spectrum is the fraction of incident flux in a random-sampled energy band. The weight or effective primary flux at depth x is

$$W(x) = W(E_1) \exp \left[- \int_0^x \sum_{pr} (E_s) dx_s \right] \quad (1)$$

where

- E_s = incident proton residual kinetic energy at depth x_s
(dummy variable)
- \sum_{pr} = the primary proton nonelastic total reaction cross section
- $W(x)$ = survival weight or attenuated flux at depth x
- $W(x_t)$ = emergent flux survival weight.

The survival weight is defined interchangeably as a function of the incident proton penetration depth or the corresponding proton residual kinetic energy at the penetration depth. For example, from Fig. 1,

$$W(x_t) \equiv W(E_2)$$

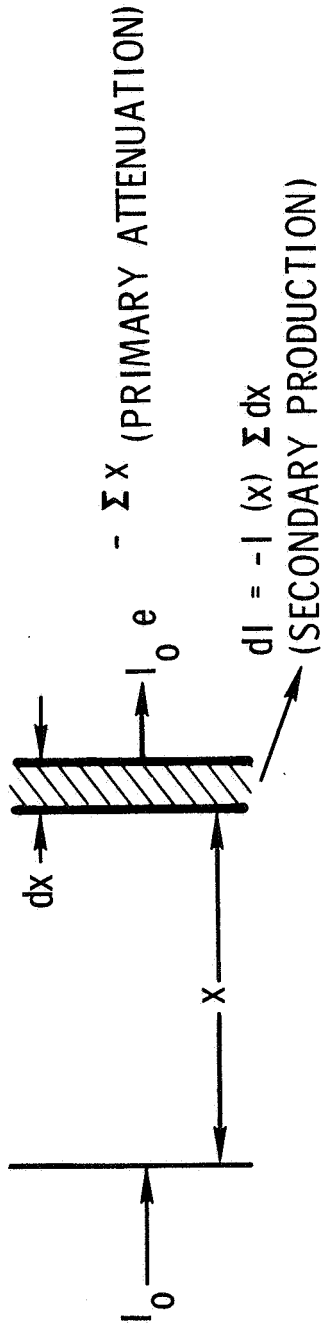
and

$$W(x=0) \equiv W(E_1)$$

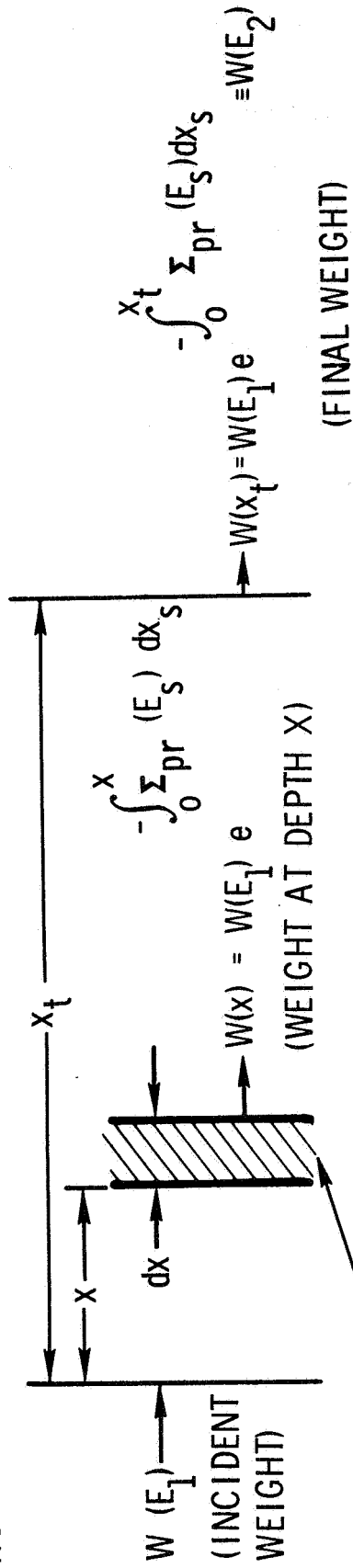
where E_1 and E_2 are the incident proton initial and final or emergent energy (Fig. 1).

The primary proton nonelastic total reaction cross section (\sum_{pr}) is an accumulation of possible significant secondary reaction cross sections

SIMPLIFIED THEORY (GAMMAS, ETC)



PROTON THEORY



$$W(x) \sum_i \ell_i \Sigma_p, \ell_i n^0 \text{ or } p^+(E_x) dx = W(x) M_r^k(E_x) dx$$

(SECONDARY PRODUCTION IN DEPTH x)

Figure 1. Primary attenuation - secondary production.

($\sum_{up,vn}$) with yield combinations (secondary protons and neutrons) for which data was available. ⁽²⁾ That is

$$\sum_{pr} = \sum_{u=0}^U \sum_{v=0}^V \sum_{up,vn} \quad (2)$$

For secondary production, the secondary nonelastic proton and neutron cross sections are $M_r^p(E)$ and $M_r^n(E)$, respectively, where

$$M_r^p(E) = \sum_{u=1}^U \sum_{v=0}^V u \sum_{up,vn} ; \quad M_r^n(E) = \sum_{u=0}^U \sum_{v=1}^V v \sum_{up,vn} \quad (3)$$

The upper limits are determined by three quantities, i.e., the number of nucleons in the target nucleus, possible significant reactions and available data. u_p and u_n refer respectively to nonelastic secondary cross section component for a yield of u protons and v neutrons.

An alternate method of determining M_r^p and M_r^n is based on the average number of emitted nucleons per nonelastic event, i.e.

$$MYP = M_r^p / \sum_{pr} \quad (4)$$

$$MYN = M_r^n / \sum_{pr}$$

where MYP and MYN are the average proton and neutron yields per nonelastic event.

The secondary model uses MYP and \sum_{pr} etc. to determine M_r^p and M_r^n from

$$M_r^p = MYP \cdot \sum_{pr} \quad ; \quad M_r^n = MYN \cdot \sum_{pr} \quad (5)$$

The average yields are derived from calculations of Bertini and Metropolis for cascade nucleons and Dresner's calculations for evaporation nucleons. ⁽²⁾ The

differential number of secondaries produced between x and $x + dx$ is

$$W(x)M_Y^k(E_x) dx; \text{ where } k = p^+ \text{ or } n^0 \quad (6)$$

The integral secondary production for a slab is defined as $N^k(E_1, E_2)$ where E_1 and E_2 are the primary protons incident and emergent energies respectively (Fig. 1).

It follows that

$$N^k(E_1, E_2) = W(E_1) \int_{E_1}^{E_2} \frac{dE}{s(E)} M_Y^k(E) \exp\left[-\int_{E_1}^E dE' \Sigma_{pr}(E')/s(E')\right] \quad (7)$$

where

k = secondary particle type (proton or neutron)

$dx = -dE/s(E)$ and $s(E)$ is the stopping power and (8)

E' = dummy variable (primary proton kinetic energy).

This integral can be simplified and expressed in tabular form as follows. The number of mean free paths, due to nonelastic collisions, for a proton of energy E is $\lambda(E)$, and

$$\begin{aligned} \lambda(E_1, E_2) &= \int_{E_1}^{E_2} \left(\frac{d\lambda}{dE} \right) dE = \int_{E_1}^{E_2} \left[-\Sigma_{pr}(E) dE/s(E) \right] \\ &= \int_{E_{min}}^{E_1} [] - \int_{E_{min}}^{E_2} [] = \lambda(E_1, E_{min}) - \lambda(E_2, E_{min}) \quad (9) \end{aligned}$$

where E_{min} is defined as 1 Mev for this model and the mean free paths and range at E_{min} are relatively negligible.

$\lambda(E) = \lambda(E, E_{min})$ is a tabular function.

From Eq. (7)

$$\frac{N^k(E_1, E_2)}{W(E_1)} = \int_{E_1}^{E_{min}} \left[-\frac{dE}{s(E)} M_r^k(E) \right] \left\{ \exp \int_{E_1}^E d\lambda(E) \right\} - \int_{E_2}^{E_{min}} [] \left\{ \right\} \quad (10)$$

Since

$$\exp \int_{E_1}^E d\lambda(E) = \exp \left[\lambda(E) - \lambda(E_1) \right]$$

$\exp - \lambda(E_1)$ can be removed from the integral. Therefore

$$N^k(E_1, E_2) = W(E_1) e^{-\lambda(E_1)} \left\{ \int_{E_{min}}^{E_1} \left[\frac{dE}{s(E)} M_r^k(E) e^{\lambda(E)} \right] - \int_{E_{min}}^{E_2} [] \right\} \quad (11)$$

$$= W(E_1) e^{-\lambda(E_1)} \left[\eta^k(E_1) - \eta^k(E_2) \right]$$

where the tabular function $\eta^k(E)$ is defined as

$$\eta^k(E) = \int_{E_{min}}^E \frac{dE'}{s(E')} M_r^k(E') e^{\lambda(E')} \quad (12)$$

Summarizing, $N^k(E_1, E_2)$ is the number of secondaries of particle type generated in the primary incident and emergent energy interval (E_1, E_2) .

POSITION OF SECONDARY GENERATION

Since the primary proton collision probability in the interval $(x, x + dx)$ i.e. $p(x)dx$ is proportional to the primary flux reduction, then from Eq. (1)

$$W(x) = -W(E_1) e^{-[\lambda(E_1) - \lambda(E)]}$$

$$p(x)dx = p(\lambda)d\lambda = -W(E_1) e^{-[\lambda(E_1) - \lambda(E)]} d\lambda(E)$$

Therefore

$$p(\lambda) = -W(E_1) e^{-[\lambda(E_1) - \lambda(E)]} \quad (13)$$

The normalized collision probability is $\xi(E)$, where

$$\xi(E) = \frac{\int_{\lambda(E)}^{\lambda(E_1)} p(\lambda) d\lambda}{\int_{\lambda(E_2)}^{\lambda(E_1)} p(\lambda) d\lambda} = \left\{ \frac{e^{-\lambda(E_1)} - e^{-\lambda(E)}}{e^{-\lambda(E_1)} - e^{-\lambda(E_2)}} \right\} \quad (14)$$

$\xi(E)$ is the probability that collision will occur at an energy greater than E .

For the primary protons which undergo collisions in the energy interval (E_1, E_2) , the incident proton residual random kinetic energy prior to a non-elastic collision (E_c) and position at collision (x_c) are determined as follows.

From Eq. (14)

$$E_c = \bar{\lambda}^{-1}(E_c); \quad \lambda(E_c) = \lambda(E_1) + \ln \left\{ 1 + \xi \left\{ \frac{e^{\lambda(E_2)}}{e^{\lambda(E_1)}} - 1 \right\} \right\}$$

$$x_c = R(E_1) - R(E_c) \quad (15)$$

where $R(E)$ is the incident protons range at energy E and

$$R(E) = R(E, E_{min}) = \int_0^x dx = - \int_E^{E_{min}} dE / s(E) = \int_{E_{min}}^E dE / s(E) \quad (16)$$

and $\bar{\lambda}^{-1}(E_c)$ refers to interpolation in the tabular function of Eq. (9), i.e.

$\lambda(E)$, to determine the primary proton residual kinetic energy (E_c) corresponding to the residual mean free paths ($\lambda[E_c]$) computed in Eq. (15).

SECONDARY ENERGY

The secondary differential energy spectrum was derived from Monte Carlo calculations of Metropolis, Dresner, Bertini, and some experimental results. ⁽⁹⁾

The subsequent empirical fits of the secondary differential spectral data are based on analysis reported in Ref. 12 and reiterated in Ref. 10. The differential secondary spectrum is defined by the following empirical equation:

$$\left(\frac{dN}{dE_{sc}} \right)_j^k (E_{sc}, E_c) = \left[\frac{1}{E_{sc} + C_j^k} \right] / C_N^k, \quad E_{sc} < E_c \quad (17)$$

$$= 0, \quad E_{sc} > E_c$$

where

E_{sc} = as the secondary nucleon kinetic energy; j, k refer to the target element and secondary nucleon type (neutron or proton) respectively

C_j^k = empirical constant which is a function of the target element atomic number and the secondary particle type

C_N^k = normalization constant for the integral spectrum

C_j^k is least square curve fitted as a function of KZ_j i.e.

$$C_j^k = \sum_{l=0}^4 b_l^k (KZ_j)^l \quad (18)$$

with

$$KZ_j = 0.46 + 1.3 \log_{10} Z$$

where Z = atomic number. Values C_j^k and KZ_j were obtained from Ref. 9.

The empirical constants (C_j^k, KZ_j) were determined subject to the constraints

$$(\bar{E}_p)_{sc} / E_c = 0.22 ; (\bar{E}_n)_{sc} / E_c = 0.17 \quad (19)$$

for $E_c = 460$ Mev

The secondary spectra includes contributions from cascade and evaporation nucleons and on the average conserves energy. However, each primary proton is weighted with the secondary nucleons multiplicity to represent the secondary nucleons emerging from the collisions. The emerging secondaries of each particle type are defined as having the same energy. Now a method of randomly selecting

the energy of each of the secondary particle types is discussed.

For normalization of the integral secondary spectrum

$$C_N^k = \int_{E_{min}}^{E_c} \left(\frac{dN}{dE_{sc}} \right)_j^k dE_{sc} \quad (20)$$

The differential secondary energy probability is proportional to the secondary differential flux; therefore

$$p(E_{sc}, E_c) dE_{sc} = \frac{dN}{dE_{sc}}(E_{sc}, E_c) dE_{sc} \quad (21)$$

Consequently, if $E_c = 2 \text{ BeV}$, the probability that $E_{sc} < E$ is $\epsilon(E)$, where

$$\begin{aligned} \epsilon(E_{sc} < E, E_c = 2 \text{ BeV}) &= \int_{E_{min}}^E \frac{dN}{dE_{sc}}(E_{sc}, 2 \text{ BeV}) dE_{sc} \quad (22) \\ &\equiv \epsilon(E, 2 \text{ BeV}) \end{aligned}$$

which is a tabular function. However, if $E_c < 2 \text{ BeV}$ and the secondary energy, $E_{sc} \neq E_c$, then

$$\epsilon(E_{sc}, E_c) = \frac{\epsilon(E_{sc}, 2 \text{ BeV})}{\epsilon(E_c, 2 \text{ BeV})} \quad (23)$$

To determine a random secondary energy using a random number, δ

$$\epsilon(E_{sc}, 2 \text{ BeV}) = \delta \cdot \epsilon(E_c, 2 \text{ BeV}); \quad E_{sc} = \epsilon^{-1}(E_{sc}, 2 \text{ BeV}) \quad (24)$$

where ϵ^{-1} refers to interpolation in the tabular function of Eq. (22) to determine the E_{sc} corresponding to $\epsilon = \epsilon(E_{sc}, 2 \text{ BeV})$.

DIFFERENTIAL ANGULAR SCATTERING OF SECONDARIES

Figure 2 depicts a secondary nucleon being scattered into the differential solid angle, $d\Omega$, at a linear angle, θ , with respect to the direction of the primary proton. The differential probability for this solid angle is

$$p(E_c, \Omega, \Omega + d\Omega, \mu) d\Omega = \frac{1}{\sigma} \left(\frac{d\sigma}{d\Omega} \right) d\Omega = \frac{d\sigma}{\sigma} \quad (25)$$

where σ is the total scattering cross section. Therefore, assuming that all the secondary flux is generated at the reaction point, the flux contained in the solid angle is

$$N^k d\sigma^k / \sigma^k$$

where k refers to particle type.

The flux (nucleons/cm²) at a distance, R , is

$$N^k \frac{d\sigma^k}{\sigma^k} / dA = \frac{N^k}{4\pi R^2} \frac{d\sigma^k}{\sigma^k d\Omega} (E_c, \mu) \quad (26)$$

The differential cross sections are assumed to be equivalent for secondary neutrons and protons. Reference 9 presents comprehensive tabulations of the differential scattering cross sections, i.e.

$$\frac{d\sigma}{\sigma d\Omega} (E_c, \mu)$$

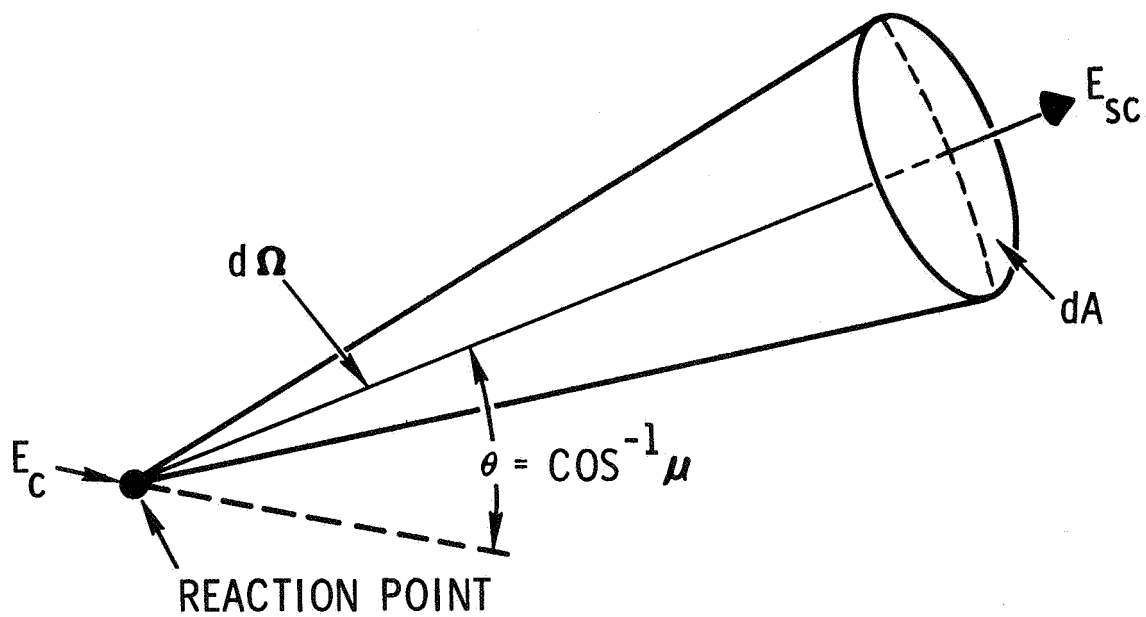


Figure 2. Differential scattering.

This tabulated data assumes equivalent differential scattering cross sections for protons and neutrons. There are 31 energy values for each of 12 μ values in this tabulated data for the secondary model.

ATTENUATION OF SECONDARY NUCLEONS

The secondary protons and neutrons are tracked from the position of secondary generation towards the dosimeter location. As secondaries traverse the segments of materials between their point of origin and the exit surface of the last or the dosimeter position, their weights are attenuated by the factor A_T where

$$A_T = \prod_{j=1}^m \exp - \left[\lambda(E_1) - \lambda(E_2) \right]_j \quad (27)$$

and

j refers to the j th material traversed

E_{1j} , E_{2j} refer respectively to the incident and emergent energies for the j th material

$\lambda(E)_j$ refers to the number of mean free paths traversed in the j th material. This attenuation factor is used to determine the secondary proton source flux reduction due to nonelastic collisions. For neutrons the inner bracketed quantity of Eq. (27) is replaced by

$$\left[\sum_{nr} (E_1) \cdot x \right]_j \quad (28)$$

where

- x_j = path length traversed in the j th material
- \sum_{nrj} = nonelastic cross section for nonhydrogenous materials and
the total cross section for hydrogenous materials
- E_{1j} = incident neutron energy for the j th material

The neutron's energy (E_{1j}) is assumed to be invariant as it traverses the various materials. The straight ahead approximation is used for neutron transport in the nonhydrogenous materials. An approximate buildup factor is used to compensate scattered neutron flux which arrives at the dosimeter by multiple elastic scattering in hydrogenous materials.

BUILDUP AND FLUX TO DOSE CONVERSION FACTORS FOR NEUTRONS

The neutron buildup factor due primarily to elastic collisions with hydrogen is approximated by a simple relationship, which was derived by Blizard and Welton and reported by Kalos. ⁽⁶⁾ This buildup factor is a function of the number of mean free paths (λ) and for tissue is approximated by

$$B(\lambda) \cong 1 + \lambda^{0.823} \quad (29)$$

for all energies. This buildup factor was derived for a plane monodirectional neutron flux normally incident on an infinite plane of water. Although the actual geometry is closer to a point source and a water sphere, the aforementioned buildup factor should be a first order approximation of the actual

buildup factor. This buildup factor is considered applicable up to 8 MeV. However, this analysis uses this buildup factor as an approximation at higher energies. The only justification for this extended application of the buildup factor is the relative insensitivity of the buildup factors to large changes in the slope of the cross-section versus neutron energy. ⁽¹⁴⁾

The neutron flux (n/cm²) to dose (rads) conversion factor (fig. 3) is a composite of first collision or surface type doses computed by Gibson ⁽⁷⁾ and the National Bureau of Standards ⁽¹⁶⁾ and reported in Ref. 15. Therefore, the depth doses are computed by determining the local flux, including buildup, and using the surface or local flux to dose conversion factor. The flux to dose conversion factor for protons is F^P where

$$F^P(E_{sc}) = \left[\text{Stopping Power} \left(\frac{\text{MeV-cm}^2}{\text{gram}} \right) \right] \times 1.6 \times 10^{-8} \frac{\text{rads-gram}}{\text{MeV}}$$

The generalized flux to dose conversion factor is defined as F^k where the superscript k refers to the particle type.

NORMALIZATION OF DOSE

The final dose computation equation incorporates all aspects of the model which have been discussed. However, it is desirable to explain their relationships to the overall model. In general, a history is defined by one direction (i.e., three random direction cosines) and ten random incident energies which are randomly selected from 10 weighted portions of the incident spectrum. For each proton the mean secondary multiplicity per unit incident flux weight is computed by Eq. 10. Then, Eq. 15 is used to randomly select the incident protons random position (X_c) of collision and its associated residual kinetic energy (E_c) before collision. In turn, Eq. 24 uses E_c to randomly select an energy (E_{sc}) from the secondary spectrum. Each secondary

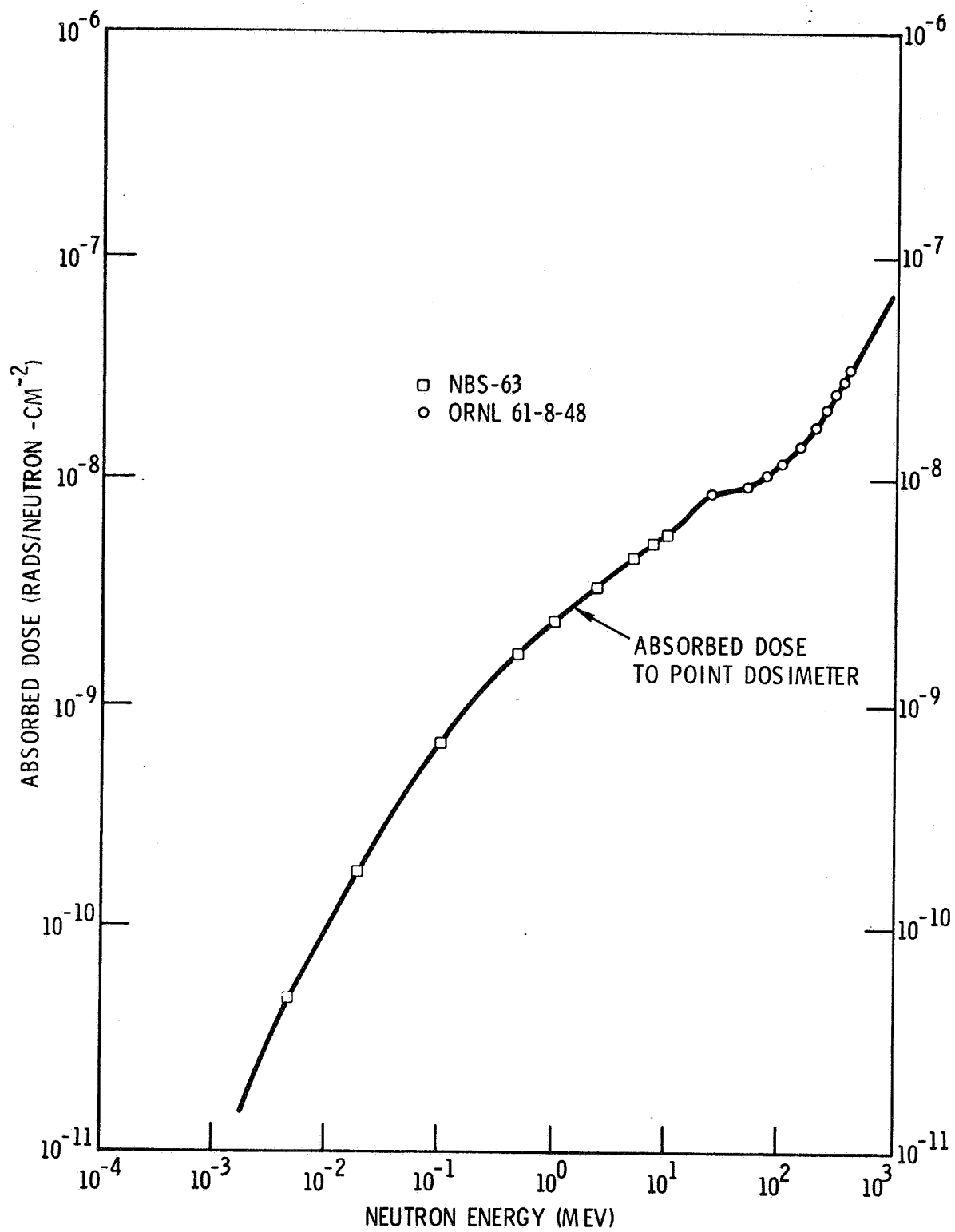


Figure 3. Neutron flux to dose conversion factor.

particle type is represented as having equal energy secondaries. However, the model does, on the average, conserve energy. The corresponding effective flux at the dosimeter is computed with Eq. 26. The proton secondaries are degraded to account for ionization energy losses before reaching the dosimeter. The aforementioned flux includes differential scattering and the $(1/R^2)$ effect. Then the secondary flux at the dosimeter (Eq. 26) is reduced by the factor A_T (Eq. 27), which accounts for non-elastic collisions of the secondary with the medium it traverses between its point of origin and the dosimeter location. For hydrogenous materials, for example tissue or water, the attenuation factor includes both elastic and non-elastic collisions. The attenuation factor (A_T) for hydrogenous materials is multiplied by the buildup factor (Eq. 29) to account for the flux which is scattered towards the dosimeter after multiple elastic collisions. Finally the flux at the dosimeter is converted to energy deposition or rad dose by the flux to dose conversion factors for protons and neutrons. The effective directional cross sectional area of the shield or spacecraft is defined as A_l where the subscript refers to the l th history.

The incident proton source is normalized to one particle per cm^2 above the minimum source energy (E_0) and the total source flux is defined as P . All of the aforementioned factors which contribute to the normalized dose equation are defined in Table I with their associated units. The normalized first generation secondary dose is D^k where

$$D^k \left\{ \begin{array}{l} L \text{ histories} \\ J \text{ energies} \end{array} \right\} = \frac{P}{L} \sum_{l=1}^L A_l \sum_{j=1}^J \left[\left(\frac{B \cdot A_T \cdot N \cdot F}{4 \pi \cdot R^2} \right) \left(\frac{d\sigma}{\sigma d\Omega} \right) \right]_{l,j}^k \quad (30)$$

Table I. Nomenclature and Units for the Dose Normalization Equation's Components

| <u>Nomenclature</u> | <u>Symbol</u> | <u>Units</u> |
|---|-------------------|---------------------------------|
| Total flux above the minimum source energy (E_0) | P | protons/cm ² > E_0 |
| Projected shield or spacecraft area | A_I | cm ² |
| Neutron buildup factor in tissue | B | none |
| Secondary flux attenuation factor | A_T | none |
| Number of secondary nucleons produced in the shield | N | nucleons |
| Distance from secondary nucleon source point to the dosimeter | R | cm |
| Differential scattering cross-section | $d\sigma/d\Omega$ | steradian ⁻¹ |

and k refers to the secondary particle type. The subscripts l and j refer the incident protons direction and energy respectively. A history comprises one random direction and J energies sampled from a corresponding number of weighted portions of the incident spectrum. The total number of sampled source protons used to compute D^k are J times L . The model computer program uses a J value of 10. The weights ($W [E_j]$) are included in N^k (see Eq. 7). For the mono-directional case with a slab target, A_l is constant and P is the total incident flux.

DISCUSSION OF THE COMPUTATIONAL MODEL

This concludes the description of the constituents of the secondary model. It has been demonstrated that simple tabular functions, derived from a logical equivalent physical model and a random number generator, can be used to construct a simple computer model for secondary dose computations. The logical discussion of the physical model is sufficient to verify its correctness. In the final analysis, however, the validity of the physical and computational model is determined by favorable comparisons with comprehensive experimental data. This comparison validates the cross sections, multiplicities, and other secondary data utilized in the model as well as the computational procedure.

The cross sections, multiplicities, etc., were supplied by ORNL, ⁽¹³⁾
and necessary empirical data fits were generated by Atomics International. ⁽⁹⁾
The initial physical model was also formulated at Atomics International and reported in the literature. ⁽¹⁰⁾ However, several modifications were necessary to improve the model and to obtain realistic secondary calculations capable of matching experimental results.

EXPERIMENTAL CONFIGURATIONS AND RELATED PURPOSES

The primary goal of the experiment of Maienschein and Blosser was to provide data for validation of calculations of proton-induced reactions in shields. Figure 4 illustrates the geometrical configuration and associated parameters. It can be shown that the direction cosine of the angle between the direction of the incident proton and the line from the emergent point to the center of the tissue equivalent sphere is $\cos \gamma$ where

$$\cos^2 \gamma = \sec^2 \alpha + \sec^2 \beta - 1$$

Three specific configurations will be used to check the generation, transport, and scattering of the proton-induced secondaries. The following outline indicates (1) the experiment geometrical parameters, (2) aluminum target areal density, (3) whether or not the primary proton is stopped in the target, and (4) the characteristics of the secondaries which each configuration is capable of checking.

First

$$\alpha = \beta = 0 \text{ degrees, } \theta = 0 \text{ degrees}$$

26.9 grams/cm² of Al target

+
p stopped

n^o generation and transport

Second

$$\alpha = \beta = 45 \text{ degrees, } \theta = 0 \text{ degrees}$$

26.9 grams/cm² of Al target

+
p stopped

n^o generation, transport, and scattering

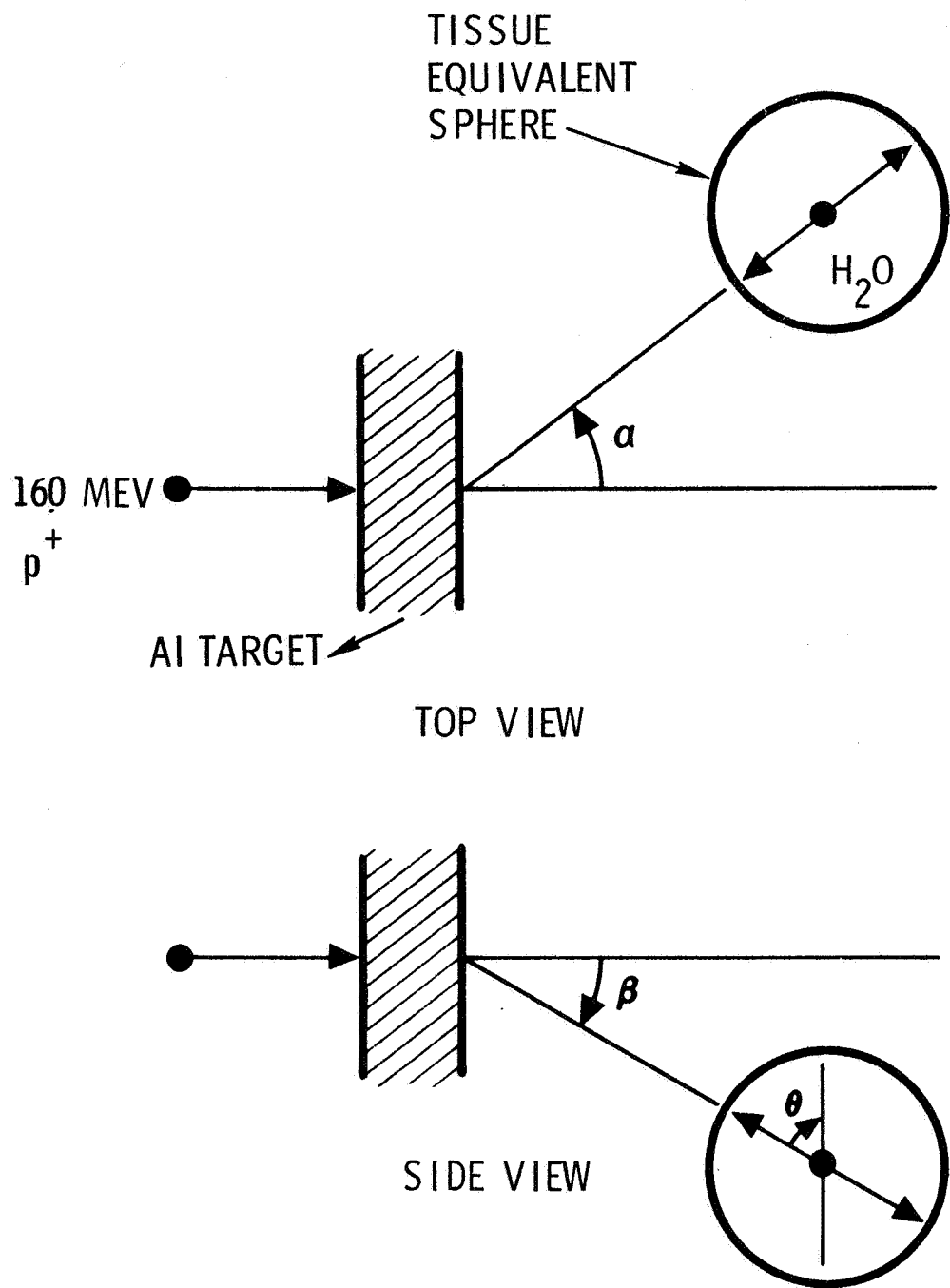


Figure 4. Experiment configuration.

Third

$$\alpha = \beta = 45 \text{ degrees, } \Theta = 0 \text{ degrees}$$

6.95 grams/cm² of Al target

p⁺ not stopped

p⁺ generation, transport, and scattering

COMPARISON OF EXPERIMENTAL AND CALCULATED DOSES

For each configuration, the calculated and experimental doses are plotted and the percentage difference between the upper or lower experimental bound is indicated relative to the calculated values. The first configuration comparison is shown in Fig. 5. There is excellent agreement at the smaller depths in the tissue equivalent phantom. However, the accuracy degenerates as the dosimeter depth increases. This implies that the discrepancy might be due to the neutron buildup factor. Inaccuracies in the buildup factor would be magnified with increasing neutron mean free paths. The agreement at smaller depths indicates comparatively accurate calculations of the secondary neutron spectra. However, the overall comparative accuracy is relatively good and within the state-of-the-art accuracies.

Figure 6 shows the comparison for the second configuration. This configuration generally indicates higher percentage differences than the other two. The calculated and experiment values (upper bound) differ by approximately a constant ratio. The percentage error decreases with phantom depth. Although, at present we have no explanation for the constant ratio, a future effort could perhaps resolve this by additional intermediate output from the computer program. The accuracies for this particular configuration, however, are comparable to the present accuracies

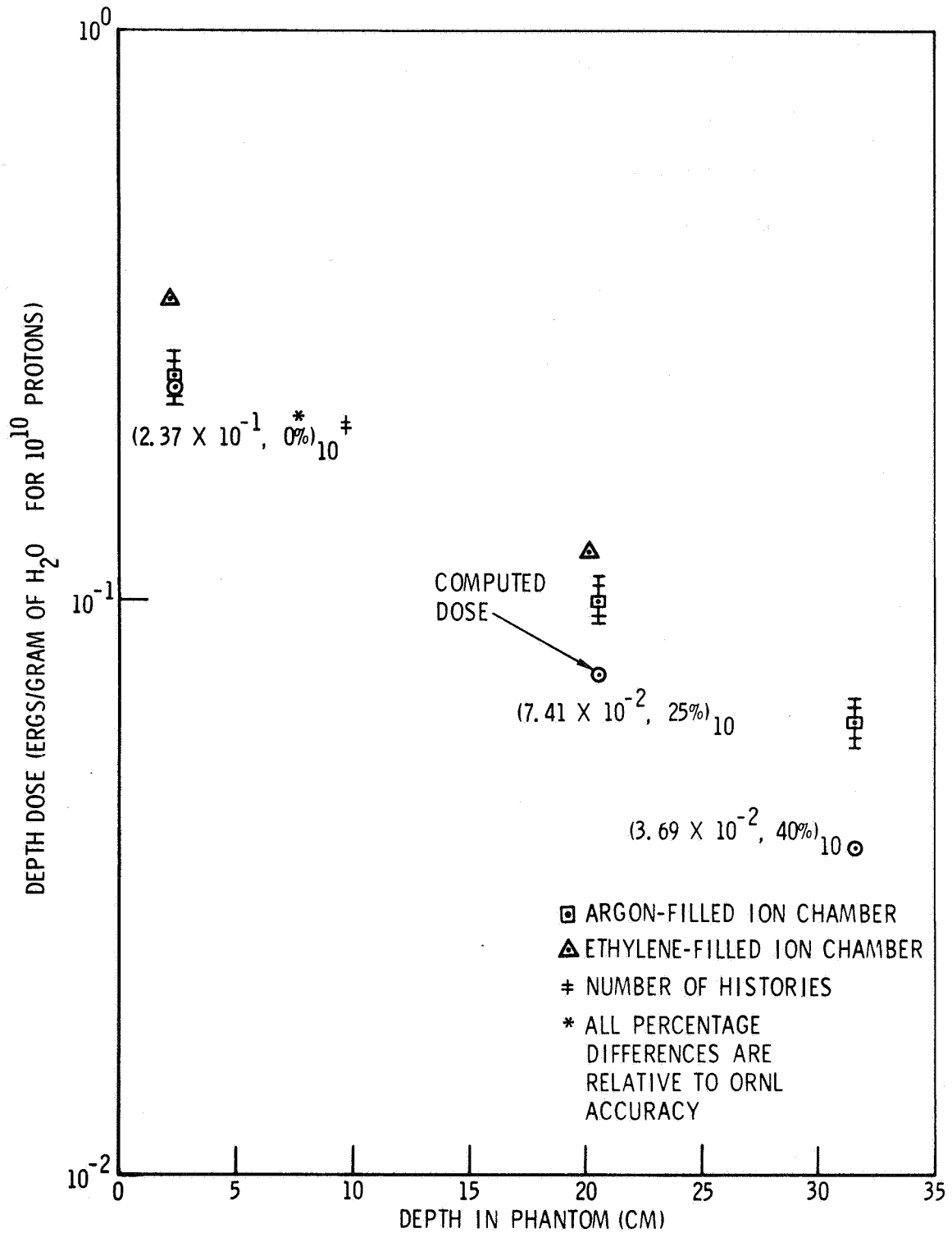


Figure 5. $\alpha = \beta = 0$ degrees, Al target, 26.9 g/cm^2 ; target-phantom distance = 48.5 cm.

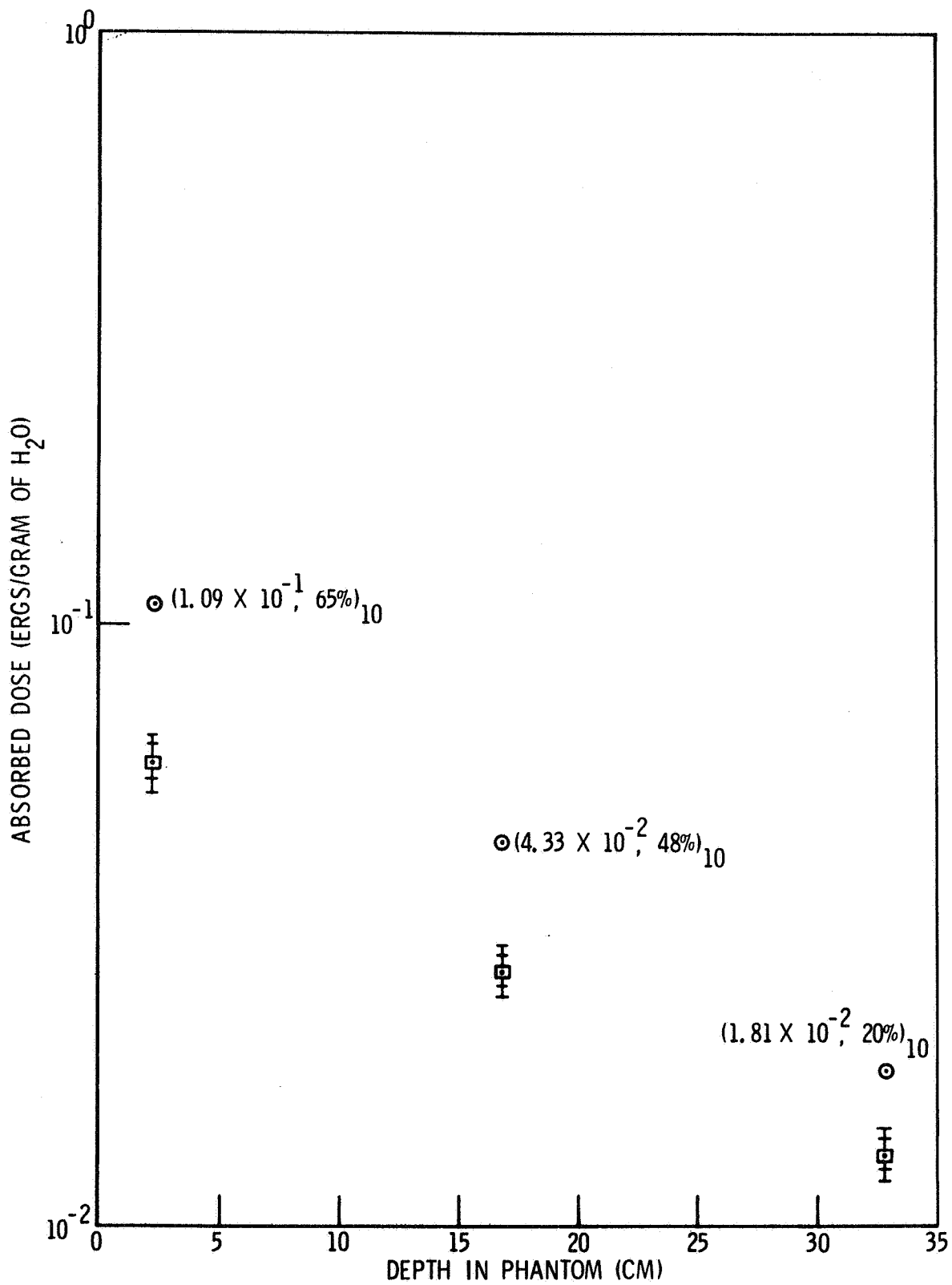


Figure 6. $\alpha = \beta = 45$ degrees, Al target, 26.9 g/cm^2 ; target-phantom distance = 53.7 cm.

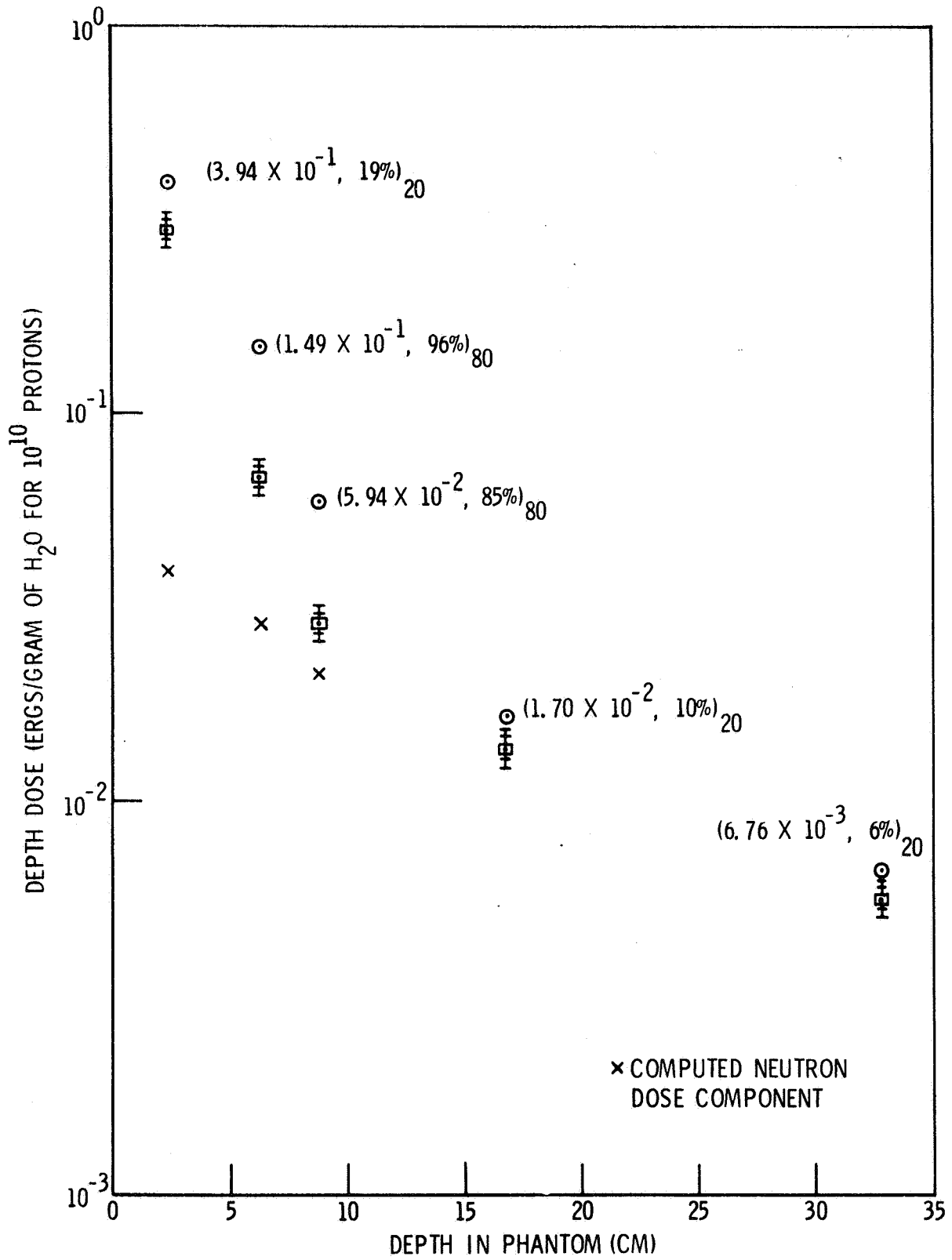


Figure 7. $\alpha = \beta = 45$ degrees, Al target, 6.72 g/cm^2 ; target-phantom distance = 53.7 cm.

for secondary computations.

The percentage differences for the third configuration are comparable to those of the first. Figure 7 shows the neutron and proton components for several points. There is good agreement and identical cross-over phantom depths for predominant secondary proton and neutron contributions (8.75 cm). Only two phantom depths (6.25, 8.75 cm) indicate an appreciable percentage difference. This tends to indicate that the calculated dose will not increase as fast as the extrapolated experimental results at lower energies. However, this difference can only be resolved by consideration of the low-energy portion of the proton emergent spectra from the Al target. Previously reported experiments have not considered the low-energy segment of the spectrum. (8)

The generally excellent agreement for the third configuration (both neutrons and proton components) tends to validate secondary-generation transport differential scattering and flux to dose conversion factors. The more favorable agreement for the third configuration could be due to more accurate differential scattering cross sections at higher reaction energies. The second configuration has a softer effective reaction energy spectrum because of two factors:

1. smaller average reaction energy of the primary protons
2. larger target absorption of the secondaries generated at higher energies.

CONCLUDING REMARKS

A detailed simple model has been presented for secondary dose computations. Agreement between the calculated and experimental results is generally better than the existing state-of-the-art accuracy which is about a factor of 2. The accuracy is also quite sufficient to validate the

analytical model. Reference 11 indicates that the translunar and lunar landing spacecrafts and space suit (including astronaut) will have areal density distribution functions with substantial solid angle at small areal densities. Therefore, the most critical secondary dose component for lunar-type missions will be the secondary proton component. This is due to the much larger secondary proton component, indicated in Table II, for thin target generated secondaries. The ratio of the secondary proton component to the secondary neutron component can be as large as a factor of 10. However, the total secondary dose will be small compared to the associate primary dose for thin targets.

Table II. Secondary Dose Components*

| No. of Histories | α | β | θ | Target Thickness (cm) | Dosimeter Depth (cm) | Proton Dose | | Neutron Dose | | Total Dose |
|------------------|----------|---------|----------|-----------------------|----------------------|--|-----|--------------|---------|------------|
| | | | | | | (ergs/gram/10 ¹⁰ p ⁺) | | | | |
| 10 | 0° | 0° | 0° | 10 | 2.5 | 0.0 | 0.0 | 0.237 | 0.237 | 0.237 |
| | | | | | 20.55 | 0.0 | 0.0 | 0.0741 | 0.0741 | 0.0741 |
| | | | | | 32.85 | 0.0 | 0.0 | 0.0369 | 0.0369 | 0.0369 |
| 10 | 45° | 45° | 0° | 10 | 2.35 | 0.0 | 0.0 | 0.109 | 0.109 | 0.109 |
| | | | | | 16.95 | 0.0 | 0.0 | 0.0433 | 0.0433 | 0.0433 |
| | | | | | 32.85 | 0.0 | 0.0 | 0.0181 | 0.0181 | 0.0181 |
| 20 | 45° | 45° | 0° | 2.5 | 2.35 | 0.354 | 0.0 | 0.0397 | 0.394 | 0.394 |
| 80 | | | | | 6.25 | 0.120 | 0.0 | 0.0290 | 0.149 | 0.149 |
| 80 | | | | | 8.75 | 0.038 | 0.0 | 0.0214 | 0.0594 | 0.0594 |
| 20 | | | | | 16.75 | 0.0 | 0.0 | 0.0170 | 0.0170 | 0.0170 |
| 20 | | | | | 32.85 | 0.0 | 0.0 | 0.00676 | 0.00676 | 0.00676 |

*The estimated computational uncertainty in each of these doses is 10% at one standard deviation.

REFERENCES

- 1 R. Wallace, P. Steward, and C. Sondhaus, "Primary and Secondary Proton Dose Rates in Spheres and Slabs of Tissue," Second Symposium on Protection Against Radiations in Space, Gatlinburg, Tenn. (12 - 14 Oct. 1964) p. 301.
- 2 R. Wilson and R. Miller, "Secondary-Particle Dose Contributions Induced by Solar Proton Radiation," First Symposium on Protection Against Radiations in Space, Gatlinburg, Tenn. (5 - 7 Nov. 1962) p. 595.
- 3 W. Kinney, R. Coveyou, and C. Zerby, "A Series of Monte Carlo Codes to Transport Nucleons Through Matter," First Symposium on Protection Against Radiations in Space, Gatlinburg, Tenn. (5 - 7 Nov. 1962) p. 608.
- 4 C. Zerby and W. Kinney, "Calculated Tissue Current-to-Dose Conversion Factors for Nucleons Below 400 Mev," ORNL-TM-1038 (May 1965).
- 5 F. Maienschein and V. Blosser, "The Depth Dose Distribution Produced in a Spherical Water Filled Phantom by the Interactions of a 160 Mev Proton Beam," ORNL-3457 (7 June 1963).
- 6 M. H. Kalos, "Neutron Penetration Through Thick Hydrogen Slabs," Nuclear Science and Engineering, Vol. 16 (1963) p. 227.
- 7 W. A. Gibson, "Energy Removed for Primary Proton and Neutron Beams by Tissue," ORNL-CF-61-8-48 (June 1961).
- 8 W. Gibson, et al, "Comparison of Measured Neutron and Proton Spectra With Calculated Spectra in the Energy Region Between 50 and 60 Mev," Second Symposium on Protection Against Radiations in Space, Gatlinburg, Tenn. (12 - 14 Oct. 1964) p. 337.

- ⁹ H. Alter, "Basic Microscopic Data for Space Shielding Analysis," AI-Memo-8853, Vols. I and II (8 Aug. 1963).
- ¹⁰ R. Blaine, K. Rooney, and E. Vaughan, "A Program for Apollo Radiation Shielding Analysis: Summary Report," AI-Memo-8855.
- ¹¹ B. Liley and G. Schaedle, "An Examination of the Relative Merits of Stochastic and Nonstatistical Method of Computing Primary Ionization Doses," Second Symposium on Protection Against Radiations in Space, Gatlinburg, Tenn. (12 - 14 Oct. 1964) p. 527.
- ¹² "Shielding Problems in Manned Space Vehicles," Lockheed Report NR 140 (1960) p. 65.
- ¹³ F. K. McGowan, et al, "Charged Particle Nuclear Cross-Section Computation," Neutron Physics Division Space Radiation Shielding Research Annual Progress Report, ORNL-3425 (1963) p. 15.
- ¹⁴ H. Goldstein, "Fundamental Aspects of Reactor Shielding," Addison-Wesley Publishing Co., Inc., 1959, p. 286.
- ¹⁵ W. R. Burrus, "Bonner Spheres and Threshold Detectors for Neutron Spectroscopy," Neutron Physics Division Space Radiation Shielding Research Annual Progress Report, ORNL-CF-62-10-99, Rev., 1962, p. 248.
- ¹⁶ "Protection Against Neutron Radiation up to 300 MeV," NBS-63 (1957) p. 7.



ANALYTIC REPRESENTATION OF NONELASTIC CROSS SECTIONS AND
PARTICLE-EMISSION SPECTRA FROM NUCLEON-NUCLEUS
COLLISIONS IN THE ENERGY RANGE
25 TO 400 MeV*

R. G. Alsmiller, Jr., M. Leimdorfer,
and J. Barish**
Oak Ridge National Laboratory
Oak Ridge, Tennessee

Analytic fits, obtained by the method of linear least squares, to the intranuclear-cascade data generated by H. W. Bertini are given. For both protons and neutrons incident on the elements C, O, Al, Cr, Cu, Ru, Ce, W, Pb, and U, analytic expressions are given for:

1. the nonelastic cross section as a function of energy;
2. the cascade neutron- and proton-emission spectra in the angular intervals $0-30^\circ$, $30-60^\circ$, $60-90^\circ$, and $90-180^\circ$;
3. the evaporation neutron- and proton-emission spectra (assumed isotropic); and
4. the cascade neutron- and proton-emission spectra integrated over all angles.

The cascade emission spectra integrated over all angles can be obtained by summing the emission spectra in the individual angular intervals. This procedure, however, leads to functions which involve many more parameters than are necessary, so separate fits for the angle-integrated spectra are given.

*Research partially sponsored by the National Aeronautics and Space Administration under Union Carbide Corporation's contract with the U. S. Atomic Energy Commission.

**Computing Technology Center, Union Carbide Corporation, Oak Ridge, Tennessee.

I. INTRODUCTION

Using an intranuclear-cascade model, H. W. Bertini has generated a large amount of data on the nonelastic cross sections and the energy and angular distributions of emitted neutrons and protons when neutrons and protons in the energy range 25 to 400 MeV are incident on a variety of targets.^{1-5*} The calculations were carried out using Monte Carlo methods and the data were presented in the form of histograms which contain, of course, statistical fluctuations. In order to make this large amount of data more accessible and to remove insofar as possible the statistical fluctuations, the data have been fitted using the method of linear least squares. In this paper, the fitting procedure is discussed, and tables of the coefficients which occur in the fitted functions are given.

For both protons and neutrons in the energy range 25 to 400 MeV, incident on the elements C, O, Al, Cr, Cu, Ru, Ce, W, Pb, and U, analytic expressions are given for:

1. the nonelastic cross section as a function of energy;
2. the cascade** neutron- and proton-emission spectra in the laboratory angular intervals $0-30^\circ$, $30-60^\circ$, $60-90^\circ$, and $90-180^\circ$;
3. the evaporation** neutron- and proton-emission spectra (assumed isotropic); and
4. the cascade neutron- and proton-emission spectra integrated over all angles.

*All of the data calculated by Bertini² have been recorded on microfilm and are available on request from the Radiation Shielding Information Center of the Oak Ridge National Laboratory. The data on pion-nucleus collisions are not considered in this paper.

**See ref. 1 for a discussion of the distinction between cascade and evaporation particles.

II. NONELASTIC CROSS SECTION

In many ways the nonelastic cross section is the easiest part of the data to fit because the Monte Carlo calculation in this case gives an estimate of the cross section at discrete energies. Let σ_{E_i} be the cross-section value given by the Monte Carlo calculation at energy E_i and let $\sigma(E)$, the assumed analytic form of the cross section, be given by

$$\sigma(E) = \frac{1}{400} \exp \left[\sum_{j=0}^{\nu} a_j \left(\frac{E}{400} \right)^j \right], \quad (1)$$

where the a_j 's are coefficients which are to be determined and ν is a parameter which must be specified. To determine the coefficients, a quantity R is defined by

$$R = \sum_{E_i} \left[\log(400 \sigma_{E_i}) - \sum_{j=0}^{\nu} a_j \left(\frac{E}{400} \right)^j \right]^2, \quad (2)$$

and it is required that R be a minimum with respect to the a_j 's. Taking the derivative of R with respect to each a_j and setting the derivative equal to zero leads to a set of linear equations for the a_j 's, which may easily be solved.

In calculating the cross-section fits, ν was in general taken to be 4. In some cases, however, this led to unphysical oscillations in the cross section. To avoid this, the derivative of σ was tested for sign changes and no more than two such changes were allowed. If $\nu = 4$ led to more than two sign changes, the fit was recalculated using $\nu = 3$, the test was again applied, and so on. In only one case - protons incident on lead - was it necessary to go to $\nu = 2$.

Figure 1 shows a comparison between the Monte Carlo cross-section values and the analytic cross section for the case of protons incident on aluminum. The points give the Monte Carlo values and the smooth curve is obtained from the fitted function. This comparison is roughly similar to the comparisons in the other cases.*

The calculated coefficients for protons and neutrons incident on all ten elements considered are given in Table 1. When these coefficients are used in Eq. 1, the cross section is given in millibarns. It should be carefully noted that the analytic expression for the cross section is valid only between E_{MIN} and E_{MAX} . If an attempt is made to use the expression outside of these limits, quite wild behavior may occur.

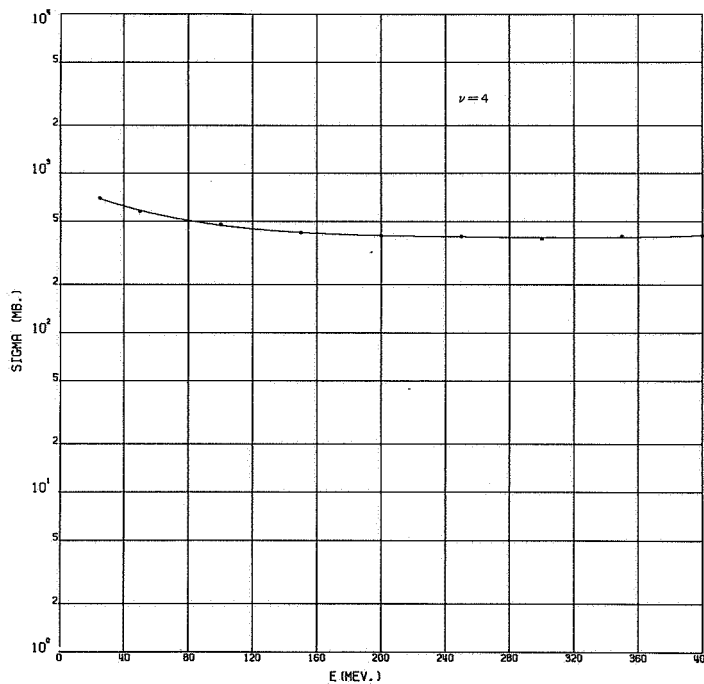


Fig. 1 Non-elastic cross section for protons on aluminum

*Graphs comparing the analytic functions with the Monte Carlo results for every fit considered in this paper have been put on microfiche and are available on request from the Radiation Shielding Information Center of the Oak Ridge National Laboratory.

TABLE I

Non-Elastic Cross Section -- $E_{\max} = 400 \text{ Mev}$ -- $E_{\min} = 25 \text{ Mev}$

| INC. PART. | ELEMENT | A0 | A1 | A2 | A3 | A4 |
|---------------|---------|---------------|----------------|---------------|----------------|---------------|
| P | C | 1.2404415E 01 | -5.8957527E 00 | 1.4181531E 01 | -1.5782847E 01 | 6.5407931E 00 |
| N | C | 1.2382795E 01 | -5.4469868E 00 | 1.1550725E 01 | -1.1297047E 01 | 4.2141600E 00 |
| P | O | 1.2491634E 01 | -4.8397415E 00 | 1.0672125E 01 | -1.1107638E 01 | 4.4098029E 00 |
| N | O | 1.2517978E 01 | -5.0931867E 00 | 1.1287781E 01 | -1.1489868E 01 | 4.4210285E 00 |
| P | AL | 1.2755232E 01 | -4.0729099E 00 | 8.3844210E 00 | -7.9828938E 00 | 2.9174227E 00 |
| N | AL | 1.2693695E 01 | -3.2955608E 00 | 4.8855736E 00 | -2.2990761E 00 | 0. |
| P | CR | 1.3086483E 01 | -3.6344494E 00 | 8.2685571E 00 | -8.5600537E 00 | 3.3101446E 00 |
| N | CR | 1.2992464E 01 | -2.7472568E 00 | 4.7781588E 00 | -3.3056928E 00 | 7.1729518E-01 |
| P | CU | 1.3124442E 01 | -2.2431584E 00 | 3.1773718E 00 | -1.4557472E 00 | 0. |
| N | CU | 1.3123691E 01 | -3.1100930E 00 | 6.8323115E 00 | -6.7329364E 00 | 2.5074524E 00 |
| P | RU | 1.3393167E 01 | -2.5932699E 00 | 4.9881883E 00 | -4.3351257E 00 | 1.4487587E 00 |
| N | RU | 1.3310216E 01 | -2.2752317E 00 | 4.4564933E 00 | -3.9346417E 00 | 1.3578885E 00 |
| P | CE | 1.3576547E 01 | -2.5932949E 00 | 5.9442778E 00 | -6.2489418E 00 | 2.4423424E 00 |
| N | CE | 1.3481119E 01 | -2.2271577E 00 | 4.6824312E 00 | -4.3243270E 00 | 1.5115106E 00 |
| P | W | 1.3738246E 01 | -2.7154819E 00 | 6.8485157E 00 | -7.8453774E 00 | 3.2812133E 00 |
| N | W | 1.3616097E 01 | -1.8728119E 00 | 3.3837169E 00 | -2.1868509E 00 | 3.4781330E-01 |
| P | PB | 1.3769213E 01 | -2.1353969E 00 | 4.4340011E 00 | -4.1898265E 00 | 1.4975631E 00 |
| N | PB | 1.3594525E 01 | -7.8999317E-01 | 5.7062252E-01 | 0. | 0. |
| P | U | 1.3808177E 01 | -1.4907267E 00 | 2.0592438E 00 | -9.3032273E-01 | 0. |
| N | U | 1.3753272E 01 | -2.0033221E 00 | 4.8844039E 00 | -5.3210571E 00 | 2.1316326E 00 |

III. PARTICLE EMISSION SPECTRA

A. Cascade Neutron- and Proton-Emission Spectra

The cascade neutrons and protons emitted from nucleon-nucleus collisions have complicated energy-angle distributions with the high-energy particles emitted predominantly at the smaller angles. The Monte Carlo results presented by Bertini² give the emission spectra in the form of a histogram, with equal energy intervals, averaged over specified angular intervals. It is these spectra which have been fitted. However, for fitting purposes, it was found that equal intervals in energy were not convenient so, before the fitting was carried out, the Monte Carlo history tapes were re-analyzed. This analysis was carried out to form a histogram with unequal energy intervals but with the same number of emitted particles in each interval. In each histogram interval, the energy, such that within the interval equal numbers of particles were emitted above and below this energy, was determined, and the histogram value was assumed to be an estimate of the energy distribution at this energy.*

Let F_{E_i} be this Monte Carlo estimate of the energy distribution (number of emitted particles per MeV per steradian per collision) averaged over a specified angular interval at the energy E_i and let $F(E)$, the assumed analytic form of the distribution, be defined by

$$F(E) = \frac{1}{E_0} \exp \left[\sum_{j=0}^{\nu} a_j \left(\frac{E}{E_0} \right)^j \right], \quad (3)$$

where E_0 is the energy of the incident particle. It is to be understood

*This procedure was varied slightly in the very highest energy interval in each histogram. The complete details of the analysis procedure are given in Appendix 1 of reference 7.

that F_{E_i} and the function $F(E)$ depend on the type of incident particle, the energy of the incident particle, the element considered, the type of emergent particle, and on the angular interval used in carrying out the average. To determine the coefficient, R was defined by the equation,

$$R = \sum_{E_i} \left[\log\left(\frac{F_{E_i}}{F_{E_0}}\right) - \sum_{j=0}^{\nu} a_j \left(\frac{E_i}{E_0}\right)^j \right]^2, \quad (4)$$

and was minimized with respect to the a_j 's.

In the calculations, ν was in general taken to be 5 or to be the number of histogram intervals minus 2 when there were less than seven intervals in the histogram.* In some cases, however, this large number of parameters led to excessive oscillation in the fitted distributions. To avoid this, the derivative of Eq. 3 was tested for sign changes and only two such changes were allowed. If more than two occurred, the fit was recalculated with ν reduced by 1 and the test was reapplied. This procedure was continued until a satisfactory fit was obtained or until $\nu = 2$ was reached. If $\nu = 2$ was reached, the fit was accepted without further testing.

In Figs. 2-5 the smooth curves obtained with the analytic fit are compared with the Monte Carlo histograms for the case of neutrons emitted from 400-MeV protons on aluminum in the angular intervals 0-30°, 30-60°, 60-90°, and 90-180°, respectively. The comparisons shown in these figures are similar to the comparisons in the other cases.

*See Appendix 1 of reference 7.

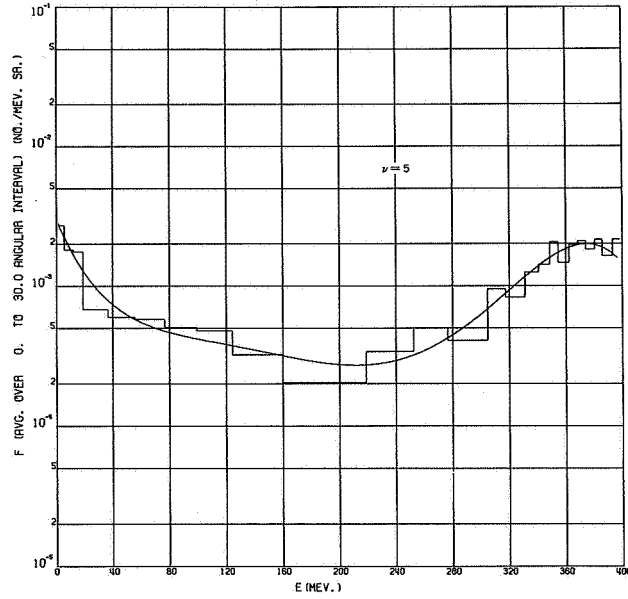


Fig. 2 Cascade neutrons from 400 MeV protons on aluminum

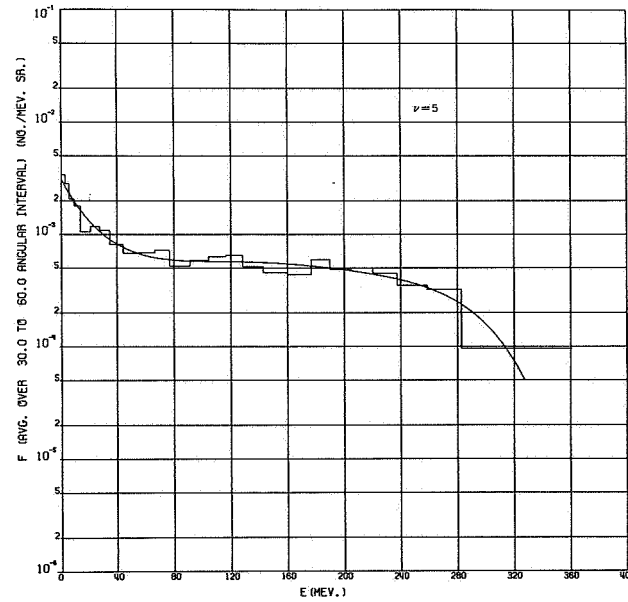


Fig. 3 Cascade neutrons from 400 MeV protons on aluminum

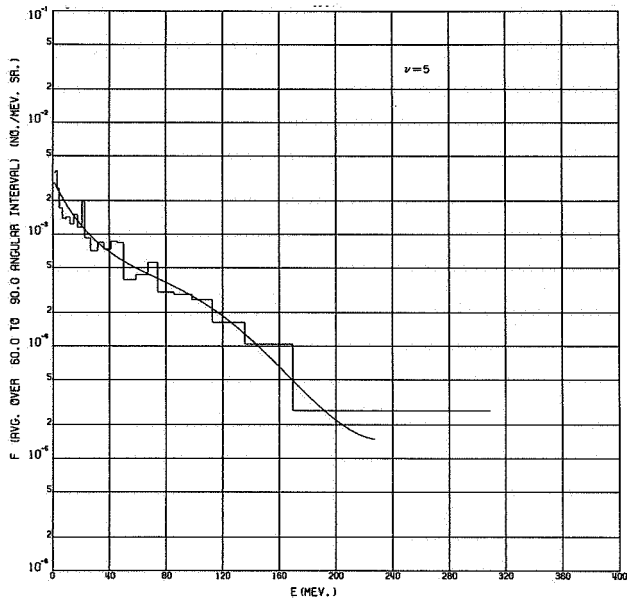


Fig. 4 Cascade neutrons from 400 MeV protons on aluminum

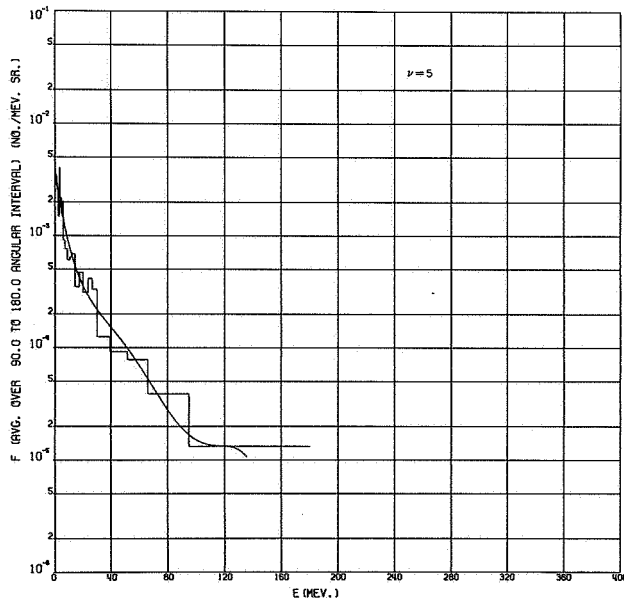


Fig. 5 Cascade neutrons from 400 MeV protons on aluminum

The coefficients for all of the cases considered are given in Tables 2 through 41.* At the top of each table, the type of incident particle, the element, and the type of emitted particle are given. The first column in the table gives the incident energy, E_0 , the second column gives the laboratory angular interval over which the data were averaged, and columns three through eight give the coefficients. When these coefficients are used in Eq. 3, the function F has the units number per MeV per steradian per collision. Here and throughout the tables the coefficients are given with eight significant figures. This is, of course, more than is justified by either the Monte Carlo data or the accuracy of the fits. The numbers given, however, are those which were used in calculating the smooth curves in the graphs. If the coefficients are truncated, curves different from those shown in the graphs may occur. At the top of each table, E_{MIN} is given and, in the last column of each table, E_{MAX} divided by E_0 is given. This E_{MIN} is a parameter which occurs in the calculations of Bertini and represents the energy below which no cascade particles are emitted. The quantity, E_{MAX} , gives the highest energy considered in doing the fitting - that is, it is the highest energy point fitted in a given angular interval. It must be understood that if the analytic functions are used outside of the energy interval E_{MIN} to E_{MAX} , very erratic behavior may occur. Finally, columns nine and ten give the number of particles of a given type emitted per collision in a given angular region and the sum of the energy of these particles divided by E_0 , respectively. The values in these columns are obtained using the fitted functions and the equations

*Only Tables 10 and 11 are given here. Tables of coefficients for all of the cases considered are given in reference 7. Values of χ^2 for each of the fits are given in Appendix 2 of reference 7.

TABLE 10

Protons Incident on Aluminum -- Protons Emitted -- $E_{min} = 1.637$ Mev

| EO (MEV) | ANG. INT. | A0 | A1 | A2 | A3 | A4 | A5 | NO. EMIT. | ENERGY EMIT./EO | EMAX /EC |
|-------------|--------------|----------------|----------------|----------------|----------------|----------------|-----------------|--------------|--------------------|-------------|
| 25 | 0 - 30 | -2.8598950E-01 | -8.3746065E 00 | 1.4048758E 01 | -7.7066813E-01 | -7.3612164E 00 | 0. | 0.177 | 0.0854 | 0.957 |
| | 30 - 60 | -1.3062827E-01 | -2.0436621E 01 | 8.9082304E 01 | -1.8677197E 02 | 1.8140328E 02 | -6.8165786E 01 | 0.216 | 0.0797 | 0.934 |
| | 60 - 90 | -2.1765171E 00 | -3.8374997E 00 | 9.3190541E 00 | -3.1356151E 01 | 2.0750142E 01 | 0. | 0.068 | 0.0159 | 0.676 |
| | 90 -180 | 0. | 0. | 0. | 0. | 0. | 0. | 0.01C | | |
| 50 | 0 - 30 | 1.8257806E-01 | -2.3093975E 01 | 1.2722191E 02 | -3.2676317E 02 | 3.8231027E 02 | -1.6264976E 02 | 0.224 | 0.1151 | 0.972 |
| | 30 - 60 | -3.3570733E-01 | -1.1392949E 01 | 4.1376191E 01 | -7.9280067E 01 | 7.7722386E 01 | -3.3976044E 01 | 0.345 | 0.1168 | 0.909 |
| | 60 - 90 | -1.6329304E 00 | -9.7002971E-01 | -1.3644498E 01 | 1.5625980E 01 | -8.0996298E 00 | 0. | 0.131 | 0.0262 | 0.699 |
| | 90 -180 | -6.1407872E-01 | -1.1350533E 02 | 1.5982764E 03 | -1.0343935E 04 | 2.9773711E 04 | -3.1130989E 04 | 0.036 | 0.0054 | 0.388 |
| 100 | 0 - 30 | 1.3209442E-01 | -1.6469012E 01 | 6.0419427E 01 | -1.2902492E 02 | 1.5556231E 02 | -7.2359787E 01 | 0.285 | 0.1599 | 0.976 |
| | 30 - 60 | 3.7192968E-02 | -1.4047568E 01 | 4.6957476E 01 | -5.9152944E 01 | 1.6642253E 01 | 6.7771571E 00 | 0.490 | 0.1677 | 0.908 |
| | 60 - 90 | -3.5567331E-02 | -2.5465483E 01 | 1.3731771E 02 | -3.5440899E 02 | 3.5570803E 02 | -1.0666662E 02 | 0.230 | 0.0393 | 0.654 |
| | 90 -180 | -1.1021602E 00 | -4.4004517E 01 | 4.2507898E 02 | -1.9017084E 03 | 2.6447520E 03 | 0. | 0.077 | 0.0072 | 0.317 |
| 150 | 0 - 30 | 2.8568012E-01 | -2.4985599E 01 | 1.2712754E 02 | -3.0996816E 02 | 3.5597885E 02 | -1.4990194E 02 | 0.313 | 0.1844 | 0.985 |
| | 30 - 60 | 4.5654287E-02 | -1.8867131E 01 | 8.7532312E 01 | -1.6791441E 02 | 1.4272974E 02 | -4.7886605E 01 | 0.565 | 0.2098 | 0.929 |
| | 60 - 90 | 1.0565200E-01 | -2.2287275E 01 | 1.3322266E 02 | -4.4821100E 02 | 6.3286058E 02 | -3.1672827E 02 | 0.292 | 0.0420 | 0.680 |
| | 90 -180 | -4.4831066E-01 | -5.5054606E 01 | 5.1695319E 02 | -3.0984696E 03 | 1.0533085E 04 | -1.5033375E 04 | 0.107 | 0.0093 | 0.322 |
| 200 | 0 - 30 | 4.6217349E-01 | -3.1754100E 01 | 1.6034585E 02 | -3.7715878E 02 | 4.1969703E 02 | -1.7295128E 02 | 0.333 | 0.2080 | 0.984 |
| | 30 - 60 | 2.2302780E-01 | -2.1803110E 01 | 1.0401002E 02 | -2.0116162E 02 | 1.6808053E 02 | -5.3071643E 01 | 0.611 | 0.2247 | 0.935 |
| | 60 - 90 | 4.5109478E-02 | -1.9698351E 01 | 9.7236922E 01 | -2.3203816E 02 | 1.6724362E 02 | 4.2739485E 00 | 0.322 | 0.0487 | 0.596 |
| | 90 -180 | -7.0727081E-01 | -1.5476547E 01 | -1.6355955E 02 | 1.3105093E 03 | -2.4552212E 03 | 0. | 0.143 | 0.0105 | 0.330 |
| 250 | 0 - 30 | 1.6113985E-01 | -1.8586426E 01 | 7.3592290E 01 | -1.6140596E 02 | 1.9080227E 02 | -8.5659566E 01 | 0.347 | 0.2103 | 0.980 |
| | 30 - 60 | 2.1609405E-01 | -1.6829088E 01 | 7.3962016E 01 | -1.4764038E 02 | 1.4781355E 02 | -6.5426473E 01 | 0.658 | 0.2281 | 0.895 |
| | 60 - 90 | 3.6170024E-01 | -3.2053589E 01 | 2.4670842E 02 | -9.0965852E 02 | 1.4432761E 03 | -8.3491192E 02 | 0.356 | 0.0535 | 0.569 |
| | 90 -180 | 7.1475114E-02 | -6.7957774E 01 | 7.6900274E 02 | -4.4299433E 03 | 1.0658509E 04 | -8.7957876E 03 | 0.155 | 0.0097 | 0.279 |
| 300 | 0 - 30 | 4.5720704E-01 | -2.5998778E 01 | 1.2439622E 02 | -2.8959208E 02 | 3.2672995E 02 | -1.3723534E 02 | 0.370 | 0.2220 | 0.989 |
| | 30 - 60 | 1.4550004E-01 | -1.8639178E 01 | 9.5442330E 01 | -2.1394247E 02 | 2.2471546E 02 | -9.44556092E 01 | 0.660 | 0.2356 | 0.890 |
| | 60 - 90 | 3.1273582E-01 | -2.8012730E 01 | 1.9876584E 02 | -6.8444590E 02 | 1.0058802E 03 | -5.4341424E 02 | 0.378 | 0.0568 | 0.592 |
| | 90 -180 | 2.0530513E-01 | -5.7542686E 01 | 4.2772115E 02 | -1.5552592E 03 | 1.9092300E 03 | 0. | 0.185 | 0.0117 | 0.353 |
| 350 | 0 - 30 | 1.8098580E-01 | -1.9295761E 01 | 8.1611531E 01 | -1.8251654E 02 | 2.1014135E 02 | -9.0568273E 01 | 0.406 | 0.2581 | 0.989 |
| | 30 - 60 | 2.4279452E-01 | -1.8740302E 01 | 9.28659942E 01 | -1.9380103E 02 | 1.8137467E 02 | -6.7187282E 01 | 0.697 | 0.2402 | 0.893 |
| | 60 - 90 | 3.4973160E-01 | -2.8989238E 01 | 2.4725092E 02 | -1.0879400E 03 | 2.1153173E 03 | -1.5445978E 03 | 0.377 | 0.0500 | 0.515 |
| | 90 -180 | -1.3351158E-01 | -3.3854347E 01 | 1.1546520E 02 | -1.8478054E 02 | 0. | 0. | 0.193 | 0.0114 | 0.296 |
| 400 | 0 - 30 | 2.6105281E-01 | -2.6420529E 01 | 1.3227442E 02 | -3.0973108E 02 | 3.4336939E 02 | -1.4025499E 02 | 0.398 | 0.2581 | 0.991 |
| | 30 - 60 | 4.0331609E-01 | -2.4677581E 01 | 1.2399120E 02 | -2.6000383E 02 | 2.5092945E 02 | -9.7773282E 01 | 0.682 | 0.2426 | 0.863 |
| | 60 - 90 | 6.2189580E-01 | -3.4078394E 01 | 2.7046140E 02 | -1.0608300E 03 | 1.7405789E 03 | -1.0138915E 03 | 0.389 | 0.0464 | 0.563 |
| | 90 -180 | 5.7044991E-02 | -3.8967300E 01 | 1.3437984E 02 | -2.2415526E 02 | 0. | 0. | 0.195 | 0.0097 | 0.319 |

TABLE 11

Protons Incident on Aluminum -- Neutrons Emitted -- $E_{\min} = 1.637$ MeV

| EO (MEV) | ANG. INT. | A0 | A1 | A2 | A3 | A4 | A5 | NO. EMIT. | ENERGY EMIT./EO | EMAX /EO |
|-------------|--------------|----------------|----------------|----------------|----------------|----------------|----------------|--------------|--------------------|-------------|
| 25 | 0 - 30 | -2.0582384E-01 | -9.4997159E 00 | 1.6672165E 01 | -4.3540535E 00 | -5.8801774E 00 | 0. | 0.146 | 0.0652 | 0.944 |
| | 30 - 60 | -1.1446529E 00 | -8.1214093E 00 | 2.0813286E 01 | -3.1285133E 01 | 2.3381931E 01 | -9.5605812E 00 | 0.138 | 0.0466 | 0.892 |
| | 60 - 90 | -3.3927871E 00 | 1.9194626E 01 | -1.3880588E 02 | 2.8451119E 02 | -1.9653423E 02 | 7.4603592E 00 | 0.045 | 0.0097 | 0.667 |
| | 90 -180 | 0. | 0. | 0. | 0. | 0. | 0. | 0.010 | | |
| 50 | 0 - 30 | -3.6829797E-01 | -6.4756619E 00 | -2.1687782E 00 | 4.0571920E 01 | -4.9442551E 01 | 1.5849463E 01 | 0.194 | 0.0943 | 0.977 |
| | 30 - 60 | -2.3771082E-01 | -1.4227494E 01 | 5.3345724E 01 | -1.1171930E 02 | 1.2058881E 02 | -5.5376545E 01 | 0.270 | 0.0817 | 0.880 |
| | 60 - 90 | -1.5328537E 00 | -4.8479594E 00 | 1.2556125E 00 | -1.1741539E-01 | -2.3087367E 01 | 2.3494169E 01 | 0.109 | 0.0208 | 0.662 |
| | 90 -180 | -2.1730779E 00 | -1.4971539E 01 | 3.8287644E 00 | 0. | 0. | 0. | 0.030 | 0.0030 | 0.302 |
| 100 | 0 - 30 | -4.4155729E-01 | -1.2675632E 01 | 5.3847844E 01 | -1.1971100E 02 | 1.3364319E 02 | -5.5862721E 01 | 0.219 | 0.1179 | 0.973 |
| | 30 - 60 | -3.9076856E-01 | -8.1103227E 00 | 3.1151018E 00 | 5.2921579E 01 | -1.0242447E 02 | 5.1938397E 01 | 0.326 | 0.0986 | 0.920 |
| | 60 - 90 | -9.6187931E-01 | 2.7676462E 00 | -1.5835605E 02 | 8.898604E 02 | -1.9222920E 03 | 1.3921981E 03 | 0.180 | 0.0279 | 0.569 |
| | 90 -180 | -2.2277075E 00 | 1.7720895E 01 | -5.1951788E 02 | 3.0644054E 03 | -6.5632992E 03 | 3.8300911E 03 | 0.070 | 0.0067 | 0.347 |
| 150 | 0 - 30 | -3.2264142E-01 | -1.1547256E 01 | 4.6767039E 01 | -1.2609027E 02 | 1.7126697E 02 | -8.1753765E 01 | 0.222 | 0.1179 | 0.971 |
| | 30 - 60 | 1.5577855E-01 | -1.9350442E 01 | 8.2721858E 01 | -1.7502570E 02 | 1.7931850E 02 | -7.5116493E 01 | 0.373 | 0.1052 | 0.853 |
| | 60 - 90 | 4.2507200E-01 | -4.2267140E 01 | 3.0238048E 02 | -9.8716519E 02 | 1.3547234E 03 | -6.6502997E 02 | 0.232 | 0.0327 | 0.567 |
| | 90 -180 | -1.2935761E 00 | -1.4182680E 01 | 4.0630659E 00 | 7.2975810E-01 | 0. | 0. | 0.108 | 0.0089 | 0.343 |
| 200 | 0 - 30 | 1.3947506E-01 | -2.0028960E 01 | 8.7609593E 01 | -2.0653109E 02 | 2.4300923E 02 | -1.0588523E 02 | 0.243 | 0.1314 | 0.984 |
| | 30 - 60 | 2.0636015E-01 | -2.0519131E 01 | 8.2051533E 01 | -1.5738658E 02 | 1.4480670E 02 | -5.5563720E 01 | 0.361 | 0.1006 | 0.891 |
| | 60 - 90 | -1.9334836E-01 | -1.4505193E 01 | 3.4930097E 01 | -4.1040539E 01 | 0. | 0. | 0.252 | 0.0359 | 0.581 |
| | 90 -180 | -7.8127718E-01 | -3.5103032E 01 | 2.5739180E 02 | -1.2198912E 03 | 2.3378928E 03 | -1.2828398E 03 | 0.117 | 0.0087 | 0.330 |
| 250 | 0 - 30 | 3.2436825E-01 | -2.1818105E 01 | 8.6052881E 01 | -1.8995783E 02 | 2.1829996E 02 | -9.4100225E 01 | 0.247 | 0.1363 | 0.988 |
| | 30 - 60 | 2.8389247E-01 | -2.3592044E 01 | 1.1299440E 02 | -2.5328671E 02 | 2.6491850E 02 | -1.0897711E 02 | 0.393 | 0.1093 | 0.836 |
| | 60 - 90 | 3.1994826E-01 | -3.4141635E 01 | 2.5962165E 02 | -9.9975438E 02 | 1.6614568E 03 | -1.0016574E 03 | 0.273 | 0.0347 | 0.566 |
| | 90 -180 | -5.7347713E-01 | -2.3563178E 01 | -3.7731193E 00 | 2.9133689E 02 | -7.0555840E 02 | 4.2424548E 02 | 0.147 | 0.0097 | 0.342 |
| 300 | 0 - 30 | 3.992348E-01 | -2.5993024E 01 | 1.1556582E 02 | -2.5271907E 02 | 2.6718572E 02 | -1.0537204E 02 | 0.242 | 0.1303 | 0.987 |
| | 30 - 60 | 2.5894607E-01 | -2.3311826E 01 | 1.1265418E 02 | -2.5781789E 02 | 2.9274532E 02 | -1.4031184E 02 | 0.412 | 0.1150 | 0.800 |
| | 60 - 90 | -1.9350901E-02 | -1.4603470E 01 | 3.5047193E 01 | -4.5029092E 01 | 0. | 0. | 0.292 | 0.0371 | 0.546 |
| | 90 -180 | -2.9438261E-01 | -3.3994011E 01 | 1.1957705E 02 | -2.0369549E 02 | 0. | 0. | 0.162 | 0.0099 | 0.337 |
| 350 | 0 - 30 | 5.0168191E-01 | -2.7785761E 01 | 1.2563141E 02 | -2.7754260E 02 | 2.9379623E 02 | -1.1540391E 02 | 0.252 | 0.1376 | 0.993 |
| | 30 - 60 | 4.2089826E-01 | -3.1528009E 01 | 1.7944133E 02 | -4.4506506E 02 | 4.9217389E 02 | -2.0344026E 02 | 0.410 | 0.1184 | 0.844 |
| | 60 - 90 | -3.4132196E-02 | -1.6777024E 01 | 4.0214362E 01 | -3.9909990E 01 | 0. | 0. | 0.275 | 0.0394 | 0.588 |
| | 90 -180 | 3.3954398E-01 | -8.4557639E 01 | 1.2611496E 03 | -1.0738830E 04 | 4.2881732E 04 | -6.3283222E 04 | 0.175 | 0.0103 | 0.271 |
| 400 | 0 - 30 | 2.0209264E-01 | -2.2766777E 01 | 1.0974841E 02 | -2.7269629E 02 | 3.1486005E 02 | -1.2989518E 02 | 0.247 | 0.1405 | 0.991 |
| | 30 - 60 | 2.8795522E-01 | -2.3432551E 01 | 1.2093044E 02 | -3.0019594E 02 | 3.5724812E 02 | -1.6810379E 02 | 0.432 | 0.1204 | 0.819 |
| | 60 - 90 | 2.3901904E-01 | -2.4639708E 01 | 1.2670547E 02 | -3.5334507E 02 | 3.5485006E 02 | -7.4924331E 01 | 0.284 | 0.0324 | 0.567 |
| | 90 -180 | 6.3134015E-01 | -8.8506657E 01 | 1.0395768E 03 | -6.7522640E 03 | 1.9881292E 04 | -2.1236545E 04 | 0.181 | 0.0085 | 0.338 |

$$\text{No. of Emitted Particles} = 2\pi[\cos \theta_1 - \cos \theta_2] \int_{E_{\text{MIN}}}^{E_{\text{MAX}}} F(E) dE \quad (5)$$

and

$$\text{Energy of Emitted Particles}/E_0 = \frac{2\pi[\cos \theta_1 - \cos \theta_2]}{E_0} \int_{E_{\text{MIN}}}^{E_{\text{MAX}}} EF(E) dE, \quad (6)$$

where θ_1 and θ_2 are the angular limits given in column two.

In those places in the tables where only three coefficients are given, the fits must be considered somewhat more approximate than when more coefficients are given. In a few cases, all of the coefficients are given to be zero. When this occurs, it means that so few particles were emitted in a given angular interval that the Monte Carlo results were not considered statistically significant and no attempt was made to obtain a fit. In these cases, the number of emitted particles is still given in column nine of the tables for comparison purposes. This number, of course, is not obtained from Eq. 5 but is taken directly from the Monte Carlo results.

B. Evaporation Neutron- and Proton-Emission Spectra

The procedure used to fit the neutron- and proton-evaporation spectra is very similar to that used in the case of the cascade spectra. The Monte Carlo results presented by Bertini give the emission spectra integrated over all angles in the form of a histogram with equal energy intervals.* The equal energy intervals were again found to be inconvenient so a histogram was constructed with unequal energy intervals determined in such a way that the probability for a particle to be emitted in each interval was the

*The evaporation particles are by assumption emitted isotropically.

same.* Within each interval, the central energy, determined by the condition that a particle within the interval be equally likely to be above and below this energy, was obtained and the histogram value was taken to be an estimate of the energy distribution at this central energy.

The analytic function, $G(E)$, used for the fitting was defined by

$$G(E) = \frac{1}{25} \exp \left[\sum_{j=0}^{\nu} a_j \left(\frac{E}{25} \right)^j \right], \quad (7)$$

and the coefficients were determined by requiring that the quantity R , defined as in Eq. 4 with E_0 replaced by 25, be a minimum. A scaling factor of 25 was used because evaporation particles with energy higher than this were not considered in the Bertini calculations. The fitting procedure was exactly the same as in the case of the cascade spectra.

In Figs. 6 and 7 the smooth curves obtained with the analytic fit are compared with the Monte Carlo histograms for neutrons and protons, respectively, emitted from 400-MeV protons on aluminum. The comparisons shown in the figures are similar to the comparisons in the other cases. In particular, the failure of the analytic curve to reproduce well the low-energy portion of the histogram in the case of evaporation protons, Fig. 7, should be noted because this is generally true of all of the fits to the evaporation proton spectra.

The coefficients for all of the cases considered are given in Tables 42 through 61.** At the top of each table the type of incident particle and the element are given. Each table contains the coefficients for both emitted

*The details of this analysis are given in Appendix 1 of reference 7.

**Only table 46 is given here. Tables of coefficients for all of the cases considered are given in reference 7. Values of χ^2 for each of the fits are given in Appendix 2 of reference 7.

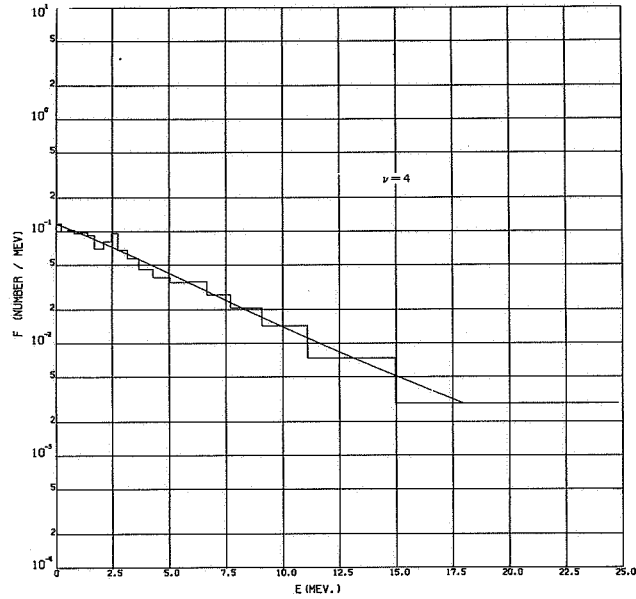


Fig. 6 Evaporation neutrons from 400 MeV protons on aluminum

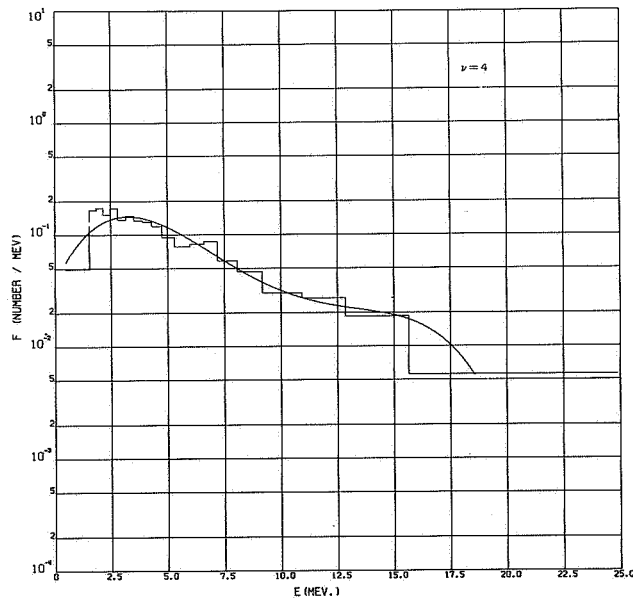


Fig. 7 Evaporation protons from 400 MeV protons on aluminum

TABLE 46

Protons Incident on Aluminum

EVAPORATION PROTONS EMITTED

| EO (MEV) | A0 | A1 | A2 | A3 | A4 | A5 | NO. EMIT. | ENERGY EMIT./EO | EPAX /EO | EMIN /EO |
|-------------|----------------|---------------|----------------|---------------|----------------|----|--------------|--------------------|-------------|-------------|
| 25 | -1.6439358E 00 | 7.3233149E 01 | -6.0039155E 02 | 1.8148050E 03 | -1.9539403E 03 | 0. | 0.549 | 0.0837 | 0.407 | .04800 |
| 50 | -1.0207356E 00 | 5.4829475E 01 | -3.8946252E 02 | 9.8531168E 02 | -8.7019916E 02 | 0. | 0.807 | 0.0712 | 0.255 | .02200 |
| 100 | 4.3604028E-02 | 3.0419367E 01 | -2.0118767E 02 | 4.3204636E 02 | -3.1756648E 02 | 0. | 0.966 | 0.0465 | 0.153 | .00900 |
| 150 | -3.1109351E-02 | 2.9154686E 01 | -1.7866441E 02 | 3.5219663E 02 | -2.3245151E 02 | 0. | 1.033 | 0.0373 | 0.116 | .00600 |
| 200 | 3.7204177E-02 | 2.5424778E 01 | -1.5401392E 02 | 3.0138553E 02 | -2.0157256E 02 | 0. | 0.988 | 0.0263 | 0.084 | .00350 |
| 250 | 6.4057857E-02 | 2.4483812E 01 | -1.4332480E 02 | 2.6748242E 02 | -1.6786420E 02 | 0. | 1.045 | 0.0239 | 0.073 | .00320 |
| 300 | 4.0095028E-01 | 1.7945763E 01 | -1.0331816E 02 | 1.7805551E 02 | -1.0448563E 02 | 0. | 1.051 | 0.0194 | 0.061 | .00267 |
| 350 | 2.4619127E-01 | 2.0067921E 01 | -1.2006985E 02 | 2.2228972E 02 | -1.3916204E 02 | 0. | 0.989 | 0.0159 | 0.052 | .00200 |
| 400 | -1.0220292E-01 | 2.5135558E 01 | -1.4211537E 02 | 2.6008143E 02 | -1.6007186E 02 | 0. | 1.027 | 0.0151 | 0.046 | .00125 |

EVAPORATION NEUTRONS EMITTED

| EO (MEV) | A0 | A1 | A2 | A3 | A4 | A5 | NO. EMIT. | ENERGY EMIT./EO | EPAX /EO | EMIN /EO |
|-------------|---------------|----------------|----------------|----------------|----------------|----------------|--------------|--------------------|-------------|-------------|
| 25 | 1.4324994E 00 | 1.3190309E 01 | -5.8212761E 02 | 4.0532078E 03 | -9.1724969E 03 | 0. | 0.355 | 0.0199 | 0.227 | 0. |
| 50 | 1.2754591E 00 | -2.1402368E 00 | -4.8553957E 01 | 1.4860894E 02 | -2.0788442E 02 | 0. | 0.479 | 0.0235 | 0.187 | 0. |
| 100 | 1.2717622E 00 | -4.0859271E 00 | -2.0870245E 01 | 6.7005758E 01 | -7.4974271E 01 | 0. | 0.562 | 0.0188 | 0.134 | 0. |
| 150 | 9.3813576E-01 | 4.2038499E 00 | -7.6231385E 01 | 1.9407449E 02 | -1.5693451E 02 | 0. | 0.566 | 0.0145 | 0.104 | 0. |
| 200 | 1.0659685E 00 | 2.4486448E-01 | -5.1984472E 01 | 1.4233685E 02 | -1.1975083E 02 | 0. | 0.558 | 0.0108 | 0.080 | 0. |
| 250 | 1.0246835E 00 | -4.1464291E 00 | -2.8276821E 00 | 0. | 0. | 0. | 0.538 | 0.0087 | 0.064 | 0. |
| 300 | 1.3576820E 00 | -1.0578617E 01 | 8.1072084E 01 | -4.6520355E 02 | 1.0286981E 03 | -7.5801758E 02 | 0.615 | 0.0080 | 0.052 | 0. |
| 350 | 1.0051489E 00 | -3.7613749E 00 | 1.2405027E 01 | -1.4653177E 02 | 3.9311022E 02 | -3.1497716E 02 | 0.561 | 0.0068 | 0.046 | 0. |
| 400 | 1.0839580E 00 | -4.3652641E 00 | -5.4889070E 00 | 9.9707985E 00 | -5.3655269E 00 | 0. | 0.562 | 0.0060 | 0.045 | 0. |

protons and emitted neutrons. The first column in each table gives the incident energy E_0 , and columns two through seven give the coefficients which occur in Eq. 7. When these coefficients are used, $G(E)$ has units number per MeV per collision. Columns eight and nine give the number of emitted particles and the energy of the emitted particles divided by E_0 . These quantities were determined using the fitted functions and the equations

$$\text{No. of Emitted Particles} = \int_{E_{\text{MIN}}}^{E_{\text{MAX}}} G(E) dE \quad (8)$$

and

$$\text{Energy of Emitted Particles}/E_0 = \frac{1}{E_0} \int_{E_{\text{MIN}}}^{E_{\text{MAX}}} EG(E) dE, \quad (9)$$

where

E_{MAX} = the highest energy point considered in the fitting,

E_{MIN} = the lowest energy particle emitted in the Monte Carlo studies.

The values of E_{MAX} and E_{MIN} divided by E_0 are given in columns ten and eleven, respectively. As before, the analytic functions are to be used only between the energies E_{MIN} and E_{MAX} .

In those places in the tables where only three coefficients are given, the fits must be considered very approximate. In some cases, all of the coefficients are given to be zero. When this occurs, it means that so few particles of a given type were omitted that the Monte Carlo results were not considered statistically significant, and no attempt was made to obtain a fit. In these cases, the number of emitted particles is still given in column eight of the tables. This number, of course, is not obtained from Eq. 8 but is taken directly from the Monte Carlo results.

C. Cascade Neutron- and Proton-Emission Spectra Integrated Over All Angles

The cascade particle-emission spectra integrated over all angles can be obtained directly from the results given in section A. The spectra obtained in this manner, however, contain many more parameters than are required to obtain a reasonable fit. To avoid this, the Monte Carlo results were integrated over angles and the resulting spectra were fitted separately.

The procedure used to form the histograms from the angle-integrated Monte Carlo data and to fit the histograms was the same as described in section A.

In Figs. 8 and 9 the analytic fits are compared with the Monte Carlo histograms for cascade protons and neutrons, respectively, emitted from 400-MeV protons on aluminum.

The coefficients for all of the cases considered are given in Tables 62 through 81.* These coefficients are to be used in conjunction with the function F defined in Eq. 4. When this is done, F has the units number per MeV per collision. It is important to note that in this section F is not expressed per steradian as in section A. The quantity E_{MAX}/E_0 , given in the last column in the tables, has the same meaning as before. In the case of the angle-integrated data, however, E_{MAX} is very close to E_0 , and one may with impunity take the analytic function to be valid from E_{MIN} to E_0 .

*Only Table 66 is given here. Tables of coefficients for all of the cases considered are given in reference 7. Values of χ^2 for each of the fits are given in Appendix 2 of reference 7.

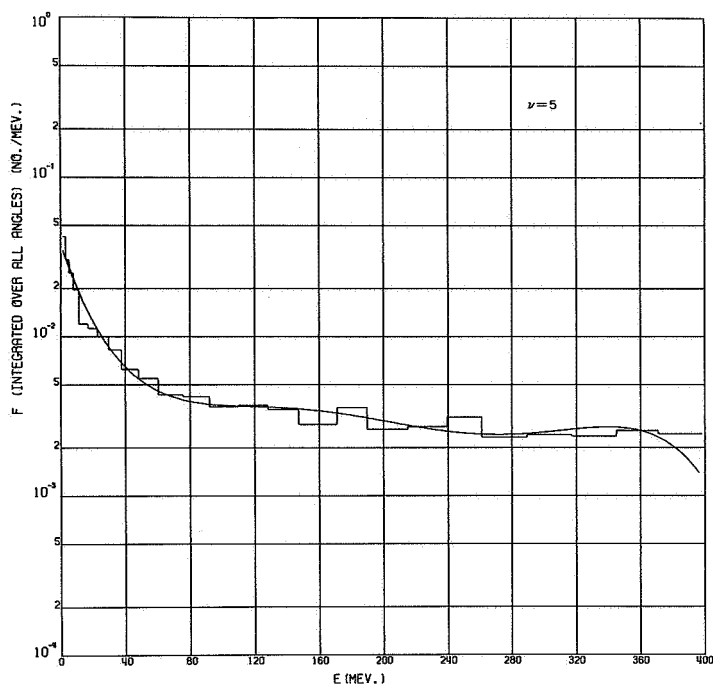


Fig. 8 Cascade protons from 400 MeV protons on aluminum

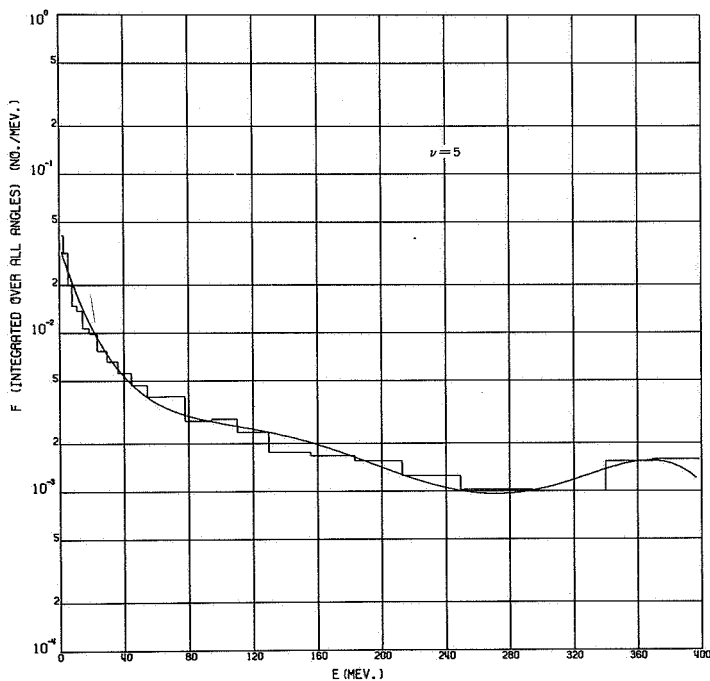


Fig. 9 Cascade neutrons from 400 MeV protons on aluminum

TABLE 66

Protons Incident on Aluminum -- $E_{\min} = 1.637 \text{ MeV}$

PROTONS EMITTED

| EO (MEV) | ANG. INT. | AC | A1 | A2 | A3 | A4 | A5 | NO. EMIT. | ENERGY EMIT./EO | EMAX /EO |
|-------------|-----------|---------------|----------------|---------------|----------------|---------------|----------------|-----------|-----------------|----------|
| 25 0 - 180 | | 1.5701524E 00 | -2.2731294E 01 | 1.0632819E 02 | -2.4756306E 02 | 2.6971120E 02 | -1.1C64C54E 02 | 0.468 | 0.1848 | 0.967 |
| 50 0 - 180 | | 1.1006405E 00 | -8.6997917E 00 | 3.3082370E 01 | -8.9465053E 01 | 1.1844078E 02 | -5.7116708E 01 | 0.726 | 0.2629 | 0.972 |
| 100 0 - 180 | | 1.9992527E 00 | -1.8626104E 01 | 8.0655761E 01 | -1.8902231E 02 | 2.1319261E 02 | -9.0184774E 01 | 1.065 | 0.3662 | 0.976 |
| 150 0 - 180 | | 2.2424504E 00 | -2.3207630E 01 | 1.1011585E 02 | -2.5689810E 02 | 2.7855399E 02 | -1.1239120E 02 | 1.263 | 0.4426 | 0.985 |
| 200 0 - 180 | | 2.4394701E 00 | -2.6780777E 01 | 1.3386653E 02 | -3.1946234E 02 | 3.4953146E 02 | -1.4118658E 02 | 1.391 | 0.4860 | 0.984 |
| 250 0 - 180 | | 2.4350781E 00 | -2.2605825E 01 | 1.0319003E 02 | -2.3803108E 02 | 2.5902389E 02 | -1.0542919E 02 | 1.530 | 0.5160 | 0.981 |
| 300 0 - 180 | | 2.5683880E 00 | -2.6023834E 01 | 1.2699013E 02 | -2.9857276E 02 | 3.2315159E 02 | -1.256C909E 02 | 1.586 | 0.5256 | 0.989 |
| 350 0 - 180 | | 2.5576099E 00 | -2.3246923E 01 | 1.0431757E 02 | -2.3180269E 02 | 2.3892895E 02 | -9.1161010E 01 | 1.678 | 0.5642 | 0.989 |
| 400 0 - 180 | | 2.7461777E 00 | -2.8681599E 01 | 1.3424366E 02 | -2.9732541E 02 | 3.0343690E 02 | -1.1511883E 02 | 1.664 | 0.5554 | 0.991 |

NEUTRONS EMITTED

| EO (MEV) | ANG. INT. | AC | A1 | A2 | A3 | A4 | A5 | NO. EMIT. | ENERGY EMIT./EO | EMAX /EO |
|-------------|-----------|---------------|----------------|---------------|----------------|----------------|----------------|-----------|-----------------|----------|
| 25 0 - 180 | | 9.1C93216E-01 | -1.3070356E 01 | 4.4623537E 01 | -9.3328805E 01 | 1.02322294E 02 | -4.4979404E 01 | 0.340 | 0.1259 | 0.962 |
| 50 0 - 180 | | 1.2493887E 00 | -9.6690089E 00 | 1.9663062E 01 | -2.7410243E 01 | 2.7864960E 01 | -1.3964418E 01 | 0.602 | 0.2019 | 0.979 |
| 100 0 - 180 | | 1.6394980E 00 | -1.4183721E 01 | 4.6672741E 01 | -9.0489986E 01 | 8.8442409E 01 | -3.3375292E 01 | 0.793 | 0.2533 | 0.973 |
| 150 0 - 180 | | 2.1467393E 00 | -2.1748714E 01 | 9.6515359E 01 | -2.3155671E 02 | 2.5997894E 02 | -1.0731072E 02 | 0.933 | 0.2694 | 0.971 |
| 200 0 - 180 | | 2.2192312E 00 | -2.2262872E 01 | 9.4302622E 01 | -2.2052400E 02 | 2.4658465E 02 | -1.0218118E 02 | 0.965 | 0.2776 | 0.984 |
| 250 0 - 180 | | 2.4183285E 00 | -2.4381478E 01 | 1.0246655E 02 | -2.2830222E 02 | 2.4022712E 02 | -9.3614579E 01 | 1.061 | 0.2959 | 0.988 |
| 300 0 - 180 | | 2.5253210E 00 | -2.7440449E 01 | 1.2521129E 02 | -2.8285324E 02 | 2.9184465E 02 | -1.1052355E 02 | 1.112 | 0.3006 | 0.987 |
| 350 0 - 180 | | 2.3642398E 00 | -2.0280829E 01 | 5.8687278E 01 | -7.5060593E 01 | 3.3746075E 01 | 0. | 1.104 | 0.3004 | 0.993 |
| 400 0 - 180 | | 2.6859617E 00 | -3.0789708E 01 | 1.4553006E 02 | -3.3627917E 02 | 3.5134779E 02 | -1.3329962E 02 | 1.151 | 0.3096 | 0.991 |

REFERENCES

1. HUGO W. BERTINI, Phys. Rev., 131, 1801 (1963); with erratum, Phys. Rev., 138, AB2 (1965).
2. HUGO W. BERTINI, "Results from Low-Energy Intranuclear-Cascade Calculations," ORNL TM-1225, Oak Ridge National Laboratory (1965).
3. HUGO W. BERTINI, HEMMA E. FRANCIS, and MIRIAM P. GUTHRIE, "Instructions for the Operation of Codes Associated with the Low-Energy Intranuclear Cascade Calculation," ORNL-3844, Oak Ridge National Laboratory (1966).
4. W. A. GIBSON et al., "Comparison of Measured Neutron and Proton Spectra with Calculated Spectra in the Energy Region Between 50 and 160 MeV," Proc. Second Symposium on Protection Against Radiations in Space, Gatlinburg, Tennessee, October 12-14, 1964, NASA SP-71, p. 337, National Aeronautics and Space Administration (1965).
5. HUGO W. BERTINI, "Energy Spectra from Inelastic Nuclear Reactions at Energies Below 450 MeV," Trans. Am. Nucl. Soc. 18, 634 (1965).
6. P. G. GUEST, Numerical Methods of Curve Fitting, Cambridge University Press, New York, 1961.
7. R. G. ALSMILLER, JR. et al., "Analytic Representation of Nonelastic Cross Sections and Particle-Emission Spectra from Nucleon-Nucleus Collisions in the Energy Range 25 to 400 MeV," ORNL-4046, Oak Ridge National Laboratory (1967).



PLANE ISOTROPIC BUILDUP FACTORS
FOR BREMSSTRAHLUNG CALCULATIONS

M. O. Burrell and J. W. Watts, Jr.

George C. Marshall Space Flight Center
Huntsville, Alabama

This report presents gamma-ray plane isotropic dose, energy flux, and energy current buildup factors for finite slabs not available until this time. Monte Carlo techniques were used to generate buildup factors for initial gamma-ray energies ranging from 0.05 MeV to 8.0 MeV with six source backings from 0 mfp to 3.0 mfp and for five source-exit plane distances from 0.5 mfp to 7.0 mfp. Differences of up to 50 percent were found in comparisons with buildup factors generated by the moments method for infinite media.

I. INTRODUCTION

Bremsstrahlung gamma-ray spectra are extremely peaked toward lower energies (below 0.5 MeV), and most of the bremsstrahlung production takes place near the entrance plane of the shield. For calculations of bremsstrahlung dose rates behind plane slab shields, available gamma-ray dose buildup factors were found to be unsatisfactory. They did not extend to the range of interest and were for infinite or semi-infinite shields. Monte Carlo methods were used to calculate the dose, energy current, and energy flux buildup factors for plane isotropic gamma-ray sources in single homogeneous slabs of aluminum, water, and lead for a variety of gamma-ray energies, slab thicknesses, and source plane positions. Emphasis was given to low energies and thin entrance-source plane distances. One may find it difficult to realize why these calculations should differ from the plane isotropic buildup factors of Goldstein [1]. However, it must be realized that Goldstein's data are for infinite media and, in most cases, were obtained using Equation (1) from point isotropic sources which were generated in a spherical rather than a slab geometry.

$$B^{Pl}(E_0, \mu |x|) = \frac{\int_{\mu|x|}^{\infty} [B^{Pt}(y)e^{-y/y}] dy}{E_1(\mu|x|)} \quad (1)$$

B^{pl} is the plane isotropic buildup factor; E is the energy; $\mu |x|$ is the source-exit plane distance in mean free paths; B^{pt} is the point buildup factor; and E is the exponential integral. For example, early calculations by Berger and Doggett [2, 3] showed that for plane monodirectional sources the infinite media calculations gave a 50 percent larger value than the finite slab case for 1.0 MeV gammas in 1 mfp ($\mu |x|$) of water. The isotropic case could then probably yield even larger differences in some cases. Figure 1 shows a comparison of Goldstein's plane isotropic buildup factors with buildup factors generated by the method described in this report.

II. METHOD

The Monte Carlo code used is a revised version of a code developed by J. F. Perkins and M. O. Burrell. The modifications to treat isotropic incidence were carried out by C. W. Hill of Lockheed Georgia Company, Marietta, Georgia. The basic geometry is shown in Figure 2.

To improve statistics, all photons were started in directions sampled systematically from a forward biased angular distribution function. Two items were incorporated in the path length probability density function used. One was an exponential transformation which stretched path lengths in the forward direction and shrank those in the backward direction. The other was path length truncation which insured that all particles stayed in the slab after each scatter.

It was given by:

$$f(r)dr = \frac{\Sigma(E)e^{-\Sigma(E)r}}{1 - e^{-\Sigma(E)Z_t \sec \theta}} dr \quad ; \quad (2)$$

$$\Sigma(E) = (1 - m \cos \theta) \mu(E) \quad (3)$$

In the above equations, E was the photon energy; Z_t was the source-exit plane distance; θ was the photon direction measured from the source plane normal; $\mu(E)$ was the mass attenuation coefficient [4]; and m was a biasing parameter between 0 and 1 (usually $\sim .9$) which determined how much the path length would be stretched. Photon path lengths were determined by random sampling from the distribution given by Equation (2). After each scatter, statistical estimation was used to calculate the probability that a photon would cross each of several boundaries established at various distances from

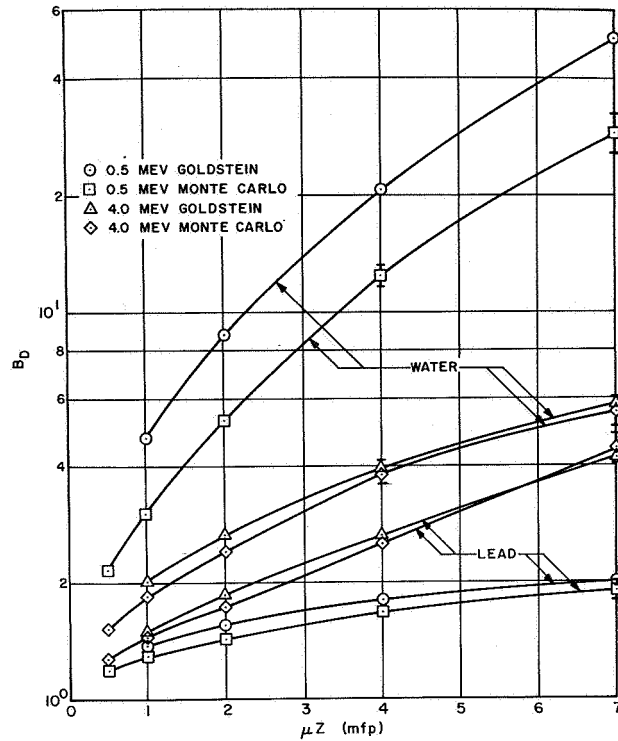


Fig. 1 A comparison of Goldstein's plane isotropic dose buildup factors with buildup factors generated by the Monte Carlo methods described

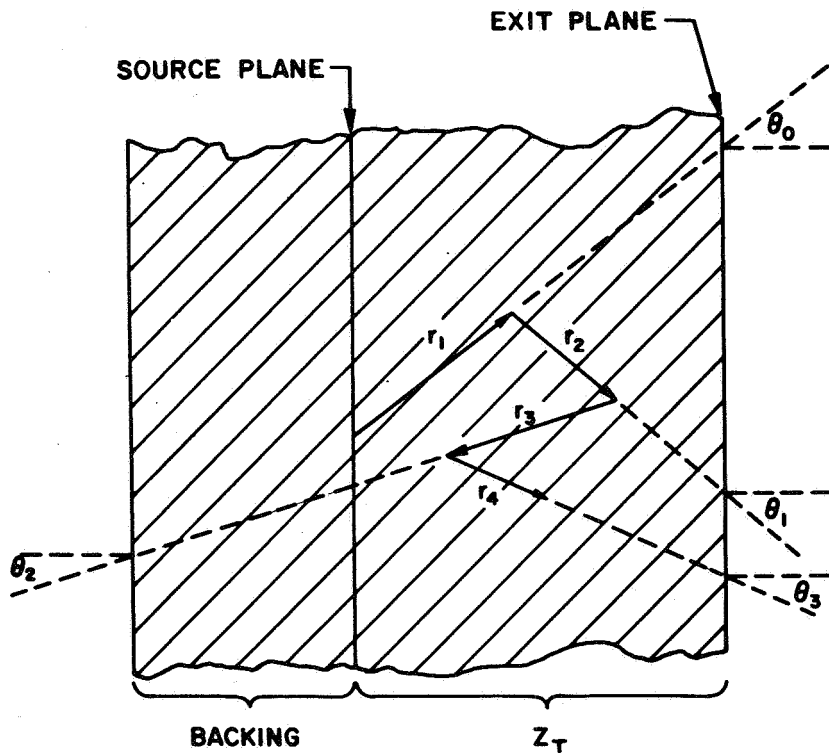


Fig. 2 The basic geometry configuration used in the calculations

the source plane so that several problems could be performed effectively and simultaneously. The transmitted scatter dose rate, energy current, and energy flux were calculated from the weighted probabilities by

$$D_s = \frac{1}{n} \sum_{k=1}^n \sum_{i=1}^{m_k} E_{ik} F(E_{ik}) W_{ik} P_{ik} \sec \theta_{ik} \quad (4)$$

$$J_s = \frac{1}{n} \sum_{k=1}^n \sum_{i=1}^{m_k} E_{ik} W_{ik} P_{ik} \quad (5)$$

$$F_s = \frac{1}{n} \sum_{k=1}^n \sum_{i=1}^{m_k} E_{ik} W_{ik} P_{ik} \sec \theta_{ik} \quad , \quad (6)$$

where E_{ik} was the energy of the k^{th} photon after the i^{th} scatter; $F(E_{ik})$ was the energy flux to dose conversion factor [1]; W_{ik} was the photon weight; P_{ik} was the probability that the photon would cross the exit plane traveling the θ_{ik} direction; m_k was the number of scatters of the K^{th} history; and N was the number of the histories. The particle histories were terminated using a Russian roulette scheme when the particle weight or energy became too small (below 0.01 MeV). The uncollided values were given by

$$D_u = \frac{E_0 F(E_0) E_1 (\mu(E_0) Z_t)}{2} \quad (7)$$

$$J_u = \frac{E_0 E_2 (\mu(E_0) Z_t)}{2} \quad (8)$$

$$F_u = \frac{E_0 E_1 (\mu(E_0) Z_t)}{2} \quad , \quad (9)$$

where E_0 was the initial energy and $E_2 (\mu(E_0) Z_t)$ is the second exponential integral. All the buildup factors were defined by the same form as the dose buildup

$$B_D = \frac{D_u + D_s}{D_u} \quad (10)$$

III. RESULTS

With careful use of biasing, reasonable statistical errors were obtained with 1000 to 4000 histories. The results of calculations performed for twelve energies ranging from 0.05 MeV to 8.0 MeV with six source backings of 0 mfp to 3.0 mfp and for five source-exit plane distances from 0.5 mfp to 7.0 mfp are shown in Table I for aluminum. Additional tables of buildup factors for lead and water are available in a NASA Technical Note (in publication) having the same title as this paper. Energy current and energy flux buildup factors for all three materials are also included. (Table II converts mean free paths to centimeters and to grams per centimeters squared.) The least reliable calculations were for water, especially the 7.0 mfp case which had estimated standard errors of about ± 10 percent about the mean for a one-sigma error band. All the other calculations were more accurate (errors ranged around 5 percent). The lead results were extremely accurate with errors of less than 1 percent over the majority of the range considered except for 7 mfp and 8 MeV where errors approached 10 percent.

IV. CONCLUSIONS

Figures 3, 4, and 5 show important results for bremsstrahlung calculations. In Figure 3, aluminum dose buildup factors are plotted as a function of energy for a slab of constant backing for various source-exit plane distances. The most striking feature is that the buildup factors begin to decrease again below about 0.2 MeV where photoelectric absorption becomes important. Thus, Goldstein's results which extend down only to 0.5 MeV cannot be extrapolated very far into the region of interest for bremsstrahlung production accurately. For lead, the photoelectric K-edge at 0.088 MeV has an interesting effect on the buildup factors for energies immediately above the edge. The dose buildup factors in Table III show a large increase between 0.08 MeV and 0.09 MeV. The buildup apparently tends to follow the same pattern as the photoelectric cross section in this region. Figure 4 shows the effect of having finite backing behind the source plane. In it, aluminum buildup factors are plotted as a function of backing for a constant source-exit plane distance and various energies. Generally, electrons incident on a slab shield deposit most of their energy near the front surface. Thus, most of the bremsstrahlung is generated there. For lower energies, the buildup factors were smaller for thin backing increasing asymptotically to a constant as semi-infinite media conditions were approached. At higher energies scattering became extremely forward in direction and backing had little effect. For higher backing and higher energies, the calculated buildup factors were in reasonable agreement with Goldstein's results.

TABLE I

Aluminum Plane Isotropic Dose Buildup Factors

BACKING= 0.00 MEAN FREE PATHS

| UZ (M.F.P.) | 0.5 | 1.0 | 2.0 | 4.0 | 7.0 |
|--------------|-------|-------|-------|--------|--------|
| ENERGY (MEV) | | | | | |
| 0.05 | 1.457 | 1.730 | 2.203 | 2.940 | 3.663 |
| 0.10 | 1.780 | 2.576 | 4.265 | 8.290 | 15.260 |
| 0.30 | 1.738 | 2.621 | 4.490 | 10.220 | 22.040 |
| 0.50 | 1.702 | 2.410 | 4.213 | 8.847 | 19.720 |
| 0.70 | 1.687 | 2.382 | 3.683 | 8.076 | 15.690 |
| 1.00 | 1.624 | 2.288 | 3.473 | 6.482 | 12.150 |
| 2.00 | 1.539 | 2.051 | 2.823 | 5.104 | 7.373 |
| 3.00 | 1.481 | 1.858 | 2.622 | 3.846 | 6.153 |
| 4.00 | 1.464 | 1.771 | 2.427 | 3.593 | 4.513 |
| 6.00 | 1.388 | 1.610 | 2.046 | 2.884 | 4.164 |
| 8.00 | 1.304 | 1.514 | 1.909 | 2.492 | 3.768 |

BACKING= 0.02 MEAN FREE PATHS

| UZ (M.F.P.) | 0.5 | 1.0 | 2.0 | 4.0 | 7.0 |
|--------------|-------|-------|-------|--------|--------|
| ENERGY (MEV) | | | | | |
| 0.05 | 1.489 | 1.757 | 2.236 | 2.956 | 3.676 |
| 0.10 | 1.834 | 2.666 | 4.417 | 8.441 | 15.360 |
| 0.30 | 1.788 | 2.663 | 4.611 | 10.330 | 22.340 |
| 0.50 | 1.742 | 2.457 | 4.275 | 8.916 | 20.000 |
| 0.70 | 1.723 | 2.423 | 3.711 | 8.150 | 16.050 |
| 1.00 | 1.649 | 2.317 | 3.503 | 6.508 | 12.160 |
| 2.00 | 1.555 | 2.064 | 2.833 | 5.108 | 7.373 |
| 3.00 | 1.491 | 1.870 | 2.628 | 3.846 | 6.153 |
| 4.00 | 1.479 | 1.775 | 2.433 | 3.593 | 4.513 |
| 6.00 | 1.396 | 1.613 | 2.048 | 2.884 | 4.164 |
| 8.00 | 1.309 | 1.516 | 1.909 | 2.492 | 3.768 |

BACKING= 0.10 MEAN FREE PATHS

| UZ (M.F.P.) | 0.5 | 1.0 | 2.0 | 4.0 | 7.0 |
|--------------|-------|-------|-------|--------|--------|
| ENERGY (MEV) | | | | | |
| 0.05 | 1.551 | 1.817 | 2.298 | 3.002 | 3.704 |
| 0.10 | 1.951 | 2.827 | 4.581 | 8.693 | 15.530 |
| 0.30 | 1.876 | 2.795 | 4.928 | 10.700 | 22.580 |
| 0.50 | 1.821 | 2.559 | 4.398 | 9.032 | 20.150 |
| 0.70 | 1.795 | 2.476 | 3.802 | 8.236 | 16.060 |
| 1.00 | 1.701 | 2.383 | 3.550 | 6.566 | 12.200 |
| 2.00 | 1.581 | 2.085 | 2.846 | 5.114 | 7.373 |
| 3.00 | 1.519 | 1.882 | 2.635 | 3.848 | 6.154 |
| 4.00 | 1.489 | 1.788 | 2.440 | 3.595 | 4.513 |
| 6.00 | 1.402 | 1.620 | 2.049 | 2.884 | 4.164 |
| 8.00 | 1.316 | 1.519 | 1.910 | 2.492 | 3.768 |

TABLE I

Aluminum Plane Isotropic Dose Buildup Factors (Concluded)

BACKING= 0.50 MEAN FREE PATHS
UZ (M.F.P.)

| | 0.5 | 1.0 | 2.0 | 4.0 | 7.0 |
|--------------|-------|-------|-------|--------|--------|
| ENERGY (MEV) | | | | | |
| 0.05 | 1.650 | 1.915 | 2.380 | 3.061 | 3.748 |
| 0.10 | 2.168 | 3.124 | 4.927 | 9.161 | 16.240 |
| 0.30 | 2.055 | 3.050 | 5.270 | 11.310 | 23.150 |
| 0.50 | 1.950 | 2.723 | 4.648 | 9.337 | 20.270 |
| 0.70 | 1.903 | 2.614 | 3.992 | 8.376 | 16.170 |
| 1.00 | 1.785 | 2.482 | 3.646 | 6.610 | 12.210 |
| 2.00 | 1.619 | 2.126 | 2.865 | 5.119 | 7.375 |
| 3.00 | 1.547 | 1.902 | 2.639 | 3.852 | 6.156 |
| 4.00 | 1.508 | 1.800 | 2.445 | 3.595 | 4.513 |
| 6.00 | 1.409 | 1.625 | 2.050 | 2.884 | 4.164 |
| 8.00 | 1.321 | 1.524 | 1.912 | 2.492 | 3.768 |

BACKING= 1.00 MEAN FREE PATHS
UZ (M.F.P.)

| | 0.5 | 1.0 | 2.0 | 4.0 | 7.0 |
|--------------|-------|-------|-------|--------|--------|
| ENERGY (MEV) | | | | | |
| 0.05 | 1.670 | 1.933 | 2.400 | 3.080 | 3.755 |
| 0.10 | 2.242 | 3.212 | 5.051 | 9.271 | 16.380 |
| 0.30 | 2.113 | 3.135 | 5.372 | 11.430 | 23.270 |
| 0.50 | 1.989 | 2.772 | 4.708 | 9.426 | 20.320 |
| 0.70 | 1.939 | 2.650 | 4.029 | 8.444 | 16.180 |
| 1.00 | 1.808 | 2.509 | 3.684 | 6.623 | 12.210 |
| 2.00 | 1.627 | 2.133 | 2.869 | 5.120 | 7.375 |
| 3.00 | 1.549 | 1.904 | 2.642 | 3.852 | 6.156 |
| 4.00 | 1.510 | 1.801 | 2.445 | 3.595 | 4.513 |
| 6.00 | 1.409 | 1.625 | 2.050 | 2.884 | 4.164 |
| 8.00 | 1.321 | 1.524 | 1.912 | 2.492 | 3.768 |

BACKING= 3.00 MEAN FREE PATHS
UZ (M.F.P.)

| | 0.5 | 1.0 | 2.0 | 4.0 | 7.0 |
|--------------|-------|-------|-------|--------|--------|
| ENERGY (MEV) | | | | | |
| 0.05 | 1.677 | 1.939 | 2.409 | 3.087 | 3.759 |
| 0.10 | 2.267 | 3.246 | 5.120 | 9.323 | 16.430 |
| 0.30 | 2.147 | 3.173 | 5.414 | 11.490 | 23.310 |
| 0.50 | 2.007 | 2.796 | 4.759 | 9.448 | 20.330 |
| 0.70 | 1.952 | 2.665 | 4.039 | 8.455 | 16.180 |
| 1.00 | 1.814 | 2.517 | 3.688 | 6.627 | 12.210 |
| 2.00 | 1.628 | 2.135 | 2.870 | 5.121 | 7.375 |
| 3.00 | 1.550 | 1.905 | 2.642 | 3.852 | 6.156 |
| 4.00 | 1.511 | 1.801 | 2.445 | 3.595 | 4.513 |
| 6.00 | 1.409 | 1.625 | 2.050 | 2.884 | 4.164 |
| 8.00 | 1.321 | 1.524 | 1.912 | 2.492 | 3.768 |

TABLE II
 Mean Free Path to Slab Thickness Conversion for Aluminum,
 Lead, and Water

| ENERGY (MeV) | Aluminum | | Lead | | Water | |
|-----------------|-----------------|-----------------------------------|-----------------|-------------------------------|-----------------|---------------|
| | 1.0 mfp (cm) | Aluminum (gm/cm ²) | 1.0 mfp (cm) | Lead (gm/cm ²) | 1.0 mfp (cm) | Water (cm) |
| 0.05 | 1.161 | 3.135 | 0.01108 | 1.256 | 4.744 | |
| 0.1 | 2.315 | 6.251 | 0.01586 | 1.799 | 5.984 | |
| 0.3 | 3.596 | 9.709 | 0.2315 | 2.625 | 8.421 | |
| 0.5 | 4.404 | 11.89 | 0.5764 | 6.536 | 10.35 | |
| 0.7 | 5.101 | 13.77 | 0.8858 | 10.04 | 11.98 | |
| 1.0 | 6.032 | 16.29 | 1.280 | 14.52 | 14.17 | |
| 2.0 | 8.573 | 23.15 | 1.955 | 22.17 | 20.27 | |
| 3.0 | 10.49 | 28.32 | 2.115 | 23.98 | 25.23 | |
| 4.0 | 11.91 | 32.16 | 2.120 | 24.04 | 29.31 | |
| 6.0 | 13.92 | 37.58 | 2.027 | 22.99 | 36.12 | |
| 8.0 | 15.24 | 41.15 | 1.917 | 21.74 | 41.22 | |

TABLE III

Dose Buildup Factors Around the Lead k-edge (0.088 MeV)
Source-Exit Plane Distance 7.0 mfp

| Backing (mfp) \ Energy (MeV) | 0.0 | 0.02 | 0.1 | 0.5 | 1.0 | 3.0 |
|------------------------------|-------|-------|-------|-------|-------|-------|
| 0.05 | 1.037 | 1.037 | 1.037 | 1.038 | 1.038 | 1.038 |
| 0.07 | 1.105 | 1.105 | 1.105 | 1.105 | 1.105 | 1.105 |
| 0.08 | 1.115 | 1.116 | 1.116 | 1.116 | 1.116 | 1.116 |
| 0.09 | 5.677 | 5.810 | 6.134 | 6.557 | 6.675 | 6.747 |
| 0.1 | 1.989 | 2.078 | 2.264 | 2.599 | 2.669 | 2.737 |
| 0.3 | 1.366 | 1.366 | 1.366 | 1.366 | 1.366 | 1.366 |

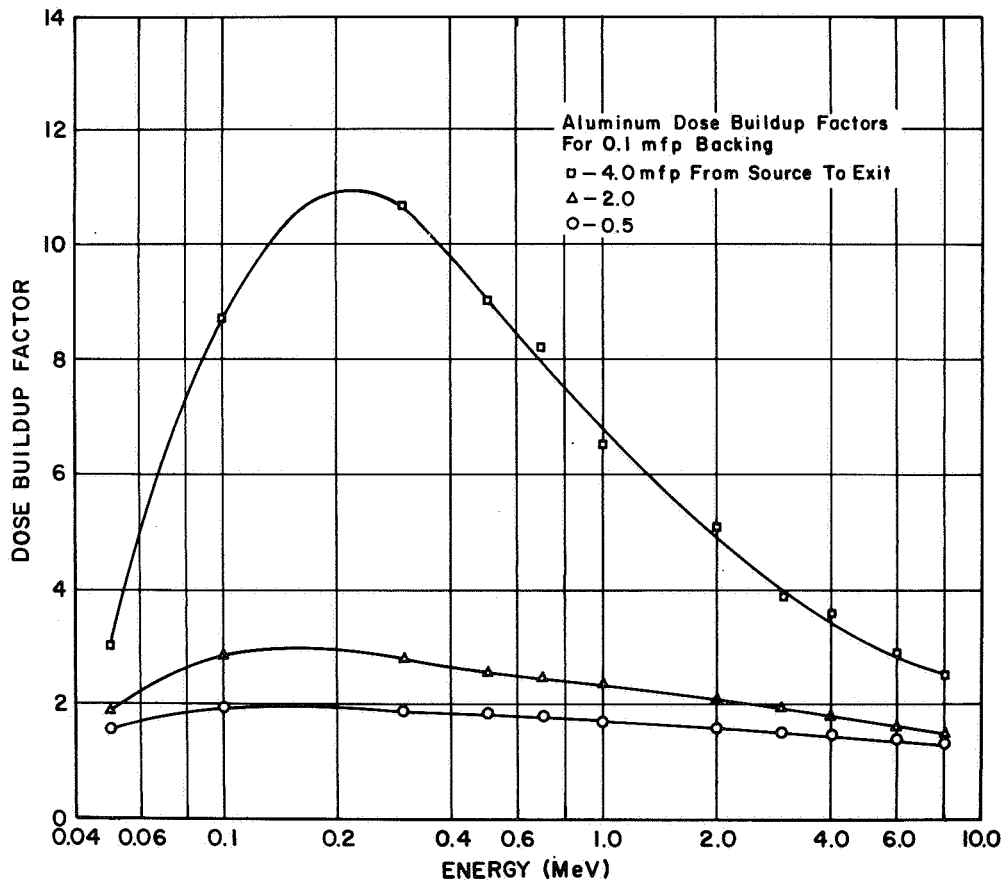


Fig. 3 Aluminum dose buildup factors as a function of energy for several source-exit plane distances

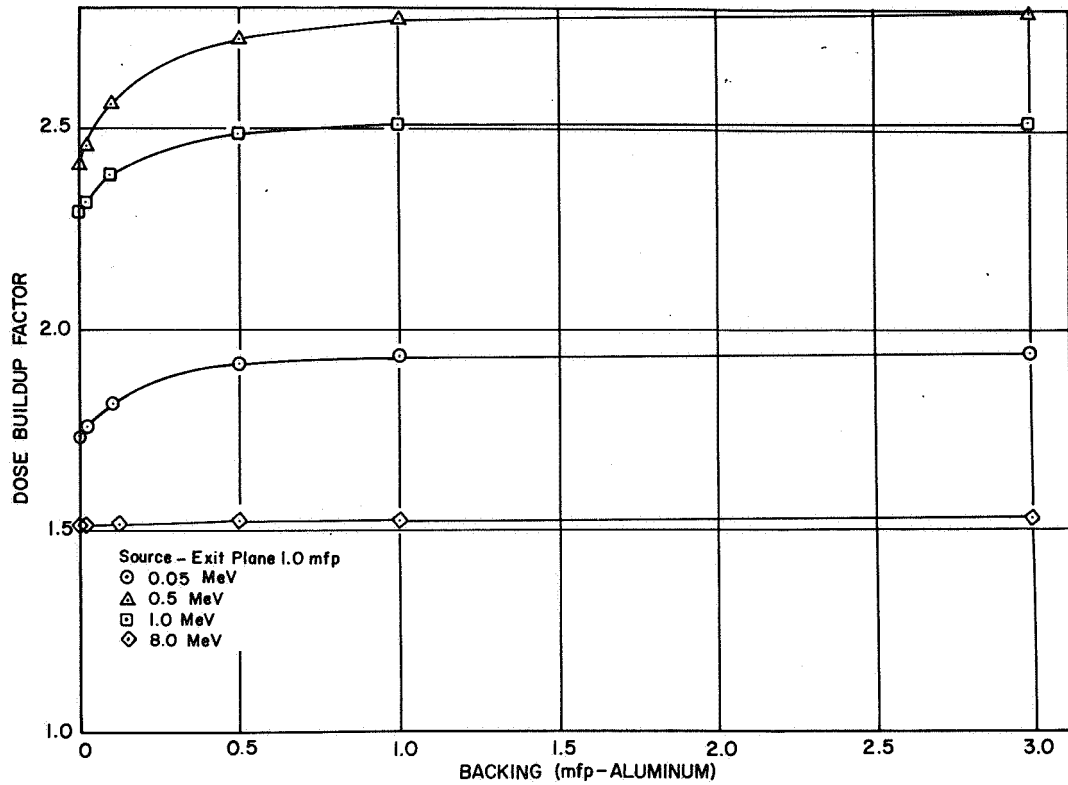


Fig. 4 Aluminum dose buildup factors as a function of backing thickness for several energies

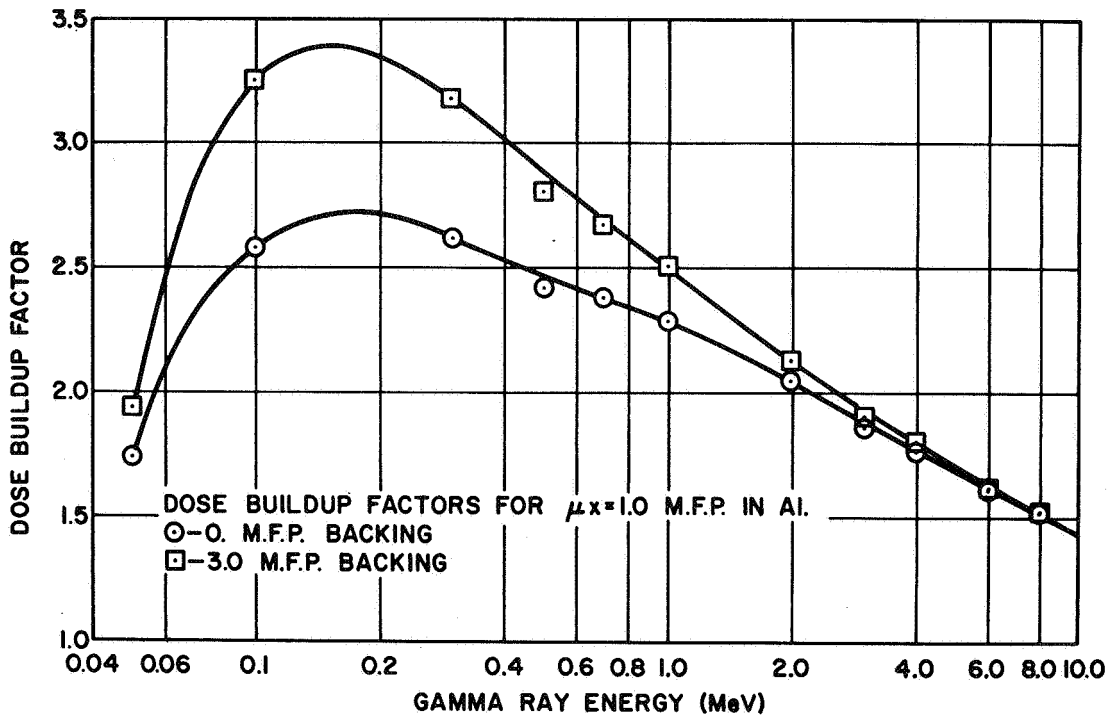


Fig. 5 Aluminum dose buildup factors as a function of energy for backings of 0. mfp and 3.0 mfp

REFERENCES

1. Goldstein, H.: *Fundamental Aspects of Reactor Shielding*. Addison-Wesley Publishing Company, Reading, Massachusetts. 1959.
2. Berger, M. J.: WASH-145, May 1953 (classified).
3. Berger, M. J. and Doggett, J.: *J. Res., National Bur. Stand., Vol. 56, No. 89C, 1956.*
4. Hubbell, J. H. and Berger, M. J.: *Photon Attenuation and Energy Transfer Coefficients, Tabulations, and Discussions*. NBS Report 8681, 1965.



N 68-26149

THE CALCULATION OF ELECTRON AND
BREMSSTRAHLUNG DOSE RATES

by

Martin O. Burrell, J. J. Wright, & John W. Watts, Jr.

Space Sciences Laboratory
The George C. Marshall Space Flight Center, Alabama

I. INTRODUCTION

The purpose of this report is to present some useful computational schemes devised by the authors for the calculation of electron penetration and the attendant bremsstrahlung in spacecraft materials. Two different methods of analysis are presented. The first uses the Monte Carlo electron energy transfer data of Berger [1]. The second is based on an analytical method devised by the writers, and additionally deals with the bremsstrahlung production and attenuation.

II. ELECTRON MONTE CARLO METHOD

The report by Berger presents the electron number and energy transmission and reflecting factors for five energies, each at five angles of incidence, for five relative thicknesses of aluminum. In the present report, electrons incident on aluminum are considered in terms of transmission and reflection factors for normal incidence with respect to electron number and energy, and isotropic incidence with respect to electron number and energy.

The isotropic transmission and reflection factors were obtained by numerical integration over plots of Berger's data. The isotropic transmission factors $T(Z)$ are expressed as:

$$T(Z) = \int_0^1 T(Z, \mu) d\mu = \int_0^{\pi/2} T(Z, \cos \theta) \sin \theta d\theta, \quad (1)$$

where Z is the depth normal to the surface, $\mu = \cos \theta$, and θ is the electron angle of incidence with the surface (Fig. 1). A point of caution should be made regarding the relative distance employed by Berger in his calculations. His transmission and reflection data are plotted against a ratio, $Z/r_0 = x$, which represents the fraction x of the average path length r_0 (that is, the average length along the zig-zag paths) traversed by the

electron in penetrating the distance Z . In the present work the extrapolated range, $R(E)$ (the maximum depth of penetration), is used in all calculations. The relationship between the average path length r_0 and the extrapolated range $R(E)$ in the present scope of work is sufficiently well approximated as:

$$r_0 = (1.33 - .019 E) R(E), \text{ in gm/cm}^2 \quad (2)$$

For aluminum, $R(E) = (0.2713E^2 + 0.0121)^{\frac{1}{2}} - 0.11$ and E is the incident electron energy in MeV [2].

At this point it is appropriate to define exactly what is meant by Berger's transmission factors. The terms $T_N(Z)$ and $T_E(Z)$ are used to denote number- and energy-transmission factors, respectively, for a shield slab of thickness Z :

$$T_N(Z, \theta) = \frac{\text{number of electrons transmitted at } Z}{\text{number of electrons incident on shield at angle } \theta} \quad (3)$$

$$T_E(Z, \theta) = \frac{\text{energy transmitted at } Z}{\text{energy incident on shield at angle } \theta} \quad (4)$$

The number- and energy-reflection factors $B_N(Z, \theta)$ and $B_E(Z, \theta)$, respectively, are similarly defined. Because particles are conserved, it follows that particles either (1) penetrate the shield, (2) are scattered back out of the slab, or (3) are absorbed between the slab surface and slab depth Z . This is represented by the following equations which are valid for number and energy current:

$$1 = T_N(Z, \theta) + B_N(Z, \theta) + \int_0^Z n(Z', \theta) dZ' \quad (5)$$

$$1 = T_E(Z, \theta) + B_E(Z, \theta) + \int_0^Z p(Z', \theta) dZ', \quad (6)$$

where $n(Z', \theta) dZ'$ and $p(Z', \theta) dZ'$ represent, respectively, the probability of electron number and energy absorption in the interval Z' to $Z' + dZ'$, and the integral of these quantities are the absorption factors to depth Z . The values of $T_N(Z, \theta)$, $T_E(Z, \theta)$, $B_N(Z, \theta)$, and $B_E(Z, \theta)$ are given by Berger. The probability density functions $n(Z', \theta)$ and $p(Z', \theta)$ for number and energy absorption are needed for the present work. According to Berger the reflection factors $B_N(Z, \theta)$ and $B_E(Z, \theta)$ become constant when the relative penetration $Z/r_0 \geq 0.3$. The writers have additionally conjectured that the transmission factors $T_N(Z, \theta)$ and $T_E(Z, \theta)$ approach one as Z approaches zero.

A convenient constancy occurred when the sum of the reflection factors and transmission factors were plotted against $x = Z/r_0$. These

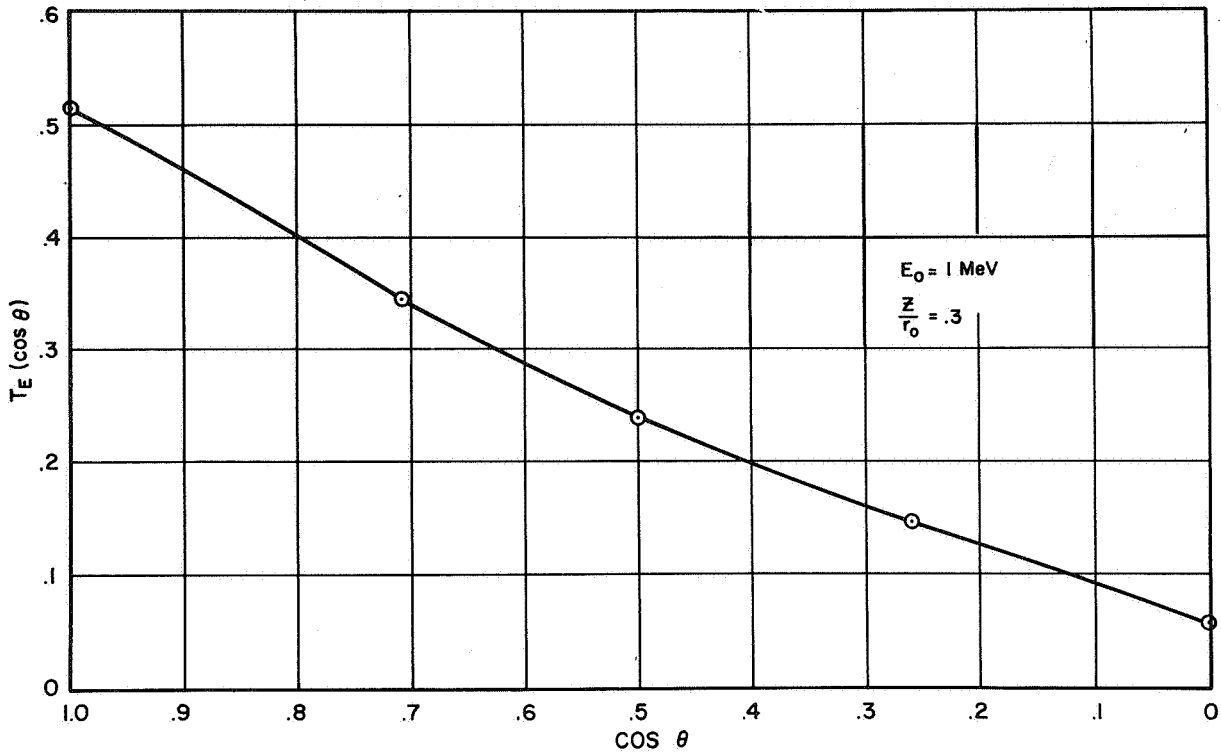


Fig. 1 Energy transmission factors as a function of electron angle of incidence

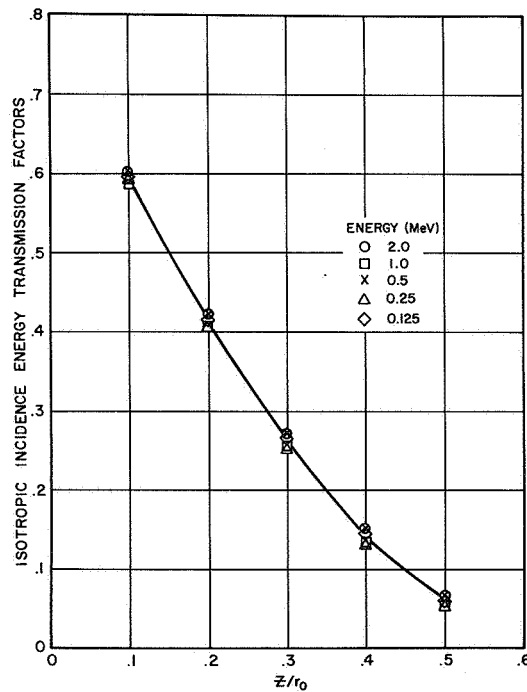


Fig. 2 Isotropic energy transmission factors versus relative depth in aluminum for different incident energies of electrons

plots, especially for isotropic incidence, showed little change with variation in electron energy (Fig. 2). These observations lead one to seek an empirical curve to describe the electron absorption factors. The following equations are expressions for curves obtained by fitting Berger's data for the four cases of interest.

I. Normal Incidence

$$\begin{aligned} \int_0^x p(x', 0^\circ) dx' &= 1 - [T_E(x, 0^\circ) + B_E(x, 0^\circ)] \\ &= 0.95 [1 - \exp(-.653x - 2.40x^2 - 6.89x^3)] \end{aligned} \quad (7)$$

$$\begin{aligned} \int_0^x n(x', 0^\circ) dx' &= 1 - [T_N(x, 0^\circ) + B_N(x, 0^\circ)] \\ &= 0.912 [1 - \exp(-.0512x + 1.128x^2 - 9.38x^3)], \end{aligned} \quad (8)$$

II. Isotropic Incidence

$$\begin{aligned} \int_0^{\pi/2} \int_0^x p(x', \theta) dx' \sin \theta d\theta &= 1 - [T_E(x) + B_E(x)] \\ &= 0.72 [1 - \exp(-2.47x + .752x^2 - 11.38x^3)] \end{aligned} \quad (9)$$

$$\begin{aligned} \int_0^{\pi/2} \int_0^x n(x', \theta) dx' \sin \theta d\theta &= 1 - [T_N(Z) + B_N(x)] \\ &= 0.63 [1 - \exp(-.152x + .479x^2 - 11.84x^3)], \end{aligned} \quad (10)$$

where $x = Z/r_0$.

With the above relationships at our disposal we see that to obtain the probability density function for electron number $n(Z, \theta)$ and energy absorption $p(Z, \theta)$ we must differentiate the above equations with respect to Z . But in order to obtain the derivatives of the above equations with respect to Z it is necessary to make the change of variables denoted by:

$$x = Z/r_0 \quad (11)$$

and

$$dx = \frac{dZ}{r_0}.$$

Thus we obtain the equations for $p(Z, 0^\circ)$, $n(Z, 0^\circ)$, $p(Z)$, and $n(Z)$ by making the proper change of variables and differentiating the above equations with respect to Z . The following results are obtained:

III. Normal Incidence:

$$\begin{aligned} p(Z, 0^\circ) &= \frac{1}{r_0} \left[0.62 + 4.56 \left(\frac{Z}{r_0} \right) + 19.64 \left(\frac{Z}{r_0} \right)^2 \right] \\ &\times \exp \left[-.653 \left(\frac{Z}{r_0} \right) - 2.40 \left(\frac{Z}{r_0} \right)^2 - 6.89 \left(\frac{Z}{r_0} \right)^3 \right] \end{aligned} \quad (12)$$

$$n(Z, 0^\circ) = \frac{1}{r_0} \left[0.467 - 2.057 \left(\frac{Z}{r_0} \right) + 25.66 \left(\frac{Z}{r_0} \right)^2 \right] \\ \times \exp \left[-.0512 \left(\frac{Z}{r_0} \right) + 1.128 \left(\frac{Z}{r_0} \right)^2 - 9.38 \left(\frac{Z}{r_0} \right)^3 \right], \quad (13)$$

IV. Isotropic Incidence

$$p(Z) = \frac{1}{r_0} \left[1.78 - 1.083 \left(\frac{Z}{r_0} \right) + 24.58 \left(\frac{Z}{r_0} \right)^2 \right] \\ \times \exp \left[-2.47 \left(\frac{Z}{r_0} \right) + .752 \left(\frac{Z}{r_0} \right)^2 - 11.38 \left(\frac{Z}{r_0} \right)^3 \right] \quad (14)$$

$$n(Z) = \frac{1}{r_0} \left[.0958 - .604 \left(\frac{Z}{r_0} \right) + 22.38 \left(\frac{Z}{r_0} \right)^2 \right] \\ \times \exp \left[-.152 \left(\frac{Z}{r_0} \right) + .479 \left(\frac{Z}{r_0} \right)^2 - 11.84 \left(\frac{Z}{r_0} \right)^3 \right], \quad (15)$$

where the dependence of the electron path length r_0 on the incident electron energy E for aluminum is given through the relationship

$$r_0 = (1.33 - .019 E) (\sqrt{.2713E^2 + .0121} - .11). \quad (16)$$

The method of employing the above functions to find the number deposition $N(Z)$ and energy deposition $D(Z)$ (dose rates) of a given differential energy spectrum incident isotropically on a shield is as follows:

$$N(Z) = K \int_{E_{\min}}^{10} \phi(E)n(Z)dE, \quad \text{in } \frac{\text{electrons}}{\text{gm} - \text{sec}} \quad (17)$$

$$D(Z) = K \int_{E_{\min}}^{10} E\phi(E)p(Z)dE, \quad \text{in MeV/gm} - \text{sec}, \quad (18)$$

where K is the constant for conversion to desired units of electron dose rates, $\phi(E)$ has the dimensions of electrons/MeV-cm²-sec, $E_{\min} = 1.92 \times (Z^2 + .22 Z)^{\frac{1}{2}}$ for aluminum, and Z is in units of gm/cm².

An example of a plot obtained through the use of equation 18 is given in Figure 3.

III. ANALYTIC METHOD AND BREMSSTRAHLUNG

The electron dose method given above does not provide a convenient way for obtaining the bremsstrahlung production; consequently, a completely different method is necessary. First we make the assumption that a straight-ahead approximation for electrons is reasonable if one uses a range formula based on the so-called extrapolated range in a

slab. The range formula chosen is:

$$R(E) = \sqrt{\frac{E^2}{a^2} + b^2} - b \quad (19)$$

In aluminum $a = 1.92$ and $b = 0.11$ for $E > 0.05$ MeV. Next we assume that an isotropic flux of electrons is incident on the shield and the incident differential electron energy spectrum at the shield is given by the relation:

$$\phi_o(E, \Omega) dE d\Omega = \frac{2\pi \phi_o(E, \mu) dE d\mu}{4\pi} \frac{\text{electrons}}{\text{cm}^2\text{-MeV-sec}} \quad (20)$$

where $\mu = \cos \theta$.

Following the methods described on pages 2-4 of reference 3, we infer that at a depth Z in the shield the incident electron differential spectrum has been severely modified; it is given by the expression:

$$\phi_Z(E^*, \mu) dE^* d\mu = \frac{1}{2} \phi_o[g(E^*), \mu] \frac{dg(E^*)}{dE^*} dE^* d\mu \quad (21)$$

where E^* is the electron energy at depth Z .

$$E = g(E^*) = a \left[\left(\frac{Z}{\mu} + t \right)^2 - b^2 \right]^{\frac{1}{2}},$$

where $t = \sqrt{\left(\frac{E^*}{a} \right)^2 + b^2}$

and $\frac{dg(E^*)}{dE^*} = \frac{E^* \left(\frac{Z}{\mu} + t \right)}{a t \left[\left(\frac{Z}{\mu} + t \right)^2 - b^2 \right]^{\frac{1}{2}}}$

Therefore the differential spectrum at depth Z is expressed as:

$$\begin{aligned} \phi_Z(E^*, \mu) dE^* d\mu \\ = \frac{1}{2} \phi_o \left[a \sqrt{\left(\frac{Z}{\mu} + t \right)^2 - b^2}, \mu \right] \frac{E^* \left(\frac{Z}{\mu} + t \right) dE^* d\mu}{a t \left[\left(\frac{Z}{\mu} + t \right)^2 - b^2 \right]^{\frac{1}{2}}} \quad (22) \end{aligned}$$

From equation 22 the electron dose at depth Z can be calculated as follows:

$$D(Z) = \frac{K}{2} \int_0^1 \int_0^{E^*_{\max}} S(E^*) \phi_Z(E^*, \mu) dE^* d\mu \quad (23)$$

where $E^*_{\max} = a \left(\left[\left(\frac{E_{\max}}{a^2} + b^2 \right)^{\frac{1}{2}} - \frac{Z}{\mu} \right] - b \right)^{\frac{1}{2}}$, K is the dose conversion factor, and $S(E^*)$ is the electron stopping power at depth Z in the

shield. The stopping power may be defined in terms of range formula equation 19 as:

$$S(E^*) = \int_0^{E^*} \frac{dE'}{R(E')} = \frac{a_0^2 t}{E^*},$$

where
$$R(E') = \sqrt{\left(\frac{E'}{a_0}\right)^2 + b_0^2} - b_0$$

and
$$t = \left[\left(\frac{E^*}{a_0}\right)^2 + b_0^2 \right]^{\frac{1}{2}}.$$

The zero subscript of the coefficients a and b indicate that these values may be changed if the electrons are stopped in a different material than the shield (for example, tissue). If one wishes to estimate the dose at the center of a spherical shell, it is approximately a factor of two higher than that of a slab having a thickness equal to the shell.

It follows from equation 23 that if one wishes to assume that electrons are incident normal to the shield surface, then $\mu \equiv 1$ and the integration becomes simply

$$D(Z) = K \int_0^{E^* \max} S(E^*) \phi_Z(E^*) dE^*. \quad (24)$$

Also one sees that this formulation provides the correct answer at the center of a spherical shell if the incident spectrum is treated as the flux integrated over 4π space. However, it is believed by the writers that this formulation will give an overestimation of the dose rate since the straight-ahead assumption for electrons is not truly valid. Equation 23 is believed to be more defensible, however, because of the increased attenuation represented by the slant thicknesses of the isotropic integration in a slab geometry. For a comparison of results of solutions of equations 23 and 18, see Figure 3. It should be noted that equation 18 gives a higher dose rate for thin shields whereas equation 23 gives a higher dose rate above approximately 1.5 gm/cm^2 . This may be in part due to the extrapolation of the Berger data to higher energies than presented in reference 1. However, the agreement is rather good considering the completely different assumptions made in the two calculations.

The bremsstrahlung generated in the shield at a given depth depends on the electron differential energy spectrum at the depth. If the radiation is isotropically incident on the shield, it seems reasonable to assume that the bremsstrahlung source can be treated as plane and isotropic at a given depth.

The bremsstrahlung source term is given by the expression

$$\begin{aligned}
 S(E_\gamma, Z)dZ &= \frac{dZ}{2} \int_0^{E_\gamma^*} \int_0^{\max \mu=1} E_\gamma \frac{f(E_\gamma, E^*)}{Z_N^2} \phi_Z(E^*, \mu) d\mu dE^* \\
 &\text{in } \frac{\text{photons}}{\text{cm}^2}, \quad (25)
 \end{aligned}$$

where dZ (shield increment) is in units of gm/cm^2 , Z_N is the atomic number of the shield material, and $f(E_\gamma, E^*)$ photons $\text{cm}^2/\text{MeV-gm}$ is the differential bremsstrahlung spectrum for electrons of energy E^* . This function is derived from the Born approximation cross section, $d\sigma_k$, given in reference 4 as formula 3BN. This formula is multiplied by a correction factor $C(E^*)$, also shown in the reference (Figure 23, p. 948).

Thus

$$f(E_\gamma, E^*) = C(E^*) 10^{-24} d\sigma_k \frac{N_0}{A} \text{ in } \frac{\text{photons cm}^2}{\text{MeV-gm electron}}, \quad (26)$$

where E^* is the electron kinetic energy in MeV, N_0 is Avagadro's number, and A is the atomic weight of the shield material.

Using the above source term and referring to Figure 4, we can write the bremsstrahlung dose rate as follows:

$$\begin{aligned}
 D_\gamma(Z_T) &= \frac{1}{2} \int_0^{E_\gamma^* \max} \int_0^{Z \max} \int_0^\infty S(E_\gamma, Z) F(E_\gamma) B(E_\gamma, Z, Z') \\
 &\times \frac{r e^{-\mu(E_\gamma) \sqrt{Z'^2 + r^2}}}{r^2 + Z'^2} dr dZ' dE_\gamma, \quad (27)
 \end{aligned}$$

where $Z \max$ is the maximum depth of electron penetration, $Z + Z' = Z_T$, (total shield thickness); $Z \leq Z \max$; $\mu(E_\gamma)$ is the gamma ray absorption coefficient; and $F(E_\gamma)$ is the energy flux to dose conversion factor.

The term $B(E_\gamma, Z, Z')$ is a plane isotropic buildup factor for gamma rays of energy E_γ at a depth Z in a shield having a distance of Z' to the detector. These buildup factors are tabulated in reference 5. (They were generated with a Monte Carlo multilayer slab code described in this reference.) Equation 27 may be simplified as follows:

$$\int_{r=0}^\infty \frac{r e^{-\mu(E_\gamma) \sqrt{r^2 + Z'^2}}}{r^2 + Z'^2} dr = E_1 [\mu(E_\gamma), Z'] = \int_{\mu Z'}^\infty \frac{e^{-y}}{y} dy. \quad (28)$$

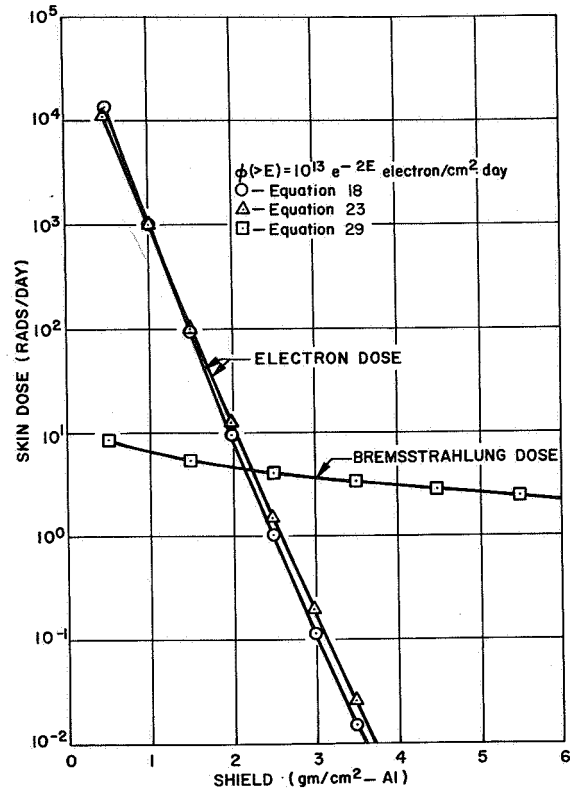


Fig. 3 Comparison of electron dose rate from two different methods and the Bremsstrahlung dose rate

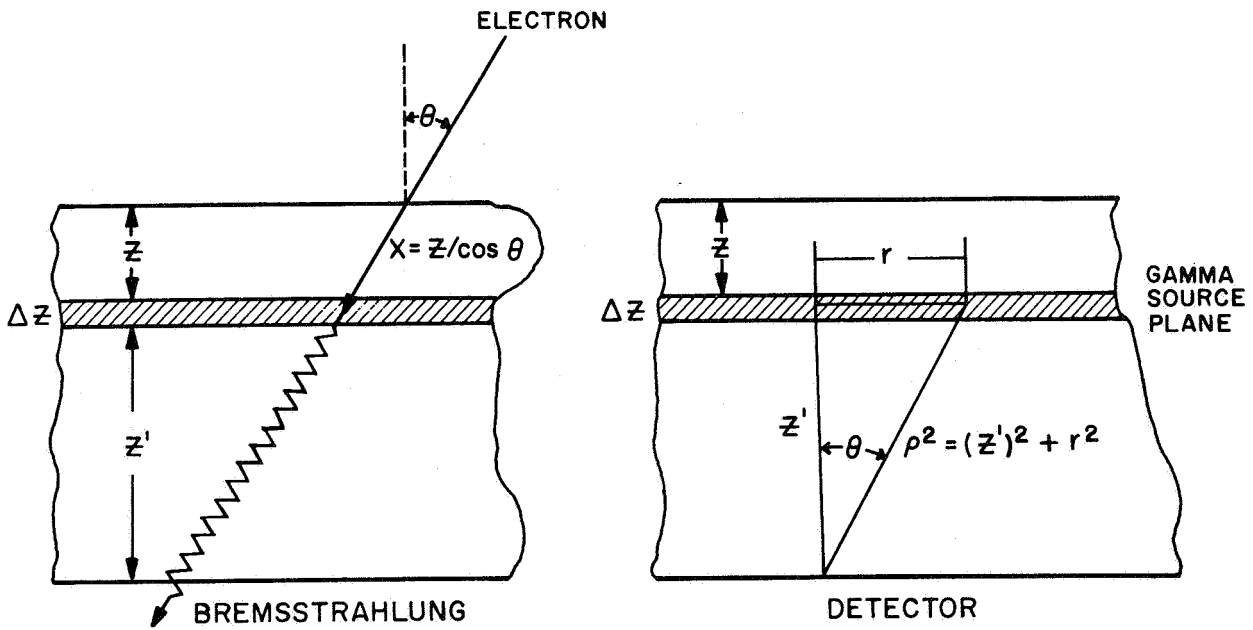


Fig. 4 Bremsstrahlung source plane from incident electrons that reach depth Z in slab

Therefore the bremsstrahlung dose rate equation is simplified to:

$$D_{\gamma}(E_T) = \frac{1}{2} \int_0^{Z_{\max}} \int_0^{E_{\gamma \max}} F(E_{\gamma}) S(E_{\gamma}, Z) \times B(E_{\gamma}, Z, Z') E_1[\mu(E_{\gamma})Z'] dE_{\gamma} dZ' . \quad (29)$$

See Figure 3 for an example of results. The one-half factor in this last equation may seem suspect but it follows from the assumption of an isotropic source term for the gamma rays. However, it seems that if one uses the straight-ahead approximation, all the photons would be directed into the forward hemisphere because the bremsstrahlung has a rather forward scattering distribution. The authors believe that if the straight-ahead assumption is used indiscriminately, the gamma ray dose will be high. For example, based on the Monte Carlo results of Berger for isotropic incidence, the electron energy current reflected from an aluminum shield is approximately 28% of the incident electron energy current. In addition, since the electrons experience many collisions inside the shield, their directions become quite random. Hence, it seems logical to assume an isotropic distribution of generated bremsstrahlung as a first approximation to the probable angular distribution.

REFERENCES

1. MARTIN J. BERGER, "Transmission and Reflection of Electrons by Aluminum Foils," Technical Note 187, Natl. Bur. Std. (April 1, 1963).
2. B. T. PRICE, C. C. HORTON, and K. T. SPINNEY, Radiation Shielding, Pergamon Press, New York (1957).
3. M. O. BURRELL, "The Calculation of Proton Penetration and Dose Rates," NASA TM X-53063 (Aug. 17, 1964).
4. H. W. KOCH and J. W. MOTZ, "Bremsstrahlung Cross-Section Formulas and Related Data," Rev. Mod. Phys., Vol. 31, No. 4, pp. 920-955 (Oct. 1959).
5. J. W. WATTS, M. O. BURRELL, and C. W. HILL, "Plane Isotropic Buildup Factors for Bremsstrahlung Calculations," Presented at the 13th Annual Meeting of Am. Nucl. Soc., San Diego, California (June 11-15, 1967).

N 68-26150

EVALUATION OF GAMMA PROBE SHIELDING VERIFICATION
FOR THE GEMINI AND APOLLO VEHICLES

By Alva C. Hardy and Joseph W. Snyder
Space Physics Division
NASA Manned Spacecraft Center
Houston, Texas

A gamma-ray probe technique for verification of analytical shielding descriptions has been utilized by the NASA Manned Spacecraft Center for shielding verification tests of the Gemini and Apollo space vehicles. The gamma probe determines, through gamma-ray attenuation measurements, the areal electron density between the source and detectors for many positions over the vehicle surface. Since for thin shields (less than a radiation length) the penetration of charged particles is largely determined by interaction with the electrons of the shielding material, the distribution of the areal electron density about a point defines the shielding of that point to a good approximation.

Radiation-dose comparison between the gamma probe data and analytical descriptions of the Gemini and Apollo vehicles indicates that the analytical descriptions produce conservatively high dose estimates.

Presented at the
Thirteenth Annual American Nuclear Society Meeting
San Diego, California
June 12, 1967

INTRODUCTION

Evaluation of the potential hazards to manned space flight from radiation encountered in space requires the determination of the doses expected to be received by the crew and equipment within the spacecraft. To determine the dose, analyses and/or measurements are required of the radiation transported through the structure, equipment, and biological tissue within the spacecraft. For vehicles of current design, most of the radiation protection is provided by the shielding offered by the vehicle structure and internal equipment, resulting in highly complex shielding configurations. The accuracy and reliability of radiation-dose and shielding computations for evaluating the radiation hazard to manned space flight are highly dependent upon the shielding description of the spacecraft.

Compilation of analytical descriptions of shielding geometries requires detailed analysis of the many drawings which describe the spacecraft and all its components. The volume of the drawings and the continual changes to the drawings during design restrict the amount of

detail which can practically be incorporated in the shielding description. Most small components are homogenized or neglected. Assessment of the reliability of such an analytical description is impossible without some type of shielding verification measurement.

The best verification of an analytical shielding description comes with inflight measurements of the radiation environment both inside and outside the spacecraft. However, with the gamma probe technique, it is possible to obtain a measurement of the inherent shielding provided by a space vehicle before it is flown, allowing the determination of the reliability of the analytical description by locating hotspots, erroneous shielding, and other errors which may have been overlooked.

GAMMA PROBE TECHNIQUE

The basis of the gamma-ray shield verification method is that the primary attenuating constituent in the passage of protons and gammas through matter is electrons. In fact, the attenuation of any type of ionizing radiation can be related with reasonable accuracy to the areal electron density of the stopping material. By making gamma transmission measurements along many paths from the outside of the spacecraft to points of interest inside, the electron density along these paths can be determined, thus allowing the computation or verification of the spacecraft shielding geometry (Ref. 1).

For the lightweight materials used in space vehicles ($Z \leq 30$) and for the gamma source used in these measurements, the Compton scattering

process accounts for more than 98 percent of the gamma cross section (Ref. 1). In the Compton process, the gamma photon scatters from an atomic electron and loses an amount of energy related to the deflection. Therefore, by measuring the number of transmitted gammas which have not been deflected by the Compton process, the areal electron density of the shield may be obtained from the relationship

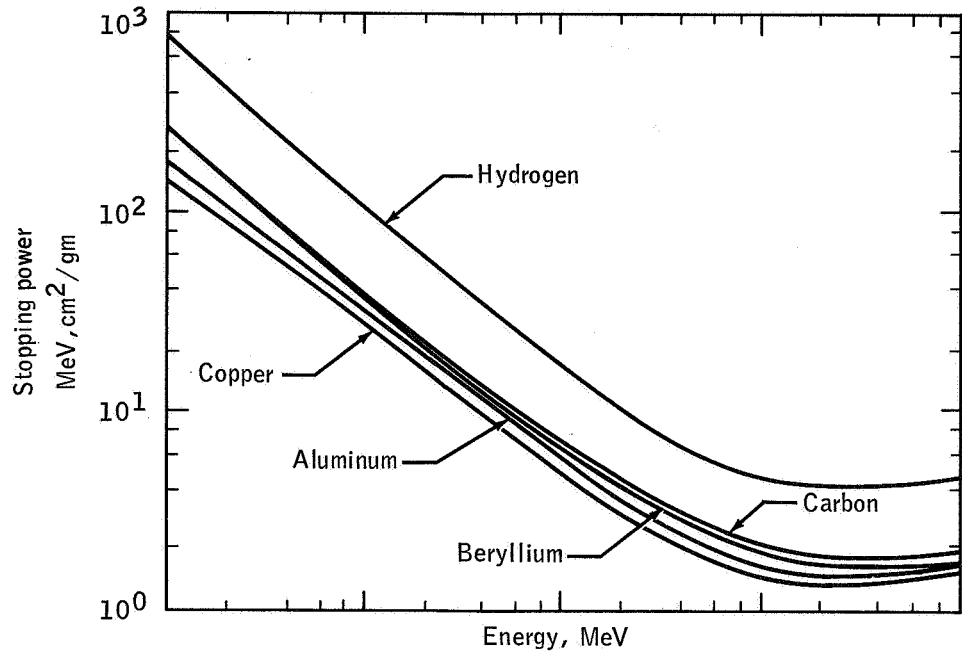
$$\int_0^t N_e dt = \frac{1}{\mu_e} \ln \left| \frac{I_0}{I} \right|$$

where t is shield thickness, N_e is electron density of the shield, μ_e is the Compton cross section per electron, I_0 is the number of incident gammas, and I is the number transmitted through the shield without scattering.

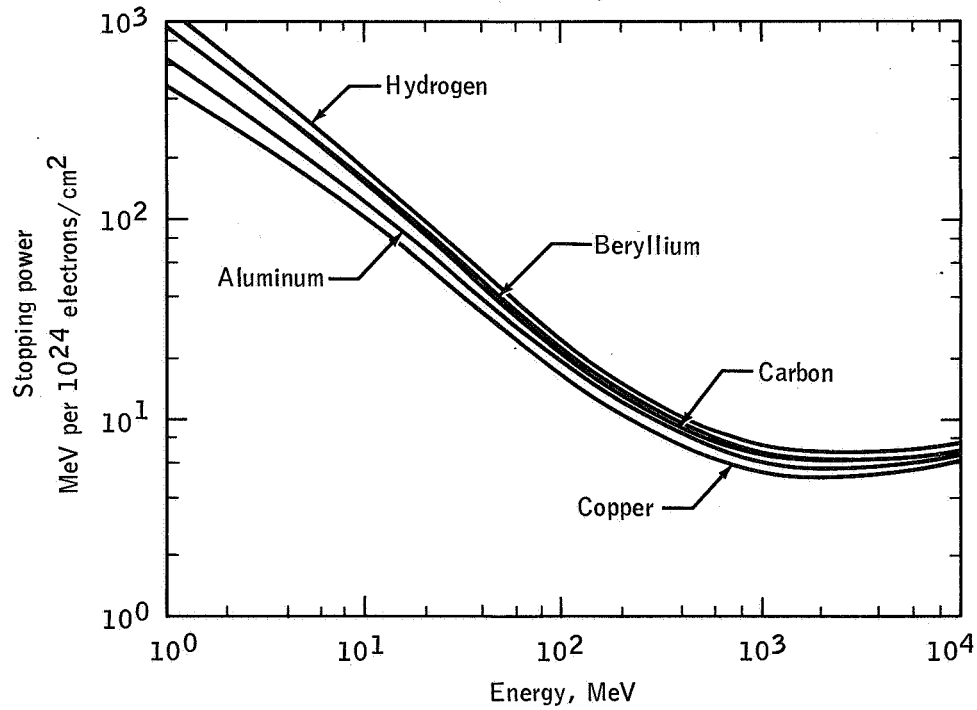
Figure 1 (Ref. 2) shows the stopping power of various materials for protons in terms of electron density and also mass density for comparison purposes. These curves show that electron density is a more uniform measure of proton attenuation and indicate the relatively small amount of error introduced by assuming an effective Compton cross section or proton stopping power.

GAMMA PROBE HARDWARE

The hardware for the gamma probe consists of several subsystems which will be described in turn.



(a) Mass density.



(b) Electron density.

Fig. 1. Proton stopping power.

The scan system places the radiation source at known positions about the spacecraft. It has a monorail track which can be leveled and made circular very accurately. Upon this track is a tripod which can be rotated by motor-driven gears. The source holder is mounted on one leg of the tripod and can be moved parallel and perpendicular to the leg by means of motor-driven gears. The gears are connected to a visual readout of the position of the source (Fig. 2).

The detector system has six 2- by 2-in. NaI(Tl) scintillators with 6-percent full width at half maximum resolution for Zn^{65} gamma-rays. Each detector has an independent system of amplifiers and scalers and may be positioned inside the spacecraft at will.

The data-readout system outputs the three coordinates of the source, the count time, and the counts from each of the detectors on punched cards and by typewriter simultaneously.

The control system controls the sequencing of moving the source, turning the scalers on and off, and starting the data readout. The control system can be operated either manually or automatically.

MEASUREMENTS

The Gemini III capsule was probed with a 4- by 4-in. grid in July 1966 using a Zn^{65} gamma source. The Gemini spacecraft and gamma probe apparatus are shown in Fig. 2.

Several difficulties were encountered because the gamma probe was designed for an Apollo spacecraft. Also, the spacecraft was completely

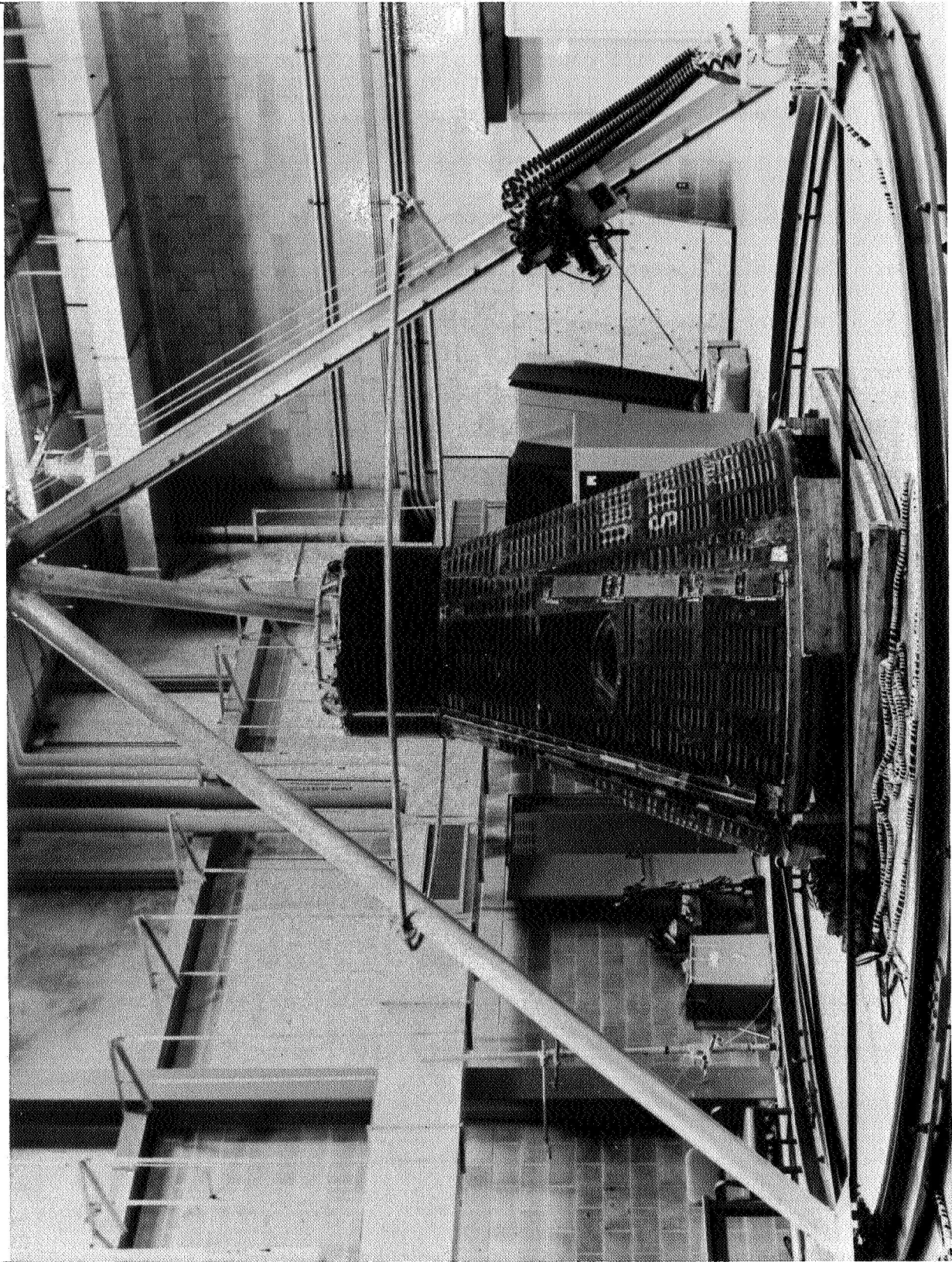


Fig. 2. The Gemini spacecraft and gamma probe apparatus.

stripped of instruments and couches, and the ablative material, heat shield, and parachute had been spent on reentry.

An Apollo Block I command module (ground-test Spacecraft 008) was probed with a 6- by 6-in. grid in December 1966 using a Zn^{65} gamma source. The Apollo spacecraft and gamma probe apparatus are shown in Fig. 3. The scan time for the Apollo spacecraft was approximately 15 hours.

The vehicle was completely equipped except for the crew couches and the hatch. An average thickness of 2.4 gm/cm^2 was assumed over the hatch area for data-reduction purposes. The effect of the missing couches is insignificant. All detectors were located above the couch positions; therefore, the couches would not have been between the source and detectors at most of the data locations. Detector arrangement is shown in Fig. 4.

To insure consistency in data quality, checks were run between each data batch (source rotation around the vehicle at a fixed height), and corrections were made for electronic drift. The data were monitored carefully so that no data were lost because of faulty printout, swamping of detectors, and so forth.

Before reducing the Apollo gamma probe data, a test with known thicknesses of aluminum was run to determine the short-term electronic drift and to check the conversion factors used in the data-reduction code. Both I and I_0 runs were made within a half hour of each other under identical (except for the aluminum shield) conditions without

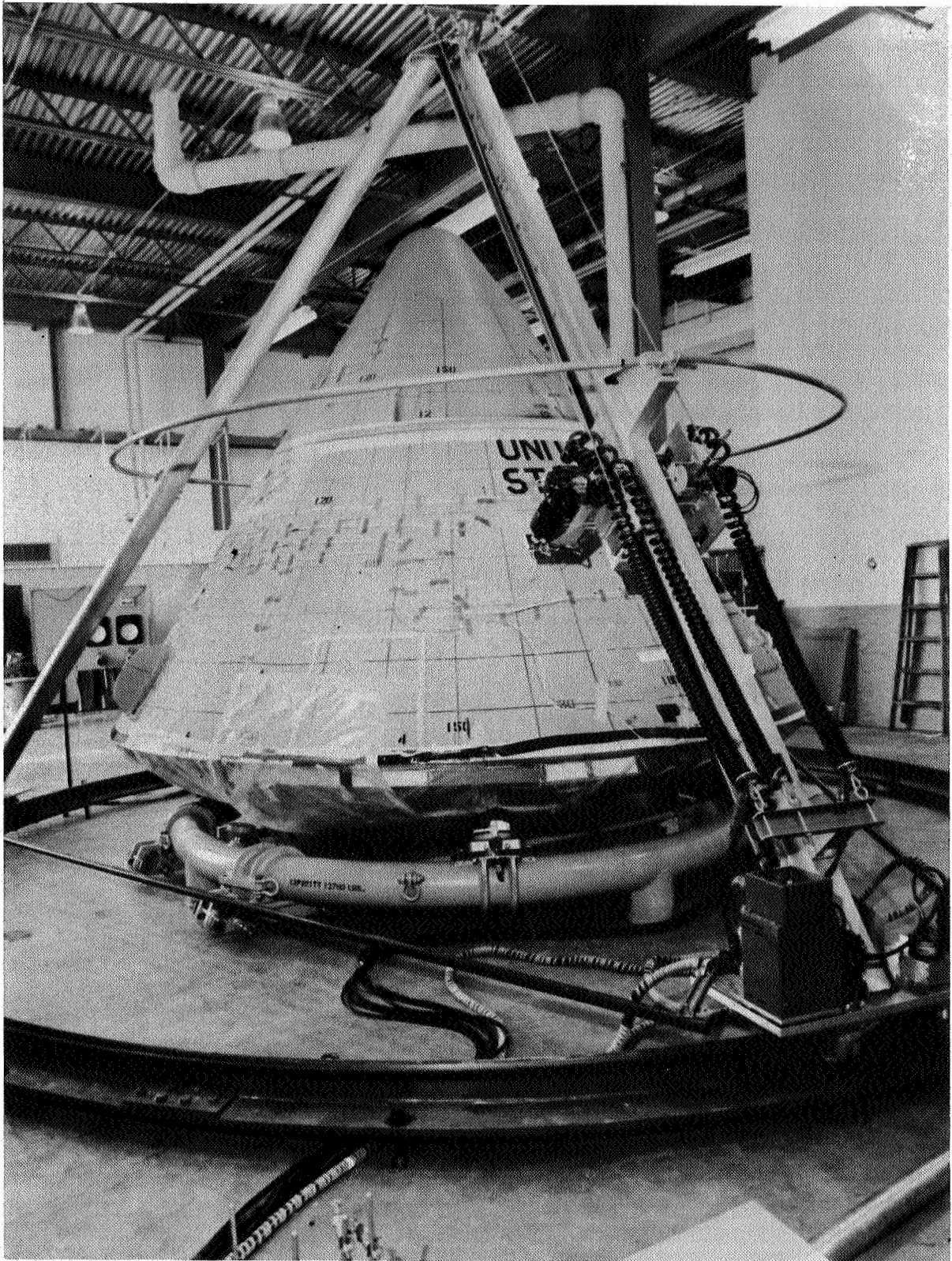


Fig. 3. The Apollo spacecraft and gamma probe apparatus.

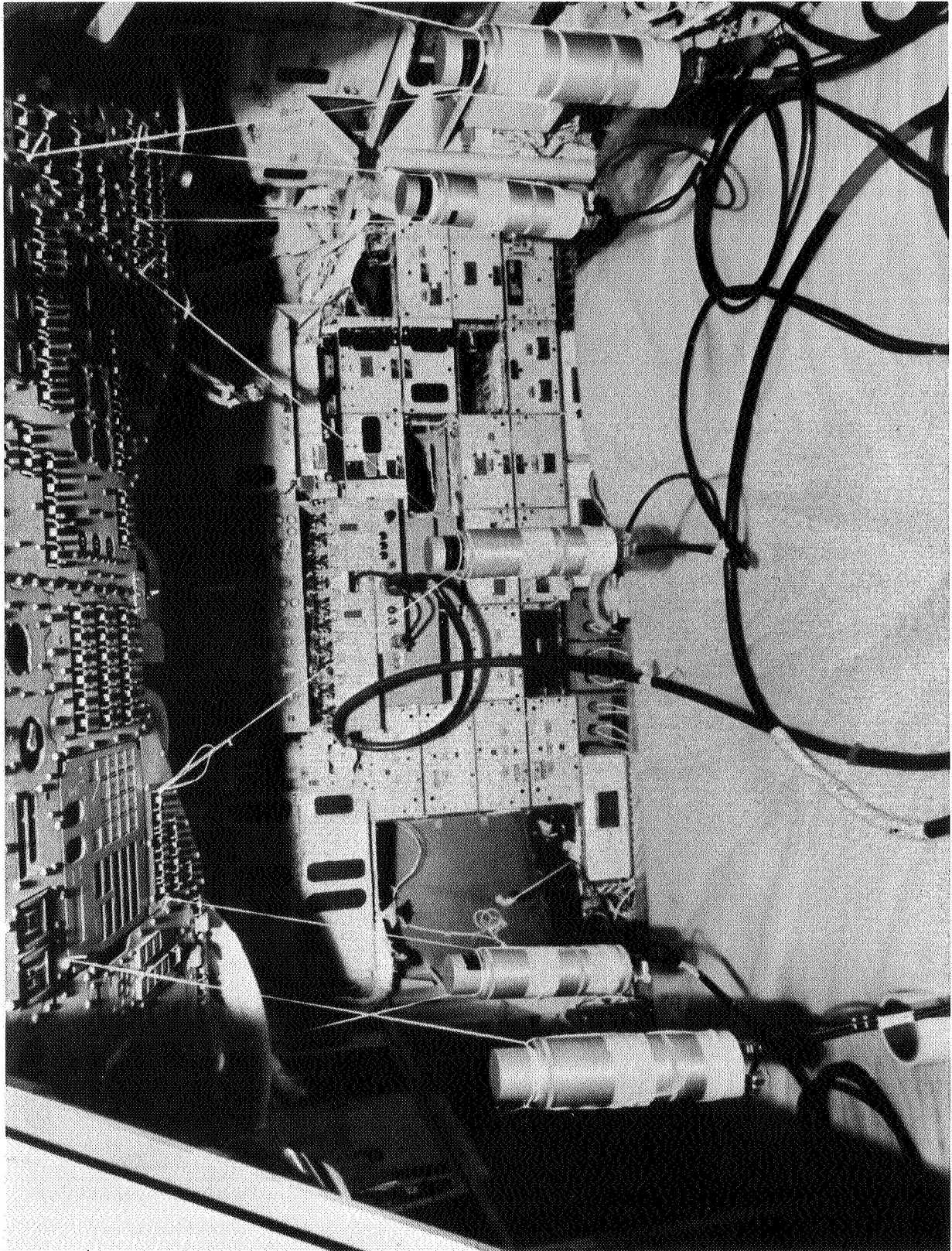


Fig. 4. Detector arrangement.

moving the source or detector. The average error in thickness from 44 trials using thicknesses of 3.43, 6.86, and 10.3 gm/cm² of Al was about 5 percent.

Data were taken for six detector locations in both the Gemini and Apollo vehicles. One detector in each spacecraft was located in the approximate position as that described by the corresponding vehicle analytical shielding breakdown. The other five detectors were placed at specific locations of interest in each vehicle.

DATA EVALUATION

Radiation-dose comparisons between the gamma probe shielding data and analytical solid-angle breakdowns of the Gemini and Apollo vehicles are in fairly good agreement, with the gamma probe data yielding slightly lower doses (Table I).

TABLE I

Gamma Probe and Analytical-Geometry Dose Comparisons

| Vehicle | Spectrum | Dose From Gamma Probe Data, rad | Dose From Analytical Geometry, rad | Dose Ratio |
|---------|---------------------|---------------------------------|------------------------------------|------------|
| Gemini | I Model event | 26.75 | 94.02 | 3.51 |
| | II Trapped protons | 1.953 | 5.194 | 2.66 |
| | III Trapped protons | 2.558 | 7.106 | 2.78 |
| Apollo | I Model event | 20.54 | 31.12 | 1.51 |
| | II Trapped protons | 0.815 | 1.364 | 1.67 |

The gamma probe data do not give a complete description of the vehicles; therefore, dose comparisons were made using only the portions of the analytical data that correspond to the vehicle surface which was probed. Portions of vehicles which were not probed include the aft heat-shield area and a small cone through the nose. These portions comprise a large percentage of the total solid angle; however, they are very heavily shielded areas from which only a small percentage of the total radiation dose can be attributed.

Gamma probe data for the Gemini spacecraft covered approximately 36 percent of the total solid angle for detector no. 5, which was located in the approximate position as that described by the U.S. Air Force solid-angle breakdown. Dose comparisons were made between the two shielding geometries for the proton spectra shown in Fig. 5. The results of these comparisons (Table I) show that the gamma probe data indicate more shielding than the analytical description.

The Apollo gamma probe data included 60 percent of the total solid angle for detector no. 6 which was located in a position corresponding to that described by the North American Aviation, Inc., Downey, California, solid-angle breakdown of the Block I spacecraft. Dose comparisons were made between the two geometries using Spectrum I and Spectrum II shown in Fig. 5. As shown in Table I, the gamma probe doses were considerably lower.

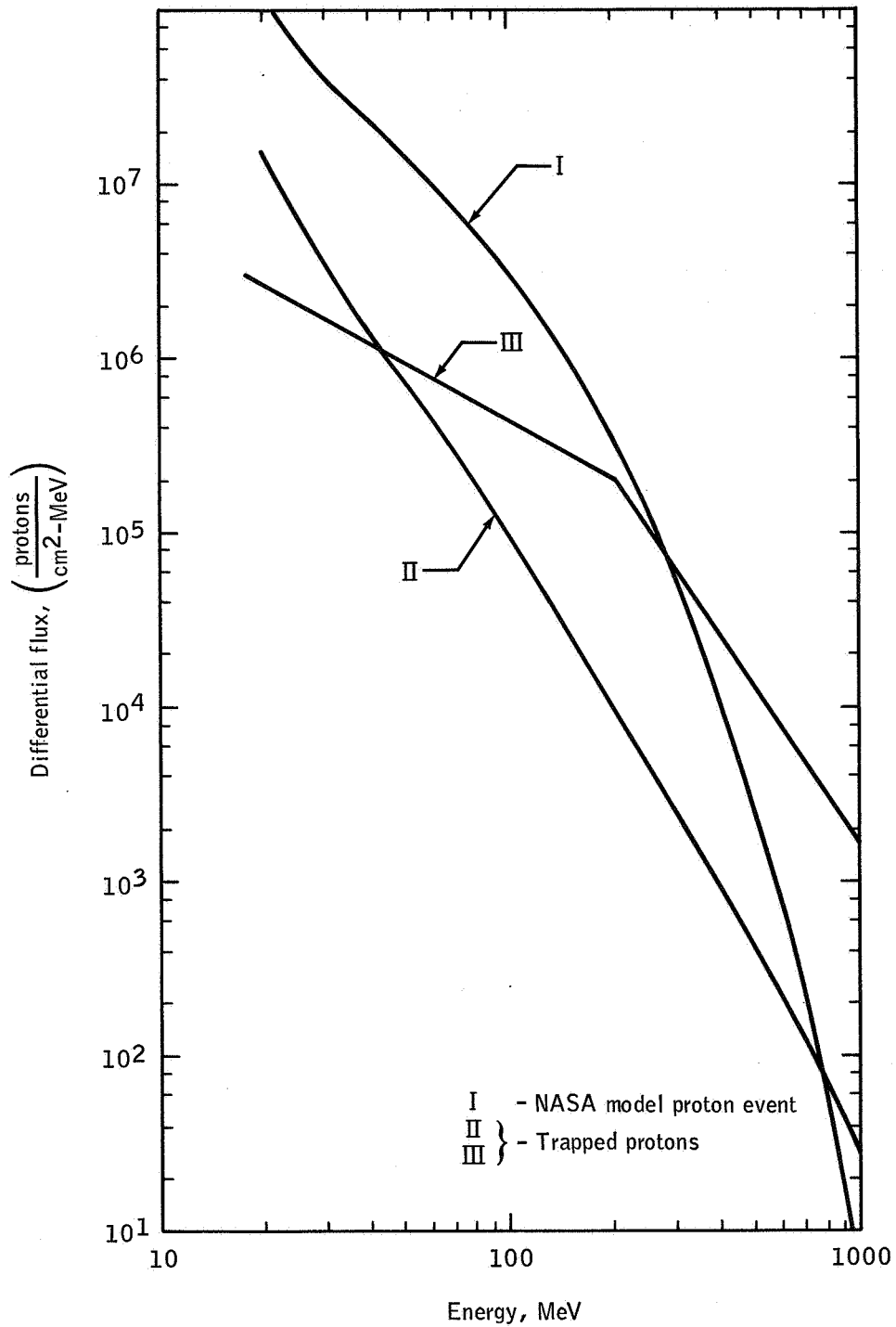


Fig. 5. Proton differential energy spectra.

Dose variations with respect to detector location for all detectors in the Apollo spacecraft are shown in Table II.

TABLE II

Dose Variation in Apollo Spacecraft — Spectrum II

| Apollo Detector Location | Dose, rad |
|---------------------------------------|-----------|
| Detector 1, eye of right astronaut | 0.346 |
| Detector 2, instrument panel | 0.490 |
| Detector 3, chest of right astronaut | 0.922 |
| Detector 4, chest of left astronaut | 0.713 |
| Detector 5, eye of left astronaut | 0.920 |
| Detector 6, chest of middle astronaut | 0.815 |

CONCLUDING REMARKS

The purpose of the gamma probe was a verification of the analytical shielding descriptions for the vehicles under consideration. The results are satisfactory and are as expected. Any analytical description of a shielding configuration tends to produce conservatively high dose estimates. Spacecraft wiring, small beams, nuts and bolts, and other minute components must necessarily be neglected, otherwise an analytical description would be virtually impossible. A weight comparison of the Gemini analytical description, for example, gave on the order of 65 percent of the true spacecraft weight, which shows that much of the actual shielding has been overlooked by the analytical shielding method. Gamma probe data,

on the other hand, describe the shielding (electron density) from all material between the gamma source and the detector.

From the gamma probe dose comparisons for the Gemini spacecraft, and from comparisons of dose measurements taken on specific Gemini flights with preflight dose calculations, it has been concluded that the analytical breakdown is conservative and always produces conservatively high dose estimates.

As shown in Table III, the analytical breakdown gave doses ranging from a factor of 1.8 to 5.0 higher than the actual measured doses.

TABLE III

Calculated and Measured Doses for Specific Gemini Flights

| Gemini Flight | Calculated Dose, rad | Measured Dose, rad | Dose Ratio |
|---------------|----------------------|--------------------|------------|
| IX | 0.09 | 0.018 | 5.0 |
| X | 1.4 | 0.77 | 1.82 |
| XI | 0.091 | 0.025 | 3.64 |

Based on the gamma probe findings, it was also concluded that the Apollo analytical geometry produces conservatively high doses.

It is planned that gamma probe evaluation will be made of the Apollo Block II spacecraft and of the ascent stage of the lunar module.

REFERENCES

1. A. D. KRUMBEIN, R. C. ROSS, and C. BEAULIEU, "A Gamma-Ray Probe System for Determining the Shielding Effectiveness of the Apollo Vehicle," Second Symposium on Protection Against Radiation in Space, NASA SP-71 (1965).
2. A. D. KRUMBEIN and F. JOHNSON, "The Use of Gamma Probing to Determine the Shielding Effectiveness of Space Vehicles," UNC-5075, United Nuclear Corp., 1964. (Also NASA CR-38783.)

RADIATION DOSIMETRY FOR MANNED SPACE FLIGHT

By Robert G. Richmond, William G. Davis,
Joseph C. Lill, and Carlos S. Warren
Space Physics Division
NASA Manned Spacecraft Center
Houston, Texas

INTRODUCTION

Since the advent of manned space flight in 1961, much effort has been directed toward the analysis of the hazards associated with exposure to extraterrestrial sources of radiation and toward the adequate measurement of these sources. With the completion of the Mercury and Gemini programs, it has been shown that radiation presents no problem to low-altitude earth-orbital flights. Limited excursions to altitudes penetrating the Van Allen belt have also been shown to be possible without overexposing the spacecraft crewmembers.

The more complex nature of Apollo lunar missions, however, infers greater uncertainty in radiation exposures. Once the spacecraft leaves the protection of the magnetic field of the earth, it is vulnerable to energetic particles accelerated by solar flares. These solar particle events vary widely in their frequency of occurrence, their intensity, and their spectra. Since this radiation environment can be significant, in terms of crew safety and mission success, an operational dosimetry system, with passive and active elements, has been developed

for Apollo. Active systems include an alpha-proton spectrometer, skin- and depth-dose-rate dosimeters, personal integrating dosimeters, and a portable, hand-held radiation survey meter. The passive dosimetry system consists of several layers of nuclear emulsions and films, packaged with a lithium fluoride thermoluminescent powder.

SYMBOLS

- B magnetic-field strength, gauss
- $\frac{dE}{dx}$ differential energy deposited per unit path length
- E total particle energy
- L the geocentric distance to the crossing of a field line, where the field line is defined by B, earth radii

DESCRIPTION OF THE SOURCE TERM

The radiation environment in space may be divided into four categories: galactic cosmic rays, solar wind, geomagnetically trapped particles (Van Allen belts), and particles associated with solar flares. A short description of each of these components of the radiation environment aids in the understanding of the dosimetry problems and techniques.

Galactic cosmic radiation, which originates outside the solar system, consists mostly of very-high-energy charged particles (about 85 percent protons and 13 percent alpha particles). The remaining constituent is heavy nuclei. These particles, because of their high

penetrating power, may be encountered essentially everywhere in space. The intensity of these particles (i.e., particles per unit area) is considered small and remains relatively constant with time, although the particle intensity varies somewhat with solar activity. Although the radiation dose deposited by cosmic galactic rays may be neglected for short-duration missions, this component will be an important contributor to the total radiation dose on long-duration missions.

The solar wind is mainly low-energy protons, caused by the hydro-magnetic expansion of the solar corona into interplanetary space. Typical particle energies are of the order of 1 to 10 keV with fluxes of approximately 10^8 particles/cm²-sec (Ref. 1). With such a large particle flux, exposed spacecraft materials and/or components could conceivably be damaged, since doses on the surface of the spacecraft could reach 10^{10} rad. (Radiation-effects testing of materials exposed to simulated solar-wind environments has been continuing for several years.) Because of their low penetrating power, solar-wind particles do not constitute a direct radiation hazard to man and will not be considered here.

In 1958, Dr. James Van Allen (Ref. 2) demonstrated experimentally that which Störmer (Ref. 3) and Singer (Ref. 4) had predicted analytically — that charged particles are trapped by the magnetic field of the earth. Protons and electrons are trapped in a region about the earth equator which extends in latitude to about $\pm 60^\circ$ and in altitude from the top of the atmosphere to the bottom edge of the

magnetosphere. Experiments have indicated (Refs. 5 and 6) that two proton maxima exist, one at $L = 1.5$ and the second at $L = 2.2$ earth radii. Although there is no clear demarcation between an inner and outer radiation belt for electrons, the separation is very sharp for protons and occurs at about $L = 2$ earth radii. In the inner radiation belt, there are protons with energies up to hundreds of MeV. In the outer radiation belt, proton energies are much lower, and fluxes are much higher.

Since 1958, seven temporary, artificial radiation belts of electrons have been made by high-altitude nuclear detonations. The most significant of these tests, which was the source of much knowledge about the particle-trapping mechanisms, was Starfish in July 1962. A distortion (anomaly) of the magnetic field of the earth in a region in the South Atlantic has caused the lower edge of the belt to "dip down" to its lowest altitude. For low earth-orbit missions, such as those conducted during the Mercury and Gemini programs, most of the radiation dose was received during the passes through the South Atlantic Anomaly (Refs. 7 to 10).

Energetic particles ejected during solar flares (solar-flare particle events) present the largest radiation hazard to lunar landing missions. The occurrence of solar particle events is essentially unpredictable. Although the occurrence of a particular event cannot presently be forecast or predicted, it has been shown that solar activity is cyclic, with a period of about 11 years. The present (20th) solar

cycle began near the end of 1964. It is expected to have a period of maximum activity before 1970 and should end in about 1975. Solar particle events generally produce protons of medium to high energy, but often include a substantial number of alpha particles as well.

After a solar-flare particle event occurs on the surface of the sun, several minutes to several hours may elapse before particles are detected in the earth-moon region. The higher-energy particles are detected first, with the maximum number of particles arriving from 1 to 10 hours after the beginning, or onset, of the event. Events may last from 1 to 4 days, depending on the size (particle fluence) of the event.

The need for development of a radiation environment to be used in mission planning and in the design of spacecraft shielding led to the establishment of a "model" solar particle event. This model event was formulated from a statistical analysis of the sparse data obtained from the 19th solar cycle. (A detailed description of the formulation of the model event can be found in Ref. 11.) This environment was found to be applicable in the earth-moon region outside of the earth's magnetosphere.

GEMINI RADIATION MEASUREMENTS

The Gemini flights, generally, have been flown at relatively low altitudes and, thus, have not been affected by radiation. It was shown during Project Mercury that the only radiation received by the

spacecraft occupants was that radiation received during brief passes through the South Atlantic Anomaly. In view of this, it was decided that the only dosimetry required on Gemini spacecraft would be that required for medical-record purposes. Since there was no requirement for dosimetry readout in real mission time, a passive system was developed which has been flown on every manned mission to date.

The passive dosimetry system is a multicomponent badge, with dimensions of 2.1 by 1.7 by 0.25 inches. It consists of 500 mg of lithium fluoride thermoluminescent powder (TLD); 600 μ of nuclear emulsions; and several standard beta-, gamma-, and neutron-sensitive films. The components are sandwiched between 0.011-inch polyvinylchloride film, to make a soft, flexible package that is installed in pockets on the astronaut's constant wear garment. Four packages are worn by each astronaut, one each on the right and left chest, one on the right thigh, and one in the helmet over the right forehead, between the helmet liner and the helmet shell.

The TLD was included because it can be read immediately after flight. The emulsions were included so that the charged-particle flux incident on the crew could be analyzed in detail. (That is, estimates of dose caused by different components could be separately considered.) The films, one double-component pair and one neutron-monitoring type, were added to provide a densitometric readout capability in the event the emulsions were overexposed. The entire photodosimeter package was assembled and analyzed by Dr. Hermann J. Schaefer of the U.S. Naval Aerospace Medical Institute at Pensacola, Florida.

Table I lists the doses measured with TLD during the Gemini Program. Except for the Gemini V, VII, and X flights, all doses were quite low. The Gemini V flight lasted 8 days and reached apogees of 200 n. mi. Gemini VII was a 160-n. mi. circular-orbit mission that lasted 14 days. These two flights, Gemini V and VII, were of much longer duration than any of the others. The Gemini X flight, although short, reached a higher altitude in the anomaly than was reached by any previous flight, spending almost 13 hours in a 158- by 413-n. mi. orbit. Four of the high-altitude orbits cut through the anomaly region. Gemini XI reached a higher altitude than Gemini X, but was programmed to attain an apogee of 750 n. mi. over Australia, deliberately away from the anomaly, to protect a nuclear-emulsion cosmic-ray experiment. Differences in doses recorded on the same flights were attributed to local shielding by spacecraft structure.

GEMINI RADIATION MONITORING SYSTEM (GRMS)

Because the Gemini X and XI missions went higher into the Van Allen belt than man had ever been, flight controllers at the Manned Spacecraft Center (MSC) thought it desirable to have a real-time dose-readout capability throughout the mission. Using prototype dosimeters developed for the Apollo Spacecraft Program, a hybrid package was built at MSC incorporating ionization chambers to read dose rate and integrated dose. This hybrid package, the Gemini Radiation Monitoring System (Fig. 1), was stowed for launch and then placed on the spacecraft wall, where it remained until reentry. Although the dose rate was negligible throughout

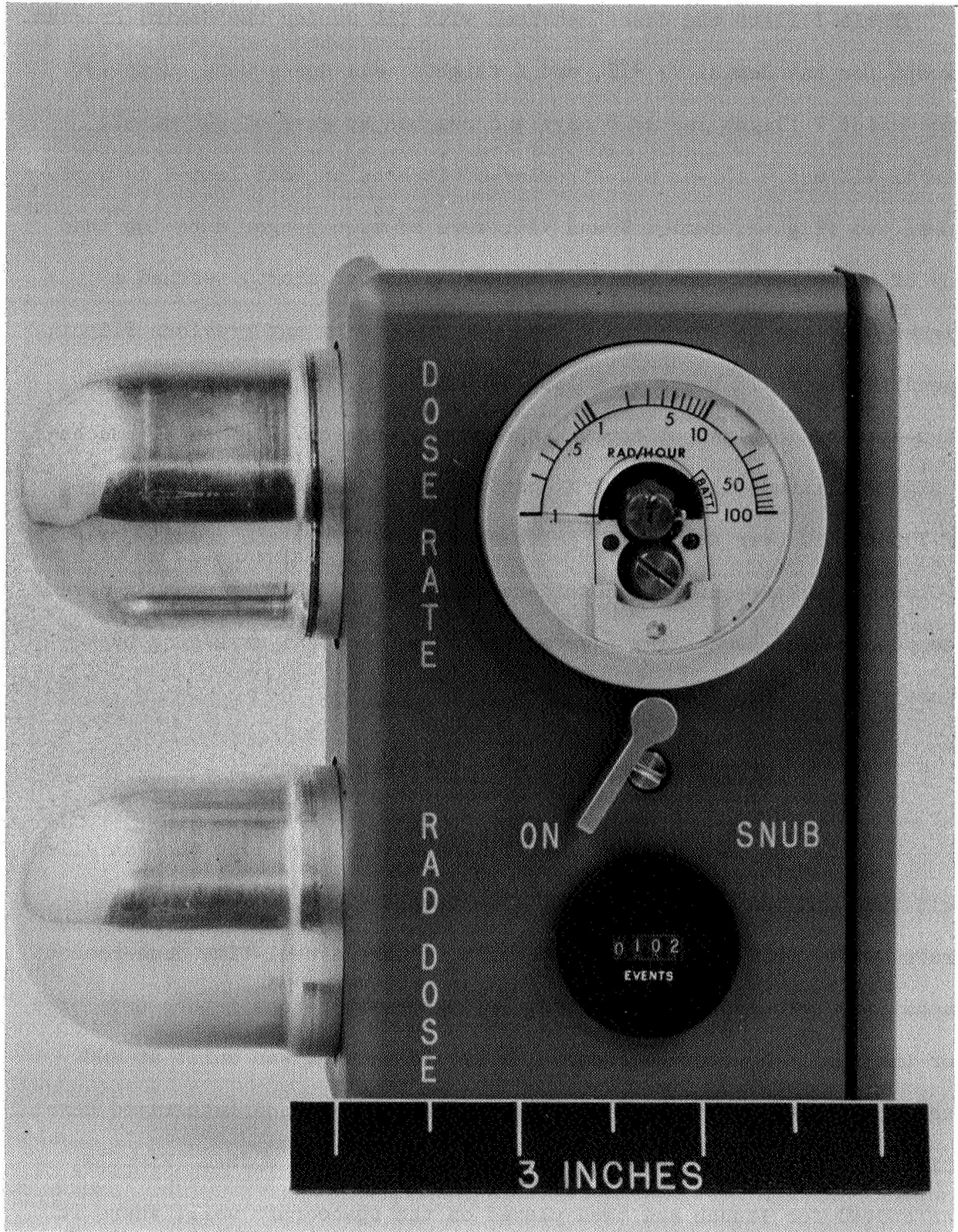


Fig. 1. Gemini Radiation Monitoring System (GRMS).

the flight, the integrated dose recorded was 910 mrad (Table I). The difference between this reading and that of the TLD was attributed to differences in local shielding by the spacecraft. The same instrument was carried on Gemini XI, but had the low reading of 30 mrad (Table I), as was expected.

In the Gemini Radiation Monitoring System (GRMS), two 10-cc tissue-equivalent ionization chambers were used, with field-effect transistors (FET) as the input element from the ion chambers to the electronics. In the rate-meter section, a three-decade logarithmic amplifier was used to cover a dose-rate range of 0.1 to 100 rad/hr. The integrating section of the dosimeter integrated the current from the ion chamber to an equivalent of 10 mrad, at which point an electromechanical register was used to accumulate the total dose in 10-mrad increments. The system operated from its own internal batteries and had an operating life of about 250 hours.

APOLLO DOSIMETRY

Dosimetry and mission operations required for crew safety on the Apollo lunar mission are more complex than those used for the Gemini missions. In addition to insuring the requirements of crew safety, Apollo dosimetry must be accurate and reliable, so as to have no adverse effect on mission success, while minimizing space, weight, and power.

TABLE I

Doses Measured with the TLD

| Flight | Location | Command Pilot | Pilot |
|-------------|-------------|---------------------------|----------------------------|
| Gemini III | Helmet | <20 | 45 ± 20 |
| | Right Chest | <20 | <20 |
| | Left Chest | <20 | 39 ± 15 |
| | Thigh | <20 | <20 |
| Gemini IV | Helmet | 45 ± 4.5 | 69 ± 3.8 |
| | Right Chest | 40 ± 4.2 | 46 ± 4.6 |
| | Left Chest | 39 ± 4.5 | 43 ± 4.7 |
| | Thigh | 43 ± 4.5 | 43 ± 4.5 |
| Gemini V | Helmet | 195 ± 19.5 | 172 ± 17.2 |
| | Right Chest | 173 ± 17.3 | 172 ± 17.2 |
| | Left Chest | 190 ± 19.0 | 140 ± 14.8 |
| | Thigh | 183 ± 18.3 | 186 ± 18.6 |
| Gemini VI | Helmet | 25 ± 2.8 | 31 ± 7.4 |
| | Right Chest | 26 ± 1.5 | 20 ± 1.5 |
| | Left Chest | 25 ± 2.1 | 24 ± 1.4 |
| | Thigh | 24 ± 1.7 | 22 ± 0.2 |
| Gemini VII | Helmet | Not used | Not used |
| | Right Chest | 113 ± 13.6 | 231 ± 9.0 |
| | Left Chest | 192 ± 10.8 | 105 ± 10.5 |
| | Thigh | 178 ± 4.5 | 163 ± 8.2 |
| Gemini VIII | Helmet | <10 | <10 |
| | Right Chest | <10 | <10 |
| | Left Chest | <10 | <10 |
| | Thigh | <10 | <10 |
| Gemini IX | Helmet | 15 ± 1 | 27 ± 1 |
| | Right Chest | 14 ± 1 | 22 ± 3 |
| | Left Chest | 18 ± 1 | 17 ± 1 |
| | Thigh | 20 ± 3 | 22 ± 1 |
| Gemini X | Helmet | 618 ± 6 | 763 ± 6 |
| | Right Chest | 725 ± 6 (GRMS — 910 mrad) | 763 ± 7 (GRMS — 910 mrad) |
| | Left Chest | 769 ± 7 (GRMS — 910 mrad) | 779 ± 13 (GRMS — 910 mrad) |
| | Thigh | 626 ± 6 | Not used |
| Gemini XI | Helmet | 39 ± 1 | 34 ± 2 |
| | Right Chest | 26 ± 3 (GRMS — 30 mrad) | 25 ± 1 (GRMS — 30 mrad) |
| | Left Chest | 27 ± 1 (GRMS — 30 mrad) | 23 ± 1 (GRMS — 30 mrad) |
| | Thigh | 28 ± 3 | 25 ± 1 |
| Gemini XIII | Helmet | <20 | <20 |
| | Right Chest | <20 | <20 |
| | Left Chest | <20 | <20 |
| | Thigh | <20 | <20 |

After considerable study, the following instrumentation was defined for sufficient and complete radiation monitoring (Ref. 12).

1. Nuclear Particle Detection System (NPDS) — a proton-alpha spectrometer, carried on the service module that telemeters spectral and flux data (Fig. 2)

2. Van Allen Belt Dosimeter (VABD) — a skin- and depth-dose-rate instrument, fixed in the command module, that telemeters dose rates

3. Apollo Radiation Survey Meter (ARSM) — a portable, hand-held, tissue-equivalent dose-rate meter carried in the command module and transferred to the lunar module for lunar operations

4. Apollo Personal Radiation Dosimeters (APRD) — integrating, tissue-equivalent ionization chambers carried by each crewman, designed to measure skin dose

5. Apollo Passive Dosimeters (APD) — carried on each crewman, as on the Gemini flights

THE NUCLEAR PARTICLE DETECTION SYSTEM (NPDS)

The NPDS is a solid-state detector-absorber telescope which measures the proton and alpha-particle spectra and rates, in cislunar space, from solar-flare particle events. Seven differential energy bands and one integral energy band are defined by the NPDS as in Table II.

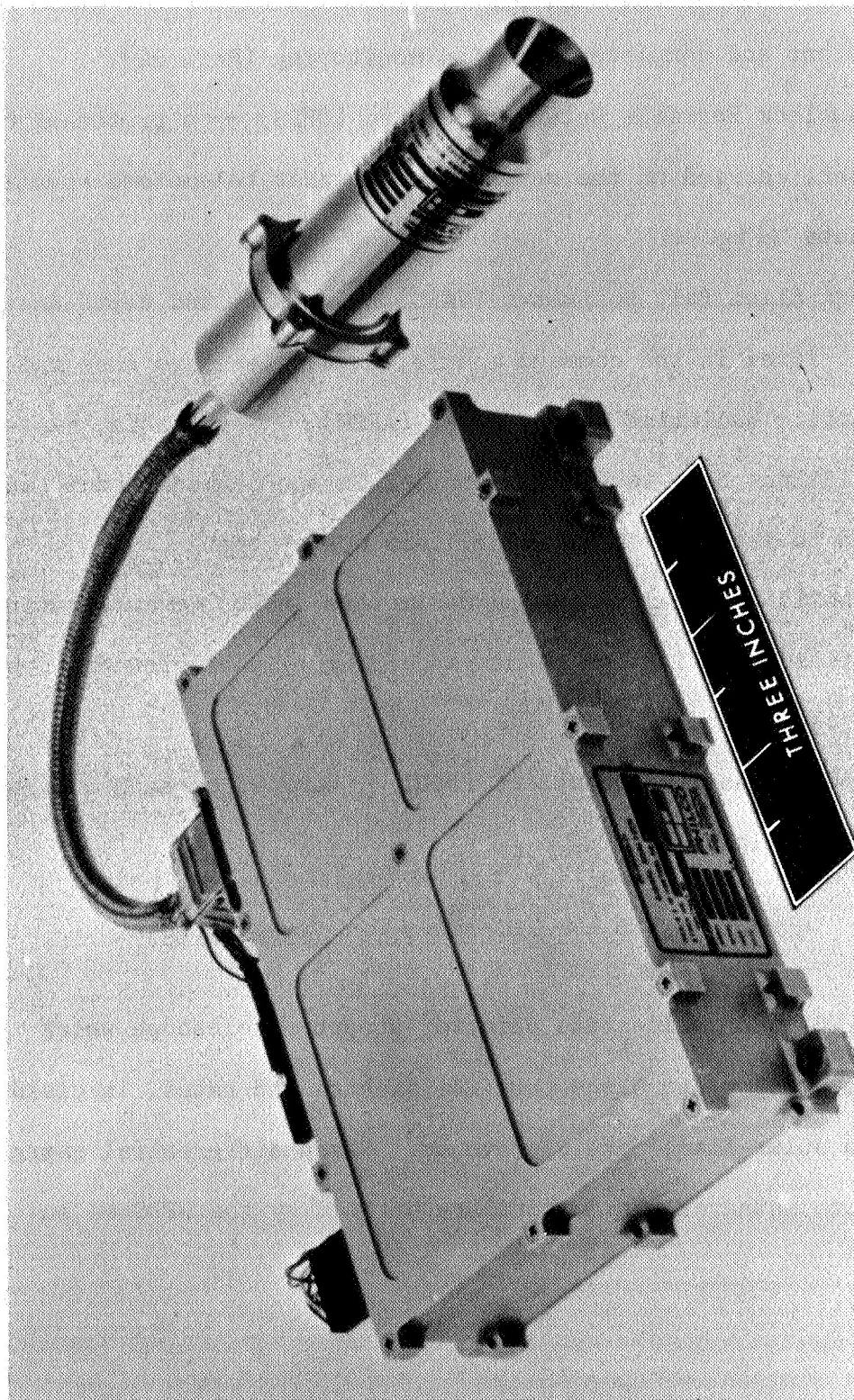


Fig. 2. Nuclear Particle Detection System (NPDS).

TABLE II

Energy Bands Defined by the NPDS

| Energy Band | Counter Rate Range |
|--------------------------------|--------------------|
| Differential — Protons | |
| 10 to 20 MeV | 0 to 100 000 cps |
| 35 to 45 MeV | 0 to 10 000 cps |
| 85 to 95 MeV | 0 to 10 000 cps |
| 130 to 170 MeV | 0 to 10 000 cps |
| Differential — Alpha Particles | |
| 40 to 50 MeV | 0 to 10 000 cps |
| 130 to 170 MeV | 0 to 10 000 cps |
| 270 to 330 MeV | 0 to 10 000 cps |
| Integral — Protons Only | |
| 15 MeV | 0 to 100 000 cps |

The sensor of the NPDS consists of three solid-state detectors and two absorbers which act as energy shifters. The first detector in the telescope is a fully-depleted, phosphorus-diffused device, 8 mm in diameter and 270 μ thick. The second and third detectors are 2-mm lithium-drifted devices that are 10 mm and 16 mm in diameter, respectively. A lucite absorber is used between the first and second detectors, and a tungsten absorber is located between the second and third detectors. Particle type and energy determination are made using dE/dx and total E techniques.

The energy intervals at which the NPDS operates are determined by setting 16 level sensors. The intersection of these level sensors with the energy cusps of the three detectors, together with the system logic, defines the energy intervals. The pulse rates, at which particles enter the various energy intervals, are integrated and fed to the appropriate rate meter. The output of the rate meter is then transmitted to the ground. The rate meters present an output which is logarithmic with count rate, changing from 0 to 5 V dc as the count rate varies over five decades.

The NPDS rate-meter outputs are specified to vary by no more than ± 160 mV or ± 3.2 percent of full-scale voltage, over the full operating temperature range (-54° to $+52^{\circ}$ C). Most units typically vary from ± 50 to ± 80 mV, or from 1.0 to 1.6 percent of full-scale voltage. The low voltage inaccuracies that develop over the wide temperature variations are equivalent to higher percentages when expressed as percent of count rate. For example, maintaining voltage to within ± 1 percent over the full temperature range represents a count-rate inaccuracy of ± 11 percent.

The sensing-band edges (cusps) depend upon amplifier gains and level-sensor thresholds. These also vary with temperature, so that the spectrometer band edges (which are set at room temperature) will vary with temperature. Preliminary testing shows that band-edge shifts with temperature can be kept under 10 percent and that, if the temperature is measured during operation, the edge shift can be calculated and interpreted in the data-reduction program.

In addition to the nuclear-band and rate requirements, this eight-channel nuclear spectrometer has been designed, and is being fabricated, to meet the general Apollo requirements of low weight, low power, and high reliability. The NPDS weighs 3.0 lb, requires only 1.6 W in operation, and has a predicted probability of success greater than 0.99 for 365 consecutive hours of operation. This is exclusive of the solid-state detectors, for which little or no reliability data are available.

The data from the spectrometer will be telemetered to ground control and will be used in three operational modes, (1) confirmation of arrival of solar particle event, (2) source term for calculation of doses in the command module, and (3) dose projection. Doses calculated from the real-time spectra will be compared with dosimeter readings, and the data will be used for a dose versus time projection to implement length-of-stay and/or abort decisions.

VAN ALLEN BELT DOSIMETER (VABD)

The VABD (Fig. 3) is a system which continuously telemeters skin- and blood-forming-organ (BFO) dose-rate information to ground control. The dose-rate information is integrated by computer, and the dose rate and accumulated dose values are displayed visually at the Space Environment Console in the Mission Control Center - Houston. These data are used with the other spacecraft radiation-instrumentation data to evaluate the hazard to the crewmembers on a real-time basis. The ability of the crewmembers to participate in providing regular visual readouts of

- SENSORS
 - 2 10cc TISSUE - EQUIVALENT ION CHAMBERS
- WEIGHT
 - APPROX 4 LBS
- VOLUME
 - APPROX 60 IN.³
- RANGE
 - 0.01-100 RAD/HR, TELEMETERED
- OPERATING LIFE
 - SPACECRAFT POWER

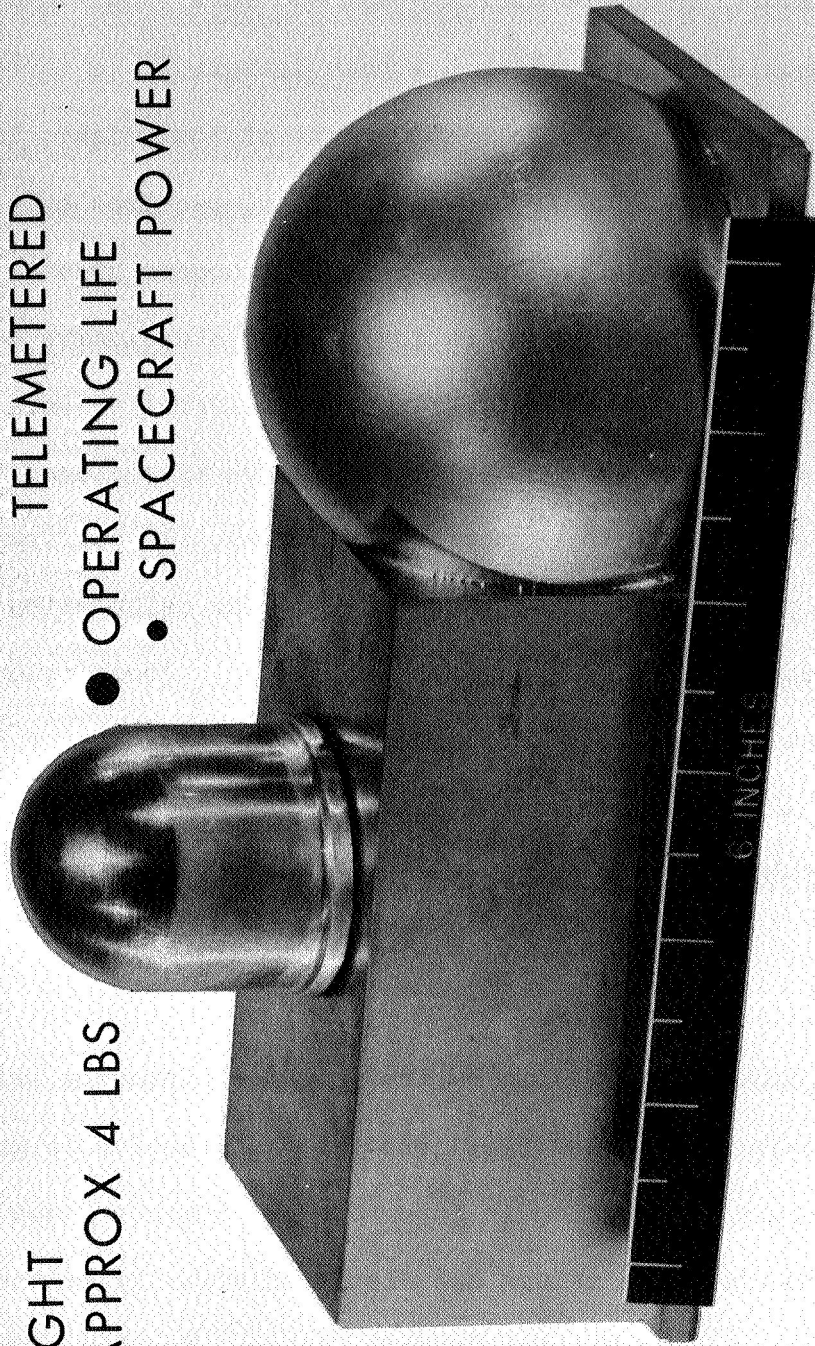


Fig. 3. Van Allen Belt Dosimeter (VABD).

the other onboard dosimeter is limited. The need to measure depth dose is a result of the difference between the proton spectra in the Van Allen belt region and the proton spectra in the solar-flare environment. The "harder" spectra in the Van Allen belt may lead to the dose limit established for the BFO being reached before the dose limit established for the skin. In the "softer" solar-flare particle-event environment the skin-dose limit could be the limiting factor.

The initial requirement for the VABD was a result of the necessity for planning a high-altitude-trajectory mission (4000-n. mi. apogee) in preparation for the lunar flight. Although the dose predictions for the mission did not exceed the established limits, it was realized that variation in the planned trajectory could cause the dose levels to approach the defined dose limit. The VABD will be provided on all manned missions which extend beyond the nominal Gemini trajectories.

In addition to its primary objective, the VABD will provide an instantaneous skin- and depth-dose ratio in the command module during a solar-flare particle event. This ratio could be used to verify the NPDS data concerning the particle-event spectra.

The sensors of the VABD are two 10-cc tissue-equivalent ionization chambers. One ionization chamber is covered by a material equivalent to 5 cm of tissue, to provide the depth-dose-rate measurement. The second ion chamber has a wall thickness approximately equal to the crew pressure-suit thickness plus 0.7 mm of tissue, to provide an equivalent skin-dose rate.

The electronic circuitry for the VABD incorporates field-effect transistors (FET) as the input stages from the ionization chambers to the logarithmic amplifiers. A wide range of dose rates is made practical by use of the logarithmic response of the output (of the system) to the input radiation field. To maintain the necessary resolution of the measurement, an automatic range switch is used which allows the 0- to 5-V system output to represent either three decades of low dose rate or three decades of high dose rate. A logic output indicates the range in which two sensors are operating.

The VABD was designed to fit a specific location in the command module, about 18 inches from the right-hand crewman. This location and the space limitation required a compromise in the selection of a material for the depth sensor. The tissue-equivalent plastic, normally used, was replaced by an equivalent thickness of aluminum. It was determined that the difference between secondary production in tissue and secondary production in aluminum, for particle energies of interest, would cause a difference of less than 5 percent in the measured dose.

APOLLO RADIATION SURVEY METER (ARSM)

The ARSM is shown in Fig. 4. The system consists of a 10-cc tissue-equivalent ionization chamber, solid-state circuitry, and self-contained power supply and readout. The detector (constructed of a tissue-equivalent plastic and filled with ethylene at 1 atm pressure)

- SENSOR
 - 10cc TISSUE-EQUIVALENT ION CHAMBER
 - WEIGHT
 - 1.60 LBS
 - VOLUME
 - 23 IN.³
 - RANGE: LINEAR
 - 0-100
 - 0-10
 - 0-1
 - 0-0.1
- } RADS/HR
- OPERATING LIFE
 - 1200 HOURS



Fig. 4. Apollo Radiation Survey Meter (ARSM).

has a gamma sensitivity of approximately 10^{-12} A/rad/hr. An FET is used in the front of the instrument, replacing the conventional electrometer tube as a stage of amplification.

The wall thickness is such that readings correspond reasonably to a skin-dose-rate measurement. The linear readout is in four ranges, 0 to 0.1, 0 to 1, 0 to 10, and 0 to 100 rad/hr. A spring-loaded snubbing switch is provided to allow the meter to be locked at any reading. The instrument will operate continuously for 1200 hours without battery replacement.

APOLLO PERSONAL RADIATION DOSIMETER (APRD)

The APRD, shown in Fig. 5, consists of a tissue-equivalent ionization chamber, necessary electronics, a self-contained battery power supply, and a signal readout. The wall thickness of the ionization chamber is approximately equal to 0.7 mm of tissue plus suit thicknesses. The battery power supply furnishes the unit with up to 2000 hours of continuous operation.

The APRD has a range of 0 to 1000 rad in 0.01-rad/pulse increments, with a minimum pulse rate of 3 pulses/sec, corresponding to a dose rate of 108 rad/hr. The ionization chamber has an active volume of 7.1 cc and has a gamma sensitivity of approximately 10^{-12} A/rad/hr. The high-impedance input circuit (containing an FET for one stage of amplification and a relay to furnish the necessary charge feedback) is sealed in an evacuated can to minimize input-circuit leakage. A five-digit

- **SENSOR**
 - 7.1cc TISSUE-EQUIVALENT ION CHAMBER
- **WEIGHT**
 - 0.4 LBS
- **VOLUME**
 - 5.46 IN.³
- **RANGE**
 - 0-1000 RADS IN 0.01 RAD INCREMENTS
- **OPERATING LIFE**
 - 2000 HOURS

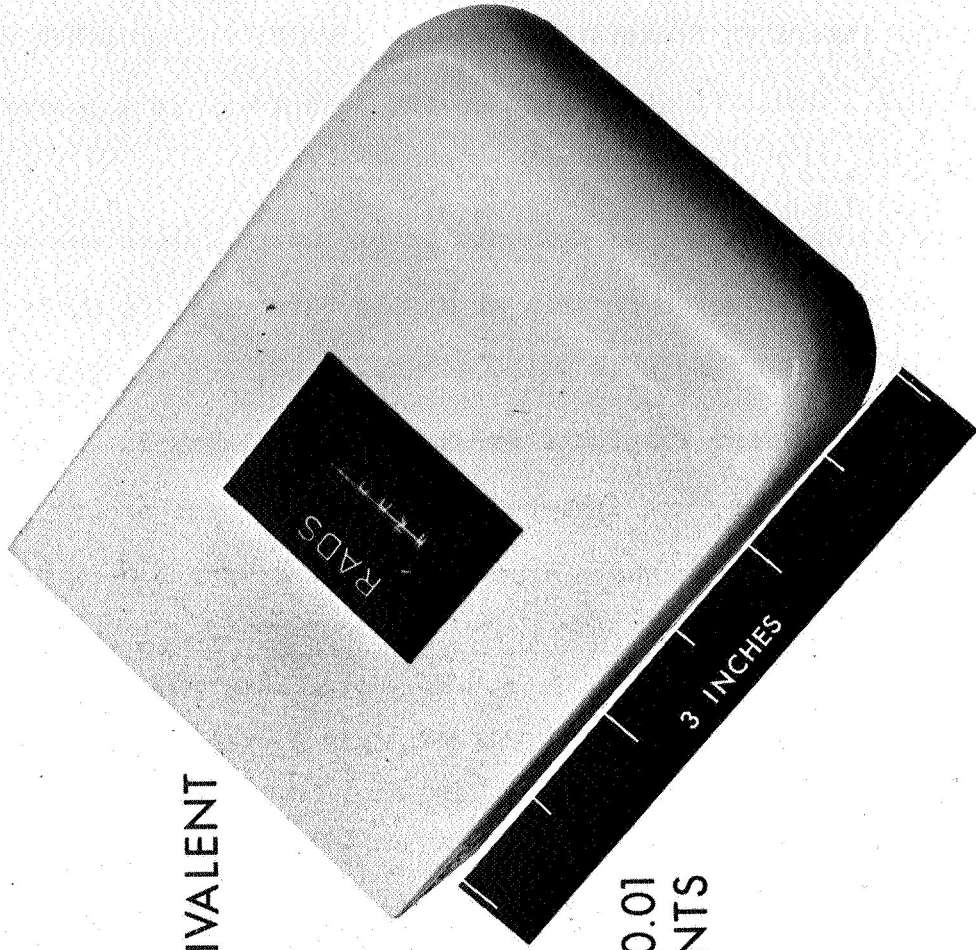


Fig. 5. Apollo Personal Radiation Dosimeter (APRD).

electromechanical register is used for readout. All circuitry incorporates the latest in transistor, welded-circuit, and/or other micromodule techniques. The APRD is located on the left thigh in a pocket of the Apollo suit.

Proton calibration experiments on prototype dosimeters were conducted at the 100-MeV cyclotron at McGill University in Montreal, Canada; at the 160-MeV cyclotron at Harvard University; and the 187-MeV cyclotron at the Gustav Werner Institute for Nuclear Chemistry in Uppsala, Sweden. The energy, angular, and dose-rate responses of each prototype were measured. These parameters have also been measured for 1.0- and 2.0-MeV electrons.

APOLLO PASSIVE DOSIMETERS (APD)

The APD are essentially the same as those flown on the Gemini missions. Four of these packets are flown in each crewmember's constant wear garment (one each at the right chest, left thigh, right ankle, and helmet locations). The packets are color-coded to match the three constant wear garment colors.

The TLD is to be read out at the Manned Spacecraft Center immediately after the mission. The readout system consists of the following:

1. A stainless-steel heating planchet, with high-current power supply
2. A photomultiplier (PM) tube and high-voltage power supply

3. A micro-microammeter and chart recorder for measurement and recording of the PM tube current as a function of the planchet temperature

A jacket with flowing, cooled carbon dioxide (CO_2) has been placed around the PM tube to lower tube temperature for minimum dark current. The dark current and tube noise have been reduced to a dose-equivalent level of less than 1 mrad.

A 50-mg sample of the TLD powder is placed in the heating planchet, and the temperature of the TLD powder is raised to 240°C in 30 sec. This heating rate and maximum temperature provide an optimum signal-to-noise ratio for data evaluation and insure that the light-curve peak will be recorded.

The lithium fluoride (LiF) light output is linearly related to gamma-ray dose, within ± 10 percent, when crystal size, heating rate, photomultiplier voltage, and thermal emission are held at "best" conditions. The best conditions occur at the PM voltage which yields maximum signal-to-noise ratio, at a crystal size between 150- and 100-mesh Tyler, and at a heating rate of $6^\circ\text{C}/\text{sec}$. The beta-gamma films and emulsions from the packets are processed, developed, and analyzed by Dr. Hermann Schaefer of the U.S. Naval Aerospace Medical Institute. The "grain-counting" technique is used to determine spatial and spectral distribution of the individual radiation components.

CONCLUSIONS

Unlike the low-altitude, earth-orbit Mercury and Gemini manned spacecraft missions, the Apollo mission profiles can provide significant radiation exposures. The radiation instrumentation described here will be sufficient for adequate monitoring of the radiation environment for the lunar landing Apollo mission. As flight durations increase, however, monitoring of the low dose-rate components (galactic cosmic rays, secondary radiation, etc.) will become more important and will result in a new generation of specialized radiation instrumentation.

REFERENCES

1. MODISETTE, JERRY L., "Design Standards Bulletin No. 55," NASA Manned Spacecraft Center (May 1967).
2. VAN ALLEN, JAMES A., "First Public Lecture on the Discovery of the Geomagnetically Trapped Radiation," SUI 60-13, State University of Iowa (1960).
3. STÖRMER, CARL, The Polar Aurora, Clarendon Press, Oxford (1955).
4. SINGER, S. F., "A New Model of Magnetic Storms," Trans. Am. Geophys. Un., 38, 2, 175 (1957).
5. FREDEN, STANLEY C., and WHITE, R. STEPHEN, "Trapped Proton and Cosmic-Ray Albedo Neutron Fluxes," J. Geophys. Res., 67, 1, 25 (1962).
6. McILWAIN, C. E., "The Radiation Belts, Natural and Artificial," Science, 142, 355-361 (Oct. 1963).
7. WARREN, CARLOS S., and GILL, WILLIAM L., "Radiation Dosimetry Aboard the Spacecraft of the Eighth Mercury-Atlas Mission (MA-8)," NASA TN D-1862, NASA Manned Spacecraft Center (August 1964).
8. WARREN, CARLOS S., and BAKER, BENNY R., "Radiation Measurements on the Ninth Mercury-Atlas Mission (MA-9)," NASA TN D-2608, NASA Manned Spacecraft Center (Feb. 1965).
9. RICHMOND, ROBERT G., DAVIS, WILLIAM G., and LILL, JOSEPH C., "Gemini Dosimetry Results," paper presented at the Health Physics Society of America Meeting, Houston, Texas (June 1967).

10. JANNI, JOSEPH W., "Measurement of Spacecraft Cabin Radiation Distributions for the Fourth and Sixth Gemini Flights," AFWL-TR-65-149 (March 1967).
11. MODISETTE, JERRY L., TERRENCE M. VINSON, and ALVA C. HARDY, "Model Solar Proton Environments for Manned Spacecraft Design," NASA TN D-2746, NASA Manned Spacecraft Center (April 1965).
12. RICHMOND, ROBERT G., and LILL, JOSEPH C., "Apollo Operational Dosimetry," paper presented at the Health Physics Society of America Meeting, Houston, Texas (June 1967).

A COMPARISON OF MEASURED TO CALCULATED DOSE FOR THE GEMINI-IV AND VI SPACE FLIGHTS AND WL-304 SPACE PROBE

Robert L. Stovall, Roger S. Case, Jr.,
Joseph F. Janni, & Marion F. Schneider

Biophysics Branch
Air Force Weapons Laboratory
Kirtland AFB, New Mexico

Both the Gemini-IV and Gemini-VI space capsules contained dosimetry experiments consisting of 2 tissue-equivalent ionization chambers designed to return a dose rate time history profile and 5 passive units used to provide total mission dose for cross-comparison with time integrated active dosimetry readings. The ionization chambers were located symmetrically on each hatch within the spacecraft cabin. The passive dosimeters were enclosed within five small aluminum canisters. The WL-304 probe contained an unshielded tissue-equivalent ionization chamber surrounded primarily, only by the vehicle skin furnishing a dose correlation with the simultaneous measurement of the external environment recorded with proton and electron spectrometers.

A complete analysis comparing doses calculated with the AFWL Space Radiation Environment Shielding (SPARES) computer codes using both the Vette model environment and the Gemini-IV on-board spectrometer data is presented. The calculations include; (1) defining the orbital path by using ephemeris information; (2) determining the McIlwain "B,L" coordinates using the 1960 magnetic field expansion of Jensen and Cain; (3) describing the radiation environment employing the Vette AP series proton and AE2 electron maps with appropriate mean life decay factors for the electron flux; (4) formulating the vehicle shielding using a detailed sectoring analysis; (5) transporting the above environment through the vehicle to the desired dose point using radiation transport models.

For the low-altitude Gemini flights which intersected the inner radiation zone only through the South Atlantic magnetic anomaly, the dose rates calculated using the Vette environment were consistently high (a factor of 2 to 4) with the corresponding mission doses again being high by a similar amount. A much better agreement was obtained by calculating the dose rate using the on-board spectrometer data (a factor of 1 to 2) for those revolutions where this information was available (36 to 52). The dose rates calculated using the Vette environment for the WL-304 probe which traversed near the heart of the inner radiation zone were in much better agreement with the total calculated dose for the probes first pass through the inner zone being higher than that observed by 50%.

I. INTRODUCTION

One prerequisite to the successful completion of future manned space missions is the gathering of adequate data concerning (1) the radiation environment, (2) its vehicle shielding interactions, and (3) the resultant

doses to be encountered. Such data are necessary to provide experimental checks on the calculational models presently being used in mission planning studies. With this in mind, experimental dose and dose rate data were taken aboard the Gemini-IV and Gemini-VI manned space flights. Similar additional information was obtained from the Air Force Weapons Laboratory WL-304 space probe. These data will be compared with the results which have been obtained from the AFWL SPARES computer codes.

Since an adequate prediction capability for manned missions is of paramount interest, more emphasis has been given to the Gemini data and the associated dose calculations than to the unmanned WL-304 space probe. It should be noted, however, that both of these experiments involved the simultaneous measurement of radiation environment and dose. Detailed shielding information was available for both vehicles, allowing correlation of the calculated and measured dose rates to be made directly.

II. GEMINI SPACECRAFT SHIELDING CONFIGURATION

The design of the mechanical structure of the Gemini spacecraft was based on the criteria of low weight, mechanical ruggedness, and thermal resistance to re-entry heat. The thickness of the spacecraft walls and interior equipment has been analyzed to ascertain areas of maximum, minimum, and intermediate shielding.

All US manned space vehicles are extremely complex combinations of materials of different compositions and thicknesses. Special alloys and organic compounds are often used. Layered slabs are also common. Hence, the study of the shielding effectiveness of these configurations can become rather involved. The following evaluation has been restricted to the ability of the spacecraft's walls and internal structure to stop charged particles and to minimize the production of bremsstrahlung.

The general configuration of the Gemini capsule is that of a truncated cone with a cylindrical extension at the small end. The large end at the base of the cone is an ablative shield. The small end is the neck of the capsule and houses much of the reentry and recovery equipment, and has a fairly high effective thickness. The sloping sides of the capsule are rather thin and constitute the critical weak spot in the capsule shielding, although some relief is given by the clustering of equipment racks on each side of the compartment. Each astronaut has a 45-degree field of view through windows placed in the cabin wall. A large "adapter" section is mounted between the second stage rocket and the main cabin. This adapter section is jettisoned shortly before reentry and must be considered as part of the shielding for normal operation.

The adapter section and heat shield subtend about 35 percent of the solid angle from a point midway between the two astronauts. The adapter section is basically a titanium and aluminum structure with a group of equipment and propellant storage tanks inside. A skin of about 0.13 gm/cm^2 of magnesium surrounds this structure.

The nose section subtends about 5 percent of the solid angle from the reference point given above. This section is covered with 0.4 to 1.1 gm/cm^2 of beryllium, the thickness varying with the location. The layer immediately

below is 0.3 gm/cm² of insulating material. Next is a 0.3 gm/cm² layer of titanium. Finally, a densely packed array of special equipment (drogue chute, orientation thrusters, etc.) is housed in the front end.

The two windows in the cabin are relatively small and affect the overall shielding only slightly for most parts of the body. The Gemini windows consist of outer, center, and inner panes. The thicknesses are 0.838, 0.965, and 0.559 centimeters, respectively. The center and outer panes are made of Corning "Vycor" 7900 high-temperature fused silica, and the inner pane is made of Corning 1723 tempered glass. The outer pane of the window is attached to the outer spacecraft skin and is essentially a heat shield. This thickness is sufficient to stop 84 Mev protons and 12 Mev electrons, and will heavily attenuate low-energy bremsstrahlung.

The conical surface section constitutes the sides of the spacecraft and subtends about 60 percent of the solid angle about the reference point and somewhat above 60 percent for the eye. The outside of this section is a 0.35 gm/cm² layer of Rene 41, a special heat-resistant alloy. The inner wall is the pressure vessel, and is composed of a double shell of titanium with a total thickness of 0.45 gm/cm². A low-density insulating material is sandwiched between the Rene and titanium, which has a thickness of about 0.15 gm/cm². The wall is sufficiently thin that an appreciable fraction of the external charged particles will penetrate. Equipment bays on both sides and underneath the astronauts increase the effective shielding thickness of several gm/cm² over about two-thirds of the conical surface section. The remaining one-third constitutes the "weak spot" in the Gemini spacecraft for radiation shielding. A large portion of this remaining third represents the hatch area.

III. THE GEMINI EXPERIMENTS

These experiments were performed to obtain precision measurements which could be applied to space-planning studies where an accurate prediction and interpretation of the biological effects produced in man would be of vital importance. Two tissue-equivalent ionization chambers and five highly sensitive passive dosimetry packages were flown aboard the Gemini-IV and Gemini-VI flights for the purpose of obtaining experimental values of instantaneous dose rate, accumulated dose, and shielding effectiveness. This experiment marked the first time that well-defined tissue dose and radiation survey measurements have been carried out in manned spaceflight operations.

The apogee and perigee for Gemini-IV were 297 kilometers to 157 kilometers. The apogee and perigee for the Gemini-VI were 311 kilometers to 161 kilometers. Gemini-IV had a mission time of 97.25 hours, and the duration of the Gemini-VI flight was 25.25 hours. Gemini-IV had an orbital inclination of 32.5 degrees; Gemini-VI had an inclination of 28.9 degrees.

The experiment was carried out using two distinct types of dosimeter systems. One system was active and required spacecraft power and telemetry, while the other consisted entirely of passive dosimeters. These detectors and the measurements obtained for each will be discussed separately.

Since these measurements were carried out under normal ambient conditions, the radiation environment consisted mainly of energetic protons and electrons from the inner Van Allen belt, which was encountered each time the Gemini spacecraft passed over the South Atlantic. In this region the radiation belt dips close to Earth because of the anomalously low strength of the Earth's magnetic

field. The instruments used in this experiment were optimized for the radiation levels that were anticipated in this geomagnetic anomaly region. In order to allow for measurement of the very low cosmic radiation intensities encountered outside of the anomaly, the dynamic range of the instrumentation was extended for detection of all energy-deposition rates above the level of 0.1 millirad/hour.

Calibration of the active dosimeters consisted of a vigorous, many-phased program to determine (1) the radiation input-to-output voltage-transfer functions for protons, electrons, and photons, (2) the radiation response time at various radiation levels, and (3) temperature-time effects on the calibration curves. The initial calibration was performed 90 days before launch, using cesium-137 and cobalt-60 gamma sources.

Duplicates of the flight instrument were also calibrated using 40 Mev and 57.8 Mev protons of various beam diameters and intensities to obtain proton calibration curves and directional responses. Similar calibration and response data were gathered using 3.0, 2.0, 1.0, and 0.5 Mev electrons. These data were compared with the photon calibrations obtained using cesium-137 and cobalt-60. The calibrations obtained with these different sources were identical with each other within the experimental error, which was not greater than 10 percent in any of the calibration.

One ionization chamber was mounted on the left hatch of the spacecraft with the other being mounted in a symmetrical location on the other hatch. The location of those detectors is shown in Figures 1 and 2. The output from each instrument was recorded continuously throughout the flight. Each instrument was capable of recording dose rates between 0.1 millirad/hour and 100 rad/hr. The active dosimeters also have an advantage in that their instantaneous outputs may be integrated to determine the total accumulated dose, for purposes of comparison with the passive dosimetry portion of the experiment.

The active portion of the experiment is discussed most conveniently in terms of two general areas: (1) experimental determination of the dose levels obtained outside of the South Atlantic anomaly region, and (2) measurement of the radiation characteristics during spacecraft passage through the inner radiation belt.

Cosmic Radiation Dose Measurements

Outside of the South Atlantic anomaly region, the principal contribution to the dose was from cosmic radiation. The average dose rate was obtained every 3.2 seconds for each revolution. The average dose rate for all "non-anomaly" revolutions analyzed here was found to be 0.15 millirad/hr.

Since the revolutions selected for analysis cover the entire span of the Gemini missions, the average dose rate presented may be readily extended to obtain excellent approximations of the total integrated dosage for the complete missions. The total integrated dosage resulting from cosmic radiation during the Gemini-IV and Gemini-VI missions was approximately 3.7 millirad/day.

During a portion of Revolution 3 and during the period of astronaut egress, the right hatch remained open and exposed one dosimeter to an essentially external space-radiation environment. The radiation levels measured by the other instrument during this time never exceeded those obtained by the exposed unit. This indicates clearly a total absence of soft-trapped radiation in those

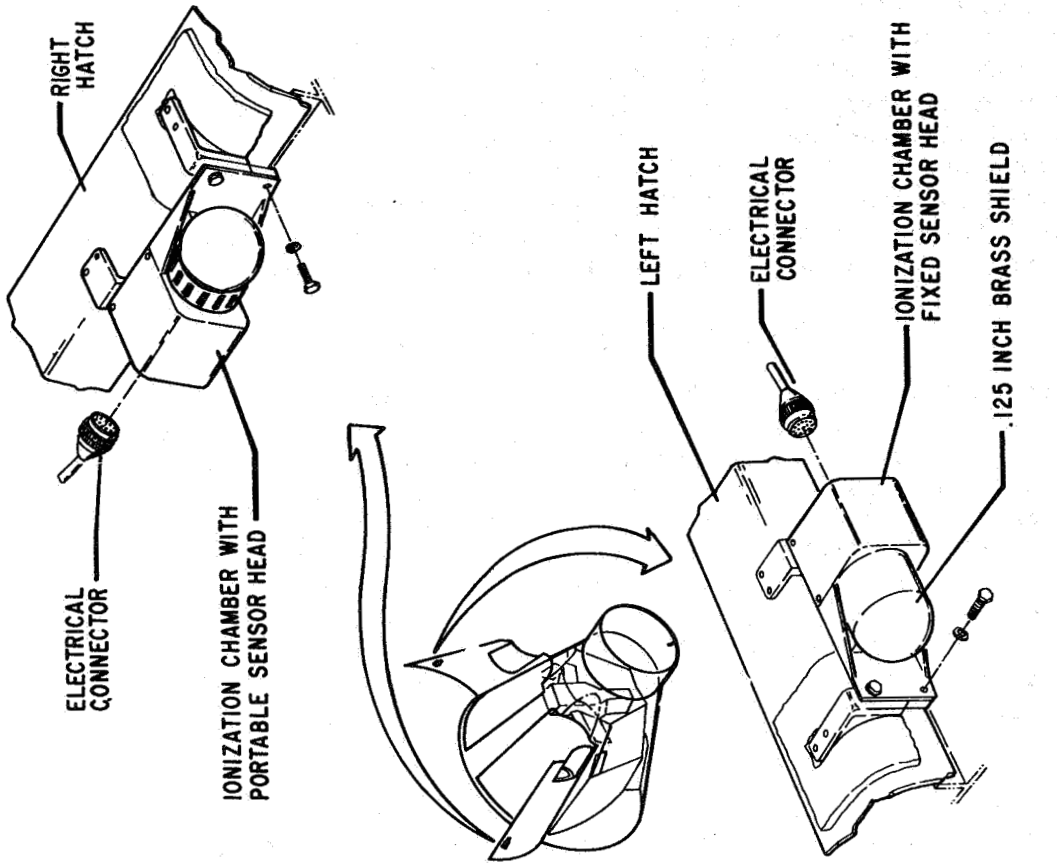


Figure 2. Location of Hatch-Mounted TEICs: Gemini-VI

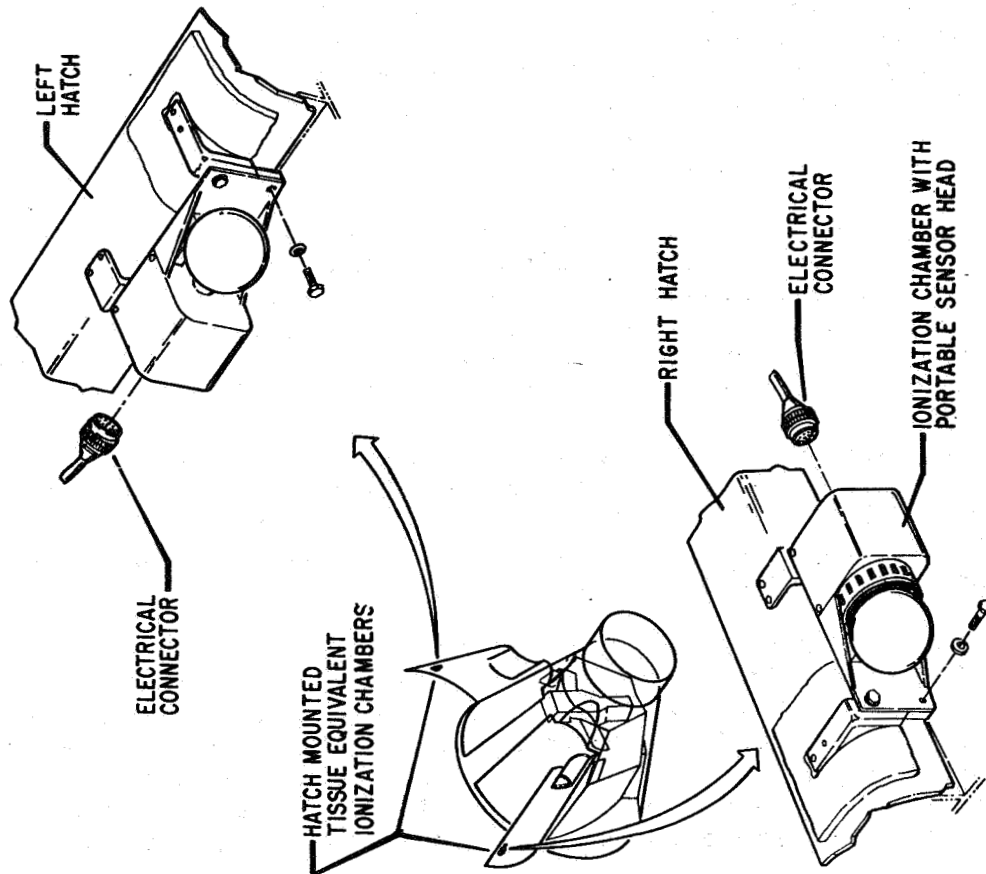


Figure 1. Location of Hatch-Mounted TEICs: Gemini-IV

regions of space where the astronaut was extravehicular. Figure 3 illustrates the cosmic radiation dose rate profile as a function of orbital elapsed time and corresponding L-shell values for Revolution 45. These profiles indicate a buildup to approximately 0.5 millirad/hour at higher L values, and a rapid drop below 0.1 millirad/hour at lower L values near ~ 1.0 earth radii. This effect is consistent with the predicted magnetic cutoff values encountered by the Gemini spacecraft. Since the spacecraft traversed only the lower geomagnetic latitudes, dosage was less than the free-space value, which nominally runs as high as 14 millirad/day during solar minimum.

Anomaly Region Dose Levels

Dose rate data obtained from the South Atlantic anomaly Region show a rapid and pronounced rise in magnitude over the cosmic radiation levels. The "anomaly" dose rate experienced during Revolution 7 of Gemini-IV, for example, rises two orders of magnitude to more than 100 millirad/hour. Figures 4 and 5 indicate the dose rate levels recorded by the two active dosimeters within the Gemini-IV spacecraft for revolutions 36 and 52. Figure 6 illustrates similar results from revolution 7 of Gemini-VI. The peak dose rate observed on Gemini-IV was 107 millirad/hr on revolution 7, while Gemini-VI experienced 62 millirad/hr on the 7th revolution of its flight. A summary of the total observed mission dose obtained by time integrating contributions from all space radiation sources is shown in Table III.

Figures 7 and 8 illustrate the spatial extent of the experimental iso-dose contours at two altitudes in the anomaly region for the Gemini-IV spacecraft, these contours representing data compiled by taking the highest reading from either ion chamber. Note that where experimental contour information was not available due to the orbital inclination (32.5°) the contours have been mirrored to connect with the measured data and to be consistent with the known extent of similar flux contours.

IV. PASSIVE DOSIMETRY

Five passive dosimetry packages were placed aboard the Gemini-IV and Gemini-VI spacecrafts at points of maximum, minimum, and intermediate shielding. Each passive dosimetry package contained the following dosimeters: photoluminescent glass, lithium fluoride, and calcium fluoride thermoluminescent dosimeters, discharge ionization chambers, nuclear emulsions, activation foils, and disks of cellulose nitrate plastic.

The passive dosimetry system consisted of five small aluminum canisters, 1/32 inch thick. Each unit was hermetically sealed and contained the detectors previously described. The units were placed at five selected locations within the spacecraft cabin. Slightly different configurations were used for Gemini-IV and for Gemini-VI.

The five passive dosimetry packages located in the spacecraft cabin were designed to ascertain both total accumulated dose and the type of radiation causing it. These packages were located at the shielding locations shown in Figures 9 and 10. Package 1 was mounted near the Type I active dosimeter to provide a comparison between the dose measured by the passive unit and the dose obtained by integrating the ionization chamber data over the total measurement time. Three other passive units were

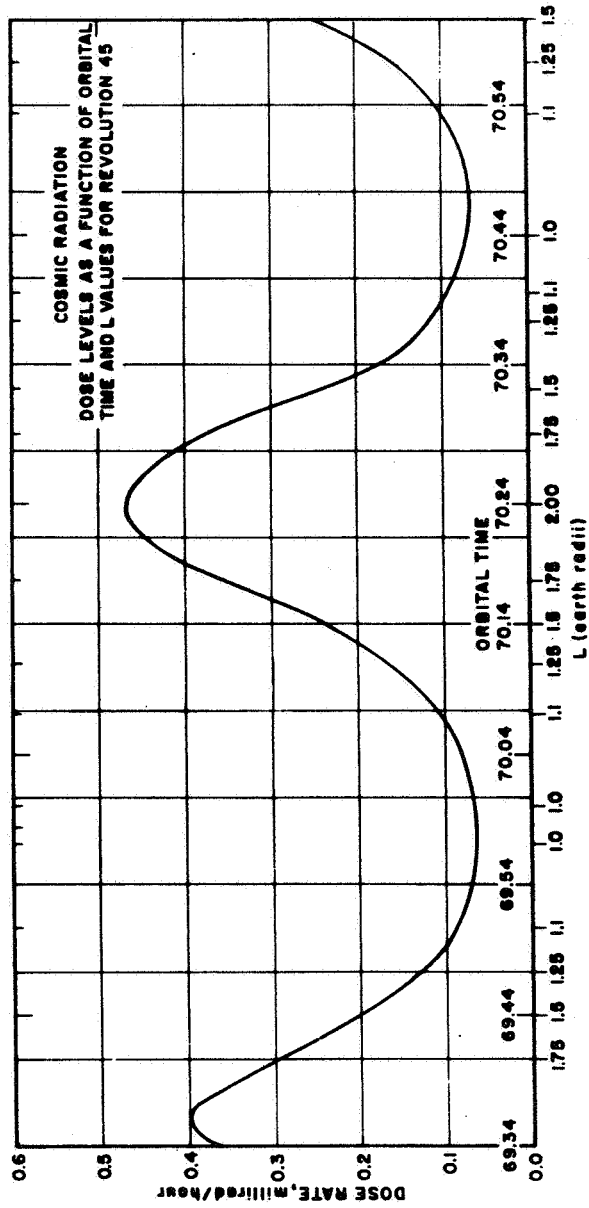


Figure 3. Cosmic Radiation Dose Levels Within Gemini-4
As a Function of Orbital Time and L Values
For Revolution 45.

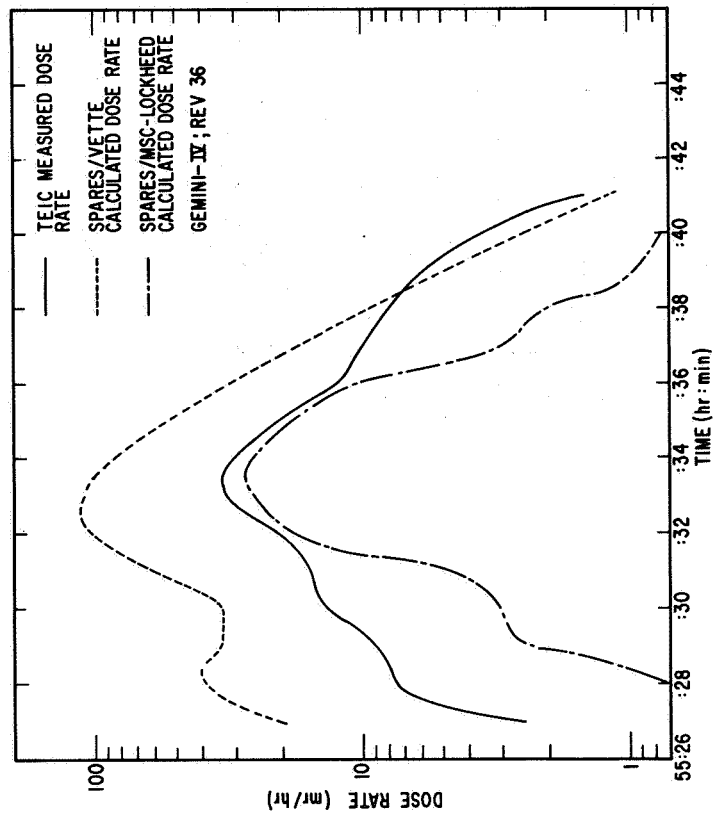


Figure 4. Orbit 36 - Measured and Calculated Dose Rate Compared

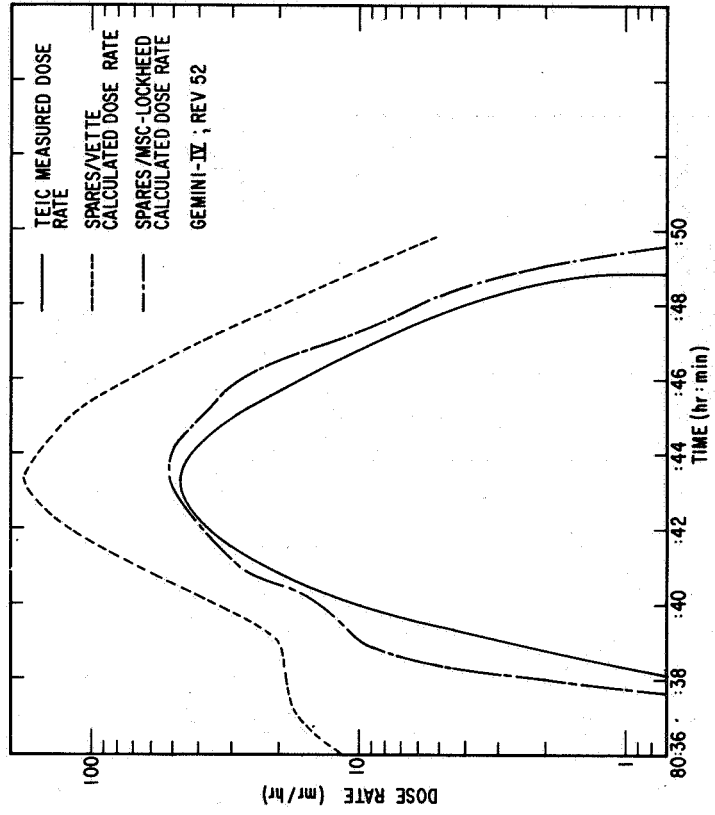


Figure 5. Orbit 52 - Measured and Calculated Dose Rate Compared

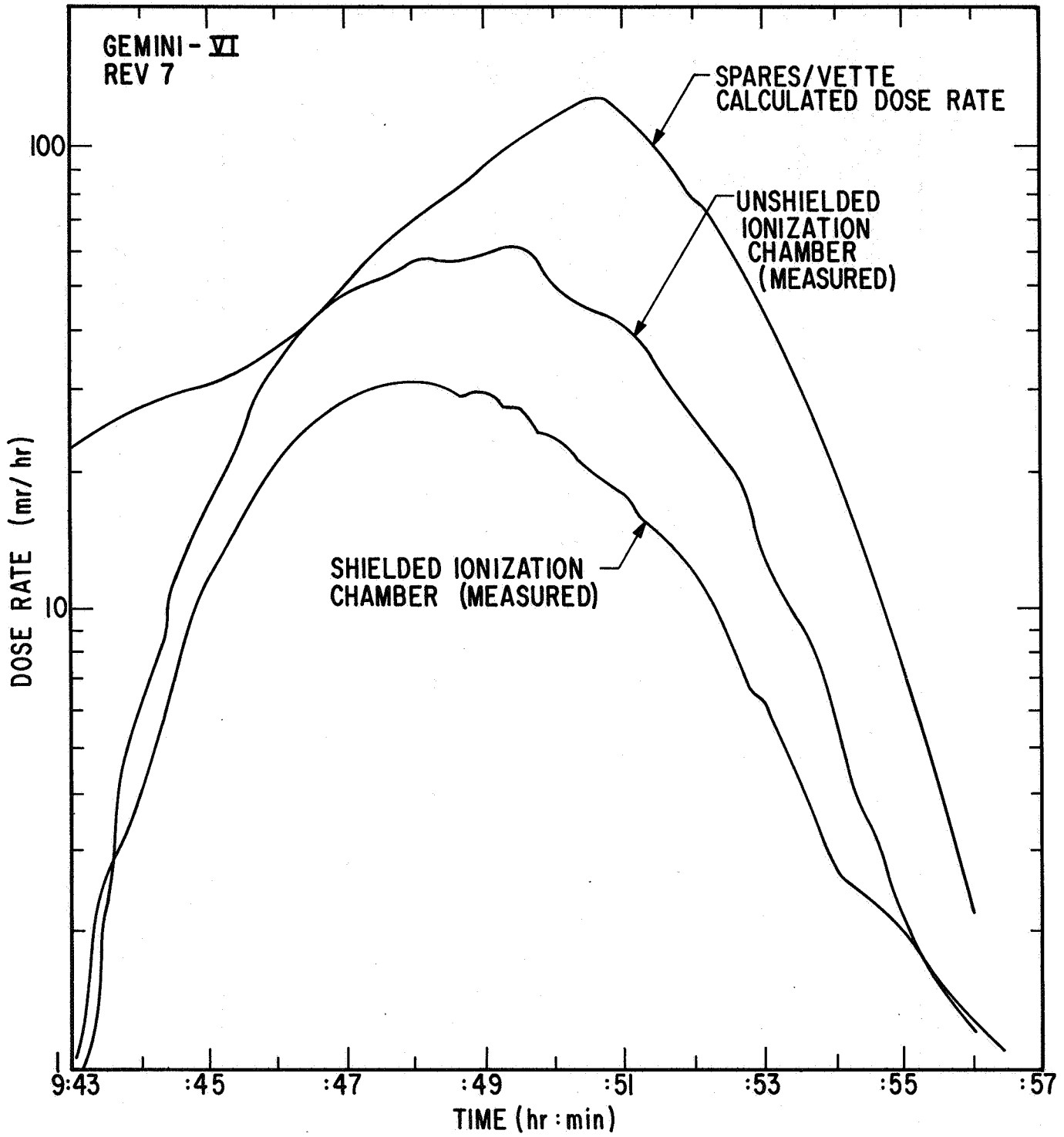


Figure 6. Orbit 7 - Measured and Calculated Dose Rate Compared

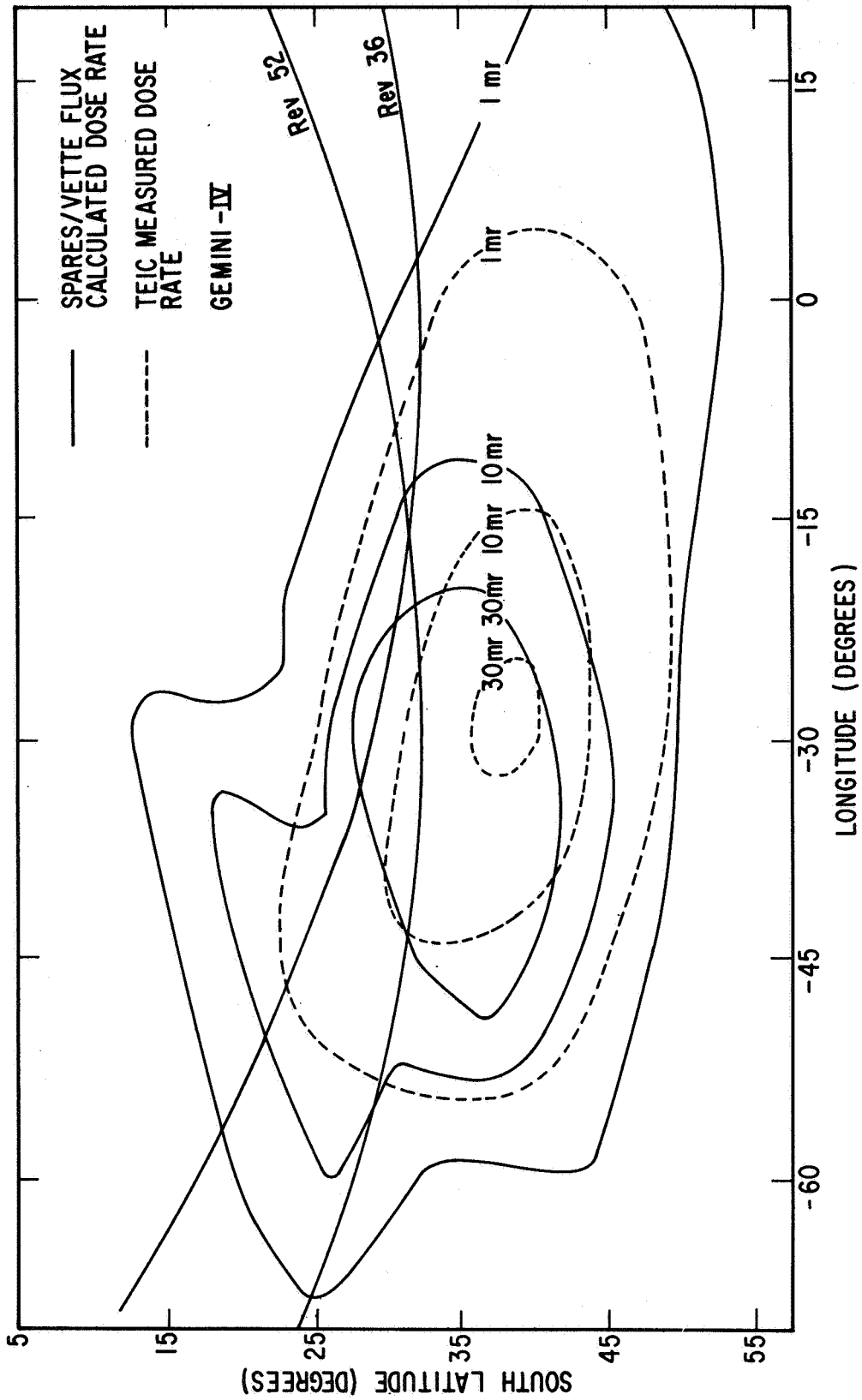


Figure 7. Isodose Contours at 200 km in the South Atlantic Magnetic Anomaly

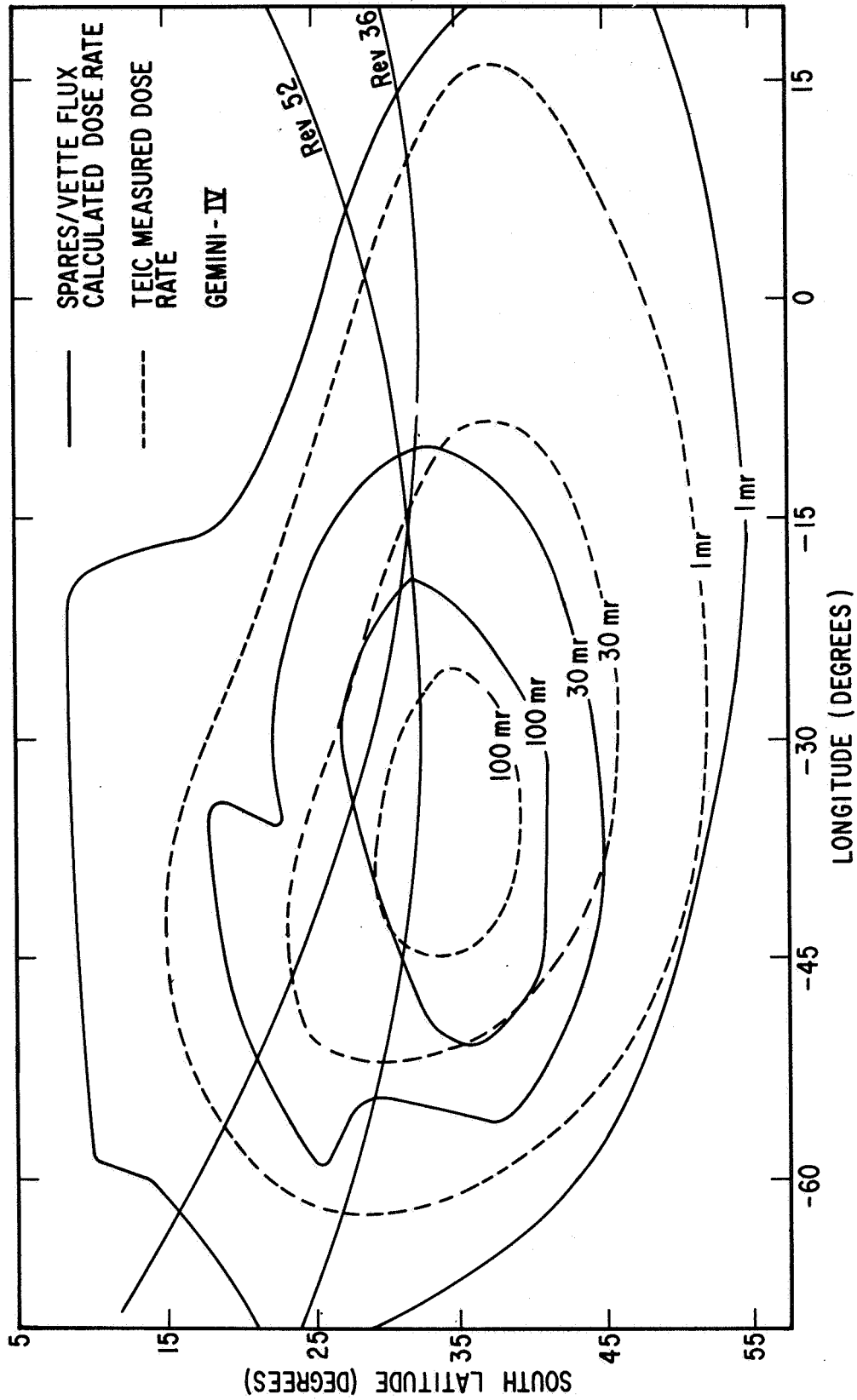


Figure 8. Isodose Contours at 300 km in the South Atlantic Magnetic Anomaly

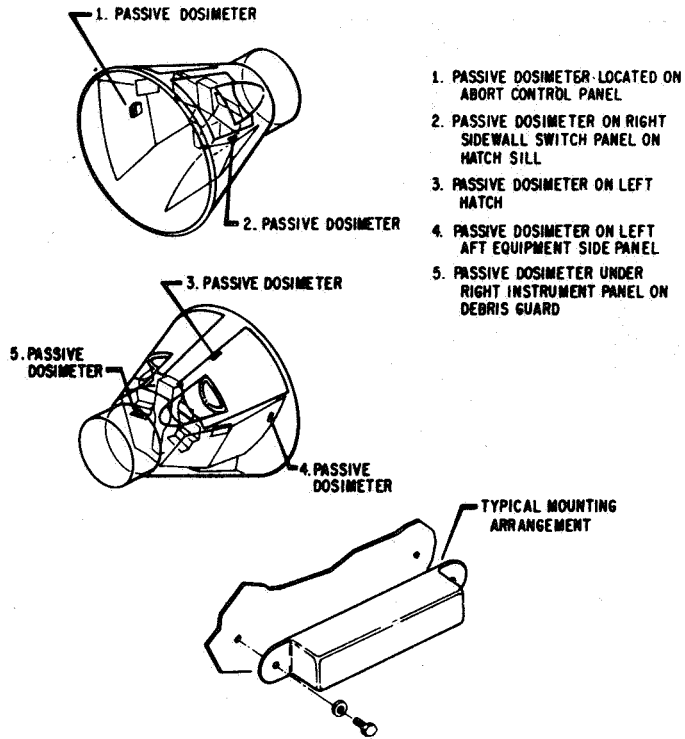


Figure 9. Mounting Locations of the Five Passive Dosimetry Canisters Aboard Gemini-IV

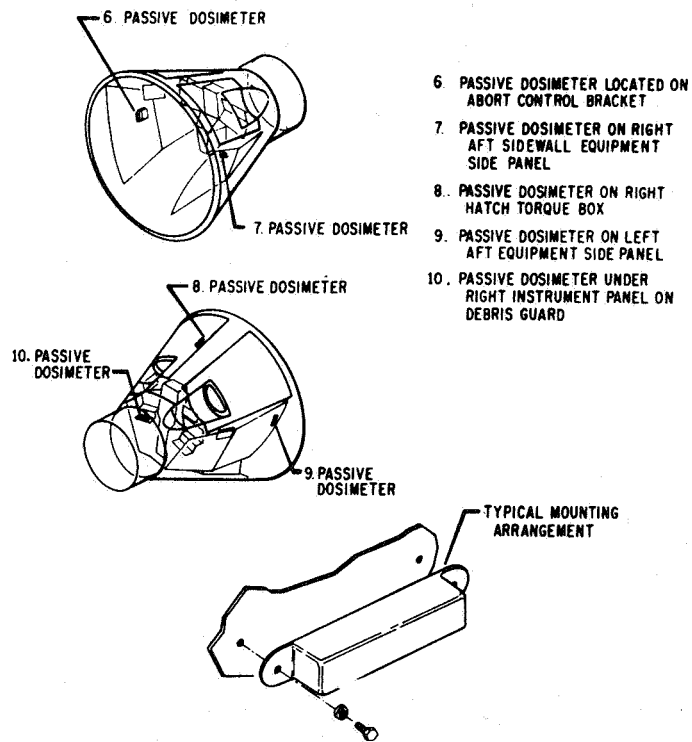


Figure 10. Mounting Locations of the Five Passive Dosimetry Canisters Aboard Gemini-VI

located at points of intermediate shielding, and a fourth unit was placed on the debris guard beneath the instrument panel, an area of heavy shielding. A summary of the passive dosimetry results is presented in Tables I and II.

Because of the close packing required, the self-shielding of each dosimeter by all of the other dosimeters within the aluminum housing cannot be neglected. Only dosimeters which were capable of detecting doses lower than those recorded on the Gemini-IV flight were placed aboard Gemini-VI. Since these canisters contained fewer dosimeters, the self-shielding effects were somewhat reduced. No corrections to the final data have been applied to compensate for self-shielding effects.

Toshiba glass* registered low readings compared to other dosimeters in the same canister. The Toshiba readings aboard Gemini-VI were not above the minimum threshold levels of this system, and hence were not statistically significant. The consistently low readings from the Gemini-IV Toshiba glass is, in part, a result of shielding by other passive dosimeters within the same package.

Dose comparison between the two lithium isotopes in the lithium fluoride dosimeters indicates that within the limits of the experimental error, which is about 20 percent of the doses received, no neutron dose occurred. This lack of neutrons was further substantiated by the activation foils. This result is reasonable in that the only neutrons expected would come from secondary radiation produced by the interaction of high energy protons with the spacecraft and its occupants. Analysis of the emulsions further substantiates the lithium-fluoride results.

The emulsion packs** indicated that over 90 percent of the tracks were caused by protons, with only residual electron, alpha, and heavy particle tracks. Nuclear disintegrations and neutron recoils were negligible when compared to the entire track count. The electron population in the flown emulsions was not statistically different from the ground controls. Less than 2 millirads of emulsion dose were caused by particles other than protons. These results are consistent with the readings obtained from the emulsion packs within each astronaut's suit.¹

The readings of the shielded and unshielded calcium fluoride dosimeters are very similar. This is significant because the charged particle response of these shielded and unshielded dosimeters is quite different and is marked by a rather distinct low energy cutoff to both protons and electrons. The sensitivity to a given energy electron below about 1.5 Mev is dissimilar because the shielded detector would record only bremsstrahlung in a field consisting exclusively of electrons. If an appreciable number of low-energy electrons had penetrated into the dosimetry package, there would have been a distinct difference in the readings of the shielded and unshielded calcium fluoride dosimeters. No such difference was found. It

*The Toshiba Glass was supplied and evaluated by Miss C. Menkes of the Naval Radiological Defense Laboratory.

**The emulsion packs were supplied and evaluated by Dr. H. Schaefer of the U.S. Naval Aerospace Medical Institute.

could be argued that a sizable distribution of both protons and electrons existed which combined to produce equivalent results. It is extremely doubtful that a set of circumstances prevailed where the proton spectrum within the spacecraft exactly offset the supposed electron contribution. Further, the emulsion clearly shows that the vast majority of the charged particles were protons, and that most of these protons were above 20 Mev.

The calcium fluoride devices have proton cutoff energies of about 7 and 21 Mev, which would have resulted in a low reading if a significant number of low-energy protons had been present. Comparison with the emulsion energy deposition distributions shows that most of the protons were energetic enough to be above the attenuation points of the calcium fluoride shields. No significant number of electrons were present within the aluminum housing around the aggregate of the individual dosimeters. However, electrons may have penetrated to some degree within the spacecraft cabin which did not penetrate the individual dosimeters.

The cellulose nitrate plastic and associated emulsions were processed and examined with an optical microscope.² About 10 tracks/cm²-day were found in the plastic detectors. Most of these were judged to be tracks of heavy recoil ions. Approximately 1 track/cm²-day was estimated to be from the primary cosmic radiation. These were the longest tracks found and were too long for recoils. Such tracks may be the result of heavy particles, such as the C, N, O group, that have been highly degraded in energy by the material of the spacecraft. They could also result from relativistic particles with an atomic number greater than 26.

When the self-shielding of all the dosimeters is considered, the differences in readings between individual dosimeters within the same dosimetry package are certainly within the statistical error and the varied charged particle energy deposition mechanisms which are characteristic of each detector.

The general trend of decreasing total dosage with increasing overall shielding was expected and is evident from the data in Tables I and II. The variation in dose with location in the spacecraft was not as pronounced as had been originally anticipated. This may be attributable to the flux maps upon which the first estimates had been based, and to considerable pre-attenuation of the low-energy particles by the spacecraft itself. Dosimeters 1, 4, 6, and 9 were least heavily shielded and were significantly exposed to the conical portion of the spacecraft mentioned previously. Numbers 2, 5, 7, and 10 were heavily shielded by both the spacecraft equipment and the astronauts. Dosimeters 3 and 8 were at points of intermediate shielding.

Although the results obtained from this experiment are not astronaut doses, they are quite consistent with the data obtained from the dosimetry which was placed within the spacesuit of each astronaut.³ The associated emulsion results have been published elsewhere.^{4,5} It should be noted that the total mission dose obtained by integrating the output from the ionization chambers is higher for both missions than that which was recorded in the passive dosimetry packs. Since wall thickness of the ionization chambers was slightly less than the total shielding of the passive dosimetry units, results of this type were logically expected.

Table I. Summary of the Passive Dosimetry Results Aboard Gemini-IV
Spacecraft* (Location: Figure 9)

| Dosimeters | 1 | 2 | 3 | 4 | 5 |
|---------------------------|----------------|----------------|----------------|----------------|----------------|
| Li ⁶ F | 50 \pm 10 | --- | 44 \pm 19 | --- | 53 \pm 18 |
| Li ⁷ F | --- | 52.5 \pm 19 | 43 \pm 12 | 50 \pm 14 | 59 \pm 14 |
| CaF ₂ : | | | | | |
| Unshielded | --- | 49.4 \pm 6.1 | --- | 57.9 \pm 6.5 | 49.4 \pm 4.7 |
| Unshielded | 54.7 \pm 7.0 | 47.1 \pm 4.1 | 55.3 \pm 5.4 | 55.7 \pm 5.1 | 48.5 \pm 6.1 |
| Shielded | 53.6 \pm 5.7 | 48.9 \pm 3.8 | 49.0 \pm 3.8 | 55.9 \pm 5.9 | --- |
| Pocket ionization chamber | 73 \pm 5.1 | 45 \pm 2.3 | 46 \pm 3.2 | 54 \pm 3.8 | 47 \pm 3.3 |
| Toshiba glass:** | | | | | |
| Unshielded | 52 \pm 23 | 27 \pm 15 | 42 \pm 20 | --- | 37 \pm 18 |
| Shielded | 37 \pm 18 | 17 \pm 12 | 37 \pm 18 | --- | 12 \pm 10 |
| Emulsion*** | 68 | --- | --- | --- | 35 |

*With the exception of the emulsion, all readings in this table are in milliroentgens equivalent exposure.

**The Toshiba glass was calibrated using Co⁶⁰; all other calibrations used Cs¹³⁷.

***The emulsion readings are in millirads. The error is less than 5 percent.

Table II. Summary of the Passive Dosimetry Results Aboard Gemini-VI
Spacecraft* (Location: Figure 10)

| Dosimeters | 6 | 7 | 8 | 9 | 10 |
|---------------------------|----------------|----------------|----------------|----------------|----------------|
| CaF ₂ : | | | | | |
| Unshielded | 19.9 \pm 2.0 | 14.2 \pm 1.8 | 20.7 \pm 2.3 | 21.9 \pm 2.4 | 13.0 \pm 1.5 |
| Unshielded | 20.2 \pm 2.1 | 13.7 \pm 1.7 | 20.3 \pm 1.9 | 18.8 \pm 2.0 | 13.7 \pm 1.8 |
| Unshielded | 20.1 \pm 2.2 | 14.3 \pm 1.9 | 18.2 \pm 2.0 | 21.0 \pm 2.1 | 14.9 \pm 1.8 |
| Shielded | --- | 14.1 \pm 1.8 | 19.0 \pm 1.8 | 20.8 \pm 2.1 | 13.7 \pm 1.7 |
| Pocket ionization chamber | 18.5 \pm 1.3 | 10.5 \pm 1.0 | 18.5 \pm 1.4 | 22.5 \pm 1.6 | 14.5 \pm 1.4 |

*All readings in this table are in milliroentgens equivalent exposure.

V. THEORETICAL CALCULATIONS

The theoretical results presented in this paper have been generated using the AFWL SPARES computer codes.⁶ These codes have been designed to predict, before the fact, the space radiation dose to be received inside a specified vehicle flown on some mission of interest. Briefly, the calculation includes defining the radiation environment to be experienced on the mission (both within and without the geomagnetic field), describing the shielding to be afforded by the space vehicle and the inherent astronaut shielding about some dose point of interest, and finally transporting the environment through the vehicle, calculating the dose at the specified point including any secondary radiations created by the primary radiation interaction with the vehicle.

VI. GEMINI DOSE CALCULATIONS

The dose calculations for the Gemini vehicle generally follow the outline described above. The spatial position versus flight time profile data (ephemeris) was obtained using NASA-furnished tracking information. The radiation environment was defined using the ephemeris data as input to the McIlwain magnetic field fit code which returns the magnetic field (B) and the L-shell parameter (L) along the orbital path. This was, in turn, used to calculate omnidirectional proton and electron fluxes using the Vette AP1-4 proton mappings and the AE2 electron mapping respectively.⁷ The electron fluxes were decayed using the energy independent mean life decay factors of Bostrom and Williams which are a function only of the L-shell considered.⁸ The magnetic field fit parameters used were those formulated by Jensen and Cain and with which the Vette flux mappings have been normalized.⁹ The vehicle sectoring information (shielding) used was that originated by the McDonald Co., the details of which remain classified.¹⁰ The shielding afforded by both astronauts and the vehicle were employed in defining the material type and thickness along 720 radials representing equal solid angles (sectors). A total of seven material types were considered. The types of radiation contributing to the calculated doses reported in this paper include only the penetrating proton and electron fluxes, with no treatment being given to any secondaries produced by these. For these missions any secondary radiations, produced by the primary flux interaction with the vehicle, contribute a negligible amount to the dose.

The radiation transport models were then used to calculate the dose, considering each sector as a small spherical shield having the appropriate material types and thicknesses on which is incident the omnidirectional fluxes. A dose was then calculated for each sector; with the total dose for the vehicle obtained by using the formula

$$\text{Vehicle Dose} = \sum_{i=1}^N \phi_i D_i$$

where ϕ_i = Solid angle for sector $i/4\pi$ Steradians

D_i = Dose calculated for sector i (Rad)

N = Total number of sectors.

The proton radiation which travels approximately in straight lines in traversing the vehicle was handled using the well established range/energy

relations, while the electrons which are subject to large scattering interactions are treated using results from a one-dimensional Monte Carlo Model.

Using the above methodology the dose due to the inner belt radiations was calculated for each pass through the magnetic anomaly region and summed to obtain total mission dose. Cosmic ray doses have been calculated using¹¹:

$$\text{Dose} = \int_{\text{time}} [0.54(L(t)-1) + 0.072] dt \quad (1 < L < 2.5)$$
$$\text{or} = \int_{\text{time}} 0.88 dt \quad (L > 2.5)$$

A comparative summary of the results obtained using the above calculational techniques and the experimental active and passive dosimetry, for the Gemini-IV and VI missions, is presented in Table III.

Specific Dose Comparisons

A complete analysis of the dose rate time history for each anomaly pass has been determined and is reported elsewhere.¹⁴ It will be the purpose of this paper to compare the experimental TEIC and theoretically calculated dose rates for Revolutions 36 and 52 of Gemini-IV, for which physical spectrometry data has recently been published.¹⁶ This physical spectrometer measured both electrons ($0.4 > E > 4.5$ Mev in 7 channels) and protons ($25 > E > 80$ Mev in 5 channels). The time history flux profile from this instrument while traversing the anomaly region compared to fluxes calculated using the Vette maps is shown in Figures 11 and 12 for these two revolutions. A similar comparison of the measured electron and proton spectral shape with that calculated using the Vette maps for the time where peak experimental fluxes were observed is shown in Figures 13 through 16.

Using this physical spectrometry data a comprehensive comparison may be made with TEIC measurements for these passes calculating the dose rate, first using the Vette flux predictions with the SPARES radiation transport models, and second, determining the dose rate using the on-board measured environment in conjunction with these same transport models. This comparison is illustrated in Figures 4 and 5 for the two Gemini-IV passes and for a typical pass of Gemini-VI in Figure 6. Experimental and calculated isodose rate contours on mercator projection maps at 200 and 300 Km for Gemini-IV are summarized in Figures 7 and 8.

VII. THE WL-304 EXPERIMENT

The WL-304 probe was one of the early experiments to measure the physical radiation environment of near-earth space, while simultaneously measuring the dose rate. Launch occurred on 9 June 1965 from Cape Kennedy.

The proton spectrometer consisted of a solid state detector and scintillator array; it determined the incident spectra by pulse height analysis into 9 channels from 1 to 200 Mev. An integral rate above 260 Kev and 1 Mev was also provided. The electron spectrometer was a telescope and consisted of an array of 4 solid state detectors. Incident electron integral spectra from 0.5 to 3 Mev were determined by 10 channel pulse height analysis. The

Table III. A Summary of Experimental and Calculated Mission Dose for the Gemini IV and VI Space Flights

| VEHICLE | RADIATION SOURCE | MISSION DOSE (MRad) | | |
|--------------------|--------------------------|---------------------|---------|------------|
| | | EXPERIMENTAL | | CALCULATED |
| | | ACTIVE | PASSIVE | |
| GEMINI-IV | Trapped [†] | 67 ± 7 | - | 228.4 |
| | Cosmic Ray ^{††} | 15 ± 5 | - | 9.2 |
| TOTAL MISSION DOSE | | 82 ± 9 | 59 ± 6 | 237.6 |
| GEMINI-VI | Trapped [†] | 16 ± 2 | - | 42.8 |
| | Cosmic Ray ^{††} | 5 ± 2 | - | 2.4 |
| TOTAL MISSION DOSE | | 21 ± 3 | 20 ± 2 | 45.2 |

[†] Dose contribution from anomaly passes only.

^{††} Represents cosmic ray dose integrated over mission duration.

Table IV. Dose Comparison for the WL-304 Space Probe[†]

| Dose Information | Peak Dose Rate (Rad/hr) | Integrated Dose (Rad) |
|------------------|-------------------------|-----------------------|
| Experimental | 13 ± 1.3 | 3.27 ± .3 |
| Calculated | 13.98 | 4.87 |

[†] Note this data summarizes only the first pass through the inner radiation belt.

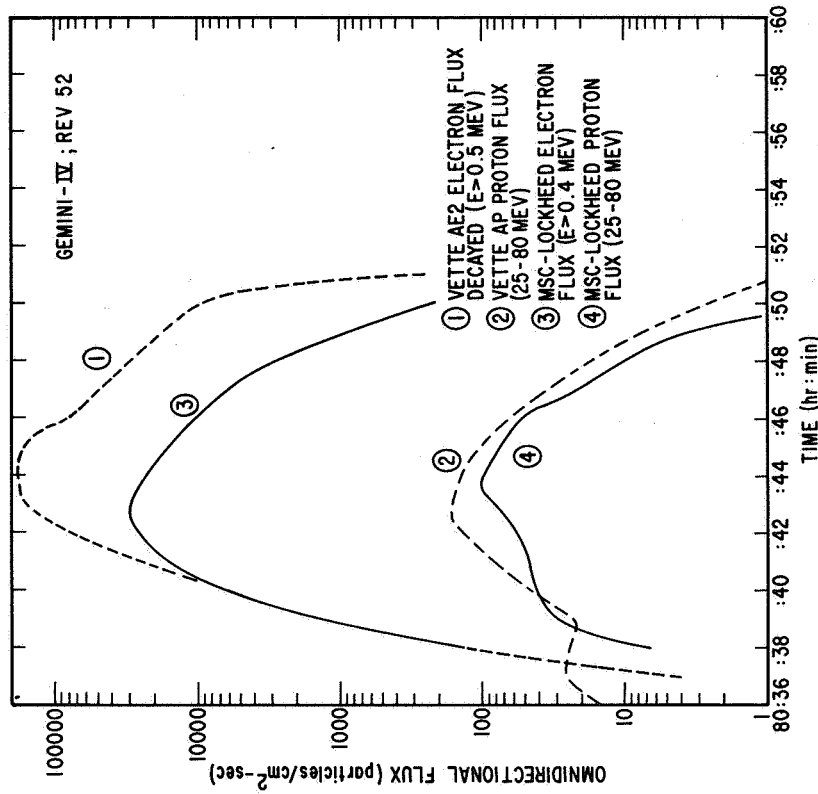


Figure 12. Orbit 52 - Measured and Calculated Omnidirectional Fluxes

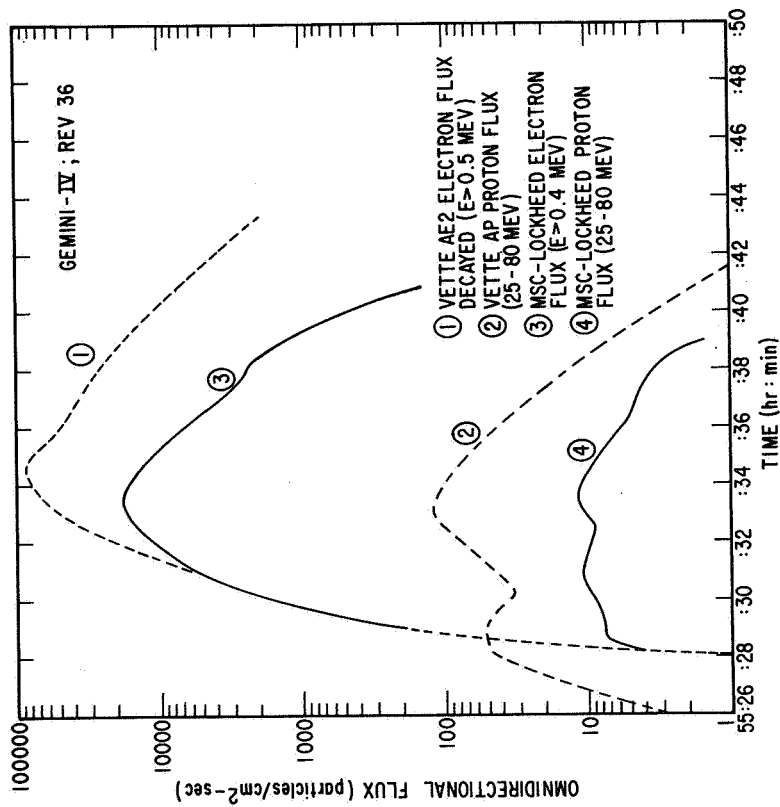


Figure 11. Orbit 36 - Measured and Calculated Omnidirectional Fluxes

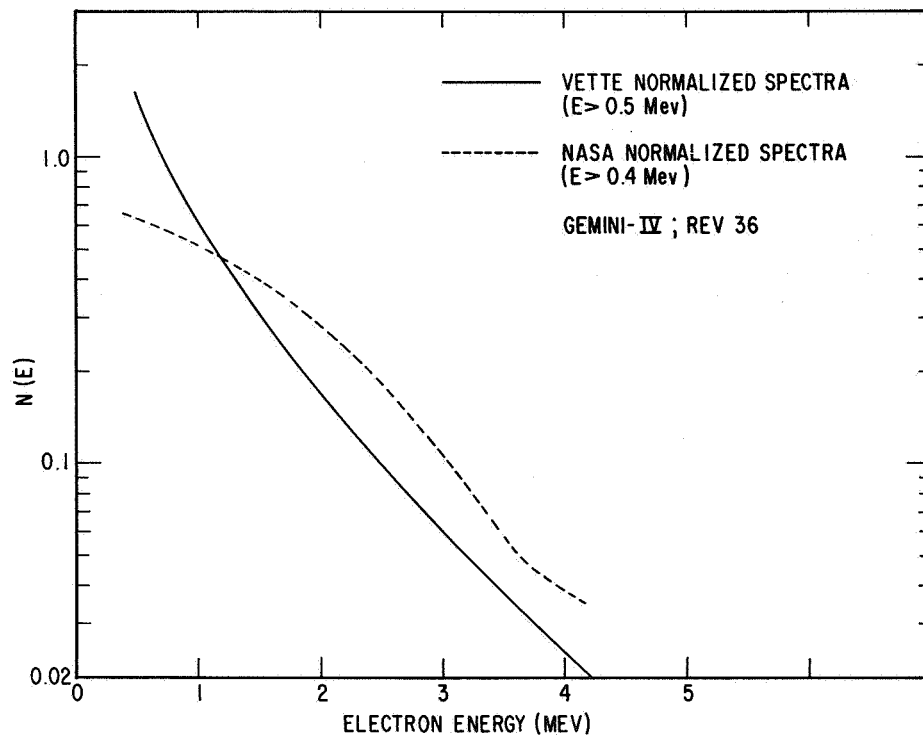


Figure 13. Orbit 36 - Peak Flux Electron Spectra Compared

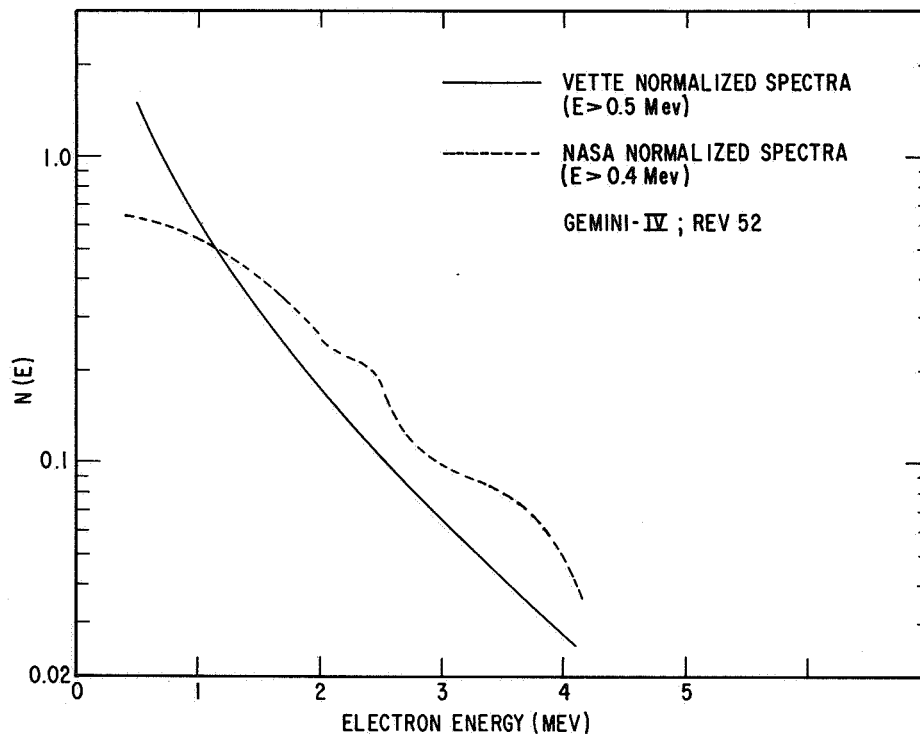


Figure 14. Orbit 52 - Peak Flux Electron Spectra Compared

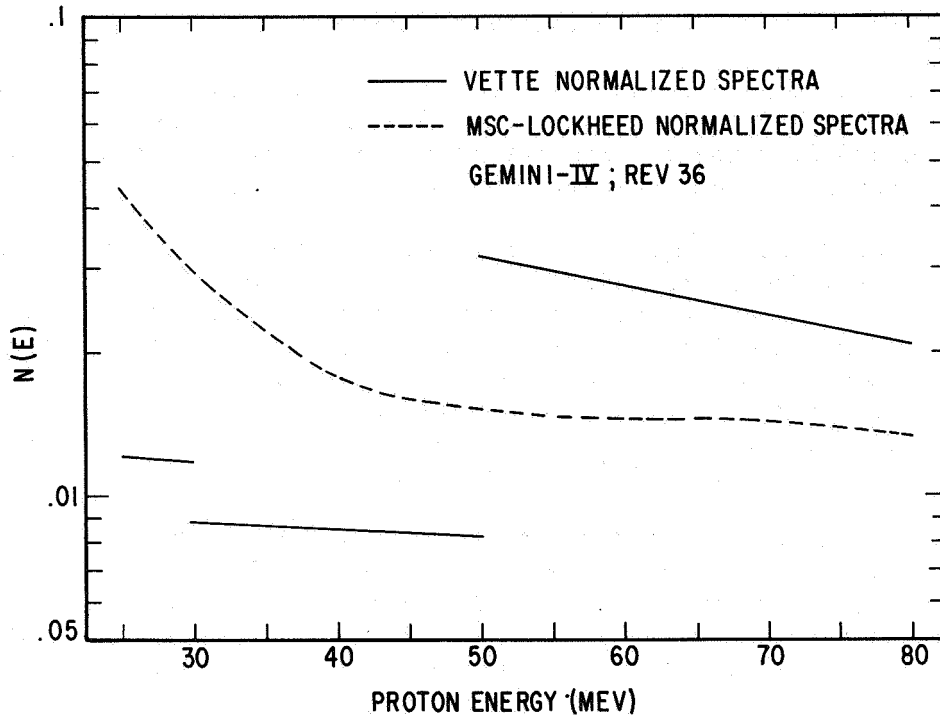


Figure 15. Orbit 36 - Peak Flux Proton Spectra Compared

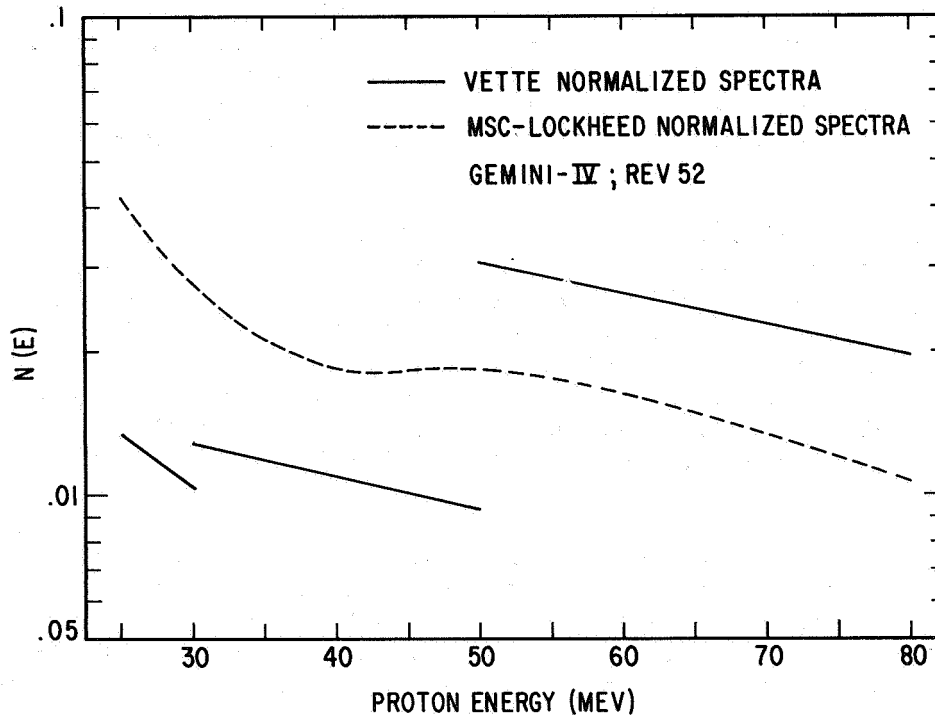


Figure 16. Orbit 52 - Peak Flux Proton Spectra Compared

anticoincidence function of the telescope was also transmitted to the ground and served as a check on the proton telescope.

Biophysical information was provided by a tissue-equivalent ionization chamber. The chamber was set to measure from 10 mrad to 500 rad per hour and was shielded from the environment by the 0.1 inch fiberglass skin of the payload and the 0.4 gm/cm² wall of the ionization chamber.

The probe contained a highly sophisticated housekeeping system. A triaxis magnetometer provided information on magnetic field and orientation in space; two voltage and current calibration points were provided; and the temperatures were monitored at five locations in the payload. A failure occurred when the batteries became so cold they could no longer supply power needed to operate the telemetry. Warming, which occurred later in the flight, restored power and allowed data to be collected. It should be noted that no performance degradation of the instrumentation was observed after power was restored.

The flight path of this probe took it from a Cape Kennedy launch to a crossing of the magnetic equator at an altitude of 4787 n.m. (.0209, 2.46, 6° s, 24.9° w),** reaching a maximum altitude of 9254 n.m. (.0069, 4.39, 83.0° e) where the last useable data was recorded. The total flight time was 4 1/2 hours. The probe returned simultaneous environment and dose data for both the inner and outer radiation zones.

VIII. WL-304 DOSE CALCULATIONS

The dose calculations for the WL-304 probe parallel very closely those performed for the Gemini vehicle. The environmental models, magnetic field description, and transport models used were the same; however, the vehicle sectoring information was generated with an AFWL version of the NASA MSC sectoring code modified to yield both material type and thickness along radials converging to the dose point.¹² This code describes the vehicle using five basic shapes (hexahedron, cone, cylinder, sphere, and hemisphere) allowing for both positive and negative shields where hollowed out regions are required.

The shielding afforded by the probe at the position of the ionization chamber was described using this code with a total of 25 shields and five material types. Again, 720 radials representing equal solid angles were used. The vehicle contained two shelves; the top one containing the ion chamber and physical spectrometers, with the shelf below this housing several gm/cm² of electronics and batteries. Above the ion chamber was only a thin fiberglass casing. With this shielding configuration, over 30% of the total solid angle subtended by the chamber had thickness from 0.5 to 1.0 gm/cm².

Here again, a dose rate calculation has been made using the Vette radiation environments in conjunction with SPARES radiation transport models. A summary of this information as it relates to the ionization chamber readings is presented in Figure 14, with a brief comparison of the peak dose rate and total dose for the probes first pass through the inner belt being shown in Table IV.

** $(B \text{ (gauss)}, L \text{ (earth radii)}, \text{Latitude (degrees)}, \text{Longitude (degrees)})$

There are limitations presently inherent in the calculational models to be kept in mind when considering the results presented here. First, although the AE2 electron map is defined for $1 < L < 6$ the exponential decay factor is calculated only in the region $1 < L < 3$. This limitation is reasonable, however, since the decay factor applies to electrons resultant from the starfish nuclear detonation which injected electrons for $L \leq 3$. Second, the API-4 proton mappings are defined only in the region $1 < L < 3$, so that any possible proton contribution is not evident for regions where $L > 3$. Note that the inner radiation zone is roughly defined as that region for which $L \leq 3$. Since there is no medium to high energy model proton environment for the outer belt at this time, the calculated dose rates for the WL-304 probe in the outer belt do not include a proton contribution.

IX. CONCLUSIONS

To fully understand the discussion of the comparison of the measured and calculated dose rate and dose for the Gemini flights, it is mandatory to first examine, in detail, the radiation environment responsible for these doses. It should be emphasized that the Gemini flights were conducted at low altitude intersecting the inner radiation zones only at its fringes where the radiation mappings have their most uncertainty. In fact, it may be necessary to include also the geographic coordinates as well as the "B, L" parameters to accurately determine the flux at these altitudes, since a definite east-west asymmetry of the fluxes in the anomaly region has been observed.^{16,17} Figures 11 through 16 illustrate differences in these fluxes, both in spectral shape and magnitude, between the Vette model environment, and that measured by the MSC on-board spectrometers. For clarity the discussion to follow will first consider the electron fluxes and then the proton fluxes.

Electron Flux*

As is shown in Figures 11 and 12, the magnitude of the measured electron fluxes are consistently lower than those calculated from the decayed Vette environment. The ratio (V36/N36) is 4.6 while (V52/N52) is 4.7 showing a consistent variation in the peak fluxes. The ratio (V52/V36) is 1.63 while (N52/N36) is 1.61 which indicates little east-west asymmetry in these electron fluxes, at least for these two revolutions. A number of similar anomaly passes yielded nearly identical and reproducible measured flux versus time profiles. The experimental results presented here represent a preliminary analysis of this spectral data, with the data having a confidence limit of ± 2 , which has been assigned by Reagan.¹⁶

*For convenience, in the following two sections the peak fluxes for revolutions 36 and 52 will be designated V36 and V52 for the Vette environment, and N36 and N52 for the MSC spectrometer flux. These terms will apply to electrons or protons depending on which section they are used in.

The spectral shape of the radiation environment has a strong affect on the calculated dose. Figures 13 and 14 clearly illustrate the relative spectral hardness of the measured spectra to that predicted; this comparison being made at the point of peak measured flux. Note that both curves have been normalized to unit area. Three separate spectral shapes have been used in determining the experimental electron spectra for revolutions 36 and 52, while the Vette AE2 spectra are calculated as a function of L-shell alone.

Proton Flux

Figures 11 and 12 illustrate that the Vette proton fluxes, as was observed with the electron fluxes, are consistently higher than those measured. Note the Vette flux has been considered only in the energy range $25 < E < 80$ Mev so that a direct comparison with the observed flux is possible. Here, the ratio (V36/N36) is 10.4 while (V52/N52) is 1.72, showing a marked difference in the flux ratios for these revolutions. The ratio (V52/V36) is 1.35 and (N52/N36) is 8.2. These ratios seem to indicate an east-west asymmetry in the measured proton flux, and a steeper gradient of this parameter in B,L space than what was calculated. Again, the measured fluxes were reported to be accurate within a factor of ± 2 .

Figures 15 and 16 illustrate the relative spectral shapes plotted at the time of peak measured flux and normalized to unity in the range $25 < \text{Energy} < 80$ Mev. Two points of interest are brought out when examining these figures. First, they emphasize the discontinuity in the Vette AP series, differential proton spectra. The Vette environment was designed to represent accurately the integral spectrum in four energy intervals (4-15, 15-30, 30-50, and >50 Mev) using a function of the form

$$J(>E, B, L) = F_i(B, L) \text{ Exp} \left[\frac{E_i - E}{E_{oi}(B, L)} \right]$$

where J = omnidirectional flux greater than energy E .

F_i = omnidirectional flux normalization value for interval i .

E_i = lower energy cutoff for interval i .

E_{oi} = characteristic energy for interval i .

This discontinuity can be important in dose calculations especially when the shielding of the vehicle is such that the minimum penetrating energy fall near or coincides with one of the interval end points.⁸ Secondly, the normalized calculated spectra predict a proportionally higher number of high-energy protons and a lower number of low-energy protons than were measured.

Dose Rate and Dose Compared

Figures 4 and 5 summarize the dose rate profile comparisons for revolutions 36 and 52 of the Gemini-IV flight. Figure 6 shows a typical anomaly pass for Gemini-VI. In general, the differences in the calculated dose rates using the Vette model environment in combination with the SPARES radiation transport models (SPARES/Vette), and the measured environment in conjunction with these same transport models (SPARES/MS),

follows the general trends observed in the flux profiles (see Figures 4 and 5). The tissue-equivalent ionization chamber (TEIC) readings shown for these passes represent the average of the fixed and portable units which were mounted symmetrically on the hatches. The ratios of the peak dose rates with both modes of calculation to that measured are:

| | | | |
|--------|---------------|------|-------|
| Rev 36 | SPARES/Vette: | TEIC | 3.4:1 |
| | SPARES/MSC: | TEIC | 0.8:1 |
| Rev 52 | SPARES/Vette: | TEIC | 3.8:1 |
| | SPARES/MSC: | TEIC | 1.1:1 |

Forming ratios similar to these for the pass doses, i.e., the time integral of the dose rate profiles, yields:

| | | | |
|--------|---------------|------|-------|
| Rev 36 | SPARES/Vette: | TEIC | 3.1:1 |
| | SPARES/MSC: | TEIC | 0.6:1 |
| Rev | SPARES/Vette: | TEIC | 4.2:1 |
| | SPARES/MSC: | TEIC | 1.3:1 |

The proton contribution to the calculated dose rate dominates the electron contribution when dose rates are calculated from the Vette model environment for revolutions 36 and 52. This domination of the proton component to the total dose rate and dose was observed for all Gemini-IV and VI anomaly passes using the SPARES/Vette system. The SPARES/MSC calculation shows this same effect for revolution 52, however, the electron component of the dose does predominate during revolution 36.

For the SPARES/Vette calculation the ratios of the proton to electron pass doses are 2.60:1 (Rev 36) and 1.85:1 (Rev 52). These same ratios for the SPARES/MSC calculation are 0.32:1 (Rev 36) and 1.55:1 (Rev 52). Even though these ratios contain errors due to the above mentioned uncertainty in the measured environment, they definitely predict the existence of a significant number of electrons within the spacecraft. No such electrons were found within the passive dosimetry packs. The dose calculations were performed for the ionization chamber shielding, not for the passive dosimetry shielding. All of the passive dosimeters were inherently more heavily shielded than the ionization chambers. For the Gemini spacecraft small amounts of additional shielding strongly attenuate the electrons which have managed to penetrate the spacecraft structure and reach the astronaut area. The integrated doses from the unshielded ionization chambers for both missions were higher than the dose recorded by any of the passive dosimeters within the packages. In all probability the ionization chambers were actually responding to both protons and electrons, while the passive dosimetry packages were devoid of electrons because they could not penetrate.

A summary of the TEIC and SPARES/Vette mission doses is presented in Table III. The calculated doses are considerably higher than any of the measured doses. The spatial extent of the variations in the isodose rate contours at 200 and 300 km is shown in Figures 7 and 8. Using the simultaneously measured physical environment lowers the calculated values considerably. This brings the SPARES/MSC calculated dose well within the

range of the experimental TEIC data, considering the possible error in the measured environment.

In the abstract of this paper published in the ANS transactions, the parameters of 1965 Cain and Hendricks magnetic field formulation were used to calculate the (B,L) coordinates.¹⁵ These coordinates were then used with the Vette flux maps and the SPARES transport models to calculate the doses summarized in the transactions. This calculation, when compared to the one presented here using the 1960 Jensen and Cain magnetic field, yields smaller peak dose rates for all anomaly passes (a factor of 2) with a similar decrease of the mission dose. Since the Vette flux maps were compiled using the 1960 magnetic field it is necessary to use this same formulation when calculating the flux with these maps.

WL-304 Dose Rate and Dose

In contrast to the low-altitude Gemini missions, the flight path of this probe took it through high radiation intensities in its pass through the heart of the inner radiation zone. Unfortunately, very little useful data was recorded for the time the probe spent in the outer zone resultant from the battery failure discussed above (see Figure 17). The measured dose rates are close to those expected for the unshielded ion chamber alone since very little shielding was afforded by the vehicle. This makes the calculated doses highly dependent on an accurate knowledge of the environment in the low-energy portion of both the electron and proton spectra. It is in just these regions of high flux and low energy where the Vette model environment should be most accurate. The assumption of omnidirectional flux made in the calculational models should also have a small effect on the calculated dose rates because of the thin shielding about the ion chamber and the fact that a large portion of the time the probe was at low geomagnetic latitude. The close agreement between the measured and SPARES/Vette calculated dose rate shown in Figure 17 verify quantitatively these arguments. A comparison of the peak dose rates, measured and calculated, for the first pass through the inner zone are within 7.5 percent. However, the integrated dose for the first pass through the inner zone is high by 49 percent.

As is illustrated in Figure 17, there is a relatively poor agreement between the calculated and measured dose rates in the outer zone. This may be attributed to the fact that first, no proton contribution is included from the proton component in this region, and second the computed electron dose rate is dependent on the environment, which has been observed to fluctuate temporally over several orders of magnitude.

Implications for Mission Planning

The dose per anomaly pass, calculated from the Gemini IV on-board physical spectrometer data compared to that integrated from the ionization chamber readings, was always within a factor of 1.7. This is based on the only two revolutions for these flights where simultaneous environment and dose information is available. The total mission doses, calculated using the most recent model environment available, were high by a factor of 2 to 4. It appears, at least in this initial analysis, that a re-evaluation of the

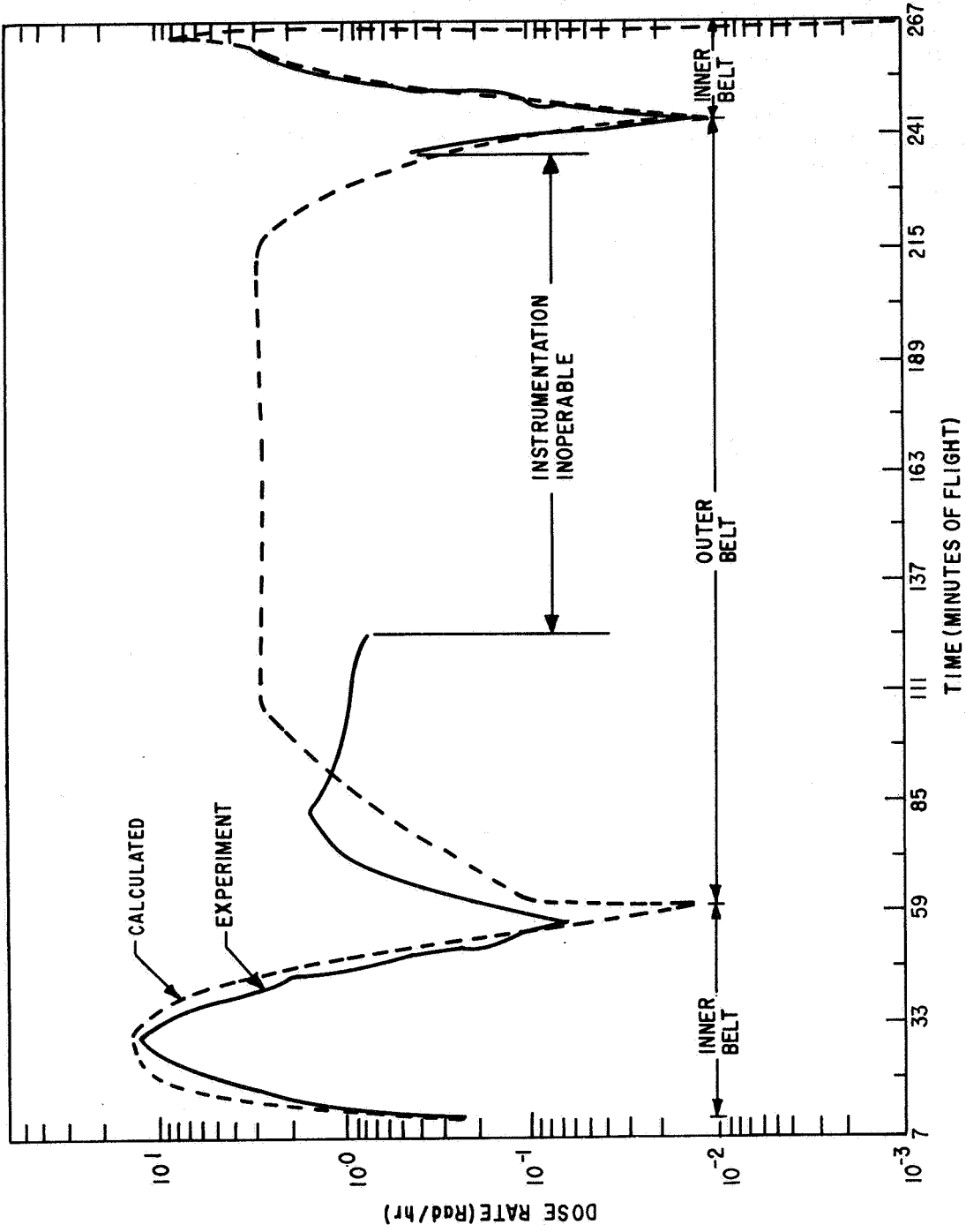


Figure 17. WL-304 Dose Rate Summary

radiation environment in the anomaly region may be appropriate; however, a more complete study considering all available anomaly passes must be performed before any firm recommendations can be made.

For higher altitudes in the inner radiation zone, using the limited data gathered on the WL-304 probe, the calculated mission dose using the model environment were more accurate than for Gemini and were within a factor of 1.5.

REFERENCES

1. Schaefer, H., Radiation Monitoring with Nuclear Emulsions on Mission Gemini IV and V, Journal of Aerospace Medicine, 38, 1, 1967.
2. Benton, E., and Collver, M., Charged Particle Tracks in Polymers; Number 2--Registration of Heavy Ions During the Flight of Gemini-VI, USNRDL-TR-1037, June 1966.
3. Richmond, R., Davis, W., and Lill, J., Gemini Dosimetry Results, presented at the Health Physics Society of America Meeting, Houston, Texas, June 1966.
4. Schaefer, H., and Sullivan, J., Radiation Monitoring with Nuclear Emulsions on Project Gemini 1; Experimental Design and Evaluation Procedures: Partial Results on Missions 4 and 5, NAMI-955, Naval Aerospace Medical Institute, 18 February 1966.
5. Schaefer, H., Radiation Monitoring with Nuclear Emulsions on Mission Gemini IV and V, Journal of Aerospace Medicine, 38, 1, 1967.
6. Barton, Mar, et al., Computer Codes for Space Radiation Environment and Shielding, WL TDR 64-71, Vol. I, August 1964.
7. Vette, Models of the Trapped Radiation Environment. NASA SP-3024. Jan 1966.
8. Bostrom, Williams, Time Decay of the Artificial Radiation Belt. JGR, Vol. 70, pg 240, 1965.
9. Jensen, Cain, An Interim Magnetic Field, JGR, 67, 3568-3569, 1962. (Abstract)
10. Chappell, D., et al., Inherent Shielding and Dose-rate Calculations for Gemini Spacecraft, St. Louis, Mo.: McDonnell Aircraft Corp., 1964.
11. Neher, Anderson, JGR, Vol. 67, pages 1309-1313, 1962.
12. Malone, Program L015: Shield Thickness Calculation Program, NASA, Manned Spacecraft Center document, Vol. I, Computer Program Users Manual, May 1965.
13. Vette, et al., Models of the Trapped Radiation Environment, Vol. III: Electrons at Synchronous Altitudes. NASA SP-3024, March 1967.
14. Schneider, Janni, Brentnall, Experiment D8: Radiation in Spacecraft, SSD-TR-66-115, May 1966.
15. Cain, Hendricks, Magnetic Field Data for Trapped Particle Evaluation, JGR, Vol. 71, page 346, Jan 1966.
16. Reagan, et al., Proton-Electron Spectrometer Experiments on Gemini IV and VII, LMSC/2-44-66-1, Sept 1966.

17. Reagan, private communication.
18. Thede, A. L., A Correlation of Dosimetric Measurements with Charged Particle Environment of the Inner Van Allen Belt, this meeting.

THE APPLICATION OF SPACE SHIELDING TECHNOLOGY
TO SPACECRAFT PROBLEMS

by

Russell D. Shelton

Space Sciences Laboratory
George C. Marshall Space Flight Center

I. INTRODUCTION

The purpose of the following discussion is to review a number of spacecraft problems which have arisen over a period of several years and to point out how our knowledge of the radiation environment and our ability to apply radiation transport techniques have been used to solve these problems. It is unnecessary to point out that many of the problems, which at one time were quite urgent, have been solved or circumvented, or found not to exist in fact, and that our views in retrospect are much more positive and enlightened than they were when the questions were being asked and answers demanded by a project-oriented management. However, the shifting interests in spacecraft and instrumentation still leave many of the same basic analytical problems with us, but with perhaps new boundary conditions and new response functions which have not been determined. In many cases of immediate interest, we still have questions about the reliability of predictions of the radiation environment, especially in situations likely to be strongly influenced by the coming increase in solar activity.

II. THE PARTICLE THRESHOLD PROBLEM

The use of energy threshold detectors to determine an energy spectrum has been a part of reactor and x-ray technology for some time. The use of anisotropic detectors to determine directional distributions in radiation has been given less attention, but has been of considerable importance in space situations and presents many of the same analytical and calibration problems. Unfortunately, it is too often the case that an experiment is analyzed and calibrated after the crucial measurements are made, rather than before, so that instrument design does not enjoy the full benefit of our

basic knowledge of radiation transport.

The use of a basic detector, such as photographic film or a scintillation counter, behind various thicknesses of absorber is an example of a threshold detector with several levels of energy discrimination. Several of the early measurements of radiation in space employed Geiger tubes behind various absorber thicknesses and scintillation detectors with restricted angles of view [1].

Ideally, a threshold detector should have a step-function response (or transmission curve if an absorber is used) such as shown in curve A of Figure 1). The actual response will, in most cases, look more like curve B of Figure 1, taken from electron transmission data calculated by Berger [2]. The effective threshold energy E_i for curve A is obviously at the transition point, but for curve B it can be defined by the equation

$$\int_{E_i}^{\infty} \phi(E) dE = \int_{E = \infty}^{E = \infty} K \phi(E) T_i(E) dE \quad (1)$$

where $\phi(E)$ is a differential energy spectrum (particles/cm²sec mev) and $T_i(E)$ is the fractional electron transmission as a function of energy and a particular absorber identified by the subscript i . Unfortunately, E_i is not clearly defined unless

$$T_i(E) = \begin{cases} 0 & E < E_i \\ 1 & E \geq E_i \end{cases} \quad (2)$$

Otherwise, E_i is a function of $\phi(E)$ and $T_i(E)$ with $\phi(E)$ being also an unknown. Nevertheless, if there are several threshold detectors, an iterative process can yield a spectrum $\phi(E)$ and a set of threshold energies appropriate for the detector-absorber system and the spectrum.

The point of the above discussion is that effective thresholds can be determined easily only for highly special cases, such as defined in Eq. (2), which is not bad for protons in simple geometries. For electrons, however, the effective energy threshold is a function of the spectrum, and moves toward energies lower than the energy corresponding to 50 percent transmission for spectra typical of space radiation. This effect, shown in Fig. 2, accounts for some of the early predictions of large radiation fluxes which were later revised downward. It should also be pointed out that much of the good theoretical and experimental work on electron transmission was performed after a number of electron measurements had been made.

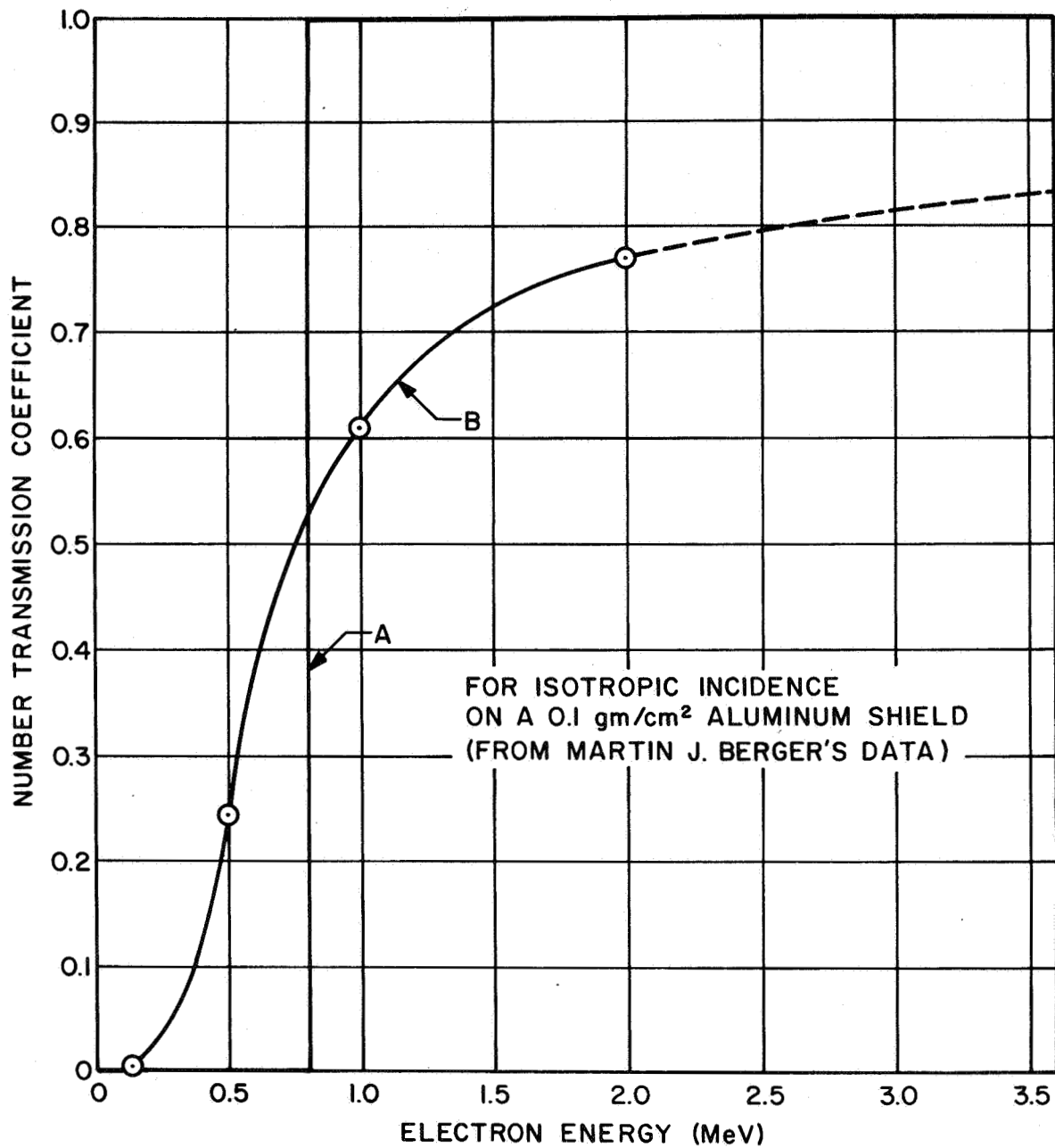


FIGURE 1. Ideal and Actual Response for an Electron Threshold Detector Shielded by 0.1 gm/cm² of Aluminum [2]

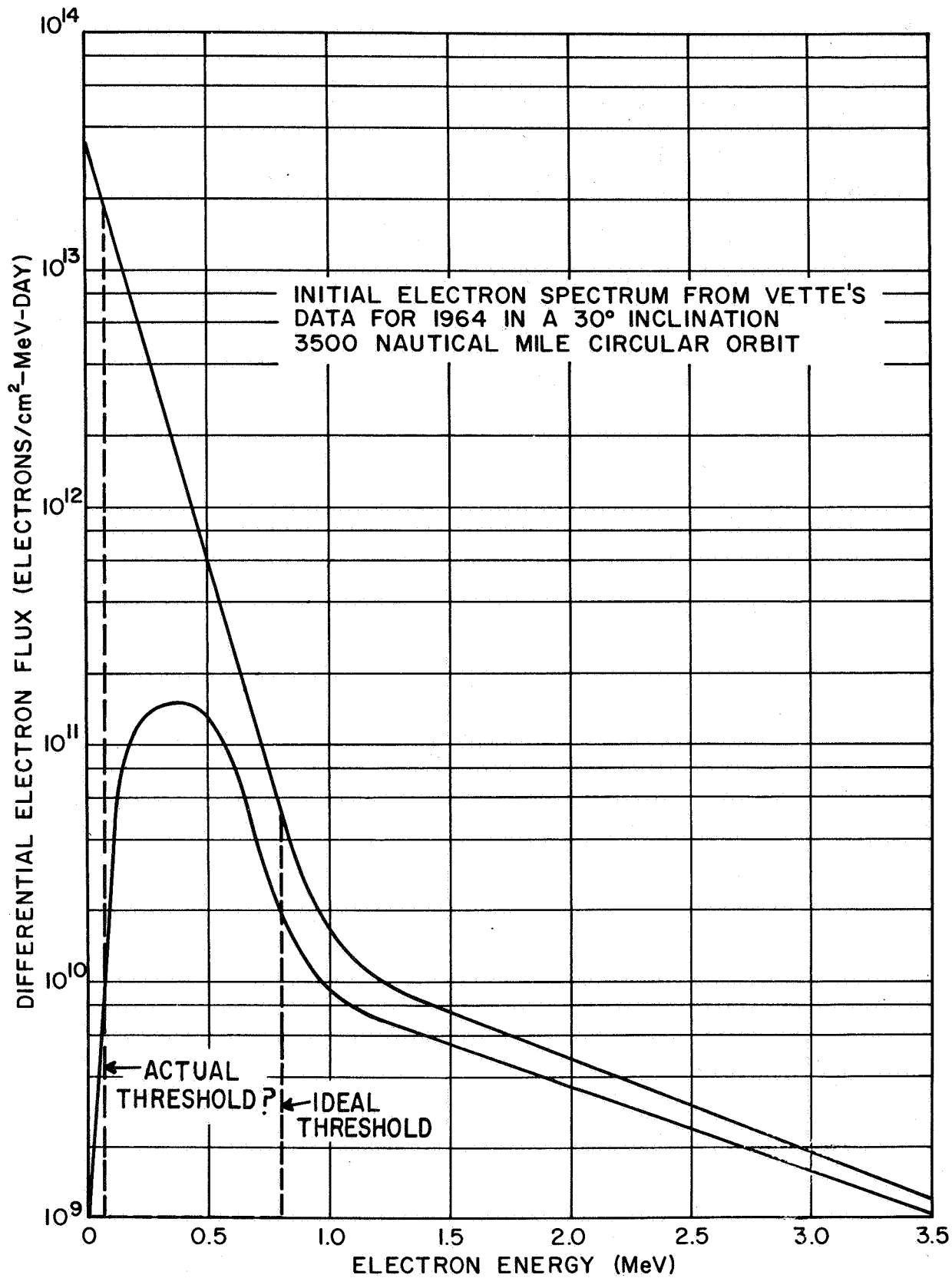


FIGURE 2. Typical Trapped Belt Electron Spectrum Transformed by an Ideal and Actual Detector Response [2, 11]

III. ANISOTROPIC DETECTORS

There is a close relationship physically and mathematically between the threshold detector problem and the problem of extracting an energy spectrum from a pulse height distribution available from a particular type of detector. In this case, the problem is that of solving the integral equation

$$N(h) = \int \phi(E) R(E, h) dE \quad (3)$$

for the energy spectrum $\phi(E)$ when the response function of the detector $R(E, h)$ is known and the pulse height distribution $N(h)$ is determined experimentally. This important problem has received much attention by Burrus [3] et al. of ORNL, and is a necessary ingredient in any radiation measurement directed toward obtaining an energy spectrum, unless the detector response $R(E, h)$ is the Dirac delta function $\delta(E, Kh)$, where K is some instrument constant. In this case, $\phi(E) = N(E/K)/K$. A similar problem was presented by the radiation measurements made in early Explorer satellites because the radiation detectors were anisotropic in their responses. In this case, the counting rate $C(\hat{\Omega})$ of a detector was a function of the counter orientation, defined by a unit vector $\hat{\Omega}$. This simple definition of counter orientation is possible only under the assumption of azimuthal symmetry for the counter anisotropy, in which case the counter response as a function of orientation can be written as

$$R(E, \hat{\Omega} \cdot \hat{\Omega}')$$

where $\hat{\Omega}$ defines the counter orientation, and $\hat{\Omega}'$ defines the direction from which radiation is arriving. Neglecting the energy dependence of the anisotropy and assuming a counter geometry such as shown in Figure 3, an attempt was made [4] to extract the directional distribution of the electron radiation from the integral equation

$$C(\hat{\Omega}) = \int_E \int_{\omega} \phi(E, \hat{\Omega}') R(E, \hat{\Omega} \cdot \hat{\Omega}') d\omega dE \quad (4)$$

where the counting rate $C(\hat{\Omega})$ as a function of direction was known and $R(E, \hat{\Omega} \cdot \hat{\Omega}')$ was guessed at with the best electron penetration data available. The results of this "directionality unraveling" process is shown in Figure 4.

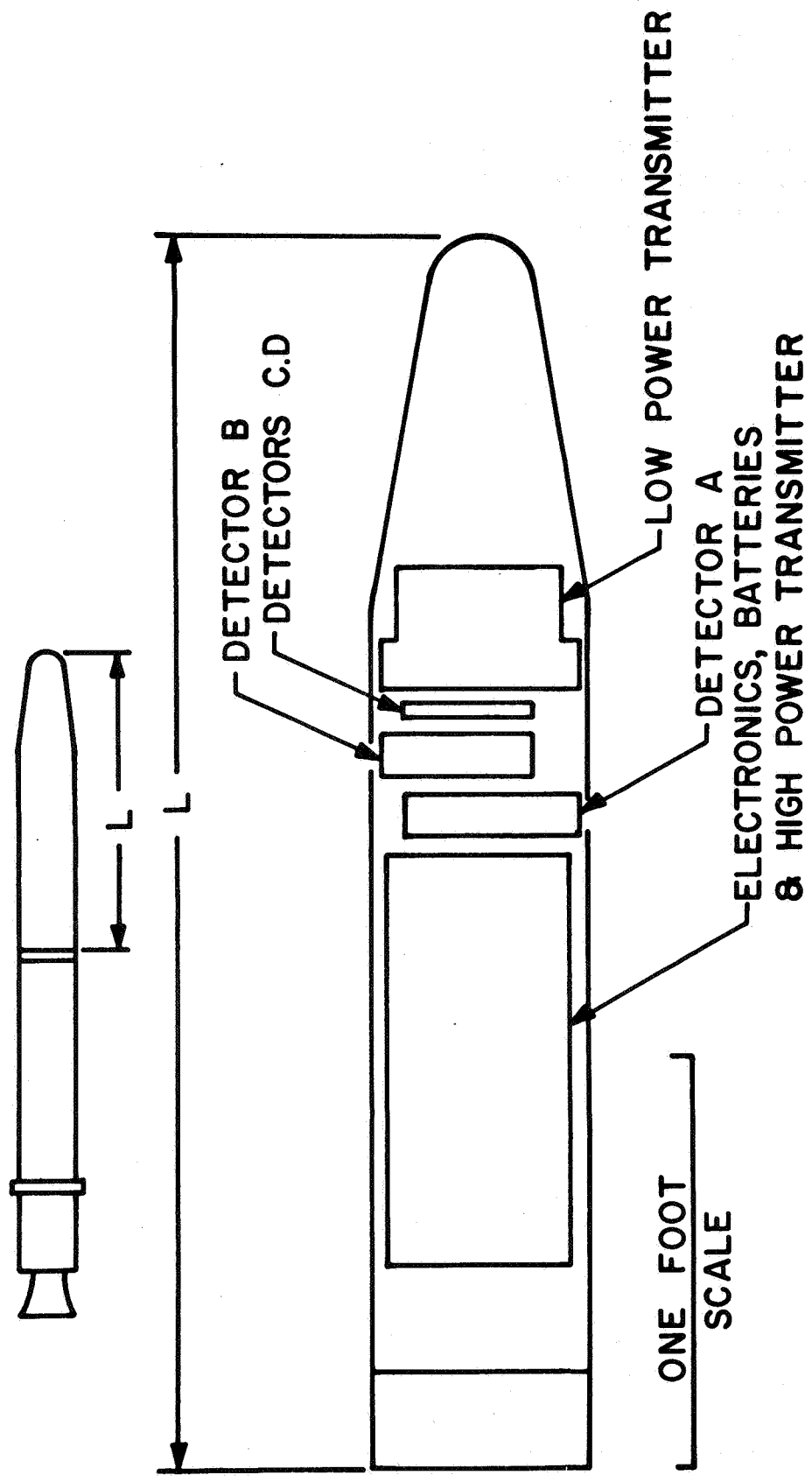


FIGURE 3. Geometry for a Simple Directional Detector [4]

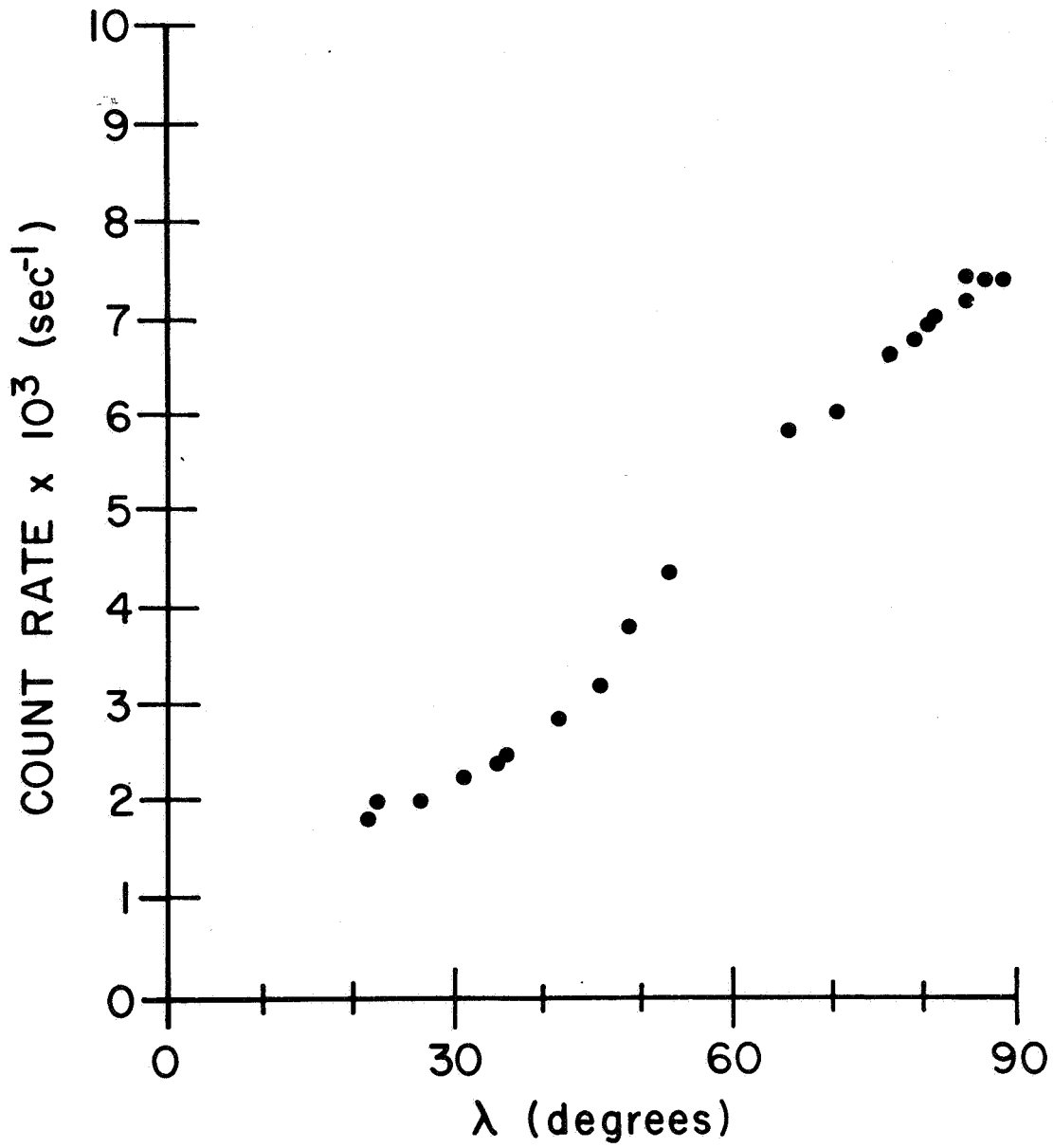


FIGURE 4. Counting Rate vs. Angle Between the Velocity and Magnetic Field Vectors [4]

An important and difficult part of determining the directional distribution of the electron radiation lay in determining the counter orientation. The orientation of the satellite, in which the detectors were fixed, was determined from a knowledge of mechanics, the observation from the ground of the signal intensity from an anisotropically radiating antenna, and a knowledge of the fact that the radiation distribution in direction should have axial symmetry about the magnetic field direction.

IV. DAMAGE TO SOLAR CELLS

Damage to solar cells by space radiation has been dealt with by developing more resistant solar cells, incorporating shielding glass in front of the solar cells, and by over-design of the power supply system. When the problem first arose, the intensity of the radiation was poorly known and the measurements of radiation effects were confined to normal incidence by monoenergetic electrons and protons on bare solar cells. As usual with such problems, the space environment had to be determined, and the results of idealized laboratory experiments had to be equated to the space radiation environments by using the theory of atomic displacements by charged particles.

We assumed [5] the damage D to a solar cell to be given by an integral of the form

$$D = \int_E \int_t \phi [\bar{F}(t), E] D(E) dE dt \quad (5)$$

where $\phi [\bar{F}(t), E]$ is the particle flux as a function of particle energy E and time t , and $D(E)$ is a damage function depending on the type of solar cell, the kind of particle radiation, and the energy and direction of the radiation. Fortunately, enough experimental data was available to determine $D(E)$ for protons and electrons with a reasonable feeling of confidence, as shown in Figure 5, but the environment was relatively unknown, as shown in Figure 6, which represents the degree of uncertainty which we faced. The comparison of actual and calculated deteriorations of solar cells for Explorer XI is shown in Figure 7. The expense of solar cells is such that information (or lack of it) on the radiation environment is worth a considerable amount of project money, which will probably be spent in over-design if information is lacking.

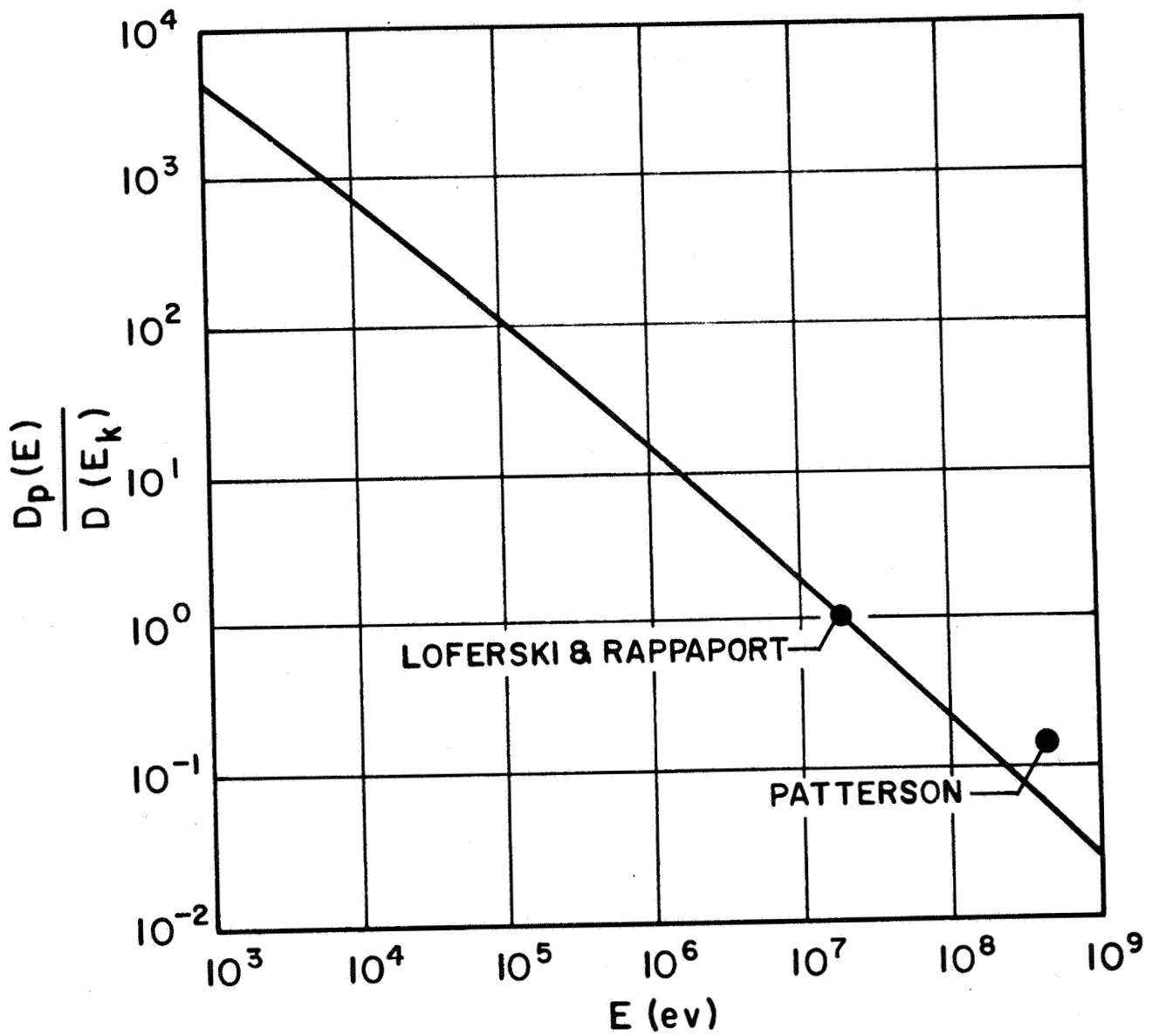


FIGURE 5. A Plot of $D_p(E)/D_p(E_k)$ Based on the Theory of Seitz and Koehler and Normalized to the 17.6 MeV Proton Irradiation of Loferski and Rappaport [1]

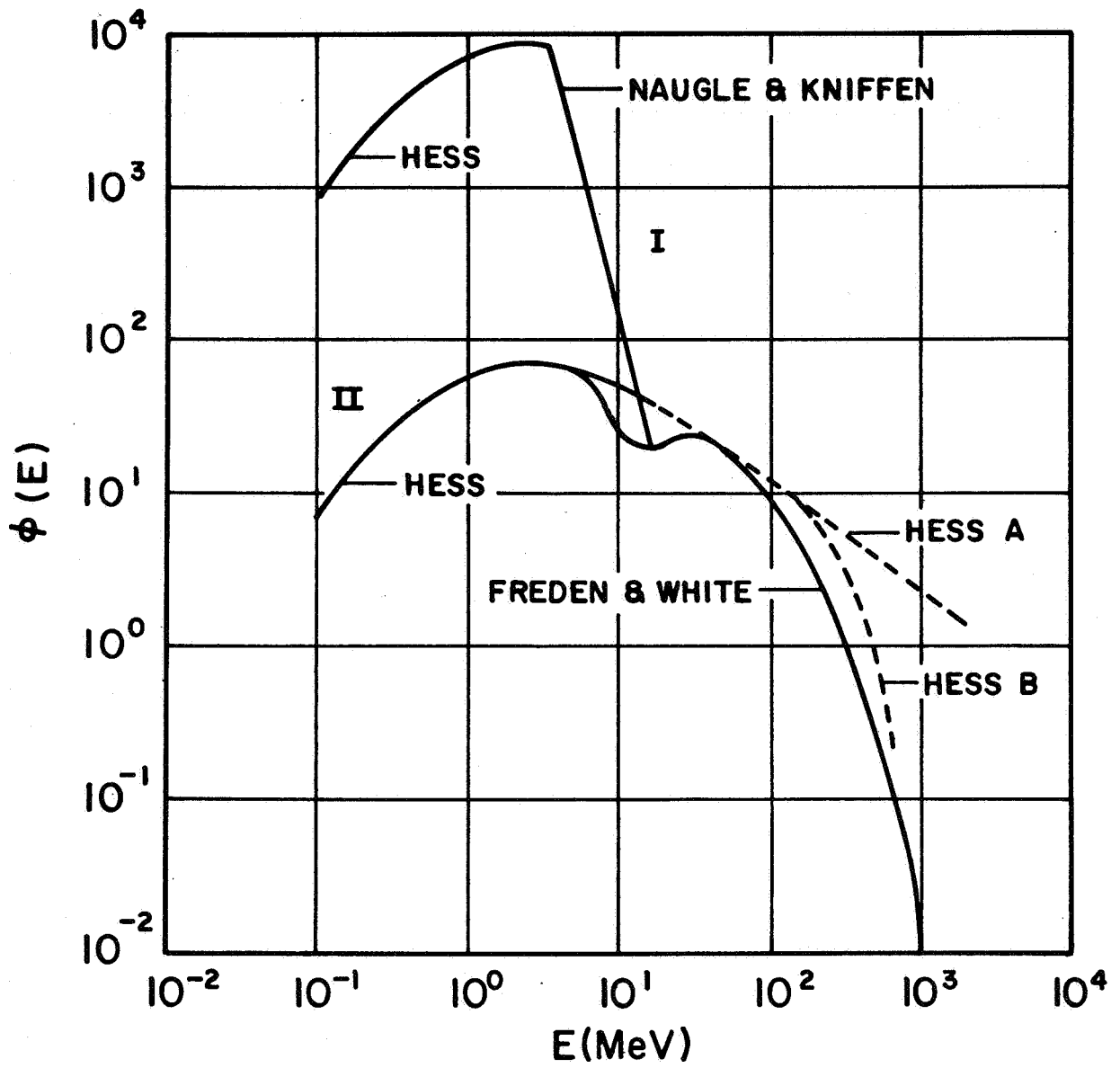


FIGURE 6. Comparison of Trapped Proton Spectra from Several Sources [1]

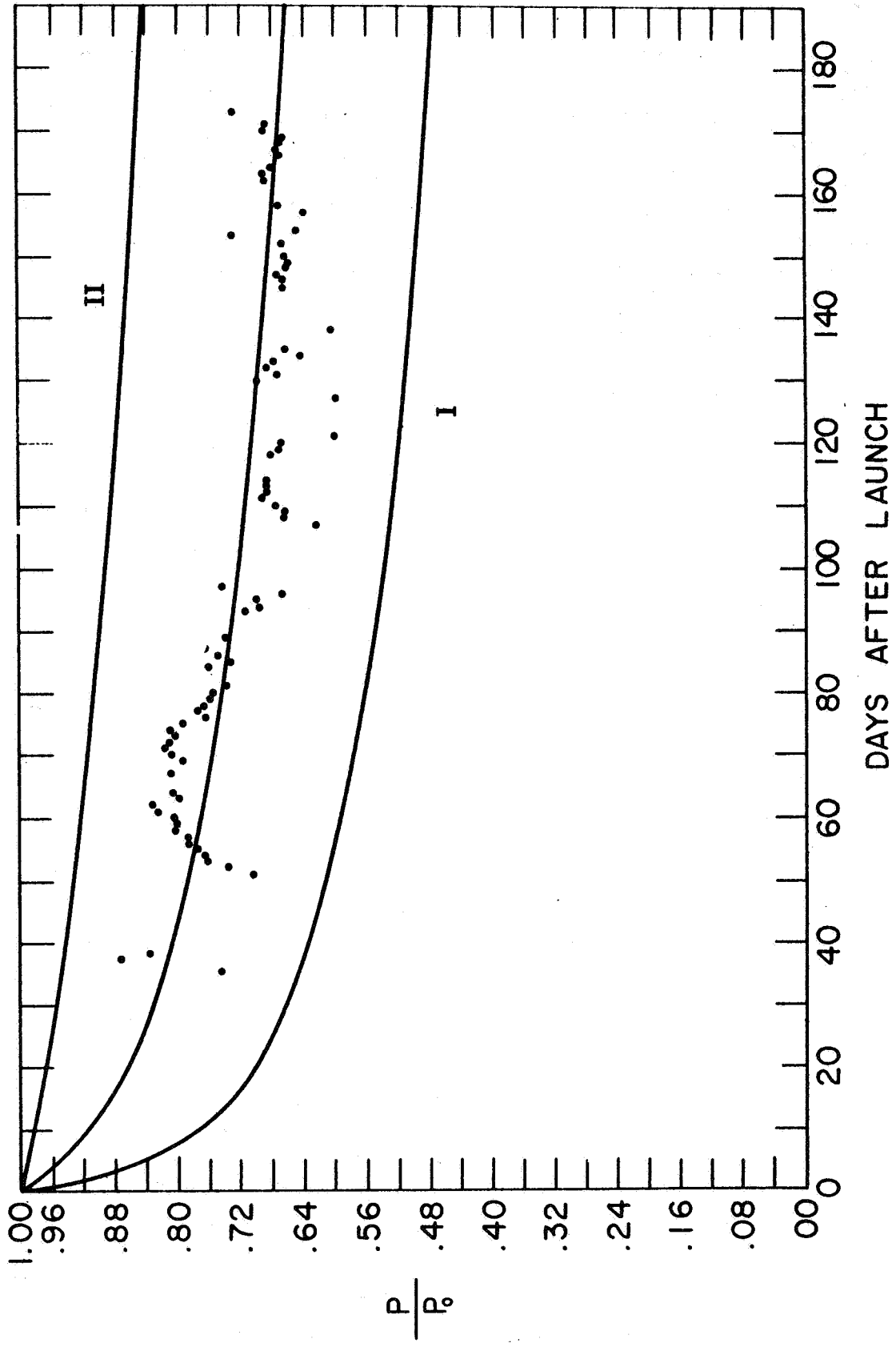


FIGURE 7. Comparison of Experimental and Predicted Behavior of Solar Cells on Explorer XI [1]

V. INSULATORS IN SPACE

One of the most interesting radiation problems arising in connection with spacecraft came to focus when it was suspected that charge storage in dielectrics, as a result of exposure to space radiation, could lead to noisy electrical discharges. Most of us have seen Lichtenberger patterns such as that shown in Figure 8, created by injecting high-energy electrons into a transparent block of dielectric and inducing a breakdown electrical discharge by touching a grounding terminal to the edge of the block.* Unlike lightning, where all trace of the path of the discharge disappears soon after the flash, the discharge path is permanently recorded in the solid dielectric.

In satellites which have large amounts of dielectrics exposed to space radiation, either directly or behind modest shielding, there is the possibility of Lichtenberger discharges on a smaller scale than shown in Figure 8, and there will be the problem of a broad spectrum of electrical noise pulses associated with these discharges. A microscopic examination of a piece of mylar insulated cable exposed to electron radiation of the proper energy will show many such patterns, each corresponding to a discharge characterized by insulator breakdown and electrical noise propagation.

The physics and mathematics of charge storage and leakage will not be discussed here. However, the general situation is much like [6] the "leaky bucket" problem of the radiation belts or the generation of a quantity of radioisotope in a reactor, except that there is a catastrophic discharge which appears to wipe the slate almost clean if the charge accumulates beyond a certain point. It is easily seen that charge injection into dielectrics is essentially a shielding or transport problem, and the leakage of charges is a matter of electrical conductivity, which is not an easy parameter to measure for good insulators, especially in a radiation field. The basic problem is to determine whether or not charges leak off quietly or build up until there is a noisy and catastrophic breakdown of the dielectric, with accompanying propagation of electromagnetic noise, such as produced by lightning in the atmosphere.

The problem of electrical noise generation by static discharges can be dealt with in several ways, such as changing spacecraft orbits so as to encounter less radiation, hardening the electronic circuitry to electrical noise, or using leaky dielectrics. Some insulation resistance decreases by a factor of ten for each 8° C rise in temperature, which means that much can be done with a little temperature rise.

* courtesy of Dr. A. M. Liebeschutz, Hughes Research Laboratories.

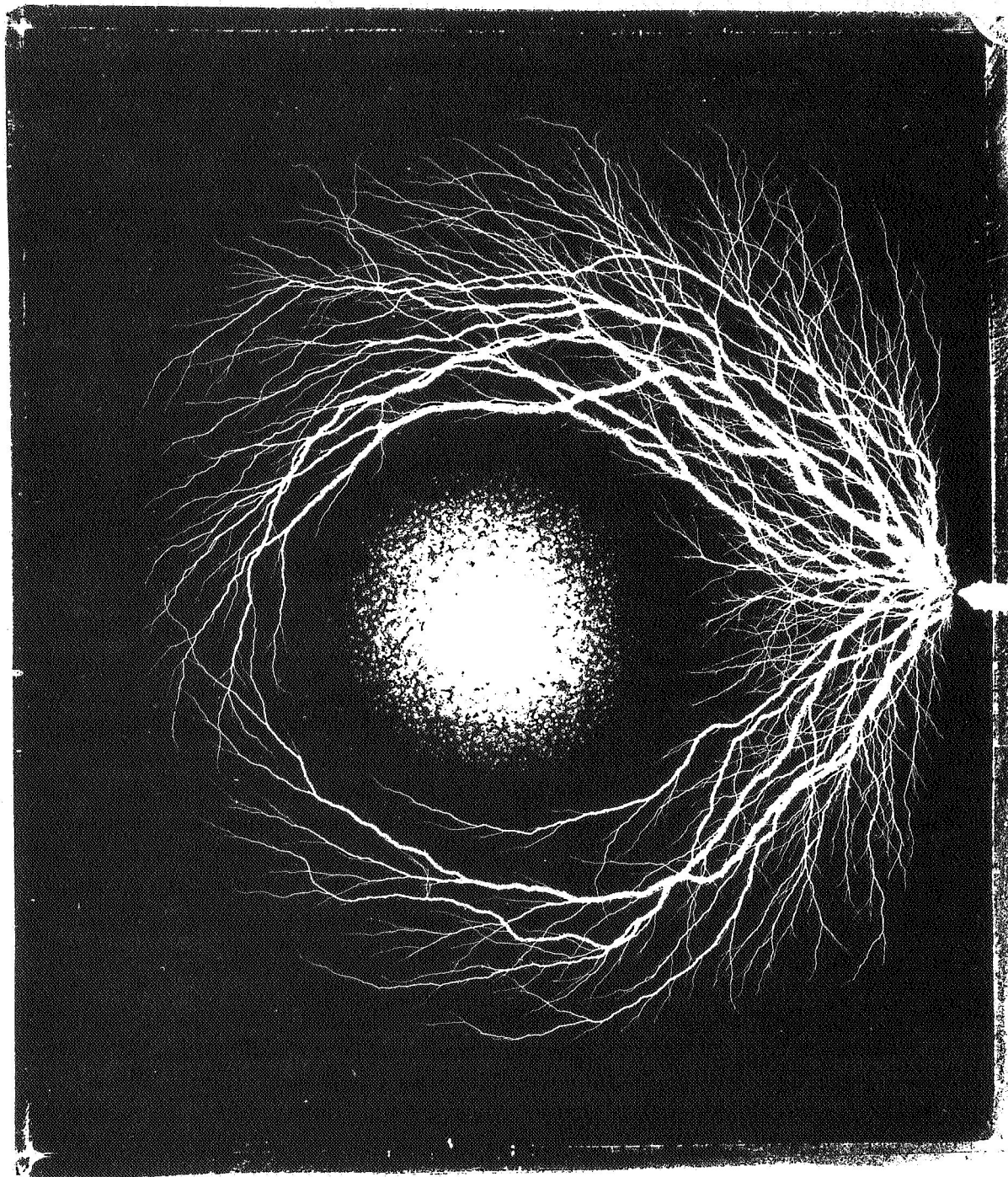


FIGURE 8. Lichtenberger Pattern for High-Energy Electrons in a Block of Plastic (courtesy of Dr. A. M. Liebeschutz, Hughes Research Lab)

As we look at the charge storage problem today, we are sure that there can be charge storage and noisy discharges under the right conditions [7], and we are reasonably sure, if we use a little ingenuity and foresight, we can design around such problems. Unfortunately, we are unable to predict accurately what values of parameters characterize the transition from quiet leakage to noisy discharges, and we will consequently pay some design penalties if we want guaranteed immunity from electrical noise.

VI. FILM FOGGING

Photographic film has been used for data recording for several satellites and spacecraft and is of particular interest in recording astronomical data. Film has been used for years as a sensitive radiation detector, and is subject to darkening when exposed to space radiation. It turns out that the radiation transport problem is easily handled and that the effect of charged particle radiation on film is reliably determined and related to CO^{60} exposures, for example. However, the radiation exposure to which the film is subjected for a particular low orbit is relatively uncertain for the next few years because of lack of faith in the B-L coordinate representations in the regions of the magnetic anomalies and because large changes in the particle populations may occur during the next solar maximum. A sample of electron flux measurements [8] in low orbits is shown in Figures 9 and 10. There is a sound physical basis and supporting experimental evidence for expecting a rise in the height of the atmosphere during the solar active period and a related decrease in the particle lifetime and particle population [9]. On the other hand, there is no body of data supporting an increase in the proton population since the last solar active period and there is a very incomplete understanding of the mechanisms for particle injection and acceleration into the radiation belts. It would not be surprising to find these mechanisms more active at times of solar maximum and increased geomagnetic disturbances.

Another aspect of the film fogging problem is the large range of sensitivity possible in photographic films, as shown in Figure 11. The horizontal lines are the dose rates which films can tolerate, for a 56-day mission at 240 N. M. and 31° inclination, without exceeding a background density of 0.2. Obviously one can avoid the degradation of photographic film by radiation by such expedencies as choosing orbits of lower inclination and altitude, choosing less sensitive film, shielding, film activation and development in orbit, etc. However these circumventions entail losses which must be weighed against our best estimates of the seriousness of the problem.

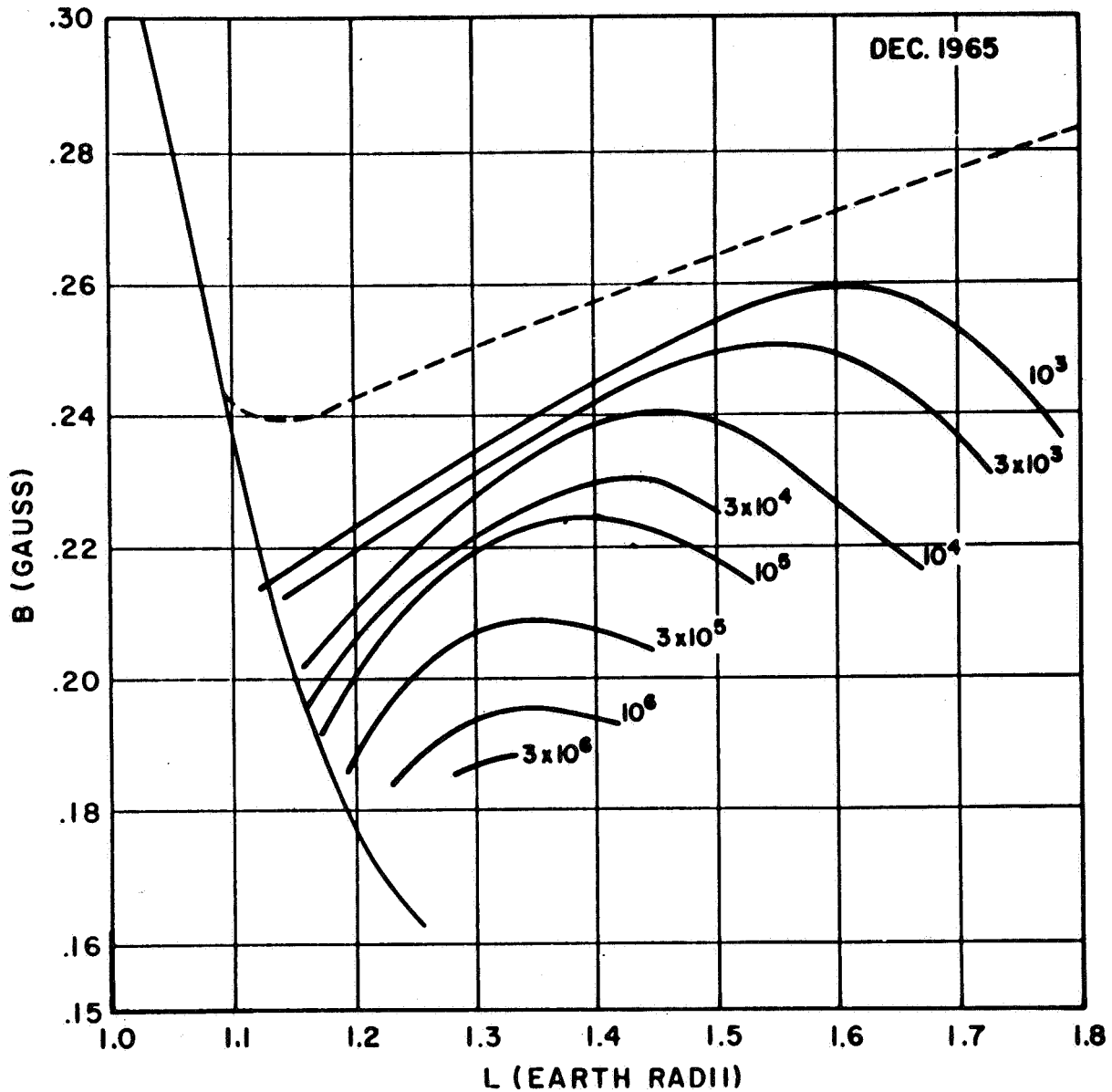


FIGURE 9. Typical Trapped Electron Flux Data as a Function of B and L Coordinates [8]

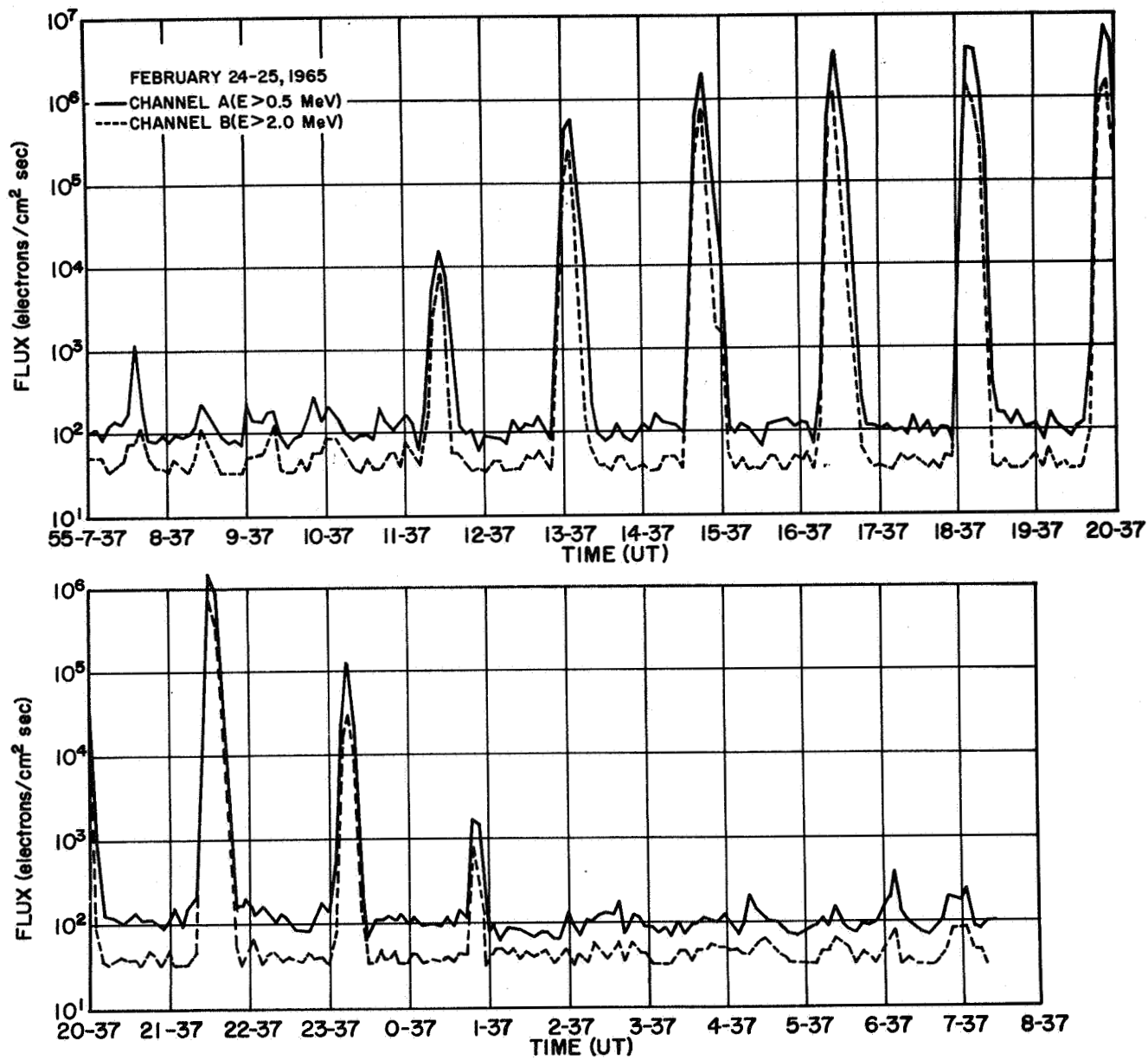


FIGURE 10. Trapped Electron Flux Data as a Function of Time in a Low Satellite Orbit [8]

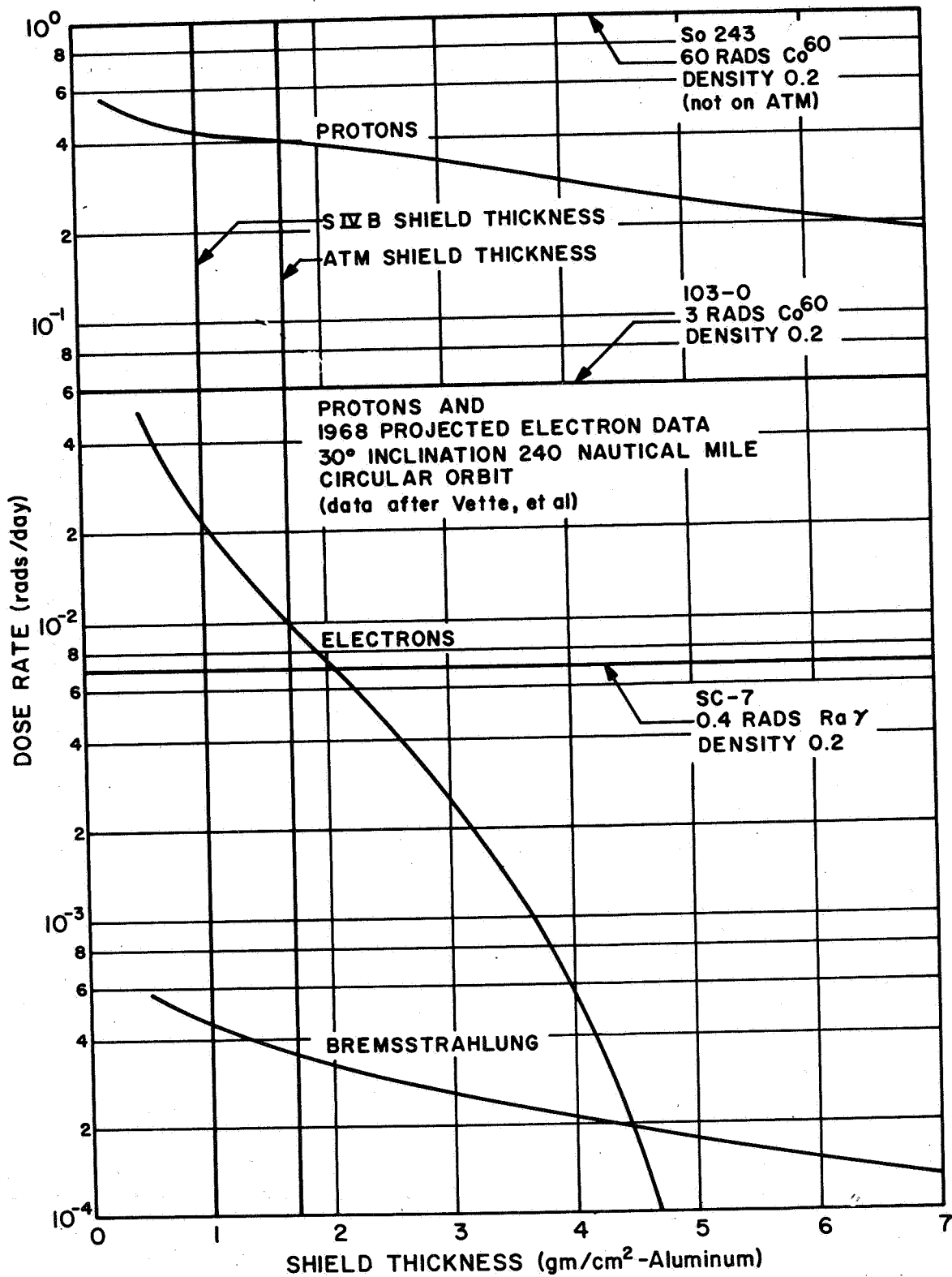


FIGURE 11. A Comparison of Dose Rates Due to Trapped Electrons, Electron-Induced Bremsstrahlung, and Protons, Plus Proton-Produced Secondary Particles, for an ATM Orbit [11, 12, 13]

Because of association of film darkening with dose, we will base our prediction of film damage on the calculation of an integral of the form

$$D = \int_E \int_t \phi[\bar{r}(t), E] \left(\frac{dE}{dx} \right) D(E) dE dt \quad (6)$$

where $\phi[\bar{r}(t), E]$ is the differential energy spectrum as a function of time t through the position vector $\bar{r}(t)$; dE/dx is the energy loss per unit path length; and $D(E)$ is the grain development per unit energy, and will be determined experimentally for films of interest. One particularly interesting aspect of $D(E)$ may be its sensitive dependence on energy under bremsstrahlung irradiation.

VII. CHARGE TRANSPORT BY NEUTRAL RADIATION

It is easy to visualize the production of Lichtenberger discharges as charged particles are deposited in insulators and dielectrics and the associated electric fields begin to increase. It is perhaps more difficult to believe that neutral radiation, such as neutrons and gammas, can result in charge separations in dielectrics sufficient to cause dielectric breakdown in spectacular discharges. Not many years ago, however, Dow-Corning was investigating the properties of glass necessary to avoid the ruining of large glass shielding windows by Lichtenberger discharges associated with charge transport by gamma radiation. This charge transport is one of the reasons why it is so difficult to measure the radiation-induced conductivity of many dielectrics.

Charge transport by neutral radiation is of more than academic interest to those engaged in studying the effects of radiation on nuclear stages. The use of hydrogen as propellant, and the possible condensation of oxygen in regions where the insulation for the hydrogen is poor, could produce a situation such that fires could be a hazard. The outgassing of combustible mixtures under irradiation is also possible. The final ingredient for a fire, namely, some means of ignition, could very easily be an electric spark produced by charge separation in dielectrics exposed to a neutral radiation field.

It perhaps seems odd to talk of radiations giving rise to electric potential differences capable of producing large sparks when every hi-fi enthusiast knows that radiation reduces the accumulation of charges on phonograph pickups. The difference in the situations is determined by ion

and electron mobility, which always acts to neutralize charges and which is relatively high in air but possibly extremely low in dielectrics.

VIII. PROTON SHIELD EVALUATION

The evaluation of proton shields directly by using proton beams is impractical for several reasons, and the use of engineering drawings is a difficult way of arriving at areal electron distributions in a shield. A very effective way is the use of x-ray techniques [10] with gamma rays having energies where Compton scattering is dominant. The problem is to determine the electrons/cm² by a source-detector geometry, such as shown in Figure 12. The best choice of source-detector geometry is by no means obvious. The experimental arrangement of Figure 12 resulted in the data of Figure 13, which should not be regarded as an illustration of the limitations of the method.

IX. SUMMARY

The preceding discussion is an enumeration of a number of problems created for spacecraft by space radiation as they have arisen and been dealt with by my associates at the Marshall Space Flight Center. No claim is made for completeness or for having solved all the problems. The uncertainties of the radiation environment are still with us for a number of interesting missions, but the transport techniques have improved steadily. The transient fears that secondary radiations, such as bremsstrahlung from electrons and gammas from inelastic collisions by high-energy protons, would provide great uncertainties in the shielding business have been somewhat allayed, but are still regarded with a degree of respect. There is still a lot of work to be done in predicting and understanding biological doses in complex geometries, but there is a general feeling that a factor of two either way is acceptable.

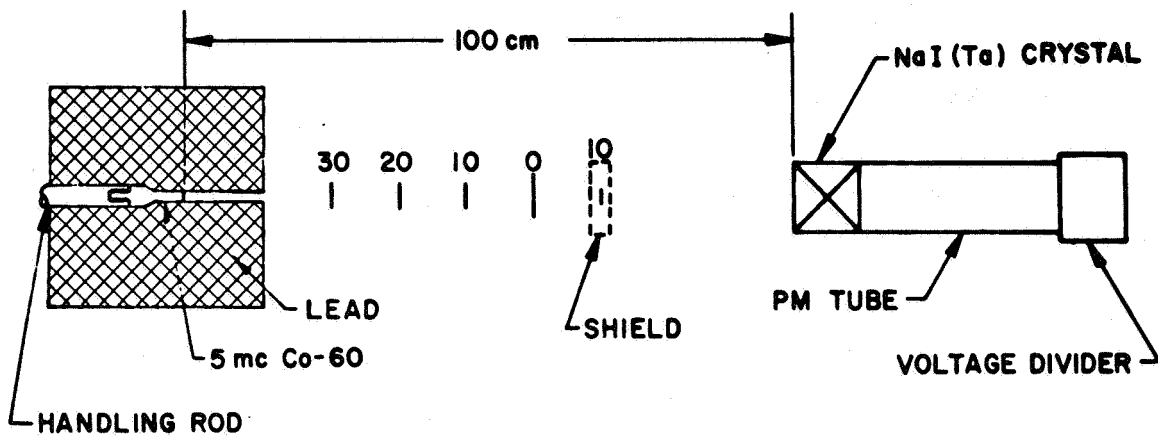


FIGURE 12. Detector Geometry for the Gamma Probing Technique (courtesy of R. Potter, MSFC)

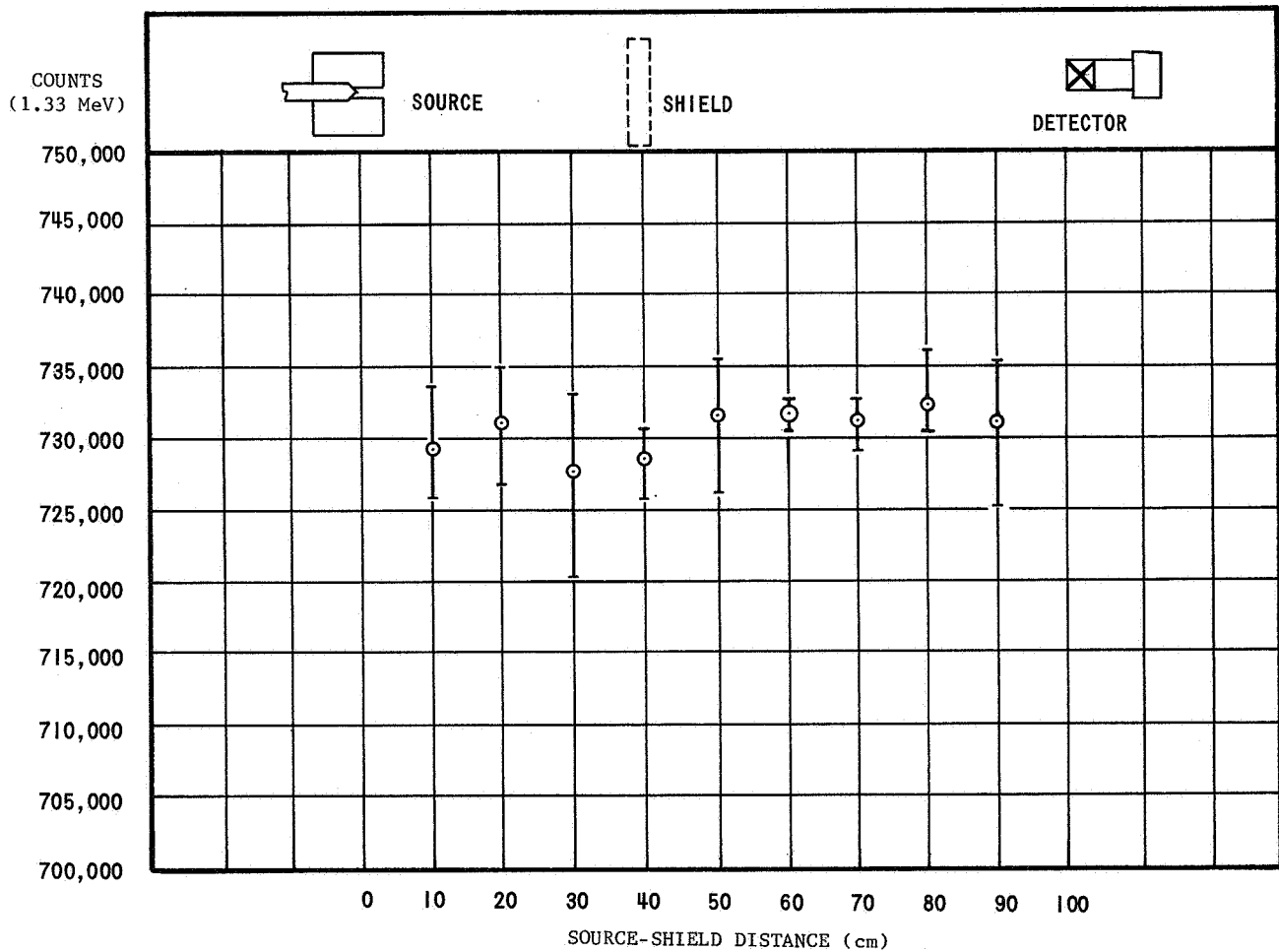


FIGURE 13. A Graph of Experimental Points Indicating the Effects of the Shield Position on the Number of Counts (courtesy of R. Potter, MSFC)

REFERENCES

1. R. D. SHELTON and A. W. THOMPSON, Objectives and Experimental Results with the Army Explorers. IRE Trans. MIL Elec., Vol. MIL-4, April-July, 1960, Nos. 2 and 3.
2. MARTIN J. BERGER, Transmission and Reflection of Electrons by Aluminum Foils. Technical Note 187, Nat'l. Bur. Stand. April 1963.
3. W. R. BURRUS, Utilization of A Priori Information by Means of Mathematical Programming in the Statistical Interpretation of Measured Distributions (Thesis). ORNL-3743. June 1965.
4. R. J. NAUMANN, Directional Dependence of Counting Rates from Explorer IV. (M. S. Thesis, University of Alabama, 1961).
5. J. W. KELLER, R. D. SHELTON, R. A. POTTER, and L. LACY, A Study of the Effect of Geomagnetically Trapped Radiation on Bare Solar Cells. Proceedings of the IRE, November 1962.
6. R. D. SHELTON, High Energy Electron Deposition in Dielectrics. Bulletin Amer. Phys. Soc. 1964.
7. ER 8582, Radiation Effects on Composite Structures, NASA Contract NAS 8-20206, Lockheed Nuclear Products, April 1966.
8. ALAN ROSEN and M. L. SANDERS (TRW Systems), and R. POTTER, R. D. SHELTON and E. URBAN (Marshall Space Flight Center), Temporal and Spatial Dependency of the "STARFISH" Belt Electrons in 1965 and Early 1966, presented at Amer. Geophys. Union Mtg., 1967.
9. ROBERT C. BLANCHARD and WILMOT N. HESS, Solar Cycle Changes in Inner Zone Protons. NASA TMX-55013. NASA, Greenbelt, Md. Goddard Space Flight Center. March 1964.
10. A. P. KRUMBEIN and F. JOHNSON, The Use of Gamma Probing to Determine the Shielding Effectiveness of Space Vehicles. UNC-5075, February 18, 1964.
11. J. I. VETTE, Models of the Trapped Radiation Environment. Vols. 1-3, NASA SP-3024 (1966, 1967).
12. M. O. BURRELL, The Calculation of Proton Penetration and Dose Rates. NASA TMX-53063, August 17, 1964.
13. M. O. BURRELL and J. J. WRIGHT, The Calculation of Electron and Bremsstrahlung Penetration and Dose Rates. To be presented at the 13th Annual Mtg. of the Amer. Nuc. Soc., June 11-15, 1967.

FIRST CLASS MAIL

POSTMASTER: If Undeliverable (Section 158
Postal Manual) Do Not Return

"The aeronautical and space activities of the United States shall be conducted so as to contribute . . . to the expansion of human knowledge of phenomena in the atmosphere and space. The Administration shall provide for the widest practicable and appropriate dissemination of information concerning its activities and the results thereof."

— NATIONAL AERONAUTICS AND SPACE ACT OF 1958

NASA SCIENTIFIC AND TECHNICAL PUBLICATIONS

TECHNICAL REPORTS: Scientific and technical information considered important, complete, and a lasting contribution to existing knowledge.

TECHNICAL NOTES: Information less broad in scope but nevertheless of importance as a contribution to existing knowledge.

TECHNICAL MEMORANDUMS: Information receiving limited distribution because of preliminary data, security classification, or other reasons.

CONTRACTOR REPORTS: Scientific and technical information generated under a NASA contract or grant and considered an important contribution to existing knowledge.

TECHNICAL TRANSLATIONS: Information published in a foreign language considered to merit NASA distribution in English.

SPECIAL PUBLICATIONS: Information derived from or of value to NASA activities. Publications include conference proceedings, monographs, data compilations, handbooks, sourcebooks, and special bibliographies.

TECHNOLOGY UTILIZATION PUBLICATIONS: Information on technology used by NASA that may be of particular interest in commercial and other non-aerospace applications. Publications include Tech Briefs, Technology Utilization Reports and Notes, and Technology Surveys.

Details on the availability of these publications may be obtained from:

SCIENTIFIC AND TECHNICAL INFORMATION DIVISION
NATIONAL AERONAUTICS AND SPACE ADMINISTRATION
Washington, D.C. 20546